MICROWAVE BACKGROUND ANISOTROPIES

ILLUSTRATION DE COUVERTURE : chacune des bandes (de deux degrés de largeur) évoque la distribution spatiale possible d'une des nombreuses sources d'émission contribuant aux fluctuations du ciel micro-onde. En allant du bas de la page de couverture vers le haut de la quatrième de couverture, on trouve successivement des fluctuations I) de température du corps noir cosmologique dans le cas d'un scénario de matière froide standard, II) du paramètre de Compton y qui détermine l'amplitude de l'effet Sunyaev-Zeldovich dans les amas de galaxies, III) des fluctuations de température induites via effet Doppler par la vitesse propre de ces même amas (toutes trois estimées par simulation numérique), IV) de l'émission des point sources, suivies (V) VI) ET VII)) des émissions synchrotron, de la poussière, et de freinage dans notre propre galaxie (extrapolées à partir des données d'Haslam à 408 MHz et IRAS à 100μm et pour finir, VIII) les modulations caractéristiques dues aux bruit en 1/f des détecteurs le long des trajectoires mesurées sur le ciel (CONCEPTION FRANÇOIS R. BOUCHET).

COVER ILLUSTRATION: each of the band (of 2° width) is meant to illustrate a possible spatial distribution of one of the many different processes contributing to the fluctuations of the microwave sky. Going upward from the bottom of the cover page to the top of the back page one successively finds I) simulated temperature fluctuations of the cosmic background in a Standard CDM scenario, II) variations of the Compton parameter y which governs the amplitude of the Sunyaev-Zeldovich effect in clusters, III) of the induced ΔT fluctuations by Doppler effect on clusters with a peculiar velocity (both estimated by numerical simulations), IV) the emission from point sources, then the synchrotron dust and free-free emissions (V) VI) ET VII)) of our own galaxy (as extrapolated from the Haslam 408 MHz and IRAS 100μm data), and finally VIII) the detector noise with characteristic stripes as imprinted by $1/f$ noise along scans (DESIGN : FRANÇOIS R. BOUCHET).

XVIth Moriond Astrophysics Meeting
MICROWAVE BACKGROUND ANISOTROPIES
Les Arcs, Savoie, France – March 16th-23rd 1996
Actes des XVIème Rencontres Astrophysiques de Moriond
ANISOTROPIES DU CIEL MICRO-ONDE
March 16th-23rd 1996

ISBN 2-86332-208-7

EDITIONS FRONTIERES
B.P. 33
91192 Gif-sur-Yvette Cedex - France

Printed in Singapore

MICROWAVE BACKGROUND ANISOTROPIES

PROCEEDINGS OF THE
XVITH MORIOND ASTROPHYSICS MEETING
LES ARCS, SAVOIE, FRANCE
MARCH 16TH-23RD 1996

EDITED BY

FRANÇOIS R. BOUCHET
Institut d'Astrophysique de Paris, CNRS

RICHARD GISPERT
Institut d'Astrophysique Spatiale, Orsay, CNRS

BRUNO GUIDERDONI
Institut d'Astrophysique de Paris, CNRS

AND

JEAN TRÂN THANH VÂN
Laboratoire de Physique Théorique des Hautes Energies, Orsay, CNRS

EDITIONS
FRONTIERES

COMITÉ SCIENTIFIQUE INTERNATIONAL
INTERNATIONAL ADVISORY COMMITTEE

J. Bergeron	ESO, Garching	Germany
J. Bleeker	RUU	Netherlands
D. Bond	CITA, Toronto	Canada
W.B. Burton	Leiden U.	Netherlands
C. Cesarsky	CEA, Saclay	France
L. Danese	SISSA, Trieste	Italy
G. Efstathiou	Oxford University	England
J. Ellis	CERN	Switzerland
B. Jones	NORDITA, Copenhagen	Denmark
R. Juszkiewicz	Copernicus Center, Varsaw	Poland
A. Lange	CalTech, Pasadena	USA
A. Lasenby	Cavendish Lab., Cambridge	England
D. Lemke	MPIA, Garching	Germany
E. Martinez	Santander University	Spain
J. Mather	GSFC	USA
R. Matsumoto	Nagoya U.	Japan
H.U. Nordgaard-Nielsen	DSRI, Copenhagen	Denmark
L. Page	Princeton U.	USA
P. Richards	U. of California, Berkeley	USA
M. Rowan-Robinson	Imperial College, London	England
J.-L. Sanz	IFC, Santander	Spain
K. Sato	Tokyo U.	Japan
G. Setti	U. of Bologna	Italy
J. Silk	U. of California, Berkeley	USA
M. Spiro	CEA, Saclay	France
G. Smoot	U. of California, Berkeley	USA
R. Sunyaev	IKI, Moscow	Russia
I.A. Strukov	IKI, Moscow	Russia
N. Vittorio	U. of Rome	Italy
S. Volonte	ESA, Paris	France
S.D.M. White	MPIA, Garching	Germany

COMITÉ D'ORGANISATION
ORGANIZING COMMITTEE

M. Bersanelli		U. of Bologna	Italy
F.R. Bouchet	(Chairperson)	IAP, Paris	France
M. Giard		CESR, Toulouse	France
R. Gispert		IAS, Orsay	France
B. Guiderdoni		IAP, Paris	France
J.-M. Lamarre		IAS, Orsay	France
N. Mandolesi		Bologna U.	Italy
J.-L. Puget		IAS, Orsay	France
J. Tauber		ESTEC, Noordwijk	Netherlands

PARRAINAGE – SPONSORS

Agenzia Spaziale Italiana (ASI), B.P.D., Commissariat à l'Energie Atomique (CEA), Centre National d'Etudes Spatiales (CNES), Centre National de la Recherche Scientifique-Formation Permanente (CNRS), Human Capital and Mobility program of the European Commission (HCM-EC), European Space Agency (ESA), Institut d'Astrophysique de Paris (IAP), Laben, le programme ACCES du Ministère de l'Education Nationale, de l'Enseignement Supérieur, de la Recherche, et de l'Insertion Professionnelle (MENESRIP)

AVANT-PROPOS

Ce livre rassemble les actes des XVIèmes Rencontres Astrophysiques de Moriond qui ont eu lieu dans la station de ski des Arcs durant la semaine du 16 au 23 mars 1996. Cette Euroconference fut consacrée à tous les aspects des *anisotropies du ciel micro-onde* d'intérêt pour les mesures à venir des fluctuations du rayonnement cosmique de fond, tout particulièrement celles faites dans l'espace.

De substantiels progrès récents de la technologie des détecteurs micro-onde et sub-millimétrique rendent possibles des missions spatiales de cartographie de tout le ciel qui augmenteraient considérablement notre connaissance du Fond Cosmique Micro-onde (FCM). Ces instruments modernes permettent un gain en sensibilité d'au moins un facteur 10 par rapport à celle du satellite COBE ($\Delta T/T$ approchant 10^{-6} par élément de résolution) et un gain simultané considérable en résolution angulaire (des 7 degrés de l'expérience DMR à quelques minutes d'arc).

Des missions spatiales conçues autour de ces possibilités étaient, au moment des Rencontres, en phase ultime de préparation, à la fois en Europe et aux Etats-Unis, et des décisions critiques sur leur financement étaient attendues dans les mois à venir. Il était donc opportun d'organiser une conférence dédiée à la confrontation des théories cosmologiques et des observations, et à l'identification du type d'observation requis pour finalement lever le voile sur des inconnues fondamentales telles que la densité et la géométrie de l'Univers, la nature de la matière noire, et l'origine des structures cosmologiques.

La théorie et le statut observationnel actuel des anisotropies du FCM, la science à faire avec une mission FCM de seconde génération, et les caractéristiques techniques requises pour obtenir des résultats décisifs furent donc le thème central des Rencontres. A l'évidence, l'impact scientifique d'une telle mission ne serait cependant pas restreint aux questions liées aux fluctuations "primaires" issues de l'Univers primordial; elle permettrait aussi de mieux cerner nombre d'autres questions astrophysiques liées à l'émission et à l'absorption des sources d'avant-plan qui contribuent également aux fluctuations micro-onde. De fait, près de la moitié des Rencontres fut consacrée aux sources connues de fluctuations "secondaires", diffusions Compton dans le gaz des amas de galaxies (l'effet Sunyaev-Zeldovich, en liaison avec l'émission en X), fluctuations dues aux sources résolues ou non, anisotropies d'origine galactique liées aux émissions synchrotron, bremsstrahlung, et de la poussière, sans oublier les techniques pour séparer ces composantes.

J'ai le plaisir de remercier les institutions qui, par leur parrainage, ont permis la tenue de ces Rencontres: le programme CHM de la commission Européenne et la formation permanente du CNRS ont permis la participation d'un grand nombre de jeunes chercheurs, le programme ACCES a rendu possible la présence de scientifiques de l'ex-URSS, les support de l'ESA, du CNES, du CEA, et de l'ASI ont contribué à la venue d'orateurs-clé, tandis que BPD et Laben nous ont aimablement fourni une aide matérielle utile. Je désire aussi exprimer ma gratitude à tous les membres du comité scientifique international et du comité d'organisation, aux présidents des séances scientifiques et aux orateurs, ainsi qu'a Jean Trân Thanh Vân et à son équipe d'organisation. Enfin mes remerciements les plus chaleureux vont à la secrétaire des Rencontres, Françoise Warin, dont la bonne humeur et l'inébranlable patience ont permis d'aplanir avec le sourire nombre de difficultés.

Je crois que ces Rencontres furent un succès. Non seulement parce qu'elles ont réuni la plus grande partie des chercheurs actifs de ce domaine, mais aussi grâce à l'esprit constructif de discussions parfois pied-à-pied. J'en suis revenu avec l'impression d'un large accord sur les principales questions scientifiques, les difficultés potentielles, et sur la manière de s'y attaquer. Au cours des mois qui suivirent, notre communauté eu la joie d'apprendre la sélection de deux missions FCM, une par la NASA et l'autre par l'ESA. La mission de la NASA, MAP, utilisera des HEMTs non-refroidis. Elle devrait voler à l'orée du siècle prochain et améliorer considérablement notre connaissance des propriétés du ciel micro–onde à l'échelle du degré, sujet de recherches intenses et fructueuses qui sont en cours à la fois du sol et de ballons. La mission de l'ESA, COBRAS/SAMBA, se propose d'effectuer, à partir de 2004, la cartographie définitive de toutes les échelles d'intérêt cosmologique en incluant de plus des bolomètres refroidis à 0.1K.

Avec deux missions spatiales d'imagerie du FCM coiffant la fournée courante d'expériences terrestres, la prochaine décade promet d'être extrêmement excitante, non seulement pour les cosmologistes, mais pour tous les physiciens, en particulier ceux des particules qui cherchent des réponses ne pouvant être obtenus qu'à des énergies si élevées que l'Univers primordial lui-même devient l'ultime et unique laboratoire possible.

François R. Bouchet

FOREWORD

This book contains the proceedings of the XVIth Moriond Astrophysics Meeting held in the ski resort of Les Arcs in France, during the week of March, the 16th–23rd, 1996. This Euroconference was devoted to all aspects of the *microwave background anisotropies* relevant for future measurements of cosmic microwave anisotropies, in particular from space.

Substantial recent progress in microwave and sub-millimeter detector technology now makes possible new generation all-sky survey missions from space which would greatly increase our knowledge of the Cosmic Microwave Background (CMB). Modern instruments allow more than an order of magnitude gain in sensitivity over the highly successful COBE satellite (i.e. $\Delta T/T$ approaching 10^{-6} per resolution element) as well as a very large simultaneous gain in angular resolution (from DMR's 7 degrees down to a few arc minutes).

Space missions based on these possibilities were at the time of the meeting in the final stages of preparation both in Europe and in the US, and critical decisions on funding were expected in the following months. It was thus timely to hold a conference dedicated to exploring the confrontation between cosmological theories and observations, and to understanding the critical observations needed to decide fundamental issues such as the density and geometry of the Universe, the nature of the unseen dark matter, and the origin of structure.

The focus of the meeting was thus on the theory and current observational status of CMB anisotropies, the science to be done with a second generation CMB mission and the technical requirements necessary to obtain decisive results. Of course, such a mission would address not only the primary (primordial) fluctuations which come from the early universe, but also a host of other astrophysical issues related to foreground emission and absorption. As a matter of fact, nearly half of the meeting was devoted to known sources of secondary fluctuations, to Compton scaterrings in clusters (the Sunyaev-Zeldovich effect and its link to X-ray emission), to the fluctuations from resolved and unresolved extragalactic sources, to the galactic ones due to dust, synchrotron and bremsstrahlung emissions, and to techniques for separating these components.

I would like to thank the institutions and sponsors that made this meeting possible: the EC-HCM Program and the "formation permanente" of CNRS enabled the participation of many young researchers, the ACCES program permitted many scientists from the former USSR to attend, the support from ESA, CNES, CEA, and ASI was crucial to help inviting key-speakers, while BPD and Laben kindly provided useful material help. I would also like to express my gratitude to all members of the International Advisory Committee and of the Organizing Committee, the chairpersons of the scientific sessions and all speakers, as well as Jean Trân Thanh Vân and his staff. Last but not least, my warmest thanks go to the meeting secretary, Françoise Warin, for her unshakable patience and good-heartedness.

I felt that the meeting was a great success. This was not only because it brought together most of the active workers in the field but also because of the positive spirit of the (sometimes heated) discussions. I went away with the feeling of a broad agreement on the main scientific issues, the potential difficulties, and on the best way to adress them. In the few months following the meeting, the CMB community was happy to learn that two CMB missions had been selected, both by NASA and ESA. The NASA mission based on uncooled HEMT's, MAP, should fly right after the turn of the century and considerably improve our knowledge of the properties of the microwave sky around the degree scale, a subject of intense and productive research nowadays both from the ground and from balloons. The ESA mission, COBRAS/SAMBA, is planned for launch in 2004; it aims at a definitive imaging of the CMB on all cosmologically relevant angular scales by also including bolometers cooled at 0.1K.

With two accepted CMB mapping missions topping the current breed of ground experiments, the coming decade should be quite an exciting one, not only for cosmologists, but also for physicists at large, and in particular particle physicists seeking answers obtainable only at very high energies when the Universe itself provides the ultimate and only laboratory.

François R. Bouchet

CONTENTS

THE CURRENT EXPERIMENTS AND PLANNED FOLLOW-UP

COMBINING CURRENT EXPERIMENTS TO CONSTRAIN THEORIES

PART III.– CMB THEORY & IMPACT OF FUTURE EXPERIMENTS

Theoretical Status for the Primary CMB Anisotropies

Anisotropies from Defects

Scientific Impact of Future Experiments

PART I

SETTING THE STAGE

THE LEGACY OF COBE

George F. Smoot
Lawrence Berkeley National Laboratory & Department of Physics,
University of California Berkeley CA 94720 USA
E-mail: SMOOT@COSMOS.LBL.GOV

Abstract

The Cosmic Background Explorer (*COBE*) was NASA's first satellite dedicated to comology and is a milestone for that and for the legacy of information that it has provided on the early Universe. Much of its results are from observations of the Cosmic Microwave Background (CMB). The CMB is a pillar of the Big Bang model and encodes information about primoridal perturbations and the geometry of the universe as well as information on critical cosmological parameters such as Ω_0, Ω_B, Ω_Λ, and H_0. *COBE's* legacy of the precise measurement of the CMB spectrum and the discovery and early mapping of the CMB anisotropy power spectrum provides a position to carry out a program to test our cosmological theories and understand the early Universe precisely.

1 Introduction

My task is to review the legacy provided by *COBE*. This review concentrates on the cosmic background radiation. The observed cosmic microwave background (CMB) radiation provides strong evidence for the hot big bang model of cosmology. Primordial nucleosynthesis calculations require a cosmic background radiation (CBR) with a temperature $kT \sim 1$ MeV at a redshift of $z \sim 10^9$. Gamow, Alpher, & Herman [2] realized that this CBR was required and predicted its evolution to a faint residual relic radiation wiht a current temperature of a few degrees.

The CMB was serendipitously discovered by Penzias & Wilson [33] in 1964 and its existence immediately interpreted by Dicke *et al.*[10] as the relic radiation manifestation of the hypothesized primordial CBR. The observed CMB spectrum is well characterized by a 2.73 ± 0.01 K blackbody spectrum. The hot big bang model predicts that the CBR should have a fairly precise thermal spectrum. The thermal coupling between the matter and radiation is extremely good at the time of primordial nucleosynthesis. A non-interacting Planckian spectrum at temperature T_i at redshift z_i transforms with the universial expansion to another Planckian distribution

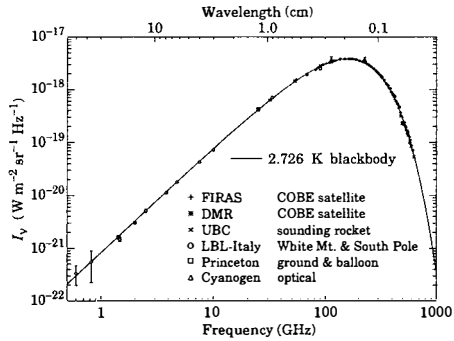

Figure 1: Precise measurements of the CMB spectrum. The line represents a 2.73 K blackbody, which describes the spectrum very well, especially around the peak of intensity. The spectrum is less well constrained at frequencies of 3 GHz and below.

at redshift z_r with temperature $T_r/(1+z_r) = T_i/(1+z_i)$. Hence thermal equilibrium, once established (e.g. at the nucleosynthesis epoch), is preserved by the expansion, in spite of the fact that photons decoupled from matter at early times. Because there are about 10^9 photons per nucleon, the transition from the ionized primordial plasma to neutral atoms at $z \sim 1000$ does not significantly alter the CBR spectrum [32]. The large ratio of photons to nucleons means that it takes a very significant release of energy or photons by the matter to have any appreciable effect on the CBR.

The *COBE* FIRAS observations [29, 13]. are the major step in the precision measurement of the CMB spectrum. The current observations of the CMB spectrum are shown in Figure 1.

The remarkable precision with which the CMB spectrum is fitted by a Planckian distribution provides limits on possible energy releases in the early Universe, at roughly the fractional level of 10^{-4} of the CBR energy, for redshifts $\lesssim 10^7$ (corresponding to epochs $\gtrsim 1$ year). These observations provide significant constraints on possible cosmologies. Combined with the observed spectrum of the first order dipole anisotropy they also provide us with the knowledge and ability to separate CMB anisotropies from the various foregrounds.

2 *COBE* DMR Four-Year Observations

2.1 Anisotropy Observations with the *COBE* DMR

The Differential Microwave Radiometers (DMR) experiment discovered cosmic microwave background (CMB) anisotropies from analysis of its first year of data [38], [8], [44], [22]. The CMB temperature fluctuations were measured at an angular resolution of 7° at frequencies of 31.5, 53, and 90 GHz. The *COBE* results were confirmed by the positive cross-correlation between the *COBE* data and data from balloon-borne observations at a shorter wavelength [14] and later by comparison of the *COBE* data and data from the ground-based Tenerife experiment [27] at longer wavelengths. The positive correlation at both longer and shorter wavelengths provides confidence in the results. The results from analysis of two years of DMR data [6] reconfirmed the results from the first year data. This talk and proceedings summarize the results and cosmological implications obtained from the full *COBE* DMR 4-year data and provide references

to further detailed reports about the data and its analysis.

A major finding of the initial *COBE* DMR discovery [38] was that the CMB was anisotropic on all observed angular scales. A key question is what these anisotropies represent. In the early 1970's the observed large scale structure and scaling arguments led to the prediction [31, 16, 45] that the primordial gravitational potential perturbations must have an equal rms amplitude on all scales. This corresponds to a matter perturbation power-law spectrum, $P(k) \propto k^n$, where k is the comoving wavenumber, with $n = 1$. At the time there were no known mechanisms for producing such a scale-invariant power spectrum of fluctuations. It is now known that topological defects naturally produce scale-invariant fluctuations. In 1982 it was found that inflationary models predicted nearly scale-invariant perturbations as a result of quantum mechanical fluctuations at very early times. Even with the proliferation of inflationary models, it is found that essentially all reasonable inflationary models predict $n \approx 1$. The translation from a scale-invariant spectrum of perturbations to the CMB temperature anisotropies depends upon angular scale and the contents of the universe. On large angular scales the results of most models are fairly similar. Including the effects of a standard cold dark matter model, *COBE* DMR should find $n_{eff} \approx 1.1$ for a Peebles-Harrison-Zeldovich $n = 1$ universe. This is consistent with the power spectrum measured by the *COBE* DMR data. The observed power spectrum of fluctuations amplitude is also consistent with models of large scale structure formation based upon primordial seeds produced by quantum fluctuations or topological defects in the early universe.

Most cosmological models do not predict the exact CMB temperature pattern that would be observed in our sky, but rather predict a statistical distribution of anisotropies. In the context of such models, the CMB temperature observed in our sky is only a single realization from a statistical distribution. Theoretical models most often predict a power spectrum in spherical harmonic amplitudes; as the physics of the models leads to primordial fluctuations that are Gaussian random fields, the power spectrum is sufficient to characterize the results. Observations of the sky are usually expressed as a spherical harmonic temperature expansion $T(\theta, \phi) = \sum_{\ell m} a_{\ell m} Y_{\ell m}(\theta, \phi)$. If the original perturbations are Gaussian random fields, the $a_{\ell m}$ are Gaussianly distributed, and the power at each ℓ is $(2\ell + 1)C_\ell/(4\pi)$, where $C_\ell \equiv \langle |a_{\ell m}|^2 \rangle$, is sufficient to characterize the results. For an idealized full-sky observation, the variance of each measured C_ℓ is $[2/(2\ell+1)]C_\ell^2$. This sampling variance (known as cosmic variance) comes about because each C_ℓ is chi-squared distributed with $(2\ell + 1)$ degrees of freedom for our observable volume of the Universe [42]. Thus, in addition to experimental uncertainties, we account for the ***cosmic sample variance*** uncertainties due to our observation of a single realization in our analyses of the DMR maps. Cosmic variance exists independently of the quality of the experiment. The power spectrum from the 4-year DMR map is cosmic variance limited for $\ell \lesssim 20$.

This talk summarizes the key and most recent results from COBE. Details can be found in the original references and in the most recent FIRAS paper [13] and in a set of DMR 4-year analysis papers [3], [4], [5], [15], [18],[19], [24], [25], [26], [43].

2.2 OBSERVATIONS

The DMR consists of 6 differential microwave radiometers: 2 nearly independent channels, labeled A and B, at frequencies 31.5, 53, and 90 GHz (wavelength 9.5, 5.7, and 3.3 mm). Each radiometer measures the difference in power between two 7° fields of view separated by 60°, 30° to either side of the spacecraft spin axis [39]. *COBE* was launched from Vandenberg Air Force Base on 18 November 1989 into a 900 km, 99° inclination circular orbit, which precesses to follow the terminator (light dark line on the Earth) as the Earth orbits the Sun. Attitude

control keeps the spacecraft pointed away from the Earth and nearly perpendicular to the Sun with a slight backward tilt so that solar radiation never directly illuminates the aperture plane. The combined motions of the spacecraft spin (75 s period), orbit (103 m period), and orbital precession ($\sim$ 1° per day) allow each sky position to be compared to all others through a highly redundant set of temperature difference measurements spaced 60° apart. The on-board processor box-car integrates the differential signal from each channel for 0.5 s, and records the digitized differences for daily playback to a ground station.

Ground data analysis consists of calibration, extensive systematic error analyses, and conversion of time-ordered-data to sky maps [24]. The DMR time-ordered-data include systematic effects such as emission from the Earth and Moon, the instrument's response to thermal changes, and the instrument's response to the Earth's magnetic field. The largest detected effects do not contribute significantly to the DMR maps: they are either on time scales long compared to the spacecraft spin sampling (e.g. thermal gain drifts) or have time dependence inconsistent with emission fixed on the celestial sphere (e.g. magnetic effects). Detected and potential systematic effects were quantitatively analyzed in detail [24]. Data with the worst systematic contamination (lunar emission, terrestrial emission, and thermal gain changes) were not used in the map making process and constitute less than 10% of the data in the 53 and 90 GHz channels. The remaining data were corrected using models of each effect. The data editing and correction parameters were conservatively chosen so that systematic artifacts, after correction, are less than 6 μK (95% confidence upper limit) in the final DMR map in the worst channel. This is significantly less than the levels of the noise and celestial signals.

We subtract a dipole T_d = 3.356 mK anisotropy signal (thermodynamic temperature in Galactic coordinates Cartesian components [X,Y,Z] = [-0.2173, -2.2451, +2.4853] mK) from the time-ordered differential data prior to forming the 4-year sky maps to reduce spatial gradients within a single pixel. A small residual dipole remains in the maps from a combination of CMB and Galactic emission. The mean signal-to-noise ratios in the 10° smoothed maps are approximately 0.5, 1.5, and 1.0 for 31, 53, and 90 GHz, respectively. For a multi-frequency co-added map the signal-to-noise ratio is $\sim$ 2. This signal-to-noise level is adequate to portray an accurate overall visual impression of the anisotropy. Visual comparison of the full sky maps at each frequency, after averaging the A and B channels, removing the CMB dipole, and smoothing to 10° effective resolution show coincident features. Well off the Galactic plane these are clearly true CMB anisotropy features. Simulated data in combination with the noise appropriate to 1-, 2-, and 4-years of DMR 53 GHz observations show the convergence of the DMR maps with the input simulated data. Increasing years of data result in the emergence of the input large scale features. We can be confident that the large scale features in the 4-year DMR maps are real features rather than confusing noise.

Given the sensitivity of the 4-year DMR maps we have extended the cut made in our previous analyses to exclude additional Galactic emission. We use the *COBE* DIRBE 140 μm map as a guide to cut additional Galactic emission features. The full sky DMR maps contain 6144 pixels. An optimum Galactic cut maximizes the number of remaining pixels while minimizing the Galactic contamination. This cut leaves 3881 pixels (in Galactic pixelization) while eliminating the strongest $|b| > 20°$ Galactic emission. Moderate changes to this cut will cause derived CMB parameters to change somewhat, but this is consistent with the data sampling differences of real CMB anisotropy features and not necessarily Galactic contamination. Likewise, derived CMB parameters also vary by the expected amount when the maps are made in ecliptic rather than Galactic coordinates since about 1/2 of the noise is re-binned.

Kogut et al. [25] examine the Galactic contamination of the high Galactic latitude regions of the DMR maps which remain after the Galactic emission cut (described above). No significant cross-correlation is found between the DMR maps and either the 408 MHz synchrotron map

or the synchrotron map derived from a magnetic field model [8]. This places an upper limit $T_{\rm synch} < 11$ μK (95% confidence) on synchrotron emission at 31 GHz.

A significant correlation is found between the DMR maps and the dust-dominated DIRBE 140 μm map, with frequency dependence consistent with a superposition of dust and free-free emission. This corresponds to a 7° rms free-free emission component of 7.1 ± 1.7 μK at 53 GHz and a dust component of 2.7 ± 1.3 μK at 53 GHz. Since this emission is uncorrelated with CMB anisotropies it constitutes < 10% of the CMB power. The amplitude of the correlated free-free component at 53 GHz agrees with a noisier estimate of free-free emission derived from a linear combination of DMR data which includes *all* emission with free-free spectral dependence. The combined dust and free-free emission contribute 10 ± 4 μK *rms* at both 53 and 90 GHz, well below the 30 μK cosmic signal. These Galactic signal analyses are consistent with the fact that the fitted cosmological parameters are nearly unaffected by removal of modeled Galactic signals [15], [18] with the notable exception of the quadrupole, which has significant Galactic contamination [25]. A search by Banday et al. [3] finds no evidence for significant extragalactic contamination of the DMR maps.

3 Interpretation

Monopole $\ell = 0$: Despite the fact that the DMR is a differential instrument, the known motion of the *COBE* spacecraft about the Earth and the motion of the Earth about the Solar System barycenter provides a means to determine the CMB monopole temperature from the DMR data. The CMB at millimeter wavelengths is well described by a blackbody spectrum [29, 13]. The Doppler effect from the combined spacecraft and Earth orbital motions creates a dipole signal $T(\theta) = T_0[1 + 3\cos(\theta) + O(\beta^2)]$, where $\beta = v/c$ and θ is the angle relative to the time-dependent velocity vector. The satellite and Earth orbital motions are well known and change in a regular fashion. allowing their Doppler signal to be separated from fixed celestial signals. We fit the time-ordered data to the Doppler dipole and recover a value for the CMB monopole temperature, $T_0 = 2.725 \pm 0.020$ K [24].

Dipole $\ell = 1$: The CMB anisotropy is dominated by a dipole term usually attributed to the motion of the Solar System with respect to the CMB rest frame. A precise determination of the dipole must account for Galactic emission and the aliasing of power from higher multipole orders once pixels near the Galactic plane are discarded. One can account for Galactic emission by using a linear combination of the DMR maps or by cross-correlating the DMR maps with template sky maps dominated by Galactic emission [25]. The high-latitude portion of the sky is fitted for a dipole with a CMB frequency spectrum using a pixel-based likelihood analysis [18]. Accounting for the smoothing by the DMR beam and map pixelization, the CMB dipole has amplitude 3.353 ± 0.024 mK toward Galactic coordinates $(l, b) = (264.^\circ26 \pm 0.^\circ33, 48.^\circ22 \pm 0.^\circ13)$, or equatorial coordinates $(\alpha.\delta) = (11^{\rm h}12^{\rm m}2 \pm 0^{\rm m}8, -7^\circ06 \pm 0.^\circ16)$ epoch J2000.

A second analysis approach utilizes a phenomenological estimate of the Galactic foreground by examining the dipole fitted parameters as a function of cuts in Galactic latitude. It was found that the largest source of error in the dipole direction was reduced by using lower Galactic latitude cuts. Using the four year data set from all six channels of the COBE Differential Microwave Radiometers (DMR), the best-fit dipole amplitude $3.359 \pm 0.001 \pm 0.023$ mK in the direction $(\ell, b) = (264.^\circ.33 \pm 0.^\circ.04 \pm 0.^\circ.17, +48.^\circ.05 \pm 0.^\circ.02 \pm 0.^\circ.07)$ where the first uncertainties are statistical and the second are estimates of the combined systematics [28].

This dipole measurement is consistent with previous DMR and FIRAS results.

Quadrupole $\ell = 2$: On the largest angular scales (e.g., quadrupole), Galactic emission is comparable in amplitude to the anisotropy in the CMB. The quadrupole amplitude is found

by a likelihood analysis which simultaneously fits the high-latitude portion of the DMR maps for Galactic emission traced by synchrotron- and dust-dominated surveys and a quadrupole anisotropy with a thermodynamic frequency spectrum [25, 18]. After correcting for the positive bias from instrument noise and aliasing, the CMB quadrupole amplitude observed at high latitude is $Q_{rms} = 10.7 \pm 3.6 \pm 7.1$ μK, where the quoted errors reflect the 68% confidence uncertainties from random statistical errors and Galactic modeling errors, respectively. The observed quadrupole amplitude, Q_{rms}, has a lower value than the quadrupole expected from a fit to the entire power spectrum, Q_{rms-PS}, but whether this is a chance result of cosmic variance or reflects the cosmology of the universe cannot be determined from *COBE* data. The 68% confidence interval for the quadrupole amplitude, 6 μK $\leq Q_{rms} \leq$ 17 μK, is consistent with the quadrupole normalization of the full power spectrum power-law fit (discussed below): $Q_{rms-PS} = 15.3^{+3.8}_{-2.8}$ μK.

Power spectrum $\ell \geq 2$: The simplest probe of the angular power spectrum of the anisotropy is its Legendre transform, the 2-point correlation function. The 2-point correlation function of the 4-year maps is analyzed by Hinshaw et al. [19], where it is shown that the 2-point data are consistent from channel to channel and frequency to frequency. The data are robust with respect to the angular power spectrum. A Monte Carlo-based Gaussian likelihood analysis determines the most-likely quadrupole normalization for a scale-invariant ($n = 1$) power-law spectrum. The results are summarized in Table 1 which also includes the results of 3 additional, independent power spectrum analyses, discussed below. The normalization inferred from the 2-point function is now in better agreement with other determinations than was the case with the 2-year data. The change is due to data selection: with the 2-year data, we only analyzed the 53 $\times$ 90 GHz cross-correlation function; with the 4-year data we have analyzed many more data combinations, including the auto-correlation of a co-added, multi-frequency map. This latter combination is more comparable to the data analyzed by other methods, and the 2-point analysis yields consistent results in that case. The combined 31, 53 and 90 GHz CMB rms is 29$\pm$1 μK in the 10° smoothed map [4], consistent with the level determined by the 2-point results.

It is also possible to analyze the power spectrum directly in terms of spherical harmonics. However, there is considerable subtlety in this because the removal of the Galactic plane renders the harmonics non-orthonormal, producing strong correlations among the fitted amplitudes. Wright et al. [43] has solved for an angular power spectrum by modifying and applying the technique described by Peebles [30] and Hauser & Peebles [17] for data on the cut sphere. They compute a Gaussian likelihood on these data and calibrate their results with Monte Carlo simulations. Górski et al. [15] explicitly construct orthonormal functions on the cut sphere and decompose the anisotropy data with respect to these modes. They form and evaluate an exact Gaussian likelihood directly in terms of this mode decomposition. The results of these analyses are summarized in Table 1. Further details, including results from other data combinations are given in the respective papers.

Hinshaw et al. [18] evaluate a Gaussian likelihood directly in terms of a full pixel-pixel covariance matrix, a technique applied to the 2-year data by Tegmark & Bunn [40]. The results of the power-law spectrum fits are summarized in Table 1. Hinshaw et al. [18] also analyze the quadrupole anisotropy separately from the higher-order modes, to complement the analysis of Kogut et al. [25]. They compute a likelihood for the quadrupole mode C_2, nearly independent of higher-order power, and show that it peaks between 6 and 10 μK, depending on Galactic model, but that its distribution is so wide that it is easily consistent with $15.3^{+3.8}_{-2.8}$ μK, the value derived using the full power spectrum.

An important lesson from fitting with different cuts and configurations and from our Monte Carlo simulations is that the best fitted parameters depend both upon the random statistics of

CMB fluctuations and on the choice of cuts and fitting parameters. Table 1 in Gorski *et al.*[15] is very indicative of the range of results obtainable using a robust and stable approach.

Tests for Gaussian Statistics: It is important to determine whether the primordial fluctuations are Gaussian. The probability distribution of temperature residuals should be close to Gaussian if the sky variance is Gaussian and the receiver noise is Gaussian. The receiver noise varies somewhat from pixel to pixel because the observation times are not all the same, but when this is taken into account the data appear Gaussian [37]. There is no evidence for an excess of large deviations, as would be expected if there were an unknown population of point sources. A search for point sources in the 2-year maps was found none [23]. Given the large beam of the instrument and the variance of both cosmic signals and receiver noise, it is still possible for interesting signals to be hidden in the data.

Kogut et al. [26] compare the 4-year DMR maps to Monte Carlo simulations of Gaussian power-law CMB anisotropy. The 3-point correlation function, the 2-point correlation of temperature extrema, and the topological genus are all in excellent agreement with the hypothesis that the CMB anisotropy on angular scales of 7° or larger represents a random-phase Gaussian field. A likelihood comparison of the DMR maps against non-Gaussian χ^2_N toy models tests the alternate hypothesis that the CMB is a random realization of a field whose spherical harmonic coefficients $a_{\ell m}$ are drawn from a χ^2 distribution with N degrees of freedom. Not only do Gaussian power-law models provide an adequate description of the large-scale CMB anisotropy, but non-Gaussian models with $1<N<60$ are five times less likely to describe the true statistical distribution than the exact Gaussian model.

4 Summary of 4-year *COBE* DMR CMB Measurements

(1) The full 4-year set of *COBE* DMR observations is analyzed and full sky maps are presented. The typical signal-to-noise ratio in a 10° smoothed map is ~ 2 in the frequency-averaged map, enough to provide a visual impression of the anisotropy.

(2) We derive a CMB monopole temperature from DMR (despite its being a differential instrument) of $T_0 = 2.725 \pm 0.020$ K [24]. This is in excellent agreement with the *COBE* FIRAS precision measurement of the spectrum of the CMB, $T_0 = 2.728 \pm 0.002$ K [13].

(3) The CMB dipole from DMR has amplitude 3.353 ± 0.024 mK toward Galactic coordinates $(l, b) = (264.^\circ26 \pm 0.^\circ33, 48.^\circ22 \pm 0.^\circ13)$, or equatorial coordinates $(\alpha, \delta) = (11^{\rm h}12^{\rm m}2 \pm 0^{\rm m}8, -7.^\circ06 \pm 0.^\circ16)$ epoch J2000. This is consistent with the dipole amplitude and direction derived by *COBE* FIRAS [13].

(4) The 95% confidence interval for the observed $\ell = 2$ quadrupole amplitude is $4\ \mu\text{K} \leq Q_{rms} \leq 28\ \mu\text{K}$. This is consistent with the value predicted by a power-law fit to the power spectrum: $Q_{rms-PS} = 15.3^{+3.8}_{-2.8}\ \mu$K [25]; [18].

(5) The power spectrum of large angular scale CMB measurements are consistent with an $n = 1$ power-law [15], [18], [13]. If the effects of a standard cold dark matter model are included, *COBE* DMR should find $n_{eff} \approx 1.1$ for a $n = 1$ universe. With full use of the multi-frequency 4-year DMR data, including our estimate of the effects of Galactic emission, we find a power-law spectral index of $n = 1.2 \pm 0.3$ and a quadrupole normalization $Q_{rms-PS} = 15.3^{+3.8}_{-2.8}\ \mu$K. For $n = 1$ the best-fit normalization is $Q_{rms-PS}|_{n=1} = 18 \pm 1.6\ \mu$K. Differences in the derived values of Q and n between various analyses of DMR data are much more dependent on the detailed data selection effects than on the analysis technique.

(6) The DMR anisotropy data are consistent with Gaussian statistics. Statistical tests prefer Gaussian over other toy statistical models by a factor of ~ 5 [26].

Technique	n [a]	Q_{rms-PS} [b] (μK)	$Q_{rms-PS\|n=1}$ [c] (μK)
No Galaxy Correction [d]			
2-point function [19]	—	—	$17.5^{+1.4}_{-1.4}$
Orthog. functions [15]	$1.21^{+0.24}_{-0.28}$	$15.2^{+3.7}_{-2.6}$	$17.7^{+1.3}_{-1.2}$
Pixel temps [18]	$1.23^{+0.26}_{-0.27}$	$15.2^{+3.6}_{-2.8}$	$17.8^{+1.3}_{-1.3}$
Hauser-Peebles [43]	—	—	—
Internal Combination Galaxy Correction [j]			
2-point function [19]	—	—	$16.7^{+2.0}_{-2.0}$
Orthog. functions [15]	$1.11^{+0.38}_{-0.42}$	$16.3^{+5.2}_{-3.7}$	$17.4^{+1.8}_{-1.7}$
Pixel temps [18]	$1.00^{+0.40}_{-0.43}$	$17.2^{+5.6}_{-4.0}$	$17.2^{+1.9}_{-1.7}$
Hauser-Peebles [43]	$1.62^{+0.44}_{-0.50}$	—	$19.6^{+2.5}_{-2.5}$

[a] Mode & 68% confidence range of the projection of the 2-d likelihood, $L(Q,n)$, on n
[b] Mode & 68% confidence range of the projection of the 2-d likelihood, $L(Q,n)$, on Q
[c] Mode & 68% confidence range of the slice of the 2-d likelihood, $L(Q,n)$, at $n=1$
[d] Formed from the weighted average of all 6 channels
[i] weighted average of 6 channels with the Galactic maps subtracted [25]
[j] from a linear combination of 6 channel maps canceling free-free emission [25]

Table 1: Summary of DMR 4-Year Power Spectrum Fitting Results.

5 Conclusions

The COBE-discovered [38] higher-order ($\ell \geq 2$) anisotropy is interpreted as being the result of perturbations in the energy density of the early Universe, manifesting themselves at the epoch of the CMB's last scattering. In the standard scenario the last scattering takes place at a redshift of approximately 1100, at which epoch the large number of photons was no longer able to keep the hydrogen sufficiently ionized. The optical thickness of the cosmic photosphere is roughly $\Delta z \sim 100$ or about 5 arcminutes, so that features smaller than this size are damped.

On the order of ten experiments have now observed CMB anisotropies. Anisotropies are observed on angular scales larger than this damping scale (see Figure 3) and are consistent with those expected from an initially scale-invariant power spectrum of potential and thus metric fluctuations. It is believed that the large scale structure in the Universe developed through the process of gravitational instability where small primordial perturbations in energy density were amplified by gravity over the course of time. The initial spectrum of density perturbations can evolve significantly in the epoch $z > 1100$ for causally connected regions (angles $\lesssim 1^\circ\ \Omega_{tot}^{1/2}$). The primary mode of evolution is through adiabatic (acoustic) oscillations, leading to a series of peaks that encode information about the perturbations and geometry of the universe, as well as information on Ω_0, Ω_B, Ω_Λ (cosmological constant), and H_0 [35]. The location of the first acoustic peak is predicted to be at $\ell \sim 220\ \Omega_{tot}^{-1/2}$ or $\theta \sim 1^\circ\ \Omega_{tot}^{1/2}$ and its amplitude increases with increasing Ω_B.

Figure 4 shows the theoretically predicted power spectrum for a sample of models, plotted as $\ell(\ell+1)C_\ell$ versus ℓ which is the power per logarithmic interval in ℓ or, equivalently, the two-dimensional power spectrum. If the initial power spectrum of perturbations is the result of quantum mechanical fluctuations produced and amplified during inflation, then the anisotropy spectrum and the fractional contribution from density (scalar) and gravity wave (tensor) perturbations are coupled. If the energy scale of inflation at the appropriate epoch is at the level

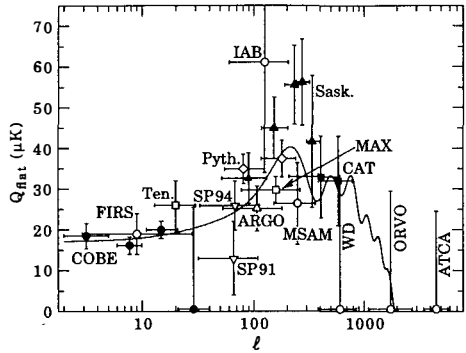

Figure 2: Current status of CMB anisotropy observations, adapted from Scott, Silk, and White (1995). Plotted are the quadrupole amplitudes for a flat (unprocessed scale-invariant spectrum of primordial perturbations, i.e., a horizontal line) anisotropy spectrum that would give the observed results for the experiment. The vertical error bars represent estimates of 68% CL, while the upper limits are at 95% CL. Horizontal bars indicate the range of ℓ values sampled. The curve indicates the expected spectrum for a standard CDM model ($\Omega_0 = 1$, $\Omega_B = 0.05$, $h = 0.5$), although true comparison with models should involve convolution of this curve with each experimental filter function.

of $\simeq 10^{16}$GeV, then detection of gravitons is possible, as well as partial reconstruction of the inflaton potential. If the energy scale is $\lesssim 10^{14}$GeV, then density fluctuations dominate and less constraint is possible.

Fits to data over smaller angular scales are often quoted as the expected value of the quadrupole $\langle Q \rangle$ for some specific theory, e.g. a model with power-law initial conditions (primordial density perturbation power spectrum $P(k) \propto k^n$). The full 4-year COBE DMR data give $\langle Q \rangle = 15.3^{+3.7}_{-2.8}$ μK, after projecting out the slope dependence, while the best-fit slope is $n = 1.2 \pm 0.3$, and for an $n = 1$ (scale-invariant potential perturbation) spectrum $\langle Q \rangle (n = 1) = 18 \pm 1.6\,\mu$K [5], [15]. The conventional notation is such that $Q^2_{\rm rms}/T^2_\gamma = 5C_2/4\pi$.

Only somewhat weak conclusions can be drawn based on the current smaller angular scale data (see Figure 3). However, new data are being acquired at an increasing rate. With future experiments and the prospect of next generation satellite missions: MAP and COBRAS/SAMBA, a precise measurement of the CMB anisotropy power spectrum is possible and likely, allowing us to decode the information that it contains [21, 20].

Acknowledgements. We are grateful to the organizers of the Moriond Conference and particularly Tran Van Than for holding the conference and inviting us. The DMR time-ordered data, map data, and ancillary data sets (including the revised Galactic cut) are publicly available through the National Space Science Data Center (NSSDC) over the WWW internet at http://www.gsfc.nasa.gov/astro/cobe/cobe_home.html. *COBE* support was provided by the NASA Office of Space Sciences (OSS). This work was supported in part by the Director, Office of Energy Research, Office of High Energy and Nuclear Physics, Division of High Energy Physics of the U.S. Department of Energy under contract No. DE-AC03-76SF00098.

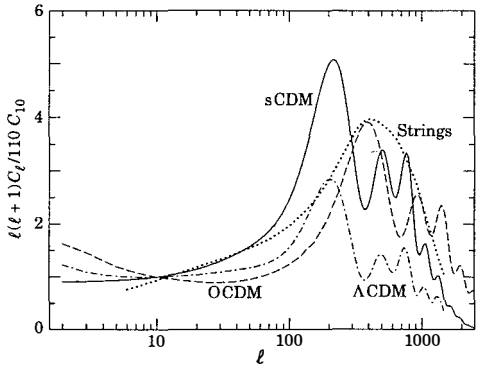

Figure 3: Examples of theoretically predicted $\ell(\ell+1)C_\ell$ or CMB anisotropy power spectra. **sCDM** is the standard cold dark matter model with $h = 0.5$ and $\Omega_B = 0.05$. **ΛCDM** is a model with $\Omega_{tot} = \Omega_\Lambda + \Omega_0 = 1$ where $\Omega_\Lambda = 0.3$ and $h = 0.8$. **OCDM** is an open model with $\Omega_0 = 0.3$ and $h = 0.75$. (See [41] for models). **Strings** is a model where cosmic strings are the primary source of large scale structure [1]. The plot indicates that precise measurements of the CMB anisotropy power spectrum could distinguish between current models.

References

[1] Albrecht, A. *et al.*, Phys. Rev. Lett., in press (1995) astro-ph/9505030

[2] R.A. Alpher & R.C. Herman 1948 Physics Today, Vol. 41, No. 8, p. 24

[3] Banday, A. et al. 1996a, ApJ, accepted, astro-ph/9601064

[4] Banday, A. et al. 1996b, ApJ, accepted, astro-ph/9601066

[5] Bennett, C. L., et al. 1996, ApJ, accepted, astro-ph/9601067

[6] Bennett, C. L., et al. 1994, ApJ, 436, 423

[7] Bennett, C. L., et al. 1993, ApJ, 414, L77

[8] Bennett, C. L., et al. 1992, ApJ, 396, L7

[9] Bennett, C. L., et al. 1991, ApJ, 391, 466

[10] R.H. Dicke, P.J.E. Peebles, P.G. Roll, and D.T. Wilkinson1965 Ap.J. 142, 414.

[11] A.G. Doroshkevich, V.N. Lukash & I.D. Novikov 1973 The Isotropization of Homogeneous Cosmological Models *Zh. Eksper. Teor. Fiz* **64**, 739–746.

[12] A.G. Doroshkevich, V.N. Lukash & I.D. Novikov 1974 Primordial Radiation in a Homogeneous but Anisotropic Universe *Astron. Zh.* **51**, 554–560.

[13] Fixsen, D. J., et al. 1996, ApJ, accepted, astro-ph/9605054

[14] Ganga, K., et al. 1993, ApJ, 410, L57

[15] Górski et al., K. M. 1996, ApJ, accepted, astro-ph/9601063

[16] Harrison, E. R. 1970, Phys. Rev. D, 1, 2726

[17] Hauser, M. G. & Peebles, P. J. E. 1973, ApJ, 185, 757

[18] Hinshaw, G., et al. 1996a, ApJ Letters, accepted, astro-ph/9601058

[19] Hinshaw, G., et al. 1996b, Ap.J Letters, accepted, astro-ph/9601061

[20] Jungman, G., Kamionkowski, M., Kosowsky, A., & Spergel, D. N. 1995, astro-ph/9512139

[21] Knox, L. 1995, Phys. Rev. **D** in press 1995 astro-ph/9504054

[22] Kogut, A., et al. 1992, ApJ, 401, 1

[23] Kogut, A., Banday, A. J., Bennett, C. L., Hinshaw, G., Loewenstein, K., Lubin, P., Smoot, G. F., & Wright, E. L. 1994, ApJ, 433, 435

[24] Kogut, A., et al. 1996a. ApJ, accepted, astro-ph/9601066

[25] Kogut, A., et al. 1996b, ApJ, accepted, astro-ph/9601060

[26] Kogut, A., et al. 1996c, ApJ, accepted, astro-ph/9601062

[27] Lineweaver, C., et al. 1995, ApJ, 448, 482-487.

[28] Lineweaver, C., et al. 199, ApJ, accepted. astro-ph/9601151

[29] Mather, J. C., et al. 1994, ApJ, 420, 439

[30] Peebles, P. J. E. 1973, ApJ, 185, 413

[31] Peebles, P. J. E. & Yu. J. T. 1970, ApJ, 162, 815

[32] P.J.E. Peebles, 1993, "Principles of Physical Cosmology," Princeton U. Press, p. 168

[33] A.A. Penzias and R. Wilson 1965, Ap. J. 142, 419.

[34] R. K. Sachs & A.M. Wolfe 1967, Ap.J. 147, 73.

[35] D. Scott. J. Silk, and M. White 1995, Science, 268, 829

[36] J. Silk 1967, Nature, 215, 1155-1156.

[37] Smoot, G. F., Tenorio, L., Banday, A.J., Kogut, A., Wright, E.L., Hinshaw, G., & Bennett, C.L. 1994, ApJ, 437, 1

[38] Smoot, G. F., et al. 1992, ApJ, 396, L1

[39] Smoot, G.F., et al. 1990, ApJ, 360, 685

[40] Tegmark, M. & Bunn. E. F. 1995, ApJ, 455, 1

[41] White, M. 1996, Phys Rev D, in press astro-ph/9601158

[42] M. White, D. Scott, and J. Silk, Ann. Rev. Astron. & Astrophys. **32**, 329 (1994)

[43] Wright, E. L., et al. 1996, ApJ Letters, accepted, astro-ph/9601059

[44] Wright, E. L., et al. 1992. ApJ, 396, L13

[45] Zeldovich, Ya B. 1972. MNRAS, 160, 1

[17] Hauser, M. G. & Peebles, P. J. E. 1973, ApJ, 185, 757

[18] Hinshaw, G., et al. 1996a, ApJ Letters, accepted. astro-ph/9601058

[19] Hinshaw, G., et al. 1996b, ApJ Letters, accepted. astro-ph/9601061

[20] Jungman, G., Kamionkowski, M., Kosowsky, A., & Spergel, D. N. 1995, astro-ph/9512139

[21] Knox, L. 1995, Phys. Rev. **D** in press 1995 astro-ph/9504054

[22] Kogut, A., et al. 1992, ApJ, 401, 1

[23] Kogut, A., Banday, A. J., Bennett, C. L., Hinshaw, G., Loewenstein, K., Lubin, P., Smoot, G. F., & Wright, E. L. 1994, ApJ, 433, 435

[24] Kogut, A., et al. 1996a, ApJ, accepted, astro-ph/9601066

[25] Kogut, A., et al. 1996b, ApJ, accepted, astro-ph/9601060

[26] Kogut, A., et al. 1996c, ApJ, accepted, astro-ph/9601062

[27] Lineweaver, C., et al. 1995, ApJ, 448, 482-487.

[28] Lineweaver, C., et al. 199, ApJ, accepted. astro-ph/9601151

[29] Mather, J. C., et al. 1994, ApJ, 420, 439

[30] Peebles, P. J. E. 1973, ApJ, 185, 413

[31] Peebles, P. J. E. & Yu, J. T. 1970, ApJ, 162, 815

[32] P.J.E. Peebles, 1993, "Principles of Physical Cosmology," Princeton U. Press, p. 168

[33] A.A. Penzias and R. Wilson 1965, Ap. J. 142, 419.

[34] R. K. Sachs & A.M. Wolfe 1967, Ap.J. 147, 73.

[35] D. Scott. J. Silk, and M. White 1995, Science, 268, 829

[36] J. Silk 1967, Nature, 215, 1155-1156.

[37] Smoot, G. F., Tenorio, L., Banday, A.J., Kogut, A., Wright, E.L., Hinshaw, G., & Bennett, C.L. 1994, ApJ, 437, 1

[38] Smoot, G. F., et al. 1992, ApJ, 396, L1

[39] Smoot, G.F., et al. 1990, ApJ, 360, 685

[40] Tegmark, M. & Bunn, E. F. 1995, ApJ, 455, 1

[41] White, M. 1996, Phys Rev D, in press astro-ph/9601158

[42] M. White, D. Scott, and J. Silk, Ann. Rev. Astron. & Astrophys. **32**, 329 (1994)

[43] Wright, E. L., et al. 1996, ApJ Letters, accepted. astro-ph/9601059

[44] Wright, E. L., et al. 1992, ApJ, 396, L13

[45] Zeldovich, Ya B. 1972. MNRAS, 160, 1

THE THEORETICAL AGENDA IN CMB RESEARCH

J. Richard Bond
Canadian Institute for Advanced Research Cosmology Program
Canadian Institute for Theoretical Astrophysics, Toronto, Ontario, Canada.

Abstract

The terrain that theorists cover in this CMB golden age is described. We ponder early universe physics in quest of the fluctuation generator. We extoll the virtues of inflation and defects. We transport fields, matter and radiation into the linear (primary anisotropies) and nonlinear (secondary anisotropies) regimes. We validate our linear codes to deliver accurate predictions for experimentalists to shoot at. We struggle at the computing edge to push our nonlinear simulations from only illustrative to fully predictive. We are now phenomenologists, optimizing statistical techniques for extracting truths and their errors from current and future experiments. We begin to clean foregrounds. We join CMB experimental teams. We combine the CMB with large scale structure, galaxy and other cosmological observations in search of current concordance. The brave use all topical data. Others carefully craft their prior probabilities to downweight data sets. We are always unbiased. We declare theories sick, dead, ugly. Sometimes we cure them, resurrect them, rarely beautify them. Our goal is to understand how all cosmic structure we see arose and what the Universe is made of, and to use this to discover the laws of ultrahigh energy physics. Theorists are humble, without hubris.

1 Theoretical Theory

Early Universe Physics is the likely source of fluctuations to input into the cosmic structure formation problem (e.g., [1]). We want to measure the CMB (and large scale structure) response to these initial fluctuations. The goal is the lofty one of peering into the physical mechanism by which the fluctuations were generated, by learning: the statistics of the fluctuations, whether Gaussian or non-Gaussian; the mode, whether adiabatic or isocurvature scalar perturbations, and whether there is a significant component in gravitational wave tensor perturbations; the power spectra for these modes (albeit over only 3 decades in wavenumber for CMB probes, Fig. 2, and fewer for large scale structure (LSS) probes).

Fluctuation Generation Mechanisms: The contenders are (1) "zero point" oscillations in scalar and tensor fields that must be there in the early universe if quantum mechanics is applicable and (2) topological defects which may arise in the inevitable phase transitions expected in the early universe.

Inflation: For quantum oscillations to be important, a period of accelerated expansion seems essential, for then the comoving Hubble length $(Ha)^{-1}$ shrinks in size, freezing the time-incoherent noise into time-coherent patterns for structure formation.[1] A major challenge for

[1] Acceleration (i.e., inflation) seems to be generic unless it is explicitly forbidden by some law of physics unknown at this time. It may be extremely improbable *a priori* that a bit of space would accelerate and yet be highly probable *a posteriori* that we would find ourselves in a region that once inflated because of the vast space created.

inflation models is a "natural" explanation of why post-inflation fluctuations should be $\sim 10^{-5}$ in size, as revealed by COBE and also LSS observations.

Many many variants of the basic inflation theme have been proposed, sometimes with radically different consequences for the appearance of the CMB sky, which is used in fact to highly constrain the more baroque models. A rank-ordering of inflation possibilities: (1) adiabatic curvature fluctuations with nearly uniform scalar tilt over the observable range, slightly more power to large scales ($n_s < 1$) than "scale invariance" ($n_s = 1$) gives, a predictable nonzero gravity wave contribution with tilt similar to the scalar one, and tiny mean curvature ($\Omega_{tot} \approx 1$); (2) same as (1), but with a tiny gravity wave contribution; (3) same as (1) but with a subdominant isocurvature component of nearly scale invariant tilt (the case in which isocurvature dominates is ruled out by $\Delta T/T$); (4) radically broken scale invariance with weak to moderate features (ramps, mountains, valleys) in the fluctuation spectrum (strong ones are largely ruled out by $\Delta T/T$); (5) radical breaking with non-Gaussian features as well; (6) "open" inflation, with quantum tunneling producing a negatively-curved (hyperbolic) space which inflates, but not so much as to flatten the mean curvature ($d_c \sim (Ha)^{-1}$, not $\gg (Ha)^{-1}$, where $d_c \equiv H_0^{-1}|1 - \Omega_{tot}|^{-1/2}$); (7) quantum creation of compact hyperbolic space from "nothing" with volume d_T^3 which inflates, with $d_T \sim (Ha)^{-1}$, not $\gg (Ha)^{-1}$, and d_T of order d_c; (8) flat ($d_c = \infty$) inflating models which are small tori of scale d_T with d_T a few $(Ha)^{-1}$ in size. It is quite debatable which of the cases beyond (2) are more or less plausible, with some claims that (4) is supersymmetry-inspired, others that (6) is not as improbable as it sounds (see Cohn, these proceedings, for a nice discussion). It is the theorists' job to push out the boundaries of the inflation idea and use the data to select what is allowed.

Defects: Gradients in the disordered field energy left by a phase transition are smoothed on the growing scale over which causal communication can occur. Topological knot-like or string-like field configurations disappear slowly enough that they can act as isocurvature seed perturbations to drive the growth of fluctuations in the total mass density. The inherent nonlinearity of these defects in the field implies many issues can only be answered with numerical simulations, and these are subject to the same computational-size-to-resolution limitations that plague the rest of nonlinear cosmology. Much analytic progress in understanding the basic observable features of defect models is being made and renewed effort is being put into doing large enough simulations to predict CMB anisotropies in both texture and string theories.

Hydro: Although hydrodynamic and radiative processes are expected to play important roles around collapsed objects and may bias the galaxy distribution relative to the mass, a global role in obscuring the early universe fluctuations by late time generation on large scales now seems unlikely.[2]

Transport: Cosmological radiative transfer is on a firm theoretical footing. Together with a gravity theory[3] and the transport theory for the other fields and particles present (baryons, hot, warm and cold dark matter, coherent fields, i.e., "dynamical" cosmological "constants", *etc.*), we propagate initial fluctuations from the early universe through photon decoupling into

[2]Not too long ago it seemed perfectly reasonable based on extrapolation from the physics of the interstellar medium to the pregalactic and intergalactic medium to suppose hydrodynamical amplification of seed cosmic structure would obscure primordial fluctuations from the early Universe. The strong limits on Compton cooling from FIRAS, in energy $\delta E_{Compton\ cool}/E_{cmb} = 4y < 6.0 \times 10^{-5}$ (95% CL), constrain the product $f_{exp}R_{exp}^2$ of filling factor f_{exp} and bubble formation scale R_{exp}, to values too small for a purely hydrodynamic origin. If supernovae were responsible for the blasts, the accompanying presupernova light radiated would have been much in excess of the explosive energy (more than a hundred-fold), leading to much stronger restrictions.

[3]Einstein's theory is invariably assumed, but deviations are expected and indeed necessary at very high energy, with potential impact on the fluctuation generation process, and, if exotic enough, on transport through decoupling to now. Eventually, as we understand the CMB sky better, the data will undoubtedly be turned to constraining or discovering modified theories of gravity.

the (very) weakly nonlinear phase, and predict *primary anisotropies*, those calculated using either linear perturbation theory (e.g., for inflation-generated fluctuations), or, in the case of defects, linear response theory. The sources driving their development are listed in the Table.

Cosmic Parameters: Even simple Gaussian inflation-generated fluctuations for structure formation have a large number of early universe parameters we would wish to determine: power spectrum amplitudes at some normalization wavenumber k_n for the modes present, $\{\mathcal{P}_{ad}(k_n), \mathcal{P}_{is}(k_n), \mathcal{P}_{GW}(k_n)\}$; "tilt" shape functions $\{n_s(k), n_{is}(k), n_t(k)\}$, usually chosen to be constant or with a logarithmic correction, e.g., $n_s(k_n), dn_s(k_n)/d\ln k$. The transport problem is dependent upon physical processes, and hence on physical parameters. A partial list includes various mean energy densities $\{\Omega_{tot}, \Omega_B, \Omega_{vac}, \Omega_{cdm}, \Omega_{hdm}\}$, the Hubble parameter h, the number of relativistic neutrinos, the abundance of primordial helium, and parameters characterizing the ionization history of the Universe, e.g., the Compton optical depth from a reheating redshift z_{reh} to the present. For a given model, the early universe power spectrum amplitude measures are uniquely related to late-time power spectrum measures of relevance for the CMB, such as the quadrupole or bandpowers for various experiments, or to large scale structure observations, such as the *rms* density fluctuation level on the $8\,h^{-1}$ Mpc (cluster) scale, σ_8.

The arena in which theory battles observation is the anisotropy power spectrum figure. Fig. 1 illustrates how primary $\mathcal{C}_\ell$'s vary with cosmic parameters. They are normalized to the 4-year *dmr*(53+90+31)(A+B) data. A "standard" CDM model, with n_s=1, Ω_{tot}=1, H_0=50, Ω_B=0.05, and a 13 Gyr age, is the upper solid curve. It has $\sigma_8 = 1.20 \pm 0.08$, far from the ~ 0.6 target value derived from cluster abundance observations. An (almost indistinguishable) dotted curve has the same parameters except that it includes a light neutrino with $\Omega_{m\nu} = 0.2$ (and $\Omega_{cdm} = 0.75$). It has $\sigma_8 = 0.83 \pm 0.06$. The upper dashed curve is a vacuum-dominated model with H_0=75 and the 13 Gyr age (and $\Omega_\Lambda = 0.73$, $\Omega_B = 0.02$, $\Omega_{cdm} = 0.24$). It has $\sigma_8 = 1.03 \pm 0.07$, which is OK for cluster abundances. An open CDM model has the $\mathcal{C}_\ell$ peak shifted to higher ℓ; the one shown has $H_0 = 60$ and the 13 Gyr age, with Ω_{tot}=0.33, Ω_{cdm}=0.30, $\Omega_B = 0.035$, and $\sigma_8 = 0.50 \pm 0.04$. By $H_0 = 70$, Ω_{tot} is down to 0.055 at this age. The lower solid curve is a CDM model with reionization at $z_{reh} = 30$, and almost degenerate with it is a tilted CDM model (n_s=0.95 but otherwise standard). Even the nearly degenerate hot/cold and CDM models shown should be distinguishable by COBRAS/SAMBA.

COMBA: Spurred on by the promise of percent-level precision in cosmic parameters from CMB satellites, a considerable fraction of the CMB theoretical community with Boltzmann transport codes compared their approaches and validated the results to ensure percent-level accuracy up to $\ell \sim 3000$ [2]. The arena shifted from figures like Fig. 1 to $\Delta\mathcal{C}_\ell/\mathcal{C}_\ell$ figures with tiny vertical range. We look forward to the happy day when such a relative difference figure will be used to reveal the remaining tiny residuals in the best fit theoretical model. An important goal for COMBA was speed, since the parameter space we wish to constrain has many dimensions. Most groups have solved cosmological radiative transport by evolving a hierarchy of coupled moment equations, one for each ℓ. Although the equations and techniques were in place prior to the COBE discovery for scalar modes, and shortly after for tensor modes, to get the high accuracy with speed has been somewhat of a challenge. There are alternatives to the moment hierarchy for the transport of photons and neutrinos. In particular the entire problem of photon transport reduces to integral equations in which the multipoles with $\ell > 2$ are expressed as history-integrals of metric variables, photon-bunching, Doppler and polarization sources, as in the Table. The fastest COMBA-validated code uses this method (Seljak, these proceedings).

Secondary: Secondary anisotropies, with sources listed in the Table, arise from nonlinear structures. They are a nuisance foreground to be subtracted to get at the *primary* primary ones, but also invaluable probes of shorter-distance aspects of structure formation theories, full

of important cosmological information. The effect of lensing is to smooth slightly the Doppler peaks and troughs of Fig. 1. $\mathcal{C}_\ell$'s from quadratic nonlinearities in the gas at high redshift are concentrated at high ℓ, but for most viable models are expected to be a small contaminant. Scattering from gas in moving clusters also has a small effect on $\mathcal{C}_\ell$, although is measurable in individual clusters. Power spectra for the thermal SZ effect from clusters are larger; examples in Fig. 1 are for a cluster-normalized σ_8=0.7 hot/cold hybrid model (solid, Ω_{hdm}=0.3) and an n_s=0.8 tilted CDM model. Although $\mathcal{C}_\ell^{(SZ)}$ may be small, because the power for such non-Gaussian sources is concentrated in hot or cold spots the signal is detectable, and often has been. $\mathcal{C}_\ell$ for a typical dusty primeval galaxy model is also shown, the larger (arbitrarily normalized) part a shot-noise effect for galaxies with dust distributed over 10 kpc, the smaller a contribution associated with clustering. Similar spectra are expected for other extragalactic point sources, e.g., radio galaxies.

2 Phenomenological Theory

Phenomenology: We have progressed from the tens of pixels of early $\Delta T/T$ experiments through the thousands for DMR and SK, and will soon be dealing with tens of thousands for long duration balloon experiments and eventually millions for the MAP and COBRAS/SAMBA satellites . How best to analyze statistically these data sets is a subject being developed largely by CMB theorists. Theorists have also taken on an increasingly phenomenological role in LSS studies and many of the same techniques are being applied to both $\Delta T/T$ and LSS data sets. This is opening up into a major subfield, a trend which we should strongly encourage. Finding nearly optimal strategies for data projection, compression and analysis which will allow us to disentangle the primary anisotropies from the Galactic and extragalactic foregrounds and from the secondary anisotropies induced by nonlinear effects will be the key to realizing the theoretically-possible precision on cosmic parameters and so to determine the winner (and losers) in theory space. Particularly powerful is to combine results from different CMB experiments and combine these with LSS and other observations. Almost as important as the end-product is the application of the same techniques to probing the self-consistency and cross-consistency of experimental results.

Current State: Current band-powers, shown in Fig. 1, broadly follow inflation-based expectations, but may still include residual signals. Consistency with the primary anisotropy frequency spectrum has been shown for DMR and for the smaller angle experiments, but over a limited range. That the level is $\sim 10^{-5}$ provides strong support for the gravitational instability theory. To get the large scale structure of COBE-normalized fluctuations right provides encouraging support that the initial fluctuation spectrum was not far off the scale invariant form that inflation (and defect) models prefer. That there appears to be power at $\ell \sim 400$ suggests the universe could not have reionized too early.

Large Scale Structure: We have always combined CMB and LSS data in our quest for viable models. Fig. 2 shows how the two are connected. As we have seen, the DMR data precisely determines σ_8 for each model considered. For the COBE-normalized density power spectra to thread the "eye of the needle" associated with cluster abundances severely constrains the parameters determining them. Similar constrictions arise from galaxy-galaxy and cluster-cluster clustering observations. Smaller angle CMB data (e.g., SP94, SK95) are consistent with these models (e.g., Bond and Jaffe, these proceedings), and will soon be powerful enough for the CMB by itself to offer strong selection, but this will definitely not diminish the combined LSS-CMB phenomenology.

Ultra-large Scale Structure: The "beyond our horizon" land in Fig. 2 is actually partly

accessible because long waves contribute gentle gradients to our observables. Constraints on such "global parameters" as average curvature are an example, $d_c > 1.1 H_0^{-1}$, though not yet very restrictive. One may also probe whether a huge bump or deficit in power exists just beyond $k^{-1} \sim H_0^{-1}$, but this has not been much explored. The remarkable non-Gaussian structure predicted by stochastic inflation theory would likely be too far beyond our horizon for its influence to be felt. The bubble boundary in hyperbolic inflation models may be closer and its influence shortly after tunneling occurred could have observable consequences for the CMB. Theorists have also constrained the scale of topology in simple models; e.g., we (Pogosyan, Sokolov and I) find $d_T/2 > 2H_0^{-1}$ for flat 3-tori and $> 1.5H_0^{-1}$ for flat 1-tori from DMR (see de Oliveira-Costa, these proceedings). A number of groups are now trying to constrain the compact hyperbolic topologies.

Futures: Let us look forward to the day phenomenological theorists will have optimally-analyzed LDBs/VSA/CBI/ChiSPI/MAP/COBRAS/SAMBA and we know the power spectrum and cosmic parameters to wonderful precision. What will it mean? It may not be clear. Take inflation as an example. There will be attempts, undoubtedly optimal ones, to reconstruct the inflaton's potential, but all of our CMB and LSS observations actually access only a very small region of the potential surface, and even this will be fuzzily determined if we allow too much freedom in parameter space. Still even a fuzzy glimpse is worth the effort. Most fun will be when phenomenology teaches us that non-baroque inflation and defect models fail and howling packs of theorists go hunting for the elusive generator following trails well marked by the data.

References

[1] Bond, J.R. 1996, *Theory and Observations of the Cosmic Background Radiation*, in "Cosmology and Large Scale Structure", Les Houches Session LX, August 1993, ed. R. Schaeffer, Elsevier Science Press, and references therein.

[2] Bertschinger, E., Bode, P., Bond, J.R., Coulson, D., Crittenden, R., Dodelson, S., Efstathiou, G., Gorski, K., Hu, W., Knox, L., Lithwick, Y., Scott, D., Seljak, U., Stebbins, A., Steinhardt, P., Stompor, R., Souradeep, T., Sugiyama, N., Turok, N., Vittorio, N., White, M., Zaldarriaga, M. 1995, ITP workshop on *Cosmic Radiation Backgrounds and the Formation of Galaxies*, Santa Barbara.

PHYSICAL PROCESSES FOR ANISOTROPY	
PRIMARY SCALAR ANISOTROPIES	
$\Phi/3$	"Naive" Sachs-Wolfe effect: Gravitational Potential
$\frac{1}{4}\frac{\delta\rho_\gamma}{\rho_\gamma}$	photon bunching (acoustic): $\frac{1}{3}\frac{\delta\rho_B}{\rho_B}$ effect, isocurvature effect
$\sigma_T \bar{n}_e \mathbf{v}_e \cdot \hat{q}$	Linear-order Thompson scattering (Doppler)
$2\int_{l.o.s.} \dot{\Phi}$	Integrated Sachs-Wolfe effect
	subdominant anisotropic stress and polarization terms
PRIMARY TENSOR ANISOTROPIES	
$\frac{1}{2}\dot{h}_{+,\times}$	gravity waves (two polarizations)
	subdominant polarization terms
SECONDARY ANISOTROPIES	
ε_{AB}	Linear Weak Lensing: 2D shear tensor
$2\int_{l.o.s.} \dot{\Phi}_{NL}$	Rees-Sciama effect: Linear Response to Φ of nonlinear structure
$\sigma_T \delta n_e \mathbf{v}_e \cdot \hat{q}$	Nonlinear Thompson scattering: Quadratic-order (Vishniac) effect,
.....	"kinematic" SZ effect (moving cluster/galaxy)
$\int_{l.o.s.} \psi_K(x)\delta(n_e T_e)$	thermal SZ effect: Compton cooling from nonlinear gas ($x = E_\gamma/T_\gamma$)
$\int_{l.o.s.} \psi_{dust}(x_d)\rho_d$	redshifted dust emission, pregalactic/protogalactic ($x_d = E_\gamma/T_d$)
FOREGROUNDS	
	extragalactic radio sources: falling, flat, rising
	IRAS sources and extrapolations to moderate z
	Galactic bremsstrahlung, synchrotron
	Galactic Dust: regular, cool, strange??

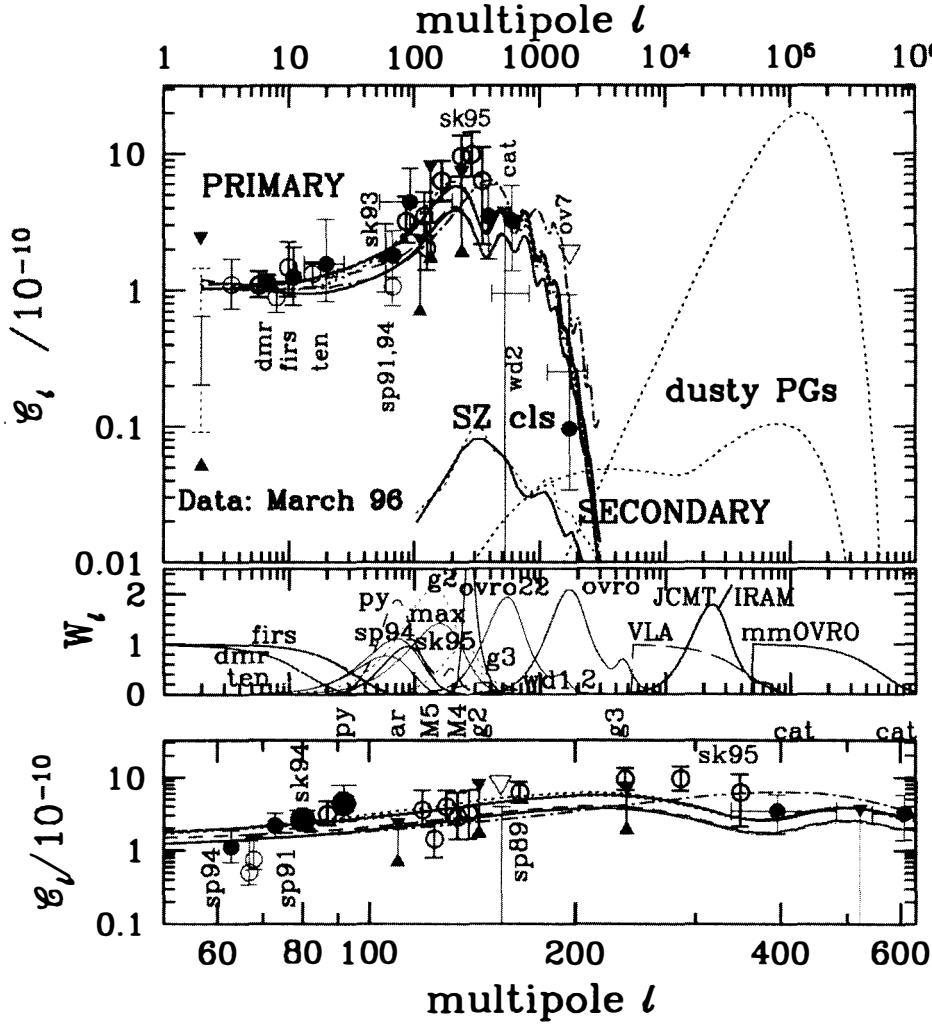

Figure 1: Sample primary and secondary power spectra, $\mathcal{C}_\ell \equiv \ell(\ell+1)\langle|(\Delta T/T)_{\ell m}|^2\rangle/(2\pi)$, are compared with the band-power estimates derived for the anisotropy data up to March 1996. The lower panel is a closeup of the first two 'Doppler peaks'. Average filter functions for a variety of experiments are shown in the middle panel. The upper solid primary $\mathcal{C}_\ell$ curve is a COBE-normalized "standard" untilted CDM model, and variants are shown with the same cosmological age and $\Omega_B h^2$, but nonzero tilt, Ω_{hdm} (i.e., $m_\nu > 0$), Ω_{vac} (i.e., $\Lambda > 0$), average curvature (i.e., $\Omega_{tot} < 1$) or weak reionization. They all broadly agree with the data. By contrast, the thermal SZ anisotropy power is way down, the kinematic SZ power is off-scale, and dusty emission power from early galaxies is concentrated at higher ℓ and higher frequency.

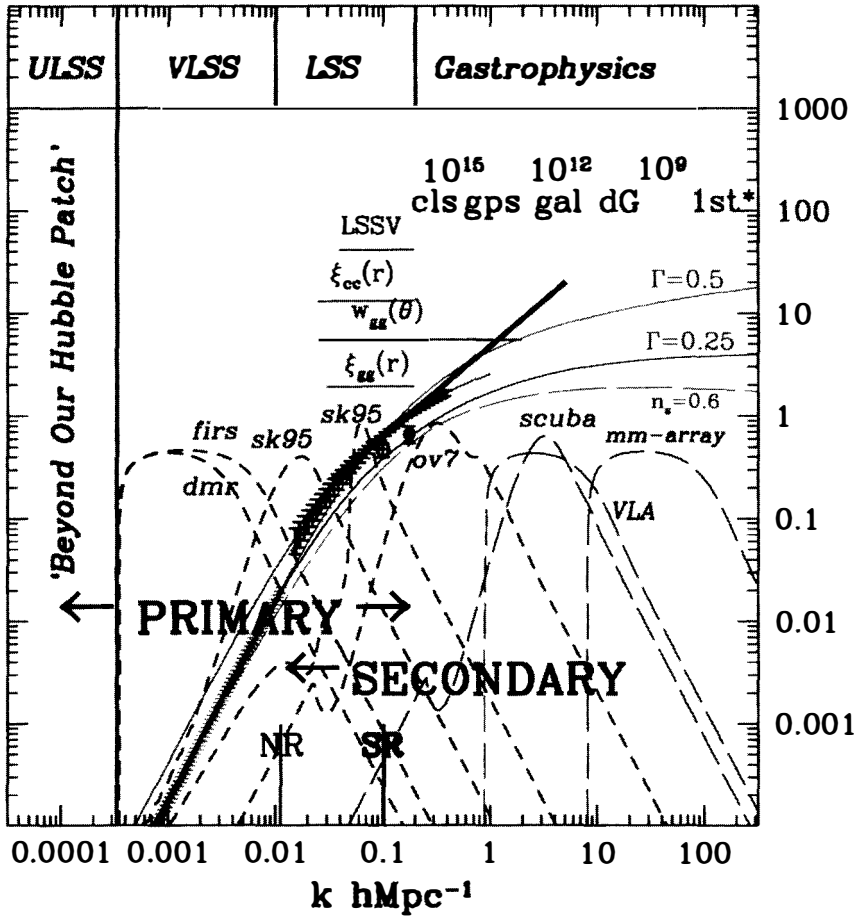

Figure 2: The bands in comoving wavenumber probed by CMB primary and secondary anisotropy experiments and by large scale structure observations are contrasted. Sample (linear) density power spectra are for the "standard" $n_s = 1$ CDM model (labelled $\Gamma = 0.5$), for a tilted ($n_s = 0.6$, $\Gamma = 0.5$) CDM model and for a model with the shape modified ($\Gamma = 0.25$) by changing the matter content of the Universe. A (uniform?) bias is allowed to raise the shapes into the hatched w_{gg} region; only the latter two fit. The solid data point in the cluster-band denotes the constraint from the abundance of clusters, and the open data point at $10\,h^{-1}$ Mpc a constraint from streaming velocities (for Ω_{tot}=1,Ω_{vac}=0).

ULTRA-LOW-NOISE HETEROSTRUCTURE FIELD-EFFECT TRANSISTOR, MILLIMETER-WAVE RECEIVERS

Marian W. Pospieszalski
National Radio Astronomy Observatory*
2015 Ivy Road
Charlottesville, VA 22903

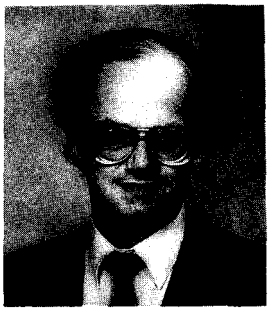

Abstract

Recent developments in ultra-low-noise heterostructure field-effect transistor receiver technology for frequencies up to W-band are discussed. The following main topics are covered:

- noise and signal properties of heterostructure field-effect transistors (HFET's), also known as high-electron mobility transistors (HEMT's), at cryogenic temperatures,
- design and examples of the realization of wideband low-noise, cryogenically-coolable HFET amplifiers and receivers in the 20 to 100 GHz range, and
- a comparison of HFET receivers with SIS mixer/HFET IF amplifier receivers.

*The National Radio Astronomy Observatory is a facility of the National Science Foundation operated under cooperative agreement by Associated Universities, Inc.

INTRODUCTION

The quest for ultra-low-noise reception has been mostly driven by applications in radio astronomy and space communications. A list of devices which at one time and at some frequency provided the lowest reported noise temperature is very long: vacuum tubes, crystal mixers, tunnel diode amplifiers, parametric amplifiers, solid-state masers, Schottky diode mixers, superconductor-insulator-superconductor (SIS) mixers, GaAs field-effect transistors (FET's) and heterostructure field-effect transistors (HFET's, HEMT's), etc.

In the early 1970's, the ultra-low-noise receiving systems employed mainly solid-state masers, cryogenically-cooled parametric amplifiers (or converters) and Schottky diode mixers [8], [17]. At the end of that decade, the advances in the technology of GaAs FET's, combined with cryogenic cooling, made the noise performance of GaAs FET amplifiers competitive with the performance of parametric amplifiers [16]. Also, a new mixing element, superconductor-insulator-superconductor (SIS) junction, capable of quantum limited detection, was developed [4], [15]. Progress in the development of SIS mixers and HFET amplifiers during the 1980's pushed the parametric amplifiers into obsolescence, and left Schottky diode mixers, in spite of strong technological advances in this field, as the lowest noise devices only for frequencies above 1 THz. Especially, the progress in the performance of FET and HFET amplifiers was quite dramatic [2], [6], [7], [9]-]12], [16]: from state-of-the-art noise temperature of 20 K at 4.75 GHz in 1980 [16] to the state-of-the-art noise temperature of 10 K at 40 GHz in 1994 [12] at the ambient temperature of 18 K. HFET receivers now compete in performance with masers and SIS mixer/HFET amplifier tandems for frequencies below 110 GHz.

NOISE AND SIGNAL PROPERTIES OF HFET'S AT CRYOGENIC TEMPERATURES

A successful design of wideband cryogenically-coolable amplifiers with optimal noise performance requires knowledge of the signal and noise properties of FET's. Modern devices for cryogenic application usually employ AlInAs/GaInAs/InP heterostructure [6], [7], [10], [12], commonly known as InP HFET's. A good example of a state-of-the-art device [7], [12] consists of a 250-nm undoped AlInAs buffer, a 40-nm GaInAs channel, a 1.5-nm undoped spacer, an 8-nm AlInAs donor layer doped to approximately 7×10^{18} cm^{-3} and, finally, a 7-nm GaInAs doped cap, all grown lattice-matched to InP on a 2-inch semi-insulating substrate. It typically exhibits an electron sheet density of 2.5 to 2.8×10^{12} cm^{-2} and a room-temperature mobility of 10,000 to 11,000 cm^2/Vs.

An example of the I-V characteristics at room and cryogenic temperatures of an InP HFET with gate dimensions .1 x 50 μm is shown in Fig. 1 [7], [12]. The equivalent circuit of this device is shown in Fig. 2.

A FET (HFET) noise model introduced in [11] is especially well suited to study the noise properties of a FET under change in ambient temperature and bias. In this model, the noise properties of a device at a given temperature and bias are fully determined by its equivalent circuit and two frequency independent constants: equivalent gate and drain temperatures, T_g and T_d, respectively. The ambient temperature determines the noise contributions of any losses of the embedding circuit or device parasitics. The equivalent gate temperature assigned to intrinsic gate resistance, r_{gs}, represents the noise process, internal to a FET, which produces perfectly correlated short circuit noise currents in gate and drain with a purely imaginary correlation coefficient. The equivalent drain temperature assigned to drain resistance r_{ds} represents a noise process, internal to a FET, which produces a noise current only in a drain circuit. For this model, the minimum noise temperature, T_{min}, in the case of intrinsic chip and small signal approximation is given by [9]:

$$T_{min} \simeq 2 \frac{f}{f_T} \sqrt{g_{ds} r_{gs} T_g T_d}$$

where $f_T = g_m/2\pi C_{gs}$ and $g_{ds} = 1/r_{ds}$. The gate temperature is, within the accuracy of an experiment, equal to the device physical temperature [9]-[14]. The drain temperature for devices at room temperature falls in the range of 1000 K to 10000 K and is strongly dependent on a device drain current [9]-[14]. For devices at room temperature under low-noise bias, the equivalent drain temperature assumes values between 1000 K to 2000 K [9], [13], [14]. For optimal noise bias at cryogenic temperatures, the values between 200 K and 700 K were observed [9], [12]. A plot of equivalent drain temperature T_d, explaining the measured noise temperature at 40 GHz at the ambient temperature T_a = 18 K for the devices of Figs. 1 and 2 and for different bias currents, is shown in Fig. 3. In obtaining the values of T_d, the equivalent circuit of Fig. 2 was used under the assumption that the only element of the equivalent circuit changing with ambient temperature and drain current is the transconductance g_m, also plotted in Fig. 3. This oversimplified approach, in the absence of good cryogenic S-parameter measurements, is used to show the same qualitative dependence of T_d vs. drain current as demonstrated in a much more accurate room temperature experiments [13], [14].

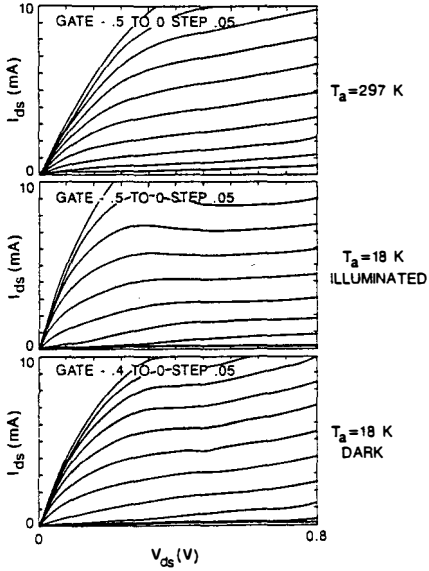

Fig. 1. Example of I-V characteristics of .1 x 50 µm AlInAs/GaInAs/InP HEMT at room and cryogenic temperatures.

INTRINSIC DEVICE	PARASITIC ELEMENTS
C_{gs} = 37. 7 fF	r_g = 3.0 Ω
r_{gs} = 4.0 Ω	r_d = 12.0 Ω
C_{gd} = 2.9 fF	r_s = 8.0 Ω
r_{gd} = 400 Ω	C_{pgs} = 6.5 fF
g_m = 50.2 mS	C_{pgd} = 2.5 fF
τ = 0.6 ps	C_{pds} = 12.0 fF
C_{ds} = 5.2 fF	L_g = 33 pH
g_{ds} = 4.1 mS	L_d = 27 pH
	L_s = 6.0 pH

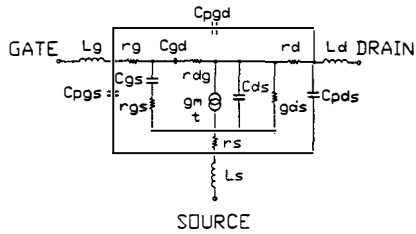

Fig. 2. An equivalent circuit of .1 x 50 µm InP HEMT at room temperature and V_{ds} = 1 V, I_{ds} = 7 mA.

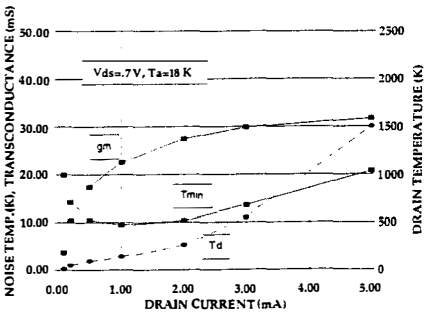

Fig. 3. The minimum noise temperature at 40 GHz, dc measured transconductance and equivalent drain temperature vs. drain current at the ambient temperature T_a = 18 K of .1 x 50 µm InP HEMT.

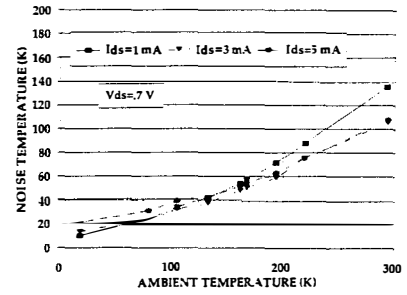

Fig. 4. Noise temperature of cryogenic Q-band amplifier versus ambient temperature for different bias currents of the AlInAs/GaInAs/InP device.

The data of Fig. 3 demonstrate how mutually compensating changes in f_T and T_d under change in drain current allow for a very shallow minimum of noise temperature T_{min}. This relative insensitivity to bias is a strong advantage of HFET's over other low-noise devices. Also, these devices have an advantage of a very graceful and predictable degradation of noise performance with increase in ambient temperature. As an example, the minimum noise temperature at 40 GHz of the device of Figs. 1-3 is shown in Fig. 4 for three different bias currents. A "rule of thumb" for a typical device is the doubling of noise temperature with the physical temperature increasing from 18 K to 80 K.

DESIGN AND PERFORMANCE OF ULTRA-LOW-NOISE CRYOGENIC AMPLIFIERS

The noise and signal models of cryogenic FET's described in the previous section are sufficiently accurate to allow for computer-aided design of cryogenic amplifiers with optimal, according to some criterion, noise bandwidth performance. The criterion for CMBR measurements could be, for example, a minimum value of the average noise temperature over a given bandwidth. Usually an amplifier has to satisfy other requirements, as the input and output return loss, unconditional stability, minimum gain and gain flatness, etc., which can also be reliably investigated in a CAD process. As a result, there are no "set-in-stone" design rules; yet the following observations could prove valuable. In similarity with an impedance matching, a "noise matching" of a FET can be done perfectly only at a single frequency. Consequently, a wideband "noise matching" is similar to wideband matching of a complex impedance to a resistive load. For a given frequency range, there is a particular gate width of a FET (HEMT) which allows for the possible largest relative bandwidth. A proper choice of the inductance in series with the gate (for example, the inductance of the gate bond wire) usually results in the simplest broadband "noise matching" network. Also, a proper value of the source inductance allows to address other requirements (stability, input return loss, gain flatness) without penalty in the noise temperature of a multi-stage amplifier.

It is well known that the minimum noise temperature of a multi-stage amplifier with sufficient gain is determined not only by the device noise figure, but also by its associated gain. A more proper figure of merit is the minimum noise measure, M_{min}, which determines the lowest noise temperature (noise figure) of an amplifier made of many identical stages. It is always useful to compare the noise performance of an amplifier design with the minimum noise measure of the device used.

The NRAO Central Development Laboratory has built a number of millimeter-wave amplifiers in the 20 to 110 GHz range for applications in radio astronomy receiving systems. A representative performance of the receivers built with the InP amplifiers is shown in Fig. 5. Also shown is the best performance expected of InP HFET receivers at any frequency calculated with a noise and signal model briefly discussed in the previous section. The amplifier examples demonstrate that for a bandwidth of around an octave or less the amplifier average noise temperature T_{nav} is approximately equal to the minimum noise measure M_{min} at the highest frequency within the band:

$$T_{nav} = \frac{1}{f_{max} - f_{min}} \int_{f_{min}}^{f_{max}} T_n \, df \simeq M_{min}(f_{max})$$

The performance of a NRAO SIS receiver (600 MHz bandwidth) has also been shown in Fig. 5 [17]. A more detailed comparison of predicted and measured noise temperatures for Ka-band [1] and E-band cryogenic HFET receivers is shown in Fig. 6 and Fig. 7, respectively.

The sensitivity of a total power radiometer is given by [5]:

$$\Delta T = T_s \sqrt{\frac{1}{B\tau} + \left(\frac{\Delta G}{G}\right)^2}$$

where B is the effective RF bandwidth, τ is the integration time, ΔG is the effective value of receiver power gain variations, G is the average predetection power gain and T_s is the system noise temperature. Obviously, for the sufficiently large bandwidth B, the radiometer sensitivity may be limited by the predetection gain variation ΔG for a given integration time τ. This is often the case with wideband HFET receivers which exhibit random, 1/f-like gain fluctuation related to the presence of traps in semiconductor [3], [18]. Consequently, a proper receiver design (Dicke, correlation) is needed to take advantage of wideband, low-noise properties of HFET amplifiers.

In conclusion, the noise performance of cryogenic HFET receivers is currently competitive with SIS mixer receivers in the 3-mm wavelength atmospheric window. HFET receivers, however, offer an advantage of instantaneous coverage of full waveguide band, as shown in the example of an E-band (60-90 GHz, WR12 waveguide) receiver.

ACKNOWLEDGEMENTS

The contributions of L. Nguyen of Hughes Research Labs, and A. R. Kerr, S.-K. Pan, W. Lakatosh, and E. Wollack of NRAO are gratefully acknowledged.

REFERENCES

[1] Carlstrom J., Joy M, Grego L., private communication.
[2] Duh K. H. G. *et al.*, 1988, *IEEE Trans. Electron Devices*, **35**, p. 249.
[3] Jarosik N., 1996, *IEEE Trans. Microwave Theory Tech.*, **MTT-44**, 2, p. 193.
[4] Kerr A. R. and Pan S.-K., 1990, *Int. J. Infrared & Millimeter Waves*, **11**, 10, p. 1169.
[5] Kraus J. D., 1986, *Radio Astronomy*, Cyprus-Quasar Books.
[6] Nguyen L. D. *et al.*, Sept. 1992, *IEEE Trans. Electron Devices*, **39**, p. 2007.
[7] Nguyen L. D. *et al.*, June 1993, in *Proc. 1993 IEEE MTT-S Int. Microwave Symp.*, p. 345.
[8] Okwit S., 1984, *IEEE Trans. Microwave Theory Tech.*, **MTT-32**, p. 1068.
[9] Pospieszalski M. W., 1989, *IEEE Trans. on Microwave Theory and Tech.*, **MTT-37**, p. 1340.
[10] Pospieszalski M. W., Sept. 1993, *Proc. of 23rd European Microwave Conf.*, p. 73.
[11] Pospieszalski M. W. *et al.*, 1988, *IEEE Trans. Microwave Theory Tech.*, **36**, p. 552.
[12] Pospieszalski M. W. *et al.*, May 1995, in *Proc. 1995 IEEE MTT-S Int. Microwave Symp.*, p. 1121.
[13] Pospieszalski M. W. and Niedzwiecki A. C., 1991, in *Proc. 1991 IEEE MTT-S Int. Microwave Symp.*, p. 1117.
[14] Tasker P. J. *et al.*, 1993, in *Proc. IEEE MTT-S Int. Microwave Symp.*, p. 1251.
[15] Tucker J. R., 1979, *IEEE J. of Quantum Electron.*, **QE-15**, p. 1234
[16] Weinreb S., 1980, *IEEE Trans. Microwave Theory Tech.*, **MTT-28**, p. 1041.
[17] Weinreb S. and Kerr A. R., 1973, *IEEE J. Solid-State Circuits*, **SC-8**, p. 58.
[18] Wollack E., 1995, *Rev. of Sci. Instruments*, **66**, 8, p. 4305.

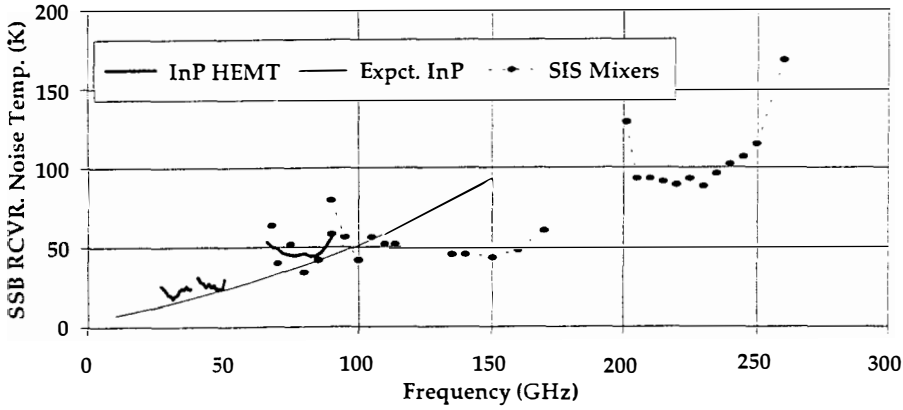

Fig. 5. Comparison of noise temperature of NRAO cryogenic receivers using InP HEMT amplifiers cooled to 20 K and SIS mixer receivers (A. R. Kerr and S.-K. Pan) cooled to 4 K.

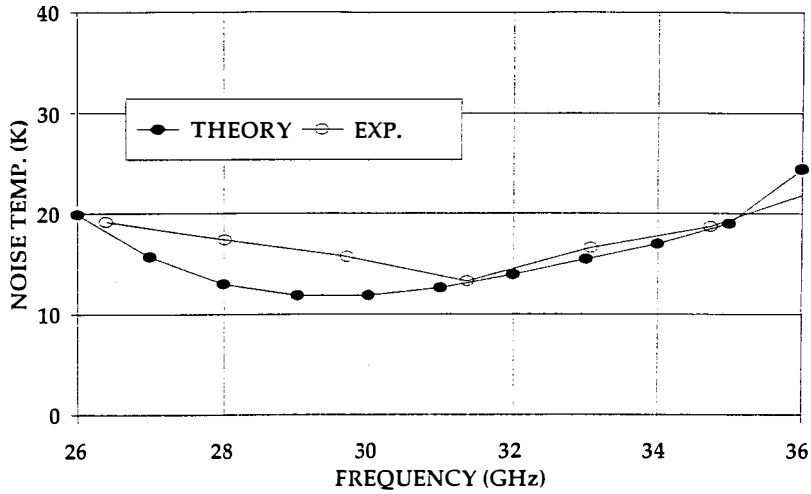

Fig. 6. Example of noise performance of cryogenic Ka-band receiver ($T_g \simeq 20$ K) compared with model prediction [1].

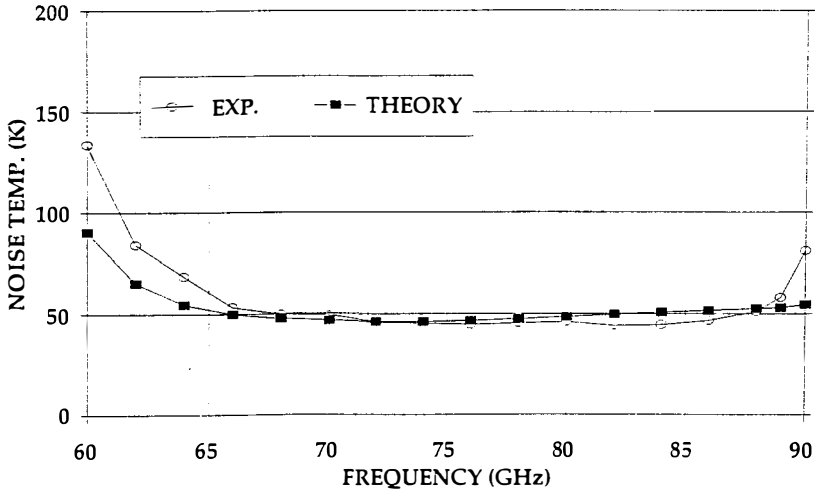

Fig. 7. Example of noise performance of E-band cryogenic receiver compared with model prediction.

BOLOMETERS : THE ULTIMATE DETECTORS FOR CMB MEASUREMENTS ?

Jean-Michel Lamarre
Institut d'Astrophysique Spatiale
CNRS-Université Paris-Sud, Orsay, France.

Abstract

The noise of an optimized bolometer depends mainly on its temperature, on its required time constant, and on the incoming power. It can be made less than the photon noise of the sky in the millimeter range provided that: (1) the bolometer frequency response required by the observation strategy does not exceed a few tens of hertz; (2) the temperature of the bolometer is low enough, i.e. 0.3 K or even 0.1 K; (3) The bandwidth of the observed radiation is large, in order to maximize the detected flux. Then, the best available bolometer technology allows photon noise limited photometry of the Cosmic Microwave Background. These conditions are met in current projects based on bolometric detection for the measurement of CMB anisotropy, and especially for COBRAS/SAMBA. The space qualification of the needed cryogenic systems has been demonstrated for 0.3 K temperatures and is in preparation for 0.1 K. For this type of wide band photometry, bolometers are the best type of detectors in the 200 μm - 5 mm wavelength range.

1 Introduction

Bolometers are used in a very wide range of frequencies, from X rays to millimeter waves. This results from the principle of thermal detection. Photons have only to be transformed in phonons, which is a very common process at nearly all frequencies. The temperature changes of the radiation absorber are then measured by a thermometer. Historically, the discovery of infrared radiations has been made with a simple mercury-glass thermometer used as a detector. The submillimeter range (200 μm - 5 mm) is now the domain of predilection of bolometric detection. At shorter wavelengths, photons are energetic enough to efficiently trig the photoconductor effect in low noise detectors that prove to be more sensitive. At longer ones and at high

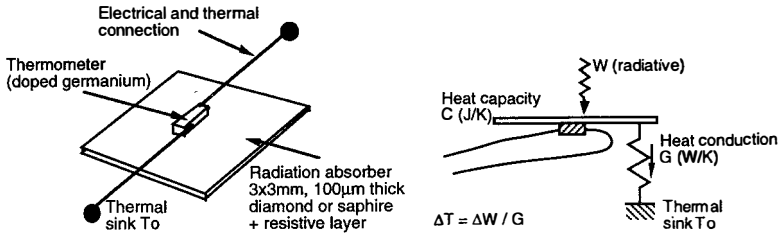

Figure 1: Representation of a conventional composite bolometer and of the simplified associated thermal scheme. The absorber insures the coupling with the radiation, while the thermometer allows to measure of the temperature changes.

It must be larger than one wavelength to achieve a good coupling with the radiation field. The absorber is thermally attached to a thermometer and to a heat leak towards a heat sink at temperature T_0. If G is the thermal conductance of the heat leak, the steady state temperature change ΔT induced by an increased absorbed power ΔW is:

$$\Delta T = \frac{\Delta W}{G} \tag{1}$$

ΔT is measured thanks to the thermometer, usually doped silicon or germanium. A wide variety of techniques are now considered for new developments. The resistance R of the thermometer changes with its temperature, and may be measured by applying a constant bias current I, and

measuring the voltage change. Taking into account the electrical power in the thermometer, the power balance can be written:

$$\Delta W + I^2 \alpha \Delta T = G \Delta T \tag{2}$$

where $\alpha = \frac{dR}{dT}$. The responsivity, i.e. the voltage change per unit of power, is

$$\frac{dV}{dW} = \frac{\alpha I}{G - \alpha I^2} \tag{3}$$

α is negative for semi-conductors. We do not consider here thermometers working at the supraconductive transient, although promising researches are currently done in this field. From (3), we can deduce that there is an optimal current, and that high responsivities can be obtained with low values of G.

The thermal time constant of a bolometer is:

$$\tau = \frac{C}{G} \tag{4}$$

Its apparent time constant when operating is modified by the feedback effect of the power deposited by the bias current, but its general behaviour follows that of equation (4) : it varies as $\frac{C}{G}$.

2.2 Sources of noises

In his nonequilibrium theory of bolometer noise [Mather, 1982], John Mather identifies five main sources of noise of independent origin: Johnson noise in the thermometer, thermal fluctuations of the bolometer, photon noise of the radiation, noise in the load resistor, and noise in the amplifier. In addition, he gathers other sources, especially low frequency electrical noise, under the denomination of excess noise. The total noise is the quadratic sum of all these contributors.

A way to improve the sensitivity of a bolometer is to increase its responsivity by decreasing the heat leak G (see equation 3). Electrical noises will not increase, and the thermal noise will only increase as the square root of $1/G$. In theory, it is possible to build infinitely sensitive bolometers by reducing G values to zero. Two phenomena will limit this search for low G values: G must be large enough to obtain a reasonably short thermal time constant (see equation 4) and also large enough to prevent excessive heating by the incident radiative power (see equation 1). Consequently, two main requirements will limit the sensitivity of a bolometer: the required frequency response f_0, which depends on the observation strategy, and the background power, i.e. the steady part of the optical power W_{bg}. These two requirements determine the two terms of a semi-empirical formula giving the Noise Equivalent Power (NEP, in $WHz^{-1/2}$) of a perfectly optimized bolometer [Mather, 1982].

$$NEP^2 = \frac{2}{\pi} k T_0 (f_0 C T_0)(\frac{9}{A} + \frac{25}{A^2}) + 4kT_0 \frac{36 W_{bg}}{A} \tag{5}$$

Where k is Boltzmann's constant, $A = -\frac{dlogR}{dlogT}$, and other variables have been previously defined. Depending on W_{bg} and f_0, the first or the second term dominate and are the main source of the NEP. The main parameter that can help is the temperature of the heat sink. Both terms depend on T_0, but the speed term is much more sensitive, since the heat capacity C of most materials is an increasing function of temperature.

Ideally, the bolometer intrinsic NEP, given by formula (5), should be significantly smaller than the photon noise, which is the fluctuation of the measured radiation itself. This determines

the ultimate sensitivity that can be obtained with any detector for a given source and with a given optical system. The photon noise with power sensitive detectors can be written [Lamarre, 1986]:

$$NEP_{ph}^2 = 2\int h\nu \frac{dW}{d\nu}\, d\nu + 2\frac{c^2}{U}\int \frac{1}{\nu^2}\left(\frac{dW}{d\nu}\right)^2 d\nu \qquad (6)$$

where h is Planck's constant, W the optical power, n the optical frequency, and U the beam étendue (in m^2sr). The first term is the shot noise produced by the detection of photons as individual events and is dominant at short wavelengths, while the second one is produced by the interference of photons and appears when the photon occupation number is large, therefore in the Rayleigh-Jeans regime. In this case, and if the frequency term in (6) can be neglected, it is possible to derive, from equations (5) and (6) , a condition on the bolometer cooling temperature T_0 to obtain a photon noise limited sensitivity while observing a blackbody at temperature T_S:

$$T_0 \leq \frac{AT_S}{18} \qquad (7)$$

If we assume a realistic value of A equal to 3 and a source temperature $T_S = 3\ K$, it comes: $T_0 \leq 0.5\ K$. From this first approach, it can be concluded that sub-Kelvin temperatures are needed for the observation of the cosmic background limited by photon noise.

2.3 Frequency requirements and actual performances

Equation (7) is independent of the technology and of the frequency requirement. Other conditions may result from the actual heat capacity and of the scanning speed needed for a given project. For example, COBRAS/SAMBA is designed to be a spin stabilized satellite rotating at 1 round per minute, and to make measurements with an angular resolution down to 4.5 minutes of arc. The resulting maximum frequency of the signal arriving on the bolometer is 95 Hz. For the best conventional bolometers, frequency is the driving requirement for the five channels and photon noise limited photometry is achievable only for two of them, even with a cooling temperature of 0.1 K. Lower heat capacities must be looked at to solve this problem. The "Spider Web" bolometer uses a resistive grid instead of a continuous metallic layer to absorb the radiation [Lange, 1996]. Simultaneous work on the thermometer size has proven to significantly decrease the heat capacity. Both improvements allow to reach bolometer NEPs not larger than twice the photon noise for all the channels. To give orders of magnitudes, the heat capacity of such a bolometer may be as low as $10^{-12}\ J/K$, and its NEP may not exceed a few $10^{-17}\ WHz^{-1/2}$. These new bolometers have also the advantage of presenting a smaller cross section for the unavoidable interaction with particles, which decreases the rate of glitches on the bolometer signal. Other developments in the similar directions are undertaken by several teams in the world [Lamarre, 1995].

For projects less demanding than COBRAS/SAMBA in term of frequency, such as FIRE or SAMBA, temperatures significantly larger than 0.1 K can be accepted. For example, 0.3 K has been considered as a baseline for FIRE as being technically simpler than 0.1 K while not compromising significantly the final sensitivity of the instrument. It can be considered that the available technology of bolometers at 0.3 K and 0.1 K covers the need for nearly photon noise limited sensitivities for the measurement of the cosmic background radiation.

3 Associated technologies

3.1 Optics

The absorber of bolometers, unlike coherent detectors, can detect radiation from any direction. Coupling a bolometer with the incoming radiation needs an efficient feed horn able to select, among all possible radiations, those coming from the telescope. This light concentrator usually feeds an integrating cavity housing the bolometer and enhancing the efficiency of the absorber by allowing multiple reflection of photons. this cavity is usually at the temperature of the bolometer, in order to prevent its self emission from being significant. One has then to take into account this cavity when assessing the mass to be cooled at sub-Kelvin temperatures.

Bolometers are sensitive to radiations at nearly all wavelengths, as indicated by the usual meaning of "bolometeric" quantities in photometry. Detection in a well defined spectral band is possible only by rejecting the unwanted radiation with efficient filters. Very high rejection ratios, up to 10^9, are needed in order to block the infrared radiation associated with warm sources. The technology of such filters has now reached a high degree of maturity for ground based and space applications. Nevertheless, these filters have to be cooled to prevent their thermal emission from being significant with respect to the measured one. Some power is absorbed in the filters and may exceed the cooling capabilities of the coldest stage of the cryogenic system. In this case, a filter blocking most of the short wavelengths must be attached to a cryogenic stage at a temperature low enough to reduce its thermal emission, but with a cooling power high enough to cope with the incident radiation. These conflicting requirements may prove to be among the most demanding for the cryogenic system.

3.2 Cryogenics

Satellites based on the use of liquid helium cryostats have been successfully flown in Europe (ISO) and in the USA (IRAS, COBE), and can provide temperatures under 2 K with a life time up to two years. On the other hand, mechanical cryo-coolers can be operated for longer periods, but can provide only 4 K and their qualification for space is not yet fully insured. Going from these 2 K or 4 K to the sub-Kelvin temperatures wanted for high sensitivity bolometers needs additional cryogenic systems.

The temperature of 0.3 K can be reached with recyclable helium 3 refrigerators using sorption pumps [Torre et al., 1985, Duband, 1995] that have cooling powers of several microwatts. When lower temperatures are required, two solutions can be contemplated. Adiabatic Demagnetization Refrigerators (ADR) can provide cooling at less than 100 mK and their space qualification is or has been studied at different places. The solution chosen for COBRAS/SAMBA is an open cycle dilution refrigerator [Benoît, 1994] and its space qualification has been undertaken under CNES sponsoring. This system, based on the mixture of helium 3 and helium 4 flows, can provide a cooling power of 100 nW or more at 100 mK with a total helium flow of less than 10 micromole per second. Tanks with reasonable size and weight ($< 20\ kg$) can insure a life time of several years.

3.3 Readout electronics

Bolometers used for detection of far-infrared radiations are traditionally biased with a DC voltage source and a high impedance load resistor that approximately behaves as a current source, as assumed in section I (figure 2). The voltage of the load resistor to bolometer connection is read by a junction transistor used in a source follower scheme as an impedance adaptor to the

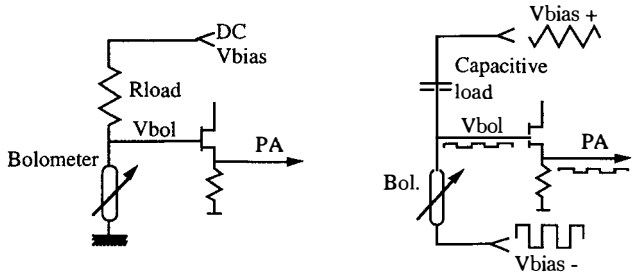

Figure 2: Principles of a conventional DC bias readout circuit (left) and of an AC bias readout using a capacitor as an impedance load (right). In the second circuit, both ends of the bridge are biased with signals that keep the middle point around zero.

Alternative biases can be used instead of DC ones. The AC voltage at the terminals of the bolometer is proportional to its resistance. In consequence, the measured optical flux appears as a modulation of the amplitude of the AC signal and can be efficiently recovered by a lock-in amplifier. One difficulty of this principle is the large dynamics of the modulated signal with respect to the amplitude changes due to the detection of radiation. The first solution that has been considered [Lange, 1996], is to use two bolometers in a differential bridge, and to amplify the difference signal. This has the same disadvantage as the sky chopping, i.e. only differential photometry can be implemented in this way. A different approach has been chosen by A. Benoît [Benoît, 1995]: both ends of the bolometer - load resistor circuit are polarized with square waves of opposite sign and with amplitudes tuned to null the mean voltage at the measurement point. This scheme can be refined by using a capacitive load instead of a resistor [Benoît, 1995].In this case, the bias voltage must be a triangle wave, in order to produce a square wave bias current (figure 2). An other track that is being studied is to use high quality components able to handle the large dynamics of the signal without adding new sources of noise. These techniques use bolometers as total power receivers able to measure DC optical powers and showing no significant 1/f noise down to less than $10^{-2}\,Hz$. This important advance opens the range of useful modulation frequencies and makes attractive the simple scanning of the sky as performed with photoconductors in the successful IRAS mission, or by balloon-borne bolometer experiments [Caux, 1986]. In the SAMBA concept, the sky is scanned along or near to a great circle by the rotation of the satellite, with no other type of optical modulation. A total power AC read-out circuit insures low noise down to the scanning frequency.

4 Conclusions

The best possible measurements of the CMB are limited in sensitivity by the statistical fluctuations of the observed radiation (photon noise) during the measurement, which is possible only if

the own noise of the detectors is low enough. The intrinsic noise of a bolometer depends mainly on the incoming power, on the specified time constant, and on its temperature. This noise can be made less than the photon noise from the sky in the millimeter range provided that three conditions are met: (1) the bolometer frequency response required by the observation strategy is not exceeding a few tens of hertz; (2) the temperature of the bolometer is low enough, i.e. 0.3 K or even 0.1 K for the fastest bolometers; (3) The bandwidth of the observed radiation is large, for example $\frac{\nu}{\Delta\nu} = 3$, in order to maximize the detected flux. In these conditions, the best available bolometer technology is good enough for photon noise limited photometry of the sub-millimeter and millimeter sky. These conditions are met in current projects based on bolometric detection for the measurement of CMB anisotropy, and especially for COBRAS/SAMBA. This is possible thanks to recent progresses in cryogenics for space and to new developments of read-out electronics allowing to use bolometers as total power measurements. For this type of wide band photometry bolometers are the best type of detectors in the 200 μm-5 mm wavelength range.

References

[1] Bennett C.L. et al., 1996, *COBE preprint* No. 96-01

[2] Benoît, A. et al., 1994, *SAE Technical Paper series* 941276.

[3] Benoît, A., 1995, *International Workshop on Bolometers for mm and submm Space Projects, Orsay, 15-16th June 1995*, IAS publication.

[4] Blanc, Y., 1996,*this conference.*

[5] Bouchet, F.R., 1996, *this conference.*

[6] Caux, E. and Serra, G., 1986, *A&A* 165, L5.

[7] Duband, L., 1995, *International Workshop on Bolometers for mm and submm Space Projects, Orsay, 15-16th June 1995*, IAS publication.

[8] Lamarre, J.-M., 1986, *Appl. Opt.* 25, 870.

[9] Lamarre, J.-M., 1995, *International Workshop on Bolometers for mm and submm Space Projects, Orsay, 15-16th June 1995*, IAS publication.

[10] Lange, A., 1996, *this conference.*

[11] Mather, J.C., 1982, *Appl. Opt.* 21, 6, 1125.

[12] Tauber, J., 1996, *this conference.*

[13] Torre, J.-P. and Chanin, G., 1985, "Miniature liquid ^3He refrigerator", *Rev.Scient. Instr.* 26, 318-320.

THE FAR INFRARED EXPLORER (FIRE)

Andrew E. Lange
California Institute of Technology, Pasadena, CA, U.S.A.

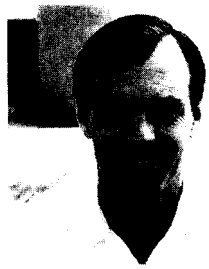

Abstract

The definitive map of the Cosmic Microwave Background (CMB) will ultimately be made by an orbital experiment operating at the earth-sun L_2 point, where systematic effects are minimized. The Far IR Explorer (FIRE) is a Midex-class mission concept designed to image the CMB over the entire sky from L_2 with 8′ resolution and 20 mK/pixel sensitivity. FIRE achieves this high performance using an advanced bolometric detector system. We describe the FIRE mission concept, with an emphasis on the detector technology developed specifically for this mission. Many aspects of the detector system developed for FIRE have been adopted by the High Frequency Instrument on COBRAS/SAMBA.

1 Introduction

The case for measuring the Cosmic Microwave Background (CMB) over the entire sky with high angular resolution and high sensitivity has been well made by other authors in this volume. Figure 1 compares the relative sensitivity of the two types of detectors currently in use to measure CMB anisotropy: high electron mobility transistors (HEMTs) and bolometers. Bolometers currently provide superior sensitivity to HEMTs over the entire range of frequency at which confusion from the Galaxy is small. Because they operate with high sensitivity at $\upsilon \geq 90$ GHz, bolometers enable higher angular resolution to be achieved with a given size aperture. In addition only bolometers currently provide the frequency coverage necessary to distinguish Sunyaev-Zel'dovich (SZ) anisotropy from CMB anisotropy, and thus to probe the

peculiar velocity field of the clusters of galaxies via the kinetic SZ effect. Finally, the stability of bolometric detector systems that has been achieved in recent years allows for simple and efficient scan strategies without the necessity of chopping to an internal load.

For all of these reasons, bolometers are an attractive choice for an orbital mission designed to measure CMB anisotropy, despite the requirement of cooling the detectors to sub-Kelvin temperatures. The FIRE mission concept grew out of an effort to understand if the advantages that bolometers possess for measurements of the CMB could be realized within the cost, volume and mass constraints of a MIDEX class mission.

The FIRE study team consisted of the science team and industry partners indicated in Table 1. The study included a substantial effort to advance the state-of-the-art of bolometric detector systems. The study was aimed at minimizing the cost and complexity of the system. The results were highly successful. As described below, advances in the detector technology made as a part of this effort reduced or eliminated all of the technical difficulties usually associated with implementing bolometric detectors and enabled high sensitivity to be achieved with a simple and flight-proven ^{3}He sorption refrigerator. Most importantly, the extremely high stability that was demonstrated enabled a scan strategy that greatly reduced the cost of the spacecraft. Due to these savings, the FIRE mission concept is surprisingly inexpensive; the total mission cost of FIRE was estimated to be well below the $70M Midex cost cap.

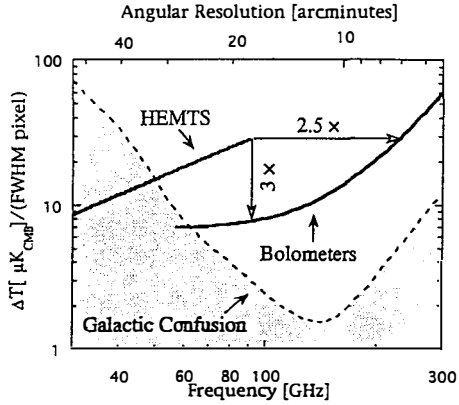

Figure 1. Bolometers have higher sensitivity than HEMTs over the entire frequency range in which confusion by Galactic emission (shown here as 3x the estimate for the Galactic pole) is at a minimum. The sensitivity that the FIRE detector system would achieve on each diffraction-limited pixel in an all-sky map is compared with that of state-of-the-art HEMT amplifiers cooled to 20K. (HEMTs operated at higher temperature would have worse performance.) At 90 GHz, the FIRE detector system provides 3x greater sensitivity than cooled HEMT amplifiers. At a given sensitivity level, the FIRE detector system is capable of operating at 2.5x greater frequency, and thus of providing 2.5x greater angular resolution (shown here for a 1.2m aperture). Not illustrated in this plot is the fact that the FIRE detector system is stable to below 0.03 Hz, eliminating the need for Dicke switching or a rapidly (>1 rpm) spinning spacecraft.

Table 1. The FIRE Study Team

Co-Investigators	Science Support Team
P.A.R. Ade, Queen Mary and Westfield College	C.A. Beichman, IPAC, California Institute of Technology
J.J. Bock, Jet Propulsion Laboratory	M. Birkinshaw, Harvard/Smithsonian Center for Astrophysics
F.R. Bouchet, Institut d'Astrophysique de Paris, CNRS	C. Cesarsky, Direction des Sciences de al Matiere, CEA
S. E. Church, California Institute of Technology	T.N. Gautier, Jet Propulsion Laboratory
M. Dragovan, University of Chicago	A.C.S. Readhead, California Institute of Technology
M.A. Janssen, Jet Propulsion Laboratory	G.H. Rieke, Steward Observatory, University of Arizona
J.M. Lamarre, Institut d'Astrophysique Spatiale	M.W. Werner, Jet Propulsion Laboratory
C. Lawrence, Jet Propulsion Laboratory	
J.L. Puget, Institut d'Astrophysique Spatiale	
J. Ruhl, University of California at Santa Barbara	
P.L. Richards, University of California at Berkeley	
D. Scott, University of British Columbia	
M. White, University of Chicago	

Participating Organizations	
Ball Aerospace Systems Division	Centre National D'Estudes Spatiales (CNES)/ Institut d'Astrophysique Spatiale (IAS) of France
California Institute of Technology	CTA Space Systems
Commissiariat à l'Energie Atomique (CEA) of France/Service de Basses Temperature	Jet Propulsion Laboratory

2 Mission Overview

FIRE is launched into an eclipse-free Lissajou orbit at L_2 using a lunar swingby, as illustrated in Figure 2. From this orbit, the Earth subtends 0.5° and is always within 5° of the Sun. The spacecraft rotates at 0.1 rpm about an axis that is always pointed directly at the Sun. The telescope boresight is oriented 90° to the rotation axis of the spacecraft. The entire sky is mapped once each six months. The FIRE mission is designed for a 20 month lifetime, providing 3 all-sky maps after reaching the L_2 orbit.

The advantages of this orbit and scan strategy are many. The orientation of the spacecraft relative to the sun is fixed. This simplifies the spacecraft, allows efficient passive cooling of the science instrument, and virtually eliminates temperature fluctuations of the optical system. Each scan in the mission is linked directly to the two ecliptic poles. Mission operations are simple, efficient and inexpensive. Data is transmitted daily without interrupting observations via a small fixed antenna pointed

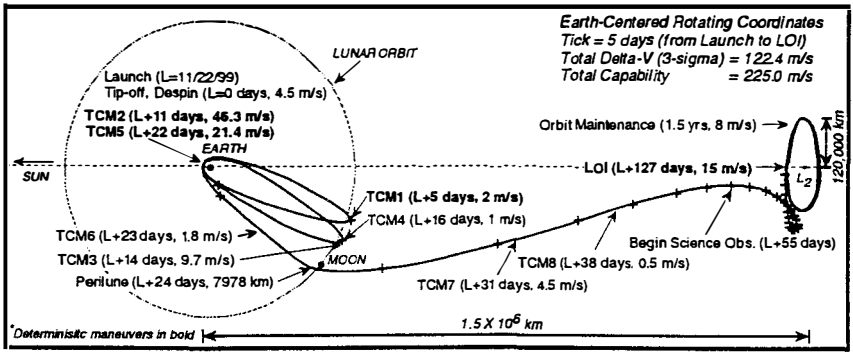

Figure 2 FIRE trajectory from launch to Lissajous orbit at L_2.

at the sun. The scan rate is sufficiently fast to ensure > 20 passes/pixel/detector at 8′ resolution, but slow enough to allow all of the data to be telemetered without onboard averaging or compression.

The FIRE instrument is shown in Fig. 3. The telescope is an all-aluminum 1.2 m, off-axis Gregorian. The secondary mirror forms an image of the primary close to the entrance aperture of a superfluid He (SfHe) cryostat that houses the detector system. The entire instrument is shaded from the Earth and the Sun by the spacecraft solar array. A passively cooled radiator intercepts conduction and radiation from the spacecraft. An analysis of the passive cooling of the science instrument is shown in Fig. 4. The predicted temperature for the telescope and the outer shell of the SfHe cryostat is 41K.

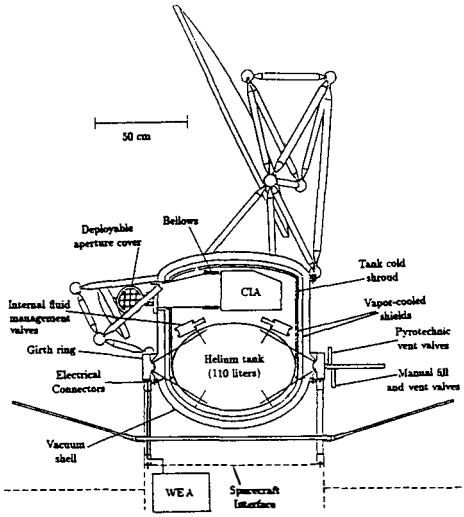

Figure 3. FIRE Science Instrument

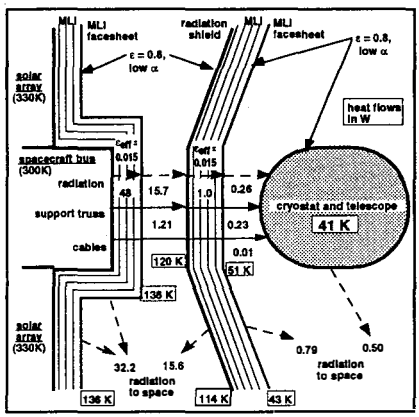

Figure 4. Thermal analysis of the FIRE passive cooling system. The predicted temperature of the telescope and cryostat outer shell is 41K. The temperature assumed in design study is a more conservative 60K.

3 Cryogenics

The focal plane instrument requires a 1.5 K heat sink. After considering several options, a conventional SfHe cryostat emerged as the optimum solution for FIRE. Passive cooling of the outer shell allows very high performance to be achieved from an otherwise conventional cryostat, as long as the mass and power dissipation of the instrument are kept small.

The FIRE cryostat, shown in Figure 3, contains 110 l of SfHe at launch, and has a wet mass of 100 kg. A comparison of the performance of the FIRE cryostat with the performance of the IRAS and COBE cryostats is given in Table 2. These estimates assume a 60 K outer shell temperature for FIRE, well above the predicted 41 K. The estimated lifetime is 29 months allowing ample margin over the 20 month

requirement. Note that the high performance relative to IRAS and COBE is due as much to the small (2 mW) instrument heat load as it is to the cold outer shell.

Table 2. Comparison of FIRE thermal performance with IRAS and COBE

	IRAS	COBE	FIRE
Vacuum Shell Temperature (K)	195	140	60
Size (liters)	540	640	110
Instrument Heat Load (mW)	16	33	2
Parasitic Heat Load (mW)	44	39	1.3
Predicted Lifetime Before Dewar Test (years)	1.06	1.04	2.5
Actual Lifetime (years)	0.88	0.84	–
% overestimate in prediction	20	24	–

The Cold Instrument Assembly (CIA) is bolted to the SfHe tank. The low mass (8 kg) of the CIA allows the full benefit of the small mass of the SfHe tank to be realized. Routine assembly tolerances provide adequate alignment between the CIA and the telescope mounting interface on the vacuum shell.

4 Cold Instrument Assembly

The CIA contains focal plane optics and filters, bolometric detectors, cooled GaAs FET pre-amplifiers, and a sub-Kelvin cooler in a single RF-tight enclosure that is designed to have a simple mechanical, thermal and electrical interface with the cryostat.

4.1 Focal Plane Optics

The FIRE focal plane, shown in Figure 5 comprises an array of 36 feeds: 4 dual–polarization feeds in each of 7 spectral bands spanning the frequency range 60 to 850 GHz, and 4 single–polarization feeds at 150 and 220 GHz. The sensitivity and angular resolution of each channel is given in Table 3.

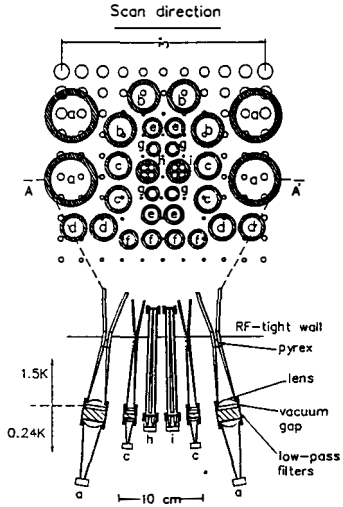

Figure 5. Schematic showing the layout of the FIRE focal plane viewed from the cold stop (above) and in cross-section (below). The calculated aberration as a function of field angle is shown superposed to scale over the feed apertures. The feeds are identified as follows: (a) 60 GHz dual-polarization (DP), (b) 100 GHz DP, (c) 150GHz DP, (d) 150 GHz single-polarization (SP), (e) 220 GHz DP, (f) 220 GHz SP, (g) 340 GHz DP, (h) 500 GHz multi-mode, (i) 850 GHz multi-mode.

Table 3. Angular Resolution and Sensitivity of the FIRE Baseline Mission[a]

Freq. [GHz]	Beam Width [arcmin]	P^{b}_{CMB} [pW]	$P^{b}_{telescope}$ [pW]	τ [ms]	NEP[c] $\times 10^{17}$ [W Hz$^{-1/2}$]	ΔT_{CMB}[d] Sensitivity [μKs$^{1/2}$]	Sensitivity/FWHM pixel[e] CMB ΔT [μK]	S-Z Δy[f] [10^{-6}]	Point Source [mJy]
60	27	0.23	0.04	170	1.5	160	7.0	7.0	43
100	18	0.25	0.08	110	1.5	120	8.3	9.0	43
150	12	0.23	0.16	75	1.5	90	9.6	13.7	37
220	8	0.14	0.28	50	1.7	120	19	–	40
340	5	0.04	0.52	30	2.0	350	81	28.7	47
500	5	0.01	1.90	30	2.4	1130	264	42.1	41
850	5	0.00	10.4	30	4.8	72000	17000	19000	54
150p[g]	12	0.12	0.08	75	1.5	260	27	38.7	105
220p[g]	8	0.07	0.14	50	1.7	350	54	–	113

[a] assumes: total optical efficiency = 40%; $\Delta\nu/\nu$ = 25%; telescope emissivity = $0.01\sqrt{\nu/340\ \mathrm{Hz}}$; telescope temperature = 60 K. Throughput: diffraction-limited at $\nu \leq 340$ GHz; $A\Omega = 10^{-2}$cm^{2}sr at $\nu \geq 500$ GHz
[b] at the detector
[c] Electrical Noise Equivalent Power of each detector, excluding amplifier and photon noise
[d] sensitivity to CMB anisotropy, including amplifier noise
[e] in the ecliptic plane for an 18 month mission
[f] sensitivity to the S-Z effect for a cluster with core radius 250 kpc, at redshift $z = 0.1$
[g] denotes polarization channels; sensitivities are for each component of linear polarization.

Each feed consists of a back-to-back feedhorn that controls the illumination pattern of the 1.5K cold stop, a filter stack that determines the spectral bandpass and provides out-of-band blocking, and a smooth-walled cone that concentrates radiation onto the detector. Each back-to-back feedhorn is embedded in the 1.5K wall of the CIA, providing an RF-tight seal.

We have built and tested a prototype 100 GHz dual-polarization feed. The measured optical efficiency is 42%, exceeding the FIRE specification. Adequate high frequency blocking was confirmed by blocking the in-band response and measuring the response to a chopped hot load.

4.2 Bolometric Detectors

Bolometric detectors have historically had five features that make them difficult to implement: cooling requirements, microphonic response, sensitivity to cosmic rays, out-of-band response and $1/f$ noise. A novel bolometer developed for the FIRE mission reduces or eliminates each of these difficulties. The detector is a composite bolometer comprising a Ge thermistor that is indium bump-bonded to a finely lithographed silicon nitride (Si_4N_3) mesh. These detectors have been developed at the JPL Center for Space Micro-electronics Technology (CSMT). Detectors based on this architecture are already in use in ground-based and balloon-borne CMB anisotropy experiments. Relative to the composite bolometric detectors that have been successfully flown on COBE and on the IRTS [1], the Si_4N_3 mesh detectors provide:

- higher sensitivity, due to the reduced heat capacity of the absorber and the thermistor
- lower microphonic response and higher strength, due to a 300x reduction in mass
- 20x smaller cosmic ray cross-section, due to the open mesh absorber
- 20x lower response to high frequency radiation, due to the open mesh absorber

- lower $1/f$ noise, due to the stress-free, low-impedance indium bump-bonded contacts
- more reproducible fabrication

The highest sensitivity is required at the lowest frequencies. A prototype detector optimized for the FIRE 60 GHz band has been fabricated and tested at 300 mK. This detector is measured to have an NEP of 1.2×10^{-17} W/$\sqrt{\text{Hz}}$ and a thermal time constant of 110 msec operated from a 310 mK heat sink. Based on conservative extrapolations from the performance of this detector to the optimization for the other frequencies, these detectors exceed all of the FIRE requirements in each band when operated from a 300mK heat sink. No further technology development is needed.

4.3 Cooled Pre-Amplifiers

The cooled preamplifiers must transform the detector impedance to <10kΩ, have gain stability of 10 ppm over 600s, have an input capacitance of <10 pF, and contribute no more than 28 nV/$\sqrt{\text{Hz}}$ to the detector output noise at the 500Hz bias frequency. Low power dissipation is critical to the lifetime of the SfHe cryostat; each channel must dissipate ≤0.03mW at 1.5K.

The baseline preamplifier is a GaAs MESFET (Metal Semiconductor Field Effect Transistor). The charge carriers in GaAs do not freeze out at low temperature. The GaAs FETs can thus be located inside the CIA and heat sunk directly to the 1.5 K stage. The proximity of detector and preamp results in high rejection of interference and minimal microphonic response.

We have successfully implemented a GaAs FET that meets all of the FIRE requirements in a prototype readout circuit, as described below. In order to probe the yield of devices that meet the voltage noise requirement, voltage noise was measured for 14 devices from 5 different manufacturing lots. Half had differential voltage noise < 22 nV/$\sqrt{\text{Hz}}$ at 500 Hz, and 12 of 14 had voltage noise < 28 nV/$\sqrt{\text{Hz}}$ at 500 Hz. The baseline sensitivity of FIRE has been calculated assuming 28 nV/$\sqrt{\text{Hz}}$.

4.4 Sub-Kelvin Cooler

The sub-Kelvin cooler must provide 1 μW of cooling power at 240 mK, and operate from a 1.5K heat sink with a time-average power dissipation of <1.0 mW.

The baseline design is based on a cooler that has been successfully operated in orbit [2][3]. The cooler is a ^{3}He sorption cooler that has no moving parts and can be recycled indefinitely with high (>95%) duty cycle. An activated charcoal cryo-pump cools ^{3}He liquid that is confined by surface tension to a silicose sponge. The cooler is recycled using gas-gap heat switches and a heater to (i) isolate the pump and thermally ground the evaporator, (ii) heat the pump to 40 K, condensing the desorbed gas in the evaporator, (iii) isolate the evaporator and ground the pump. The IRTS cooler was successfully cycled 3 times in orbit during the 40 day IRTS mission and each time achieved a temperature of 301 mK.

The FIRE baseline cooler is a two-stage cooler, each stage of which closely resembles the IRTS cooler. The thermal circuit of the two stage FIRE cooler is shown in Figure 6. The first stage thermally buffers the second and cools a thermal guard ring that creates a stable thermal environment for the detectors.

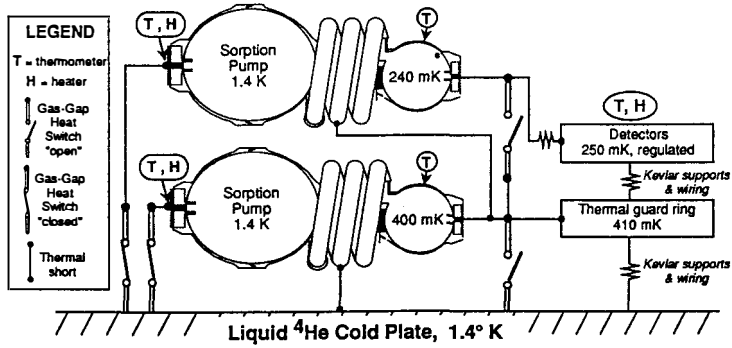

Figure 6. The thermal circuit of the FIRE sub-Kelvin cooler.

The performance of the FIRE cooler has been analyzed using the same models that successfully predicted the performance of the IRTS cooler on orbit. Each stage contains 100 STP liters of ^{3}He. The first stage achieves a temperature of 400 mK, a lifetime between re-cycles of 220 days and a duty cycle efficiency of 98%. The second stage achieves a temperature of 240 mK and a lifetime of 750 days between recycles. Its temperature will elevate to 300 mK during the 2% of the mission that the first stage cooler is being recycled. The total time-averaged power dissipation to the 1.4 K heat sink is 0.9 mW.

5 Warm Electronics Assembly

The WEA (Figure 7) resides in the spacecraft and contains all of the warm electronics that support the science payload module. These include: 44 channels of chopper stabilized, low-noise amplifiers for the focal plane, two PID temperature control circuits that regulate the 250 mK stage, A/D converters and multiplexors, drive electronics for the cryostat thermometry and motor-operated lid, an RTIOU control/interface to the 1553 spacecraft data bus, and DC/DC switching power regulators. These electronics are distributed among nine slices that are isolated from each other. The WEA is 31 cm x 31 cm x 19 cm, has a mass of 8.66 kg and dissipates 45 W.

5.1 Readout Electronics

The warm readout electronics provide a stable measure of the bolometer signals. They must have <10 nV/$\sqrt{\text{Hz}}$ input noise, 10 ppm gain stability over 100s and a dynamic range adequate to resolve 50 nV on a DC level of 10 mV.

A block diagram of the baseline design is shown in Figure 7. A prototype of this circuit has been built and tested. The measured performance, shown in Figure 8 meets the requirement of the FIRE Baseline Mission.

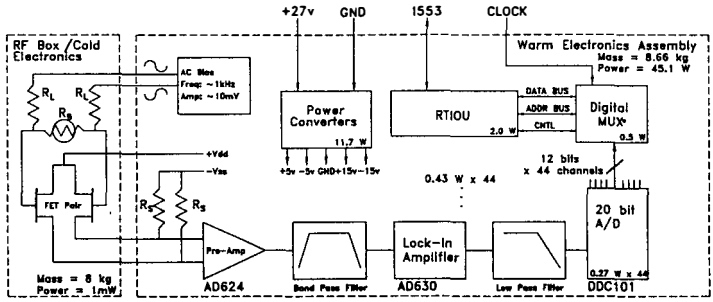

Figure 7. The FIRE readout electronics have been fully prototyped and tested, from detector through 20bit A/D. Shown here is a block diagram of the readout electronics contained in the CIA and the WEA. Interface with the spacecraft consists of a clock line, 1553 data bus, and unregulated power. The performance of the prototype readout electronics is shown in Figure 8.

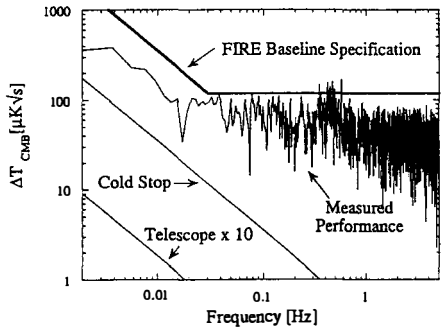

Figure 8. The stability of the FIRE prototype detector system exceeds specifications. The uppermost curve shows the requirement for the noise power spectral density in order that the $1/f$ noise makes a negligible contribution to the final map at the baseline 0.1 rpm spin rate. The data are the measured noise spectrum of a prototype 100 GHz detector coupled to the proto-flight electronics shown in Figure 7. The voltage noise has been scaled to ΔT_{CMB} sensitivity using the measured optical efficiency of the prototype 100 GHz radiometer. The feature near 0.5 Hz is due to the active temperature control of the detector heat sink. Also shown are the two contributions to $1/f$ noise that cannot be simulated in the laboratory, scaled to 100 GHz: (1) fluctuations in telescope temperature driven by a 10 C° p-p fluctuation at the spacecraft, (2) fluctuations of the cold stop temperature driven by a 10% change in CIA power dissipation to the SfHe bath (equivalent to a 100% change in sub-Kelvin cooler power dissipation). Both contributions are well below the baseline specification at all frequencies.

Each detector is sampled at 16Hz. The 2 LSB and the 6 MSB of the 20 bit signal are discarded, leaving a digital signal with resolution equal or better than the rms noise level and a 12 bit dynamic range, adequate to observe the brightest sources in the sky without saturation. The 20 bit A/D ensures that the DC bolometer level will not saturate the A/D under any operating conditions. Discarding the 6 MSB is a simple and

effective means of data compression that removes the absolute zero level from the high bandwidth data. The full 20 bit samples are recorded at a lower (1 Hz) sampling rate as part of the housekeeping data stream.

The 36 element focal plane is divided into 4 stand-alone modules, each driven by an independent bias oscillator. The entire science instrument upstream of the digital multiplexor is thus protected against single point failure.

6 Conclusions

The results of our design study indicate that passive cooling to T < 60 K is straightforward given the proper orbit and scan strategy. This outer shell temperature together with a low instrument heat load allow a SfHe cryostat containing 110 l of SfHe and with mass 100 kg to provide cooling to T < 1.5 K with a lifetime of over 2 years. The SfHe cryostat creates no acoustic or electrical noise, consumes no power on orbit, and allows full testing of the detector system just before launch. The most difficult constraint in incorporating a SfHe cryostat into a Midex mission is schedule, since the cryostat presents a long lead-time item that must be completed before system integration can begin.

A flight-ready bolometric detector system developed at Caltech and JPL meets all of the specifications for FIRE at a heat sink temperature of 300 mK, and provides high sensitivity from 60 to 1000 GHz. The broad spectral coverage allows accurate separation of CMB anisotropy from Galactic and extra-galactic foregrounds, and allows the SZ effect to be cleanly separated from intrinsic CMB anisotropy. The demonstrated stability of the detector system reduces demands on the spacecraft attitude control, data handling and telemetry, resulting in a substantial cost and mass savings. As a result, the FIRE concept fits will within the Midex cost, mass, and volume constraints.

Though FIRE was not selected for flight within the Midex program, many of the technologies developed for FIRE have been adopted for use in the High Frequency Instrument on COBRAS/SAMBA.

This work was supported by a NASA New Mission Concept award (RTOP No. 440-50-00-10), by NASA Innovative Research Grant NAGW-4754, and by JPL. The FIRE concept study was initially stimulated by Peter Mason of JPL. The FIRE science team benefited greatly from the superb technical, management and costing support provided by JPL during the concept study. We are particularly grateful to Charles Elachi, Steve Levin, Peter Mason, Bill McLaughlin, Sylvia Miller, Bob Oberto, Leigh Rosenberg, and Rod Zeiger for their support of this effort.

References

[1] Devlin et al. 1993, *IEEE Trans. on Nuc. Sci.*, **40**, 162
[2] Duband et al. 1992, *Cryogenics*, **30**, 263
[3] Lange et al. 1994, *Astrophys. J.*, **428**, 384

SAMBA
SAtellite for Measurements of Background Anisotropies

Yvan Blanc
Centre National d'Etudes Spatiales, 18, avenue E.Belin, 31055, Toulouse, France

ABSTRACT

SAMBA is a proposal for a small space mission, whose goal is to provide mapping of the CMB fluctuations at angular resolutions from 20 arcmin to several degrees with a sensitivity and an angular resolution more than one order of magnitude than COBE. The purpose of this paper is neither to describe the scientific goals of SAMBA, neither details on detectors or other hardware but to briefly describe some particulars aspects and technical developments of the SAMBA mission.

1.INTRODUCTION

The SAMBA concept was born as an answer the call for new idea for small missions made by CNES in 1993 and was translated to answer the ESA/AO for M3 missions. This concept merged with the COBRAS proposal gave the COBRAS/SAMBA mission. On the US side, the FIRE mission with similar goals but different solutions for cryogenics is being submitted to the MIDEX AO.
The SAMBA project is presented to CNES by several scientific institutes with IAS (Institut d'Astrophysique Spatiale) as payload PI (Principal Investigator). It is now under phase A by CNES to be concluded in April 96, and completes for the first opportunity of a launch as early as mid 2000. The final choise will occur by mid 96.

2.SCIENTIFIC GOALS

The basic goal of SAMBA is to produce mapping of the CMB fluctuations in several channels (0.3 - 6mm range) with a sensitivity per pixel full sky 2 years mission $\partial T/T \approx 10^{-6}$ and an angular resolution between 20 arcmin to 7 degrees. Secondary goal is to measure the Sunyaev-Zeldovich effect on several hundred clusters of galaxies and to obtain constraints on the fundamental cosmological parameters (Ω_0, H, Ω_B).

3.MISSION PROFILE

The scientific goals previously described will be satisfied by a space mission using very sensitive detectors like bolometers to survey the sky in the 0.3 - 6 mm range.
The volume of the budget of the "small mission" program favors a cheap orbit. A preliminary mission analysis showed that a sun synchronous orbit at 825 km to 1000 km with a zenital line of sight offers (figure 1):
- a complete sky coverage over a period of 6 months,
- the orbit plan rotates as to the sun perpendicular to the line of sight,
- Moon shadows zones of 3 by 40° appear near the ecliptic plane (space out 27°). Over one year period, a shift of 9° permit to observe the hiden zones of the before half-year.

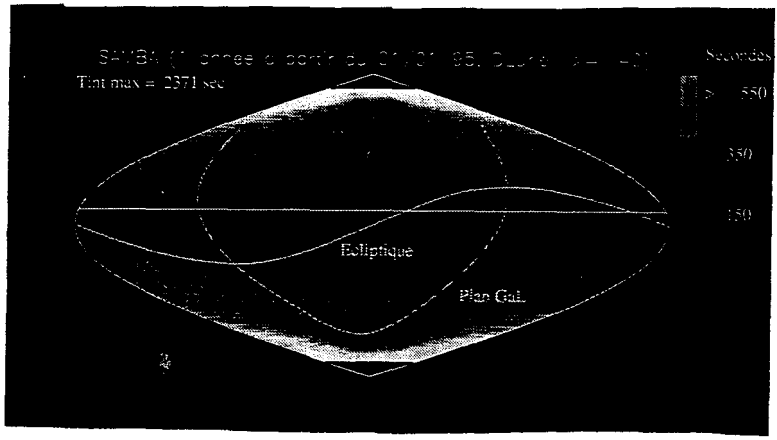

Figure 1: SAMBA sky coverage (one year of observations integration time)

The low altitude of the orbit implies careful payload design from the straylight rejection and thermal stability.
The SAMBA mission is compatible with several launchers (EUROCKOT, TAURUS, LLV ,PSLV).

4.MODEL PAYLOAD

The model payload (figure2) presently under study includes:
- a telescope with a 80 cm primary mirror focusing the signal to be detected on the focal plane assembly called also bolometer box,
- a system of baffles at respectively 150 K and 100 K, these baffles are also the sunshades of the telescope,
- the associated subsystems necessary to the operationnal running of the instrument, like cooling system (figure 3) and associated electronic boxes.

The low temperature required by the bolometers (0.1 K) must be provided by an active precooling system 60K and 4K cryocoolers (RAL and MMS developments sponsored by ESA) coupled to an open-cycle He dilution refrigerator (CRTBT/Grenoble sponsored by CNES). A cooling dilution system power of 100 nW at 0.1K has been demonstrated.

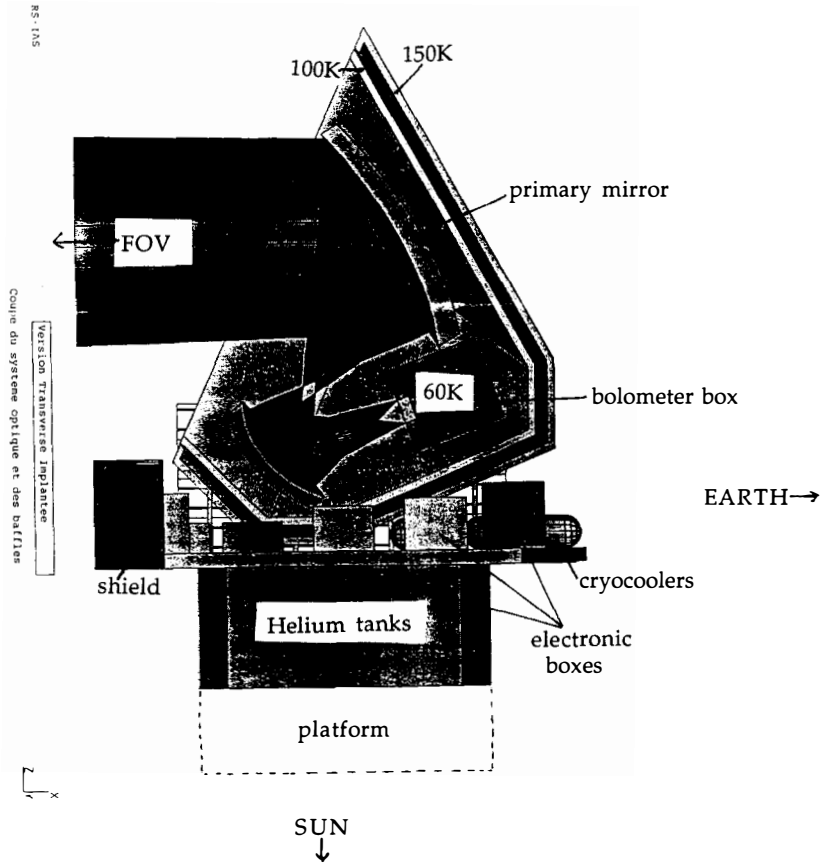

Figure 2: SAMBA model payload

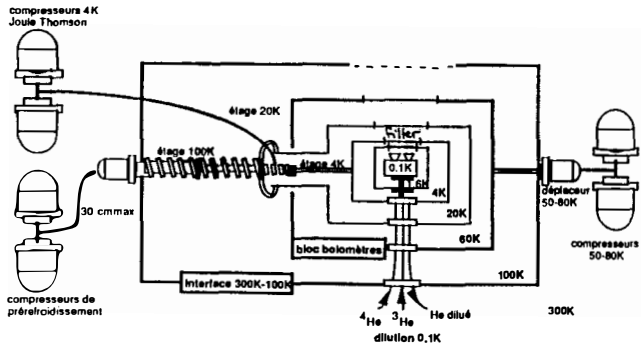

Figure 3: SAMBA cooling system

The bolometer box (figure 4) includes the detectors, the 0.1 K dilution refrigerator stage, the light concentrators, the filters to select wavelengths, the different shields and boxes necessary for thermal reasons.
At this time, seven channels have been selected to cover the range (857 to 53 GHz) with previous sensitivities per pixel over a full sky 2 years mission giving in figure 5.

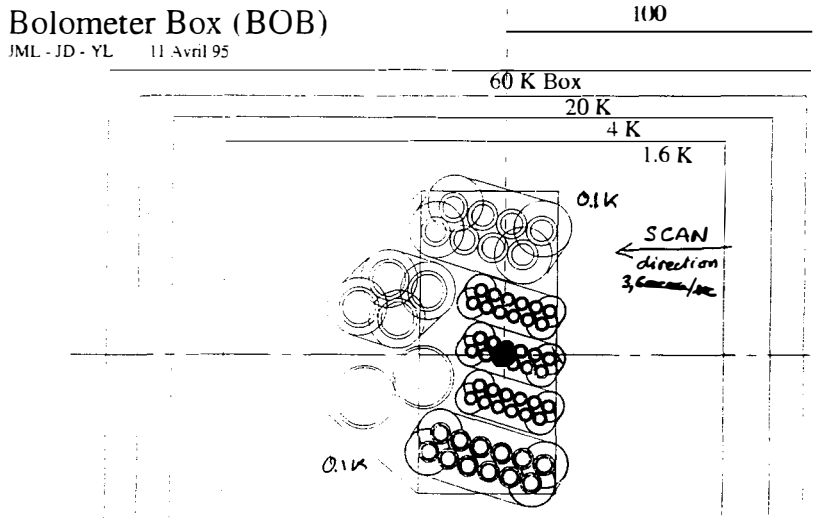

Figure 4: SAMBA bolometers box

Channels	1	2	3	4	5	6	7
Central Frequency (GHz	857	545	353	217	150	90	53
Central Wavelength (mm)	0.35	0.55	0.85	1.38	2.00	3.33	5.66
Pixel diameter (arcmin)	7.8	7.8	7.8	12.7	18.4	30	52
ΔT Sensitivity per pixel full sky 2 years mission (μK Rayleigh-Jeans)	0.45	0.7	1.2	0.85	0.85	0.9	0.66

Figure 5: SAMBA channels

5.PAYLOAD PROGRESS REPORT OF TECHNOLOGY

Payload phase A studies have been achieved:

- the optical design of the telescope consists in an off-axis tilted Gregorian system with a parabolic primary mirror of 0.80 m. This size is restricted by the fairing envelope. A possible increase of this size will be studied during phase B,

- simulations demonstrate that the final sensitivity is not affected by the side lobe rejections constraints,

- general CAO establishments have been performed,

-mechanical studies (first mode, impact resistance, clamping system, efforts on the colfinger tip) confirm the design,

- thermal studies with thermal decoupling between the payload and the platform show a thermal environnement of telescope and bolometers box near 100 K.

Several actions of research and technologic program and parallel developments are in progress:

- the MOB program (Matrix Of Bolometers) funding by CNES consists in the development of 2 lines of 4 bolometers cooling at 0.1 K. The objective is to produce bolometers with a NEP $\approx 10^{-17}$ w$\sqrt{Hz}$ (IAS development)

- the SYMBOL program (SYstem aspects for Measurement by BOLometers) funding by CNES procures a complete testing bench for matrix of bolometers (like temperature fluctuations compensations,read out electronics...) (IAS development)

- an other very crucial action is a common action funding by CNES and ESA is called "300 K- 0.1 K demonstrator".
This action consists to assembly and spatialize the cryogenic architecture of SAMBA with a precooling 300 K to 4 K by mechanical cryocoolers developed by RAL and MMS-Bristol, and the final cooling 4K to 0.1K with the dilution system developed by CRTBT/Grenoble. The other goal of this action is to validate the use of this architecture with bolometers.
At this time an engeneering prototype model 1.6K to 0.1K has been manufactured by CRTBT. The principle of the cryogenic architecture and the zero-g compatible 0.1K stage have been succesfully tested in vibrations and thermal performances.
The fully demonstration of this action (IAS development) is expected by end 1997.

The DIABOLO ground experiment consisting in a photometer with 2 bolometers (1 and 2 mm diameter) has validated the assembly of the 0.1K cryogenic dilution with bolometers and original read-out electronics during ground observations (IRAM telescope...).

6.THE SPACECRAFT

SAMBA has been studied in the context of the CNES Small Satellite Initiative concerning the development of a reconfigurable multimission platform called PROTEUS. This initiative concerns a new satellite product line with a total cost of 300 MF (≈ 50 MUSD) and a 2-3 years development phase. Three potential missions have been selected mid-95. These missions are for astronomy SAMBA and COROT and the Topex Poseidon Follow On mission for earth studies.
SAMBA is fully compatible with the PROTEUS concept and the main caracteristics of the mission in this context are listed in figure 6.
The satellite is 3-axis stabilized with a zenital field of view. The total mass is approximatively 500 kg and dimensions are compatible with a 2 m fairing diameter small launcher (Rockot,LLV,Taurus). The restitution of the LOS telescope is assumed with a star tracker aligned with it. Telemetry data collection and communications are assumed by a 2 Giga-octets on-board memory and a dedicated band-S ground station.

7.CONCLUSION

We have shown that an existing CMB measurements mission can be planned with a small budget (60 M$). Working in a low orbit, it will be able to output calibrated full-sky maps ranging in frequency from 75 to 850 GHz and in angular resolution from 20 arcmin to 7°.
Developp PROTEUS seems a strong recommendation of the French government to CNES and the first mission in this context will be the TPFO one wich flight is scheduled in 99.
Scientists have an unique advisability to have SAMBA as the second PROTEUS mission with a launch mid 2000 (figure 7).

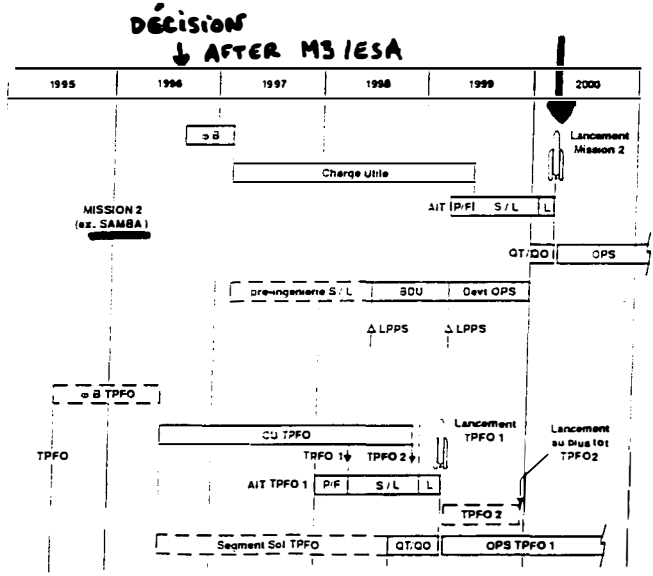

Figure 7: SAMBA schedule

SAMBA

Scientific goals

Measurements of the CMB anisotropies (2.726 K) at angular resolution from 20 arcmin to 7°, with a sensitivity per pixel $\Delta T/T \approx 10^{-6}$, in the frequency range 75 to 850 GHz.
Detection of the Sunyaev-Zeldovich effect in 3 channels
Constraints on the fundamental cosmological parameters ($\Omega 0, H, \Omega B$)

Payload

Télescope - off-axis Gregorian (primary Ø 80 cm, secondary Ø 45cm)
- passive cooling at 100 K (baffes at 150K and 100K

Focal plane - bolometers cooled at 0.1 K
- wavelength channels 6 mm to 0.35 mm
- precooling by mechanical cryocoolers at 60 K
- cooling of the focal plane by cryocoolers at 4 K associated with a Helium dilution refrigerator at 0.1 K

Observation mode sky coverage by zenital pointing and rotation of the orbit plane
Lifetime 1.5 to 2 years (limited by the Helium tanks capacities)

Satellite

Type 3-axis stabilization with a zenital line of sight (LOS)
Mass 470 kg(platform 220 kg and payload 250 kg)
Structure 3.2m heigh x 2m diameter
Electric power 400 W maxi.by deployed solar panels (payload:240 W nominal,114 W launch)
Pointing precision of 0.2° , stability 0.07° per second restitution 0.02° by startracker calibrated with the payload LOS
Communications dedicated S-band ground station, TC=4 Kbps, TM<300 Kbps
Storage on board memory 480 Mbits/day
Launch >2000 (LLV,Taurus,Rockot...)
Orbit 825 km sun synchronous orbit(820 to 1000 km) period of 101.4 min

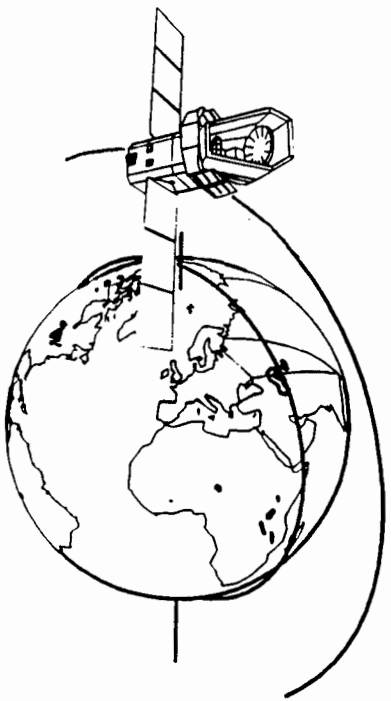

CT/ED/TV/EI - Y.BLANC

Figure 6: SAMBA mission characteristics

COBRAS/SAMBA
The definitive Cosmic Microwave Background anisotropy mission

Jan A. Tauber[1]
European Space Agency, Space Science Department, Keplerlaan 1, 2201AZ Noordwijk, The Netherlands

Abstract

The primary objective of the COBRAS/SAMBA mission is to image the temperature anisotropies of the Cosmic Microwave Background (CMB) radiation field, to a sensitivity level of $\Delta T/T \sim 2\times10^{-6}$ (T$\sim$ 2.726 K) and with an angular resolution of 10 arcminutes. To achieve this objective, it will survey the whole sky in nine frequency bands ranging between 30 GHz and 900 GHz, with an angular resolution varying between 30 and 4.5 arcminutes. The spectral information will be used to subtract from the observed signal the emission due to our own and other galaxies, and recover the primordial (CMB) information. The maps of the CMB fluctuations will be used to test models of the early Universe, determine fundamental cosmological parameters to a precision of a few percent, investigate the initial conditions for the formation of structure, and constrain the nature of the dark matter. In addition, detection of the Sunyaev-Zeldovich effect in thousands of rich clusters of galaxies will allow the study of their properties and evolution. Finally, catalogues of extragalactic sources and maps of our own Galaxy will yield a wide spectrum of astrophysical science.

1 Introduction

COBRAS/SAMBA is a mission devoted to the study of the temperature fluctuations - often called anisotropies - of the Cosmic Microwave Background radiation field (CMB). The scientific objectives and capabilities of COBRAS/SAMBA are presented elsewhere in these proceedings, and thus we here concentrate on a brief description of its technical characteristics. For completeness' sake a summary of the scientific areas addressed by COBRAS/SAMBA is shown in Table 1. A general overview of the technical description is shown in Table 2.

[1]This article is based on the results of ESA's COBRAS/SAMBA Phase A Study, which are presented in more detail in the Phase A Report, ESA D/SCI(96)3. The Science Team leading the Study included M. Bersanelli, M. Griffin, J.M. Lamarre, N. Mandolesi, H.U. Norgaard-Nielsen, O. Pace (Study Manager), J. Polny, J.L. Puget, J. Tauber (Study Scientist), and S. Volontè. The industrial part of the study was carried out by a team of engineers from Matra Marconi Space (Toulouse), led by C. Koeck. Technical support was also provided by specialists from the ESA Technical Directorate (ESTEC) and the Directorate of Operations (ESOC). Many other people contributed to various scientific and technical aspects of the Study; their names are too numerous to list here, but we wish at least to acknowledge the substantial contributions by F. Bouchet and G. Efstathiou.

But first, a word of history: in response to ESA's call for M3 proposals, two projects were presented devoted to the study of the anisotropies of the CMB. COBRAS (Cosmic Background Radiation Anisotropy Satellite) and SAMBA (Satellite for Measurement of Background Anisotropies) were both conceived as 1 meter-class telescopes, each carrying broad-band detection systems at four different frequencies, in the case of COBRAS in the range 30 to 130 GHz, and in that of SAMBA 140 to 800 GHz. COBRAS and SAMBA together span a range of frequencies which, due to technical limitations, would be impossible to achieve for each of them alone. Early on in the Assessment phase it was recognized that to meet its scientific objectives COBRAS/SAMBA would have to provide the widest possible frequency range. Therefore, the two original (COBRAS and SAMBA) instruments were merged into a single payload. Since then, the combined project has been studied at the Assessment and Phase A levels by ESA, and shown both to be capable of meeting its scientific objectives and of fitting within the (financial and technical) constraints of a medium-sized mission.

Table 1. Scientific areas addressed by COBRAS/SAMBA

Component	Area	Highlights
CMB	Cosmology & origin of structure	• Initial conditions for structure evolution • Constraints on particle physics at energies $>10^{15}$ GeV: – Origin of primordial fluctuations – Testing and characterizing inflation – Testing and characterizing topological defects • Constraints on the nature and amount of dark matter • Determination of fundamental parameters: – Ω_0, H_0, Λ to 1% – Ω_b, Q_{rms}, n_s to a few %
SZ	Cosmology & structure evolution	• Measurement of y in $>10^4$ clusters • Estimate of H_0 from y and X-ray measurements • Cosmological evolution of clusters • Bulk velocities (scales >300 Mpc) out to $z \simeq 1$ with $\Delta v \simeq 50$ km/s
Extragalactic sources	Cosmology & structure formation	• Source catalogues of – IR and radio galaxies – AGNs, QSOs, blazars – inverted-spectrum radio sources • Far-infrared background fluctuations • Evolution of galaxy counts
Dust emission	Galactic studies	• Dust properties • Cloud and cirrus morphology • Systematic search for cold cores
Free-free and synchrotron		• Determination of spectral indices • Cosmic ray distribution • Magnetic field mapping

2 Scientific Requirements

The ambitious scientific objectives of COBRAS/SAMBA can only be met by fulfilling a number of stringent experimental specifications:

- Very high sensitivity ($\Delta T/T \sim 10^{-6}$), requiring the use of state-of-the-art detection techniques.
- The ability to probe all angular scales between ~10 arcminutes and 180° . The 10' angular resolutions sets the size of the effective aperture of the payload telescope to be of order 1 meter in diameter.
- The ability to survey a large fraction of the sky, to improve the statistical properties of the data set.
- Coverage of a large range of frequencies, to monitor and separate the emission from all potential foreground sources. By simulation the required frequency range has been specified as ~30-800 GHz, requiring two technologically different types of detectors: tuned radio receivers at low frequencies and bolometers at high frequencies.

In addition to these basic requirements, the payload must be designed with the goal of reducing its sensitivity to systematic effects, mainly those due to straylight and thermal modulation.

The COBRAS/SAMBA mission is designed to comply with all of these requirements. In fact, our best current knowledge indicates that at the 10' angular scale, residual foreground fluctuations will limit any attempt to exceed the goal sensitivity levels of COBRAS/SAMBA , thus justifying its description as a "definitive" experiment.

Table 2. COBRAS/SAMBA Mission Summary

PAYLOAD									
Telescope	1.5 m Diam. Gregorian; shared focal plane; system emissivity 1% Viewing direction offset 70° from spin axis.								
Center Frequency (GHz)	31.5	53	90	125	143	217	353	545	857
Detector Technology	HEMT radio receiver arrays				Bolometer arrays				
Detector Temperature	~100 K				0.1-0.15 K				
Cooling Requirements	Passive				Cryocooler + Dilution system				
Number of Detectors	4	14	26	12	8	12	12	12	12
Angular Resolution (arcmin)	30	18	12	12	10.3	7.1	4.4	4.4	4.4
Optical Transmission	1	1	1	1	0.3	0.3	0.3	0.3	0.3
Bandwidth ($\frac{\Delta\nu}{\nu}$)	0.15	0.15	0.15	0.15	0.37	0.37	0.37	0.37	0.37
$\frac{\Delta T}{T}$ Sensitivity per res. element (14 months, 1σ, 10^{-6} units)	7.8	7.5	14.4	35.4	1.2	2.0	12.1	76.6	4166

SPACECRAFT	
Launcher	Ariane 5 (Dual- or triple-launch Configuration, SILMA Fairing)
Orbit	Lissajous around Sun-Earth L2 point
Stabilization	Spinner at 1 rpm
Pointing (2σ)	2'.5 a posteriori
Lifetime	1.5 yrs baseline, 5 yrs extended
Operations	10-11 hr per day contact; one ground station
Total mass	1523 kg
Total power	693 W

3 Model Payload Architecture

There are three basic payload components: (1) a telescope and baffling system, providing the angular resolution and rejection of straylight; (2) the Low Frequency Instrument (or LFI) – arrays of tuned radio receivers, based on HEMT amplifier technology, and covering the frequency range ~30 - 135 GHz; and (3) the High Frequency Instrument (or HFI) – arrays of bolometers covering the frequency range ~116 - 900 GHz. The LFI and HFI are both placed in the focal plane formed by the telescope, and share the focal area equally. This arrangement maximizes the optical throughput to each instrument, while keeping off-axis aberrations to an acceptable level.

The temperature requirements of the two types of detector are very different, the HEMTs giving adequate performance at 100 K (achievable by passive cooling), while the bolometers must operate at temperatures between 0.1 and 0.15 K to achieve the required performance. Thus, while the LFI will simply consist of an array of corrugated horns feeding miniaturized receivers, the bolometers must be placed inside a "cold box" consisting of a series of nested radiation shields, and cooled by an open-cycle dilution refrigerator coupled to a mechanical 4 K cooler.

A schematic overview of the arrangement of the payload is shown in Figure 1(a).

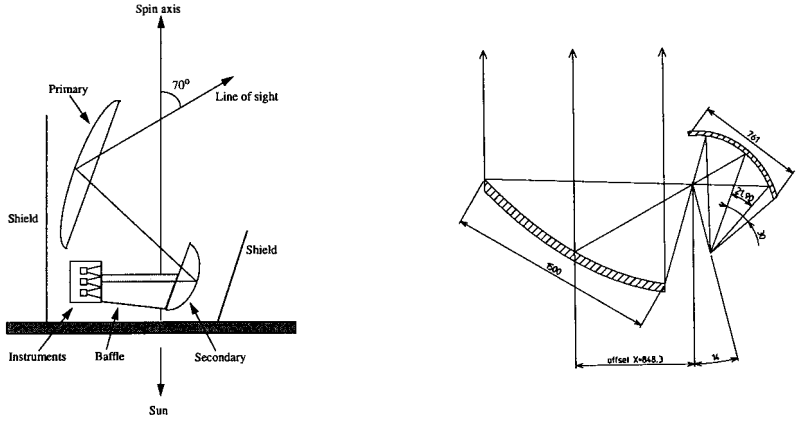

Figure 1: (Left) A sketch of the geometric architecture of the payload. (Right) A sketch of the configuration of the mirrors. Linear dimensions are in mm and angular dimensions in degrees. The offset of the main mirror is marked in the direction perpendicular to the telescope boresight.

3.1 The telescope and baffling system

The telescope (see Figure 1b) consists of an off-axis tilted Gregorian system, offering the advantages of no blockage and compactness. The eccentricity and tilt angle of the secondary mirror, and the off-axis angle obey the so-called Dragone-Mizuguchi condition, which allows the system to operate without significant degradation in a large focal plane array, while simultaneously minimizing the polarization effects introduced by the telescope.

The baffling system is composed of two elements. The first (the "shield") is a large, self-supporting, and roughly conical structure covered with MLI, which surrounds the telescope and focal plane instruments. Together with the payload platform or optical bench, it defines the payload (or optical) "enclosure" (see Figure 1). It has an important function in reducing the level of straylight (which at the chosen orbit is in large part due to the spacecraft itself) and in promoting the radiative cooling

of the enclosure towards deep space. The second element (the "baffle") consists of one half of a conically shaped surface that links the focal plane instruments to the bottom edge of the subreflector; its function is to shield the detectors from thermal radiation originating within the enclosure.

The primary and secondary mirrors will be fabricated using Carbon Fibre (CFRP) technology, taking advantage of the experience accumulated in the design and development of the FIRST (the Far Infrared and Submillimetre Telescope, an ESA cornerstone mission) telescope.

3.2 The Low Frequency Instrument

The LFI (see Figure 2) is designed to cover the 30 - 135 GHz band, with an array of 56 detectors split into 4 channels, centered at 31.5, 53, 90, and 125 GHz. Radiation will be coupled from the telescope to the detectors via conical corrugated feedhorns exploiting the two orthogonal polarizations at a given frequency. Thus, each horn feeds two receivers. Each receiver consists of a pair of amplification/detection chains connected in parallel via so-called hybrid rings, and constitutes a "continuous-comparison" device. In this scheme, the difference between the inputs to each of the chains (the signal from the telescope and that from a reference blackbody respectively) is continuously being observed. Each amplification stage will be provided by High Electron Mobility Transistors (HEMTs). This technology offers at present the best compromise between sensitivity and ease of implementation in the frequency range of the LFI. Total power receivers based on Monolithic Microwave Integrated Circuit (MMIC) technology, in which the whole receiver is packed into a device a few centimeters across, are state-of-the-art but already available commercially with characteristics close to those required by COBRAS/SAMBA .

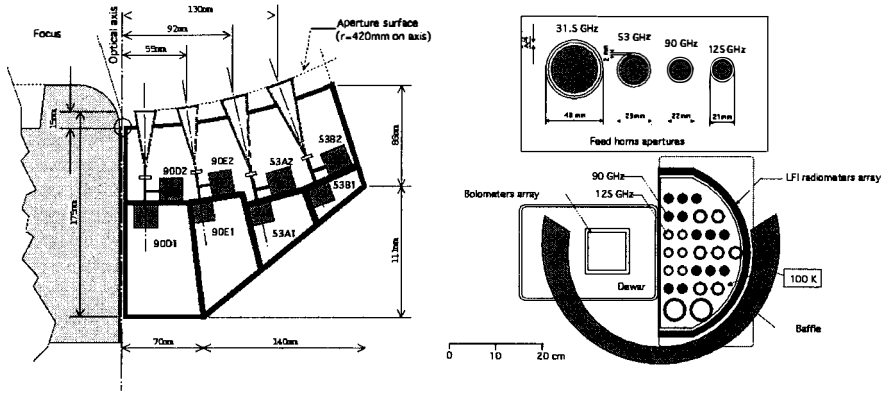

Figure 2: Side and top view of the LFI, the former showing the horn/receiver arrangement, and the latter the layout of the feed apertures in the focal plane.

3.3 The High Frequency Instrument

The HFI (see Figure 3) will cover the high frequency part of the COBRAS/SAMBA range. The heart of the HFI – the detectors – are bolometers, solid-state devices in which the incoming radiation dissipates its energy as heat that increases the temperature of a thermometer. For a bolometer, the temperature increase is inversely proportional to the heat capacity of the bolometer. The cooling of these detectors to very low temperatures provides for the low heat capacity needed for high sensitivities. In the case of COBRAS/SAMBA , the HFI bolometers must be cooled to temperatures of ~ 0.1 K.

The total number of bolometers will be 56, split into 5 channels at central frequencies of 143, 217, 353, 545, and 857 GHz. The placement of the channels in frequency space has been optimized

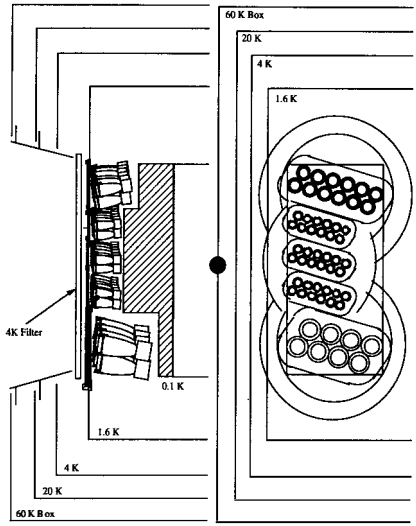

Figure 3: A conceptual view of the HFI "cold box", which consists of nested radiation shields maintained at various temperatures by the active cooling system. The side view shows the optical arrangement, including the 4 K blocking and 1.6 K bandpass filters, and the Winston cones. The top view shows the detector layout and filter outlines.

not only to remove the foregrounds (mainly dust emission at these high frequencies) and recover the CMB, but also for the detection of the Sunyaev-Zeldovich effect. Filters provide the necessary frequency selectivity for each channel, and also block the thermal radiation coming from the telescope itself. Light from the telescope will enter the cold box through an initial blocking stage at 4 K, proceed through a second bandpass filter at 1.6 K made from interfering cross-shaped grids embedded in a polyethylene matrix, and will finally be concentrated on the detectors by Winston cones. The entrance apertures of the cones define the fields of view of the detectors; they are sized to the diffraction pattern in the three low frequency channels, and oversized in the two highest frequency channels in order to cope with the aberrations of the telescope. The bolometers are read out via J-FETs located very close to them, in a box which is physically located inside the cold box of the HFI, but thermally insulated from it. The readout electronics are based on the principle of AC bias that has successfully demonstrated (in ground-based experiments) its capability to detect signals at very low frequency without sky-chopping.

The low temperature required by the bolometers (0.1 K) must be provided by an active cooling system, which will consist of a number of Stirling-cycle mechanical coolers coupled to an open-cycle He dilution refrigerator. The mechanical coolers will provide precooling of ^{3}He and ^{4}He cryogen down to 4 K, as well as control of the temperature of the outermost radiation shield of the HFI to ~65 K; the dilution system (consisting of an initial Joule-Thompson stage followed by the ^{3}He/^{4}He dilution refrigerator) carries the cooling down to 0.1 K. The overall system is very similar to that which will be used by FIRST (an approved ESA cornerstone mission).

The basis of the COBRAS/SAMBA mechanical cooler technology is the development by Oxford University and Rutherford Appleton Laboratory (RAL) of an 80 K cooler that was space qualified for the ISAMS instrument, and the further development at RAL of a two stage Stirling Cycle Cooler achieving 20-50 K, and a closed cycle Joule-Thomson Expansion Cooler achieving 4 K. British Aerospace (now Matra Marconi Space), funded by ESA, has successfully transferred this technology to an industrial level and can provide space qualified 4 K coolers. The long life and high reliability of

these systems result from the use of a frictionless compressor that has demonstrated successful space operation for periods of years.

The Open Cycle Dilution/Joule-Thomson Refrigerator has been developed at the Centre de Recherches des Très Basses Temperatures (CRTBT) in Grenoble (France). It uses a new dilution principle based on friction that does not need gravity to operate. Its cooling power depends on the gas flow, which is very low and thus allows sufficient gas storage to achieve long mission life. The principle of this cryogenic architecture and its ± 1 g operation have been successfully proven with a demonstration model, and qualification of this system for space operation is in progress.

4 Payload Requirements

In addition to requiring large sky coverage, instrumental effects demand that the observing pattern be repetitive with a periodicity of order 1 minute. These requirements indicate a solution in which the telescope line of sight sweeps large areas of the sky periodically with a period of $\sim$1 minute. This situation is most naturally arrived at with a spinning spacecraft where the telescope line-of-sight is offset from the spin axis by an angle (the so-called "scan angle" -70° - see Fig. 1), and thereby describes a circle on the sky. A spinning period of 1 r.p.m. fulfills the one minute periodicity requirement.

The control of straylight and thermal variations imposes severe constraints on the payload. Variations can be either random or systematic (e.g. synchronized with the observing pattern); the latter are the most severe since their effect does not average out by integration. Simulation of the instrumental sensitivity to temperature fluctuations of critical components results in stability requirements of a fraction of a milliKelvin for the optical surfaces and elements in the focal plane.

The main source of systematic temperature variations within the payload enclosure is spin-synchronized modulation of solar illumination on the spacecraft. The optimal situation is encountered when the payload is permanently maintained in solar shadow, and the spin axis is parallel to the Sunwards vector. This condition can be met if the payload is pointed in the anti-Sun direction and thus protected from direct solar illumination by the rest of the spacecraft, and in addition, if the motion of the spin axis is restricted to comply with the shadow condition. From the latter, it follows that to obtain the required sky coverage the scan angle (i.e. the angle between the spin axis and the viewing direction) must be large (e.g. 90° corresponds to tracing meridian circles on the sky, and achieving full sky coverage). Secondary sources of thermal modulation of the focal plane are caused by passages of the Earth and Moon through the field of view. These must be reduced by the choice of orbit.

One of the most significant issues in the payload design is to achieve adequate rejection of unwanted radiation, which include local (satellite) sources and Solar System sources. The requirements in this area are met not only by appropriate optical design, but also by specifying the allowed orientation of the spacecraft with respect to the major sources of straylight. The rejection required of the brightest source, the Sun, is $\sim$93 dB at the most critical frequency (31.5 GHz). For the next brightest sources, Earth, Moon and Jupiter, the rejection requirements are 79 dB, 67 dB and 43 dB, respectively (assuming a sensitivity of order $\Delta T/T \sim 10^{-6}$). Due to the orientation possibilities of the spin axis, these requirements mean that the radiation suppression should be better than $\sim$-93 dB for $\theta > 165°$ and better than $\sim$-67 dB for $\theta > 150°$ (θ being the angle from the spin axis). The required rejection is of course most easily achieved if the enclosure is continuously pointed diametrically away from the Sun. Detailed electromagnetic simulations of the optical enclosure, which take into account the angular response of individual detectors, have shown that by combining an appropriate optical design and observing strategy, it will be possible to cope with the straylight problem adequately.

A compromise between achieving large sky coverage, maintaining thermal stability, and rejecting solar straylight, results in a choice of scan angle of 70° . The geometry of the spacecraft (constrained by the launcher fairing) is such that the payload will remain in the shadow of the Sun for spin-axis to Sun-vector angles of up to 15° . Thus, ecliptic latitudes as large as ± 85 degrees will be available for observation, or more than 99% of the whole sky.

The basic anti-Sun pointing strategy reduces the effects of solar radiation to a minimum; however, the Earth and Moon can also be intense sources of both straylight and thermal modulation, and

reducing their effects drives the choice of orbit. Near-Earth orbits are eliminated mainly because the large thermal influx renders it extremely difficult to reach temperatures near 100 K in the focal plane, or to achieve the required thermal stability and straylight rejection. The nearest far-Earth orbit possible is that around one of the Lagrangian points of the Earth-Moon system (L4 or L5); this orbit (which shares the Lunar motion around the Earth) suffers from the fact that the Earth or the Moon are often not very far from the telescope line-of-sight. Simulations indicate that if this orbit were chosen, at least 35% of the acquired data would have to be discarded due to poor thermal or straylight conditions, leading not only to lower sky coverage but also to a less efficient removal of systematic effects. The optimal choice of orbit, resulting from a tradeoff of the various payload requirements, several spacecraft technical constraints (most importantly related to telecommunications to ground), and the transfer-to-orbit cost, is a Lissajous orbit around the L2 Lagrangian point of the Earth-Sun system. At this location, the Sun, the Earth, and the Moon are all located behind the payload, where their undesirable effects are at the lowest possible level, both in terms of location and of flux. In addition, this is the only orbit in which the antennas which provide telemetry and telecommand (TM/TC) for the spacecraft are also continually pointed away from the payload, thereby minimizing the potential effects of RF interference.

5 Mission aspects

COBRAS/SAMBA is designed to fit into the lowest cost launch scenario available after the year 2003 for ESA space science missions, i.e.:

- it will be one of two (or three, if this option is available) passengers on an Ariane 5 launcher;
- the launch window and target transfer orbit are dictated by the most likely co-passenger(s) - telecommunications satellites in geostationary orbits - rather than by COBRAS/SAMBA itself.

More specifically, the Ariane vehicle will inject COBRAS/SAMBA into the standard Geostationary Transfer Orbit, and transfer and injection into the final operational orbit will be accomplished using the on-board propulsion system of the spacecraft. The best-case transfer trajectory, lasting approximately 6 months, is shown in Figure 4.

As mentioned before, the operational orbit will be a Lissajous orbit around the L2 point of the Earth-Sun system; the semi-major amplitude of the orbit will be ~400,000×100,000 km. In this orbit COBRAS/SAMBA will move around the L2 point with a period of about 180 days.

6 The Observing Plan

The basic observing strategy is based on the antisolar orientation of the spin axis, as outlined previously. To maintain this orientation, the spin axis must be displaced along the ecliptic plane by 1° every day. This is done in individual steps for ease of operations. An appropriate value for the amplitude of each step is 5′ ; thus, the basic plan consists of one 5′ displacement of the spin axis along the ecliptic plane every 2 hours.

A perturbation to the basic motion along the ecliptic plane will be purposely introduced to optimize the distribution of integration time (and thus of achieved sensitivity level) over the sky. The strategy is to add to the basic (5′) ecliptic-plane manoeuver a component which brings the spin axis out of the ecliptic plane, by an amount which is to first order sinusoidal with time, has a period of order months, and a maximum amplitude of 15° .

The scan angle of 70° implies that one (>90%) sky coverage can be achieved after ~7.3 months of observations. The need to control systematic effects requires that at least two full sky coverages be achieved. This sets the minimum mission duration as that allowing routine observations of more than ~15 months, although clearly a longer duration of operations is desirable as it would lead to increased sensitivity, and better control of systematics.

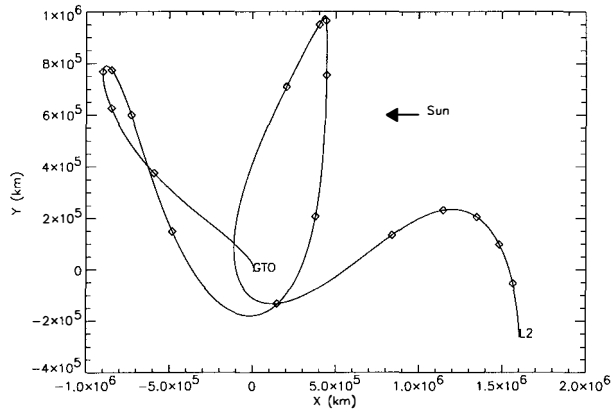

Figure 4: Best case transfer trajectory from Geostationary Transfer Orbit (GTO) to a Lissajous orbit (projection onto ecliptic plane, launch on 3 March 2003). Ticks are marked along the trajectory at 10 day intervals, starting at launch. Orbital motion within GTO is not shown in this plot. In most transfer cases, an inclination change manoeuver occurs about 30 days after launch, and a final injection manoeuver about 6 months after launch.

7 Scientific Operations

Routine scientific operations will commence during transfer to L2, approximately 3 months after launch, or 4 months before insertion into the Lissajous orbit. Once routine operations are initiated, the observing mode will be unique. Routine operations will be tied to the period of visibility afforded by one ground station (Kourou), which varies according to the season between 10.1 and 11 hours. During the visibility period, the data of the preceding obscuration period will be telemetered to ground, interleaved with the ongoing observations. During routine operations, the spacecraft will operate in a pre-programmed, automatic manner. The observing pattern (consisting of a series of manoeuvers to be carried out at 2 hour intervals) will be known far in advance.

Calibration of the science data (both absolute and relative) will not require a special mode of operation, but will be an ongoing process during sky observations. Various sources will be used for this purpose, most notably the well-known dipole component of the CMB, passages through the galactic plane, extragalactic point sources, and planets present in or near the field of view (Jupiter, Saturn, Mars). At high frequencies the absolute calibration will be tied to COBE-FIRAS observations of the galactic plane.

8 Scientific Data Products

Final data processing consists mainly of two steps: generation of maps of the surveyed area from the raw data, and separation of the various components from the maps to obtain both the cosmological signal, and the foreground emissions.

There will be three levels of scientific data products:

1. time series of the data acquired by each detector, after basic calibration, removal of systematic features, and attitude reconstruction;
2. maps of the sky in nine frequency bands;
3. maps of the sky for each of the main underlying components (CMB, SZ, dust, free-free, and possibly synchrotron).

9 The Spacecraft

Two separate modules, the payload module (PLM) and the service module (SVM) have been conceived to keep simple and clear interfaces, thus optimizing the development, integration and testing activities (see Figure 5).

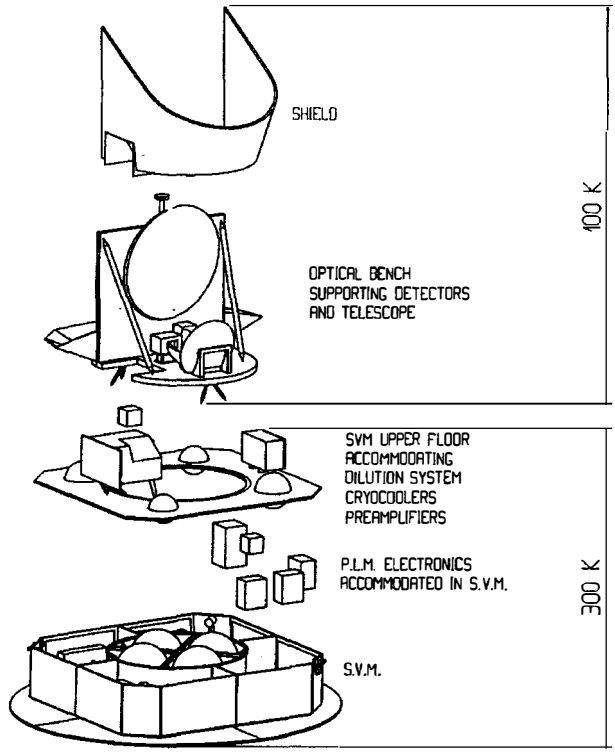

Figure 5: A three-dimensional exploded view of the spacecraft.

The PLM houses all the payload equipments requiring cryogenic temperatures : the detection units of the instruments, the telescope, the baffle and the outer flared shield. All this is mounted on a cold optical bench, together with a cryogenic radiator of nearly 3 m^2, fixed vertically onto the main mirror support. The optical bench is attached to the SVM top platform by means of glass fiber struts. Cryo coolers and cryogenic dilution system equipment are also mounted on this top platform, and the whole constitutes a mechanically and thermally autonomous assembly.

The SVM houses all the warm electronics of the payload, together with the subsystems of the spacecraft. It is a flat octagonal box, whose design is driven by the need to maximize inertia about the spin axis. All equipments are attached to lateral walls, which simplifies their passive thermal control. Four fuel tanks are accommodated inside the central cylinder. The solar array is fixed, non deployable, and of annular shape. Its outer diameter is 4 m, the maximum allowable for the Ariane 5 SILMA fairing. It is mounted at the base of the SVM, with the active side facing away from the SVM and PLM.

PART II

OBSERVATIONAL STATUS OF CMB ANISOTROPIES & IMPLICATIONS

THE CMB DIPOLE: THE MOST RECENT MEASUREMENT AND SOME HISTORY

Charles H. Lineweaver
Université Louis Pasteur
Observatoire Astronomique de Strasbourg
11 rue de l'Université, 67000 Strasbourg, France
charley@cdsxb6.u-strasbg.fr

ABSTRACT

The largest anisotropy in the cosmic microwave background (CMB) is the $\approx$ 3 mK dipole assumed to be due to our velocity with respect to the CMB. Over the past ten years the precision of our knowledge of the dipole has increased by a factor of ten. We discuss the most recent measurement of this dipole obtained from the four year COBE Differential Microwave Radiometers (DMR) as reported by Lineweaver et al. (1996). The best-fit dipole is $3.358 \pm 0.001 \pm 0.023$ mK in the direction $(\ell, b) = (264°.31 \pm 0°.04 \pm 0°.16,\ +48°.05 \pm 0°.02 \pm 0°.09)$, where the first uncertainties are statistical and the second include calibration and systematic uncertainties. The inferred velocity of the Local Group is $v_{LG} = 627 \pm 22$ km/s in the direction $\ell = 276° \pm 3$, $b = 30° \pm 2$. We compare this most recent measurement to a compilation of more than 30 years of dipole observations.

1 Introduction

The Sun's motion with respect to the rest frame of the cosmic microwave background (CMB) is believed to be responsible for the largest anisotropy seen in the COBE DMR maps: the ≈ 3 mK dipole in the direction of the constellation Leo. A high precision measurement of this Doppler dipole is important because it

- tells us our velocity with respect to the rest frame of the CMB.
- will be used as the primary calibrator for an increasing number of ground, balloon and satellite anisotropy experiments (Bersanelli et al. 1996). Small scale experiments are becoming sensitive enough to use the dipole to calibrate (Richards 1996). Thus the typical 10-20% absolute calibration accuracy of ground and balloon-borne experiments can be improved by more than an order of magnitude to the 0.7% absolute calibration accuracy of the DMR dipole.
- permits the accurate removal of the Doppler dipole and Doppler quadrupole from anisotropy maps thus improving the precision of the anisotropy results.
- calibrates bulk flow observations which yield independent but much less precise dipole values.
- permits an eventual test of the Doppler origin of the CMB dipole in which it is compared to the dipoles in other background radiations (Lineweaver et al. 1995).

In this paper we discuss the most recent determination of the precise direction and the amplitude of the dipole observed in the DMR four-year data. We discuss contamination from Galactic emission as well as other factors contributing to the error budget (see Lineweaver et al. (1996) for details). We then compare our results to a compilation of more than 30 years of dipole results.

2 Minimizing the Error Due to Galactic Foreground, CMB Background and Instrument Noise

2.1 Galactic Plane Cuts

We estimate the influence of Galactic emission on the measurement by solving for the dipoles for a series of Galactic plane latitude cuts. The dipole amplitude and direction results from each channel and each Galactic cut are shown in Figure 1. Galactic emission produces a dipole which pulls the solutions towards it. This is easily seen in Figure 1 from the locations of the 0° and 5° cut solutions relative to the cluster of higher cut results on the right. Since the Galactic dipole vector is nearly orthogonal to the CMB dipole vector, it is almost maximally effective in influencing the CMB dipole direction and almost minimally effective in influencing the CMB dipole amplitude.

In Figure 1, the general increase of the dipole amplitudes seen in the top panel as the Galactic cut increases from 0° to 5° to 10° can be explained by the fact that the Galactic dipole vector contains a component in the direction opposite to the CMB dipole (the Galactic center is $\approx 94°$ away) and thus reduces the total dipole in the maps.

Figure 1 clearly shows the influence of the Galaxy for the 0° and 5° cuts as well as the relative agreement of the independent channel results for both amplitude and direction. It

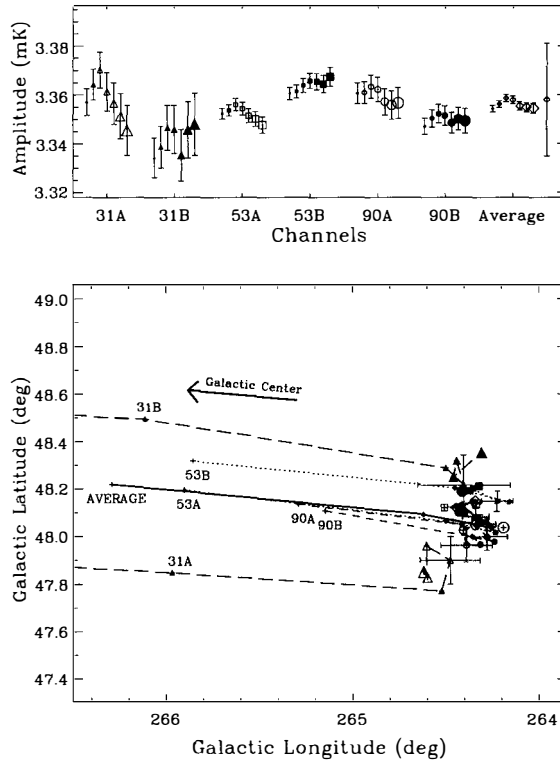

Figure 1. Dipole Amplitudes (top) and Directions (bottom) The results for each channel and Galactic plane cut (from left to right in the top panel), $|b| >$ 0°, 5°, 10°, 15°, 20°, 25°, 30° are shown. Channels and cuts are denoted with the same point type and size in both panels. Solutions for the dipole where no effort has been made to eliminate Galactic emission (i.e., 0° Galactic cuts) are labeled with the channel names "53A", "53B", "90A" and "90B". The 31 GHz labels indicate the 5° cut solutions since their 0° cut solutions are off the plot at longitude $\approx$ 271°. For each channel, the successive Galactic cuts are connected by lines (31: long dashes, 53: dots, 90: short dashes, Average: solid). The direction of the Galactic center is toward higher latitudes for the same reason that one flies north-west from London to arrive at New York. The latitude and longitude ranges were chosen to display an approximately square piece of the sky. For each channel, the direction error bars on the 15° Galactic cut solutions are shown. Our final dipole amplitude, including the calibration uncertainty is the point in the far right of the top panel. The grey box in the bottom panel denotes the 68% confidence levels of our final dipole direction (cf. Fig. 1, Lineweaver et al. (1996)).

is also apparent that to first approximation a 10° cut is sufficient to remove the effect of the Galaxy on the direction of the best-fit dipole; increases of the cut from 10° to 15° and so on, do not push the directions away from the Galactic center or in any other particular direction. The results tend to cluster together. The directional precision of the various channels and Galactic cuts is seen to be $\sim 0°.3$ and it is perhaps reassuring to note that at the bottom and the top of the cluster are the least sensitive 31A and 31B solutions.

Galactic emission significant enough to affect the dipole results will tend to pull the three channels in approximately the same direction and favor a spectral behavior typical of synchrotron or free-free emission. This is easily seen for the 0° and 5° cuts (cf. Figure 2, Lineweaver et al. 1996). The absence of this behavior for the 10° and 15° cuts and larger is evidence that the Galaxy is no longer the major contributor to the directional uncertainty of the dipole.

2.2 Higher Multipole CMB as Unwanted Contamination

For the purposes of determining the dipole there are two sources of noise; instrument noise with a power law spectral index $n \approx 3$ and the $n \approx 1$ CMB signal. At 10° scales the CMB signal to noise ratio in the maps is ~ 2 (Bennett et al. 1996). Thus on larger scales the CMB

signal dominates the instrument noise and correspondingly, the uncertainties on the dipole from the CMB signal are larger than those from the instrument noise. The uncertainties from *both* are reduced by lowering the Galactic plane cut. This is further supported by the fact that for $|b| \gtrsim 20°$, the combined free-free and dust emission from the Galaxy at 53 and 90 GHz produces only $\sim 10\,\mu$K rms (Kogut et al. 1996a) while the CMB signal rms is $\sim 35\,\mu$K (Banday et al. 1996).

To estimate the uncertainty in the dipole results due to the CMB signal we simulate $n = 1.2$, $Q_{rms-PS} = 15.3\,\mu$K CMB skies for $2 \leq \ell \leq 25$. We superimpose these maps on a known dipole and solve for the dipole using a 15° Galactic plane cut. No bias is detected and the rms's of the results around the input values are $3.3\,\mu$K in amplitude, 0°.127 in longitude and 0°.062 in latitude. We include these CMB contamination uncertainties in our estimate of the systematic errors.

We have found that Galactic cuts greater than 15° are not useful corrections which eliminate more and more Galactic contamination; they introduce systematic errors associated with large Galactic cuts due to the increasingly non-orthogonal basis functions $Y_{\ell m}(\theta, \phi)$, over the increasingly limited and thus noisier input data.

We conclude that the Galactic cuts of 10° and 15° are the best compromise to minimize the combined effect of CMB aliasing, Galactic contamination and noise. The high precision of our dipole direction results depend on this conclusion. Note that this choice for the optimal Galactic cut is smaller than the $\approx 20°$ cut used when one is trying to compute the correlation function or determine the $\ell \geq 2$ components of the power spectrum of the CMB signal which are smaller than the dipole by a factor of ~ 200. For such determinations, the similar compromisefor simultaneously minimizing Galactic contamination, instrument noise and other procedural/systematic effects demands a larger cut.

3 Results

Taking the averages of the 10° and 15° cuts and the weighted average of all six channels we obtain a best-fit dipole amplitude $3.358 \pm 0.001 \pm 0.023$ mK in the direction $(\ell, b) = (264°.31 \pm 0°.04 \pm 0°.16,\ +48°.05 \pm 0°.02 \pm 0°.09)$, where the first uncertainties are statistical and the second are estimations of the combined systematics. In celestial coordinates the direction is $(\alpha, \delta) = (11^h 11^m 57^s \pm 23^s, -7°.22 \pm 0°.08)$ (J2000). The uncertainty in the dipole amplitude is dominated by the absolute calibration of the DMR instrument (Kogut et al. 1996b). This is easily seen in Figure 1 by comparing the large error bars on our final result (far right) with the noise-only error bars on the channel results. The calibration uncertainty plays no role in the directional uncertainty for the same reason that the directions of vectors $\vec{x}$ and $a\vec{x}$ (where a is any positive constant) are the same.

Under the assumption that the Doppler effect is responsible for the entire CMB dipole, the velocity of the Sun with respect to the rest frame of the CMB is $v_\odot = 369.0 \pm 2.5$ km/s, which corresponds to the dimensionless velocity $\beta = v_\odot/c = 1.231 \pm 0.008 \times 10^{-3}$. The associated rms Doppler quadrupole[1] is $Q_{rms} = 1.23 \pm 0.02\ \mu$K with components $[Q_1, Q_2, Q_3, Q_4, Q_5] = [0.91 \pm 0.02, -0.20 \pm 0.01, -2.04 \pm 0.03, -0.91 \pm 0.02, 0.18 \pm 0.01]\,\mu$K. The velocity of the Local Group with respect to the CMB can be inferred; following Kogut et al. (1993) we obtain $v_{LG} = 627 \pm 22$ km/s in the direction $\ell = 276 \pm 3$, $b = 30 \pm 2$.

[1] $Q^2_{rms} = \frac{4}{15}[\frac{3}{4}Q_1^2 + Q_2^2 + Q_3^2 + Q_4^2 + Q_5^2]$ where the components are defined by $T_o \frac{\beta^2}{2}(2cos^2\theta - (2/3)) = Q_1(3sin^2 b - 1)/2 + Q_2 sin2b\, cos\ell + Q_3 sin2b\, sin\ell + Q_4 cos^2 b\, cos2\ell + Q_5 cos^2 b\, sin2\ell$, where T_o is the mean CMB temperature and θ is the angle between the dipole direction and the direction of observation: (ℓ, b).

4 Historical Discussion

We have compiled more than 30 years of dipole measurements in Table 1 and these numbers were used to make Figure 2. This plot may a good example of scientific progress. We acknowledge support from the French Ministère des Affaires Etrangères.

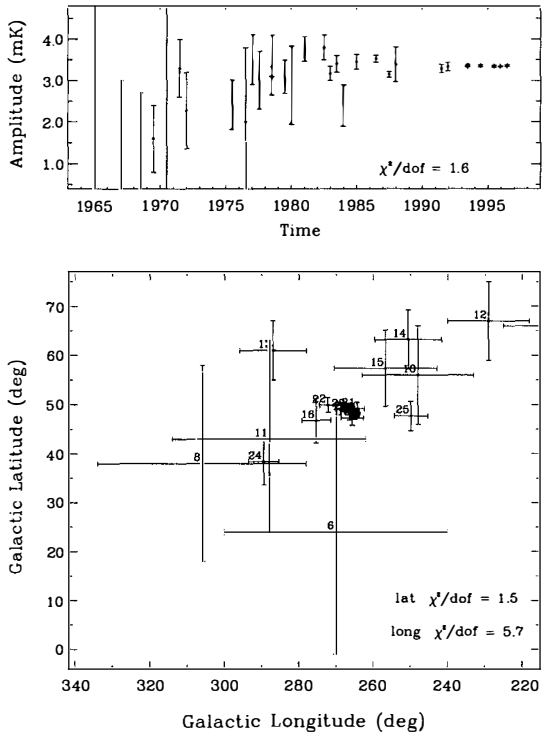

Figure 2. 30 Years of CMB Dipole Measurements
These results and the number labels in the bottom panel correspond to the references in Table 1. To see how realistically the dipole community has estimated its errors we have calculated the χ^2 per degree of freedom for the amplitudes, galactic longitudes and latitudes of the reported results. They are respectively 1.6, 5.7 and 1.5 (approximately correct error estimates yield $\chi^2/dof \sim 1$). Thus, the amplitude and latitude estimates are believable while the reported errors on longitude have been underestimated. This can probably be attributed to the various ways in which Galactic emission has (or has not) been accounted for since a line fit to the set of dipole directions passes through the Galactic center ($\ell = 360°, b = 0$). This plot may be a good example of scientific progress.

Table 1: CMB Dipole Measurements

#	Reference	Amplitude D(mK)	$\pm\sigma$	Longitude[a] ℓ(deg)	$\pm\sigma$	Latitude[a] b(deg)	$\pm\sigma$	Freq (GHz)
1	Penzias & Wilson(1965)	< 270						4
2	Partridge & Wilkinson(1967)	0.8	2.2					9
3	Wilkinson & Partridge(1969)	1.1	1.6					9
4	Conklin(1969)	1.6	0.8	96	30	85	30	8
5	Boughn et al. (1971)	7.6	11.6					37
6	Henry(1971)	3.3	0.7	270	30	24	25	10
7	Conklin(1972)	> 2.28	0.92	195	30	66	10	8
8	Corey & Wilkinson(1976)	2.4	0.6	306	28	38	20	19
9	Muehler(1976)	2.0	1.8	207		-11		150
10	Smoot et al. (1977)	3.5	0.6	248	15	56	10	33
11	Corey(1978)	3.0	0.7	288	26	43	19	19
12	Gorenstein(1978)	3.60	0.5	229	11	67	8	33
13	Cheng et al. (1979)	2.99	0.34	287	9	61	6	30
14	Smoot & Lubin(1979)	3.1	0.4	250.6	9	63.2	6	33
15	Fabbri et al. (1980)	2.9	0.95	256.7	13.8	57.4	7.7	300
16	Boughn et al. (1981)	3.78	0.30	275.4	3.9	46.8	4.5	46
17	Cheng(1983)	3.8	0.3					30
18	Fixsen et al. (1983)	3.18	0.17	265.7	3.0	47.3	1.5	25
19	Lubin (1983)	3.4	0.2					90
20	Strukov et al. (1984)	2.4	0.5					67
21	Lubin et al. (1985)	3.44	0.17	264.3	1.9	49.2	1.3	90
22	Cottingham(1987)	3.52	0.08	272.2	2.3	49.9	1.5	19
23	Strukov et al. (1987)	3.16	0.07	266.4	2.3	48.5	1.6	67
24	Halpern et al. (1988)	3.4	0.42	289.5	4.1	38.4	4.8	150
25	Meyer et al. (1991)			249.9	4.5	47.7	3.0	170
26	Smoot et al. (1991)	3.3	0.1	265	1	48	1	53
27	Smoot et al. (1992)	3.36	0.1	264.7	0.8	48.2	0.5	53
28	Ganga et al. (1993)			267.0	1.0	49.0	0.7	170
29	Kogut et al. (1993)	3.365	0.027	264.4	0.3	48.4	0.5	53
30	Fixsen et al. (1994)	3.347	0.008	265.6	0.75	48.3	0.5	300
31	Bennett et al. (1994)	3.363	0.024	264.4	0.2	48.1	0.4	53
32	Bennett et al. (1996)	3.353	0.024	264.26	0.33	48.22	0.13	53
33	Fixsen et al. (1996)	3.372	0.005	264.14	0.17	48.26	0.16	300
34	Lineweaver et al. (1996)	3.358	0.023	264.31	0.17	48.05	0.10	53

[a] Galactic coordinates

References

1. Banday, A., et al. 1996, Ap.J., submitted
2. Bennett, C.L., et al. 1994, Ap.J., 436, 423
3. Bennett, C.L., et al. 1996, Ap.J., in press
4. Bersanelli, M., et al. 1996, A&A in press
5. Boughn, S.P. et al. 1971, Ap.J., 165, 439
6. Boughn, S.P. et al. 1981, Ap.J., 243, L113
7. Cheng, E.S. et al. 1979, Ap.J. 232, L139
8. Cheng, E.S. 1983 Ph.D. thesis, Princeton Univ.
9. Conklin, E.K. 1969, Nature, 222, 971
10. Conklin, E.K. 1972, IAU Symposium 44, ed. D.S. Evans (Dordrecht: Reidel), p 518
11. Corey, B.E. 1978, Ph.D. thesis Princeton U.
12. Corey, B.E. & Wilkinson D. T., 1976, Bull. Amer. Astron. Soc, 8, 351
13. Cottingham, D.A. 1987, Ph.D. thesis, Princeton Univ.
14. Fabbri, R., et al. 1980, PRL, 44, 1563, erratum 1980, PRL, 45, 401
15. Fixsen, D.J., Cheng, E.S. & Wilkinson, D.T. 1983, PRL, 50, 620
16. Fixsen, D.J., et al. 1994, Ap.J., 420, 445
17. Fixsen, D.J., et al. 1996, Ap.J., submitted
18. Ganga, K., Cheng, E., Meyer, S., Page, L. 1993, Ap.J., 410, L57
19. Gorenstein, M.V. 1978, Ph.D. thesis, U.C.Berkeley
20. Halpern, M., et al. 1988 Ap.J., 332, 596
21. Henry, P.S. 1971, Nature, 231, 516
22. Kogut, A., et al. 1993, Ap.J., 419, 1
23. Kogut, A., et al. 1996a, Ap.J.L., in press
24. Kogut, A., et al. 1996b, Ap.J., in press
25. Lineweaver, C.H., et al. 1995, Astrophysical Letters and Comm., 32, pp 173-181
26. Lineweaver, C.H., et al. 1996, Ap.J., in press
27. Lubin, P.M., Epstein, G.L., Smoot, G.F. 1983, PRL, 50, 616
28. Lubin, P.M. et al. 1985, Ap.J., 298, L1
29. Meyer, S.S., et al. 1991, Ap.J., 371, L7
30. Muehler, D. 1976, in Infrared and Submillimeter Ast., ed G.Fazio, D.Reidel, Dordrecht, p63
31. Partridge, R.B. & Wilkinson, D. T., 1967, PRL 18, 557
32. Penzias, A.A. & Wilson, R. W. 1965, Ap.J., 142, 419
33. Richards, P., (comment at this Moriond Meeting)
34. Smoot, G.F., Gorenstein, M. V. & Muller, R. A. 1977, PRL, 39, 898
35. Smoot, G.F. & Lubin, P. 1979, Ap.J. 234, L83
36. Smoot, G.F., et al. 1991, Ap.J., 371, L1
37. Smoot, G.F., et al. 1992, Ap.J., 396, L1
38. Strukov, I.A., Skulachev, D.P. 1984, Sov. Ast. Lett. 10, 3
39. Strukov, I.A., Skulachev, D.P., Boyarskii, M.N., Tkachev, A.N. 1987, Sov. Ast. Lett. 13, 2
40. Weinberg, S. 1972, Gravitation and Cosmology, (NY:Wiley), p 521
41. Wilkinson, D.T. & Partridge, R.B. 1969, Partridge quoted in American Scientist, 57, 37

COSMIC MICROWAVE BACKGROUND ANISOTROPY IN THE *COBE* DMR 4-YR SKY MAPS

Krzysztof M. Górski [1,2,3]
[1] *Hughes/STX, NASA/GSFC, Code 685, Greenbelt, MD 20771, USA.*
[2] *TAC, Juliane Maries Vej 30, 2100 Copenhagen Ø, Denmark* (present address).
[3] on leave from *Warsaw University Observatory, Warsaw, Poland.*

Abstract

The *COBE* satellite has provided the only comprehensive multi-frequency full-sky observations of the microwave sky available today. Assessment of the observations requires a detailed likelihood analysis to extract the maximum amount of information present in the noisy data. I present a specific method for estimating the CMB anisotropy power spectrum independent of any assumptions about the underlying cosmology, and then use standard image processing techniques to generate the most revealing corresponding maps of the signal. The consistency of the data at the three available frequencies provides strong support to the assertion that we are being provided with our first glimpse of the last scattering surface.

1 Introduction

Operations of the Differential Microwave Radiometer instruments (DMR), the last active experiment on board NASA's COsmic Background Explorer (*COBE*) satellite, were terminated in December 1993, concluding four years of measurements of anisotropy of the cosmic microwave background (CMB) radiation. The final product of the DMR-team work — full sky maps of the microwave sky at 31.5, 53, and 90 GHz — were released to the astronomical community in January 1996. A generic description of the final DMR dataset and brief summary of the results of the DMR-team analysis were given in [4]. The issues of prime concern in the DMR-team work included the following:

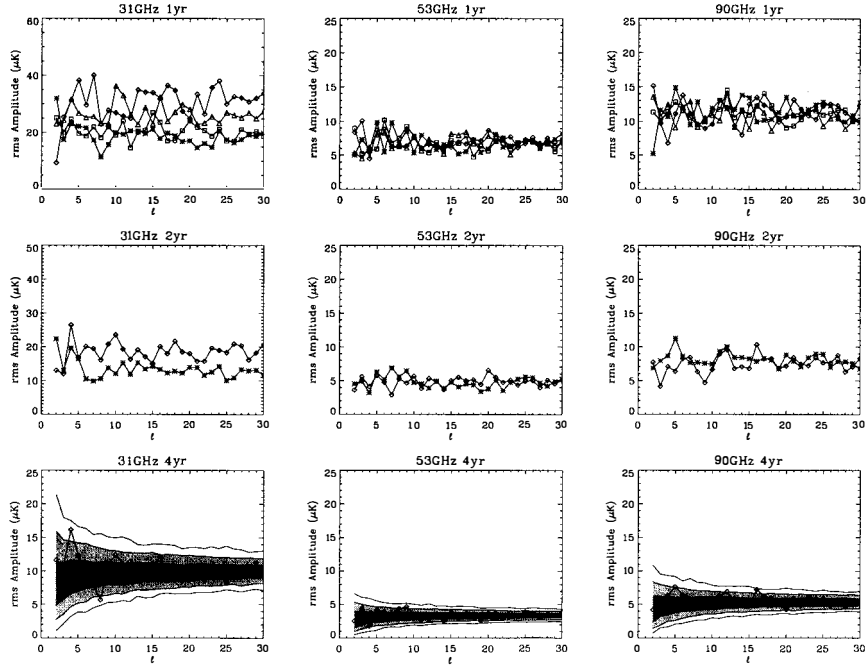

Figure 1: Power spectra of the DMR (galactic frame, extended Galaxy cut, 3881 pixels) difference maps, (A-B)/2, at each frequency of observations, for each yearly sky maps (top row, stars — year one, squares - year 2, triangles — year 3, diamonds — year 4), for two 2-year sky maps (middle row, stars — years 1 and 2, diamonds — years 3 and 4), and for the final four-year product (bottom row, diamonds). Bottom row plots include the 68, 95, and 99% confidence regions (heavy to light grey) from Monte Carlo simulations of instrumental noise in the sky maps.

1) modeling and removal of identified systematic artifacts from the data (see [13]) to produce sky maps suitable for cosmological studies,
2) studies of potential signal contamination by the Galaxy [11], and/or the extragalactic sources [1],
3) testing of the hypothesis of primordial origin of the measured CMB anisotropy [2] by evaluation of the frequency dependence of the $(\delta T/T)_{rms}$ in the sky maps,
4) testing of the hypothesis of gaussianity of statistics of the measured anisotropies [12],
5) evaluation and analysis of the auto- and cross-correlation functions of the sky maps [9],
6) determination of the angular power spectrum of the CMB anisotropy [8], [10], [16].
Other analyses of the 4 year data presented so far include [5], [15], and Bond and Jaffe in these Proceedings.

In this contribution I will focus on two aspects of the interpretation and visualisation of the *COBE*-DMR data: 1) derivation of the angular power spectrum of the CMB anisotropy using a data reduction method which is *independent* of the cosmological model, and 2) linear filtering

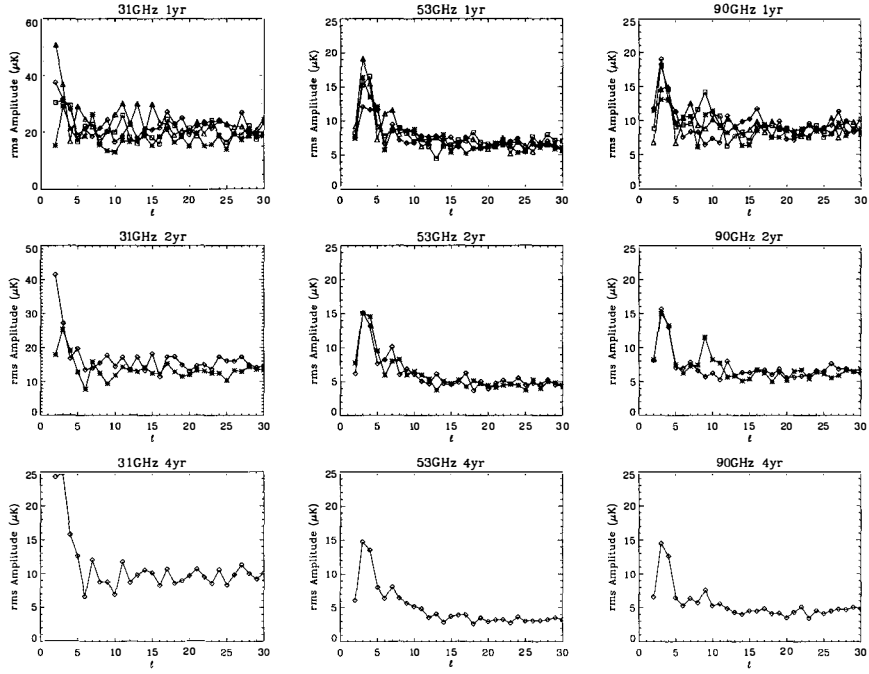

Figure 2: Power spectra of the DMR (galactic frame, extended Galaxy cut, 3881 pixels) inverse-noise-variance weighted sum maps, at each frequency of observations, for all yearly, 2-year, and 4-year sky maps (same coding as in Figure 1.) Variance weighting of the A and B sides makes the yearly and bi-yearly effective noise levels in the 31GHz map more consistent with one another than in the corresponding difference maps (with fifty-fifty noise contributions from the A and B sides), and the effective noise level in the sum maps somewhat lower than in the corresponding difference maps at all three frequencies.

of the sky maps. Both these goals are pursued within the mathematical framework for analysis of the DMR data which was originally described in [6], and [7]. I will briefly describe the DMR data, address the necessary technical points, and proceed to presentation of the results and discussion.

2 Data

The main result of the *COBE*-DMR mission is a set of full sky maps, comprised of two maps (A and B sides) at each frequency of 31.5, 53, and 90 GHz, pixelized in both galactic and ecliptic coordinates. The angular resolution of the instrument was $\sim 7°$FWHM, and the sky maps are divided into 6144 nearly equal area pixels.

A record of the sensitivity of each detector and the number of observations per pixel in each map are provided with the sky maps. This allows for stochastic modelling of the instrument noise, which is essential for a proper interpretation of the results of the data analysis and

subsequent inference of a parametric description for the cosmological signal. [Indeed, except for the dipole anisotropy and the galactic plane emission, the CMB anisotropy signals detected in the DMR maps are weak compared to typical noise contamination even at 53 GHz — rms signal $\sim 35\,\mu$K vs. rms noise $\sim 80\,\mu$K in a single pixel.]

Since the monitoring of the multichannel instrument performance was very long, DMR is to date unparalelled among the CMB anisotropy experiments in terms of noise control.

Using the customized Fourier tools introduced in [6] for the analysis of the incomplete sky of the Galaxy-excised DMR sky maps one can extract from the data the cut-sky power spectra of the sum and difference maps at each frequency, which are shown in Figures 1 and 2. Quantities plotted there are the rms values of the cut-sky harmonic coefficients (the usual $(2\ell+1)$ degrees of freedom per ℓ-mode).

One should appreciate from Figure 1 the steady decrease with time ($\sim 1/\sqrt{t}$) of the rms noise amplitude, the excellent consistency of the yearly performances of the 53 and 90 GHz instruments, and very good consistency of the measured noise properties with the Gaussian model.

Figure 2 shows the power spectra of signal and noise. Even the totality of the 31.5 GHz data remains substantially noisier than the higher frequency channels, which together with uncertainties in the galactic foreground contribution renders its interpretation more problematic. Visual inspection of the 53 and 90 GHz power spectra provides a sense of strong consistency between these independent data sets.

3 Maximum likelihood estimation of the angular power spectrum of CMB anisotropy

A method of cut-sky Fourier decomposition and maximum likelihood analysis of the DMR data to infer the parameters of a theoretical spectrum of CMB anisotropy was presented in [6]. The application of this formalism to derive the maximum likelihood estimates of the overall amplitude and shape parameters for power law spectrum fits to the 2-yr and 4-yr DMR data was given in [7], and [8], respectively. Here I demonstrate how this formalism allows one to derive a maximum likelihood estimate of the individual multipoles $C_\ell = \langle |a_{\ell m}|^2 \rangle = a_\ell^2$, where $\delta T/T(\Omega) = \sum_{\ell m} a_{\ell m} Y_{\ell m}(\Omega)$.

A proper analysis of a relatively complex data set such as DMR and the correct inference of a parametrisation of the sky distribution of CMB anisotropy requires the simultaneous treatment of several interrelated problems, which include:

1) incomplete sky coverage and resulting multipole coupling after excision of the galactic plane region from the analysed maps;

2) removal of the cosmologically irrelevant low order, $\ell = 0$, and 1 modes, preferably without affecting the higher order modes, which do carry cosmological information;

3) modeling of the nonuniform noise distribution;

4) identification and removal of possible diffuse foreground emission in the areas outside the galactic cut;

5) execution of an unbiased, or least-biased, parameter inference, preferably using the probability density which describes the tested model of anisotropy in an exact manner.

A program of analysis of the DMR data which addressed all of these points was conducted in [6], [7], and [8]. An important feature of this method of analysis is that it employs geometrically constructed orthogonalized spherical harmonics, which are *independent* of any cosmological theories that one might endeavour to test with the DMR data. This is radically different from the possible Karhunen-Loève type methods, where one builds the basis of modes for sky map

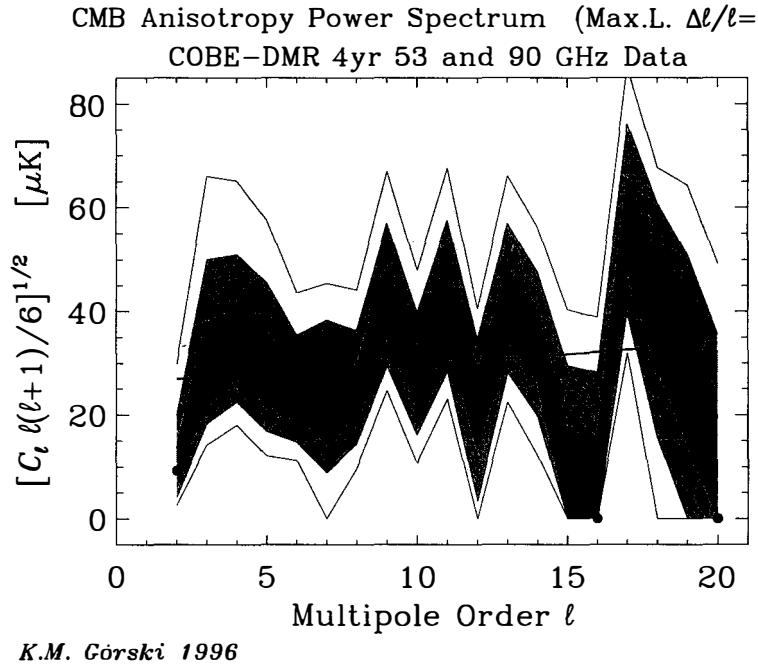

Figure 3: Power spectrum of the CMB anisotropy derived by the maximum likelihood method with each C_ℓ coefficient treated as a separate parameter (hence $\Delta\ell/\ell = 0$). Noise and incomplete sky coverage induce correlations, impossible to show on the plot, between the derived confidence intervals on each C_ℓ. One should note that a correct estimator of excess variance in signal over noise in the data was applied, hence no negative C_ℓ values were obtained. A low-ℓ tail of the CDM model CMB anisotropy spectrum (independently fitted to the same data) is shown as a slightly tilted solid line.

decomposition using a specific theoretical spectrum of CMB anisotropy (e.g. Bond and Jaffe in this volume).

Let us now establish how the method introduced in [6] can be used to compute an estimator of the full sky angular power spectrum, i.e. the coefficients C_ℓ which can be determined from the data. Since we work with the Fourier amplitudes $\mathbf{c}$ which are linear combinations of pixel temperatures (as they are integrals on the cut-sky of the map products with the cut-sky orthogonalized spherical harmonic basis functions), their joint probability distribution is Gaussian (see [6] for formal details)

$$P(\mathbf{c})\, d\mathbf{c} = \frac{d\mathbf{c}}{(2\pi)^{N/2}\sqrt{\det(\mathbf{S}+\mathbf{N})}} \exp\left(-\mathbf{c}^T \cdot (\mathbf{S}+\mathbf{N})^{-1} \cdot \mathbf{c}\,/2\right), \tag{1}$$

where $\mathbf{C} = \mathbf{S} + \mathbf{N}$, and $\mathbf{S}$ and $\mathbf{N}$ are covariance matrices of the signal and noise, respectively. For the maximum likelihood calculations I use the likelihood function defined as

$$F(\mathbf{A}|\hat{\mathbf{c}}) = \det[\mathbf{S}(\mathbf{A}) + \mathbf{N}] + \hat{\mathbf{c}}^T \cdot [\mathbf{S}(\mathbf{A}) + \mathbf{N}]^{-1} \cdot \hat{\mathbf{c}}, \tag{2}$$

where the full sky signal variance matrix has the form

$$\mathbf{A} = \mathrm{diag}[\underbrace{a_2^2, \ldots, a_2^2}_{5 \text{ times}}, \underbrace{a_3^2, \ldots, a_3^2}_{7 \text{ times}}, \ \cdots \ , \underbrace{a_{\ell_{max}}^2, \ldots, a_{\ell_{max}}^2}_{(2\ell_{max}+1) \text{ times}}]. \tag{3}$$

The maximum likelihood problem as formulated in eqs. (1-3) — seeking the coefficients C_2-$C_{\ell_{max}}$ given the data vector $\hat{\mathbf{c}}$ — involves the assumption of a Gaussian distribution of both noise and CMB anisotropies, and the statistical isotropy of the field of temperature perturbations (hence only the ℓ dependence of $\langle |a_{\ell m}|^2 \rangle$), but does not imply any relation between C_ℓ-s at different values of ℓ — hence we are solving for the power spectrum of CMB anisotropy fully *indpendently* of any specific cosmological model.

A maximum likelihood search for the power spectrum that best matches the distribution of signal on the sky simply entails finding a minimum of the function $F(\mathbf{A})$ in the $\ell_{max} - 1$-dimensional space. In the present case it is greatly facilitated by our ability to write down easily the expression for the gradient $\partial F / \partial a_\ell$, and implement a standard numerical routine for an extremum search with gradient zeroing. The solution to this problem for the DMR 4yr galactic frame data is shown in Figure 3. Our power spectrum estimator is really an estimator of excess variance in signal over noise in the data. One should note in Fig. 3 the asymmetry of the confidence intervals around the maximum likelihood solutions for the C_ℓ-s, and the fact that no derived values go negative. If there is no signal content in the data that can be attributed to a given C_ℓ, an upper limit is established, as e.g. for $\ell = 16$. The signal to noise ratio in Fourier space drops to ~ 1 at $\ell \sim 15$ in the DMR 4yr data. It is important to see that nearly all multipoles within that range are determined with great significance. As for the confidence intervals, the plot can not convey the notion of correlations between the errors on different multipoles. These correlations are quite small, and more significant for multipoles separated by $\Delta\ell = 2$ than otherwise. Because of the nontrivial (non-Gaussian) structure of confidence interval correlations it is difficult to implement an exact method of fitting of the theoretical model of CMB anisotropy to the DMR data by using the power spectrum, compressed rendition of the data. For such applications the accurate linear methods, as e.g. [7], should be preferred.

4 Linear filtering of the DMR sky maps

When the statistical properties of the signal, polluted by noise in the data, are known, one can apply powerful tools of image processing to improve, oftentimes visually quite dramatically, the presentation of the measurements. The best known device for linear filtering of noisy data is the celebrated Wiener filter. Alternatives, usually referred to as sub-optimal filters, do exist, and on occasion provide a preferred means of treating the noisy data. In the case of the DMR raw data the signal to noise ratio is pretty poor even in the 4yr data set. The Wiener filter, which practically "annihilates" those components of the data which are assesed to be noise dominated, when applied to data of low quality usually renders the impression of "over-smoothing". I choose to apply another device, called the power-equalization filter, which is constructed as follows.

First let us define the measurement, signal, and noise vectors, and their covariance matrices:

$$\mathbf{m} = \mathbf{s} + \mathbf{n}, \ \ \langle \mathbf{s} \cdot \mathbf{s}^T \rangle = \mathbf{S}, \ \ \langle \mathbf{n} \cdot \mathbf{n}^T \rangle = \mathbf{N}, \ \ \langle \mathbf{m} \cdot \mathbf{m}^T \rangle = \mathbf{S} + \mathbf{N}. \tag{4}$$

Next, define the filtered data vector, and the filter matrix:

$$\mathbf{f} = \mathbf{F} \cdot \mathbf{m} = \mathbf{F} \cdot (\mathbf{s} + \mathbf{n}). \tag{5}$$

If the filter is constructed from the requirement that the mean square deviation between the filtered and the true signal, $\epsilon = \langle(\mathbf{f}-\mathbf{s})^T \cdot (\mathbf{f}-\mathbf{s})\rangle = \mathrm{tr}\langle(\mathbf{f}-\mathbf{s}) \cdot (\mathbf{f}-\mathbf{s})^T\rangle$, is minimized, one obtains the Wiener filter

$$\mathbf{F}_W = \mathbf{S} \cdot (\mathbf{S}+\mathbf{N})^{-1}. \tag{6}$$

Another possibility for sub-optimal filtering, which renders the power equalization filter, arises when $\mathbf{F}$ is chosen such that

$$\langle \mathbf{f} \cdot \mathbf{f}^T \rangle = \mathbf{S}, \quad \text{i.e.} \quad \mathbf{F}_{PE} \cdot (\mathbf{S}+\mathbf{N}) \cdot \mathbf{F}_{PE}^T = \mathbf{S}. \tag{7}$$

Equation (7) means that on average over many applications the power-equalization filter renders filtered data, whose statistical distribution matches that of the underlying signal.

Using Choleski decomposition of the relevant matrices, and the following auxiliary matrices, we can construct the power equalization filter as follows:

$$\mathbf{S}^{-1} = \mathbf{L}_{\mathbf{S}^{-1}} \cdot \mathbf{L}_{\mathbf{S}^{-1}}^T, \qquad \mathbf{\Gamma}_{\mathbf{S}^{-1}} = \mathbf{L}_{\mathbf{S}^{-1}}^{-1}, \qquad \mathbf{S} = \mathbf{\Gamma}_{\mathbf{S}^{-1}}^T \cdot \mathbf{\Gamma}_{\mathbf{S}^{-1}}, \tag{8}$$

$$(\mathbf{S}+\mathbf{N})^{-1} = \mathbf{L}_{(\mathbf{S}+\mathbf{N})^{-1}} \cdot \mathbf{L}_{(\mathbf{S}+\mathbf{N})^{-1}}^T, \quad \mathbf{\Gamma}_{(\mathbf{S}+\mathbf{N})^{-1}} = \mathbf{L}_{(\mathbf{S}+\mathbf{N})^{-1}}^{-1}, \quad \mathbf{S}+\mathbf{N} = \mathbf{\Gamma}_{(\mathbf{S}+\mathbf{N})^{-1}}^T \cdot \mathbf{\Gamma}_{(\mathbf{S}+\mathbf{N})^{-1}}, \tag{9}$$

and as a result:

$$\mathbf{F}_{PE} = \mathbf{\Gamma}_{\mathbf{S}^{-1}}^T \cdot \mathbf{L}_{(\mathbf{S}+\mathbf{N})^{-1}}^T \tag{10}$$

This is an upper triangular matrix, hence filtering of a given mode in the cut-sky data vector $\hat{\mathbf{c}}$ does not mix in the information from lower order modes, preserving the information ordering imposed by the construction of orthonormal modes (see [6]).

For the presentation purposes of this contribution I constructed separate filters for the DMR4 53 and 90 GHz maps. The tremendous advantage of DMR is clearly visible here. We can internally compare two sets of decent quality observations at 53 and 90 GHz, and we are able to quantify and visualize the consistency with which the instrument reveals the image of the last scattering surface.

5 The first image of last scattering surface

It should be realized that the *COBE*-DMR observations *did* allow us to make a first reliable picture of the last scattering surface. Recognition of this fact is somewhat obscured by the memory of the picture of the first DMR all sky map that was circulated in 1992 - a picture which was substantially distorted by noise features.

Four years after that presentation, the quality of DMR data is now substantially better, but it is still somewhat difficult to argue about its validity as an image of the last scattering surface, as there is simply no other data at microwave frequencies at the same angular scales to allow a direct image to image comparison with DMR. However, since DMR observed the sky at three frequencies, and two of these have rendered sky maps of decent quality, an internal image comparison is possible.

What I present here is a result of a fairly long chain of events: separate instruments (with different noise properties) were used to observe the sky (looking at different directions at the time of observations!), the data were separately analysed and corrected for the systematic effects, the maps were made separately, all the subsequent data reduction was performed separately, and in the end different filters were constructed and applied.

The end product of these operations is visible in two panels on the left side of the color plate as the DMR 53 and 90 GHz, power-equalisation filtered sky maps. To facilitate the comparison

and assessment of consistency of these maps I add and subtract them. This is shown in the remaining panels of the color plate in both Mollweide and spherical polar projections.

It is immediately clear that the 53 and 90 GHz maps contain many common features on large angular scales (and, as shown in [1], [11], [8], they can not be attributed to foreground emission from either the Galaxy, or nearby extragalactic objects). The epistemological value of this result of the *COBE*-DMR mission should not be underestimated, as this is the first time ever that we are afforded a reliable picture of the most remote regions of the universe. (I shall stress that I do not attempt to make an argument about the wonders of image processing, but about our truly good luck with the DMR's splendid performance at two different frequencies!)

The rms anisotropy in the $(53 + 90)/2$ PE filtered map is 35μK, while the rms in the $(53 - 90)/2$ map is about 15μK. These numbers define the accuracy to which *COBE*-DMR has revealed to us a most elusive astronomical realm, and provided a first direct glimpse at the universe in its embryonic state.

Acknowledgements. I gratefully acknowledge the efforts of the *COBE* team and the support of the Office of Space Sciences at NASA. I am grateful to A.J. Banday for help with preparation of the manuscript.

References

[1] Banday A.J. *et al.*, 1996, *Astrophys. J.* **468**, L85

[2] Banday A.J. *et al.*, 1997, *Astrophys. J.* in press

[3] Bennett C.L. *et al.*, 1994, *Astrophys. J.* **436**, 423

[4] Bennett C.L. *et al.*, 1996, *Astrophys. J.* **464**, L1

[5] Bunn, E., & White, M., 1996, *astro-ph* 960735

[6] Górski K.M., 1994, *Astrophys. J.* **430**, L85

[7] Górski K.M. *et al.*, 1994, *Astrophys. J.* **430**, L89

[8] Górski K.M. *et al.*, 1996, *Astrophys. J.* **464**, L11

[9] Hinshaw G. *et al.*, 1996, *Astrophys. J.* **464**, L25

[10] Hinshaw G. *et al.*, 1996, *Astrophys. J.* **464**, L17

[11] Kogut A. *et al.*, 1996, *Astrophys. J.* **464**, L5

[12] Kogut A. *et al.*, 1996, *Astrophys. J.* **464**, L29

[13] Kogut A. *et al.*, 1996, *Astrophys. J.* **470**, 653

[14] Smoot G.F. *et al.*, 1992, *Astrophys. J.* **396**, L1

[15] Tegmark M., 1996, *Astrophys. J.* **464**, L34

[16] Wright, E.L., 1996, *Astrophys. J.* **464**, L21

CONSTRAINING TOPOLOGY WITH THE CMB

Angélica de Oliveira-Costa[1], George F. Smoot[2] & Alexei A. Starobinsky[3]
[1]*Max-Planck-Institut für Astrophysik, Garching, Germany.*
[2]*Lawrence Berkeley National Laboratory, Berkeley, USA.*
[3]*Russian Academy of Sciences, Moscow, Russia.*

Abstract

We present a new data analysis method to study rectangular T^3 "small universes" with one or two of its dimensions significantly smaller than the present horizon (which we refer to as T^1- and T^2-models, respectively). We find that the 4 year $COBE$/DMR data set a lower limit on the smallest cell size for T^1- and T^2-models of $3000h^{-1}$Mpc, at 95% confidence, for a scale invariant power spectrum (n=1).

1 Introduction

In the past few years, mainly after the discovery of CMB anisotropies by $COBE$/DMR [11], the study of the topology of the universe has become an important problem for cosmologists and some hypotheses, such as the "small universe" model [4], have received considerable attention. From the theoretical point of view, it is possible to have quantum creation of the universe with a multiply-connected topology [16]. From the observational side, this model has been used to explain the "observed" periodicity in the distributions of quasars [7] and galaxies [1].

Almost all work on "small universes" has been limited to the case where the spatial sections form a rectangular basic cell with sides L_x, L_y, L_z and with opposite faces topologically connected, a topology known as toroidal. The three-dimensional cubic torus T^3 is the simplest model among all possible multiply-connected topologies, in which all three sides have the same size $L \equiv L_x = L_y = L_z$. In spite of the fact that cubic T^3-model has been ruled out by $COBE$ results [2, 8, 12, 13, 14], the possibility that we live in a universe with a more anisotropic topology, such as a rectangular torus T^3, is an open option that has not been ruled out yet. For instance, if the toroidal model is not a cube, but a rectangle with sides $L_x \neq L_y \neq L_z$ and with one or two of its dimensions significantly smaller than the horizon R_H ($\equiv 2cH_0^{-1}$), this small rectangular universe cannot be completely excluded by any of the previous analyses:

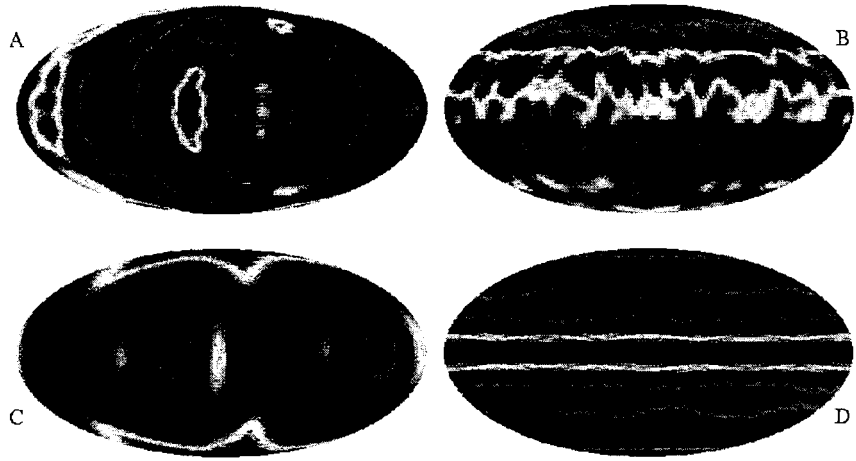

Figure 1: Simulated sky maps for the T^1- and T^2-models and their S-maps. (A) T^1-model with dimensions $(L_x, L_y, L_z) = R_H(3,3,0.3)$; (B) T^2-model with dimensions $(L_x. L_y, L_z) = R_H(0.3,0.3,3)$; (C) S-map of the T^1-model shown in (A); (D) S-map of the T^2-model shown in (B). Both models are plotted in galactic coordinates and have a scale invariant power spectrum (n=1).

constraints from the DMR data merely require that at least one of the sides of the cell be larger than R_H.

As pointed out by [5] and [13], if the rectangular T^3-universe has one of the cell sizes smaller than the horizon and the other two cell sizes are of the order of or larger than the horizon (for instance, $L_z \ll R_H$ and $L_x. L_y \gtrsim R_H$), the values of $\delta T/T$ are almost independent of the z-coordinate, *i.e.*, the large scale CMB pattern shows the existence of a symmetry plane formed by the x and y-axes; and if it has two cell sizes smaller than the horizon and the third cell size is of the order of or larger than the horizon (for instance, $L_x, L_y \ll R_H$ and $L_z \gtrsim R_H$), the temperatures $\delta T/T$ are aproximately independent of both x and y. *i.e.*, the CMB pattern shows the existence of a symmetry axis: values of $\delta T/T$ are almost constant along rings around the z-axis. We call the former case a T^1-model because the spatial topology of the universe becomes just T^1 in the limit $L_x, L_y \to \infty$ with L_z being fixed. The later case is denoted a T^2-model for the same reason (the corresponding limit is $L_z \to \infty$ with L_x, L_y being fixed). See Figures 1A (upper left) and 1B (upper right).

Our goal is to show that the $COBE$/DMR maps have the ability to test and rule out T^1- and T^2-models. We use a new approach to study these models in which we constrain their sizes by looking for the symmetries that they would produce in the CMB, obtaining strong constraints from the 4 year $COBE$/DMR data.

2 The method

The analysis of T^1- and T^2-models is not an easy task, since there are infinitely many combinations of different cell sizes and cell orientations. In order to study these models, we

choose a statistic in which we calculate the function $S(\hat{\mathbf{n}}_i)$ defined by [3]

$$S(\hat{\mathbf{n}}_i) \equiv \frac{1}{N_{pix}} \sum_{j=1}^{N_{pix}} \frac{[\frac{\delta T}{T}(\hat{\mathbf{n}}_j) - \frac{\delta T}{T}(\hat{\mathbf{n}}_{ij})]^2}{\sigma(\hat{\mathbf{n}}_j)^2 + \sigma(\hat{\mathbf{n}}_{ij})^2}, \tag{1}$$

where N_{pix} is the number of pixels that remain in the map after the Galaxy cut has taken place, $\hat{\mathbf{n}}_{ij}$ denotes the reflection of $\hat{\mathbf{n}}_j$ in the plane whose normal is $\hat{\mathbf{n}}_i$, *i.e.*,

$$\hat{\mathbf{n}}_{ij} = \hat{\mathbf{n}}_j - 2(\hat{\mathbf{n}}_i \cdot \hat{\mathbf{n}}_j)\hat{\mathbf{n}}_i, \tag{2}$$

and $\sigma(\hat{\mathbf{n}}_j)$ and $\sigma(\hat{\mathbf{n}}_{ij})$ are the r.m.s. errors associated with the pixels in the directions $\hat{\mathbf{n}}_j$ and $\hat{\mathbf{n}}_{ij}$. $S(\hat{\mathbf{n}}_i)$ is a measure of how much reflection symmetry there is in the mirror plane perpendicular to $\hat{\mathbf{n}}_i$. The more perfect the symmetry is, the smaller $S(\hat{\mathbf{n}}_i)$ will be. When we calculate $S(\hat{\mathbf{n}}_i)$ for all 6144 pixels at the positions $\hat{\mathbf{n}}_i$, we obtain a sky map that we refer to as an S-map. This sky map is a useful visualization tool and gives intuitive understanding of how the statistic $S(\hat{\mathbf{n}}_i)$ works.

In order to better understand $S(\hat{\mathbf{n}}_i)$, we first consider the simple model of a T^1-universe with $L_z \ll R_H$. For this specific model, the values of $\delta T/T$ are almost independent of the z-coordinate, so we have almost perfect mirror symmetry about the xy-plane or, in spherical coordinates, $\delta T/T(\theta,\phi) \approx \delta T/T(\pi-\theta,\phi)$. When $\hat{\mathbf{n}}_i$ points in the direction of the smallest cell size (*i.e.*, in the z-direction), we have $S(\hat{\mathbf{n}}_i) \approx 1$; otherwise, $S(\hat{\mathbf{n}}_i) > 1$. An S-map for a T^1-model $(L_x, L_y, L_z) = R_H(3,3,0.3)$ can be seen in Figure 1C (lower left). Notice in this plot that the direction in which the cell is smallest can be easily identified by two "dark spots" at $\hat{\mathbf{n}}_i \approx \hat{\mathbf{z}}$ and $\hat{\mathbf{n}}_i \approx -\hat{\mathbf{z}}$. For T^2-models, the only difference will be that in the place of the two "dark spots", we have a "dark ring" structure in the plane formed by the two small directions. See Figure 1D (lower right), an S-map of the T^2-model $(L_x, L_y, L_z) = R_H(0.3,0.3,3)$.

From the two S-maps, we can infer two important properties: first, the direction in which the S-map takes its minimum value, denoted S_o, is the direction in which the universe is small. For a large universe such as $L_x, L_y, L_z \gg R_H$, the S_o-directions obtained from different realizations are randomly distributed in the sky. Secondly, the distribution of S_o-values changes with the cell size, *i.e.*, as the universe becomes smaller, the values of S_o decrease. From the definition of the S-map, it is easy to see that the value of S_o is independent of the cell orientation. In other words, if we rotate the cell, we will just be rotating the S-map, leaving its minimum value S_o unchanged.

From here on, we will present our results in terms of the cell sizes R_x, R_y and R_z, usually sorted as $R_x \leq R_y \leq R_z$ and defined as $R_x \equiv L_x/R_H$, $R_y \equiv L_y/R_H$ and $R_z \equiv L_z/R_H$. We remind the reader that the results are identical for all six permutations of R_x, R_y and R_z.

3 Data Analysis

If the density fluctuations are adiabatic and the Universe is spatially flat, the Sachs-Wolfe fluctuations in the CMB are given by [10]

$$\frac{\delta T}{T}(\theta,\phi) = -\frac{1}{2}\frac{H_0^2}{c^2}\sum_{\mathbf{k}} \frac{\delta_{\mathbf{k}}}{k^2} e^{i\mathbf{k}\cdot\mathbf{r}}, \tag{3}$$

where $\mathbf{r}$ is the vector with length $R_H \equiv 2cH_0^{-1}$ that points in the direction of observation (θ,ϕ), H_0 is the Hubble constant (written here as $100h$ km s^{-1} Mpc^{-1}) and $\delta_{\mathbf{k}}$ is the density fluctuation in Fourier space, with the sum taken over all wave numbers $\mathbf{k}$.

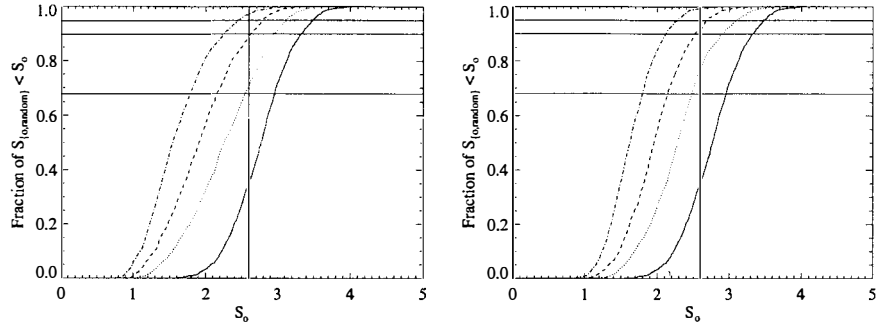

Figure 2: Cumulative probability distribution of $S_\circ$ for T^1- and T^2-models obtained from Monte Carlo simulations. A, left plot: Simulations for T^2-universes with dimensions (R_x, R_y, R_z) = (0.5,0.5,3) or dot-dashed line, (0.6,0.6,3) or dashed line, and (0.7,0.7,3) or dotted line. B, right plot: Simulations for T^1-universes with dimensions (R_x, R_y, R_z) = (0.5,3,3) or dot-dashed line, (0.6,3,3) or dashed line, and (0.7,3,3) or dotted line. In both pictures the model (R_x, R_y, R_z) = (3,3,3) is represented by a solid line, $S_\circ^{DMR} = 2.59$ (vertical straight line) and the horizontal solid lines indicate the confidence levels of 95%, 90% and 68% (from top to bottom).

In a Euclidean topology the universe is isotropic, and the sum in (3) is normally replaced by an integral. However, in a toroidal universe this is not the case. In this model, only wave numbers that are harmonics of the cell size are allowed. As a result, we have a discrete $\mathbf{k}$ spectrum [6, 15]

$$\mathbf{k} = \frac{2\pi}{R_H}\left(\frac{p_x}{R_x}, \frac{p_y}{R_y}, \frac{p_z}{R_z}\right), \tag{4}$$

where p_x, p_y and p_z are integers.

From equation (3), we can construct simulated skies by calculating [3]

$$\frac{\delta T}{T}(\theta,\phi) \propto \sum_{p_x,p_y,p_z} \left[g_1 \cos(2\pi\gamma) + g_2 \sin(2\pi\gamma)\right] \alpha^{\frac{n-4}{4}} e^{-(R_H \Theta k_\perp)^2/2} + n(\theta,\phi), \tag{5}$$

where g_1 and g_2 are two independent Gaussian random variables with zero mean and unit variance, $\gamma = \left(\frac{p_x}{R_x}x + \frac{p_y}{R_y}y + \frac{p_z}{R_z}z\right)$, $\alpha \equiv \left(\frac{p_x}{R_x}\right)^2 + \left(\frac{p_y}{R_y}\right)^2 + \left(\frac{p_z}{R_z}\right)^2 \propto k^2$ and n is the spectral index of the scalar perturbations. The term $e^{-(R_H\Theta k_\perp)^2/2}$ represents the experimental beam function, where $k_\perp$ is the length of the $\mathbf{k}$-component perpendicular to the line of sight and Θ is the width of the Gaussian beam given by $\Theta = \mathrm{FWHM}/\sqrt{8\ln 2} \approx 0.43\ \mathrm{FWHM}$, where FWHM is the full width of the beam at its half maximum. Finally, we model the noise $n(\theta,\phi)$ at each pixel i as independent Gaussian random variables with mean $\langle n_i \rangle = 0$ and variance $\langle n_i n_j \rangle = \sigma_{ij}\delta_{ij}$ [9].

We generate our simulated skies as standard DMR maps with 6144 pixels for n=1, with a Galaxy cut of 20°, FWHM = 7°, the monopole and dipole removed, add noise and normalize to $\sigma_{7^\circ} = 34.98\mu$K (the r.m.s. value at 7° extracted from our DMR map, a 4 year combined 53 plus 90 GHz map with monopole and dipole removed). Fixing a cell size, we construct a simulated sky according to (5), we smooth this once more by 7° and use the statistic defined in (1) to obtain an S-map from which we extract its minimum value $S_\circ$. Repeating this procedure 1000 times, we obtain the probability distribution of $S_\circ$ for that fixed cell size. When we repeat this same procedure for different cell sizes, we are able to construct plots as shown in Figure 2.

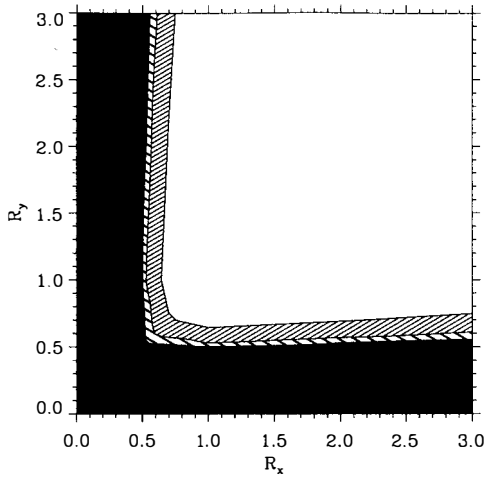

Figure 3: Grid of cumulative probability distributions of S_o for T^1- and T^2-models obtained from Monte Carlo simulations. The thin-shaded, thick-shaded and grey regions correspond, respectively, to the models ruled out at 68%, 90% and 95% confidence.

In Figure 2A (left plot), we show the cumulative probability distribution of S_o obtained from the Monte Carlo simulations for the cell sizes $(R_x, R_y, R_z) = (0.5,0.5,3)$, $(0.6,0.6,3)$, $(0.7,0.7,3)$ and $(3,3,3)$. The horizontal lines indicate the confidence levels of 95%, 90% and 68% (from top to bottom). Comparing these curves with the value $S_o^{DMR} = 2.59$ (represented in the plot by the vertical straight line), where S_o^{DMR} is the S_o value extracted from our data set, we conclude that T^2-models with smallest cell sizes R_x, $R_y \lesssim 0.5$ can be ruled out at 95% confidence. As the second cell size R_y is increased, the curves shift to the left of the T^2-models and we can rule out T^1-models for $R_x \lesssim 0.5$ at a similar confidence level, see Figure 2B (right plot). In this plot, we show the cumulative probability distribution of S_o obtained from Monte Carlo simulations for the cell sizes $(R_x, R_y, R_z) = (0.5,3,3)$, $(0.6,3,3)$, $(0.7,3,3)$ and $(3,3,3)$.

A more complete picture of the cell size limits is obtained when we construct a two-dimensional grid for different values of the cell sizes (R_x, R_y, R_z) with $R_z = 3.0$ and $0.2 < R_x, R_y < 3.0$ (see Figure 3). The thin-shaded, thick-shaded and grey regions correspond, respectively, to the models ruled out at 68%, 90% and 95% confidence. Notice in this plot that all contours are almost L-shaped, which means that, to a good approximation, the level in which a model (R_x, R_y) is ruled out depends only on the *smallest* cell size, $R_{min} \equiv min\{R_x, R_y\}$. We see that $R_{min} \gtrsim 0.5$ at 95% confidence.

4 Conclusions

We have shown that the $COBE$/DMR maps have the ability to test and rule out T^1 and T^2 topological models. We have presented a new statistic to study these anisotropic models which quantifies the "smallness" of a sky map in a single number, S_o, which is independent of the cell orientation, is precisely sensitive to the type of symmetries that small universes produce, is easy to work with and is easy to interpret.

From the *COBE*/DMR data, we obtain a lower limit for T^1- and T^2-models of $R_x \gtrsim 0.5$, which corresponds to a cell size with smallest dimension of $L=3000h^{-1}$Mpc. This limit is at 95% confidence and assumes $n=1$. Since the topology is interesting only if the cell size is considerably smaller than the horizon, so that it can (at least in principle) be directly observed, these models lose most of their appeal. Since the cubic T^3 case has already been ruled out as an interesting cosmological model [2], and T^1- and T^2-models for small cell sizes are ruled out, this means that *all* toroidal models (cubes and rectangles) are ruled out as interesting cosmological models.

Acknowledgements. We would like to thank Jon Aymon and Al Kogut for the help with the *COBE* library subroutines and Max Tegmark for many useful comments on the manuscript.

References

[1] Broadhurst, T.J., Ellis, R.S., Koo, D.C. & Szalay, A.S. 1990, *Nature* **343**, 726

[2] de Oliveira-Costa, A. & Smoot, G.F. 1995, *Astrophys. J.* **448**, 447

[3] de Oliveira-Costa, A., Smoot, G.F. & Starobinsky, A.A. 1996, *Astrophys. J.* **468**, in press

[4] Ellis, G.F.R. & Schreiber, G. 1986, *Phys. Lett. A* **115**, 97

[5] Fang, L.Z. 1993, *Mod. Phys. Lett. A* **8**, 2615

[6] Fang, L.Z. & Houjun, M. 1987, *Mod. Phys. Lett. A* **2**, 229

[7] Fang, L.Z. & Sato, H. 1985, *Gen. Rel. and Grav.* **17**, 1117

[8] Jing, Y.P. & Fang, L.Z. 1994, *Phys. Rev. Lett.* **73**, 1882

[9] Lineweaver, C. et al. 1994, *Astrophys. J.* **436**, 452

[10] Peebles, P.J.E. 1982, *Astrophys. J.* **263**, L1

[11] Smoot, G.F. et al. 1992, *Astrophys. J.* **396**, L1

[12] Sokolov, I.Y. 1993, *JETP Lett.* **57**, 617

[13] Starobinsky, A.A. 1993, *JETP Lett.* **57**, 622

[14] Stevens, D., Scott, D. & Silk, J. 1993, *Phys. Rev. Lett.* **71**, 20

[15] Zel'dovich, Ya B. 1973, *Comm. Astrophys. Space Sci.* **5**, 169

[16] Zel'dovich, Ya B. & Starobinsky, A.A. 1984, *Sov. Astron. Lett.* **10**, 135

NORMALISATIONS OF COSMOLOGICAL MODELS FROM *COBE*–DMR 4YR DATA

Radek Stompor
Astrophysics, Nuclear and Astrophysics Laboratory, University of Oxford, Keble Road, Oxford 3RH, U. K.

Abstract I summarise the results of the precise fitting of the broad set of cosmological models to the *COBE*–DMR 4 year data. The obtained normalisations, expressed in terms of Q_{rms-PS}, are provided in the form of useful approximate (good within 3%) fitting formulae.

1 INTRODUCTION

The detection[1] of the cosmic microwave background anisotropies (CMB) by the *COBE* satellite provide unambiguous means enabling precise normalisation of the models of structure formations. The significance of that was utterly expressed by the enormous number of recently published papers analyzing practically all popular cosmological models in the light of the *COBE*-DMR data. Most of the analyses to date where however based on the data obtained during two first years of the *COBE* mission. Here, I present precise normalisations for a broad set of cosmological models obtained with the linear fitting method as described by Górski[2,3].

In the presented analysis[4], special care has been taken of the systematic uncertainties arising as a consequence of the non-uniqueness of the possible data selection. To account on that we considered two coordinate frames choice, two different galactic cuts and performed the fittings with and without the quadrupole term. More detailed descriptions and the discussion of those effects as well as their influence on the final result in a case of the power-law spectra can be found elsewhere[5].

The set of considered here models includes adiabatic: critical density, spatially flat with non-zero cosmological constant and open models. In most of the cases we vary not only background cosmological parameters (e.g. Hubble constant or total density) but also the shape of the primordial fluctuations power spectrum. Also we allow for existence of non-zero gravity wave contribution. The standard thermal scenario is assumed everywhere in this paper. Obtained normalisations are expressed in terms of Q_{rms-PS}[6].

The analysis of the consequences of the 4year DMR normalisations for cosmological models can be found elsewhere[7].

2 CRITICAL DENSITY MODELS

The critical density models, though just a subset of spatially flat (or open) models, used to attract particular attention in the past, therefore here we consider them separately. As in a case of the 2 year analysis[8], we find negligible dependence of the results on the cosmological background parameters (for $h \in [0.3,\ 0.8]$ and Ω_b as constrained by standard nucleosynthesis).

• **tilted scalar:** we found that the best fit values can be summarized in that case by the following formula (n_S stands for the tilt of the primordial power spectrum):

$$Q_{rms-PS}[\mu K] = 17.7^{+3.0}_{-3.0} \exp((0.8 \pm 0.04)(1 - n_S)), \qquad (1)$$

here the quoted errors correspond to 2σ statistical deviations, including systematic error $\sim 1\mu K$ (but depending slightly on n_S). The galactic–ecliptic frame difference for a given galactic

cut stands at most for $\sim 1\mu K$. The changes of the '2σ' contours with different data selections are depicted in Figure 1a.

• **tilted with non-zero gravity wave contributions:** here we fix the relations between the index of primordial spectrum of scalar perturbations (n_S) and that of gravity wave (n_T) according to a power-law inflation prediction[9] i.e. $n_T = n_S - 1$, but allow for the changes of the relative contributions (denoted $r \equiv Q^T_{rms-PS}/Q^S_{rms-PS}$) of both components (canonical power-law inflation value of r is $7(1-n_S)$). We manage to craft the following fitting function:

$$Q_{rms-PS}[\mu K] = 17.7^{+3.0}_{-3.0}(1 + 0.83(1 - n_S)) - 4.1(2.1 - 1.1n_S)r^{1.6}, \qquad (2)$$

Again the quoted errors correspond to 2σ deviations. The above formula works well for $1.0 \geq n_S \geq 0.7$, and $r \leq 1$, and is more precise than the more general fit given below (eqns. (3) and (4)) especially in the regime of large tilts ($n_s \leq 0.85$).

3 SPATIALLY FLAT MODELS

In that case not only obvious dependence of Ω_0 but also residual dependence of h for low $\Omega_0(\leq 0.2)$ has to be taken into account what makes the form of the fit more cumbersome. We restrict our analysis to $h \in [0.5, 0.8]$ and $\Omega_0 \in [0.1, 1.0]$. Then it is usefull to consider two generic cases:

•**Harrison-Zel'dovich** ($n_S = 1,\ r = 0$) **case :**

$$Q_{rms-ps}[\mu K] = 17.7^{+3.0}_{-3.0} + 8.83^{+1.4}_{-1.4}h^{0.6}\exp(-11.37(\Omega_0 - 0.02/h)^2 h^{0.25}), \qquad (3)$$

where given ranges for coefficients correspond to 2σ deviations. Those account also for a systematic error, which is of the order of $\sim 1\mu K$ for high values of Ω_0 and increases to $\sim 2\mu K$ at $\Omega_0 \leq 0.2$ (see Figure 1b).

In a case of those models the 2 year data enabled[8,10] putting a 95% lower confidence limit on Ω_0 equal to 0.15. The analogous analysis based on 4 year data sets the similar limit, if a full range of acceptable values of Ω_0 (i.e. $0 \leq \Omega_0 \leq 1$) is considered. That limit can be increased up to ~ 0.2 if only cases with the included quadrupole are taken into account. In those cases also the almost critical density is the most preffered one. In the case with the excluded quadrupole both lower 95% confidence limit as well as the most likely value of total density are shifted down to $\Omega_0 \sim 0.15$ and $\Omega_0 \sim 0.3 - 0.4$ respectively, however, with a critical density model always comfortably acceptable.

• **tilted with non-zero gravity waves contributions** ($n_T = n_S - 1$)**:** Using notation as in a case of critical density models, we find that, for $1.0 \geq n_s \geq 0.8$, $r \leq 1$, and others

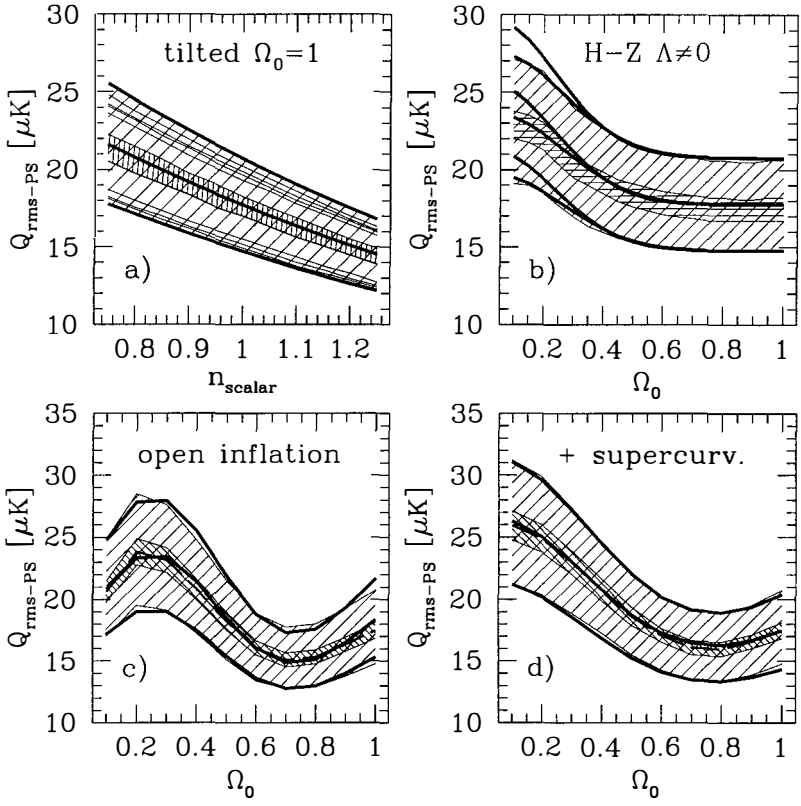

Figure 1: The dependence of the fitted Q_{rms-PS} on cosmological parameters for four different sets of models: (a) tilted critical density models (no gravity waves); (b) non-zero cosmological constant models with Harrison-Zel'dovich initial conditions; (c) open models with open inflation initial conditions; and (d) open models with bubble inflation initial conditions including super-curvature mode contribution. In each panel the thick lines are described by the approximate formulae (average values and '$\pm 2\sigma$') as given in the text. The narrow densely shaded strip shows the size of the systematic errors as investigated in this analysis. The broken line (overlapping within the width of the lines with the approximations in panel (a) and (b)) shows the exact averaged ('best') normalisation. In addition, in (a) the thin almost horizontal lines show the differences of the positions of '$\pm 2\sigma$' bands for each of 4 possible data selections in a galactic coordinate frame. In (b) two sets of three thick lines described by the formula (3) correspond to two values of Hubble constant: $h = 0.5$ - lower (shaded) triplet, $h = 0.8$ - higher at low Ω_0 end of the panel.

parameters specified as above, the following approximate formula can be successfully applied.

$$Q_{rms-PS}[\mu K] = Q_{rms-PS}(n_S = 1, r = 0)\frac{(18 + (13 - 5(1 - \Omega_0))(1 - n_S))}{18(1 + ((0.575 + 0.45(1 - \Omega_0)^4)r)^2)}. \quad (4)$$

Here the multiplicative factor $Q_{rms-PS}(n_S = 1, r = 0)$ (denoting amplitude for H-Z models without gravity waves) is given by the formula (3) above.

4 OPEN MODELS

For open universes we focus only on pure scalar mode, considering four different possible choices of initial conditions (and $\Omega_0 \in [0.1, 1.0]$ and $h \in [0.5, 0.8]$). It appears that the shape of the power spectra depend much weaker on the value of the Hubble constant than in spatially flat, low density case, and that dependence can be safely neglected for entire range of considered Ω_0 and h as specified above. The initial conditions considered include scale invariant[11], open inflation[12,13] and bubble inflation[14], and bubble inflation plus superhorizon perturbations[15]. The fitting formulae are as follows:

- **scale invariant :**

$$Q_{rms-PS}[\mu K] = 15.0^{+2.95}_{-2.5} + 3.25^{+0.6}_{-0.8}\sin(2\pi(1 + 0.25\Omega_0)(\Omega_0 + 0.05) - 1.25), \quad (5)$$

the errors of that formula are of the order of 3%, for $\Omega_0 \in [0.1, 1.0]$ reaching level of 4% only at the ends of that interval. The variations caused by the different values of the Hubble parameter are of the same order as the inaccuracies of given above fitting function itself.

- **open and bubble inflation :** we consider both cases together while the differences of the resulting CMB power spectra are generally negligible:

$$Q_{rms-PS}[\mu K] = 19.0^{+3.5}_{-3.25} + \left(4.95^{+2.5}_{-1.2} - \Omega_0\right)\sin\left(2\pi(1 - 0.25(\Omega_0 - 1.1))(\Omega_0 - 0.05)\right). \quad (6)$$

The quoted uncertainties correspond to a 2σ region. The inaccuracies of the fitting function are around $\sim 2\%$ (but $\Omega_0 \sim 1$ where they reach $\sim 3.5\%$ level) in a case of the open inflation, and are slightly larger ($\sim 3\%$ for $\Omega_0 \leq 0.9$ and $\sim 4\%$ for larger Ω_0) for the bubble scenario.

As in the models with non-zero cosmological constant the lower 95% confidence limit depends on the inclusion or exclusion of the quadrupole. The conservative value is around $\Omega_0 \sim 0.17$. Similarly, the most likely values of total density are around 0.7 with included quadrupole, and ~ 0.4 otherwise. In all considered cases flat model provides only somewhat worse fit to the data than the most favourable one.

- **bubble inflation plus superhorizon perturbations :** adding supercurvature contribution[16] connected with the infinitely long perturbation[15] decreases the effective spectral

index n_{eff} of the power spectrum. Hence the COBE-DMR preffered values of Q_{rms-PS} go up for low Ω_0 models as compared with the previous case. The very accurate fitting (within $\sim 1-1.5\%$) function in that case reads as follows,

$$Q_{rms-PS}[\mu K] = 21^{+3.7}_{-4.0} + (5.55^{+1.1}_{-1.1} - \Omega_0)\cos\left(1.25\pi(1-0.25(\Omega_\bullet - 1.1))(\Omega_0 - 0.05)\right). \quad (7)$$

The 4 year 95% lower confidence limit on Ω_0 is ~ 0.16 (though it might be as high as 0.28 in cases with the excluded quadrupole) as compared with the value 0.36 obtained with the analysis of 2 year data[17]. The most likely values of Ω_0 are ~ 0.7 when the quadrupole term is excluded, and $\sim 0.4-0.45$ otherwise, again with a critical density model well within a domain of acceptability.

Acknowledgments: This report is based on the common work with Krzysztof Górski and Tony Banday. This work was supported by the grant from UK PPARC.

REFERENCES

1. Bennett, C. L., *et al* 1996, COBE preprint
2. Górski, K. M. 1994, ApJ, **430**, L85
3. Górski, K. M., *et al* 1994, ApJ, **430**, L89
4. Górski, K. M., Stompor, R., & Banday, A. J. 1996, *in preparation*
5. Górski, *et al* 1996, COBE preprint
6. Smoot, G. F., *et al* 1992, ApJ, **396**, L1
7. Stompor, R., Górski, K. M., & Banday, A. J. 1996, *in preparation*
8. Stompor, R., Górski, K. M., & Banday, A. J. 1995, MNRAS, **277**, 1225
9. Davis, R. L., *et al* 1992, Phys. Rev. Lett. **69**, 1856
10. Bunn, E., & Sugiyama, N. 1995, ApJ, **441**, L9
11. Wilson, M. L. 1983, ApJ, **273**, 2
12. Lyth, D. H, & Stewart, E. D. 1990, Phys. Lett. B., **252**, 336
13. Ratra, B., & Peebles, P.J.E. 1995, Phys. Rev., **D52**, 1837
14. Bucher, M., &, Turok, N. 1995, Phys. Rev., **D52**, 5538
15. Yamamoto, K., Sasaki, M., & Tanaka, T. 1995, ApJ, **455**, 412
16. Lyth, D. H., & Woszczyna, A. 1995, Phys. Rev., **D52**, 3338
17. Yamamoto, K., & Bunn, E., 1995, Ap.J. *in press*

Spatial–Frequency Analysis of the COBE Data and the CMB Anisotropy Spectrum

D. P. Skulachev, A. A. Brukhanov, I. A. Strukov, T. V. Konkina
Space Research Institute, Russian Academy of Sciences, ul. Profsoyuznaya 84/32, Moscow, 117810 Russia

E-mail: istrukov@esoc1.iki.rssi.ru, virgo@relict.iki.rssi.ru

Abstract

The problem of obtaining estimates for the cosmic microwave background (CMB) anisotropy spectrum when applying the Galaxy-removal procedure is discussed. A method of two-step spatial–frequency filtering that retains the orthogonality of spherical harmonics is proposed. This method is used to analyze the four-year COBE data. After the analysis of the difference maps containing noise alone, the l = 13,14, 23, and 25 multipoles have been excluded from the data under consideration because the noise power in these multipoles in the difference maps turned out to be statistically anomalous. This procedure is shown to introduce no significant systematic errors for the noise-spectrum model employed. Once the multipoles that are anomalous in terms of noise have been removed, the analysis has yielded a power-law index of the the CMB anisotropy power spectrum of $n = 1.87 \pm 0.25$ and a quadrupole mean of $Q_{rms-PS} = 13.79 \pm 3.0$ for 53 GHz, and $n = 1.51 \pm 0.24$ and a quadrupole mean of $Q_{rms-PS} = 15.58 \pm 2.9$ for 90 GHz.

1 Introduction

The large-scale cosmic microwave background (CMB) anisotropy carries information about the spectrum and amplitude of primordial metric perturbations, and its shape reflects the composition and evolution of the Universe. Having high sensitivity and several frequency channels, the COBE experiment (Smoot et al. 1992) considerably extends our knowledge of the structure and the spectrum of the microwave background. Unfortunately, the Galaxy emission dominates the CMB radiation even at millimeter wavelengths. There are several methods to remove the Galaxy emission from radio maps. If we have a complete a priori knowledge about the Galaxy radiation, then we may simply subtract the corresponding signal from the measured data. The reminder part in this case is free from the Galactic emission. The method is the best but unreal: nobody knows the Galaxy emission with the necessary precise. With the advent of multi-frequency experiments, one would think that it become possible to directly separate the blackbody CMB component from the frequency-dependent Galactic emission. However, this procedure cannot be implemented with the required accuracy due to an apparatus noise and due to variations in the spectral composition of the Galactic radio sources. Since the bulk of the Galaxy emission comes from a rather narrow region along the Galactic plane, the next method is to "cut out" this region and study the properties of high-latitude domain only, as if the Galaxy is simply absent. The third and usually used method is a combine one: to "cut off" the Galaxy plane vicinity and subtract the residual Galactic emission using a priori data or data of other frequency channels. In this case the data of other frequencies may be used in two ways. The first is to to subtract the data of one channel from other with a priori known spectral index and to take into account a change of a cosmological signal. The second way is to subtract the part of the measured signal that correlates with other frequency channel in which the cosmological signal is a priori negligible, for example with very low or very high frequency channel (Kogout et al. 1996). However, this widely accepted technique is quite adequate only in analysis of variance of the data. In analysis of the spatial spectrum, the orthogonality of spherical functions on the rest of the sphere is lost, and, as a consequence, the harmonics begin to influence each to other. This problem can be partly resolved by introducing a new basis that is orthogonal only on part of the sphere (Gorski 1994) or orthogonal only to the monopole and dipole, whose removal on the incomplete sphere has the strongest effect on the spectrum (Wright et al.1994). The spectra obtained in this way may differ from the actual spectra (Bunn et al. 1994), leading to essentially different conclusions in the interpretation of the results.

We propose a method of all-sky map data analysis on the spatial frequencies domain. We do not use any "Galactic cut" at the radio maps. The Galaxy foreground removal in this case is done by a help of Galactic "spatial frequency cut", when some of spatial harmonics are removed from the overall spatial spectrum. Proposed method of analysis gives the greatest resolution in spatial harmonics without losing their mutual orthogonality. The technique consists in CMB filtering after a spherical-harmonic expansion of the radio-brightness temperature map and involves two filtering steps. In the first step, spatial filtering is performed: some spectrum components related to the Galaxy structures are excluded from the overall spatial spectrum, resulting in a considerable reduction in the amplitude of the Galactic microwave emission. And only after applying this procedure, is a frequency "cleaning" made in the second step: several frequency channels are used to filter out the Galactic foreground in accordance with the Galactic-emission model chosen. Nowhere do both these steps lead to the loss of orthogonality of the signal spherical harmonics.

Table 1:

Frequency, GHz	$\sigma_{(A+B)/2}$, μK	$\sigma_{(A-B)/2}$, μK	σ_{Sky}, μK
Initial data (antenna temp.)			
31.5	585.43	71.31	581.07
53.0	175.11	23.99	173.47
90.0	109.93	34.00	104.54
Spatial cleared data (antenna temp.)			
31.5	193.19	66.80	181.28
53.0	64.36	21.82	60.55
90.0	44.57	32.04	30.98
Spatial and frequency cleared data (thermod.temp)			
53.0	59.80	52.48	28.70
90.0	52.66	45.72	26.16

2 COBE data analysis

We used the freely available four-year COBE DMR data for the entire sky obtained at frequencies of 31.5, 53, and 90 GHz as input data. As a tracer of the Galaxy emission we use COBE DIRBE 140 μ data but smoothed to DMR beam size. All the data were expanded to multipoles:

$$\Delta T(\theta,\varphi) = \sum a_{lm} Y_{lm}(\theta,\varphi)$$

Because of a strong antenna reduction of the signal amplitude if multipole number $l > 25$, we restricted the expansion with the l =2...25. We used the DIRBE 140 μ map to determine the "strong" spatial harmonics that are greater than 7 MJy/sr. All this harmonics are ejected from DMR maps. Such procedure strongly reduced the residual Galactic signal on the DMR maps. The criteria we used to determine the "strong" Galactic components is near optimal, but not critical. If we use smaller value we obtain the same results, only total amount of harmonics in analysis are reduced. Using a much larger value we increase the residual Galactic signal, but may find it as a part of DMR spatial spectrum that is correlated with DIRBE spectrum. After this spatial spectrum filtering we additionally subtract from the rest data a signal of free-free Galactic emission with the fixed spectral index of -2.15. Taking into account an increasing of the CMB signal after the last procedure, we multiply the result to an appropriate value. Then we calculated for this maps the spatial spectrum parts correlated with the DIRBE map, and this parts are subtracted from the spectra. The RMS of the correlated part is less then 10 μK. The result "clear" maps are free from any emission with the spectral index of -2.15, and also are free from emission of the Galaxy structures that may be seen at DIRBE 140 μ map. We also used 408 MHz all sky map (Haslam et al., 1981) as the Galaxy tracer . Because of a strong correlation between the 408 MHz and the DIRBE 140 μ maps, we obtain very close results. Then, using maximum likelyhood method (Brukhanov et al., 1996) we may get the estimation of cosmological parameters: a power-law index of the the CMB anisotropy power spectrum n, and a quadrupole mean Q_{rms-PS}.

The results of the analysis are accumulated in Table 1 and in the first row of Table 2.

The last column in Table 2 represent the data obtained COBE team using Galaxy corrected coadded map with custom 20° Galactic plane cut (Gorski et al. 1996). One can see that proposed method gives the possibility to get very close result, but without destroying the

Table 2:

53 GHz		90 GHz		Gorski et al.1996	
n	Q_{rms-PS}	n	Q_{rms-PS}	n	Q_{rms-PS}
1.23 ± 0.23	17.7 ± 2.8	1.25 ± 0.22	17.27 ± 2.7	1.24 ± 0.25	15.5 ± 3.1
1.87 ± 0.25	13.79 ± 3.0	1.51 ± 0.24	15.58 ± 2.9		

spatial harmonics orthogonality. More accurate, we have to emphasize that proposed method is more precise, because it does not distort the signal spectral components used in analysis.

3 COBE (A-B)/2 sky maps analysis

We have tested the statistical properties of spatial spectra in the DMR 4-year (A-B)/2 sky maps. These difference maps represent estimations of total noise on the maps. Based on the difference maps and on the model of the noise power, we can find the noise power spectrum amplitudes. Such an analysis indicates that individual noise harmonics exhibit an excess power. The excess power, lager than two standard deviation may be found at 31.5 GHz (A-B)/2 map spectrum for l = 25,at 53 GHz - for l =23, 25, at 90 GHz - for l =6, 14. The same analysis for the resulting map after subtracting free-free component shows the excess power at l =6, 14, 13, 25.

4 COBE (A+B)/2 sky maps analysis after additional filtering

The strong spectrum power couple and triple components may by cased by a noise stochastic nature, but probability of such event is less than 0.5%. More probable, they are a result of some systematic effects: gain instability, calibration errors, residual errors in mapping and Earth magnetic field removal, and so on. In any case the anomalous spectrum components are questionable, and we have ejected they from the analysis. After this additional filtration we calculated mean noise intensity in the rest components and corrected noise model specification. We use the noise model based on the number of observations in every pixel. Next, we again used the maximum likelyhood estimation for cosmological parameters n and Q_{rms-PS}. If the noise power spectrum outliers are low probable but happened stochastic events, then the removal the outliers leads to the bias in the estimations: $.07 \pm 0.08$ for n and -0.4 ± 0.8 μK for Q_{rms-PS}.

The results are represented in the last row in Table 2.

5 CONCLUSIONS AND IMPLICATIONS

The problem of eliminating systematic effects and foreground Galaxy emission arises virtually in any CMB anisotropy experiments. Conventional techniques for suppressing the Galaxy emission (Galactic-plane cut) destroy the spatial harmonics orthogonality and may conceal systematic errors. It necessitate a separate consideration of the procedure of removing the monopole and dipole components. Introducing an orthogonal basis, together with spatial-frequency

filtering of the Galaxy emission, allows these types of systematic effect to be eliminated. At the same time, it becomes possible to analyze and remove finer effects that produced uncertainties in the spectrum parameters. Assuming that the instrument noise is Gaussian, removal the questionable spatial components cannot result in a statistically significant change of the cosmological signal spectrum parameters. Our parameters of the cosmological-signal spectrum differ somewhat from those derived in the previous studies that used the same data for analysis. This difference is more likely a result of removing harmonics exhibiting anomalous noise than the procedure of spatial-frequency filtering of the Galactic emission employed. The harmonic exclusion became possible because the spherical harmonics retain their orthogonality.

6 ACKNOWLEDGMENTS

The COBE data were obtained at NASA/GSFC by the COBE Science Working Group and were provided by NSSDC. The COBE DIRBE smoothed data were kindly provided by K. Gorski. We are grateful to K. Gorski, A. Klypin and M. Sazhin for numerous discussions and useful remarks. This study was supported in part by the KOSMION Research and Educational Center and the Russian Foundation for Basic Research (projected no. 96-02-17619 and 96-02-17595).

7 References.

Bunn E., Hoffman Y., Silk J. Astrophys.J. 1994. V.425. P.359.

Brukhanov A.A., Skulachev D.P., Strukov I.A., Konkina T. V. Astronomy Letters, N3, 1996

Gorski K.M., Hinshaw G., Banday A.J., Bennet C.L. et.al. Astrophys.J.(Letters) 1994. V.430. L89.

Gorski K.M. et.al. COBE Preprint No.96-03

Haslam C.G.T. et al. 1981, A&A, 100,209

Kogut A. et al. COBE Preprint No.96-02

Smoot G.F., et.al. Astrophys.J.(Letters) 1992. V.396. L1.

Wright E.L. et al. 1994, Astrophys. J., vol. 436, p. 443.

PRECISION MEASUREMENTS OF THE CMB POWER SPECTRUM

P. M. Lubin
Department of Physics, University of California, Santa Barbara, CA 93106-9530, USA and Center for Particle Astrophysics, University of California, Berkeley, CA 94720, USA

Abstract

Within the next 5–10 years it will be possible to make precision maps of the CMB from both sub-orbital and orbital experiments. Maps covering a significant portion of the sky at high sensitivity and small beam sizes ($\ll$ horizon size at decoupling) will, in theory, allow for the extraction of fundamental cosmological parameters. These measurements of the CMB power spectrum promise to revolutionize our understanding of the early universe.

1 Introduction

Potentially, studies of the Cosmic Microwave Background (CMB) angular power spectrum can provide some of the most precise determinations of the fundamental cosmological parameters we can make. These measurements are also among the most difficult and challenging to make and we will have to await the next generation of experiments to see if the promise is fulfilled. The simplest fundamental assumptions made over half a century ago about a homogeneous and isotropic universe are still consistent with our current knowledge of the universe. We now know from studies of the CMB that the assumption of isotropy is valid to an astonishing level, one which has profoundly affected the theoretical concepts of how we view the very early universe. Our field has historically been one where even upper limits on detections could profoundly affect the theoretical framework. It is only in the past few years that this has changed from strict upper limits to hints of detection in 1991 to detection of structure and the beginning of measurements of the power spectrum today. We now have a rudimentary knowledge of the CMB power spectrum sufficient to constrain and even make preliminary measurements of the fundamental parameters such as total density, baryon fraction, etc. The challenge in the coming 5-10 years will be to extend these measurements to large sky coverage and broader frequency

coverage with beam sizes substantially smaller than 1 degree. Given the extremely small level of signal we have to contend with and the potential for systematic error, the convergence of a number of experiments will be required. Combining maps of the CMB with maps from other surveys, such as optical and IR LSS surveys, will provide a database we could only dream about even a decade ago. The potential for knowledge is enormous and while potential pitfalls are possible, we are much more confident today than we were even 5 years ago based on recent measurements.

2 Approaches to the Problem

Discovery comes awkwardly at first in many fields and it is no less true in this one. Not knowing the amplitude or shape of the power spectrum or the precise form of the galactic and extragalactic foregrounds has made our task that much more difficult. The experimental response has largely been to try many different experiments over a large angular and frequency range. We now have reasonably good agreement on the measurements and feel optimistic that we are truly measuring the cosmological power spectrum. If we concentrate on the degree scale and below measurements, we find a highly varied approach experimentally. Ground based and balloon borne systems have very different atmospheric emission and other systematic errors. For example, the atmospheric emission at 40 GHz varies from 10 K at some low ground based sites to 5 K at the South Pole to less than 1 mK at balloon altitudes. At 200 GHz ground based sites are extremely difficult to use for anisotropy measurements and even balloon borne measurements suffer from some non-trivial atmospheric contamination at the higher frequencies. In spite of the atmospheric emission sub orbital approaches have produced by far the most sensitive measurements, indeed our 1991 ground based measurements at the South Pole still have the smallest errors per pixel. This is in spite of the fact that the atmosphere is more than 5 orders of magnitude larger than the cosmological signal. Ideally we would like to map the CMB with infinite signal to noise and infinitely small beam size, i.e. make a "pencil beam" survey. In practice however we will have to incrementally approach the problem, rather than have one "ultimate" experiment. With at least two space missions now planned, MAP in the US and COBRAS-SAMBA in Europe, and possibly RELICT-II in Russia, spaced based observations will be well represented. The MAP mission may produce data as early as 2002 while the COBRAS-SAMBA mission would be a few years later. Ground based and balloon-borne measurements will also vigorously be pursued with very exciting results expected within a few years.

3 Balloon Borne Missions

The primary differences between a terrestrial and an orbital mission fall into several distinct areas. The main differences are the addition of the atmosphere as a source of emission, side-lobe instrument response reduction in extended orbit missions, possible reduction in optics temperature in orbit and the ability to make a more uniform dataset from space.

3.1 Atmosphere

The atmosphere effects a mission in a number of ways. The primary effect is that the atmosphere emits ,and absorbs, millimeter wavelength radiation in a complicated way depending on the wavelength and pressure and temperature profile in the air. The primary atmospheric

constituents that are responsible are O_2, O_3 and H_2O. Many other molecular species exist but in general are not significant for us. Pressure broadening of the lines is such that at sea level the emission spectrum is a "blur" of the individual lines into a slowly changing (in wavelength) continuum of emission. At high altitudes the pressure broadening is small enough that the individual lines become distinct and the ratio of the peak to the valley, where the tails of distinct lines meet, in the line spectra becomes very large. In Figure 2 we show an example of the atmospheric emission at low and high altitudes. At sea level the typical emission in the wavelength range of interest (1–10 mm) is several to many times the CMB itself. There is little distinct line emission apparent except near the 60 GHz oxygen cluster and a few other lines. At high altitudes available to balloons the emission is distinctly line-like with peak to valley ratios exceeding 1000 and a overall reduction from sea level emission in the most favorable windows of 10^4 from 10 K to 1 mK or even less. Note however that this kind of reduction is only possible for very narrow band systems that can observe between the lines. This is a distinct advantage of narrow band coherent systems, HEMTs for example, over broad band incoherent systems (bolometers). The situation becomes even worse at high frequencies as the flux (or equivalent antenna temperature) of the CMB becomes smaller as shown in Figure 2. Indeed, an interesting comparison is that our HEMT measurements at 30 GHz at the South Pole, 4 Km, had comparable atmospheric emission to the bolometric emission at balloon altitudes (35 Km) at 200 GHz, whereas our HEMT observations at balloon altitudes were a factor of 1000 lower. This is of fundamental importance to our ability to make 2-D maps from balloon altitudes with HEMTs. For the very sensitive instruments we now have, another aspect of observing through the atmosphere becomes important, namely "atmospheric noise". There are three issues here. The first is that the atmosphere increases the total effective system noise since the atmosphere adds a background (shot noise). The second is that the atmosphere varies both temporally and spatially. The third is that beam chopping through the atmosphere will add noise unless the beam precisely repeats its position. For example, a 1 arc second error in beam elevation will introduce a signal of 7T microK where T is the vertical atmosphere in Kelvin. There are two cases of interest here. One is that the instrument may oscillate slightly, as certainly occurs in balloon borne instruments. A one arc-minute amplitude oscillation would give a 400T microK amplitude signal. This is not negligible. A typical pendulation amplitude of 1 arc-minute would give such an amplitude. The vertical atmospheric emission (T) depends on the observing band and altitude. As mentioned above, this number can be of order 1 mK for HEMTs and 0.1–1 K for bolometers which for a 1 arc-minute pendulation would give a signal of 0.4 microK for a HEMT and 40–400 microK for a bolometer based experiment. This can be a critical issue for bolometer experiments. A related issue is the "altitude noise" of the instrument. In particular, the instrument will have short term variation in the elevation position due to excitation of various modes in the balloon, flight train and payload. An amplitude of 10–60 arc seconds is not atypical. This can add noise as well as an aliased signal. The level of noise and signal is a complicated function of the sampling, scan, excitation modes and pendulation frequency. The very low level of the atmospheric emission for balloon borne HEMT measurements makes possible a 2 dimensional scan mode that allows a map to be directly generated. This is the basis for our balloon borne ACE experiment, for example.

3.2 Sidelobes

The small level of the cosmological signal requires extremely good rejection of other sources of millimeter radiation. There are a number of sources to be concerned about. These include the earth, moon, sun, atmosphere and galaxy as the dominant contributors. The earth is the primary problem for most of the relevant experiments. With an effective temperature near 300

K and a desired instrument sensitivity of 10 microK rejection of the earth of $> 10^8$ is desired. In terms of antenna response the relevant factor is the comparison between the main beam size, assume it to be 10 arc minutes, and the solid angle of the earth, (2π steradians). This gives another factor of 10^6. Therefore, ideally, we would like to reject the earth at a level of $> 10^{14}$ or 140 db. This is nearly an impossible number to achieve in practice and indeed is overly pessimistic. The reason is that the earth does not present a unity contrast target for the system and that the chopped response is far less. Indeed in our tests of the ACME instrument to detect earth sidelobe emission *in situ* by looking close to the horizon we have not been able to detect it except at extremely small angles near the horizon. It is also important to note that to mimic a cosmological signal the earth signal would have to change at the celestial rate or be aliased into it.

3.3 Optics Temperature Issues

At balloon altitudes the typical air temperature is $-20°$ to $-50°$ C. In low earth orbit radiatively cooled optics reach 100 K depending on the shielding and in far earth orbit (e.g., L2) optics temperatures of 50 K are possible. The typical emissivity of aluminum is $7 \times 10^{-4} \cdot (\mathrm{Freq}/100\ \mathrm{GHz})^{1/2}$. This is based on bulk aluminum conductivity and measured in flight performance at 90 GHz. At frequencies substantially higher than 100 GHz emissivities rise well above this, so that 1% emissive surfaces are not unheard of at sub-millimeter wavelengths. If we assume 0.1% emissivity, for a 100 GHz receiver, and balloon optics an effective optics emission of 200 mK is reasonable per mirror surface. To be able to resolve 10 microK cosmological signals places a requirement on the allowed synchronous optics temperature variation of $< 0.01°$ C. With 1% emissive optics this would be $< 0.001°$ C. Again the fact that the cosmological signal varies at the sidereal rate helps us as does a rapid chop. In a space environment the fact that there is no air makes this issue easier to deal with.

3.4 Data Uniformity

One of the difficulties we have had in sub-orbital measurements is the piecing together of different datasets to draw global conclusions. Some of the scatter we see in the present power spectra measurements is no doubt due to this problem and to the issue of varying systematics and calibrations between experiments. This is a key area where a single space based experiment will have an enormous advantage over sub-orbital measurements. Very long duration balloon experiments will also have some of this advantage. Sub-orbital experiments can overcome some of this limitation by restricting the power spectra estimates to higher "l" where these issues are less critical. *In situ* calibration is also important to tie together non-uniform datasets.

4 Current Status

4.1 Early Power Spectrum Estimates

We now know we had detected degree scale structure and had a preliminary measurement of power spectrum prior to COBE announcement in 1992, though like any new result it required confirmation. Subsequent measurements by us and others showed that our earlier measurements were indeed consistent. Prior to the COBE launch in 1989, our Advanced Cosmic Microwave Explorer (ACME) payload had made two balloon flights and one South Pole expedition making measurements from 0.3 to 3 degrees with SIS and bolometric detectors. Prior to the April 1992

COBE announcement, ACME had flown four times and made two South Pole trips with a total of seven measurements. Our 1988 South Pole trip with ACME outfitted with a sensitive SIS (Superconductor-Insulator-Superconductor) receiver resulted in an upper limit at 0.5° of $\Delta T/T \leq 3.5 \times 10^{-5}$ at 0.5° for a Gaussian sky. This was very close to the "minimal predictions" of anisotropy and, as we were to subsequently measure, just barely above the level of detectability. In the Fall of 1989, we had our first ACME-MAX flight with a subsequent flight the next summer (so-called MAX-II flight). This flight resulted in structure being detected consistent with a cosmological origin. This data was taken in a low dust region and showed no evidence for galactic contamination. This data in the Gamma Ursa Minoris region ("GUM data") was first published in Alsop et al. (1992)[3] *prior* to the COBE detections. At the time, our most serious concern was of atmospheric stability, so we revisited this region in the next ACME flight in June 1991. In the meantime, ACME was shipped to the South Pole in October 1990 for more ground based observations, this time with both an SIS detector and a new and extremely sensitive HEMT (High Electron Mobility Transistor) receiver. At scales near 1°, close to the horizon size, results from the South Pole using the ACME with a HEMT-based detector place an upper limit to CMB fluctuations of $\Delta T/T \leq 1.4 \times 10^{-5}$ at 1.2° (Gaier et al., 1992).[4] This upper limit for a Gaussian auto correlation function sky was computed from the highest frequency channel. This data set however has significant structure in excess of noise. Because the beam size varies inversely as the frequency and because of the "step scan" used, a "negative effective" spectral index is expected. Without more data the spectral information was ambiguous. Under the assumption that the structure seen is cosmological, a four-channel average of the bands yields a detection at the level of $\Delta T/T = 1 \times 10^{-5}$. This is consistent with the signal measured in an adjacent strip in SP91 (Schuster et al. 1993) as well as measured subsequently in the SP '94 dataset in another adjacent strip. Analysis of dust and synchrotron maps from the area of the sky surveyed, with reasonable assumptions about the spectral indices, predict that the signal level we observed is not consistent with expected dust or synchrotron.

Additional analysis of the 1991 ACME South Pole data using another region of the sky and with somewhat higher sensitivity shows a significant detection at the same level of $\Delta T/T = 1 \times 10^{-5}$ (Schuster et al., 1993).[5] Again, the low frequency synchrotron maps do not show similar morphology and would predict an amplitude that is much smaller (< 7 μK). The amplitude is also inconsistent with known dust emission. No evidence for point source contamination was found either. The 1σ error measured per point in this scan is 14 μK or $\Delta T/T = 5 \times 10^{-6}$. Per pixel, this is the most sensitive CMB measurement to date at any angular scale. The relevant measurements just prior to the COBE announcement are summarized in Fig. 1. While this early data was quite confusing at the time, particularly the rise in the power spectrum from 1.5 to 0.5 degrees, it is now seen with our additional measurements to be consistent with a similar rise now seen in the Sasskatoon data. The large angular scale data was provided by the COBE data in 1992, and as shown in Fig. 5, the earlier degree-scale measurements are consistent with the COBE detections.

4.2 Recent Results

The recent Sasskatoon 95 data, SK95, support the rise in the power spectrum seen in the earlier ACME data, though with a somewhat higher overall normalization. However the SK 95 data has an overall 30% uncertainty in calibration and hence it cannot be yet concluded if there is any discrepancy. Very recently the CAT interferometer results at l=400-600 combined with the degree scale measurements tentatively show that there is a fall in the power spectrum at large "l" with a peak somewhere around l=200-300. This is consistent with the other upper limits at large "l". The new SK 95 data also support this conclusion. With refined results at l=100-500

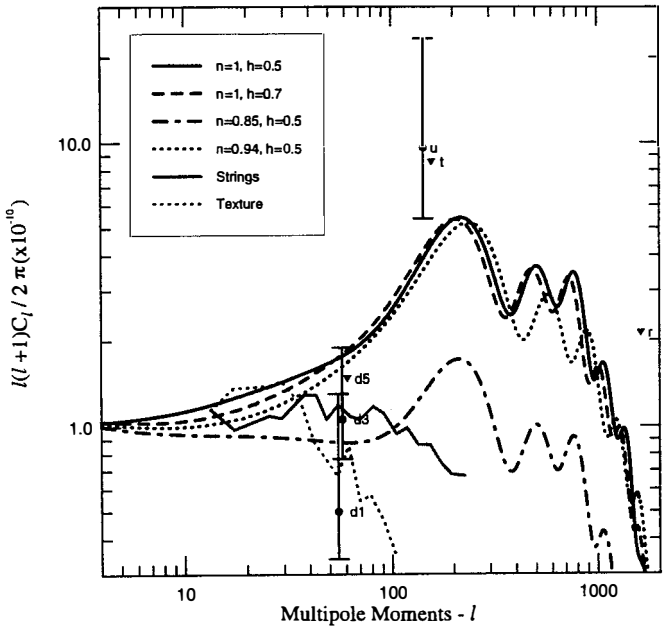

Figure 1: ACME CMB power spectrum data prior to the COBE detection. Theoretical curves are from Steinhardt and Bond (private communication). See KEY in Fig. 5 caption.

from ground and balloon data expected in the next few years, we will get good estimates of Ω and the baryon fraction.

5 Foreground Issues

In the microwave region, the primary extraterrestrial foreground contaminants are galactic synchrotron and thermal bremsstrahlung emission. Below 50 GHz, both of these contaminants have significantly different spectra than CMB fluctuations. Because of this, multi frequency measurements can distinguish between foreground and CMB fluctuations (provided there is large enough signal to noise).

Above 50 GHz, the primary contaminant is interstellar dust emission. At frequencies above 100 GHz, dust emission can be distinguished from CMB fluctuations spectrally, also using multi frequency instruments.

At all observation frequencies, extragalactic radio sources are a potential concern. Extragalactic radio sources have the disadvantage that there is no well-known spectrum which describes the whole class of sources. For this reason, measurements over a very large range of frequencies and angular scales are required for CMB anisotropy measurements in order to achieve a sensitivity of $\Delta T/T \approx 1 \times 10^{-6}$. As we proceed towards smaller beams sizes the problem becomes progressively more difficult for point source contamination. However as we

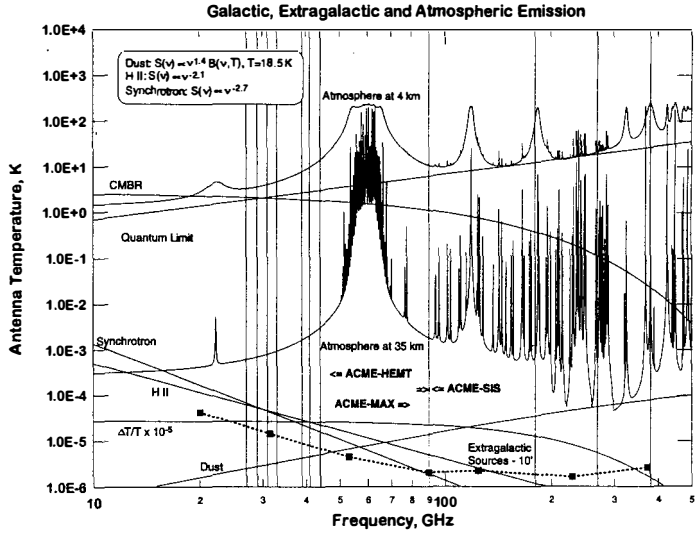

Figure 2: Relevant backgrounds for terrestrial measurements at the South Pole and at balloon altitudes (35 km). Representative galactic backgrounds are shown for synchrotron, bremsstrahlung, and interstellar dust emission as well as the various ACME (center) wavelength bands.

Date	Site	Detector System	Beam FWHM (deg.)	Sensitivity
1988 Sept	Balloon^{P}	90 GHz SIS receiver	0.5	4 mKs$^{1/2}$
1988 Nov-1989 Jan	South Pole	90 GHz SIS receiver	0.5	3.2
1989 Nov	Balloon^{FS}	MAX photometer (3, 6, 9, 12 cm^{-1}) ^{3}He	0.5	12, 2, 5.7, 7.1
1990 Jul	Balloon^{P}	MAX photometer (6, 9, 12 cm^{-1}) ^{3}He	0.5	0.7, 0.7, 5.4
1990 Nov-1990 Dec	South Pole	90 GHz SIS receiver	0.5	3.2
1990 Dec-1991 Jan	South Pole	4 Channel HEMT amp (25–35 GHz)	1.5	0.8
1991 Jun	Balloon^{P}	MAX photometer (6, 9, 12 cm^{-1}) ^{3}He	0.5	0.6, 0.6, 4.6
1993 Jun	Balloon	MAX photometer (3, 6, 9, 12 cm^{-1}) ADR	0.55–0.75	0.6, 0.5, 0.8, 3.
1993 Nov-1994 Jan	South Pole	HEMT 25–35 GHz	1.5	0.8
1993 Nov-1994 Jan	South Pole	HEMT 38–45 GHz	1.0	0.5
1994 Jun	Balloon	MAX photometer (3, 6, 9, 14 cm^{-1}) ADR	0.55-0.75	0.4, 0.4, 0.8, 3.
1996 Feb	Balloon	HACME HEMT 38–45 GHz	0.7	0.4, 0.5, 0.8
1996 Jun	Balloon	HACME HEMT 38–45 GHz	0.7	0.4, 0.5, 0.8

Table 1: CMB measurements made with ACME.
Sensitivity does not include atmosphere which, for ground-based experiments, can be substantial.

P–Palestine, TX
FS–Fort Sumner, NM

show in Figures 2 the estimated contribution for 10' beam surveys is still encouraging. We can make an estimate of the portions of the sky that are likely to be contaminated by galactic emission by combining the low and high frequency galaxy maps with our "knowledge" of the spectral indexes of the various species. In Fig. 3, we show such an estimate for the fraction of sky uncontaminated by the direct emission from our galaxy. Keep in mind that this is only an estimate based on our present data. While additional galactic surveys would help to determine the galactic component better, it is assumed at the current time that the best data on galactic contamination will come from the future CMB maps themselves. Additional ground based surveys of point sources and H-II emission will be a great aid in CMB studies however. For our SP '94 data set we have made a point source survey at a number of frequencies to determine the spectra of the brightest point sources in our field (Gundersen et al., 1997). No evidence of significant point source contamination was found for this data set. Ideally, such point source surveys could be carried out for the entire sky. Such a task is daunting however considering the number of known, let alone unknown, point sources. For example, in ACME, the sensitivity to point sources is about 47 microK per Jansky at 40 GHz. This is for a 1 degree beam. A 10' beam size experiment will face a point source sensitivity of about 1 mK per Jansky. A 1 ppm per pixel survey of the CMB at 10' resolution will require milli-Jansky point source rejection ability.

A summary of the various observations with this instrument is given in Table 1.

6 ACME Results

There have been a total of 13 ACME observations/flights from 1988 to 1996. Over 20 articles and proceedings have resulted from these measurements as well as ninen Ph.D. theses. ACME-

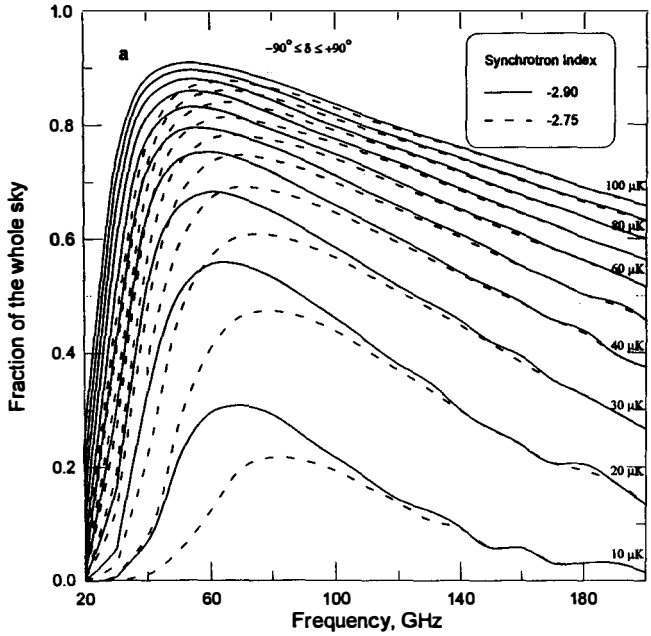

Figure 3: Galactic model estimates for the fraction of sky uncontaminated below a given level. The model includes synchrotron, bremsstrahlung, and dust emission. The synchrotron model is given for two different spectral indices. Far off the galactic plane (where we are most interested in measuring), the steeper spectral index is more appropriate. The dust model is based on the IRAS 100 micron map combined with our dust data from the mu-Pegasus region.

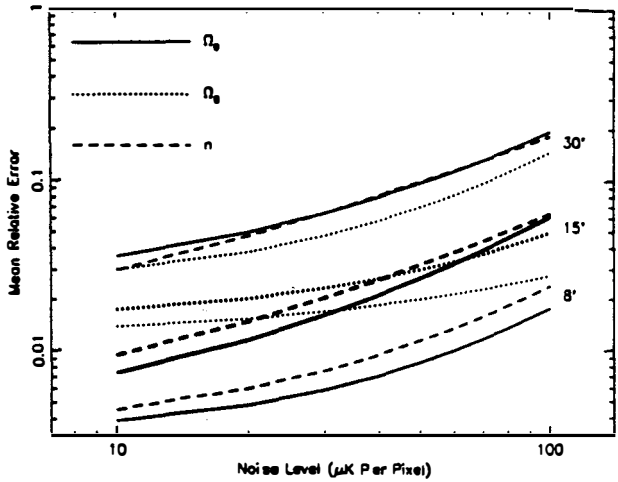

Figure 4: Estimated cosmological parameter extraction uncertainty versus sensitivity

SIS and ACME-HEMT articles by Meinhold and Lubin (1991),[6] Meinhold et al. (1992),[7] Gaier et al. (1992),[4] Schuster et al. (1993),[5] Gundersen et al. (1995),[8] and ACME-MAX articles by Fischer et al. (1992),[9] Alsop et al. (1992),[3] Meinhold et al. (1993),[10] Gundersen et al. (1993),[11] Devlin et al. (1994),[12] Clapp et al. (1994)[13] Tanaka et al. (1996)(15) and Lim et al. (1996)(16) summarize the results to date.

7 Future

This is a particularly exciting time in our field as we are on the verge of making precision maps of the CMB at sub-degree scales over large regions of the sky. Within the next 3-5 years we will get data from balloon borne mapping instruments as well as ground based interferometers. The range from 0.1 - 10 degrees should be relatively well quantified over a large range of wavelengths. Although we have now made measurements sensitive enough to extract many of the cosmological parameters we lack the sky coverage to reduce the sample and cosmic variance to a reasonable level. We are now at a point, both technologically and in our understanding of the relevant CMB signals and non cosmological backgrounds, that we can seriously contemplate making a precision measurement of the CMB power spectrum. What is needed is not necessarily more sensitivity, though more is always welcome, but more samples of the sky. Some of the current and past confusion in measurements of the power spectrum are undoubtably due to small statistics. For example in Figure 4 we show the estimated cosmological parameter extraction precision versus beam size and pixel sensitivity for an experiment that cover 50% of the sky. While the extraction procedures and error estimates are still being debated, it appears feasible to get precision in measuring the various parameters to the percent level within the next decade. This implicitly assumes a cosmological model that is "well behaved" and assumes no additional pathological foregrounds. We will soon know if these are reasonable assumptions or not.

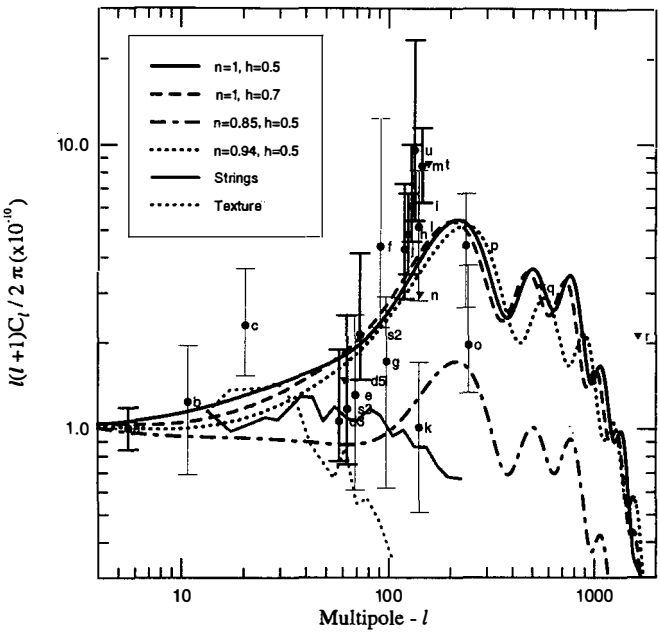

Figure 5: Recent ACME results (in BOLD) along with results from other groups. Key: a-COBE, b-FIRS, c-Tenerife, d1-SP91 9 pt. 4 channel analysis-Bond '93, d3-SP91 9+13 pt. 4 channel analysis-Bond '93, d5-SP91 9 pt. Gaier et al. '92, e-Big Plate, f-PYTHON, g-ARGO, h-MAX4-Iota Dra, i-MAX4-GUM, j-MAX4-Sig Herc, k-MSAM2, l-MSAM2, m-MAX3-GUM, n-MAX3-mu Peg, o-MSAM3, p-MSAM3, q-Wh. Dish, r-OVRO7, s2-SP94-Q, s3-SP94-Ka, t-SP89, u-MAX2-GUM, many from Steinhardt and Bond by private communication.

Publication	Configuration	Beam FWHM (deg.)	$\Delta T/T \times 10^{-6}$
Meinhold & Lubin '91	ACME-SIS SP '89	0.5	<35
Alsop et al., '92	ACME-MAX-II (GUM)	0.5	45^{+57}_{-26}
Gaier et al., '92	ACME-HEMT SP '91	1.5	<14
Meinhold et al., '92	ACME-MAX-III (μ Peg - upper limit)	0.5	<25
Meinhold et al., '92	ACME-MAX-III (μ Peg - detection)	0.5	15^{+11}_{-7}
Schuster et al., '93	ACME-HEMT SP '91	1.5	9^{+4}_{-2}
Gundersen et al., '93	ACME-MAX-III (GUM)	0.5	42^{+17}_{-11}
Devlin et al., '94	ACME-MAX-IV (GUM)	0.55-0.75	37^{+19}_{-11}
Clapp et al., '94	ACME-MAX-IV (Iota Draconis)	0.55-0.75	33^{+11}_{-11}
Clapp et al., '94	ACME-MAX-IV (Sigma Hercules)	0.55-0.75	31^{+17}_{-13}
Gundersen et al., '95	ACME-HEMT SP '94	1	$15^{+5.7}_{-2.5}$
Lim et al., '96	ACME-MAX-V (μ Peg)	0.5	<13
Tanaka et al., '96	ACME-MAX-V (HR5127)	0.5	12^{+4}_{-3}
Tanaka et al., '96	ACME-MAX-V (Phi Herculis)	0.5	19^{+7}_{-4}

Table 2: Recent ACME degree-scale results.

8 Mapping Techniques

To date, essentially all the sub degree experiments have been done in a one dimensional scan mode and have not been able to make a "true map". This has been done because of the atmospheric emission restricting us to make one dimensional, constant elevation angle chops. All of the ACME measurements are of this type. An orbital mission does not suffer from this problem, of course. However even then one is making 1-D strips and then "sewing" them together to make a map. The COBE mission was no exception. The only "real maps" so far have been made by interferometers, and then a "map" must be carefully scrutinized since the data weighting is far from uniform. With the exception of interferometers, experiments have been either differential or "total" power (this means a direct measure of the flux is made). Virtually all experiments (including our own) have opted for the differential technique as it is less demanding on various system stabilities. Recently experiments have shown that a direct "total" power measurement is possible and the era of sub-degree resolution maps is about to begin. It is easy to see why this is difficult. The typical equivalent noise of a state-of-the-art detector is 10–30K. This is to be compared to the desired sensitivity of 3–30 micro Kelvin. This requires a system stability of the order of 1-10 ppm.

9 Polarization

The CMB is characterized by the four Stokes parameters I, Q, U and V in each direction and at each frequency observed. I characterizes the overall spectrum (flux) while Q and U give the linear polarization and V the circular polarization. Very little effort has been directed towards the measurement of the polarization of the CMB compared to the effort in anisotropy

detection. In part, this is due to the low level of linear polarization expected. Typically, the polarization is only 1–30% of the anisotropy and depends strongly on the model parameters. This is an area which, in theory, can give information about the reionization history, scalar and tensor gravity wave modes, and large-scale geometry effects. It is now possible to measure CMB polarization to a sensitivity of better than 1 ppm on limited portions of the sky. In the future, this may be a very fruitful area of inquiry, particularly when combined with overlapping anisotropy measurements. In particular the polarization-anisotropy cross correlation is a very powerful technique in understanding and breaking degeneracies in the parameter extraction. Dedicated polarization measurements designed to reach a level of sensitivity of 1 ppm or better are possible. At mm and cm wavelengths this is possible to do from the ground since the atmosphere is essentially unpolarized at these wavelengths.

10 Orbital vs. Sub Orbital Missions

There are currently several major proposed (and now started) satellite missions. The European COBRAS-SAMBA proposal is a combined HEMT and bolometer mission, and would cover from about 1 to 10 mm with resolution varying from about 4 to 40 arc minutes depending on the frequency. In the U.S., the Mid-Explorer class MAP mission is a HEMT based mission that will cover from 3 to 15 mm with a beam size from 20 to 60 arc minutes. There are significant differences in technical and programmatic approaches being taken with the European being a more ambitious, and hence, more costly experiment. The U.S. Mid-Explorer mission is designed with more limited objectives, but at a significantly lower price and at a possibly shorter time scale to launch. Either of these missions would provide invaluable data that could revolutionize our understanding about early universe physics. Currently, it can be assumed that these missions will not produce data before 2002 at the earliest for the US mission, and 2004 for the European one, and hence, it is to be anticipated that continued vigorous ground-based and suborbital experiments will continue to produce valuable data.

Indeed per pixel sensitivities with suborbital missions in the μK region are now achievable with current and new technologies, HEMTs, and bolometers over hundreds to hundreds of thousands of pixels and possibly over large portions of the sky. With the HEMT and bolometer array receivers that are being planned now for sub-orbital measurements, it is quite likely that the integrated sensitivity and resolution of these measurements will exceed that of the US mission. The major issue will be atmospheric stability, control of sidelobes and getting a uniform dataset. Ideally, to reduce systematic effects, full-sky coverage would be best, and this is one area where a space-based measurement will excel. In a number of ways the sub-orbital and orbital missions will be complimentary and allow for a very powerful combined dataset.

Acknowledgements. This work was supported by the National Science Foundation Center for Particle Astrophysics, the National Aeronautics and Space Administration, the NASA Graduate Student Research Program, the National Science Foundation Polar Program, the California Space Institute and the University of California. Its success is the result of the work of a number of individuals, particularly the graduate students involved with the experiment and our collaborators, notably Paul Richards and Andrew Lange for the ACME-MAX flights. The exceptional HEMT amplifier was provided by NRAO. Robert Wilson, Anthony Stark, and Corrado Dragone, all of AT&T Bell Laboratories, provided critical support and discussion regarding the early design of the telescope and receiver system. We would like to thank all of the South Pole support staff for highly successful 1988–1989, 1990–1991 and 1993–1994 polar

summers. In addition, we want to acknowledge the crucial contributions of the entire team of the National Scientific Balloon Facility in Palestine, Texas for their continued excellent support.

References

[1] Lubin P. et al., 1985, Astrophys. J. **298**, L1.

[2] Pospieszalski, M. W. et al., 1990, IEEE MTT-S Digest, 1253

[3] Alsop, D. C. et al., 1992, Astrophys. J. **317**, 146

[4] Gaier, T. et al., 1992, Astrophys. J. **398**, L1

[5] Schuster, J. et al., 1993, Astrophys. J. **412**, L47

[6] Meinhold, P. R. and Lubin, P. M., 1991, Astrophys. J. **370**, L11.

[7] Meinhold, P. et al., 1992, Astrophys. J. **406**, 12

[8] Gundersen, J. O. et al., 1995, Astrophys. J. **443**, L57

[9] Fischer, M. et al., 1992, Astrophys. J. **388**, 242

[10] Meinhold, P. et al., 1993, Astrophys. J. **409**, L1

[11] Gundersen, J. O. et al., 1993, Astrophys. J. **413**, L1

[12] Devlin, M. et al., 1994, Astrophys. J. **430**, L1

[13] Clapp, A. et al., 1994, Astrophys. J. **433**, L57

[14] Wollack, E. et al., 1994, Astrophys. J. **419**, L49

[15] Lim, M. et al., in press (1996).

[16] Tanaka, S. et. al., in press (1996).

[17] Smoot, G. F. et al., 1992, Astrophys. J. **396**, L1

[18] Gundersen, J. O. et al., 1997, to be submitted to Astrophys. J.

RATAN-600 "COLD EXPERIMENT" AND CMB ANISOTROPY

Parijskij Y., Chepurnov A., Bursov N.
Special Astrophysical Observatory
Karachai- Cherkessia
357147 Nizhnij Arkhyz,
Russia

Here we present summary and future plans of the "Experiment Cold" at RATAN-600, which we began more than 15 Years ago. All details may be found in Parijskij, Korolkov, 1986 with first results on the CMB anisotropy estimates after reduction of the part of 1980-1981 data.

The main features of our "Cold" experiments are the following one.

1. Deep multi-wavelengths survey of the selected area down to the limit, set by the extra-terrestrial backgrounds (Galaxy, radio sources, CMB).

2. "Free-scale" approach for the measurements from the scale 6 arcsec. to 360 deg. using equatorial pole as a reference region. But we concentrated our efforts on the scales of Sakharov Oscillations, the most informative region in many respects.
3. We use "Between Synchrotron and Dust" strategy.

   We suggest, that free-free emission has only one parameter, brightness at any wavelength in the optically thin range. Dust has at least 5 parameters. Synchrotron radiation has 3 parameters for the simple curved spectrum. More over, only for the free-free dominated region we can hope, that there are no pixel-to-pixel variations of the parameters.

4. Absolute calibration problem are very important for the big scales, but looking for "Sakharov oscillations" ($100 < l < 1000$) we can use simple correlation approach with no absolute calibration .at all, if survey region is big enough..
5. "Two-Ways" approach was suggested, accumulating CMB data a n d discrete radio structures as well in the same selected area, including HZ Radio Galaxies. Last population gives us information about the epoch of the formation of the first stellar system and giant black

holes."BIG TRIO" project (RATAN-600, VLA, 6-meter Russian telescope) was realized and first results may be found in Kopylov et al., 1995. It was shown, that about 30000-100000 discrete objects of Early Universe available on the Sky, which appeared in the first billion Years after Big Bang, and can be studied by present day facilities using proper selection criteria.

At present, about 440 daily 24-hours scans, collected during 1980-1986 period available for the "Cold" S.A. at 9 wavelengths from 1 to 31 cm with best sensitivity at 7.6 cm. The data acquisition system changed during this period, and now we are re- writing all data on the CD's in the common format for quick access. We hope to realize theoretical sensitivity (about 10 micro- Kelvins) within factor 2-3 at cm. waves.

Future plans: "Between COBE and COBRAS \ SAMBA". Following changes in our strategy appeared last Years.

1. To use modern receivers we have to cool RATAN-600 as deep as possible. Now we constructed special 2-meters screens above and below the working surface of each 900 panels, that is about 8000 sq.m. It dropped the spill over effect drastically, below CMB level.

2. Short wavelengths receivers have to be improved greatly. Now we installed new set of HEMPT cryogenic receivers, which are by factor 5–30 better, than old one.
3. Some preliminary tests were made of the focal plane phased array (8 receivers from 32 in project) were used to use unprecedently big (300 beam widths at high elevation angle) unaberration field in multi-beams mode. (Pinchuck et al., 1995). In principal, it is possible to use RATAN-600 as a 900 elements phased array (Parijskij, 1995). But we are at the beginning of the road in this direction.
4. We are going to improve polarization facilities of RATAN-600, to use small scale Faraday rotation effect for better filtration of the Galactic free-free screen radiation.

We can use our 7.6cm data available now to improve greatly the upper limit on the Galactic noise. For that purpose we estimated the amplitudes of 10000 Fourie harmonics of the 24-hours long strip and converted them in the Legendre terms, taking into account the number of Legendre terms per 1 Fourie harmonic for given angular scale and the losses due to the one-dimensional scanning.We calculated power at different scales for sum and difference of two subset of monthly observations. At the scale about half to quoter of degree we have seen signal

at the level more than 5 sigma with amplitude about 100 micro-K. For the same range of the scales the noise is below 20 micro-K. If we suggest, that we see some Sky signal, which is a mixture of Galactic and CMB anisotripy, we can estimate the upper level of contribution of the synchrotron and thermal Galaxy noise components, as well as the accuracy of their measurements converted to the frequency which we are interested in. For 1cm, which we shall use as the best for next generation RATAN-600 experiment, we have the following values: 1.72, 1, 0.9, 0.9, 0.4, 0.3, 0.16, 0.1 micro K at the scales 0.75, 0.5, 0.38, 0.25, 0.21, 0.19, 0.17 degrees even if all Galactic and Extragalactic noise we see at 7.6 cm.is free-free emission only. Error of measurments transported from 7.6 cm to 1cm for this case is less than 0.1 micro K. For synchroton noise the situation will be even better. At the same time , the atmospheric noise will be much greater at 1cm then at 7.6 by factor 10 and good filtration of it should be done using the multi- wavelengths approach or big angle scanning. The later happened to be efficient one at RATAN-600 because of the big aperture and near field zone conditions for the atmosphere.

We hope, that next 10 years will be extremely important for the cosmology and particle physics. Realization of the new generation of space based missions (as

COBRAS/SAMBA, RELICT-3 and others), balloon, ground based experiments should improve the accuracy of the measurements by factor 10-100 and not only choice of the galaxies formation scenario will be possible, but also the determination of the main cosmological parameters with 1% accuracy can be made (see these Proceedings) and even some problems of high energy physics and Theory Of Everything (TOE) may be solved. This work was supported by RFFI Grants 95-02-16597, 95-02-03783 and COSMION.

References

Kopylov A., Goss W.M., Parijskij Y., Soboleva N., Zhelenkova O., Temirova A., Vitkovskij Va., Naugolnaja M., Verkhodanov O., 1995, Astron. J. (Russian) v. 72, 613

Parijskij Y., Korolkov D., 1986, Astroph.&Space Sci., v 5, 40

Parijskij Y, 1994, IEEE Antenna Propag. Magazine, v 35, 7

Pinchuck G., Parijskij Y., Majorova E., Shannikov D., 1994, IEEE Antenna Propag. Magazine, v 36, 12

Millimetric observations of CMB anisotropy from Tenerife

R. Rebolo [1], B. Femenía [1], L. Piccirillo [2], N. Kachwala [2], M. Limon [2], C.M. Gutiérrez [1], J. Nicholas [2], R.A. Watson [1], R.K. Schaefer [2]

[1] *Instituto de Astrofísica de Canarias, 38200, La Laguna, Spain*

[2] *Bartol Research Institute, University of Delaware, Newark, DE 19716*

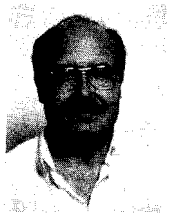

Abstract

Results of a ground-based CMB anisotropy experiment conducted at the Teide Observatory (Tenerife) are presented. The instrument is a four channel (3.1, 2.1, 1.3 and 1.1 mm) bolometer system coupled to a telescope consisting of a chopping off-axis parabolic primary mirror and an off-axis hyperbolic secondary. The resultant configuration is sensitive to structures on angular scales of about 1°-2°. We use the two higher frequency channels to monitor the atmospheric emission and correct the lower frequency ones. A simple scaling method proved to be very efficient in significantly reducing the atmospheric contribution in each individual scan. Our final 3.1 and 2.1 mm scans at Dec.=+40°, obtained adding those from independent observing nights, reach sensitivities of about 40 μK per beam. The statistical analysis show the presence of common signals. A joint likelihood analysis of these two channels using gaussian autocorrelation functions gives a detection of fluctuations with an intrinsic amplitude $C_0^{1/2} = 76^{+23}_{-21}$ μK at $\theta_c = 1.3°$. We consider these fluctuations to be dominated by CMB signal, they cannot be explained in terms of galactic foreground contamination or residual atmospheric noise.

1 Introduction

The Galaxy provides a suitable window at wavelengths around 2-3 mm for the search of Cosmic Microwave Backgrond (CMB) anisotropies. At these frequencies and at intermediate angular scales, the strength of the CMB is considerably higher than the expected signal of galactic processes such as free-free, synchrotron and dust emission. The detection of CMB fluctuations is hampered, however, by the atmospheric emission forcing most millimetric experiments to be carried out using balloons.

We present here the first results of a new intermediate scale ground-based millimetric CMB experiment conducted at the Teide Observatory (Tenerife) by the Bartol Research Institute and the Instituto de Astrofísica de Canarias. The observing site, located at an altitude of 2400 m, is well known for the transparency and stability of its atmosphere providing frequent seeing conditions better than 1″.

2 Instrumental Set-Up

The telescope is shown in Fig 1, together with the cryostat. In summary, the optics consists of a primary off-axis parabolic mirror (45 cm diameter) coupled to a secondary off-axis hyperbolic mirror (28 cm diameter). A more complete description can be found in ([10, 11]). The detector is a four channel photometer equipped with ^{3}He bolometers with bands centered at 3.3, 2.1, 1.3 and 1.1 mm (channels 1 to 4 respectively) as defined by a combination of resonant mesh filters. High frequency leaks are blocked by a combination of fluorogold, black polyethylene and Pyrex glass filters. The bolometers are cooled to 0.33 K by means of a closed cycle ^{3}He refrigerator. The telescope is surrounded by 45° aluminum radiation shields. The beam and side-lobes have been extensively checked by placing a distant Gunn source oscillating within the Channel 1 (3.3 mm) band. An accurate determination of the beam has been obtained looking for far field side lobe structures down to about −60 dB. These analyses show that the beam response can be approximated by a Gaussian with FWHM=2.°4.

The beam throw in the sky is achieved by chopping the primary mirror, according to $\theta(t) = \theta_0$, $\phi(t) = \phi_0 + \alpha_0 \sin(2\pi f_w t + \psi)$ where $\phi(t)$ and $\theta(t)$ denote the azimuth and elevation respectively, $\hat{\mathbf{n}} = (\phi_0, \theta_0)$ is the initial position of the antenna and $\alpha_0 = 2°.6$ is the zero-to-peak azimuthal chopping amplitude at a reference frequency $f_w = 4$ Hz. Data are sampled at 80 Hz for each of the four bolometer channels so as to have 20 samples per sinusoidal cycle per channel. Afterwards the data are demodulated in software at the first (4 Hz) and second (8 Hz) harmonic of the reference (chopping) frequency, so that we obtain response functions resembling the familiar "2-beam" and "3-beam" patterns respectively. Here we will limit our analysis to the "3-beam" data.

The calibration constants were obtained by requiring a 1 K signal for an input source filling the positive lobe and with a temperature of 1 K. The calibration in the laboratory was performed using cold loads and it was checked with observations of the Moon, which agreed within a 20% absolute accuracy with our very naive Moon models. We expect better agreement with more elaborated Moon models.

The window function for the experiment is shown in Fig. 1. It is placed in the multipole range $l = 38-77$, attaining its peak at $l = 56$. This intrument helps to fill the gap in l between the Tenerife experiment ([6]) and the ACME South Pole ([4]) and Saskatoon experiments ([9]).

3 Observations and Data processing

The data presented here were collected between June 10th and August 10th 1994. During a large fraction of the observing time the precipitable water vapor in the atmosphere was below 3 mm. and 10% of the time it was below 1.5 mm. We observed on the South Meridian and at fixed elevation correspondig to a band centered at dec 40°. We collected about 550 hours of data in the region of interest, and observations of the Moon were also performed to check the laboratory calibration. In order to avoid contamination from solar radiation the experiment only collected data at night.

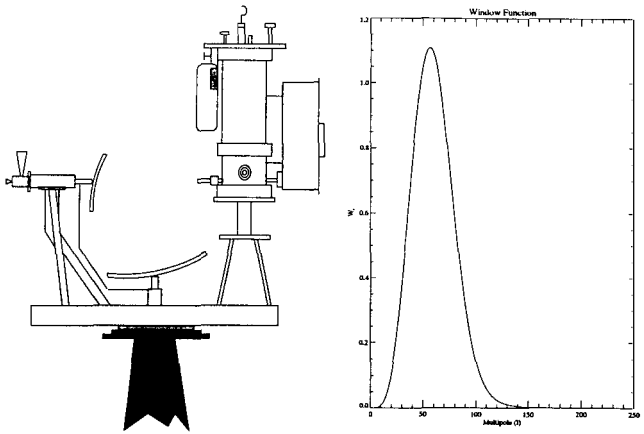

Figure 1: **Left**: Diagram showing the telescope and cryostat. The ground shields are not displayed.**Right**: Window function for the second harmonic demodulated data ("3-beam" data)

The main source of noise in our system proved to be atmospheric emission. The measured sky noise was of the order of 10 mK$\sqrt{(s)}$ during average observing nights, decreasing down to 3-4 mK$\sqrt{(s)}$ in excellent nights. The extremely high correlation between all channels and the fact that all channels are looking through the same atmospheric column suggested that we could reduce the atmospheric noise by using one of the channels as an atmospheric monitor. We choose channel 4 (1.1 mm band) as monitor since it is the most affected by atmosphere. The procedure is basically to compute the correlated signal between channel i and channel 4, scale down to channel i and substract it to this channel. At each channel we have a superposition of sky signal and atmospheric signal: $\Delta T_i = \Delta T_i'^{sky} + \Delta T_i^{atm}$, being all these terms expressed in *antenna temperature* units. Since the bulk of the signal in all channels is atmospheric, and we see extreme high correlation, we can express the atmospheric signal in channel i as $\Delta T_i^{atm} = \alpha_i \Delta T_4^{atm}$ where α_i is obtained from the linear fit of channel i versus channel 4. From the atmospheric data (water vapor content, pressure and temperature) we can compute the opacities due to water vapor and oxygen ([1]). At the end, for each channel we have to solve the following equation to obtain the sky signal:

$$\Delta T_i = \frac{f_i}{c_i}\Delta T_i^{sky} + (\Delta T_4 - \frac{f_4}{c_4}\frac{1}{\rho_{i4}}\Delta T_i^{sky}) \times \alpha_i \qquad (1)$$

where ΔT_i and ΔT_4 are the data in channels i and 4; f_i and f_4 are the atmospheric transparencies at channels i and 4; c_i and c_4 are the RJ to thermodynamic conversion factors; ΔT_i^{sky} is the sky signal in thermodynamic temperature and $\Delta T_i'^{sky}$ in antenna temperature ($\Delta T_i'^{sky} = \frac{1}{c_i}\Delta T_i^{sky}$) and ρ_{i4} is the fraction of the sky signals seen at channels i and 4 ($\rho_{i4} = 1$ for CMB signal, $\rho_{i4} \neq 1$ for Galactic emission such as the area of the Galactic Plane crossing).

This procedure is applied on the 10 s binned data, a bin size big enough for the atmospheric noise to become dominant over the instrumental noise. After cleaning, the 10 s binned scans are binned again to 4 minute bin size (1° in RA), so the beam is sampled with at least three points. Residual baselines are then removed by fitting and substracting linear combinations of sinusoidal functions with a minimum period of 72° which guarantees we are not removing signal at the scales at which our instrument is sensitive. The reduction process described here

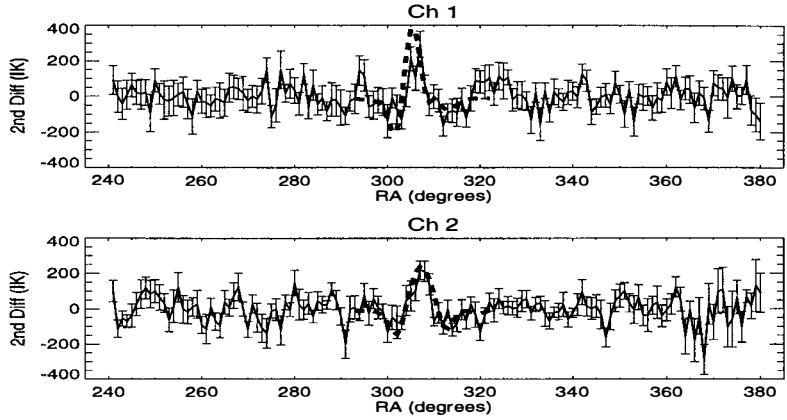

Figure 2: Second temperature differences in μK versus right ascension for channel 1 (3.1 mm) and 2 (2.1 mm) final scans. In both channels the Galactic Plane crossings (the most prominent feature) show good agreement with our estimations from available maps (bold dashed line). See text for details.

has only been applied to the 3-beam data. Finally, we form the final data sets for channels 1 and 2 (bands at 3.3 mm and 2.1 mm respectively) by performing a weighted average of the individual scans where the cleaning routine performed well. The number of points used in this average was typically of 14 and 9 independent points for channels 1 and 2 respectively. The error bars in these final scans are obtained from the weighted dispersion of the independent points. These final data sets are shown in Fig. 2 where the most prominent features are the Galactic Plane (GP) crossings. They agree pretty well with our estimations based on the low frequency maps at 408 and 1420 MHz ([7],[13]) for the synchrotron and free-free contributions, and the 140 and 240 μm DIRBE maps for the dust emission. The dust emission was modelled as a combination of two grey bodies at 20.4 and 4.77 K ([15]) with a spectral index $\gamma = 1.5$ in the regions outside the GP, while $\gamma \sim 1.7$ was obtained from the fit (pixel by pixel) to the 140 and 240 μm DIRBE maps. The free-free + synchrotron emission were modelled with a single power law: $T(\nu) \propto \nu^{-\beta}$, adopting $\beta = 2.1$ for the GP (free-free emission dominates here) and the value obtained from the fit of the 408 and 1420 MHz maps at high galactic latitudes. We also observe a larger uniformity in the size of the error bars for channel 1 due to the larger number of points used for this channel. The mean error-bar in both data sets is of about 70 μK in a 1° bin in RA.

4 Statistical Analysis

We have analyzed statistically the data of channels 1 and 2 in the ranges $\mathrm{RA_1}$=241° − 285° and $\mathrm{RA_2}$=331° − 20° which correspond to the two sections of our data at Galactic latitudes $|b| \gtrsim 15°$. We first conducted a cross-correlation analysis to check for the presence of common structure in both channels. We computed the correlation function $C(\theta) = \sum_{i,j} \Delta T_i \Delta T'_j \omega_i \omega'_j / \sum_{i,j} \omega_i \omega'_j$, where ΔT_i and $\Delta T'_j$ are the measured differences in temperature subtending an angle θ, and $\omega_i \equiv \sigma_i^{-2}$, $\omega'_j \equiv \sigma'^{-2}_j$ are the weights.Fig. 3 shows the most relevant results obtained. We observe

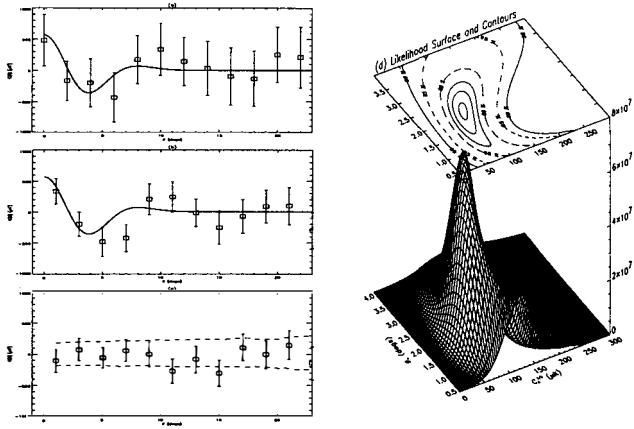

Figure 3: Statistical Analysis. The panel(a) shows the cross-correlation between channels 1 and 2. In panel (b) we show the auto-correlation of the combined analysis (Ch 1+ Ch 2)/2. In these two panels the solid lines correspond to the expected correlation for a model using the parameters yielding the peak of the likelihood surface. In panel (c) we show the auto-correlation of the difference scan (Ch 1 - Ch 2)/2. The dashed lines represent the 68% CL for uncorrelated noise. The likelihood surface and contours for the joint anlysis on channel 1 and 2 and in the whole range $RA_1 + RA_2$ is in panel (d). The peak is attained for a GAFC model with $C_0^{1/2} = 86\mu K$ and $\theta_c = 2.1°$. For the angle of highest sensitivity of our instrument ($\theta_c = 1.3°$) we obtain $C_0^{1/2} = 76\mu K$.

a shape as one would anticipate taking into account both the experimental configuration and the expected correlation in the sky signals on the angular scales at which our intrument is sensitive.

To assess the value of any signal we then conducted a likelihood analysis. If we assume that the noise and the signals are Gaussian fields, then they are completely specified by their correlation functions, and the sum of noise and signal is also a Gaussian random field with its properties completely determined by the correlation matrix. In the present analysis we have assumed a Gaussian auto-correlation function (GACF) for the CMB signal:$C_{intr}(\theta) = C_0 \exp(-\theta^2/2\theta_c^2)$. The GACF models together with its limitations and connections to more realistics scenarios have been widely discussed in the literature (seeWhite & Scott 1994) and we adopt it to quote preliminary results. The likelihood analysis was performed on each separate range and channel, on both ranges simultaneously (RA_1+RA_2) for each channel, the joint likelihood of channels 1 and 2 on each range and, finally, the joint likelihood of channels 1 and 2 on the range RA_1+RA_2. Table 1 presents a summary of the results for the coherence angle of highest sensitivity ($\theta_c = 1.32°$). Upper limits and detections are quoted at 95 % C.L. and 68 % C.L. respectively. The analysis of channel 1 do not show evidence of signal in any of the two ranges considered with a limit $C_0^{1/2} < 72$ μK, while for channel 2 we detect signal in both RA ranges. We made also a joint likelihood analysis on channel 1 and 2 assuming that both channels have been measuring the same signal. This gives a detection $C_0^{1/2} = 76^{+23}_{-21}$ μK. These results, even compatible between them, clearly indicates a possible dependence in frequency of the detected signal. A two-dimensional (in the plane C_0-θ_c) joint analysis of both channels (see

	RA_1	RA_2	RA_1+RA_2
Ch 1	< 92	25^{+37}_{-25}	< 72
Ch 2	94^{+44}_{-36}	109^{+49}_{-42}	101^{+30}_{-28}
Ch1 & Ch 2	72^{+36}_{-31}	79^{+35}_{-29}	76^{+23}_{-21}

Table 1: Likelihood results in μK.

Fig. 3 (d)) shows a well defined peak at $C_0^{1/2}$=86 μK, $\theta_c = 2.1°$; the expected correlation in our data for such a signal is plotted as the solid lines in Fig. 3-left top and middle. We recall that the uncertainty in the absolute calibration introduces an additional error bar of about 20% of the measured signal.

5 Conclusions

Preliminary results from a ground-based millimetric experiment devoted to the measurement of CMB fluctuations have been presented. A very simple and effective technique to greatly reduce the noise is discussed. With this technique we have been able to push down atmospheric noise to levels at which one would expect to observe CMB fluctuations. In fact we observe fluctuations at levels which are compatible with an intrinsic CMB signal $\sim$ 60 μK if we consider that the results of both channels are the result of a combination of CMB signal and some residual atmospheric contribution and assume an spectral index $\sim$ 2 for this last signal. Considering the approximate relations given by White & Scott 1994 this sky signal would correspond to a Q_{flat} = 30 μK in agreement with the values expected in standard scenarios. A more careful analysis on the spectral index of the signals in each channel is essential and it is under progress. We also expect an improvement in the data quality since more data have been collected during May and June 1996, under better weather conditions and with an improved instrument.

References

[1] Cernicharo, J., 1985, *IRAM Internal Report* **52**

[2] Davies, R.D., Watson, R.A., Gutiérrez, C.M., 1996, *MNRAS* **278**, 925

[3] De Bernardis, P., Masi, S.,Vittorio, N., 1991,*Astrophys. J.* **382**, 515

[4] Gundersen, J. O., *et al.*, 1995, *Astrophys. J.* **443**, L57

[5] Gutiérrez, C.M. 1992, PhD, Universidad de La Laguna

[6] Hancock, S., *et al.*, 1994, *Nature* **367**, 333

[7] Haslam et al, 1982, *Astr. Astrophys.* **100**, 209

[8] Lineweaver, C.H. *et al.*, 1995, *Astrophys. J.* **448**, 482

[9] Netterfield, C.B., Jarosik, N., Page, L., Wilkinson, & Wollack, E., 1995, *Astrophys. J.* **445**, L69

[10] Piccirillo L., 1991, *Rev. Sci. Instr.* **62**, 5

[11] Piccirillo L. & Calisse P., 1993, *Astrophys. J.* **411**, 529

[12] Piccirillo L. et al, 1996, *Astrophys. J.* **s**, ubmitted

[13] Reich, P., Reich, W., 1986, *Astr. Astrophys. Suppl. Ser.* **63**, 205

[14] White, M. & Scott, D., 1994 in CMB ANISOTROPIES: TWO YEARS AFTER COBE, Ed. L.M. Krauss, World Scientific

[15] Wright et al, 1991, *Astrophys. J.* **381**, 200

Observation of Cosmic Microwave Background Structure with the Tenerife Experiments

C. M. Gutiérrez[1]
[1] *Instituto de Astrofísica de Canarias, 38200 La Laguna, Tenerife, SPAIN.*

Abstract

The Tenerife Cosmic Microwave Background (CMB) experiments are mapping a region of 5000 square degrees on the sky. Several beam-switching radiometers at frequencies of 10, 15 and 33 GHz have been operating at the Teide Observatory (Tenerife) for more than ten years. Here we present the current observational status of the experiments, with special attention to the data at Dec.=+35°. In this strip, the data at 15 GHz have a signal to noise ratio ~ 2 and show clear evidence for the presence of individual features at high Galactic latitude. Assuming a Harrison-Zel'dovich spectrum for the primordial fluctuations, a likelihood analysis of this data at 15 GHz shows the presence of a signal with amplitude $Q_{RMS-PS} = 20^{+8}_{-6}$ μK, in agreement with our previous results at Dec.=+40° and with the results of COBE DMR. From the results at 10 GHz we conclude that the possible difuse Galactic contamination at 15 GHz should be $\leq$ 25 % of the detected signal. A preliminary comparison between our results and COBE DMR predictions for the Tenerife experiments clearly indicates the presence of individual features common to both. The invariance in amplitude along such a large range in frequency (10 – 90 GHz) is strongly indicative of an intrinsic cosmological origin for such structures.

1 Introduction

The study of the CMB has progressed decisively in recent years, with the detection of the fluctuations by the COBE DMR instrument [1, 11], the direct observation of features [5] and the statistical detections of signals on angular scales larger than a few minutes (see [6] for a summary of the observational status). The current observations constrain the CMB power spectrum to multipoles ~ 700, allowing the overall level of normalization to be determined and presenting good evidence of the existence of the Doppler peak predicted by standard inflationary scenarios.

Nevertheless, a determination in detail of the CMB spectrum will require more observations, extending the angular range, the region observed and the spectral range.

The Tenerife CMB experiments are a collaboration between the University of Manchester, the IAC Tenerife and MRAO Cambridge. The instruments consist of three independent two-channel receivers, operating at 10, 15 and 33 GHz, installed at the "Observatorio del Teide" on the island of Tenerife (Spain). The three instruments operate using a double-difference technique, with a beam response of the form -0.5, $+1$, -0.5, with three beams (FWHM$\sim$ 5°): the positive in the meridian and the other two displaced 8°.1 in declination. The three instruments use high electron mobility transistor (HEMT) amplifiers with resulting theoretical sensitivities, including both channels, of 5.6, 3.4 and 2.2 mK$\times$Hz$^{-1/2}$ at 10, 15 and 33 GHz respectively. We observe strips of the sky separated by 2°.5 covering declinations 30° to 45°. Our objective is to obtain a map in this band, with sensitivities of 50 μK at 10 GHz, and 20 μK at 15 and 33 GHz. Table 1 shows the current sensitivity of our observations in the region RA=160°$-$250°. CMB fluctuations with an amplitude of $Q_{RMS-PS} \sim 20$ μK should produce an rms in our scans ~ 30 μK. With the sensitivity achieved, we can use the data at 10 GHz to constrain the Galactic contribution at higher frequencies, whilst at 15 GHz it is possible to detect and map directly CMB features. At 33 GHz a large fraction of data are rejected due to atmospheric contamination, and only the data at Dec.=+40° have similar sensitivities to those at 15 GHz.

Table 1: Standard error (in μK) per beam sized area.

Dec. (deg.)	10 GHz	15 GHz	33 GHz
30.0	-	20	-
32.5	54	24	42
35.0	56	20	33
37.5	41	19	33
40.0	44	19	21
42.5	63	22	50
45.0	80	26	-

Figure 1 shows the stacked scans at 15 GHz. The highest intensity in these scans lies in the Galactic plane crossings at RA$\sim$300°$-$310° and shows the typical triple beam response of our instruments. The weak crossings are at RA$\sim$60°$-$90°. Comparing the amplitudes of such crossings at 10, 15 and 33 GHz we have demonstrated that the main source of signal in the Galactic plane at these frequencies is free-free emission with spectral index ~ 2. The search for intrinsic CMB structure (see next section) has been conducted at high Galactic latitude in the RA range 160° to 250°, where no structures are seen on this intensity scale.

2 Data at high Galactic latitude

The contribution due to known point-sources has been calculated using the Kuhr catalogue [9], the VLA calibrators, and the Michigan and Metsahovi monitoring programme. In the band of the sky observed by our instruments the more intense radio-sources at high Galactic latitude are 3C345, 0923+379 and 3C286. All these sources have been detected in our scans,

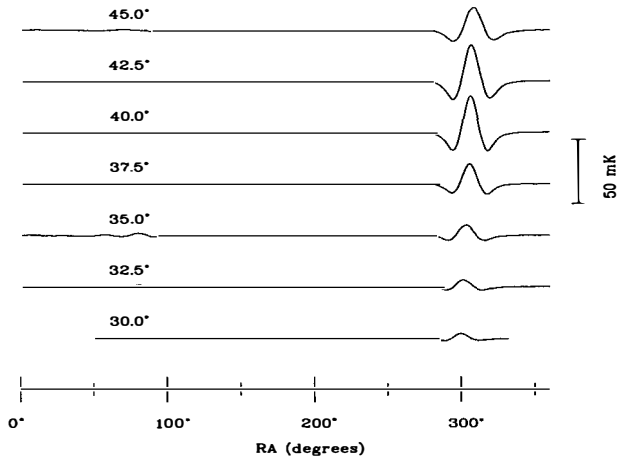

Figure 1: Stacked scans at 15 GHz showing the strong (RA$\sim$ 300° – 310°) and the weak (RA $\sim$ 60° – 90°) crossings of the Galactic plane.

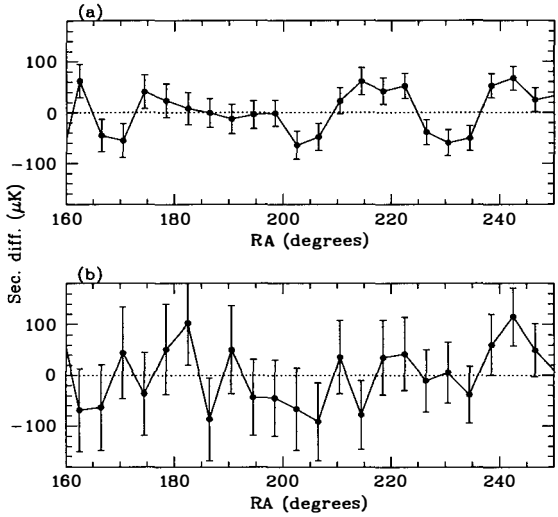

Figure 2: Section of data at high Galactic latitude in the band at Dec.=+35°. *a*/ 15 GHz and *b*/ 10 GHz.

with the expected amplitudes and shapes. The contamination by a foreground of unresolved radio-sources is expected to have an rms $\lesssim 30$ μK, $\lesssim 15$ μK and $\lesssim 3$ μK at 10, 15 and 33 GHz respectively [4]. We have demonstrated [3] the unreliability of the predictions of the difuse Galactic foreground using the low frequencies surveys at 408 [7] and 1420 MHz [10]. Nevertheless, it is possible to infer such a contribution in our data from a comparison between our own measurements at 10 and 15 GHz and the COBE DMR results at 31, 53 and 90 GHz (see below).

After subtraction of the known point-source contribution, we have applied a likelihood analysis [5] to the data at 10 GHz and 15 GHz (the analysis of the data at 33 GHz is in progress). We selected the section of the data at RA=160° − 250° and assume a Harrison-Zel'dovich spectrum for the primordial fluctuations. A summary of the results is given in Table 2. Upper limits and detections are quoted at 95 % C.L. and 68 % C.L. respectively. The results in all strips at 15 GHz are consistent with a CMB signal $Q_{RMS-PS} \sim 20$ μK, whilst at 10 GHz the data are in some cases not sensitive enough to detect CMB signals and seem to have some degree of Galactic contamination. The results at 15 GHz correspond to values only sligthly larger than the level of the signal present in the COBE DMR data ($Q_{RMS-PS} = 18 \pm 1.5$ μK, [1]) and indicate that most of the signal observed in our data at 15 GHz is intrinsic CMB structure. At 10 GHz a foreground-contamination ~ 2 times higher than at 15 GHz is expected. For instance comparing the likelihood results of the 15 GHz data at Dec.=+35° with the COBE DMR normalization, we estimate that the foreground contamination would contribute with $\Delta T_{RMS} \leq 8$ μK at 15 GHz. This value is in agreement with the strong limits placed by the 10 GHz data and implies that even at 10 GHz more than half of the signals are due to CMB fluctuations.

Table 2: Results of the likelihood analysis (expected Q_{RMS-PS} in μK) for data over RA=160°–250°.

Dec. (deg.)	10 GHz	15 GHz
30.0	-	22^{+10}_{-6}
32.5	33^{+18}_{-13}	25^{+12}_{-11}
35.0	≤ 33	20^{+8}_{-6}
37.5	35^{+16}_{-13}	19^{+8}_{-7}
40.0	≤ 31	23^{+11}_{-9}
42.5	≤ 44	29^{+12}_{-10}
45.0	59^{+22}_{-17}	21^{+14}_{-10}

3 Comparison with COBE DMR data

A Wiener filter, assuming a CDM model, was applied [2] to the two-year COBE DMR data at 53 and 90 GHz. From this filtered map the prediction for the Tenerife experiment was computed over the region 35° $\leq$Dec.$\leq$ 45°. At high Galactic latitude, the most significant features predicted in the Tenerife data are two hot spots with peak amplitudes $\sim 50 - 100$ μK around Dec.=+35°, at RA$\sim$ 220° and $\sim$ 250°. A comparison between the reconvolved results of our data using Maximum Entropy [8] and this prediction is plotted in Fig. 3. At 15

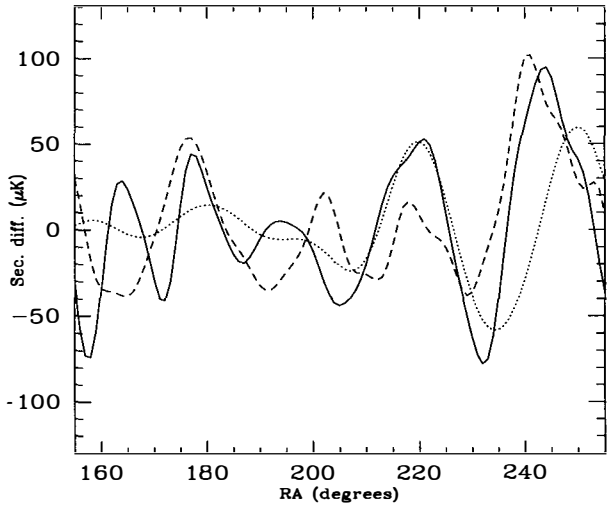

Figure 3: Comparison between COBE DMR and Tenerife at Dec.=+35°. Solid and dashed lines correspond to the Tenerife data at 15 and 10 GHz respectively; dotted are the COBE DMR predictions.

GHz the two most intense structures agree in amplitude and position whith the predicted ones, with only a slight shift in position for the feature at RA~250°; this structure is also detected in the 10 GHz results. The 10 and 15 GHz data also show a possible third positive feature at RA~ 180° with little evidence of this in the prediction. The global agreement between our data and COBE DMR predictions strongly suggests that the main structures detected at Dec.=+35° are cosmological in origin.

4 Future programme

Data collection with the radiometers will continue in order to give a coverage of Dec.=+30° to 45° at the full sampling separation of 2°5 (half the FWHM). We plan to reach rms sensitivities in a 5° beam of 20 μK at 15 and 33 GHz, and 50 μK at 10 GHz. This combination of sensitivities will enable us to detect CMB fluctuations, and at the same time, to determine the Galactic contribution to better than 5 μK at the highest frequency.

A 33 GHz two-element interferometer has been constructed at Jodrell Bank and installed at the Teide Observatory in collaboration with the IAC. This interferometer has a resolution of 2°5, with full sine and cosine correlation in a 3 GHz bandwidth. The low noise amplifiers used are cryogenically cooled HEMTs, and the anticipated sensitivity is 0.7 mK$\times$Hz$^{-1/2}$. Preliminary analyses of the data taken at Decs.=+41° and +58°, demonstrate the consistency of the data and the detection of several radio-sources. In the stacked scans at Dec.=+41° and 58° the sensitivity is about 50 μK per degree in RA, or 30 μK per fringe; these figures need to be compared with the expected levels ($\sim$ 15 μK) of the CMB signal in our instrumental configuration. With the expected improvement of the efficiency of the instrument due to the

change of the horns, we expect, in reasonable time-scales of 6-8 months, to reach in a single strip at constant declination, a signal to noise ratio ~ 2 for CMB signals, allowing a delineation of CMB features with reasonable detail.

The collaboration between MRAO, NRAL and IAC will continue with the Very Small Array (VSA) [see other contributions in this volume]. Operating at frequencies around 30 GHz at the Tenerife site, the VSA will have the capability of imaging primordial CMB structure to a sensitivity of a few μK over the angular range $10'$ to $2\overset{\circ}{.}5$.

Acknowledgements. The Tenerife experiments are supported by the UK Particle Physics and Astronomy Research Council, the European Community Science programme contract SCI-ST920830, the Human Capital and Mobility contract CHRXCT920079 and the Spanish DGICYT science programme PB92-0434-C02.

References

[1] Bennett, C.L. et al. preprint astro-ph/9601067

[2] Bunn, Hoffman, & Silk preprint astro-ph/9509045

[3] Davies, R.D., Watson, R.A. & Gutiérrez, C.M. 1996, MNRAS, 278, 925

[4] Franceschini, A., Toffolatti, L., Danese, L., & De Zotti, G. 1989, ApJ, 344, 35

[5] Hancock, S. et al. 1994, Nature, 367, 333

[6] Hancock, S. et al. 1996, MNRAS (submitted)

[7] Haslam, C.G.T., Salter, C.J., Stoffel, H., & Wilson, W.E. 1982, AASS, 47, 1

[8] Jones, A.W. et al. 1996, MNRAS (submitted)

[9] Kuhr, H., Witzel, A., Pauliny-Toth, I.I.K. & Kaiser, U. 1981, AAS, 45, 367

[10] Reich, P. & Reich, W. 1988, AASS, 74, 7

[11] Smoot, G.F. et al. 1992, ApJ, 396, L1

RECENT RESULTS FROM THE MEDIUM-SCALE ANISTROPY MEASUREMENT/TOPHAT PROGRAM [1]

Robert F. Silverberg
NASA/Goddard Space Flight Center, Code 685, Greenbelt, MD 20771, USA.

Abstract

We describe a program of complementary balloon-borne measurements to study both the anisotropy in the Cosmic Microwave Background Radiation (CMBR) and astrophysical foregrounds on angular scales of $\sim 0.^{\circ}5$. The first series of measurements, at frequencies in the range 5-22 cm^{-1} with the Medium Scale Anisotropy Measurement (MSAM1) was completed in 1995. We report here on a comparison of recent results from those flights where we have repeated measurements. In the second phase of the program we will observe at lower frequencies (2-5 cm^{-1}) using a multi-channel radiometer and a smaller ($\sim 20'$) beam. The third phase of the program will use a lightweight experiment, TopHat, mounted on the top of a balloon to provide high sensitivity and reduced systematic errors. It will take advantage of the long duration balloon capabilities now available from Antarctica.

[1]The MSAM/TopHat research program is currently being carried out by a collaboration including members from the NASA/Goddard Space Flight Center, the Bartol Research Institute, Brown University, the University of Chicago, the Danish Space Research Institute and the University of Toronto.

1 Introduction

Recent papers [4], [7], [6] have shown that detailed measurements of the Cosmic Background Radiation (CMBR) anisotropy on angular scales of 0.°1 to 1° can be used to determine cosmological parameters and thus allow discrimination among various classes of models of the early universe. While a number of measurements of anisotropy near 1° scales have been reported [11], [10], [3], systematic errors at levels comparable to the level of the detections are still of concern [12]. Although future experiments will have greater *raw* sensitivities than the current generation of instruments, it is clear that systematic effects and foregrounds must be carefully understood if greater *system* sensitivities are to be achieved.

With control of systematic errors in mind, we have embarked on a program of observations to study the CMBR anisotropy and the foreground emissions using several balloon-borne instruments. The first of these instruments, designed to study the CMBR anisotropy and the foreground from warm Galactic dust, uses a four channel cryogenic bolometric radiometer cooled to 300 mK and operates at frequencies from 5-22 cm^{-1} with a 0.°5 beam and 1.°4 maximum beam separation. It has been flown three times; we report on recent results from these flights below.

The second phase of the program (MSAM2) is currently being prepared for its maiden flight. This instrument uses a new cryogenic radiometer with an adiabatic demagnetization refrigerator (ADR). The radiometer cools an array of five bolometric detectors to ~100 mK and operates at frequencies from ~2-5 cm^{-1}. This instrument will have a 20′ beam and will be capable of beam separations up to ~2.°5. The single mode system is expected to have improved sidelobe response from the multi-mode system used on MSAM1. Because of the lower frequency range it will be insensitive to warm Galactic dust in low dust regions and more sensitive to free-free emission and bremsstrahlung than MSAM1. Details of the observing plans for MSAM2 are presented at this conference by Knox [8].

The third phase of our program, currently under construction, is an instrument that can take fuller advantage of high altitude balloon-borne platforms. Conventional balloon-borne instruments are suspended below the balloon. The balloon and the support structure are in the instrument sidelobes and may represent potential sources of significant systematic errors at the higher sensitivities being sought in newer experiments. We have designed one-meter class telescopes and radiometers using 300 mK bolometric detectors to be used on packages mounted on the *top* of a balloon where nearly half the sky is clear from obstructions. One of these top-mounted packages uses an off-axis telescope and is designed to make high sensitivity observations at mid-latitudes. The other instrument uses an on-axis telescope and will fly for about two weeks on a long duration balloon flight from Antarctica. A description of these instruments and the observing strategy to be used is provided by Meyer [9] at this conference.

2 Recent Results

Our group has reported detections of CMBR anisotropy at the $\Delta T/T \sim 2 \times 10^{-5}$ level at correlation angles near 0.°5 [1]. In a second flight (MSAM1-94) in 1994, we re-observed portions of the same region as in the 1992 flight [2] to test for systematic errors and confirm our results despite different observing conditions and some changes in our instrumentation. Observations in MSAM1-92 and MSAM1-94 scanned two nearly identical strips in the sky at declination 81.°8 ± 0.°1 from right ascension ~15-20 hours.

For both flights, the secondary mirror executed a three position chopping pattern (left, center, right). The data were demodulated in two different ways. In one case, single-difference

demodulation, the detector signal when the secondary mirror is to the right is subtracted from the detector signal when the secondary mirror is to the left. This demodulation is sensitive to atmospheric gradients. The second method, double-difference demodulation, sums data when the secondary is in the central position and subtracts the data when the secondary is on offcenter positions. These two demodulations allow us to sample different angular scales. Initial results of the comparison [2] showed good agreement for the double-difference demodulation of the data, but a poorer agreement when comparing the single-difference data.

Recently, we have completed a more detailed comparison of the MSAM1-92 and MSAM1-94 flights [5]. In this comparison, we have taken care to ensure that only regions that are spatially overlapping to a high degree are considered. Our spatial binning algorithm uses larger bins than our original analysis; data are only compared when they fall in the same 0.24° bin, approximately the size of the central plateau on our beam and about half our beam FWHM.

Figure 1 shows the central positions for the 1992 and 1994 data. The filled symbols show those data that overlap between the two flights. The raw binned data from each detector cannot be directly compared because of drifts, offsets, and small differences in the electronics which were changed from flight to flight. Even after removing the drifts, offsets, and the effects of cosmic rays striking the detectors, the comparison is more robust if all the channels are combined to recover the sky signal.

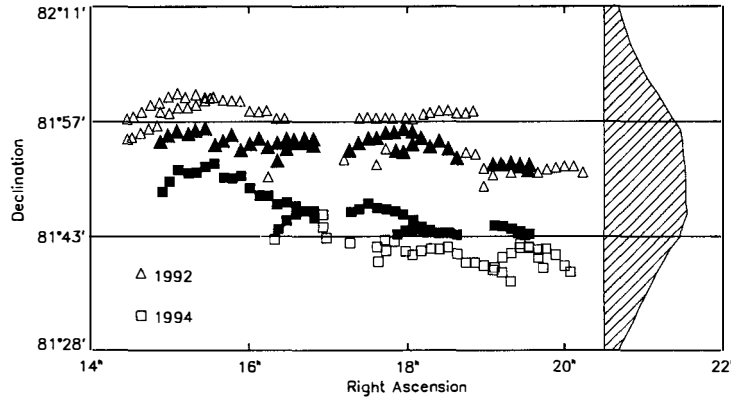

Figure 1: The weighted positions for each sky bin for MSAM1-92 and MSAM1-94 are shown. Triangles mark the 1992 centers and the squares mark the 1994 centers. The declination scale has been expanded relative to the RA scale to highlight the detailed pointing differences. The filled symbols are the weighted centers for the bins used in the comparison ($\langle\delta\rangle = 81°50'$). The declination bin boundaries (every 0°.24) are marked by the horizontal lines. Differences in the angular orientation of our chop on the sky are ignored in this plot, but are not in the analysis. On the right of the figure, the vertical beam profile is plotted in the hatched region.

We therefore fit the demodulated and dedrifted data, t_{ck}, for each channel c and each sky bin k to a two component model for the sky representing the CMBR anisotropy and emission

from Galactic dust:

$$t_{ck} = \int d\nu \, F_c(\nu) \left[D_k \left(\frac{\nu}{\nu_0} \right)^{\alpha} B_\nu(T_{\rm D}) + t_k \left. \frac{dB_\nu}{dT} \right|_{T_{\rm CMBR}} \right], \quad (1)$$

Here $F_c(\nu)$ is the spectral response of the channel, $B_\nu(T)$ is the Planck function at temperature T, $T_{\rm D} = 20\,{\rm K}$ is the Galactic dust temperature, $\alpha = 1.5$ is the spectral index of the dust, $\nu_0 = 22.5\ {\rm cm}^{-1}$ is the reference frequency, $T_{\rm CMBR} = 2.73\,{\rm K}$ is the temperature of the CMBR, and D_k and t_k are free parameters. The fits are not very sensitive to the dust spectral index or the dust temperature. The resulting decomposition of the sky signals gives a DUST and CMBR anisotropy component for each demodulation of the data for each of the flights.

3 Discussion

For both the CMBR and DUST components of the decomposition, the data from the identical bins on the sky are combined to form a sum data set, *92+94*, and a difference data set, *92−94*. A χ^2 statistic is computed with the noise estimated from the variance of the demodulated data. Table 1 shows the statistical analysis of the separate comparisons of the CMBR and DUST components for both demodulations. For both the single-difference and double-difference data we find that the *92−94* components have χ^2_ν statistically consistent with the absence of a signal. The χ^2_ν of the *92+94* components of the signals is statistically inconsistent with an assumption of no common sky signal.

Table 1. Comparison of 1992 and 1994 Data Sets .

Type	Data Set	χ^2_ν	P
Single-Difference Data			
CMBR	*92−94*	1.16	0.22
	92+94	1.98	1×10^{-4}
DUST	*92−94*	1.04	0.41
	92+94	3.22	2×10^{-12}
Double-Difference Data			
CMBR	*92−94*	0.73	0.91
	92+94	2.62	2×10^{-8}
DUST	*92−94*	1.40	0.04
	92+94	2.42	4×10^{-7}

Note: The table shows a comparison of the MSAM1-92 and MSAM1-94 data. The third column gives the reduced χ^2 for the 45 degrees of freedom (DOF) in the data set. The fourth column shows the cumulative probability of the occurrence of the observed χ^2_ν under the assumption that no signal is present in the data. Relative calibration uncertainties between the two flights are less than 6%. The effect of this uncertainty gives $|\Delta\chi^2_\nu| \leq 0.04$ which makes little change in the χ^2_ν shown in the table.

While the ability to make repeated observations with similar instrumentation is strong evidence for signals orginating from the sky, a compelling argument can also be made for making observations of the same region using different instrumentation and techniques. The Princeton Group [10] has recently completed an analysis of the polar cap region using data from their receiver operating at 26-46 GHz (SK95). During their observing program they

observed the same region as MSAM1-92. They have synthesized the MSAM double difference pattern and used a sum/difference analysis similar to the one we have used above. Although the mean pointing error between the two data sets differs by about 0°.14, their results show remarkable agreement with the CMBR data we have presented here. This agreement is despite very significant differences in our respective experiments. In particular, Table 2. highlights these differences. The χ^2_ν for the mean of the sum of the SK95 and MSAM1-92 data sets is 3.43, while the χ^2_ν for the mean of the difference of the data sets is 1.05. This agreement is a powerful constraint on systematic errors and residual foreground for both experiments. It is significant that we have reproduced our own results and that two experiments are seeing the same signal from the sky, despite the different frequencies, systematic errors, and expected contamination from foregrounds.

Table 2. Differences between SK95 and MSAM1-92 Experiments.

Characteristic	**SK95**	**MSAM1**
Frequency	26-46 GHz	170-690 GHz
Observing Platform	ground-based	balloon-borne
Observing Mode	fixed elevation	small elevation changes
Principal Foreground	synchrotron, free-free	dust
Observing Time Scale	days	~hours
Detector Technology	HEMT	bolometers
Configuration	single mode	multi-mode
Calibration	Cas A	Jupiter

Acknowledgements. We are grateful to NASA's Office of Space Science, Astrophysics Division which has supported this research through grants NTG 50720 and 50908 and RTOP 188-44.

References

[1] Cheng, E. S. et. al., 1994, *Astrophys. J.* **422**, L37

[2] Cheng, E. S. et. al., 1996, *Astrophys. J.* **456**, L71

[3] Gundersen, J. O. et. al. 1995, *Astrophys. J.* **443**, L57

[4] Hu,W. and White, M., 1996, *Astrophys. J.* submitted, *preprint* `astro-ph/9512006`

[5] Inman, C. A. et. al., 1996, *Astrophys. J. Lett.* submitted, *preprint* `astro-ph/9603017`

[6] Jungman, G., Kamionkowski, M., Kosowsky, A., and Spergel, D., 1995, *Phys. Rev. D* submitted, *preprint* `astro-ph/9512139`

[7] Knox, L., 1995, *Phys. Rev. D* **52**, 4307

[8] Knox, L., 1996, This conference

[9] Meyer, S. S., 1996, This conference

[10] Netterfield, C. B. et. al., 1996, *Astrophys. J.* submitted, *preprint* `astro-ph/9601197`

[11] Ruhl, J. E., et. al., 1995, *Astrophys. J.* **453**, L1

[12] Wilkinson, D., 1995. A Warning Label for Cosmic Microwave Background Anisotropy Experiments. In Astbury, A. et. al., editors, *Particle Physics and Cosmology, Proceedings of the Ninth Lake Louise Winter Institute*, page 110, Singapore. World Scientific.

THE MAX AND MAXIMA EXPERIMENTS

S. Hanany [1,2], and the MAX[1,2,3] and MAXIMA[1,2,4,5,6,7] Collaborations
[1] *The Center for Particle Astrophysics, University of California, Berkeley.*
[2] *University of California, Berkeley.*
[3] *University of California, Santa Barbara.*
[4] *University of Rome.*
[5] *IROE-Firenze.*
[6] *California Institute of Technology.*
[7] *Queen Marry and Westfield College.*

Abstract

We summarize the performance of the MAX experiment during its 5 years of operation and present a compilation of the results to date. We describe MAXIMA, a balloon borne experiment employing an array of detectors in the focal plane, that will provide sensitive measurements of the power spectrum between $l \sim 60$ and $l \sim 650$.

1 MAX

The Millimeter wave Anisotropy eXperiment (MAX) was a balloon borne experiment that measured the cosmic microwave background anisotropy (CMBA) on half degree angular scale from 1989 to 1994. It was a collaboration between groups in the University of California, Santa Barbara and Berkeley. Between 1989 and 1994 the instrument was launched 5 times and scanned 9 regions of the sky for CMBA. First detection of CMBA signals was reported by Alsop *et al.* [1]. Table 1 summarizes the flights, the regions scanned, flat band power results, and CMBA papers published.

1.1 Overview of the MAX experiment

Several papers describe the MAX instrument [1, 2, 3], here we only summarize selected aspects of the experiment. Particular details of the experiment, e.g. exact beam size, frequency bands,

and bolometer temperature, where modified during the duration of the program. The numbers that will be quoted here refer to the last flight of the program, MAX-5, unless otherwise noted.

MAX had a single pixel photometer at the focal plane of an off-axis Gregorian telescope. The telescope provided a beam of 0.5 degree FWHM. The beam was split inside the photometer to 4 frequency bands by means of dichroic mesh-filters.

During an observation the beam was modulated on the sky with two frequencies. The secondary mirror modulated the beam sinusoidally, in cross-elevation direction, at a frequency of 5.4 Hz and amplitude of 1.4 deg. Simultaneously the entire gondola was scanned in azimuth at constant velocity at an amplitude of 4 degrees and a frequency of 0.0075 Hz. The center of the gondola scan tracked the location of a bright star for the duration of the observation. The fast secondary mirror chop provided effective discrimination against low frequency electronic noise which had a $1/f$ knee at $\sim$ 3 Hz. The slow scan enabled the subtraction of temporal variations in the bolometer temperature and the atmosphere brightness.

The MAX detectors were composite bolometers operating at 300 mK for the first three flights and at 85 mK for the last two. The MAX-5 bolometer for the 450 GHz band was background limited. At the lower frequency bands phonon and Johnson noise was dominant. During the duration of the program sensitivity to CMB temperature differences improved significantly. For example, the sensitivity of the 180 GHz channel improved by a factor of 10 from $\sim$ 2 mK$\sqrt{\text{sec}}$ [2] to 0.24 mK$\sqrt{\text{sec}}$ [9].

The optical chop at $\sim$ 5 Hz, which was chosen as an optimum in the trade-off between the bolometer time constants and the onset of low frequency noise, determined MAX's l space coverage to a single window function. The window function peaked at $l = 150$ and had half power points at $l = 72$ and $l = 248$.

MAX was calibrated by observing a planet once during the flight and then using a partially reflecting membrane as a transfer standard for additional periodic calibrations. The typical absolute calibration error was 10% which was dominated by uncertainties in the brightness temperature of the planets observed.

1.2 MAX results

MAX provided seven detections of CMBA signals at an angular scale of $\sim$ 0.5 degrees. For these seven detections the wide frequency coverage, up to 4 channels between 90 GHz and 450 GHz, enabled unambiguous spectral discrimination against emission from galactic dust. Extrapolation of the fluctuations observed in the 408 MHz Haslam map to the MAX frequency bands, using the expected spectral dependence of either synchrotron or Bremstrahlung radiation, yields a fluctuations' amplitude of typically less than 10% of the amplitude observed. Thus it is unlikely that synchrotron or Bremstrahlung are the dominant source of the detected fluctuations. Searches in available catalogs found no sufficiently intense radio sources in the regions observed. The treatment of potential temporal variations in the signal due to atmosphere variability, beam motion relative to the balloon or earth, moon location, etc. are discussed in the references mentioned in Table 1. Two measurements near the star μ-Pegasi, where 100μ IRAS maps indicate significant dust contrast, were expected to reveal dust signals. Indeed, the dust signature detected was morphologically consistent with IRAS. Only upper limits on the CMB fluctuation power were derived in these regions.

Most cosmological models predict an increase in the power spectrum of the CMB fluctuations near the peak of MAX's window function. The MAX results are suggestive of a combined flat band power larger than that detected by the COBE/DMR experiment. Statistical analysis to combine the seven detections to a single estimate of the CMB fluctuation power within MAX's window function is in progress.

Flight/Year/ Region Observed	$(\Delta T/T)_{flat}$	Publication
MAX-1 / 1989		Fischer *et al.* 1992 [2]
MAX-2 / 1990 / GUM*	$2.9^{+4.3}_{-1.8}$	Alsop *et al.* 1992 [1]
MAX-3 / 1991 / GUM*	$2.7^{+1.1}_{-0.7}$	Gundersen *et al.* 1993 [4]
MAX-3 / 1991 / μ-Pegasi	< 1.6	Meinhold *et al.* 1993 [5]
MAX-4 / 1993 / GUM*	$2.0^{+0.6}_{-0.4}$**	Devlin *et al.* 1994 [6]
MAX-4 / 1993 / σ-Herculis	$1.8^{+0.8}_{-0.6}$**	Clapp *et al.* 1994 [7]
MAX-4 / 1993 / ι-Draconis	$1.9^{+0.7}_{-0.4}$**	Clapp *et al.* 1994 [7]
MAX-5 / 1994 / HR5127	$1.2^{+0.4}_{-0.3}$	Tanaka *et al.* 1996 [8]
MAX-5 / 1994 / ϕ-Herculis	$1.9^{+0.7}_{-0.4}$	Tanaka *et al.* 1996 [8]
MAX-5 / 1994 / μ-Pegasi	< 1.3	Lim *et al.* 1996 [9]

Table 1: Summary of MAX results. Values of $\Delta T/T$ are for flat band $\langle \frac{l(l+1)C_l}{2\pi} \rangle^{1/2}$, 95% confidence interval. (*) GUM stands for the region near the star Gamma Ursa Minoris. (**) Original results were revised as described by Tanaka *et al.* (1996).

2 MAXIMA

The goal of next generation experiments is to make precise measurements of the CMBA power spectrum. Theoretical work within the last several years has demonstrated that the optimal observing strategy to constrain the power spectrum, in the absence of systematic errors or foregrounds, is to observe as many sky pixels as possible with modest (~ 1) signal to noise per pixel [10]. It has also been argued that small to intermediate scale measurements, at $100 \lesssim l \lesssim 1500$ covering the region where CDM models predict adiabatic peaks, could discriminate between various cosmological models [11, 12] and provide information about the cosmological parameters independent of the underlying cosmological model [13].

The Millimeter wave Anisotropy eXperiment Imaging Array (MAXIMA) was designed to address these scientific requirements by scanning many pixels on the sky within a single flight, providing large l space coverage and high l resolution, while improving on the systematic-error rejection achieved for MAX. MAXIMA is a balloon borne program designed to constrain the CMBA power spectrum on a range of angular scales between $l \sim 60$ and $l \sim 650$. It is a collaboration between groups at the University of California, Berkeley, University of Rome, IROE – Florence, Queen Mary and Westfield College – London, and the California Institute of Technology.

2.1 Experimental Configuration

MAXIMA will observe 14 sky pixels simultaneously with 0.18 degree FWHM beams. The attached Figure shows the experiment, the focal plane and its orientation on the sky. The 14 single frequency photometers detect radiation in three frequency bands centered around 150 GHz, 240 GHz, and 420 GHz. The bolometers will be maintained at 100 mK to provide high sensitivity and short time constants. The experiment is designed for up to 24 hour of observations and it will fly in north America.

2.1.1 optics The optical system is a three mirror off-axis f/1.8 Gregorian telescope. The primary mirror is a 1.3 meter diameter off axis section of a parabola. The secondary and tertiary mirrors (21 cm and 18 cm in diameter respectively) are conic sections with aspheric components which compensate the aberrations introduced by the primary mirror. The secondary and tertiary mirrors and a Lyot stop are mounted in a well baffled box inside the cryostat and are

The MAXIMA Experiment

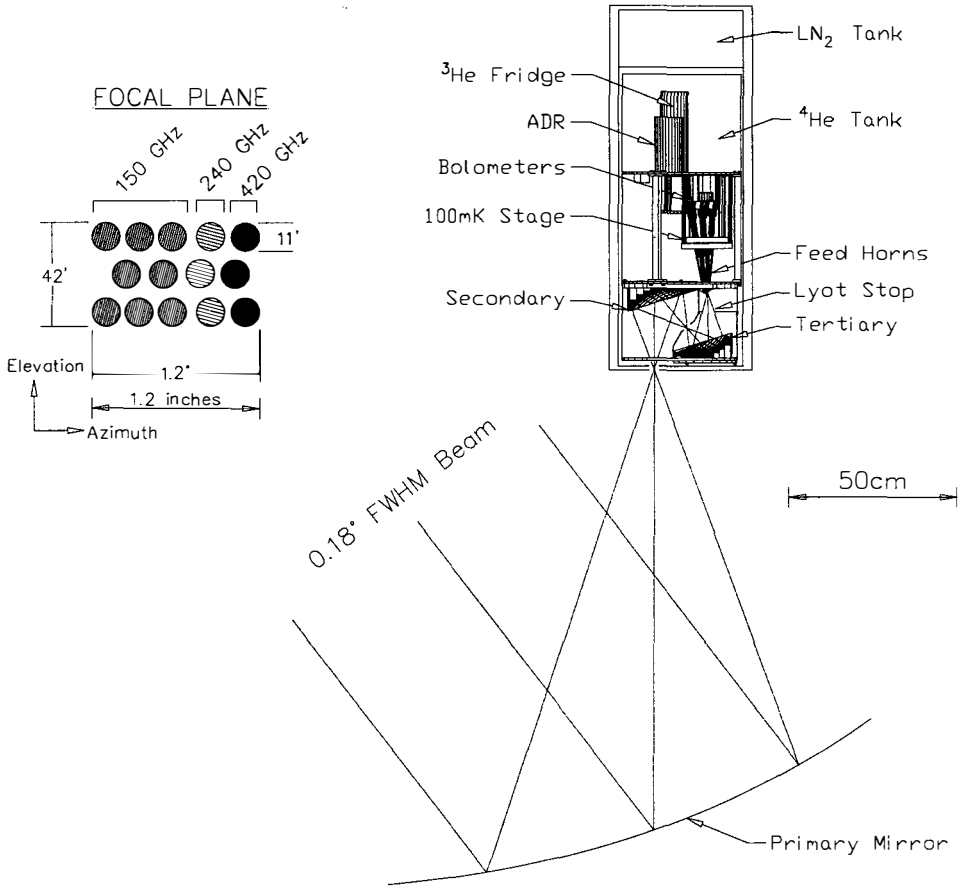

cooled to liquid helium temperature. The cold Lyot stop provides excellent sidelobe rejection and cooling the secondary optics reduces the optical loading on the bolometers. A three mirror system was designed to provide for a diffraction limited $\sim 1 \times 1$ deg^2 field of view at 150 GHz. The secondary and tertiary mirrors are fixed and the light, 11 kg, primary mirror can be modulated around the optical axis of the telescope (the line connecting the center of the primary and the center of the secondary).

2.1.2 Cryogenics, Detectors and Electronics The cryostat was designed for a north-American flight of up to 24 hours. The bolometers will be cooled to 100 mK by means of an adiabatic demagnetization refrigerator (ADR). The heat of magnetization generated during the ADR cycle will be sunk into a ^{3}He refrigerator operating at 300 mK with a cooling capacity of 25 Joules. The resulting cooling capacity of the ADR is 93 mJoules. With expected heat loads both the ADR and the ^{3}He refrigerator will maintain cooling capacity much longer than the cryostat.

Spider-web bolometers [15] operating at 100 mK will be used to detect the incoming radiation[1]. Extrapolation from measurements at 300 mK, and preliminary measurements at 100 mK, indicate that the detectors will be background limited and will have time constants $\lesssim 10$ msec. We expect a detector NET of 60 μK$\sqrt{\text{sec}}$ (90 μK$\sqrt{\text{sec}}$) at the 150 GHz (240 GHz) frequency band.

The detectors will be AC-biased at a frequency of several hundred Hz[1]. The post lock-in noise of the readout electronics was measured to be less than 10 nV$\sqrt{\text{Hz}}$, down to frequencies smaller than 100 mHz.

2.1.3 Gondola and Attitude Control The gondola provides for pointing in azimuth and elevation. Pointing control is achieved with a 5 Hz feedback loop control relying on a two axis magnetometer for coarse pointing (± 2 degrees) and on a CCD camera as a fine sensor. The CCD camera and its associated f/0.7 lens provide a field of view of 7.4 degrees in azimuth and 5.5 degrees in elevation, and pixel resolution of 0.8 arcmin/pixel and 0.9 arcmin/pixel, respectively. The on board image processing is expected to provide sub-pixel resolution. Overall pointing stability is expected to be 1 arcminute RMS or better.

2.2 Observing Strategy and l Space Coverage

MAXIMA's beam will be scanned in azimuth with two frequencies. The primary mirror will modulate the beam in a triangular wave with frequency f_1 and amplitude A_1, while the gondola will be simultaneously scanned in azimuth at a slower rate. Here we discuss the choice of f_1 and A_1.

A bolometer with time constant τ acts as a single pole low pass filter on the detected optical signals. The -3 dB point of this filter is used to set a criterion on the maximum speed that the beam can be scanned across the sky. The signal detected by a fast bolometer ($\tau \simeq 0$) when a Gaussian beam with width $\sigma = 0.425 \times$ FWHM crosses a point source at constant speed $\dot{\theta}$ has a Gaussian frequency distribution with width $\tilde{\sigma} = \dot{\theta}/(2\pi\sigma)$. If we require that the -3 dB roll-off of a real bolometer will be larger than $3\tilde{\sigma}$ we obtain a relation between the maximum scan speed and the bolometer time constant

$$\frac{1}{2\pi\tau} \geq \frac{3\dot{\theta}}{2\pi\sigma} \;\Rightarrow\; \dot{\theta} \leq \frac{\sigma}{3\tau} = \frac{\text{beam FWHM}}{7\tau}. \qquad (1)$$

[1]See also a paper by Debernardis in these proceedings. The bolometers, readout electronics, and attitude control system are shared technology between BOOMERanG and MAXIMA.

For a 0.18 degrees FWHM beam width and $\tau = 10$ msec, $\dot{\theta} \leq 2.6$ degrees/sec. By moving the beams across the sky at this (or somewhat lower) speed the bolometers remain sufficiently sensitive to all spatial frequencies up to ~ 1/beam size.

The amplitude A_1 is determined by requiring that the scan frequency f_1 be higher than the knee of the $1/f$ noise. preliminary measurements during the first flight of MAXIMA suggest that $f_1 \simeq 0.5$ Hz is appropriate. For a triangular wave

$$4A_1 f_1 = \dot{\theta} \leq 2.6 \text{ deg/sec}, \tag{2}$$

so that $A_1 = 1.3$ degrees. Larger amplitudes are possible with shorter bolometer time constants.

This scan strategy is efficient and enables the synthesis of multiple window functions in a single scan. In combination with the 11 arcminute beams we expect an l space coverage between $l = 60$ and $l = 650$. (see also a companion paper in this proceedings [16].)

2.3 Status and Flight Program

The MAXIMA set of measurements is being comissioned in stages. In the first flight, which was launched from Palestine, Texas, on Sept. 2, 1995, we flew the single beam receiver used on MAX-4, and MAX-5. Most other flight systems, including the gondola, the pointing system, AC-bias electronics, and chopping primary mirror, were new. The flight goals were to test all new flight systems, scan regions of the sky for CMBA signals, and test new scan strategies. All of these have been successfully accomplished. Data analysis is in progress.

The 14-beam array is presently under construction and is scheduled to be launched as MAXIMA-2 in the spring of 1997.

References

[1] Alsop, D. *et al.* 1992, ApJLett, 395, 317

[2] Fischer, M. L. *et al.* 1992, ApJ, 388, 242

[3] Meinhold, P., *et al.* 1993, ApJ, 406, 12

[4] Gundersen, J. O. *et al.* 1993, ApJ, 413, L1

[5] Meinhold, P., *et al.* 1993, ApJ, 409, L1

[6] Devlin, M., et al. 1994, ApJ, 430, L1

[7] Clapp, A. C., *et al.* 1994, ApJ, 433, L57

[8] Tanaka, S. T., *et al.* 1996, ApJ, in publication

[9] Lim, M. A., *et al.* 1996, ApJ, in publication

[10] Knox, L. 1995, Phys. Rev. D, 52, 4307

[11] M. White, & W. Hu 1996, these proceedings

[12] M. Magueijo, A. Albrecht, D. Coulson, & P. Ferreira 1996, Phys. Rev. Lett, 76, 2617

[13] W. Hu, & M. White 1996, these proceedings

[14] Jungman, G., Kamionkowski, M., Kosowsky, A., & Spergel, D. N. 1996, Phys. Rev. D, in press

[15] Bock, J. J., Chen, D., Mauskopf, P. D., & Lange, A. E. 1994, Proceedings of The Future of IR and MM-Wave Astronomy, Saclay, France.

[16] Lee, A. T., *et al.* 1996. these proceedings.

Future plans for CMB anisotropy measurements with the MAXIMA array

Adrian Lee[1], Peter Ade[2], James Bock[3], Andrea Boscaleri[4], Sarah Church[3], Paulo de Bernardis[5], Jason Feldman[1], Ken Ganga[3], Shaul Hanany[1], Viktor Hristov[3], Andrew Lange[3], Enzo Pascale[5], Philip Mauskopf[3], Paul Richards[1], George Smoot[1], Stacy Tanaka[1], Celeste Winant[1], and Johnny Wu[1]

[1]*Center for Particle Astrophysics and Department of Physics, University of California, Berkeley CA, 94720*

[2]*Queen Mary and Westfield College, London, UK*

[3]*California Institute of Technology, Pasadena CA, 91125*

[4]*IROE-CNR, Firenze, Italy*

[5]*Dipartimento di Fisica, Universita' La Sapienza, Roma, Italy*

Introduction

The Millimeter-Wave Anisotropy eXperiment Array (MAXIMA) experiment is an evolution of the degree-scale CMB anisotropy experiment MAX. MAXIMA is also based on a balloon-borne telescope and Adiabatic Demagnetization Refrigerator (ADR) cooled bolometers operated at 100 mK. The new experiment is designed to dramatically increase the amount of CMB anisotropy power spectrum information gathered compared to MAX. There are three main components to this improvement: (1) A large increase in sky coverage per flight is made possible by a large increase in the instrument sensitivity and an efficient observation strategy. (2) High resolution in ℓ-space and sensitivity to high values of ℓ is achieved by the total power mode observation strategy and small (11' FWHM) beams. (3) Robust checks for instrumental systematics and foregrounds are made by repeated measurements of the same area of sky on several time scales and wide frequency coverage.

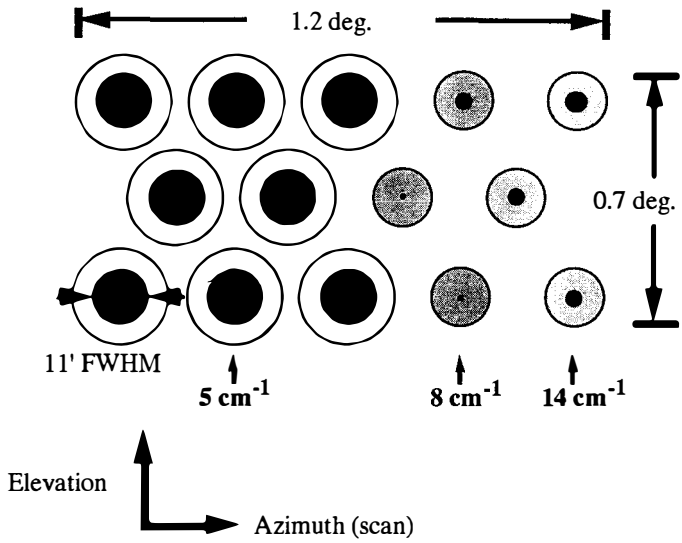

Fig. 1. MAXIMA focal plane array. Largest circles indicate aperture of horn. Filled intermediate size circles indicate FWHM beam size. Small filled circles indicate RMS aberrations.

Array configuration

A focal-plane array of bolometers will be implemented for MAXIMA to increase the rate of sky coverage. A high-optical-efficiency single-color photometer will be located at each pixel in the focal plane. There will be 8 photometers with a central frequency of 5 cm^{-1}, and 3 each with central frequencies of 8 cm^{-1} and 14 cm^{-1} (see Fig. 1). All the pixels will have a 11' FWHM beamsize. Multiple frequencies within a large range allows discrimination of foreground sources from the CMB. A large field-of-view is made possible by the cold reimaging optics.[1] The focal plane is arranged to have several 5 cm^{-1} channels, a 8 cm^{-1}, and a 14 cm^{-1} channel in each row (see Fig. 1). As the array is scanned, each pixel is measured at all three frequencies

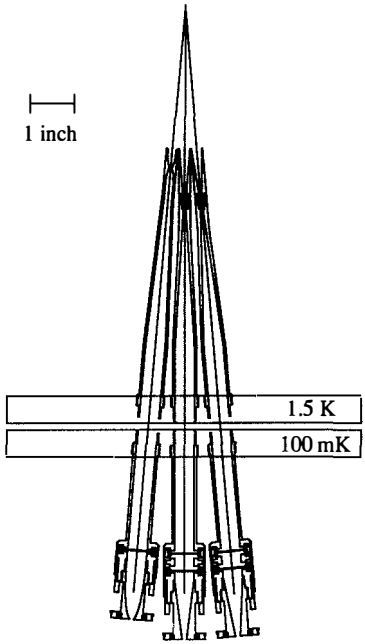

Fig. 2. Bolometer feeds. Multi-mode feed (left) uses back-to-back Winston cones and single-mode feed (middle and right) use smooth-wall conical horns. 100 mK stage is supported mechanically by Vespel tubes.

Bolometer feeds

A cutaway view of the focal-plane bolometer feeds is shown in Fig. 2. The feed horns illuminate a cold Lyot stop (defined to be at an image point of the primary mirror).[1] The 5 cm^{-1} channel is close to diffraction limited at 11' FWHM given the primary mirror diameter of 1.3 m and the illumination edge taper. The 5 cm^{-1} feed utilizes a waveguide-cutoff high-pass filter which provides a sharp band edge and restricts the radiation to a single spatial mode. The input diameter

of the horn is ~1.6Fλ, which is an optimum value in the trade-off between aperture efficiency and beam size.

The 8 cm^{-1} and 14 cm^{-1} bolometer feeds propagate multiple spatial modes and therefore Winston cones were chosen. An F/# 1.7 back-to-back Winston determines the illumination of the Lyot stop and defines the beam size.

The 5 cm^{-1} bolometer feed incorporates two metallic-mesh high-pass filters (the second filter is needed to reject a resonance in the first) manufactured at Queen Mary and Westfield College. The 8 cm^{-1} and 14 cm^{-1} feeds utilize metallic-mesh bandpass filters.

Observation strategy

MAXIMA's primary mirror will be rapidly (f ~ 1/2 Hz) modulated in an azimuth sawtooth pattern (~6° peak-to-peak) to scan the array on the sky. (The primary mirror is made of Al honeycomb with a graphite-epoxy face sheet and weighs 11 kg.) This rapid scan is made possible by the low thermal response time of the Si_3Ni_4 "spider web" bolometers ($\tau < 10$ ms) that will be used.[2,3] The rapid primary mirror scan reduces the effects of low-frequency atmospheric drifts, gondola elevation changes, and telescope pointing variations. Modulation of the primary mirror, rather than a secondary mirror, allows scans over large angles in azimuth and should give low "offsets" since the illumination from the receiver (in the reverse optical sense) is roughly constant on the primary.

The total power mode mirror scan allows anisotropy on multiple angular scales to be measured simultaneously. The number of independent window functions is comparable to the number of independent pixels on the sky (>30 for MAXIMA's mirror scan), and the highest ℓ value explored is proportional to 1/beamsize ($\ell_{max} \sim 650$ for 11' FWHM beam).

We will scan the gondola in azimuth slowly while the mirror scans rapidly and the telescope elevation is fixed. As the sky rotates a large fraction of the sky is observed (~2% in 3 hours). A repeat measurement of the same sky region with the telescope at a different elevation

allows for observations with a different orientation. This cross-linking of pixels allows two-dimensional maps to be produced. The measurement of each pixel is repeated on the time scales of the mirror scan, the gondola scan, and the cross-linked measurement which allows instrumental drifts to be measured and systematic errors to be reduced. MAXIMA's maximum sensitivity to the CMB power spectrum occurs at $\ell > 200$, past the theoretical primary peak of a standard CDM model.

References

1. see paper by Shaul Hanany in these proceedings for discussion of MAXIMA cold reimaging optics.

2. J. J. Bock, D. Chen, P. D. Mauskopf and A. E. Lange, Proceedings of The Future of IR and mm-wave Astronomy, Saclay, France, 1994

3. see paper by Paulo De Bernardis in these proceedings for discussion of bolometers, readout electronics, and attitude control system. All of these are shared technology between the MAXIMA and BOOMERanG experiments.

BOOMERanG: BALLOON OBSERVATIONS OF MILLIMETRIC EXTRAGALACTIC RADIATION and GEOPHYSICS

P. de Bernardis[1], P. Ade[2], E. Aquilini[3], J. Bock[4], A. Boscaleri[5], P. Cardoni[3], K. Ganga[4], M. Giacometti[1], M. Griffin[2], S. Hanany[6], V. Hristov[4], A. Lange[4], A. Lee[6], L. Martinis[3], S. Masi[1], P. Mauskopf[4], F. Melchiorri[1], P. Palangio[7], E. Pascale[1], A. Raccanelli[1], P. Richards[6], G. Romeo[7], F. Scaramuzzi[3], D. Sforna[1]

[1] *Dipartimento di Fisica, Universita' La Sapienza, Roma, Italy*
[2] *Queen Mary and Westfield College, London, UK*
[3] *ENEA, Frascati, Italy*
[4] *California Institute of Technology, Pasadena, USA*
[5] *IROE-CNR, Firenze, Italy*
[6] *Physics Department U.C.B., Berkeley, USA*
[7] *ING, Roma, Italy*

Abstract

The BOOMERanG experiment is an international effort to measure the Cosmic Microwave Background (CMB) anisotropy at an angular resolution of $12 \div 20$ arcmin, with unprecedented sensitivity, sky and spectral coverage. The telescope will be flown from Antarctica by NASA-NSBF with a long duration stratospheric balloon (7-14 days), and is presently scheduled for a test flight in 1996 and an Antarctic flight in 1997. The experiment is designed to measure the power spectrum of the CMB anisotropies up to $\ell \sim 700$ and to produce an image of the CMB sky with high sensitivity and angular resolution. It will be an important precursor of future space-borne missions, producing crucial cosmological data and testing new technologies which are essential to the design of a CMB mapping satellite experiment.

1 General design of the experiment

Antarctic ballooning is very attractive for CMB anisotropy experiments for two reasons. The first is that the flight duration can be between 7 and 20 days, thus allowing for a substantial

sky coverage and for a deep check for systematic effects; the second is that very low foreground regions are observable exactly in the direction opposite to the sun during the Antarctic summer. The lowest dust contrast region in the IRAS Sky Survey Atlas is at R.A. $\sim$ 4.5 hours, dec. $\sim$ -45^o, and is more than 1000 square degrees in area. The contrast in the dust emission corresponds to CMB temperature anisotropy of less than 3 μK rms in the 4-7 cm^{-1} band, a value negligible with respect to the rms level of the sub-degree CMB anisotropies. A good signal to noise map of the CMB in this region will provide a very strong test for gaussianity of the CMB anisotropies. A much larger region can be observed with a dust contribution lower than 20 μK in the same frequency band. Such an observation could provide a very precise measurement of the power spectrum of CMB anisotropies. We plan to have a test flight from North America, with a $\sim$ 15% sky coverage, and an Antarctic flight with similar sky coverage and higher signal to noise ratio [1]. A general view of the experiment is shown in fig.1. A simulation of the anisotropy power spectrum measurements for both flights is shown in fig.2. In the simulations we have assumed we are operating in a differential observation mode in order to guarantee negligible drifts in the data. We are also assuming that such observation mode is effective in removing completely residual atmospheric fluctuations, an issue still to be experimentally investigated, especially at low ℓ-s.

There are, however, a number of problems peculiar to Antarctic ballooning. The long flight duration requires special cryogenic systems. The cosmic rays flux in polar regions is enhanced by a factor about ten with respect to our latitudes, thus increasing the noise in standard bolometric detectors. The long duration balloon flights are performed during the Antarctic summer: the presence of the sun is a general concern for the thermal performance of the payload and for the sidelobes pickup of the telescope. The balloon is far from the ground equipement, so special data collection / telemetry systems have to be used, and interactivity with the system is reduced.

2 Detectors and Feed Optics

Spider web bolometers have been developed to avoid cosmic rays glitches [2]. These bolometers use micromesh absorbers and support structures patterned from thin films of low stress silicon nitride and have been designed for operation at 0.3 K with a radiation load lower than 1 pW. The small geometrical filling factor of the micromesh absorber provides 20$\times$ reduction in heat capacity and cosmic ray cross section relative to a solid absorber with no loss in infrared absorption efficiency. The support stucture is mechanically robust and has a thermal conductance, G $< 2 \times 10^{-11}$ W/K, which is 4 times smaller than previously achieved at 300 mK. The temperature rise of the bolometer is measured with a neutron transmutation doped Ge thermistor attached to the absorbing mesh. The achieved detector NEP at 0.3 K is $1.2 \times 10^{-17}\ W/\sqrt{Hz}$ with a 20 ms time constant. The bolometers are mounted in multiband photometers and single pixel detectors in the focal plane. We have developed both single mode and overmoded feeds with high optical efficiency which allows us to optimize the focal plane for angular resolution (12' at 150 GHz) and/or optical sensitivity (35 $\mu K\sqrt{s}$ at 90 GHz).

To read out these detectors, we use an AC stabilized "total power" amplifier for individual bolometers mounted on a temperature regulated stage. This system contains a cooled FET input stage and contributes less than 7 nVrms/$\sqrt{\text{Hz}}$ noise at all frequencies within the bolometer signal bandwidth down to 20mHz. The warm readout circuit has a gain stability of $<$ 10 ppm/°C and has a rejection of EMI of -120 dB. This readout scheme combined with the temperature control of the 300 mK stage makes it possible to implement scan strategies for total power mapping with bolometers.

Fig.1 : The BOOMERANG Payload

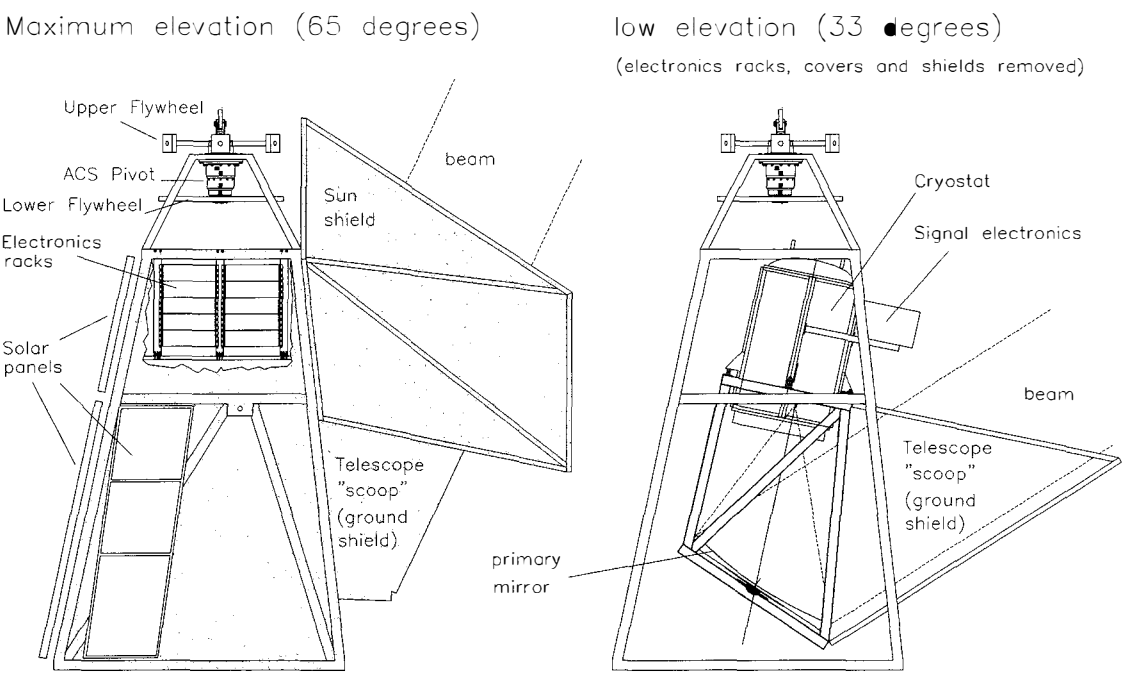

Fig.2 : simulation of BOOMERanG power spectrum measurements

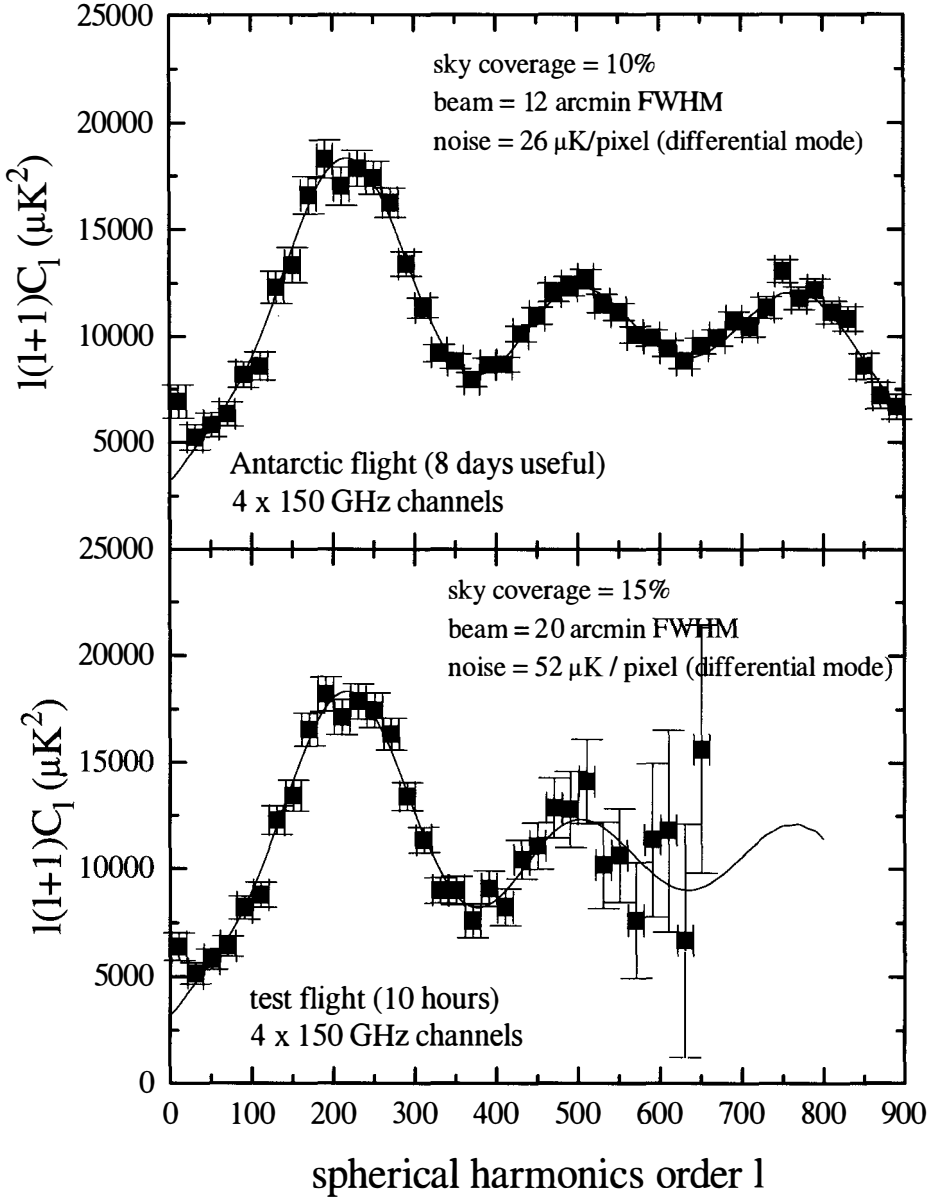

3 Cryogenic system

A "heavy duty" ^{3}He fridge and a large ^{4}He cryostat have been developed specifically for the BOOMERanG experiment. The main ^{4}He cryostat has to be large enough to contain refocusing optics and a wide focal plane with several multiband photometers. The total volume occupied by the cryogenic section of the receiver is about 0.5 m^3. The design hold time is about 20 days; the helium tank volume is 60 liters, the nitrogen tank volume is 70 liters. Conduction thermal input is reduced by suspending both the tanks with Kevlar ropes (1.6 mm diameter). The vibration frequencies of these structures are all above 20 Hz, and the amplitude of the vibrations excited during the flight is expected to be very small. Radiation thermal input on the nitrogen tank is reduced by means of 110 layers of aluminized mylar for superinsulation. The total thermal input on the nitrogen bath is about 3 W. The radiative thermal input on the helium bath is reduced by the use of a copper shield between the He tank and the Nitrogen tank. The shield is mantained at around 25 K by the vapours evaporationg from the He tank. The total thermal input on the helium bath is about 50 mW. The bolometers are cooled by a self contained ^{3}He fridge. The charge is 34 liters STP at 40 bars. The measured working temperature is 0.29 K (in flight), raising to 0.31 K when the ^{4}He bath is at normal pressure (lab tests). The measured hold time is longer than 15 days.

4 Optics

The optical system must be able to define a sharp field of view for the detectors, collecting the largest possible amount of power from the selected region of the sky and rejecting efficiently emission from off-axis sources and foreground radiation. We have developed an off/axis system based on an ambient temperature primary mirror that is a paraboloid with 1.2 m projected diameter, 1.28 m focal length, and 45^o off-axis angle. Two aluminum refocussing mirrors (off axis paraboloid and ellipsoid) are mounted at 4.2 K, inside the dewar. Radiation from the sky is reflected by the primary mirror (the primary is underfilled to improve sidelobes), crosses a thin polypropilene window, and is concentrated at the focus, inside the ^{4}He dewar. A filter reflecting high frequencies is mounted on the 77K shield, and a mesh filter is mounted on the 4 K shield, at the entrance of the refocussing optics box. Eccosorb vanes inside the box reject stray rays. The last mirror defines the cold Lyot stop of the system. The two off axis mirrors produce a large curved focal plane above the optics box. The useful size of the focal plane is 30 by 20 cm. This corresponds to more than 4 by 2.5 degrees in the sky. The large focal plane allows both a large number of detectors and the ability to synthesize many different window functions by differencing between various pixels in order to optimally reject low-ℓ sources of noise. The bolometers are arranged in single-band (S) and multi-band (M) photometers as listed in table 1.

Table 1: Focal plane of the BOOMERanG receiver

flight	band (GHz)	FWHM arcmin	feeds	NET $\mu K\sqrt{s}$
T	90 S	40	2	35
T	150 S	20	4	60
A	90 S	20	4	80
A	150 M	12	4	90
A	250 M	12	4	140
A	350 M	12	4	1000

A set of shields, partially visible in fig.2, is used to achieve high thermal stability of the telescope and to reduce efficiently sidelobes spillover from the sun and the ground.

5 Attitude Control System

The ACS must be able to point a selected sky direction, and track it or scan over it with a reasonable speed. The specs are 1 arcmin rms for pointing stability, with a reconstruction capability better than 0.5 arcmin maximum. Our main modulation is obtained scanning in azimuth, with a saw-tooth scan, with an amplitude of 20 deg (p-p) and a scan rate of about 1 deg/s. A different scan mode, useful to get a wider sky coverage during North America flights, is the full azimuth rotation of the payload at a speed of about one r.p.m.. An ACS capable of the above mentioned performances has been developed from the ACS systems used for ARGO and MAX-5. It is based on a Pivot which decouples the payload from the flight chain and controls the azimuth, plus one linear actuator controlling the elevation of the inner frame of the payload. The pivot has two flywheels, moved by powerful torque motors with tachometers. On the inner frame, which is steerable with respect to the gondola frame, are mounted both the telescope and the detectors cryostat. The observable elevation range is between 25 and 65 deg. The sensors are different for night (North America) and day (Antarctic) flights. For night flights we have a magnetometer and an elevation encoder; additional information on the attitude is obtained by means of a sensitive tilt sensor. A CCD camera is used outside the feedback loop for absolute attitude reconstruction. For day time antarctic flights we have a set of low and high resolution sun sensors and the tilt sensor. A flight programmer CPU takes care of commands handling and observations sequencing; a feedback loop controller CPU is used for digitization of sensors data and PWM control of the current of the three torque motors. A similar system has been tested in the MAX-5 flight in september 1995, with good overall performance.

6 Conclusions

The use of total power readout with overmoded bolometers at 300 mK allows us to get an unchopped sensitivity of $\sim 80\mu K\sqrt{s}$ for the 3 cm^{-1} (20' FWHM) channel; $\sim 90\mu K\sqrt{s}$ for the 5 cm^{-1} (12' FWHM) channel, $\sim 140\mu K\sqrt{s}$ for a 8 cm^{-1} (12' FWHM) channel. If we scan a $50^o \times 50^o$ region (6% of the sky, more than 20000 pixels for the 20' channel and more than 60000 pixels for the 12' channels) for 8 days with four detectors per band, we get an unchopped sensitivity of $7\mu K$/pixel at 3 cm^{-1}, $13\mu K$/pixel at 12 cm^{-1}, and $18\mu K$/pixel at 8 cm^{-1}. Real sensitivity will be degraded from this depending on the level of atmospheric noise, on the analysis algorithm and on the in-flight performance of the system. However, these numbers give already an idea of the high quality and enormous amount of information which will be produced by BOOMERanG.

References

[1] Lange A., et al. 1995, *Space Sci. Rev.* **74**, 145

[2] Bock J., et al. 1995, *Space Sci. Rev.* **74**, 229

RESULTS FROM CAT AND PROSPECTS FOR THE VSA

Michael E. Jones
Mullard Radio Astronomy Observatory, Cavendish Laboratory, Madingley Road, Cambridge CB3 0HE, UK.

Abstract

We have produced an image of the microwave sky with 30′ resolution in a 2° field using the Cosmic Anisotropy Telescope (CAT). Analysis of data taken at three frequencies near 15 GHz indicates that most of the signal is due to the CMB, with an equivalent broad-band power of $\Delta T/T = 1.9^{+0.5}_{-0.5} \times 10^{-5}$ at angular scales corresponding to multipoles $l = 320$–500, and $\Delta T/T = 1.8^{+0.7}_{-0.5} \times 10^{-5}$ at $l = 500$–680. We are now building a more advanced instrument, the Very Small Array (VSA), which will cover the range $l = 130$–1800 with a sensitivity per resolution element of $\Delta T/T \sim 10^{-6}$.

1 Introduction

Measurements of the anisotropy in the cosmic microwave background radiation (CMB) in the vicinity of the expected 'Doppler peaks' (10′–2°) are crucial for the determination of cosmological parameters such as Ω and H_0, and for discriminating between competing theories of structure formation. Most results on these scales so far have come from balloon-borne switched-beam bolometer systems (eg [1, 2]) or ground-based switched-beam heterodyne systems at dry sites (eg [3, 4]). We have been developing centimetre-wave *interferometers* which offer several advantages over these techniques. These include rejection of groundspill and other signals that do not move with the sky, freedom from $1/f$ noise problems in the receivers, and the rejection of atmospheric emission fluctuations, giving the ability to operate from less extreme sites[5, 6]. The Cosmic Anisotropy Telescope (CAT) is a prototype interferometer designed to test the concepts and technology for a more comprehensive imaging interferometer, the Very Small Array (VSA). In this paper we briefly discuss interferometric imaging of the CMB, review the CAT results and then describe the VSA.

2 Interferometric imaging and power-spectrum estimation

Each antenna pair of an interferometer measures one Fourier component of the part of the sky seen by the envelope (or primary) beam of the antennas, i.e. if a sky brightness distribution $T(\mathbf{s})$ is observed with an interferometer of baseline $\mathbf{u}$ (in wavelengths) then the measured quantity is the *visibility*

$$V(\mathbf{u}) = \frac{2k}{\lambda^2} \int T(\mathbf{s}) B(\mathbf{s}) \mathrm{e}^{i\mathbf{s}.\mathbf{u}} \, \mathrm{d}\mathbf{s}, \tag{1}$$

where $B(\mathbf{s})$ is the power reception pattern (primary beam) of the antennas, and the factor $2k/\lambda^2$ converts from temperature to flux density (the units of an interferometric map being Jy beam^{-1}). Thus a CMB interferometer measures (almost) what the theorist wants to know—$|V(\mathbf{u})|^2$ is proportional to the two-dimensional power spectrum of the sky, but convolved with the square of the Fourier transform of the primary beam. This places a limitation on the resolution with which the power spectrum can be obtained. With a fixed number of antennas of a given aperture, there is a maximum area of aperture plane that can be covered; this fixes the range over which the power spectrum can be measured, or equivalently, the number of resolution elements in the image. A sparsely sampled aperture plane (e.g. the CAT, see Fig. 2) can be inverted to yield a map, but the poor sampling in the aperture leads to long-range correlations in the image. This can be ameliorated by deconvolving the image, using for example the CLEAN algorithm, but such an image must be treated cautiously, since this is equivalent to interpolating the visibilities into regions of the aperture where none were measured. However, a well-sampled aperture plane can be inverted to yield a faithful image of the sky, subject to the resolution limit imposed by the maximum baseline, and the low spatial-frequency cut-off of the shortest baseline.

A image contains both amplitude and phase information; however, if the sky is Gaussian the phases of the Fourier components are random and all the information is contained in the one-dimensional power spectrum. This can naïvely be obtained by averaging the visibilities, first radially into independent bins, then azimuthally, squaring them, and subtracting the variance of the noise from each bin. However, in the case of low signal-to-noise this can result in negative estimates for the power spectrum in some bins. A better method is to calculate the covariance matrix expected of the data under different power-spectrum models, and adopt a maximum-likelihood approach to finding the best model[7, 8].

3 CAT

The CAT[9] is a three-element interferometer operating at 15 GHz, with a primary beam of 2° FWHM and a resolution of $\sim 30'$. The three conical horn-reflector antennas provide a primary beam with sidelobes less than -60 dB, minimising pick-up from the surroundings and from bright astronomical sources. The antennas are steered in elevation by rotating the reflectors, allowing the cryostats containing the HEMT receivers to remain fixed relative to the horn and the turntable, which provides the azimuth drive. The whole telescope is contained within a 5-m-high earth bank lined with aluminium, so that all stray ray paths are reflected on to the sky. The signals are down-converted at the turntable and sent via coaxial cable to a control hut ~ 100 m away, where the 500-MHz-bandwidth IFs are correlated using an analogue phase-switched correlator. Both linear polarizations are used, but the design of the antennas means that the polarization of each channel rotates on the sky as the telescope tracks.

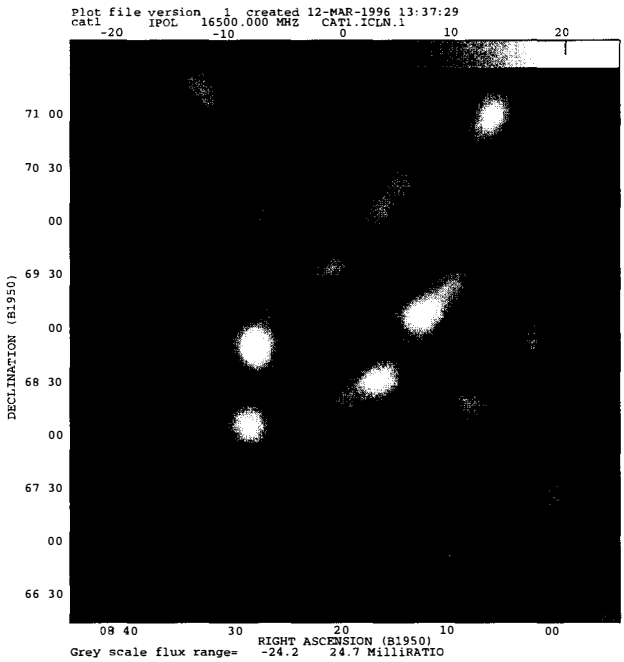

Figure 1: Combined map of 13.5-, 15.5- and 16.5-GHz CAT data, weighted as ν^2 to maximise the CMB component. The map has been CLEANed to remove the long-range correlations due to the sparse sampling of the aperture plane. The greyscale units are mJy beam^{-1}

3.1 Source subtraction

The most important contaminating signal for the CAT is discrete extragalactic radio sources. We select fields at 5 GHz (the highest available frequency with near all-sky coverage) to have minimum source content, but sources still contribute many times the total flux expected from the CMB aniotropies. It is therefore essential to observe these sources at higher flux sensitivity and higher resolution, and at close to the same frequency. This is done using the Ryle Telescope (RT). The RT compact array has five 13-m diameter antennas, giving a flux sensitivity at 15.4 GHz of 200 μJy in 12 h over a 6′ FWHM field of view, with 30″ resolution. The flux sensitivity at each of the three CAT frequencies described in the next section is 7 mJy; the RT can map $(0.5°)^2$ with a noise level of 1 mJy in 12 h. Therefore in 16 × 12 h the RT can map the entire CAT field with sufficient sensitivity to remove all sources to well below the CAT sensitivity.

3.2 CAT results

First results at 13.5 GHz[10] for a field centered at $08^h20^m + 69°$ (B1950) (the 'CAT1' field), showed evidence for a fluctuation level, after subtraction of discrete sources, of 18 mJy beam^{-1}, equivalent to temperature fluctuations of about 35 μK rms. Subsequent observations at 15.5

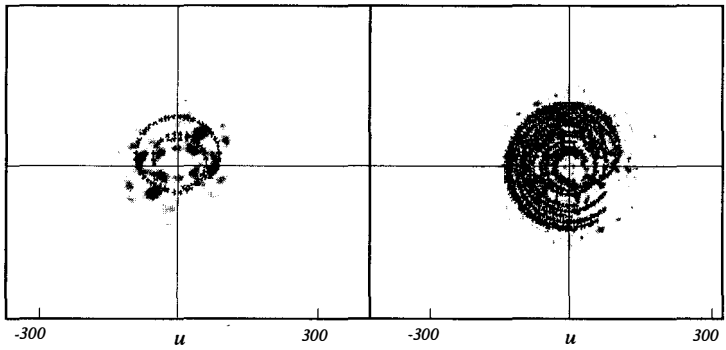

Figure 2: Sample 2-d power spectrum for a standard CDM model, with aperture-plane sampling function of the CAT (left) and the VSA with 4° horns (right). Note the smaller convolution scale of the power spectrum in the case of the VSA due to the larger primary beam.

and 16.5 GHz[8] allow us to estimate the foreground Galactic component and the level of the CMB signal.

The aperture-plane coverage of the CAT results in two independent radial bins, centred at multipole numbers $l = 410$ and $l = 590$. We use a maximum likelihood technique, modelling the CMB and Galactic signals as independent Gaussian signals with variable powers in the two bins, with a fixed flux spectral index of 2 for the CMB and variable in the range $[0, -1]$ for the Galaxy. We then calculate the expected correlation matrix of the visibilities for each model, ranging over the five-dimensional parameter space, and find the maximum likelihood with respect to the data. Marginalising over the Galactic parameters gives the best estimate of the CMB power in the two bins. The data are consistent with most of the signal at 16.5 GHz being due to the microwave background. Taking the square root of the power, the results are $\Delta T/T = 1.9^{+0.5}_{-0.5} \times 10^{-5}$ for the bin covering the range $l = 410 \pm 90$, and $\Delta T/T = 1.8^{+0.7}_{-0.5} \times 10^{-5}$ for the bin at $l = 590 \pm 90$. Given these results, we can combine the three maps at different frequencies, weighted as ν^2, to produce an image that is mostly CMB fluctuations (Fig. 1). This image, unlike the one in [8], has been CLEANed to remove some of the long-range correlations and allow the eye to see more easily the regions of highest and lowest temperature (but note the caveats in section 2 above).

In conjunction with other CMB results, these points provide evidence for the existence of the first Doppler peak, and hence place constraints on the cosmological parameters Ω and H_0 (see Hancock, and Rocha, this volume).

4 The Very Small Array

The CAT is the prototype for the Very Small Array, which is designed to make high-quality images of the CMB. The VSA, which has just received funding (March 1996), will have 15 antennas and a 2-GHz bandwidth analogue correlator, using exactly the same technology as has been successfully tested in the CAT; the specifications are given in Table 1. The operating frequency will be in the range 26–36 GHz, decreasing the effect of discrete sources and Galactic

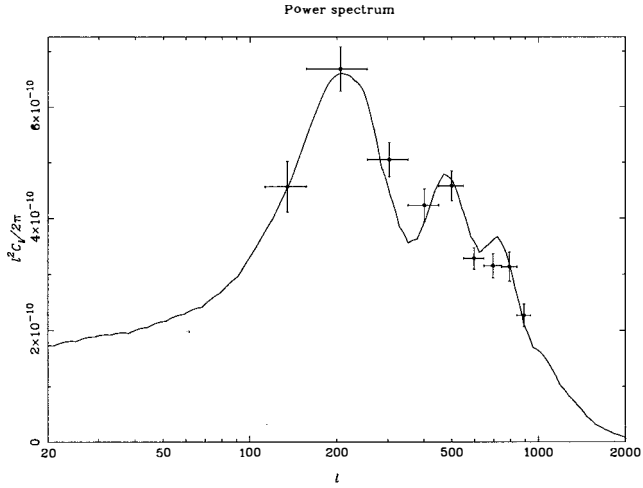

Figure 3: Simulation showing the ability of the VSA to recover the Doppler peaks of the CMB power spectrum. The solid line is a standard CDM power spectrum with $H_0 = 50$, $\Omega_b = 0.03$ and $n = 1$, normalised to COBE. The points are the recovered power spectrum from simulated observations of twelve 4° FWHM fields, representing one year's VSA observations. The simulation includes the effects of removal of discrete sources and diffuse galactic foregrounds. The horizontal error bars represent the width of the independent bins sampled in l-space.

emission compared with the CAT frequency range, but increasing the level of atmospheric fluctuation emission. To alleviate the latter effect, the VSA will be sited at the Teide Observatory in Tenerife, alongside the Jodrell Bank–Tenerife switched-beam experiment. Observations with the Tenerife experiment, and a prototype 33-GHz interferometer (R. Watson, priv. comm.) indicate that the atmospheric conditions at Teide will allow the VSA to operate essentially unhindered by the atmosphere for > 50% of the time.

Source subtraction will be as important for the VSA as for CAT; again, the Ryle Telescope with its higher resolution and flux sensitivity will be vital. Since the RT observing frequency is a factor of 2 lower than the VSA, the RT will have to survey the VSA fields to a flux sensitivity a factor of 2^α better than the flux sensitivity of the VSA, where α is the maximum expected spectral index of sources in the field. Once all the sources which might be significant at the VSA frequency have been found at 15 GHz, measuring their fluxes at $\sim$ 30 GHz will require

	Frequency range (GHz)	Number of antennas × polarizations	Field-of -view	Reso-lution	Temperature sensitivity in 300 h	Flux sensitivity in 300 h	Statistical sensitivity
CAT	13.5–16.5	3 × 2	2°	30′	35 μK	7 mJy	9 μK
VSA	26–36	15 × 1	4(2)°	30(15)′	7 μK	5(1.3) mJy	0.7 μK

Table 1: Comparison of specifications of the CAT and the VSA. The temperature sensitivity is per pixel after 300 h observation (as in each of the three CAT maps in [8]). The statistical sensitivity is the temperature sensitivity divided by the square root of the number of independent pixels. Numbers in parentheses for the VSA are for the second array with larger horns.

only a very short time on a large telescope, e.g. the Bonn 100-m.

The VSA will operate consecutively with two sets of horns; one set of $\sim$ 15 cm aperture giving a 4° beam, and a second set of $\sim$ 30 cm aperture giving a 2° beam. Using the larger horns will allow the VSA to extend to higher angular resolutions without compromising the filling factor of the aperture plane. The CAT, with only three baselines, samples the aperture plane very sparsely, giving only two independent points in the one-dimensional power spectrum. The VSA will measure $\sim$ 100 independent points in the aperture plane, giving $\sim$ 10 independent points on the 1-D power spectrum (see Fig. 3). The width in l of each bin is fixed by the primary beam, i.e. the antenna diameter; the range of l is fixed by the range of baselines possible with 15 antennas and the requirement to sample the aperture plane uniformly. The resolution and range of the measured power spectrum can be changed by changing the size of the antennas. With these two arrays we will be able to measure the power spectrum from $l = 130$–1800 with a resolution $\Delta l = 100$ at low l and $\Delta l = 200$ at high l.

Acknowledgements. Thanks to Mike Hobson and Klaus Maisinger for the VSA power-spectrum simulations. CAT and the VSA are funded by PPARC.

References

[1] Cheng E.S., Cottingham D.A., Fixsen D.J., Inman C.A., Kowitt M.S., Meyer S.S., Page L.A., Puchalla J.L., Ruhl J.E., Silverberg R.F., 1996, *Astrophys. J.* **456**, L71

[2] Clapp A.C., Devlin M.J., Gundersen J.O., Hagmann C.A., Hristov V.V., Lange A.E., Lim M., Lubin P.M., Mauskopf P.D., Meinhold P.R., Richards P. L., Smoot G.F., Tanaka S.T., Timbie P.T., Wuensche C.A., 1994, *Astrophys. J.* **433**, L57

[3] Ruhl J.E., Dragovan M., Platt S.R., Kovac J., Novak G., 1995, *Astrophys. J.* **453**, L1

[4] Netterfield C.B., Jarosik N., Page L., Wilkinson, D., Wollack, E., 1995, *Astrophys. J.* **445**, L69

[5] Saunders R., 1986, in *Highlights of Astronomy* **7**, ed Swings J-P., Reidel

[6] Church S.E., 1995, *MNRAS* **272**, 551

[7] Hobson M.P., Lasenby A.N., Jones M., 1995, *MNRAS* **275**, 863

[8] Scott P.F., Saunders R., Pooley G., O'Sullivan C., Lasenby A.N., Jones M., Hobson M.P., Duffet-Smith P.J., Baker J., 1996, *Astrophys. J.* **461**, L1

[9] Robson M., O'Sullivan C.M., Scott P.F., Duffett-Smith P. J. 1994, *Astr. Astrophys.* **286**, 1028

[10] O'Sullivan C., Yassin G., Woan G., Scott P.F., Saunders R., Robson M., Pooley G., Lasenby A.N., Kenderdine S., Jones M., Hobson M.P., Duffet-Smith P.J., *MNRAS* **274**, 861

RESULTS FROM THE FIRST FLIGHT OF BAM

G. S. Tucker[1], H. P. Gush[1], M. Halpern[1], W. Towlson[2]
[1] *Dept. of Physics and Astronomy, University of British Columbia, Vancouver, BC V6T 1Z1, Canada*
[2] *Dept. of Physics and Astronomy, University College London, London WC1E 6BT, England*

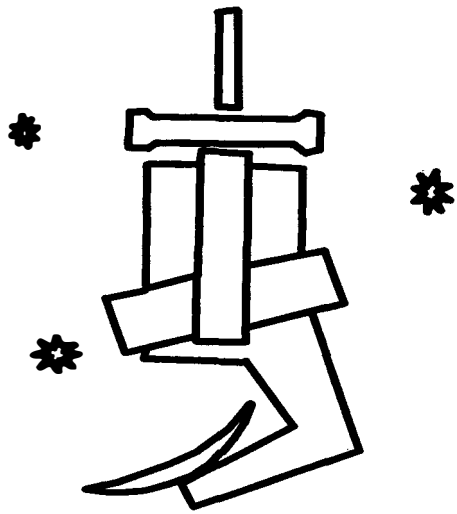

Abstract

A new instrument, BAM (Balloon-borne Anisotropy Measurement), designed to measure cosmic microwave background (CMB) anisotropy at medium angular scales was flown for the first time in July of 1995. BAM is unique in that it uses a cryogenic differential Fourier transform spectrometer coupled to a lightweight off-axis telescope. The very successful first flight of BAM demonstrates the potential of the instrument for obtaining high quality CMB anisotropy data.

A new instrument, BAM (Balloon-borne Anisotropy Measurement), designed to measure the optical spectrum of cosmic microwave background (CMB) anisotropies was flown for the first time in July 1995. The instrument is sensitive to anisotropies on angular scales from 3/4 to a few degrees, scales just larger than those typically predicted for the first so-called Doppler peak in the anisotropy angular power spectrum [1]. Therefore, measurements made by BAM will be used for a sensitive test of the angular power spectrum of *primordial* anisotropies. In this paper preliminary results obtained from the first flight are described.

The BAM receiver is a differential Fourier transform spectrometer, previously used for a measurement of the CMB intensity spectrum from a sounding rocket [2], [3], coupled to a lightweight prime-focus telescope. All of the optical elements of the spectrometer are at $\sim$2 K except for the bolometric detector assembly, which operates at 0.26 K. Rapid scanning of a mirror assembly in the cryostat varies the optical path length difference in the interferometer, and produces interferograms at the bolometers whose amplitudes are proportional to the brightness difference between the two spectrometer inputs. Spectra are obtained *a posteriori* by Fourier transformation of the interferograms with respect to optical delay. Useful anisotropy data are obtained in five spectral channels with central frequencies from 3.1 cm^{-1} to 9.2 cm^{-1}. Unlike most other instruments designed to measure the CMB anisotropy, which employ an ambient temperature chopping mirror to switch the beam on the sky, BAM obtains a differential measurement with no warm moving optical element; the only moving optical element is the moving mirror assembly located in the cryostat.

A diagram of BAM in cartoon form, adapted from the official decal (in color), is shown on the title page. The two inputs to the differential spectrometer are displaced from each other in a direction perpendicular to the plane of the drawing. The inputs are located near to the optic axis of the 70 cm focal length paraboloidal primary mirror, resulting in two beams 0.7° FWHM on the sky separated by 3.6°. Collimators [4] define the acceptance of the two inputs. The

collimators view the same portion of the primary mirror, thus the instrument is insensitive to thermal gradients across the primary mirror. This was tested late in the flight by heating one side of the mirror to produce a 2 K gradient across the mirror; no change in signal is detected.

The BAM gondola structure is relatively large in order to accommodate the off-axis optical design. The gondola stands 4 m high in the laboratory, and the ground shield is 4.5 m across at the widest point. Nevertheless, the application of aerospace-like design and construction techniques has produced a lightweight gondola. For example, the arm holding the primary mirror is a riveted sheet aluminum structure similar to an airplane wing. The undercarriage of the gondola, which absorbs the impact of landing, is made from aluminum honeycomb panels supported by a frame made from welded chrome-molybdenum steel. The 1.65 m diameter aluminum primary mirror itself is also lightweight, weighing 26 kg. The launch weight of BAM is 660 kg, not including ballast.

BAM was launched from the U.S. National Scientific Balloon Facility in Palestine, Texas at 00:45 UT on 8 July 1995 (sunset on 7 July 1995 local time). An animation of the launch and other images can be viewed at http://cmbr.physics.ubc.ca. The gondola reached a float altitude of 41.4 km approximately five hours after launch; a little over three hours was spent performing the experiment at float. Data acquisition was terminated when the balloon neared the end of telemetry range. The instrument was recovered with only minor damage.

Figure 1 shows a chronology of events during the flight. Just before reaching a stable float altitude the telescope was unlatched and scanned across the planet Jupiter to calibrate the instrument and to confirm the beam shape. The instrument was then rotated to look north and a series of observations was begun near to transit above the north celestial pole. Shortly afterwards a memory chip in the pointing system telemetry electronics became intermittent and then failed, corrupting some parts of the telemetry from the pointing system. As a result, the ground station sent erroneous corrective commands at a rate

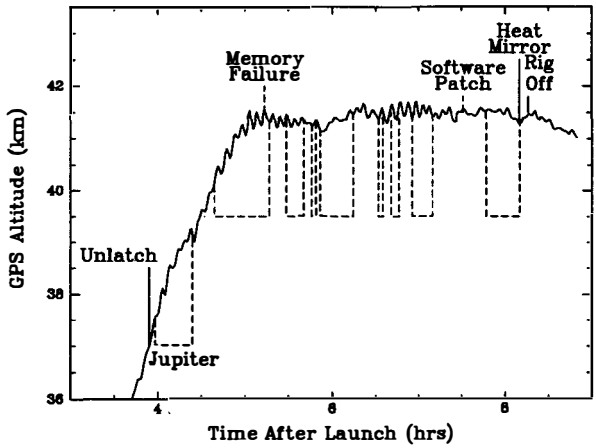

Figure 1. Chronology of events during the flight. Jupiter was scanned several times and provides the primary calibration for the instrument. Regions indicated by the dashed lines indicate periods during which data analyzed here were acquired. The disjoint nature of these regions is largely due to the problems encountered by the failure of a memory chip in the pointing system as described in the text.

exceeding the capabilities of the command transmitter, so successful command transmission became unreliable. The telescope remained locked to guide stars and data were collected, but the precise sequence of observations was difficult to control. After understanding the problem a switch was made to a redundant telemetry channel not intended for use during flight, and a software patch for the ground station was developed. As a result, reliable commanding of the gondola was restored for the last half hour of observation.

It had been intended to obtain an interleaved set of double difference measurements by slewing the telescope in azimuth by an angle corresponding to the beam separation every three minutes. We were not entirely successful in this regard. Since slewing is controlled by commands from the ground the memory failure limited the number of double differences obtained. As a result,

preliminary results based on analysis of single differences are presented; single difference measurements were obtained on ten fields on the sky.

The spectrum of the optical signal from the sky is contained in the cosine component of the phase-corrected Fourier transforms of the interferograms. The sine component is orthogonal to signals from the sky and thus provides a monitor of systematic effects in the measurement. Using a likelihood analysis technique and assuming that the sky can be described by a Gaussian autocorrelation function [5], it is found that the 90% confidence interval for the cosine component is not consistent with zero. Although the peak of the likelihood function for the sine component is not at zero power, the sine amplitude is consistent with zero. The detected optical signal can be expressed as the square root of the band power or $Q_{\rm flat}$ (after [6]). It is found that $Q_{\rm flat} = 35.9^{+17.7}_{-6.3}$ μK at an effective spherical harmonic of $\overline{\ell} = 74$. Details can be found in [7]. Figure 2 shows this result along with the results of other current CMB anisotropy measurements.

Statistically significant fluctuations in the microwave sky have been observed, but not with the sensitivity required to attribute these fluctuations definitively to cosmic origin; in particular it has not been possible to constrain the amplitude of the fluctuations and their optical spectral signature simultaneously. The modest sensitivity obtained in this flight is the result of mechanical and electrical malfunctions, coupled with the short observing time accepted for the initial flight of a new instrument, and it is not the result of any fundamental limitation of the instrument. Avoiding a repeat of these malfunctions poses no serious technical challenge or risk. With a longer flight and some improvements to the receiver, an improvement in the signal-to-noise ratio of at least a factor of five is conservatively anticipated.

Acknowledgements This research was supported by the Canadian Space Agency, the Natural Sciences and Engineering Research Council of Canada, and the Particle Physics and Astronomy Research Council of the U.K.

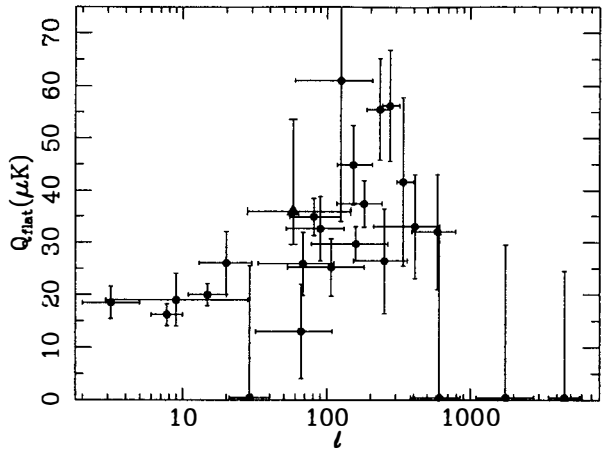

Figure 2. Current measurements of CMB anisotropy. The BAM result is shown as a triangle. Measurements of CMB anisotropy are a measurement of variance and are thus biased away from zero. Thus in regions where there are more measurements one expects a larger scatter as evidenced in this figure. This figure is adapted from [8].

References

[1] White, M., Scott, D., & Silk, J. 1994, *ARA&A* **32**, 329

[2] Gush, H. P., Halpern, M., & Wishnow, E. 1990, *Phys. Rev. Lett.* **65**, 537

[3] Gush, H. P., & Halpern, M. 1992, *Rev. Sci. Inst.* **63**, 3249

[4] Welford, W. T., & Winston, R. 1989, *High Collection Nonimaging Optics*, Academic Press

[5] Readhead, A. C. S., et al. 1989, *Astrophys. J.* **346**, 566

[6] White, M., & Scott, D. 1994, in *CMB Anisotropies Two Years After COBE*, ed. L. Krauss, World Scientific

[7] Tucker, G. S., Gush, H., Halpern, M., & Towlson, W. 1996, *submitted to Astrophys. J.*

[8] Smoot, G., & Scott, D. 1996, *Phys. Rev. D.*, in press

IMAGING AND CALIBRATION OF THE CMB ANISOTROPIES BELOW 130 GHz

M.Bersanelli [1], N.Mandolesi [2], D.Maino [1], N.Vittorio [3], P.F.Muciaccia [3], P.Natoli [3]
[1] *Istituto di Fisica Cosmica, CNR, Milano, Italy* [2] *Istituto TESRE, CNR, Bologna, Italy*
[3] *Dipartimento di Fisica, Universita' di Tor Vergata, Roma, Italy*

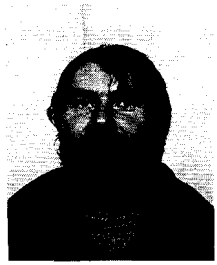

Abstract

We outline the main features of the COBRAS/SAMBA Low Frequency Instrument (LFI), which is designed to image the CMB anisotropies in the frequency range 30–130 GHz. The instrument is based on an array of corrugated feed horns coupled with passively cooled, low–noise HEMT receivers employing microwave integrated circuits technology. We describe the receiver concept and present simulations of the in–flight instrument calibration using the CMB dipole signal.

1 Introduction

Extensive imaging of the Cosmic Microwave Background (CMB) anisotropies with sufficient sensitivity and angular resolution provides a unique tool to discriminate among different structure formation models, and yields information on physics at the ultra–high energies ($\sim 10^{15}$ GeV) which characterize the early universe [1]. An accurate reconstruction of the temperature fluctuation power spectrum up to high–order multipoles ($\ell \simeq 1000$) allows the determination of all fundamental cosmological parameters with an accuracy of few percent [2]. The COBRAS/SAMBA mission[1] is conceived to provide high-sensitivity ($\Delta T/T \sim 10^{-6}$), high-resolution ($\sim 10'$), near–full–sky maps of the microwave sky in order to decode the great scientific information contained in the CMB anisotropies [3]. One of the main drivers of the COBRAS/SAMBA payload design and orbit choice is to ensure a high level of rejection of spurious signals and systematic effects [4], [5]. The orbit and the payload thermal architecture optimize the stability and absolute level of the operating temperature, which are critical

[1]COBRAS/SAMBA is an European Space Agency candidate for the M3 mission, and has recently completed the feasibility (*Phase A*) study.

for both actively and passively cooled detectors. A distinctive feature of COBRAS/SAMBA is the strong control of foreground emissions, achieved by performing multifrequency observations on both sides of the optimum spectral window for CMB observations ($\sim$ 90–200 GHz). The non–cosmological diffuse emissions (mainly synchrotron and free–free at low frequencies, and interstellar dust components at high frequencies) and point sources can be recognized and accounted for by observing their spectral behavior over a sufficiently wide frequency range [6]. Simulations have shown that the COBRAS/SAMBA observations in the range 30–1000 GHz can safely disentangle these components [3].

In order to maximize spectral coverage two different types of detector technologies must be used. The focal plane instrument will incorporate nine bands provided by arrays of cryogenically cooled bolometers in the range 120–1000 GHz (High Frequency Instrument, HFI), and arrays of passively cooled, low noise radiometers in the range 30–130 GHz (Low Frequency Instrument, LFI). The simultaneous observations of the sky with two widely different types of detectors has the additional benefit of a powerful cross-check of possible residual instrumental effects. In this work we report on some of the work that has been carried out during the ESA Phase A Study to develop a baseline for the Low Frequency Instrument.

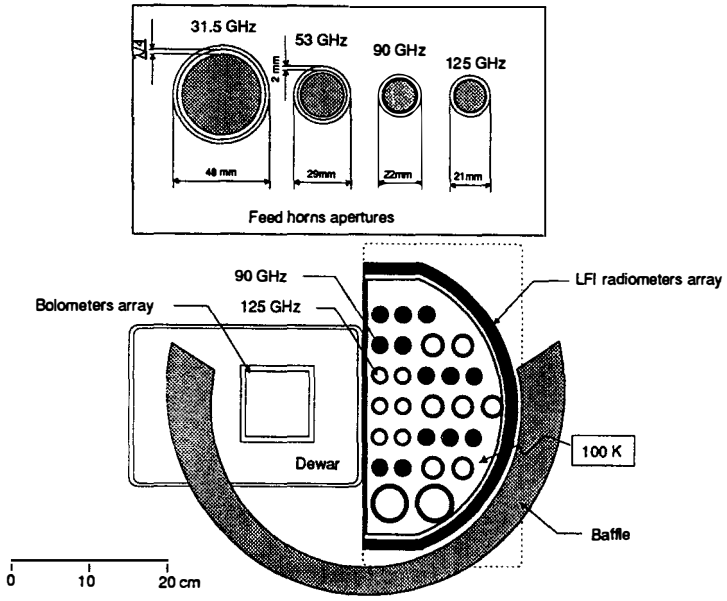

Figure 1 — Schematic of the Low Frequency Instrument (top view). The inset shows the aperture of the corrugated feed horns at the four operating frequencies.

2 Concept of the Low Frequency Instrument

The baseline LFI consists of an array of 28 corrugated feed horns, each coupled with two miniaturized coherent receivers exploiting the two orthogonal polarization modes. The 56 receivers will be based on MMIC (Monolithic Microwave Integrated Circuits) technology, with HEMT (High Electron Mobility Transistor) low noise amplifiers [7]. Currently available HEMT devices show high reliability and low-noise performance. Since the whole LFI system will be passively cooled ($T \simeq 100$ K) it can be operated for a duration limited only by spacecraft consumables (up to 5 years). The receivers (Figure 1) will operate in four frequency bands (31.5, 53, 90, and 125 GHz), with the three lowest bands matching the COBE-DMR channels.

The most straightforward receiver concept for the proposed measurements would be a total power receiver, which was first assumed in our original COBRAS proposal [9]. However, the limitations due to $1/f$ noise in the HEMT amplifiers [8] would imply a factor of ~ 3 degradation in the LFI sensitivity. Rapid switching is required to overcome this effect. The alternative receiver concept presented here (Figure 2) is a solution to this problem, and is presently assumed as the baseline. This solution requires moderate compromises on other radiometer characteristics (notably a $\sqrt{2}$ factor in sensitivity, higher front-end insertion loss, complexity). The total power concept could become again the best choice if the rapidly improving technology of transistor amplifiers can sufficiently reduce the $1/f$ instability.

A double hybrid–coupler system allows a difference measurement between the input voltages from the antenna, A, and from a reference load, R. Each hybrid coupler unit is a four-ports device, with two inputs, IN1 and IN2, and two outputs Σ_+ and Σ_- with alternate 90 degrees phase shift of the signals. If A and R are the amplitudes of the two input electric fields, the two outputs will be $(1/\sqrt{2})\ (iA + R)$ and $(1/\sqrt{2})\ (A + iR)$, respectively. After amplification through the two independent HEMT chains $G1$ and $G2$ (with $G1 \approx G2$), the signals go through the second hybrid ring, and the components in phase are recombined before detection.

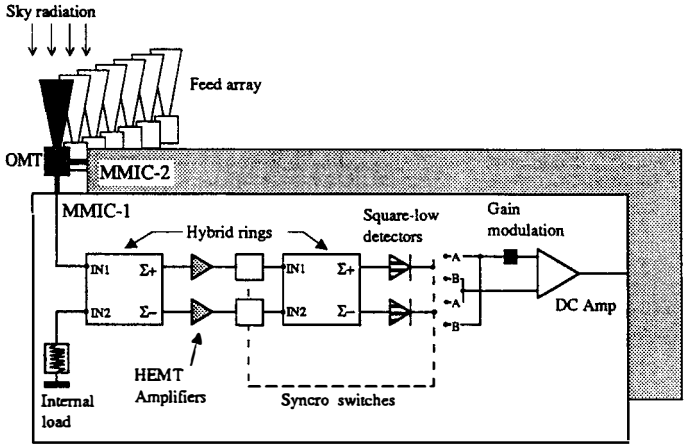

Figure 2 — Schematic of the concept of the LFI differential receivers.

The two detected signals will be, to first order, simply proportional to A and R. Thus the radiometer is effectively performing a continuous comparison between the signal from the sky and the signal from the reference load. This scheme has a factor $\sqrt{2}$ better sensitivity than a classical Dicke–switched system. Gain modulation in the post–detection section of the radiometer is used in order to balance the receiver. The synchronized phase switches, as indicated in Figure 2, have the function of inverting at fast rate ($\sim$ 1 kHz) the two signals before detection, so that possible instability of the detectors will be removed. The switches will act synchronously in the post-detection section to preserve the sign of the detected difference.

Besides the feed antenna, the entire receiver, together with the reference load, is mounted on a single carrier. The radiometer will consist of several chips cascaded together on a carrier of typical size 10×20 mm. Each chip is has a function such as a 4-stage low noise amplifier (LNA), phase switch, bandpass filter, or detector. It is the compact design of MMICs that allows the construction of efficient radiometer arrays in the relatively small focal plane area.

3 Feed Horns

Optimum designs for corrugated feed horns at high frequencies turn out to be critical for a reliable, accurate fabrication. At frequencies $\gtrsim$ 100 GHz the typical groove width is of the order of a fraction of a millimeter with depth more than 1 mm. An optimized design has a groove depth increasing in the narrow throat section, where it should reach roughly $\lambda/2$,which often can't be achieved with direct machining. We have developed a technique to fabricate high quality, high–frequency corrugated feed horns using silver electro-formation. A pure–aluminum master is machined, and used to collect silver ions in a low–current bath with the master mounted on a spinning support. After dissolving the aluminum master the corrugated internal surface of the antenna is cleaned with an ultra–sound device. Different techniques to obtain gold–coating on the inner silver surface were also successfully tested. The first prototypes have been produced and tested up to frequencies of 140 GHz.

4 Calibration

An important aspect to consider in the design of the LFI is the calibration of the detected sky signals, i.e., its conversion into physical (antenna temperature) units [10]. The modulation of the observed signal due to the presence of the CMB dipole, whose value has been accurately measured by COBE–DMR [11], can be used as a calibration source. In fact, in the COBRAS/SAMBA scanning scheme the field of view will systematically scan large circles in the sky ensuring an observed dipole modulation of a few mK throughout the year. We have simulated the LFI observations in order to demonstrate the accuracy achievable with dipole calibration [12]. We reproduced the microwave sky (CMB dipole and Galactic synchrotron, free-free and dust, properly scaled) as observed at each LFI frequency, and simulated the 70°, 1–rpm scan pattern with the sensitivity characteristic of each channel. We associate to each observed pixel i, in a given scan circle, a signal

$$V_i = \frac{1}{G}\,(T_{D,i} + T_{Gal,i}) + \sigma_i \qquad (1)$$

where G is the calibration constant and σ_i is gaussian noise characteristic of each LFI radiometer. For each pixel we then calculate the difference $\Delta V_i = V(\hat{\gamma}) - V(-\hat{\gamma})$ between opposite pixels in the circle. We minimize Galactic contamination by eliminating all the pixels for which

$\Delta T_{Gal,i}/\Delta T_{D,i} < \rho$, where ρ is an adjustable threshold. We determine the value and uncertainty of the calibration constant by minimizing

$$\chi^2 = \sum_{i=1}^{N/2} \frac{(\Delta V_i - G^{-1}\Delta T_{D,i})^2}{\sigma_i^2} \tag{2}$$

where $\Delta T_{D,i}$ is the value of the dipole temperature difference inferred from the COBE–DMR data. In order to achieve accurate calibration one needs $\rho \simeq 0.003$–0.02, depending on the frequency. The results (Figure 3) show that absolute calibration with statistical error below the 0.7% uncertainty limit of the DMR dipole measurement can be obtained every 5 to 15 days by each LFI channel throughout the mission, even with the very conservative assumptions made on the effect of the Galactic emission.

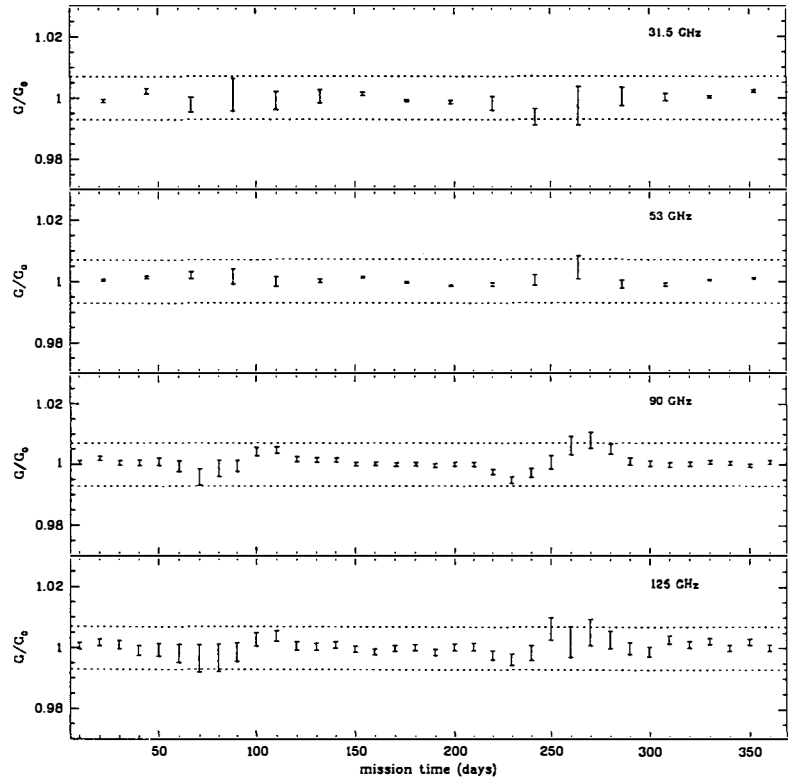

Figure 3 — Simulated calibration of the LFI channels during one year of mission. The horizontal dotted lines are the ±0.7% DMR uncertainty on the dipole amplitude.

An overall calibration accuracy significantly better than the DMR dipole limit can be achieved after one year of LFI observations by exploiting the Doppler effect due to the accurately known seasonal motion of L2 ($\sim$ 30 km/sec) around the sun. Simulations show that an accuracy of order 0.2% can be achieved.

5 Conclusions

A baseline receiver concept for the COBRAS/SAMBA Low Frequency Instrument has been developed in order to overcome the well known limitations of $1/f$ noise in HEMT amplifiers. A technically feasible solution has been described, with acceptable compromises with other system performances. The highest frequency LFI channels (90–125 GHz) present the most significant technical challenges. At these frequencies, first–generation prototypes of both MMIC receivers and corrugated feed horns have been produced and are currently being tested at ITESRE–CNR, Bologna and IFCTR–CNR, Milano. The LFI array can rely for calibration on the COBE–DMR measurement of the CMB dipole, making the non-trivial implementation of an active calibration system not necessary. The LFI is based on simple, reliable technology and is capable of reaching the required sensitivity with passive cooling in deep space environment. The simultaneous observations by the LFI and HFI with widely different foregrounds and instrumentation make the COBRAS/SAMBA mission extremely robust against any possible residual systematic effects in the CMB anisotropy maps.

References

[1] White, M., Scott, D., & Silk, J. 1994, ARAA, 32, 319.

[2] Jungman, G., Kamionkowski, M., Kosowsky, A. & Spergel, D.N., 1996, in press, Astro–ph/9512139 Astro–ph/9507032.

[3] M.Bersanelli, F.Bouchet, G.Efstathiou, M.Griffin, J.M.Lamarre, N.Mandolesi, H.U. Norgaard-Nielsen, O.Pace, J.Polny, J.L.Puget, J.Tauber, N.Vittorio, S.Volonte'; COBRAS/SAMBA Report on the Phase A Study, ESA, D/SCI(96)3, February 1996.

[4] Danese, L. et al. 1996, Astroph. Lett & Comm., 33, 257.

[5] Muciaccia, F., et al. 1996, A&A Suppl, in press.

[6] Toffolatti, et al. 1995, Astrophys. Lett. & Comm., 32, 125.

[7] Pospieszalski, M.W., 1996, these proceedings.

[8] Janssen, M., et al. 1996, ApJ, submitted, Astro–ph/9602009.

[9] Mandolesi, N., et al. 1993, COBRAS proposal - ESA/M3.

[10] Kogut, A., et al. 1996, ApJ, submitted, Astro–ph/9601066

[11] Lineweaver, C., et al. 1996, ApJ, in press.

[12] Bersanelli, M. et al. 1996, A&A Suppl., in press.

A FIRST DETERMINATION OF THE POSITION OF THE 'DOPPLER' PEAK

Stephen Hancock and Graca Rocha
MRAO, Cambridge, UK.

Abstract

Cosmological theories for the origin and evolution of structure in the Universe are highly predictive of the form of the angular power spectrum of cosmic microwave background fluctuations. We present new results from a comprehensive study of CMB observations which provide the first measurements of the power spectrum all the way down to angular scales of ~ 10 arcminutes. On large scales a joint likelihood analysis of the COBE and Tenerife data fixes the power spectrum normalisation to be $Q_{rms-ps} = 21.0 \pm 1.6\mu$K for an initially scale invariant spectrum of fluctuations. The combined data are consistent with this hypothesis, placing a limit of $n = 1.3 \pm 0.3$ on the spectral slope. On intermediate scales we find clear evidence for a 'Doppler' peak in the power spectrum localised in both angular scale and amplitude. This first estimate of the angular position of the peak is used to place a new direct limit on the curvature of the Universe, corresponding to a density of $\Omega = 0.7^{+1.0}_{-0.4}$. Very low density open Universe models are inconsistent with this limit unless there is a significant contribution from a cosmological constant.

1 Introduction

Observations of the Cosmic Microwave Background (CMB) radiation provide information about epochs and physical scales that are inaccessible to conventional astronomy. In contrast to traditional methods of determining cosmological parameters, which rely on the combination of results from local observations[31], CMB observations provide direct measurements[5, 48] over cosmological scales, thereby avoiding the systematic uncertainties and biases associated with conventional techniques. Assuming that the fluctuations conform to a random Gaussian field, then all of the statistical properties are contained in the angular power spectrum and consequently tracing out the form of the CMB power spectrum is a key goal of observational

cosmology[5, 3, 4, 40, 22, 24, 33]. CMB observations on different angular scales are probing different physical effects (see White *et al.* 1995 [48] and Scott *et al.* 1995 [40] for comprehensive reviews). On scales $\gtrsim 2°$, which is the size of the horizon at last scattering of the CMB photons, the gravitational redshifting of the CMB photons through the Sachs-Wolfe effect is the dominant process. The presence of either a background of primordial gravity waves and/or mass fluctuations at recombination, would lead to fluctuations in the CMB. The scalar mass density fluctuations lie outside the horizon and are predicted by inflationary theory to have a scale-invariant flat power spectrum *i.e.* $n = 1$. In Section 2 we use the combined large scale COBE and Tenerife observations to delimit the spectral slope n and to fix the power spectrum normalisation Q_{rms-ps}.

On scales of $\sim 0.2° - 2.0°$ the scattering of the CMB photons during acoustic oscillations of the photon-baryon fluid at recombination [13] is expected to imprint characteristic 'large' amplitude peaks into the CMB power spectrum. The position l_p of the main peak reflects the size of the horizon at last scattering of the CMB photons and is determined almost entirely by the geometry of the Universe. As a result one finds that [22, 23] l_p depends directly on the density of the Universe according to $l_p \propto 1/\sqrt{\Omega}$. The height of the peak is directly proportional to the fractional mass in baryons Ω_b and also varies according to the expansion rate of the Universe as specified by the Hubble constant H_0; in general [22] for baryon fractions $\Omega_b \lesssim 0.05$, increasing H_0 reduces the peak height whilst the converse is true at higher baryon densities. Consequently by measuring the amplitude of the intermediate scale CMB fluctuations relative to the CMB fluctuations resulting from scalar density perturbations on large scales we can trace out the CMB power spectrum and hence directly estimate Ω, Ω_b and H_0 from the position and amplitude of the main peak. In Section 3, we use current CMB observations, including new data from the CAT, Tenerife and COBE experiments to build up a conservative and consistent picture of the CMB power spectrum on large and intermediate scales and hence to obtain a first estimate of both the position and amplitude of the Doppler peak.

2 Joint likelihood analysis of COBE and Tenerife observations

Both the COBE satellite observations [2] and the ground-based observations from the Tenerife experiments [11] are on sufficiently large angular scales that they probe fluctuations that are beyond the horizon scale at recombination and are hence still in the linear growth regime. Such data can therefore be used to investigate the spectral slope of the initial primordial fluctuation spectrum generated in the early Universe. Numerous attempts [42, 19, 20, 45, 2, 16] have been made to determine both the slope and normalisation of the power spectrum at small multipoles. The approach detailed in Hancock *et al.* [19] and reviewed here differs from previous analyses in that for the first time the COBE and Tenerife data have been used *together* taking into account *all* correlations between the two data sets. This method, developed in collaboration with Max Tegmark, uses a direct brute force calculation of the likelihood function for the combined data.

We apply the likelihood analysis to the COBE two-year [1] data and the Tenerife dec +40° scan [19, 20], assuming a power law model with free parameters n and Q_{rms-ps}. The COBE Galaxy-cut two-year map consists of 4038 pixels, whilst the Tenerife Galaxy cut (RA 161°−230°) scan contains 70 pixels, requiring a 4108 × 4108 covariance matrix for a joint likelihood analysis of the data. We arrange the pixels in a 4108-dimensional vector $\mathbf{\Delta T} = (\Delta T_1, \Delta T_2, ...\Delta T_{4108})$ and compute the likelihood function $L(n, Q_{rms-ps}) \propto \exp -(\mathbf{\Delta T^T V^{-1} \Delta T})$ as in Tegmark and Bunn 1995 [45] by Cholesky decomposition of the 4108 × 4108 covariance matrix $\mathbf{V}$ at a dense grid of points in the (n, Q_{rms-ps})-parameter space, marginalizing over the four "nuisance parameters" that describe the monopole and dipole. The covariance matrix consists of three

parts: a 70×70 block with the covariance between the Tenerife pixels, a 4038×4038 block with the covariance between the COBE pixels, and off-diagonal 4038×70 blocks containing the covariance between the Tenerife and COBE pixels. In this way, we fully account for intrinsic correlations due to the CMB structure and correlations due to sampling with the different instruments. Additionally in forming the likelihood function we have intrinsically incorporated the effects of cosmic and sample variance for the two data sets, plus random noise and the interdependence of the model parameters.

The resulting normalised joint likelihood function depicted in Figure 4 of Hancock *et al.* (submitted [19]) thus provides an accurate description of the constraints placed on n and Q_{rms-ps} by the joint data set. The likelihood is seen to peak at $n = 1.37$, $Q_{rms-ps} = 16.1\mu$K, with a 68% confidence region (uniform prior) encompassing 0.90 to 1.73 in n for Q_{rms-ps} in the range from 12.1 to 22.9 μK. Margenalising over Q_{rms-ps} one finds $n = 1.3 \pm 0.3$, whilst conditioning on $n = 1$, one finds a power spectrum normalisation of $Q_{rms-ps} = 21.0 \pm 1.6$. These results using COBE 2-year and Tenerife dec $+40°$ data are comparable to those obtained using the COBE 4-year data [2], for which $n = 1.2 \pm 0.3$ and $Q_{rms-ps} = 18 \pm 1.6\mu$K for $n = 1$. The joint analysis of the COBE 4-year data plus a significantly extended Tenerife sky area is in progress and is expected to improve on these limits. However, it is clear that the current Tenerife and COBE results offer a consistent picture on large scales and do not favour values of n less than unity. In the case of power law inflation, such large values of n do not allow for a significant contribution from tensor modes, giving us confidence in normalising the scalar power spectrum to the large scale anisotropy data. In the following, we will *assume* that this is the case and will proceed to compare the large and intermediate scale anisotropy measurements to test for the presence of a Doppler peak.

3 The CMB Power Spectrum

Reconstructing the CMB power spectrum over large and intermediate angular scales requires the simultaneous use of data from a number of different experiments, all with their own classes of uncertainties. At the time of writing, there are numerous CMB experiments operating worldwide, and it is appropriate here to restrict ourselves to the subset of experiments which have produced conclusive evidence for the detection of CMB anisotropy. Clear detections have now been reported by a number of different groups, using observations from satellites (COBE[42, 2]), ground-based switching experiments (Tenerife[19],[20], Python[36], South Pole[17], Saskatoon[30]), balloon mounted instruments (ARGO[12], MAX[44], MSAM[6, 7]) and more recently ground-based interferometer telescopes (CAT[41]). Given the difficulties inherent in observing CMB anisotropy, it is possible and indeed likely, that some of these results are contaminated by foreground effects[35]. Determining the form of the CMB power spectrum in order to trace out the Doppler peak requires a careful, in-depth consideration of the CMB measurements from the different experiments within a common framework as presented in Hancock *et al.* (submitted [21]); the full details including a discussion of foreground contamination are presented in Rocha *et al.* (in preparation[35]). In this paper and the following contribution [34], we present our principal findings. We consider all of the latest CMB measurements, including new results from COBE, Tenerife, MAX, Saskatoon and CAT, with the exception of the MSAM results and the MAX detection in the Mu Pegasi region which is contaminated by dust emission[14]. On the largest scales corresponding to small l, new COBE [2] and Tenerife [19] results improve the power spectrum normalisation, whilst significant gains in knowledge at high l are provided by new results from the Saskatoon and CAT experiments. The full data set spans a range of 2 to ~ 700 in l, sufficient to test for the main Doppler peak out to $\Omega = 0.1$.

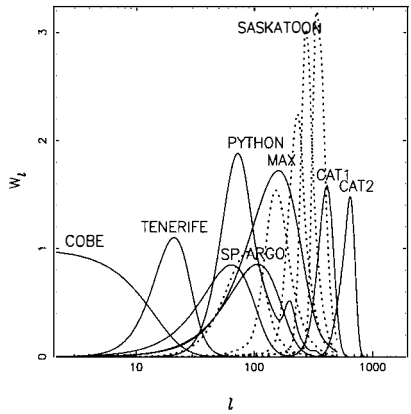

Figure 1: The experimental window functions W_l.

3.1 The flat bandpower approximation

The competing models for the origin and evolution of structure predict[5, 22], the shape and amplitude of the CMB power spectrum and its Fourier equivalent, the autocorrelation function $C(\theta) =< \Delta T(\mathbf{n_1})\Delta T(\mathbf{n_2}) >$ where $\mathbf{n_1} \cdot \mathbf{n_2} = \cos\theta$. Expanding the intrinsic angular correlation function $C(\theta)$ in terms of spherical harmonics one obtains: $C(\theta) = \sum_{l\geq 2}^{\infty}(2l+1)C_l P_l(\cos(\theta))/4\pi$, where low order multipoles l correspond to large angular scales θ and large l-modes are equivalent to small angles on the sky. The different experiments sample different l-modes according to their window functions W_l, as shown in Figure 1 : for a detailed discussion of window functions see [47, 46]. The observed power in CMB fluctuations as seen through a window W_l is given by

$$C_{obs}(0) = \left(\frac{\Delta T_{obs}}{T}\right)^2 = \sum_{l\geq 2}^{\infty}(2l+1)C_l W_l/4\pi. \qquad (1)$$

The C_l are predicted by the cosmological theories and contain all of the relevant statistical information for models described by Gaussian random fields[5]. Given W_l, then for the C_l's corresponding to the theoretical model under consideration it is possible to obtain the value of ΔT_{obs} one would expect to observe using the chosen experiment. This value can then be compared to the value actually observed to test the cosmological model.

We take the reported CMB detections and convert them to a common framework of flat bandpower results[3, 4] as given in Table 1 of the contribution by Rocha and Hancock (this volume). In order to use the observed anisotropy levels to place constraints on the CMB power spectrum one must in general know the form of the C_l under test. However, in most cases the form of C_l can be represented by a flat spectrum $C_l \propto C_2/(l(l+1))$ over the width of a given experimental window, so that the bandpower is $\Delta T_l/T = \sqrt{C_{obs}(0)/I(W_l)}$, where we define $I(W_l)$ according to Bond (1995)[3, 4] as $I(W_l) = \sum_{l=2}^{\infty}(l+0.5)W_l/(l(l+1)$. This bandpower estimate is centred on the effective multipole $l_e = I(lW_l)/I(W_l)$. In many instances experimenters now report results directly for a flat spectrum and when this is not so we have converted the quoted power in fluctuations into the equivalent flat band estimate. Each group has obtained limits on the intrinsic anisotropy level using a likelihood analysis (see *e.g.* Hancock *et al.* 1994[20]), which incorporates uncertainties due to random errors, sampling variance[39]

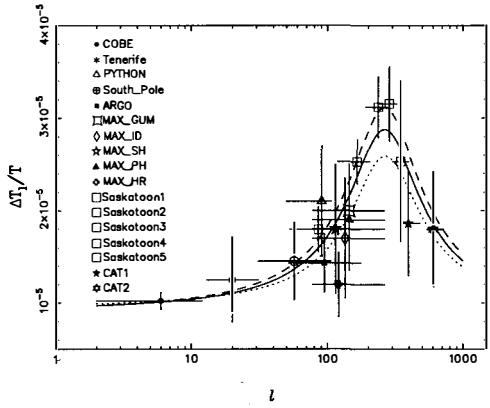

Figure 2: The data points from Table 1 (see [34]) are shown compared to the best fit analytical CDM model. The dotted and dashed lines show the best fit models which are obtained when the Saskatoon calibration is adjusted by $\pm 14\%$. The data points from the MAX experiment are shown offset in l for clarity

and cosmic variance[38, 37]. The form of the likelihood function is not necessarily Gaussian, and strictly one requires a method that will utilise the full likelihood functions from all experiments consistently. However, given the relatively large error bars on most of the reported data points it is sufficient for our purposes here to approximate all likelihood results as originating from a Gaussian distribution, giving the one-sigma error bounds in column three of Table 1 (see [34]) by averaging the difference in the reported 68% upper and lower limits and the best fit ΔT_l. This bias introduced by this averaging is discussed in [35].

Results from the MSAM experiment are not included here, because they do not provide an independent measure of the power spectrum since their angular sensitivity and sky coverage are already incorporated within the Saskatoon measurements. Netterfield *et al.* [30] report good agreement between the MSAM double difference results and Saskatoon measurements, although the discrepancy with the MSAM single difference data is yet to be resolved.

3.2 Estimating the parameters of the Doppler Peak

The data points from Table 1 (see [34]) are plotted in Figure 2, in which the horizontal bars represent the range of l contributing to each data point. There is a noticeable rise in the observed power spectrum at $l \simeq 200$, followed by a fall at higher l, tracing out a clearly defined peak in the spectrum. In the past several groups [40, 24, 33] have attempted to determine the presence of a Doppler peak, but only now are the data sufficient to make a first detection and to put constraints on the closure parameter Ω. As a first step, we adopt a simple three parameter model of the power spectrum, which we find adequately accounts for the properties of the principal Doppler peak for both standard Cold Dark Matter (CDM) models [10, 13] and open Universe ($\Omega < 1$) models [24]. The functional form chosen is a modified version of that used in Scott, Silk & White [40] — we choose the following:

$$l(l+1)C_l = 6C_2 \left(1 + \frac{A_{peak}}{1+y(l)^2}\right) / \left(1 + \frac{A_{peak}}{1+y(2)^2}\right) \qquad (2)$$

where $y(l) = (\log_{10} l - log_{10}(220/\sqrt{\Omega}))/0.266$. In this representation C_2 specifies the power spectrum normalisation, whilst the first Doppler peak has height A_{peak} above C_2, width $\log_{10} l = 0.266$ and for $\Omega = 1.0$ is centred at $l \simeq 220$. By appropriately specifying the parameters C_2, A_{peak} and Ω it is possible to reproduce to a good approximation the C_l spectra corresponding to standard models of structure formation with different values of Ω, Ω_b and H_0. Such a form will not reproduce the structure of the *secondary* Doppler peaks, but we have checked the model against the overall form of the $\Omega = 1$ models of Efstathiou and the open models reported in Kamionkowsky *et al.* [24] and find that this form adequately reflects the properties of the main peak. This satisfies our present considerations since the current CMB data are not yet up to the task of discriminating the secondary peaks. Varying the three model parameters in equation (2) we form C_l spectra corresponding to a range of cosmological models, which are then used in equation (1) to obtain a simulated observation for the ith experiment, before converting to the bandpower equivalent result $\Delta T_l[C_2, A_{peak}, \Omega](i)$. The chi-squared for this set of parameters is given by

$$\chi^2(C_2, A_{peak}, \Omega) = \sum_{i=1}^{nd} \frac{(\Delta T_l^{obs}(i) - \Delta T_l[C_2, A_{peak}, \Omega](i))^2}{\sigma_i^2},$$

for the *nd* data points in Table 1 (see [34]) and the relative likelihood function is formed according to $L(C_2, A_{peak}, \Omega) \propto \exp(-\chi^2(C_2, A_{peak}, \Omega)/2)$. We vary the power spectrum normalisation C_2 within the 95 % limits for the COBE 4-year data [2] and consider A_{peak} in the range 0 to 30 and values of the density parameter up to $\Omega = 5$. The data included in the fit are those from Table 1 (see [34]), which with the exception of Saskatoon include uncertainties in the overall calibration. There is a $\pm 14\%$ calibration error in the Saskatoon data, but since the Saskatoon points are not independent this will apply equally to all five points [30]. The likelihood function is evaluated for three cases: (i) that the calibration is correct, (ii) the calibration is the lowest allowed value and (iii) the calibration is the maximum allowed value. In each case the likelihood function is marginalised over C_2 before calculating limits on the remaining two parameters according to Bayesian integration with a uniform prior.

4 Results and Discussion

In Fig. 3 the likelihood function obtained from fitting the model C_l spectra to the data of Table 1 (see [21]) is shown plotted as a function of the amplitude and position (Ω) of the Doppler peak. The highly peaked nature of the likelihood function in Fig. 3 is good evidence for the presence of a Doppler peak localised in both position (Ω) and amplitude. In Fig. 4 we show the 1-D conditional likelihood curve for Ω, obtained by cutting through the surface shown in Fig. 3 at the best-fit value of A_{peak}. The best fit value of Ω is 0.7 with an allowed 68% range of $0.30 \leq \Omega \leq 1.73$.

In Figure 2 the best fit model, represented by the solid line, is shown compared to the data points, assuming no error in the calibration of the Saskatoon observations. The chi-squared per degree of freedom for this model is 0.9, implying a good fit to the data. The peak lies at $l = 263^{+139}_{-94}$ corresponding to a density parameter $\Omega = 0.70^{+1.0}_{-0.4}$; the height of the peak is $A_{peak} = 9.0^{+4.5}_{-2.5}$. The dashed and dotted lines show the best fit models ($\Omega = 0.70^{+0.92}_{-0.37}$, $A_{peak} = 11.0^{+5.0}_{-4.0}$ and $\Omega = 0.68^{+1.2}_{-0.4}$, $A_{peak} = 6.5^{+3.5}_{-2.0}$ respectively) assuming that the Saskatoon observations lie at the upper and lower end of the permitted range in calibration error. These likelihood results using the analytic form for the C_l and the results from a more detailed analysis using exact models (see Hancock *et al.* submitted [21]; Rocha and Hancock, this volume) imply

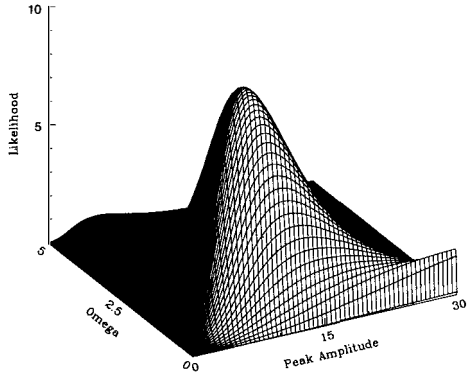

Figure 3: The likelihood surface for Ω and A_{peak}. (The nominal Saskatoon calibration is assumed.)

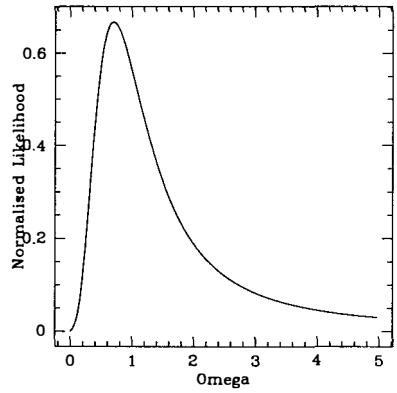

Figure 4: The 1-D conditional likelihood curve for Ω.

that independent of calibration uncertainties in the data, current CMB data are inconsistent with cosmological models with $\Omega < 0.3$.

5 Conclusions

Our current results provide good evidence for the Doppler peak, verifying a crucial prediction of cosmological models and providing an interesting new measurement of fundamental cosmological parameters. In Rocha *et al.* [35], a detailed comparison of the CMB data is made with the theoretical power spectra predicted by a range of flat, tilted, reionized, open models and models with non-zero cosmological constant. The existence of the Doppler peak has important consequences for the future of CMB astronomy, implying that our basic theory is correct and that improving our constraints on cosmological parameters is simply a matter of improved instrumental sensitivity and ability to separate out foregrounds. New instruments such as VSA [26], MAP and the proposed COBRAS/SAMBA satellite [29] will provide this improved sensitivity and should delimit Ω and other parameters with unprecedented precision.

Acknowledgements. Thanks to all the members of the CAT and Tenerife teams for their help and assistance in this work. and to B. Netterfield for supplying the Saskatoon window functions. S. Hancock wishes to acknowledge a Research Fellowship at St. John's College, Cambridge, U.K.

References

[1] Bennett, C.L. et al. 1994, ApJ., 436, 423

[2] Bennett C.L. *et al.* , 1996, ApJ., 464, L1

[3] Bond J.R., 1995, "*Cosmology and Large Scale Structure*" ed. Schaeffer, R. Elsevier Science Publishers, Netherlands, Proc. Les Houches School, Session LX, August 1993

[4] Bond, J.R., Astrophys. Lett. and Comm., in press

[5] Bond, J.R., Efstathiou, G.P., 1987, MNRAS, 226, 655

[6] Cheng E.S. *et al.* , 1994, ApJ., 422, L37

[7] Cheng E.S. *et al.* , 1996, ApJ., 456, L71

[8] Copi C.J., Schramm D.N., Turner M.S., 1995, Science, 267, 192

[9] Crittenden, R., Bond, J.R., Davis, R.L., Efstathiou, G., Steinhardt, P.J., 1993, Phys. Rev. Lett., 71, 324

[10] Davis, M., Efstathiou, G., Frenk, C.S., White, S.D.M, 1992, Nature, 356, 489

[11] Davies, R.D. et al. 1996, MNRAS, 278, 883

[12] De Bernardis P. *et al.* , 1994, ApJ., 422, L33

[13] Efstathiou, G.P., 1987, in "*Physics of the Early Universe*", proceedings of the thirty-sixth Scottish Universities Summer School in physics 1989, ed. by Peacock *et al.*

[14] Fischer, M.L. *et al.* , 1995, ApJ., 444, 226

[15] Freedman, W.L. *et al.* , 1994, Nature, 371, 757

[16] Gorski, K.M. et al. 1994, ApJ., 430, L89

[17] Gundersen, J.O *et al.* ,1995, ApJ., 443 L57

[18] Guth, A.H., 1981, Phys. Rev. D, 23, 347

[19] Hancock, S. *et al.* , submitted to MNRAS

[20] Hancock, S. *et al.* , 1994, Nature, 367, 333

[21] Hancock, S., Rocha, G., Lasenby, A.N. and Gutierrez, C.M., submitted to MNRAS

[22] Hu W., Sugiyama N., 1995, ApJ., 444, 489

[23] Kamionkowsky, M. *et al.* , 1994a, ApJ., 426, L57

[24] Kamionkowsky, M. *et al.* , 1994b, ApJ., 434, L1

[25] Kennicutt, R.C., Freedman, W.L., Mould, J.R., 1995, ApJ., 110, 1476

[26] Lasenby, A.N., Hancock, S., 1995, Proc. of : *"Current Topics in Astrofundamental Physics: The Early Universe"*, p327, eds. Sanchez, N., Zichichi, A., Kluwer

[27] Liddle, A.R., Lyth, D.H., 1992, Phys. Letters, B291, 391

[28] Magueijo, J. Albrecht, A., Coulson, D., Ferreira, P., Phys. Rev. Lett., in press

[29] Mandolesi, N. *et al.* , 1995, Planetary and Space Science, 43, 1459

[30] Netterfield C.B. *et al.* , submitted to ApJ.

[31] Ostriker, J.P., Steinhardt, P.J., 1995, Nature, 377, 600

[32] Pierce, M.J. *et al.* , 1994, Nature, 371, 385

[33] Ratra, B. *et al.* , submitted to ApJ. Lett.

[34] Rocha, G. and Hancock, S. this volume.

[35] Rocha, G., Hancock, S., Lasenby, A.N., Gutierrez, C.M. in preparation.

[36] Ruhl, J.E. *et al.* , 1995, ApJ., 453, L1

[37] Scaramela N., Vittorio N., 1990, ApJ., 353, 372

[38] Scaramela N., Vittorio N., 1993, ApJ., 411, 1

[39] Scott D., Srednicki M., White M., 1994, ApJ., 241, L5

[40] Scott D., Silk, J., White, M., 1995, Science, 268, 5212

[41] Scott, P.F. *et al.* , 1996, ApJ., 461, L1

[42] Smoot, G.F. *et al.* , 1992, ApJ., 396, L1

[43] Steinhardt, P., 1993, *Proc. of the Yamada Conference XXXVII "Evolution of the Universe and its Observational Quest"*, p159

[44] Tanaka, S.T. *et al.* , submitted to ApJ.

[45] Tegmark, M., & Bunn, E.F. 1995, ApJ., 455, 1

[46] White M., Srednicki M., 1995, ApJ., 443, 6

[47] White M., Krauss L.M., Silk J., 1993, ApJ., 418, 535

[48] White, M., Scott, D., Silk, J., 1994, Ann. Rev. Astron. Astrophys., 32, 319

THEORETICAL IMPLICATIONS OF MICROWAVE BACKGROUND RADIATION ANISOTROPY EXPERIMENTS

Graca Rocha and Stephen Hancock
MRAO, Cambridge, UK.

Abstract

Observational results from several experiments like COBE, SP, Saskatoon, PYTHON, ARGO, MAX, MSAM, Tenerife and CAT are considered and a comparison is made with predictions from several models. Conclusions are reached about the viability of current structure formation models.

1 Introduction

Cosmic microwave background (CMB) radiation anisotropies provide a direct probe of the structure of the universe at early times and constrain the values of key cosmological parameters such as Ω_0, H_0 and Ω_b. Experiments are now producing reliable measurements of the anisotropy on a variety of angular scales. They provide useful information about the process of structure formation, avoiding the systematic uncertainties and biases of conventional techniques. For Gaussian random fields all the statistical information is included in the angular power spectrum of the CMB temperature fluctuations. This being so, to determine the shape of this angular power spectrum constitutes one of the main goals of observational cosmology. We proceeded with a intercomparison of data and models in order to get the best-fit shapes of the angular power spectrum and constrain the model parameters. We present an extension of the work carried out by Hancock *et al.* [12], in which we used an analytic approximation to current CMB models and compared them with recent data. Here we consider some of the exact COBE normalised angular power spectrum models for the four-year COBE data, and apply the analysis to 4 of the 8 binned angular power spectrum points [26] for the COBE experiment in conjunction

with Tenerife, Python, South-Pole, Saskatoon, MAX, ARGO and CAT experiments. We find that low values of Ω are excluded by these exact models, in agreement with the results presented by Hancock *et al.* [12]. For a flat standard Cold Dark Matter dominated Universe we use our results in conjunction with Big Bang nucleosynthesis constraints to determine the value of the Hubble constant as $H_0 = 30 - 70\,\mathrm{km\,s^{-1}\,Mpc^{-1}}$ for baryon fractions $\Omega_b = 0.05$ to 0.2. For $H_0 = 50\,\mathrm{km\,s^{-1}\,Mpc^{-1}}$ we find the primordial spectral index of the fluctuations to be $n = 1.1 \pm 0.1$, in agreement with the inflationary prediction of $n \simeq 1.0$. Flat models with a contribution from a cosmological constant Λ seem to be consistent with the data. Models in which the fluctuations originate from cosmic strings appear to be consistent with the observations if we do not consider the higher calibration Saskatoon data. Textures model are only allowed for the lower calibration Saskatoon data. A more extensive discussion of these models will appear in Rocha *et al.* [19] (in preparation).

2 Models

Models of structure formation [4, 13] predict the shape and amplitude of the CMB power spectrum and its Fourier equivalent, the autocorrelation function $C(\theta) = \langle \Delta T(n_1) \Delta T(n_2) \rangle$ where $n_1.n_2 = \cos\theta$. The intrinsic angular correlation function $C(\theta)$ may be expanded in terms of spherical harmonics: $C(\theta) = \sum_{l \geq 2}^{\infty} (2l+1) C_l P_l(\cos(\theta))/4\pi$, where low order multipoles l correspond to large angular scales θ and large l-modes to small angular scales. The coefficients C_l are predicted by the cosmological models and contain all of the relevant statistical information for models described by Gaussian random fields [4]. We consider the following models: flat CDM models with Ω_b=0.01-0.3 and H_0=30-100 km s^{-1} Mpc^{-1} (G. Efstathiou, priv. comm.); open models with values for (Ω_0,h_0) (where $h_0 = H_0/(100\,\mathrm{km\,s^{-1}\,Mpc^{-1}})$) of (0.1,0.75), (0.2,0.7), (0.3,0.65), (0.4,0.65), (0.5,0.6) (N. Sugiyama, priv. comm.); models with a cosmological constant, Λ and no reionization, with (Λ,h_0,Ω_b) of (0.6,0.5,0.05), (0.6,0.5,0.03), (0.6,0.8,0.06), (0.7,0.5,0.05), (0.2,0.5,0.05); a string model (J. Magueijo, priv.comm.); and texture models with (Ω,h_0,Ω_b)=(1,0.5,0.05), (1,0.7,0.05) (N. Turok, priv. comm.).

We also consider the case of tilted models with the spectral index n of the primordial fluctuations varying in the range $n = 0.7 - 1.4$ with (h_0,Ω_b)=(0.3,0.2), (0.45,0.1), (0.5,0.07), for direct comparison with scale invariant flat CDM models.

3 Data

We consider all the latest CMB measurements, including new results from COBE, Tenerife, MAX, Saskatoon and CAT, with the exception of the MSAM results and the MAX detection in the Mu Pegasi region (for details on data selection see Hancock *et al.* [12]). We also consider all 8 multipole bands of the angular power spectrum extracted from the 4-year COBE data [26]. In order to avoid eventual correlations between these data points we have applied the fitting analysis to the 4 even or 4 odd multipole bands in conjunction with the remaining data points. The results are similar whether we use the even or the odd multipoles. The use of 4 instead of one multipole is particularly useful in discriminating the value of the spectral index n. The different experiments sample different angular scales according to their window functions [28, 27], W_l, as shown in Fig. 1. On the left hand side we present the window functions for 4 of the 8 multipoles of the COBE experiment. The conversion of data to a common framework in terms of flat bandpower estimates [2, 3] follows the same procedure as in Hancock *et al.* [12]. In Table 1 we display these bandpower estimates $\Delta T_l \pm \sigma$ where l_l and l_u represent the lower and

upper points at which the window function for each configuration reaches half of its peak value. For each experiment the uncertainties of the intrinsic anisotropy level have been calculated using a likelihood analysis (see *e.g.* Hancock *et al.* [10]), which incorporates uncertainties due to random errors, theoretical uncertainty (cosmic variance) [21, 22] and enhancement of cosmic variance due to partial sky coverage (sample variance) [23]. The errors in ΔT_l quoted in column 3 are 68 % confidence limits and have been obtained by averaging the difference in the reported 68 % upper and lower limits and the best fit ΔT_l. This procedure introduces a small bias into the results since the likelihood function is in general only an approximation to a Gaussian distribution.

4 Comparison

4.1 Method

For a given theoretical model it is possible to compute the value of ΔT_{obs} one would expect to observe using the angular power spectrum C_l's as predicted by the model and the window function corresponding to the experimental configuration W_l. We convert this to the bandpower equivalent result ΔT_l and compare with ΔT_l^{obs}. We then compute the chi-squared for this set of C_l's for the nd data points in Table 1, and the relative likelihood function is formed according to: $L \propto exp(-\chi^2/2)$ (for details see Hancock *et al.* [12]). As mentioned above the process by which the error bars quoted in Table 1 are computed introduces a small bias into the results. In order to assess the significance of this we applied the fitting analysis to an alternative set of data which consisted of the mean value of the data and corresponding error bars. We find no significant difference in the results obtained. We also vary the power spectrum normalization within the 95% limits for the COBE 4-year data [1]. The data included in the fit are those from Table 1, which, with the exception of Saskatoon, include uncertainties in the overall calibration. There is a $\pm 14\%$ calibration error in the Saskatoon data, but since the Saskatoon points are not independent this will apply equally to all five points [17]. The likelihood function is evaluated for three cases: (i) that the calibration is correct, (ii) the calibration is the lowest allowed value and (iii) the calibration is the maximum allowed value. We consider that a given model offers an acceptable chi-squared fit when $P(\chi^2) \geq 0.05$.

4.2 Results

We have applied the analysis to the COBE normalised flat CDM models (provided by G. Efstathiou) considering only one multipole for COBE namely C_2 obtained from the value of the Q_{rms-ps}. The models offering an acceptable chi-squared fit ($P(\chi^2) \geq 0.05$) to the CMB power spectrum whilst simultaneously satisfying nucleosynthesis constraints [5], comprehend $0.05 \leq \Omega_b \leq 0.2$, $30\,\mathrm{km\,s^{-1}\,Mpc^{-1}} \leq \mathrm{H_0} \leq 50\,\mathrm{km\,s^{-1}\,Mpc^{-1}}$. Considering the highest Saskatoon data calibration the constraints become $0.1 \leq \Omega_b \leq 0.2$, $30\,\mathrm{km\,s^{-1}\,Mpc^{-1}} \leq \mathrm{H_0} \leq 35\,\mathrm{km\,s^{-1}\,Mpc^{-1}}$. Allowing for the lowest Saskatoon data calibration relaxes the constraints up to $\mathrm{H_0} = 70\,\mathrm{km\,s^{-1}\,Mpc^{-1}}$ and $0.02 \leq \Omega_b \leq 0.2$ (see Hancock *et al.* [12]). In general, recent optical and Sunyaev-Zel'dovich observations of the Hubble constant [18, 8, 14, 15] imply $\mathrm{H_0}$ in the range $50 - 80\,\mathrm{km\,s^{-1}\,Mpc^{-1}}$.

Applying this analysis to the open models we conclude that $\Omega \leq 0.3$ is not compatible with the data, while the value of $\Omega = 0.4$ is only allowed for the lower Saskatoon calibration data. A value of $\Omega = 0.5$ offers an acceptable chi-squared fitting for both case (i) and (ii) calibrations. This confirms the results obtained using the approximate formula of Hancock *et al.* reassuring

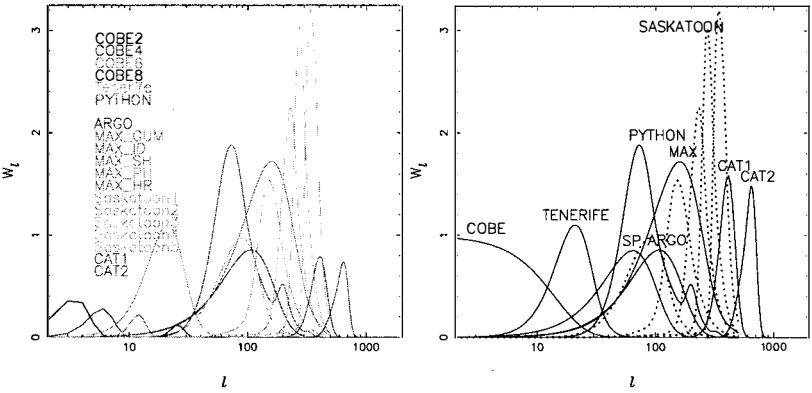

Figure 1: The window functions for the experiments listed in Table 1

us that the generalized parametrized formula previously used constitutes a good approximation given the uncertainties in the data.

The models with low Ω and a non-zero cosmological constant Λ seem to be consistent with the data, with large values of Λ providing the best fit. In Fig. 2 left hand side we present the best candidates of both the open and Λ models compared with a flat CDM model with $h_0 = 0.45$ and $\Omega_b = 0.1$ assuming case (i) calibration. Models in which structure formation is initiated by cosmic strings [16] are consistent with the data, but are excluded for the higher calibration Saskatoon data. Texture models are also only allowed if one considers the lower calibration for the Saskatoon data. In Fig . 2 right hand side we present a cosmic string model and the best candidate of the texture models (with $\Omega = 1$, $h_0 = 0.5$ and $\Omega_b = 0.05$) for comparison with the flat CDM model of Fig. 2 using case (i) calibration.

We also consider some of the best candidates of the flat CDM models: (1) $h_0 = 0.3$, $\Omega_b = 0.2$, (2) $h_0 = 0.45, \Omega_b = 0.1$ and (3) $h_0 = 0.5$, $\Omega_b = 0.07$ in which we allow for the tilting of the power spectrum to vary within $n = 0.7 - 1.4$. The fitting for the spectral index n of the primordial fluctuations was done considering two sets of data: (a) one multipole, (b) 4 multipole bands for the COBE experiment and case (i) for the calibration. For case (a) we get for model (1) a value of $n = 0.94 \pm 0.06$, for model (2) $n = 1.03 \pm 0.07$ and for model (3) $n = 1.08 \pm 0.07$. For case (b) we find for model (1) $n = 0.99 \pm 0.07$, for model (2) $n = 1.08 \pm 0.07$ and for model (3) $n = 1.11 \pm 0.07$ (68 % confidence interval). Allowing for the three calibration cases and taking extreme limits the uncertainties are altered as follows: for case (a) for model (1) $n = 0.94 \pm 0.1$, model (2) $n = 1.03 \pm 0.1$ and model (3) $n = 1.08^{+0.09}_{-0.12}$ while for case (b) for model (1) $n = 0.99^{+0.11}_{-0.13}$, model (2) $n = 1.08 \pm 0.1$ and model (3) $n = 1.11^{+0.09}_{-0.11}$. In particular fixing $H_0 = 50\,\mathrm{km\,s^{-1}\,Mpc^{-1}}$ we find $n = 1.1 \pm 0.1$ (68 % confidence interval) allowing for the three calibration cases and taking extreme limits. This tight limit rules out a significant contribution from gravity wave background for these models, in the case of power law inflation, but is consistent with the prediction of $n \simeq 1.0$ for scalar fluctuations generated by inflation. In Fig. 3 left hand side we present the model (3) and its 68 % confidence interval assuming the case (i) for the calibration. On the right hand side is displayed the likelihood function for the parameter n for model (3) which peaks at $n = 1.1$ showing a significant estimate of the spectral index parameter based on the actual CMB data.

Table 1: Details of data results used

Experiment	ΔT_l (μK)	σ (μK)	l_e	l_l	l_u	Ref
COBE2	25.4	8.1	3	3	12	[26]
COBE4	28.1	3.9	5	5	8	[26]
COBE6	22.3	4.2	11	10	15	[26]
COBE8	31.9	24.3	25	22	30	[26]
Tenerife	34.1	12.5	20	13	31	[11]
PYTHON	57.2	16.4	91	50	107	[20]
South Pole	39.5	11.4	57	31	106	[9]
ARGO	39.1	8.7	95	52	176	[6]
MAX GUM	54.5	13.6	145	78	263	[25]
MAX ID	46.3	17.7	145	78	263	[25]
MAX SH	49.1	19.1	145	78	263	[25]
MAX PH	51.8	15.0	145	78	263	[25]
MAX HR	32.7	9.5	145	78	263	[25]
Saskatoon1	49.0	6.5	86	53	132	[17]
Saskatoon2	69.0	6.5	166	119	206	[17]
Saskatoon3	85.0	8.9	236	190	274	[17]
Saskatoon4	86.0	11.0	285	243	320	[17]
Saskatoon5	69.0	23.5	348	304	401	[17]
CAT1	50.8	15.4	396	339	483	[24]
CAT2	49.0	16.9	608	546	722	[24]

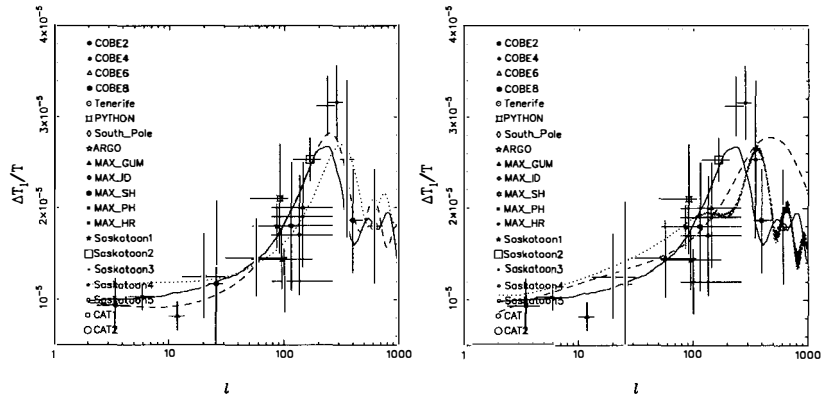

Figure 2: The data points from table 1 compared to the exact forms of the C_l for on the left hand side: an $\Omega = 1$, $h_0 = 0.45$ and $\Omega_b = 0.1$ standard CDM model (bold line), an $\Omega = 0.5$, $h_0 = 0.6$ open model (dot line) and a flat $\Omega_\Lambda = 0.7$, $h_0 = 0.5$ and $\Omega_b = 0.05$ model (dashed line). For on the right hand side: the same standard CDM model compared with a cosmic string model (dashed line) and an $\Omega = 1$, $h_0 = 0.5$ and $\Omega_b = 0.05$ texture model (dot line).

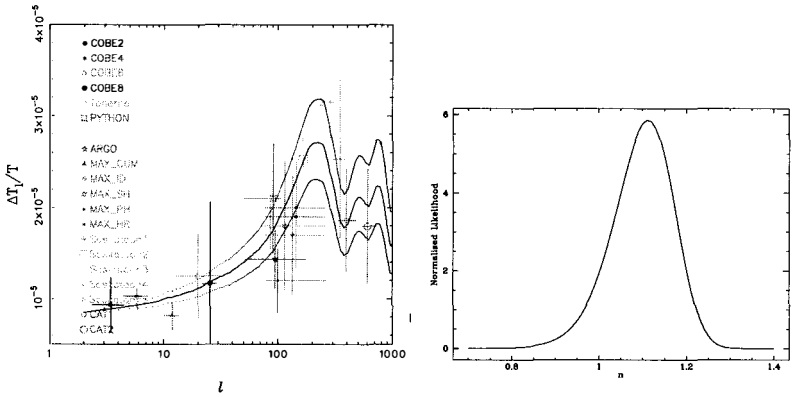

Figure 3: Tilted model with $h_0 = 0.5$, $\Omega_b = 0.07$, $n = 1.1$ and its 68 % confidence interval (left hand side), likelihood function for the parameter n (right hand side).

References

[1] Bennett C.L. *et al.* , 1996, ApJ., 464, L1

[2] Bond J.R., 1995, "*Cosmology and Large Scale Structure*" ed. Schaeffer, R. Elsevier Science Publishers, Netherlands, Proc. Les Houches School, Session LX, August 1993

[3] Bond, J.R., Astrophys. Lett. and Comm., in press

[4] Bond, J.R., Efstathiou, G.P., 1987, MNRAS, 226, 655

[5] Copi C.J., Schramm D.N., Turner M.S., 1995, Science, 267, 192

[6] De Bernardis P. *et al.* , 1994, ApJ., 422, L33

[7] Fischer, M.L. *et al.* , 1995, ApJ., 444, 226

[8] Freedman, W.L. *et al.* , 1994, Nature, 371, 757

[9] Gundersen, J.O *et al.* ,1995, ApJ., 443 L57

[10] Hancock, S. *et al.* , 1994, Nature, 367, 333

[11] Hancock, S. *et al.* , submitted to MNRAS

[12] Hancock S., Rocha G., Lasenby A.N., Gutierrez C.M., submitted to MNRAS

[13] Hu W., Sugiyama N., 1995, ApJ., 444, 489

[14] Kennicutt, R.C., Freedman, W.L., Mould, J.R., 1995, ApJ., 110, 1476

[15] Lasenby, A.N., Hancock, S., 1995, Proc. of : *"Current Topics in Astrofundamental Physics: The Early Universe"*, p327, eds. Sanchez, N., Zichichi, A., Kluwer

[16] Magueijo, J. Albrecht, A., Coulson, D., Ferreira, P., Phys. Rev. Lett., in press

[17] Netterfield C.B. *et al.* , submitted to ApJ.

[18] Pierce, M.J. *et al.* , 1994, Nature, 371, 385

[19] Rocha, G., Hancock, S., Lasenby, A.N., Gutierrez, C.M. in preparation.

[20] Ruhl, J.E. *et al.* , 1995, ApJ., 453, L1

[21] Scaramela N., Vittorio N., 1990, ApJ., 353, 372

[22] Scaramela N., Vittorio N., 1993, ApJ., 411, 1

[23] Scott D., Srednicki M., White M., 1994, ApJ., 241, L5

[24] Scott, P.F. *et al.* , 1996, ApJ., 461, L1

[25] Tanaka, S.T. *et al.* , submitted to ApJ.

[26] Tegmark, M., 1996, *Astrophys. J.* ,, 464, L35

[27] White M., Srednicki M., 1995, ApJ., 443, 6

[28] White M., Krauss L.M., Silk J., 1993, ApJ., 418, 535

COSMIC PARAMETER ESTIMATION COMBINING SUB-DEGREE CMB EXPERIMENTS WITH COBE

J. Richard Bond [1] & Andrew H. Jaffe [1,2]
[1] *Canadian Institute for Theoretical Astrophysics, Toronto, Ontario, Canada.*
[2] *Center for Particle Astrophysics, UC Berkeley, Berkeley CA USA.*

Abstract

We describe the Bayesian-based signal-to-noise eigenmode method for cosmological parameter estimation, show how it can be used to optimally compress large CMB anisotropy data sets to manageable sizes, and apply it to the DMR 4-year, South Pole and Saskatchewan data, individually and in combination. A simple prior probability method is used to include large scale structure observations. Estimates of the Hubble parameter, vacuum energy density, baryon fraction and primordial spectral tilt derived from the combined data are given.

1 Introduction

As CMB anisotropy experiments have gotten more ambitious, our need for powerful statistical methods has become more urgent. For the CMB data sets that have been obtained up to now, including COBE [1] (*dmr4*), the 1994 South Pole data of [2] (*sp94*) and the 1993-95 Saskatoon data of [3, 4] (*sk95*), which we analyze jointly here, it is possible to do a relatively complete Bayesian statistical analysis if the primary anisotropies are assumed to be Gaussian and the non-Gaussian Galactic foregrounds are not large. Even for these experiments, this is feasible only because of compression, in which the data set is acted upon by linear operators which project it onto subspaces of the full data. In the past the linear combinations of the data were defined by what made intuitive sense (e.g., weighted sums of different frequency channels or weighted averages of pixel separations below the beam scale), and could still leave too many pixels to deal with in a complete analysis. Here we use the rigorous signal-to-noise eigenmode approach to data compression [5] to reduce the sets to the manageable $\lesssim 1000$ important combinations. As we approach the era of megapixel data sets promised by MAP and COBRAS/SAMBA, via the era of tens of thousands of pixels promised by long duration balloon experiments, the question of how to come as near to optimal compression as possible given computer limitations becomes of paramount importance. This happy day of too many pixels is now upon us.

The goal is to estimate the parameters $\{y_A\}$ of a target set of theories with angular power spectra $\mathcal{C}_\ell$[1] by first determining the likelihood function $\mathcal{L}(\{y_A\})$ for each theory, and then comparing the likelihoods as a function of the parameters. Using Bayes' theorem, we can write the probability of the theoretical parameters, given the observations and the class of

[1] $\mathcal{C}_\ell \equiv \ell(\ell+1)\mathrm{C}_\ell/(2\pi)$, where $\mathrm{C}_\ell = \langle |a_{\ell m}|^2 \rangle$ is the CMB power spectrum as usually defined and the $a_{\ell m}$ are the spherical harmonic coefficients of the temperature fluctuations for the theoretical signal.

theories being tested, $P(\{y_A\}|\mathrm{OBS, TH}) \propto \mathcal{L}(\{y_A\})P(\{y_A\}|\mathrm{prior})$, where the assumed prior probability distribution $P(\{y_A\}|\mathrm{prior})$ can reflect *a priori* maximal ignorance, or take into account constraints from other information such as large scale structure observations. The proportionality constant is related to the probability that the class of theories is correct given the observations. To give preferred values and errors for a specific cosmological parameter of interest such as the Hubble parameter, one often integrates (marginalizes) over the other parameters, such as the density fluctuation power amplitude on cluster scales, σ_8, and the primordial density fluctuation spectral index n_s.

In this paper, we assume the inflationary model for structure formation with Gaussian adiabatic (scalar) density perturbations and possibly gravitational wave (tensor) perturbations. We explore constraints in the parameter space $\{t_0, \mathrm{h}, \Omega_{tot}, \Omega_B\mathrm{h}^2, \Omega_{vac}, \Omega_{hdm}, \Omega_{cdm}, \nu_s, \nu_t, \sigma_8\}$. We assume reheating occurs sufficiently late to have a negligible effect on $\mathcal{C}_\ell$. The total density parameter, $\Omega_{tot} = \Omega_B + \Omega_{cdm} + \Omega_{hdm} + \Omega_{vac}$, is expressed in terms of the densities in baryonic cold, hot and vacuum matter, of which $\Omega_{nr} = \Omega_B + \Omega_{cdm} + \Omega_{hdm}$ can cluster. The age of the Universe is t_0 and h is the Hubble parameter in units of 100 km s^{-1} Mpc^{-1}; ht_0 is a function of $\{\Omega_{vac}, \Omega_{tot}\}$, so one parameter is redundant. The scalar and tensor tilts are $\nu_s = n_s - 1$ and ν_t.[2] With current errors on the data, this space is too large for effective parameter estimation. Instead we restrict our attention to various subregions, such as $\{\sigma_8, n_s, \mathrm{h} \,|\, \mathrm{fixed}\, t_0, \Omega_B\mathrm{h}^2\}$, where either $\Omega_{tot} = 1$ and Ω_{vac} is a function of ht_0 or $\Omega_{vac} = 0$ and Ω_{tot} is a function of ht_0. The t_0's we choose are (11, 13, 15 Gyrs) with $\Omega_{vac} \geq 0$, but $\Omega_{tot} = 1$. For these cases, the "standard" nucleosynthesis value $\Omega_B\mathrm{h}^2 = 0.0125$ was chosen. We constrain $0.5 \leq n_s \leq 1.5$, $0.5 \lesssim h \leq 1$. For $\Omega_{tot} = 1$ models, we have roughly $\Omega_{vac}(h) \sim 0.9[0.3(\mathrm{h}/\mathrm{h}_1 - 1)^{0\,3} + 0.7(\mathrm{h}/\mathrm{h}_1 - 1)^{0.4}]$, where $h_1 \equiv 0.5(13\mathrm{Gyr}/t_0)$. A recent estimate for globular cluster ages is $14.6^{+1.7}_{-1.6}$ Gyr [6]. For the case $\Omega_{vac} = 0$, we have also let $\Omega_B\mathrm{h}^2$ vary, over the range $0.003125 \leq \Omega_B\mathrm{h}^2 \leq 0.05$, and we have also done a limited exploration of the 13 Gyr, $\Omega_{tot} < 1$, $\Omega_{vac} = 0$, space with tilt, using $\mathcal{C}'_\ell s$ from Bond and Souradeep. The reason for restricting the paths through parameter space is because of the length of time required for a complete statistical treatment of each data set per model $\mathcal{C}_\ell$.

In Fig. 1, the bandpowers [7] associated with current experiments are compared with some of the $\mathcal{C}_\ell$'s in the parameter space we are exploring, here the 13 Gyr, $H_0 = 50$, tilted sequence with gravity waves included and the 13 Gyr $\Omega_{vac} > 0$ sequence with $n_s = 1$, with amplitude normalized to best-fit the 4-year DMR data. In both cases, $\Omega_B\mathrm{h}^2 = 0.0125$. The curves are very similar if we allow for a mix of hot and cold dark matter with the same Ω_{nr} as these CDM models, and the other parameters fixed. The solid dark curve is the "standard" untilted CDM model. The bandpowers for the three experiments analyzed here, *dmr4*, *sp94*, *sk95*, are the darker heavier data points. Because of the differing angular scales involved we gain a long lever arm with which we can constrain cosmological parameters more strongly than with any individual experiment. The lower panels in the figures are closeups of the first and second "Doppler peak" regions. Fig. 2 gives the best fit models, described in § 5.

[2]The ratio of gravitational wave power to scalar adiabatic power is $\mathcal{P}_{GW}/\mathcal{P}_{ad} \approx (-4\nu_t)/(1 - \nu_t/2)$, apart from small corrections. This determines the level of tensor anisotropies compared with scalar. The tensor tilt is related to the deceleration parameter q of the Universe during inflation by $\nu_t/2 \approx 1 + q^{-1}$ plus small corrections. Here, we take one of two cases. (no-GW case): $\nu_t = 0$, thus no gravity wave contribution (for nearly critical acceleration, $q \approx -1$, as in natural inflation). (GW case): $\nu_t = \nu_s$ if the scalar tilt is negative (subcritical but nearly uniform acceleration) and $\nu_t = 0$ if the scalar tilt is positive.

2 Signal-to-Noise Eigenmode Method

We are given the data in the form of a measured mean $\overline{\Delta}_p$ of the anisotropy in the pth pixel, along with the variance about the mean σ_{Dp}^2 for the measurements. In general, there are pixel–pixel correlations in the noise, defining a correlation matrix $C_{Dpp'}$ with off-diagonal components as well as the diagonal $\sigma_{Dp}^2 = C_{Dpp}$. Also there is usually more than one frequency channel, with the generalized pixels having frequency as well as spatial designations. The theoretical signal also has a correlation matrix, $C_{Tpp'}$, which is a linear combination of a product of the $\mathcal{C}_\ell$ times a "window function matrix" $W_{pp'}(\ell)$ encoding the possibly frequency-dependent beam, the chopping strategy, sky coverage, etc. for the experiment: $C_{Tpp'} = \sum_\ell \mathcal{C}_\ell W_{pp'}(\ell)(\ell + \frac{1}{2})/[\ell(\ell+1)]$ (see e.g., [7]). The "window function" usually reported for an experiment is $\overline{W}_\ell = (1/N_{pix}) \sum_{p=1}^{N_{pix}} W_{pp}(\ell)$.

The likelihood function is

$$\ln \mathcal{L}(\{y_A\}) = -\tfrac{1}{2}\overline{\Delta}^\dagger (C_n + C_T)^{-1} \overline{\Delta} - \tfrac{1}{2} \ln \det(C_n + C_T) - N_{pix} \ln \sqrt{2\pi}\,. \qquad (1)$$

Here † denotes transpose. The noise correlation matrix $C_n = C_D + C_{res}$ consists of the pixel errors C_D and the correlation of any unwanted residuals C_{res}, such as Galactic or extragalactic foregrounds. One can think of C_{res} as increasing the noise for selected correlation patterns in the medium. With a large enough noise in these patterns, they are effectively projected out from the data.

Constraints such as averages, gradients (dipoles, quadrupoles) and known spatial templates, which may be frequency dependent (e.g., IRAS or DIRBE combined with appropriate extrapolations) can also be modelled in the total Δ_p, as "nuisance variables" to be integrated (marginalized) over. Denoting each constraint c on pixel p by $\kappa_c \Upsilon_{pc}$, where the template for constraint c is Υ_{pc} and the amplitude is κ_c, we need only replace $\overline{\Delta}_p$ in eq. (1) by $\overline{\Delta}_p - \sum_c \Upsilon_{pc}\kappa_c$, then integrate over the amplitudes κ_c, assuming some prior probability distribution. This is most easily done if we assume the κ_c are distributed as very broad Gaussians, reflecting our ignorance of their values (or, if we know their likely range, incorporating that as prior information in the Gaussian spreads). The integration over κ_c then yields eq.(1) with the residual noise matrix given by $C_{res} = \Upsilon K \Upsilon^\dagger$, where $K_{cc'} = \langle \kappa_c \kappa_{c'} \rangle$ is the assumed prior variance for the constraint amplitudes. As the eigenvalues of K become very large, the effect of the constraint matrix is to project onto the data subspace orthogonal to that spanned by Υ_{pc}. Although one can directly use the likelihood equation in this projection limit (using $\delta^{(N_c)}(\kappa)$ for the constraint prior), it is computationally simpler to use the Gaussian prior. (Taking into account constraints with amplitudes that are not linear multipliers times the template is much more complex.) A suitable C_{res} can also allow us to focus attention only on a specified band in ℓ-space for power spectrum estimation.

In practice, we do not compute the quantities $\overline{\Delta}^\dagger (C_T + C_n)^{-1} \overline{\Delta}$ and $\det[C_T + C_n]$ directly; instead we go to a basis (i.e., linear combination of the data) in which C_T and C_n are diagonal. First, we whiten the noise matrix using the nonorthogonal transformation provided by its "Hermitian square root," $C_n \to C_n^{-1/2} C_n C_n^{-1/2} = I$; we apply the same transformation to C_T and diagonalize this in turn with the appropriate matrix of eigenvectors, R: $C_T \to R C_n^{-1/2} C_T C_n^{-1/2} R^\dagger = \mathrm{diag}(\mathcal{E}_k)$, which has units of $(S/N)^2$. We then transform the data into the same basis, $\overline{\Delta} \to R C_D^{-1/2} \overline{\Delta} = \overline{\xi}$, now in units of (S/N). The transformed theory matrix $\mathcal{E}$ still depends on the theoretical amplitude (σ_8, etc.) as a simple multiplier, which enables the likelihood to be easily calculated as a function of this parameter. In the new basis, the noise and signal have diagonal correlations and $\langle \xi_k^2 \rangle = 1 + \mathcal{E}_k$, so $\overline{\xi}_k^2$ is useful as a theory-dependent S/N power spectrum which gives a valuable picture of the data and shows how well the target theory fares (Fig. 5)[8, 5, 9].

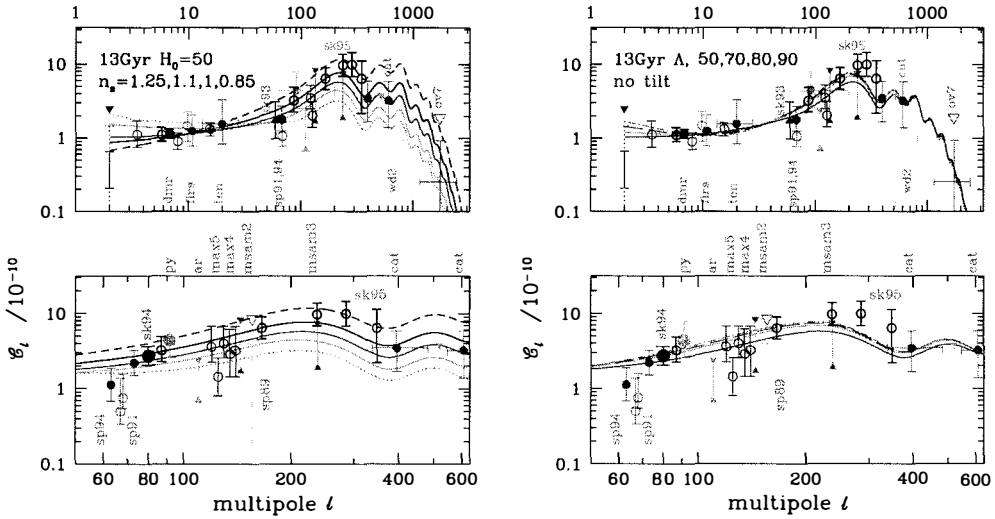

Figure 1: 13 Gyr sequences, varying n_s with $\Omega_{vac} = 0$, and varying H_0, hence Ω_{vac}, with $n_s = 1$.

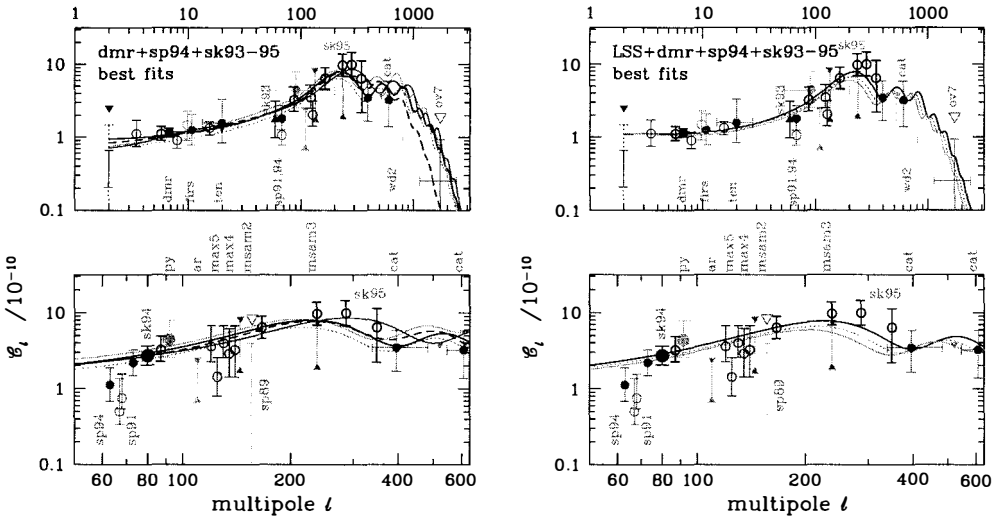

Figure 2: Best-fit models using DMR+SP94+SK95 on the left, and adding LSS on the right, for 11, 13 and 15 Gyr Λ sequences. The left also shows 13 Gyr open and baryon sequence best fits. Parameters defining these models are given in Table 2.

The modes are sorted in order of decreasing S/N-eigenvalues, $\mathcal{E}_k$, so low k-modes probe the theory in question best. This expansion is a complete (unfiltered) representation of the map. The optimal method for data compression is to use sharp signal-to-noise filtering, keeping only those high S/N modes with $k < k_{cut}$ and deleting low S/N ones. We also find it extremely useful to look carefully at the power in the low S/N modes to determine whether further residuals need to be added to the generalized noise: a poor model for the noise can give false indications of what the data is saying and misrepresent the signal. Filtering using S/N-modes has a long history in signal processing where it is called the Karhunen-Loeve method [10], and it is now being widely adopted for analysis of astronomical databases.

For an all-sky experiment with uniform, uncorrelated pixel variances, the eigenmodes are the spherical harmonics, and the eigenvalues the expected coefficients $a_{\ell m}$. For a more complicated experiment, the high-S/N modes probe the peak of the experiment's window function in ℓ-space. Low-S/N modes are more complex. For experiments with more than one frequency channel, differences between channels should show no CMB signal, and so the eigenvalue should be 0. Nearby pixels, oversampling the beam, should also show very little signal—the smooth fall from high S/N to low traces the beam in much the same way that the window function falls as a Gaussian $\propto \exp[-\ell^2/\ell_s^2]$ at high ℓ. We expect these low S/N modes to be largely independent of the theory used to calculate the appropriate C_T, which enables these modes to be used as a diagnostic of both the analysis procedure and the experiments themselves.

3 The Experiments Analyzed

We now discuss the anisotropy experiments we use. The six COBE/DMR four-year maps [1] are first compressed into a (A+B)(31+53+90 GHz) weighted-sum map, with the customized Galactic cut advocated by the DMR team, basically at $\pm 20°$ but with extra pixels removed in which contaminating Galactic emission is known to be high, and with the dipole and monopole removed. Galactic coordinate pixels are used; slight differences arise with ecliptic coordinate pixels. Although one can do full Bayesian analysis with the map's $(2.6°)^2$ pixels, this "resolution 6" pixelization of the quadrilateralized sphere is oversampled relative to the COBE beam size, and there is no effective loss of information if we do further data compression by using "resolution 5" pixels, $(5.2°)^2$ [5, 1]. The weighted sum of channels is an exact use of our optimal signal-to-noise compression. The resolution degradation is not optimal but is nearly so ($C_T(\theta)$ is nearly constant for separations θ below the scale of the beam, so adjacent pixel differences have tiny signal but the usual data-noise). The Galactic cut is also not optimal, but could be made so by using explicit templates for Galactic foregrounds to include in C_n, as described above. The combined effect reduces the pixel number from 6×6144 to 999. Further compression by a factor of two or so is possible without much information loss [5]. A strong indication of the robustness of the *dmr* data set is the insensitivity of the band-powers to the degree of signal-to-noise filtering and to which frequencies are probed. For C_{res}, we include templates for the monopole, dipole and quadrupole, the latter allowing for a Galactic foreground contaminant, which we know is there at low ℓ in the 31 GHz channel. The DMR data probes $\ell \sim 2-15$ well, with useful information out to ~ 30.

The *sp94* experiment [2] is similar to a classic single-differencing chopping experiment, except that differencing is associated with the oscillation of the beam about the pixel position. It probes $\ell \sim 30-120$. The number of frequency channels and spatial pixels is sufficiently small (301) that no compression is needed: all 7 frequencies in the Ka and Q bands at ~ 30 and ~ 40 GHz are simultaneously analyzed. There are 14 constraints, average and gradient removals for each frequency. Taking differences in $\Delta T/T$ in frequency at the same spatial position is

insensitive to the primary signal but has the usual pixel noise for each channel, so S/N filtering would tend to remove those modes and strong compression would result. Because the beams do vary somewhat with frequency, however, the compression would remove some information, unlike for COBE.

The *sk95* experiment [4] probes a much larger band in ℓ-space, from ~ 50 to ~ 400. Even before the data was delivered to us a significant amount of frequency and spatial compression already took place. In this paper, for parameter estimation, we use the "CAP" data (2016 pixels, including rebinned ¡ data from *sk94*, with 48 constraints associated with average removals). The SK experiment measured the temperature directly by making slightly-curved radial scans from the North Celestial Pole about 8 degrees in length, which covered the CAP as the earth rotated. The data was binned in RA, but, instead of binning in declination, it was projected in software onto what are in effect 3 to 19 beam "chopping" configurations. Adding the RING data to the CAP, involving sweeps in a ring around the NCP at $\sim 8°$ brings the total to 2400 pixels, with 52 constraints. In [9], we show that the "CAP" and "CAP+RING" parameter estimates agree to much better than "one sigma" even though the RING adds substantially more data. One potential concern is that only one HEMT band is represented in the data. We have also extensively analyzed the SK94 data set on its own [3], with 1344 pixels and 28 constraints, which has only 3 to 9 beam template projections and substantially fewer hours of integration than the 94+95 data, but the advantage of having both Ka and Q band information so the frequency spectrum can be checked. We agree with [3] that the spectrum of the SK94 3 to 9 templates is consistent with a CMB origin, and inconsistent with likely Galactic foregrounds. (We come to the same conclusion for the *sp94* data, in agreement with [2].) SK95 had data only from the Q-band.

In analyzing SP94 and SK94-95, it is essential to include errors in the overall calibration of ΔT. For SK94-95 it is estimated to be a Gaussian with standard deviation $\varepsilon = 0.14$; for SP94, $\varepsilon = 0.10$. Let $\mathcal{L}_0(\sigma_8)$ denote the calculated likelihood assuming no such errors; then the likelihood with the uncertainty included is $\mathcal{L}(\sigma_8) = \int d\sigma_8' \exp[-(\sigma_8 - \sigma_8')^2/(2\varepsilon^2\sigma_8^2)]\mathcal{L}_0(\sigma_8')$. It is unfortunate that after all of the effort that has gone into these superb experiments, an astronomical issue like the brightness of Cas A (for SK95) results in a substantially poorer constraint on σ_8 than one obtains assuming no such calibration uncertainty.

4 Phenomenology, S/N Power Spectra and Data Compression

As we mentioned in § 1, we have chosen to order our path through parameter-space using the cosmological age of the models, t_0. To examine the phenomenology of the experiments we shall use a one-parameter sequence of $\mathcal{C}_\ell$ shapes, with the overall bandpower of the experiment (or the related σ_8) as another parameter. While it was usual in the past to use a power law in $\mathcal{C}_\ell$, $\sim (\ell + \frac{1}{2})^{\nu_{\Delta T}}$ [8], it is evident from Fig. 1 that this would be a very bad fit to the *sk95* data, although it is a reasonable representation over the limited ℓ range for both the *dmr4* and *sp94* data. The sequence we use is the first panel in Fig. 1, the tilted CDM sequence for the standard CDM model, i.e., $H_0 = 50, \Omega = 1, \Omega_B = 0.05$, with n_s variable. We use the GW case, i.e., $\nu_t = n_s - 1$ if $n_s < 1$, $\nu_t = 0$ otherwise. These models have an age of $t_0 = 13$Gyr.

Fig. 3 shows $1, 2, 3, \ldots$ sigma contours of $\mathcal{L}(\sigma_8, n_s)$, with ν-sigma defined by $\mathcal{L}/\mathcal{L}_{max} = \exp[-\nu^2/2]$. It is clear from the right hand panel that fixing $n_s = 1$ and $t_0 = 13$, but varying h, and therefore Ω_{vac}, is not a good sequence to use for phenomenology since there is very little difference in the $\mathcal{C}_\ell$'s as h varies. The Fig. 4 $\mathcal{L}(\sigma_8, \mathrm{h})$ contour map shows that indeed the data does not determine the Hubble parameter very well.

With the most recent experiments ($N_{pix} \gtrsim 2000$), the computer power required to calcu-

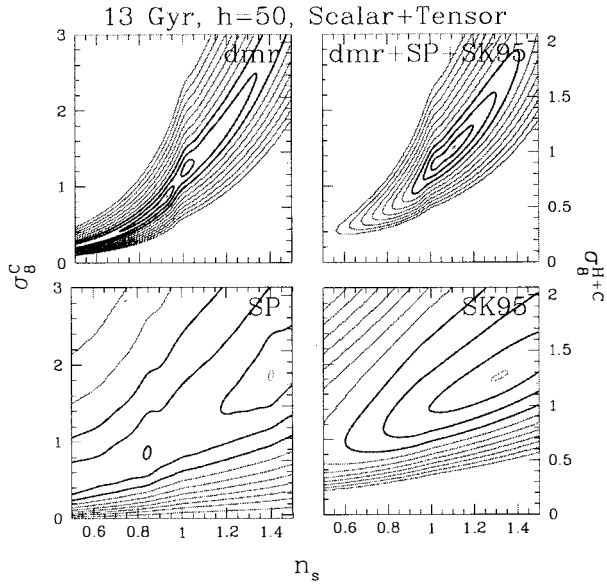

Figure 3: Contour plots of the likelihood of σ_8 and n_s for fixed $h = 0.5$. The contours are at $\mathcal{L} = \exp[-\frac{1}{2}\{1, 4, 9, \ldots\}]\mathcal{L}_{max}$ (with an extra contour around $\mathcal{L}_{max}$ to show where it is). In every panel, the lefthand σ_8 axis is for the CDM sequence, while the righthand σ_8 axis is for a $\Omega_{hdm} = 0.2\Omega_{nr}$ mixed dark matter model. σ_8 inferred from cluster abundances is ~ 0.6.

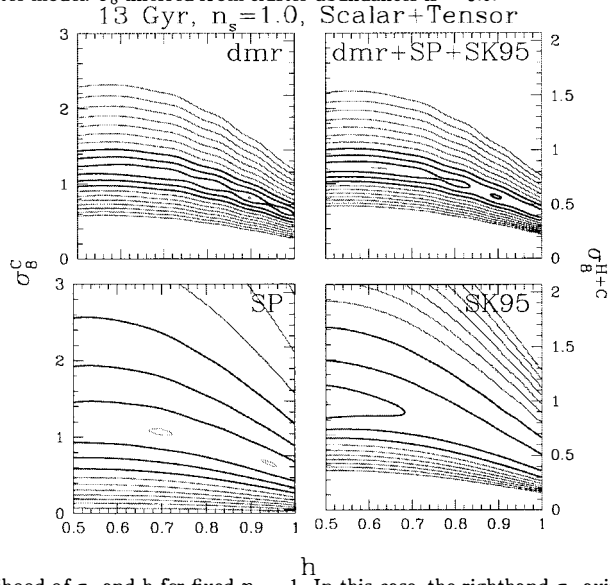

Figure 4: Likelihood of σ_8 and h for fixed $n_s = 1$. In this case, the righthand σ_8 axis strictly applies only for the h=0.5 line.

late the likelihood over a sufficiently wide model space is becoming prohibitive. The S/N-eigenmodes also provide a form of data compression which can drastically reduce the required analysis time. By rotating to a basis in which some "canonical theory" with correlation matrix C_{T*} is diagonalized by the matrix R_*, but only retaining some fraction of the modes, we efficiently remove parts of the data dominated by noise (i.e., modes with very low $S/N \ll 1$), but retain the Gaussian character of the likelihood for the remaining modes. For other theories, the transformed theory matrix $(R_* C_n^{-1/2} C_T C_n^{-1/2} R_*^\dagger)$ will no longer be diagonal, so the full matrix calculation must still be performed, but now on the smaller space of observations restricted to the modes with the highest "canonical" S/N. Moreover, for these theories, the S/N-modes will be somewhat different, so the compression will not be as efficient (i.e., we will have thrown out a bit "more signal and less noise"). Still, we have achieved compression as good as 90% for experiments (like SK94) with two channels and 65% for the full SK94-95 dataset, which has already been re-binned to remove some of the redundancy in beam oversampling and channel-to-channel differences. Because the cost of the matrix calculations involved scales as N^3, these result in significant speedups: from ~ 1 hour to ~ 10 minutes per point in parameter space for *sk95* (which is actually significantly worse than the expected $(1 - 0.65)^3 \simeq 1/25$ speedup due to overhead).

In Fig. 6, we show $1, 2, 3, \ldots$ sigma likelihood contours for the SK94-95 CAP dataset, as in Fig. 3. The lower left panel superposes the contours of the $k_{cut} = 700$ case upon those with all 2016 modes included. The similarity of the contours shows that both the amplitude and the index determinations are not compromised by S/N cuts. For the $k_{cut} = 500$ case, contours ≥ 2 are very similar as well. Thus we can achieve significant degrees of compression without loss of information. In the following, we apply no data compression to the analysis of the DMR and SP data, but for SK95 we present results using the top 700 modes from the canonical standard CDM theory, the $n_s = 1$ model in the $t_0 = 13$ Gyr sequence.

The reason the compression works can be understood by examining the S/N power spectra, shown in Fig. 5. The curve is the theoretical spectrum $1 + \mathcal{E}_k$ given by the eigenmodes, for a "standard CDM" model with amplitude $\sigma_8 = 1.2$, the value suggested by COBE. The points are the observations $\bar{\xi}_k^2$, with the same binning as the theory curve. (The bins require a certain signal-to-noise when summed, but a minimum number are required to define a bin so that the error bars are not too large.) The error bars contain both variances associated with the pixel noise and with the theoretical cosmic variance (noise-noise, noise-signal and signal-signal terms). To be a good fit to the data, the error bars should pass through the theory curve. After the top few hundred modes, the eigenvalues have $S/N \ll 1$ so we do not expect them to contribute significantly to the likelihood. We emphasize that it is legitimate to use any mode subset: the relative likelihoods we obtain will tell us which theory is preferred for those modes. It is just that we do not want to build any prior prejudice for a theory by compressing the data in a way which may be biased in its favour over the other theories we are testing. Thus we choose to go far into the S/N tail, retaining 700 modes. The S/N mode formalism also can be used to design experiments to discriminate particular theories (e.g., Knox, these Proceedings).

5 Combining Experiments and Parameter Estimation

Combining experiments to get a total likelihood is straightforward. If the pixels are uncorrelated, either because they overlap little on the sky or in ℓ, we only need to multiply the individual likelihoods together. This is the case for COBE/DMR, SP94, SK94-95. If there is significant overlap, then the experiments should ideally be combined and considered to be one larger experiment, with C_T connecting the pixels in one experiment with the pixels in the other,

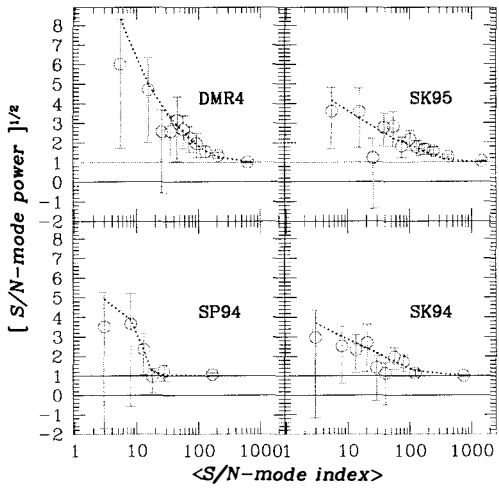

Figure 5: Observed and theoretical S/N-spectra with 1σ errors (including pixel noise and cosmic variance), using "standard" CDM, with $\sigma_8 = 1.2$, the DMR4 value, for the theory.

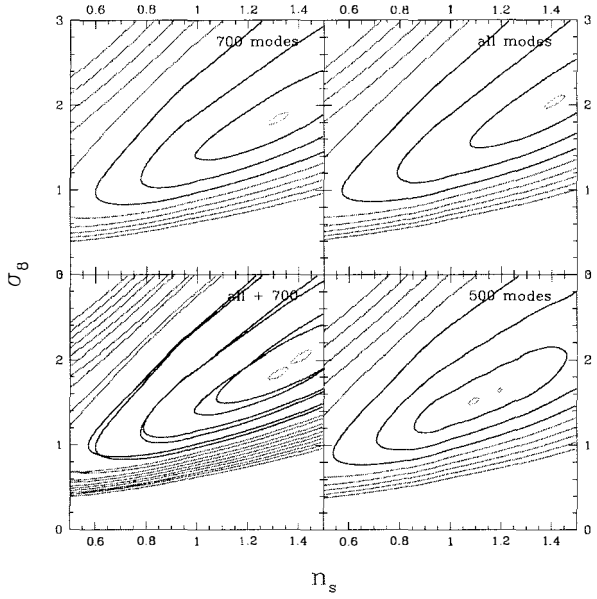

Figure 6: How σ_8-n_s likelihood contours change with the SK95 S/N cut: for 500, 700 and all ($\sim$ 2000) modes.

although the cross-pixel C_D will be zero. We have applied this to the SK95+MSAM dataset, in joint work with Charbonneau and Knox, but will not describe it here.

The upper right panel of Fig. 3 shows the likelihood for the $H_0 = 50$, GW, 13 Gyr, tilted sequence. Each experiment individually constrains the amplitude, σ_8, better than the shape, n_s: the window functions cover a narrow range of ℓ. Note that the SK experiment does better than DMR at determining the slope. The calibration uncertainty for SK95 is the reason that σ_8 is not more tightly constrained. Fig. 3 shows the advantage offered by combining the results of different experiments: the long baseline in ℓ helps considerably in localizing the n_s contours. In Fig. 4, we see that the DMR data does not restrict the value of h, and thus not of Ω_{vac}, whereas the SK data does, yet the combined data focusses the σ_8 determination, but not the h determination. The SK95 data prefers more power than is predicted by the DMR data for "standard" models. Thus, the $n_s = 1$, $H_0 = 50$, $\Omega_B h^2 = 0.0125$ model has $\sigma_8 = 1.20 \pm 0.08$ for DMR, while for SK95 it is $\sigma_8 = 1.48^{+0.26}_{-0.20}$. Increasing $\Omega_B h^2$ to 0.2 brings them closer into line, $\sigma_8 = 0.89 \pm 0.06$ for DMR, while for SK95 it is $\sigma_8 = 0.82^{+0.15}_{-0.11}$; and this model is much preferred statistically to the 0.0125 one.

We could repeat the contour maps for the 11 and 15 Gyr vacuum sequences, for the fixed t_0 open models, and for the variable Ω_B sequence, but it is more concise to quote single numbers, our estimates of the individual cosmological parameters. To that end, we marginalize over the other parameters in the sequence, assuming a prior probability for the parameters. If it is uniform we get the results in the left columns of Table 1. The idea that first motivated this project was that the SK94 and SP94 data looked sufficiently robust to return to the multiresolution approach combining experiments to get best possible constraints, e.g., [7], and this would significantly improve the COBE-only errors on n_s. The SK94+SP94+DMR4 column is the culmination of that effort. However, the SK95 data took us to significantly higher ℓ and the promise of greater discrimination among models based on how they rise to the Doppler peak. Notice the rather large shift in n_s when we pass from the 1300 pixel 2-channel SK94 data, which had chopping templates from 3 to 9, to the SK95 set, which had 10-19 projections as well as much more 3-9 data, but only for the Q-band. A worry is that non-cosmic signals at high ℓ might be contaminating the 10-19 template projections.

We now wish to add some large scale structure constraints, by constructing prior probabilities that roughly correspond to the restrictions arising from observations of galaxy clustering and cluster abundances.[3] The linear power spectrum for density fluctuations is often characterized by the shape parameter, $\Gamma \approx \Omega_{nr} h\, e^{-[\Omega_B(1+\Omega_{nr}^{-1}(2h)^{1/2})-0.06]}$, which is 0.48 for the standard CDM model. Here $\Omega_{nr} = \Omega_B + \Omega_{cdm} + \Omega_{hdm}$. Assuming a linear bias model for how the galaxy distribution is amplified over the mass distribution, the clustering data implies $0.15 \lesssim \Gamma + \nu_s/2 \lesssim 0.3$. The abundance as a function of X-ray temperature also heavily constrains σ_8. Values from 0.5 up to 0.7 are obtained for $\Omega_{nr} = 1$ CDM-like models. For $\Omega_{vac} > 0$, the value is higher, scaling roughly as $\Omega_{nr}^{-0.56}$. There are also many estimates of the combination $\sigma_8 \Omega_{nr}^{0.56}$ that are obtained by relating the galaxy flow field to the galaxy density field inferred from redshift surveys, which all take the form $[b_g \sigma_8]\, \beta_g$, where b_g is the galaxy biasing factor and β_g is a number whose value depends upon data set and analysis procedure: [11] give 0.64 ± 0.27 for an average of a number of estimates in the literature, and 0.55 ± 0.10 for a determination using a maximum likelihood technique for the IRAS survey and the Mark III velocity field data set, while a higher (~ 0.7) number is obtained using POTENT on this data set. It is usual to take $b_g \approx \sigma_8^{-1}$ for galaxies, which gives a σ_8 consistent with the cluster value, but b_g can depend

[3]We can also augment the prior probability with likelihoods for CMB experiments that we have neither the data nor the time to analyze properly, by using the quoted flat bandpower alone, along with the appropriate window function. Many groups are now using this technique exclusively to estimate CMB parameters; in joint work with Knox we show how well this extreme form of compression works.

case		DMR4	SK94+SP94 +DMR4	SK94-95 +SP94+DMR4	LSS+DMR4	LSS+DMR4 +SK94-95+SP94
13 Gyr Ω_{vac} sequence, with GW						
H_0=50	n_s	$1.02^{+.23}_{-.18}$	$0.95^{+.05}_{-.08}$	$1.12^{+.11}_{-.09}$	$0.76^{+.03}_{-.03}$	$0.85^{+.02}_{-.02}$
H_0=70	n_s	$1.12^{+.26}_{-.24}$	$0.92^{+.05}_{-.05}$	$1.12^{+.09}_{-.12}$	$0.99^{+.03}_{-.02}$	$0.99^{+.03}_{-.02}$
All H_0	n_s			$1.11^{+.11}_{-.10}$	$1.02^{+.40}_{-.06}$	$1.07^{+.13}_{-.08}$
n_s=1	H_0	< 90	< 65	< 65	68 ± 3	67 ± 3 ($\Omega_{vac} \approx 0.60$)
All n_s	H_0			< 76	< 68	70 ± 4 ($\Omega_{vac} \approx 0.66$)
15 Gyr Ω_{vac} sequence, with GW						
H_0=43	n_s	$1.02^{+.22}_{-.18}$	$0.93^{+.05}_{-.06}$	$1.04^{+.13}_{-.06}$	$0.84^{+.03}_{-.03}$	$0.91^{+.03}_{-.04}$
H_0=70	n_s	$1.28^{+.21}_{-.33}$	$0.89^{+.08}_{-.08}$	$1.02^{+.16}_{-.06}$	$1.25^{+.04}_{-.04}$	$1.26^{+.03}_{-.04}$
All H_0	n_s			$1.05^{+.12}_{-.08}$	$1.17^{+.15}_{-.18}$	$1.03^{+.14}_{-.04}$
n_s=1	H_0	< 76	< 51	< 61	54 ± 3	53 ± 2 ($\Omega_{vac} \approx 0.50$)
All n_s	H_0			< 63	< 57	55 ± 4 ($\Omega_{vac} \approx 0.52$)

Table 1: Some results for n_s and H_0 from our analysis for various combinations of experiments as indicated. Upper limits and error-bars are "1-σ" ones determined using likelihood ratios $\mathcal{L} = e^{-1/2}\mathcal{L}_{max}$. In rows 1, 2 and 4 for each case, H_0 or n_s is fixed and only σ_8 is marginalized. The other two marginalize over H_0 or n_s as well as σ_8. In all cases, we have fixed $t_0 = 13$ Gyr, $\Omega_B h^2 = 0.0125$, $\Omega_{tot} = 1$ and included tensor modes for $n_s < 1$. Note that whether the small angle experiments are added to LSS+DMR4 or not has little impact on the n_s (H_0) estimation if H_0 (n_s) is fixed.

DMR4+SP94+SK94-95 BEST FIT MODELS, with GW					
case	H_0	n_s	Ω_{vac}	σ_8	
13 Gyr B	50	1.15	0	1.8 (1.24)	($\Omega_B = 0.013$)
13 Gyr B	50	1.0**F**	0	0.9 (0.62)	($\Omega_B = 0.17$)
15 Gyr Λ	43	1.05	0	1.1 (0.76)	($\Omega_B = 0.068$)
13 Gyr Λ	50	1.15	0	1.3 (0.90)	($\Omega_B = 0.05$)
13 Gyr Λ	60	1.0**F**	0.43	1.22	($\Omega_B = 0.035$)
11 Gyr Λ	59	1.2	0	2.2 (1.54)	($\Omega_B = 0.036$)
13 Gyr OPEN	55	1.05	Ω_{tot}=0.60	1.0	($\Omega_B = 0.041$)
LSS + DMR4+SP94+SK94-95 BEST FIT MODELS, with GW					
15 Gyr Λ	55	1.0	0.52	0.97	(best fit)
13 Gyr Λ	65	1.0	0.56	1.17	(1σ down)
11 Gyr Λ	85	1.05	0.69	1.49	(2σ down)

Table 2: "Best fit" models for various regions in the scanned parameter space. The top panel considers the combined likelihoods from the CMB experiments. In the σ_8 column, the numbers in parentheses are the equivalent values for a cold+hot dark matter universe with $\Omega_{hdm} = 0.2$. For the Λ cases, Ω_B is not varied separately, but fixed at $\Omega_B h^2 = 0.125$. The bottom panel adds in the prior information from large-scale structure and lists the best fit model for each age, as well as their relative likelihoods. **F** means the parameter value was forced to be the one indicated.

upon the galaxy types being probed, upon scale, and could be bigger or smaller than σ_8^{-1}.

We want to choose priors for σ_8, Ω_{vac} and ν_s that reflect these LSS ranges, but we certainly don't want to be too miserly in our choice of allowed ranges. A straight Gaussian tends to be overly supportive of the mean, while a tophat error has no probability in the wings. Using priors which convolve a Gaussian with a tophat and have different upper and lower errors give us the flexibility we require. It is similar to specifying both a statistical and a systematic error. For the exercise shown in the tables, we required that $\Gamma + \nu_s/2$ be $0.22^{+0.07+0.08}_{-0.04-0.07}$ and $\sigma_8 \Omega_{nr}^{0.56}$ be $0.65^{+0.02+0.15}_{-0.02-0.08}$. The latter has a high probability at 0.55, but little at 0.50 (although some authors actually prefer this value). Sample LSS+CMB numbers are given in Table 1.

The tiny error bars when LSS constraints are added to the CMB data are amusing, but are far from definitive at this stage. The reason the errors are small is typically that the CMB data pushes for a likelihood peaked at high $\sigma_8 \gtrsim 1$, and this multiplies the LSS likelihood peaking at 0.6 or so. The product of the two has a narrow peak but also a small likelihood. This asymmetry is not as pronounced for the hot/cold hybrid models.

Table 2 gives the parameters for the best fits to the data for the various cases. The associated C_ℓ's are shown in Fig. 2. Note that the models which best fit the CMB data for a given age often have positive tilts. While positive scalar tilt is possible in inflation models, it requires special constructs in the inflaton potential in a region corresponding to just where we can observe it with the CMB. More likely are negative tilts. If we restrict our attention to these (e.g., second row), then the best fit for the Ω_B sequence (13 Gyr, $H_0 = 50$) is $n_s \approx 1$ and $\Omega_B \approx 0.17$, high not low. In the lower LSS part of Table 2, the 13 Gyr best fit is one sigma down from the 15 Gyr best fit, and the 11 Gyr is two sigma down.

The analysis shows that n_s lies close to the value predicted by inflation. The H_0 limits are suggestive, but better CMB data is needed to strengthen the constraint to usable values. Of course when the LSS data are included, $\Omega_{vac} > 0$ is suggested for $n_s = 1$ CDM models, though it is not needed for hot/cold hybrids with $\Omega_{hdm} = 0.2\Omega_{nr}$. Table 1 shows adding SK95 and SP94 to LSS and DMR4 does not add much further discrimination, but this should change dramatically in the next few years, with the advent of long duration balloon experiments, interferometers, MAP and COBRAS/SAMBA.

We would like to thank Barth Netterfield and Lyman Page for helping us understand how to model their data and Lloyd Knox for useful conversations.

References

[1] C. Bennett et al. , 1996, Ap. J. Lett.**464**, L1; and 4-year DMR references therein.

[2] J.O. Gundersen et al. , 1995, Ap. J. Lett., **443**, L57 *sp94*.

[3] C.B. Netterfield, N. Jarosik, L. Page & D. Wilkinson, 1995, Ap. J. Lett. **455**, L69. *sk94*.

[4] C.B. Netterfield, M.J. Devlin, N. Jarosik, L. Page & E.J. Wollack, 1996, Ap. J., submitted *sk95*.

[5] J.R. Bond, 1994, Phys. Rev. Lett. **74**, 4369.

[6] B. Chaboyer et al. , 1996, Science, in press.

[7] Bond, J.R. 1996, *Theory and Observations of the Cosmic Background Radiation*, in "Cosmology and Large Scale Structure", Les Houches Session LX, August 1993, ed. R. Schaeffer, Elsevier Science Press.

[8] J.R. Bond, 1995, Astrophys. Lett. & Comm., **32**, 63.

[9] Bond, J.R. & Jaffe, A., 1996, CITA preprint.

[10] C.W. Therrien 1992, Discrete Random Signals in Statistical Signal Processing, ISPN0-13-852112-3 (Prentice Hall).

[11] M. Strauss, & J. Willick, J. 1995, *Phys. Rep.* **261**, 271

The Cosmic Microwave Background and Large-Scale Structure

Joseph Silk
Departments of Astronomy and Physics, and Center for Particle Astrophysics
University of California, Berkeley, CA 94720, USA

Abstract

I discuss reconstruction of the underlying matter fluctuation power spectrum from cosmic microwave background temperature fluctuations. There is a remarkable concordance, to within a factor of a few, between the observed power over comoving scales spanning tens to thousands of megaparsecs and the canonical inflationary cold dark matter model, although detailed comparison with large-scale structure requires serious revision of the simplest model.

1 Introduction

There are two distinct approaches to inferring the primordial fluctuation spectrum that seeded large-scale power. One works either with cosmic microwave background fluctuations or with the large-scale matter distribution as measured in deep redshift surveys. Neither approach is without its problems, but the systematic uncertainties are largely complementary. Moreover, one is ultimately comparing the matter power spectrum $P(k)$ at $z \sim 1000$ with its value at the present epoch, and this is not only cosmological-model dependent, but can provide a test of whether structure grows by gravitational instability from infinitesimal primordial density fluctuations in a Gaussian random field.

2 Reconstruction

Detection of cosmic microwave background temperature anisotropies over scales from tens of degrees to tens of arc minutes allows reconstruction of the underlying matter fluctuation power spectrum that is responsible for generating the temperature fluctuations on the last scattering surface. One proceeds by assuming a set of model parameters and a matter power spectrum, computing the resulting $\delta T/T$ on the last scattering surface, and then inverting this calculation, which is linear on the perturbed quantities, to infer $P_m(k)$ over a band of k that projects into the window function of the CMB experiment. One finds, not surprisingly, that the shape of $P_m(k)$ is fit by $n \approx 1$, as the DMR experiment sets the normalization. Most models give an acceptable fit, although lowering n runs into difficulty with the high CMB fluctuation detections in at least one degree scale experiment.

Comparison with large-scale structure data is necessary in order to make further progress. This has been accomplished with two distinct data sets. Use of galaxy surveys has provided a means of measuring the rms fluctuations in the galaxy number counts. This has been done with the APM survey of some 4×10^6 galaxies in two dimensions, as projected on the sky. Inversion of the 2-d survey into 3-d via Limber's equation yields a three-dimensional power spectrum, that probes the universe to 18th B magnitude, appropriate to an L_* galaxy at $z \approx 0.1$ or $300h^{-1}$Mpc.

An alternative way of recovering the power spectrum utilizes galaxy redshift surveys. The disadvantage is that the resulting power spectrum is three-dimensional in redshift space, that is the third dimension is given by redshift. Distortions arise in conversion from redshift to three-dimensional space. The advantage is that one is directly sampling the three-dimensional universe, albeit in a distorted space. The three-dimensional surveys performed to date sample relatively small numbers of galaxies, up to 25000 in the Las Campanas redshift survey. Hence one approach has been to reduce the statistical uncertainties by combining results from several independent surveys. This requires normalizing the surveys to a common denominator. For example, IRAS-selected galaxies are less clustered than B-selected galaxies whereas galaxy clusters and radio galaxies are more strongly clustered. Peacock and Dodds renormalized some 6 surveys to the IRAS survey, by adopting a bias factor based on the correlation length, and made a correction for non-linear behavior of the power spectrum:

$$\langle \frac{\delta\rho_{gal}}{\rho_{gal}}(r)^2 \rangle = b^2 \langle \frac{\delta\rho}{\rho}(r)^2 \rangle = \frac{b^2}{2\pi^2} \int_0^\infty P_m(k) W(kr) k^2 dk.$$

It is convenient to use the data representation with least noise, although it should be borne in mind that systematic errors may be significant.

Figure 1 shows a comparison of the Peacock and Dodds data with the COBE-normalized CMB data and a standard CDM power spectrum. The interpretation of this figure confirms the well-known result that standard CDM produces excessive large-scale power on galaxy scales. Biasing of the luminous matter was proposed as a possible resolution, but one cannot avoid generating pairwise galaxy velocities of $\sim 1000\,\mathrm{km\,s^{-1}}$ on Mpc scales, significantly more than the measured value $\sim 500\,\mathrm{km\,s^{-1}}$.

The power overproduction can be avoided with a slight tilt. Reducing the primordial spectrum index of the fluctuation spectrum from the scale-invariant value $n = 1$ to $n = 0.8 - 0.9$ produces reasonable agreement with large-scale power. Alternative possibilities include mixed dark matter (CDM with a 20 percent admixture of hot dark matter), a flat, cosmological constant-dominated universe (with $\Omega_\Lambda = 0.7$) , and an open model ($\Omega_o = 0.3$). The COBE-normalized low Ω_o models, and even the MDM model, also overproduce power, to a lesser extent than CDM, and this can be rectified by a slight tilt, to $n \approx 0.9$.

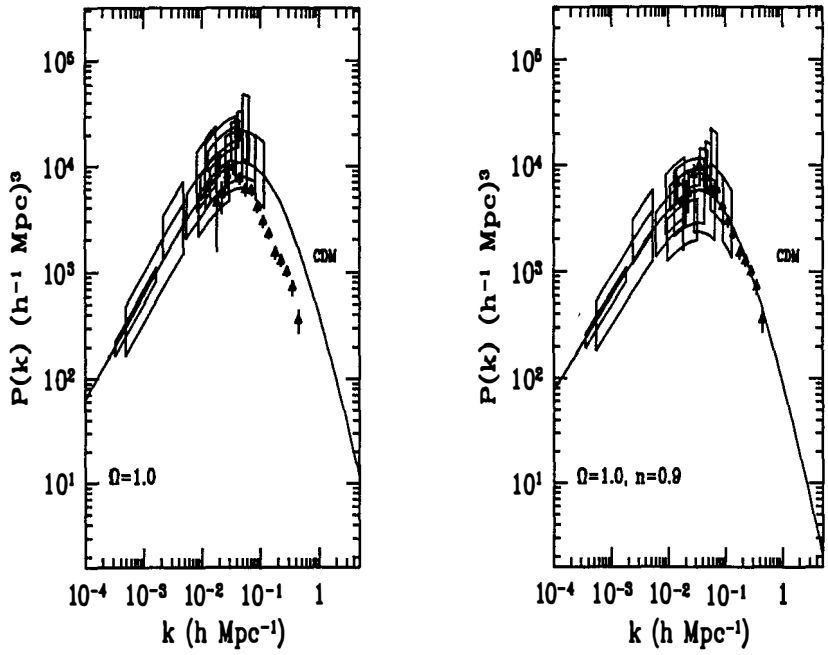

Figure 1. The matter power spectrum, $P(k)$, as reconstructed from large–scale structure and cosmic microwave background data (updated from [1]). Boxes are $\pm 1\sigma$ values of $P(k)$ inferred from CMB measurements, assuming CDM ($\Omega_0 = 1$, $h = 0.5$, $\Omega_B = 0.03$) with $n = 1$ and $n = 0.9$. The overall amplitude of the LSS data (triangles), taken from a compilation by Peacock and Dodds [3], is uncertain to $\sim$20%.

3 Peculiar velocities

Rather than use fluctuations in galaxy counts to determine $P_m(k)$, a procedure that is subject to bias of dark matter relative to luminous matter, one can apply maps of the peculiar velocity field, which has been measured out to $\sim 80h^{-1}$ Mpc. Peculiar velocities provide an unbiased measure of $P_m(k)$:

$$\langle v(r)^2 \rangle = \frac{H_o^2 f^2(\Omega)}{2\pi^2} \int_o^\infty P_m(k) W(kr) dk,$$

where $f(\Omega) \approx \Omega^{0.6}$ if $\Omega < 1$.

Now one can relate the velocity field to the density field by the linear theory of gravitational instability. From the velocity field map, it is possible to reconstruct $P_m(k)$ without any additional assumption about bias. Use of a Wiener filtering technique results in a best fit $\Omega = 1$ model that is slightly tilted: $\Omega \approx 0.8 - 0.9$ and can account for the large-scale velocity fields provided that $h \approx 0.7$. Use of lower h or less tilt overproduces the amplitudes of the peculiar velocities. However if $\Omega_b h^2$ is in the canonical range of 0.015 ± 0.005, the cosmic microwave background fluctuations in this model are too low on degree scales, unless $h \leq 0.5$

4 High baryon models

One possible solution is to increase $\Omega_b h^2$ by a factor of ~ 2 [4]. This is consistent with reports of low primordial D at high redshift, fit by $\Omega_b h^2 = 0.024(\pm.006)$ and the high baryonic fraction found in rich galaxy clusters of $(0.1 - 0.2)h^{-3/2}$. Raising the baryon abundance enhances the acoustic peak height at $l \approx 220$ without affecting $P_m(k)$ appreciably as long as $\Omega_o = 1$: the matter power spectrum is suppressed by a factor $\sim \exp(-\Omega_b - \Omega_b/\Omega_o)$. Yet another long-standing problem may also be resolved, to do with the formation of galactic disks. With a conventional baryon fraction of 5 percent, galaxy formation in dark halos results in disks that are far too small. This is because angular momentum transfer is too efficient via tidal torquing of dissipative baryonic clumps against the dark halo. The naive estimate, that if the dimensionless angular momentum parameter λ , found by analytic theory and simulations to be ~ 0.06, characterizes the initial rotation of the protogalaxy of radius r_i prior to collapse, the final disk radius is $\sim \lambda r_i$, overestimating the actual disk size by a factor of ~ 5 according to numerical simulations. Increase of the initial baryon fraction by a factor of $3 - 4$ is likely to resolve this problem: after all, a purely baryonic halo forms a disk that is far too large, of radius $\sim \lambda^{1/2} r_i$.

If the baryon fraction is as high as 25 percent, one may expect to find a unique signature in the matter power spectrum. Acoustic oscillations in the baryons gravitationally couple to the dark matter, so that there is an oscillatory signature in $P_m(k)$. The natural scale for this is set by the sound horizon at last scattering, and on scales that are smaller by $n\pi$, for $n = 1, 2, 3...$ It remains to be seen whether such a signature in wave-number space survives the projection into physical space to be observable in the observable domain of redshift space. However it is of possible relevance to note that power spectrum features on a scale of $\sim 100h^{-1}$Mpc in deep redshift surveys have persisted [2], although their degree of significance has not yet been reliably established.

5 Mapping $\delta T/T$

Future redshift surveys (the AAT 2DF survey and the Sloan digital sky survey) will obtain 250,000 and 10^6 galaxy redshifts, respectively, to 19th B magnitude or to a depth of $\sim 500h^{-1}$Mpc for L_* galaxies. One will be able to produce a map of the luminous matter distribution for some 100 independent volumes at comparable sampling to that spanned by the CfA2 and Mark III catalogs and the IRAS redshift surveys which until now have provided the best maps of the local density field. One should be able to use this information to simulate the statistical properties of cosmic microwave background fluctuations on the last scattering surface, if one relaxes the usual, but unjustified, assumption that the primordial fluctuations are Gaussian distributed. The equivalent angular scale that a similar comoving volume subtends at high redshift is $\sim 1°$. Future experiments will map the sky at a resolution of $\geq 5 - 10$ arcmin, equivalent to the scale of present-day non-linearity. Hence one may have $\sim 2 \times 10^4$ independent patches of high latitude sky (but if foregrounds proved to be a problem, one could imagine that there might be only $\sim 10^3$ patches of clean sky) probed at a resolution in $\delta T/T$ comparable to what is feasible in the deep redshift surveys for the linear power spectrum of density fluctuations at the present epoch. One should now be able to study the phases as well as the amplitudes of the density fluctuation field in the very early universe.

To demonstrate the potential richness of such map comparisons, we have performed the following experiment. The Mark III catalog has been used to generate the local linear density field over a volume of $80h^{-1}$Mpc, which has then been projected back via linear gravitational

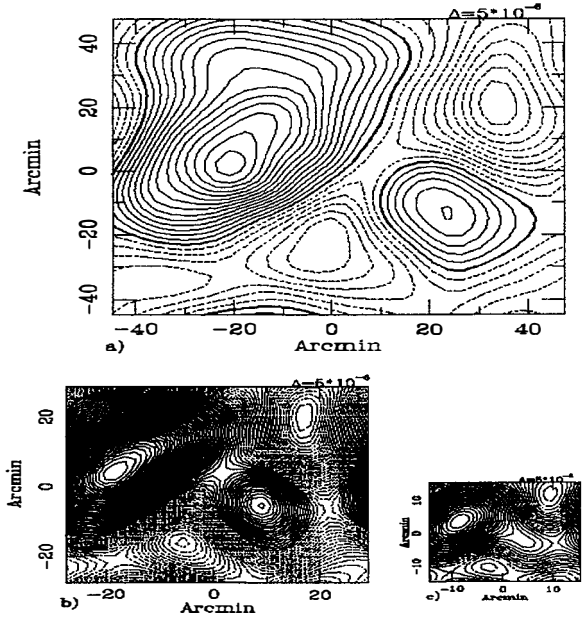

Figure 2. (a) Contour map of $\Delta T/T$ produced from our local patch of the universe. The supergalactic plane is assumed to be the last scattering surface seen by a distant observer. The map is produced assuming $\Omega = 1$, $h = 0.5$ and $\Omega_b = 0.0125h^{-2}$. The contours are spaced with 5×10^{-6} in $\Delta T/T$. (b) The same as (a) but for a flat universe with $\Omega = 0.3$ and $\lambda = 0.7$. (c) The same as in (a) but for an open universe with $\Omega = 0.3$ From [5].

instability theory into the very early universe prior to last scattering. A cosmological model is assumed, since the fluctuation growth rate is model-dependent, and phase information is preserved. One can now take this matter distribution and evolve it forward in time with coupling to the photons via the Boltzmann equation. The resulting CMB maps for different cosmological models differ in two distinct ways (Figure 2). The angular scale–redshift relation is model and geometry-dependent: hence the characteristic features imposed by the local structure differ in angular scale. The flat Λ model is smaller-scale than the $\Omega = 1$ model, and the open models, with geodesic curvature, are considerably smaller in angular scale, for the same underlying physical density fluctuations. Moreover, the shapes of the features differ significantly from model to model. This is because there are contributions to $\delta T/T$ from Sachs-Wolfe or potential fluctuations, from the intrinsic fluctuations in the radiation, and from Doppler-induced scattering, with the latter contribution being 90° out of phase. Since these various effects peak on specific but differing physical scales associated with the sound horizon at last scattering, corresponding to potential minima, maximum compression and maximum velocity, respectively, for the perturbations, one has what is in effect a differential filter that operates in combination

with the (θ, z) relation to modify the $\delta T/T$ map via the phase distribution as the cosmological model in charged. The ratio of Doppler to Sach-Wolfe contributions for example is a function of angular scale that effectively distorts the initial map of density fluctuations.

At present, with only a single predicted map, one cannot say anything about a comparison with observed CMB maps. However with $\sim$ 100 such maps derived from the deep redshift surveys, one should be able to develop a statistical comparison of the universe as seen at $z \sim 1000$ with that directly inferred from large-scale structure studies.

One could examine whether linear gravitational instability has operated since $z \sim 1000$ to amplify the primordial fluctuations. While an autocorrelation of either set of maps ($\delta\rho/\rho$ or $\delta T/T$) would provide a test of gaussianity at a particular epoch, cross-correlation provides a means of extracting the projection effects due to the integrated Sachs-Wolfe effect. In the context of a particular model, one could separate the CMB maps into local (at last scattering) and projected (due to integrated Sachs-Wolfe effect) components, and thereby enable a more direct comparison of power spectra to be made.

Curvature plays a dramatic role in modifying the angular scales and even the phases via the Doppler/acoustic/Sach-Wolfe contributions to the maps. The most direct application would be to a statistical measure of the curvature of the universe. One can also distinguish the effect of the volume element, since this also modifies the (θ, z) relation: for example in a flat model, the contribution of Λ can be extracted from the map comparisons.

6 Conclusions

This is an exciting time to be studying the cosmic microwave background radiation fluctuations. Two major satellite experiments have been approved by ESA and by NASA, and there are also projects underway using ground-based inteferometers and balloon-borne bolometer arrays that are capable of being competitive on a shorter time-scale. Over the next few years, our sampling of large-scale structure via deep redshift surveys will increase by an order of magnitude. While there are almost certainly surprises in store, it is no exaggeration to anticipate that comparison of the power spectrum of radiation with that of matter fluctuations will dramatically improve our knowledge of the underlying cosmological model parameters.

Acknowledgements. This work was done in collaboration with E. Gawiser and S. Zaroubi. I am indebted to my various collaborators for many discussions of topics covered in this lecture. This research has been supported in part by a grant from NASA.

References

[1] Scott, D., Silk, J. and White, M., *Science*, **268** (1995) 829.

[2] Landy, S. *et al.*, *Astrophys. J.*, **456** (1996) L1.

[3] Peacock, J. A. & Dodds, D. D., *Mon. Not. R. astr. Soc.* **267** (1994) 1020.

[4] White, M., Liddle, A. R., Scott, D. and Viana P. T. P., *preprint* (1996).

[5] Zaroubi, S., Sugiyama, N., Silk, J., Hoffman, Y. and Dekel, A., *preprint* (1996).

CONSTRAINTS ON REIONIZATION FROM CMB FLUCTUATIONS

P. de Bernardis[1], A. Balbi[2], G. de Gasperis[2], A. Melchiorri[1], N. Vittorio[2]
[1] *Dipartimento di Fisica, Universita' di Roma "La Sapienza", Roma, Italy*
[2] *Dipartimento di Fisica, Seconda Universita' di Roma "Tor Vergata", Roma, Italy*

Abstract

We study the anisotropy of the cosmic microwave background (CMB) in mixed dark matter models, with non scale-invariant primordial power spectra (i.e. $n \neq 1$) and a late, sudden reionization of the intergalactic medium at redshift z_{rh}. We test these models against recent detections of CMB anisotropy at large and intermediate angular scales. Our likelihood analysis indicates that mixed dark matter models with blue power spectra ($n \simeq 1.24$) and a reionization at $z_{rh} \sim 20$ are most consistent with the presently available CMB anisotropy data

1 Introduction

If and when the universe underwent through a phase of early reionization of the intergalactic medium is an interesting and still open question. From the Gunn and Peterson test we know that the universe must have been highly reionized at redshift $z \simeq 5$, and the presence of heavy elements in the intracluster gas suggest that a considerable energy release occurred during the earliest stages of galaxy formation and evolution. The recent detections of cosmic microwave background (CMB) anisotropy at degree angular scales provide a new and powerful way for investigating this issue. In fact, reionization damps power in the primary anisotropies under the horizon scale at last scattering as $\exp[-2\tau]$ where τ is the optical depth of the universe. Thus, using large and intermediate angular scale anisotropy measurements we can in principle discriminate among different assumptions for the thermal history of the universe.

2 Theoretical calculations

We consider a flat universe ($\Omega_0 = 1$) composed by baryons ($0.03 < \Omega_b < 0.07$), one family of massive neutrinos ($\Omega_\nu = 0.3$), cold dark matter ($\Omega_{CDM} = 1 - \Omega_b - \Omega_\nu$), photons and two families of massless neutrinos. From age considerations we fix $h = 0.5$. The power spectrum of CMB anisotropies is calculated by solving the radiative transport equations for each cosmological fluid. We refer to de Bernardis at al. 1996 [2] for a complete presentation of the procedure. We model the thermal history of the universe after recombination as a sudden and homogeneus reionization of the intergalactic medium from redshift z_{rh} up to the present. The correlation function (acf) of the temperature fluctuations can be written as

$$C(\alpha, \theta_B) = \frac{\mathcal{A}^2 A_{COBE}}{4\pi} \sum_{\ell=2}^{\infty} (2\ell+1) C_\ell P_\ell(\cos\alpha) \exp[-(\ell+1/2)^2 \theta_B^2] \tag{1}$$

where θ_B is the dispersion of a gaussian approximating the angular response of the beam an the quantities C_ℓ denotes the power spectrum of CMB anisotropies. We define the parameter $\mathcal{A}^2 = A/A_{COBE}$ as the amplitude A of the power spectrum (considered as a free parameter) in units of A_{COBE}, the amplitude needed to reproduce $C(\alpha = 0^o, \theta_B = 4.24^o) = (29\mu K)^2$, as observed by COBE-DMR (Bennet at al. 1996) [1].

3 Data Analysis

We have selected a set of 20 different anisotropy detections obtained by different experiments, or by the same experiment with different window functions and/or at different frequencies. For each detection, labeled by the index j, we report in Table 1 the detected mean square anisotropy, $\Delta_j^{(exp)}$, and the corresponding 1–σ error, $\Sigma_j^{(exp)}$. Theoretically, the mean (over the ensemble) squared anisotropy is given by a weighted sum of the C_ℓ's:

$$[\Delta_j^{(th)}] = \frac{1}{4\pi} \sum_\ell (2\ell+1) C_\ell W_{\ell,j} = \frac{1}{4\pi} \overline{C_{\ell_{eff}}} \sum_\ell (2\ell+1) W_{\ell,j} \tag{2}$$

where the window functions $W_{\ell,j}$ contain all the experimental details (chop, modulation, beam ,etc.), and $\overline{C_{\ell_{eff}}}$ is the mean value of the C_ℓ's over the window function. The effective multipole number $\ell_{eff,j}$ is defined as follows:

$$\ell_{eff,j} = \sum \ell(2\ell+1) C_\ell W_{\ell,j} / \sum (2\ell+1) C_\ell W_{\ell,j}$$

and is listed in Table 1 for a scale invariant model without reionization. Using numerical simulations, which take into account scan strategy and experimental noise, we verify that the expected distribution for $\Delta_j^{(exp)}$ is well approximated by a gaussian, with average $\Delta_j^{(th)}$ and cosmic/sampling variance

$$\Sigma_j^{(th)} = \frac{1}{f_j} \frac{1}{8\pi^2} \sum_\ell (2\ell+1) W_{\ell,j}^2 C_\ell^2 \tag{3}$$

Here f_j represents the fraction of the sky sampled by each experiment and it is also listed in Table 1. Given the Gaussian distribution of $\Delta_j^{(exp)}$, we compute the likelihood of the 20 (assumed independent) CMB anisotropy detections as follows:

$$\mathrm{L}(\mathcal{A}, n, z_r h) = \prod_j \frac{1}{\sqrt{2\pi[\mathcal{A}^4 (\Delta_j^{(th)})^2 + \Sigma_j^2]}} \exp\{-\frac{1}{2} \frac{[\Delta_j^{(exp)} - \mathcal{A}^2 \Delta_j^{(th)}]^2}{\mathcal{A}^4 (\Delta_j^{(th)})^2 + \Sigma_j^2}\} \tag{4}$$

As already stated, this is a function of three parameters: the amplitude $\mathcal{A}$, the spectral index n and the reionization redshift z_{rh}.

4 Results

For each pair $n - z_{rh}$ we select the value $\mathcal{A}_{max}$ which maximizes the Likelihood. The 2-D, conditional distribution $L(n, z_r|A_{max}) \equiv \mathrm{L}(\mathcal{A}_{max}, n, z_{rh})$ has a quite distinctive peak at $n \simeq 1.24$ and $z_{rh} \simeq 20$. We checked the stability of this result by applying a jack-knife analysis to the considered data set, and we have seen that the results are reasonably stable. The position of the maximum likelihood does not change by more than ± 0.02 for n and ± 10 for z_{rh} unless the COBE data are excluded. The 95% confidence contours in the $n - z_{rh}$ plane include a wide range of parameters combinations: this means that the presently available data set is not sensitive enough to produce "precise" determinations for n and z_{rh}; systematic and statistical errors in the different experiments are still significant. For example ($\Omega_b = 0.05$) we have the following 95% C.L. bounds: $1.05 < n < 1.30$ for $z_{rh} = 15$; $1.10 < n < 1.35$ for $z_{rh} = 30$; $1.20 < n < 1.45$ for $z_{rh} = 45$; $1.30 < n < 1.50$ for $z_{rh} = 60$; $z_{rh} < 80$ for any n.

If we exclude an early reionization of the intergalactic medium ($z_{rh} = 0$) we get at the 95% confidence level the following estimate for the spectral index: $1.01 \leq n \leq 1.28$ ($\Omega_b = 0.03$); $1.00 \leq n \leq 1.26$ ($\Omega_b = 0.05$); $0.96 \leq n \leq 1.24$ ($\Omega_b = 0.07$). Note that the "standard" flat model with no reionization is close but not always inside the 95% confidence contour. These results have to be compared to the results from COBE-DMR alone: $n = (1.3 \pm 0.3$, at the 68% confidence level (Bennet at al. 1996). So, in spite of their still low signal to noise ratio, the degree scale experiments already allow to better constrain the spectral index, although still at the 10% level. Also, since the Doppler peak is an evident feature of our best fit model, our analysis confirms that a Doppler peak in the C_ℓ spectrum, centered at $\ell \sim 200$, is perfectly consistent with the considered data set.

References

[1] Bennet C.L., et al. 1996, *Ap.J.Lett.* Submitted

[2] de Bernardis P., Balbi A., de Gasperis G., Melchiorri A., Vittorio N., 1996, *Ap.J.Lett.* Submitted

TABLE 1

CMB Anisotropy Detections Used in the Analysis

experiment	ref.	$\Delta T^2(\mu K^2)$	68%+, (μK^2)	68%-, (μK^2)	sky coverage	ℓ_{eff}
COBE	1	841	58	57	0.6580	5.8
Tenerife	2	1770	840	670	0.0124	20.1
South Pole Q	3	480	470	160	0.0005	49.4
South Pole K	4	2040	2330	790	0.0005	65.7
Python	5	1940	1890	490	0.0006	129.0
ARGO Hercules	6	360	170	140	0.0024	118.9
ARGO Aries	7	580	150	130	0.0055	118.9
MAX HR	8	2430	1850	1020	0.0002	162.0
MAX PH	9	5960	5080	2190	0.0002	162.0
MAX GUM	10	6580	4450	2320	0.0002	162.0
MAX ID	11	4960	5690	2330	0.0002	162.0
MAX SH	12	5740	6280	2900	0.0002	162.0
MSAM 3F	13	4680	4200	2450	0.0007	181.3
Saskatoon	14	1990	950	630	0.0037	99.9
Saskatoon	15	4490	1690	1360	0.0037	175.4
Saskatoon	16	6930	2770	2140	0.0037	235.2
Saskatoon	17	6980	3030	2310	0.0037	283.2
Saskatoon	18	4730	3380	3190	0.0037	347.8
CAT 1	19	1180	720	520	0.0001	414.9
CAT 2	20	760	760	360	0.0001	579.7

References.— (1) Bennet et al., 1996; (2) Hancock et al. 1994; (3,4) Gundersen et al. 1994; (5) Dragovan et al. 1994; (6) de Bernardis et al. 1994; (7) Masi et al. 1996; (8,9,10,11,12) Tanaka et al. 1996; (13) Cheng et al. 1994; (14, 15, 16, 17, 18) Netterfield et al. 1996; (19, 20) Scott et al. 1996

PART III

CMB THEORY & IMPACT OF FUTURE EXPERIMENTS

DO WE KNOW THE GEOMETRY OF THE UNIVERSE?

Marc Kamionkowski* and Nicolaos Toumbas
Department of Physics, Columbia University, New York, New York 10027

Abstract

It is quite remarkable that seventy years after Hubble discovered the expansion of the Universe, we still have no idea in which of the three Friedmann-Robertson-Walker geometries we live. Most of the current literature has focussed on flat or open models. Here, we construct a viable model of the Universe which has closed geometry even though the nonrelativistic-matter density is less than critical. Furthermore, in this model, the cosmic microwave background could come from a causally-connected region at the antipode of the closed Universe. This model illustrates that the geometry of the Universe is unconstrained by current data. We discuss observations which may reliably determine the geometry of the Universe in the near future.

*kamion@phys.columbia.edu

Remarkably, we have no idea in which of the three Friedmann-Robertson-Walker (FRW) geometries we live, even seventy years after the discovery of the expansion of the Universe. An open Universe accounts simply for a nonrelativistic-matter density Ω_0 that appears to be substantially less than unity. Theoretical arguments, such as the Dicke coincidence and inflation, favor a flat Universe. Theorists have recently emphasized that the Universe may be flat, even if $\Omega_0 < 1$, with a nonzero cosmological constant. There are also heuristic arguments for a closed Universe. However, given the current observations, it requires some *chutzpah* to suggest that $\Omega_0 > 1$. Here, we describe a closed Universe with $\Omega_0 < 1$, which at low redshifts is entirely indistinguishable from a standard open FRW Universe with the same Ω_0. We also address how future observations may determine the geometry of the Universe.

If matter with an equation of state $p = -\rho/3$ exists, then its energy density decreases as a^{-2} with the scale factor a of the Universe, and thus mimics a negative-curvature term in the Friedmann equation. In this case, the Universe could be closed and still have a nonrelativistic-matter density $\Omega_0 < 1$.[1-4]

The energy density contributed by a scalar field with a uniform gradient-energy density would scale as a^{-2}, but, such a scalar-field configuration would generically collapse within a Hubble time. Davis[1] pointed out that if there was a manifold of degenerate vacua with nontrivial mappings into the three-sphere, then a texture—a topological defect with uniform gradient-energy density—would be stabilized provided that it was wound around a closed Universe[1]. Non-intersecting strings would also provide an energy density that scales as a^{-2}.[3]

Moreover, if this energy density is chosen properly, the observed cosmic microwave background (CMB) comes from a causally-connected patch at the antipode of the closed Universe[5]. Although unusual, this model at least looks remarkably like a standard open Universe at low redshifts, even though the largest-scale structure differs dramatically.

The Friedmann equation for a closed Universe with nonrelativistic matter and matter (perhaps a stable texture) with an equation of state $p = -\rho/3$ is

$$H^2 \equiv \left(\frac{\dot{a}}{a}\right)^2 = \frac{8\pi G}{3}\rho_m + \frac{\gamma - 1}{a^2}$$
$$= H_0^2[\Omega_0(1+z)^3 + (1-\Omega_0)(1+z)^2] \equiv H_0^2[E(z)]^2, \qquad (1)$$

where $H = \dot{a}/a$ is the Hubble parameter (and the dot denotes derivative with respect to time), $z = (a_0/a) - 1$ is the redshift, G is Newton's gravitational constant, ρ_m is the density of nonrelativistic matter, and γ is a parameter that quantifies the contribution of the energy density of the texture. The second line defines the function $E(z)$. This is exactly the same as the Friedmann equation for an open Universe with the same Ω_0, so this closed Universe has the same expansion dynamics. At the current epoch (denoted by the subscript "0"),

$$\Omega_0 = 1 + \frac{1-\gamma}{a^2H^2} = 1 - \Omega_t + \frac{1}{a_0^2H_0^2}, \qquad (2)$$

where $\Omega_t = \gamma(a_0H_0)^{-2}$ is the contribution of the texture to closure density today. So, $\Omega_0 < 1$ if $\gamma > 1$ even though the Universe is closed, and we require that $\Omega_t + \Omega_0 > 1$.

If the metric of a closed Universe is written as

$$ds^2 = dt^2 - a^2(t)\left[d\chi^2 + \sin^2\chi(d\theta^2 + \sin^2\theta d\phi^2)\right], \qquad (3)$$

then the polar-coordinate distance between a source at a redshift z_1 and another source along the same line of sight at a redshift z_2 (for $\Omega_0 < 1$) is

$$\chi_2 - \chi_1 = \sqrt{\Omega_0 + \Omega_t - 1} \int_{z_1}^{z_2} \frac{dz}{E(z)}. \tag{4}$$

If Ω_t is chosen so that the polar-coordinate distance of the CMB surface of last scatter is $\chi_{LS} \simeq \pi$, then the CMB we observe comes from a causally-connected patch at the antipode of the Universe. From Eq. 4, the condition on Ω_t for this to occur is

$$\Omega_t \simeq \left[\frac{\pi\sqrt{1-\Omega_0}}{\mathrm{arcsinh}(2\sqrt{1-\Omega_0}/\Omega_0)} \right]^2 + 1 - \Omega_0. \tag{5}$$

With this imposed, the texture density Ω_t increases from 1.6 to 2.5 for Ω_0 between 0.1 and 1.

Is this a realistic possibility? As we discuss below, this model is fully consistent with our current knowledge of the Universe.

Incidentally, one could also "close" a low-density Universe with a large cosmological constant (although such a model with the CMB at the antipode is likely ruled out by quasar-lensing statistics[6]). However, the Friedmann equation is altered in such a model, so the expansion rate affects the classical cosmological tests. In the model discussed here, the expansion is identical to that in an open FRW Universe. Therefore, quantities that depend only on the expansion, such as the deceleration parameter, the age of the Universe, or the distribution of quasar absorption-line redshifts, do not probe Ω_t. Furthermore, the growth of density perturbations is the same as in a standard open Universe, so dynamical measurements of Ω_0 (e.g., from peculiar-velocity flows) will also be insensitive to Ω_t. Effects due to geometry arise only at $\mathcal{O}(z^3)$ since $\sin\chi$ and $\sinh\chi$ differ only at $\mathcal{O}(\chi^3)$; therefore, this Universe will differ from an open Universe only at $z \gtrsim 1$.

We now turn to cosmological tests that probe the geometry of the Universe. Underlying these is the angular-diameter distance between a source at a redshift z_2 and a redshift $z_1 < z_2$,

$$d_A(z_1, z_2) = \frac{\sin(\chi_2 - \chi_1)}{(1+z_2)H_0\sqrt{\Omega_0 + \Omega_t - 1}}. \tag{6}$$

The angular size of an object of proper length l at a redshift z is $\theta \simeq l/d_A(0,z)$. With Ω_t fixed by Eq. 5, one finds that the angular sizes in a flat matter-dominated Universe can be very similar to those in a low-density closed Universe[4]. Proper-motion distances of superluminal jets in radio sources at large redshift may provide essentially the same probe as do flux-redshift relations. The difference between the angular sizes for the standard FRW Universe and the closed model for the same value of Ω_0 is quite a bit more dramatic than the difference between open FRW and flat Λ models. It has been proposed that evolutionary effects may conceivably be understood well enough to discriminate between open and flat Λ models[7]. If so, then the distinction between these and the closed model will be even clearer.

In the low-density closed Universe, the differential number of galaxies per steradian per unit redshift is,

$$\frac{dN_{\rm gal}}{dzd\Omega} = \frac{n_0 \sin^2[\chi(z)]}{H_0^3(\Omega_0 + \Omega_t - 1)E(z)}, \tag{7}$$

where n_0 is the local number density of galaxies, and the number per comoving volume is assumed to remain constant. Again, one finds that the number-redshift relation for a flat matter-dominated Universe may be mimicked by a low-density closed Universe.

The redshift thickness δz and angular size $\delta\theta$ of a roughly spherical structure that grows with the expansion of the Universe will have a ratio[8)]

$$\frac{1}{z}\frac{\delta z}{\delta\theta} = \frac{E(z)\sin[\chi(z)]}{z\sqrt{\Omega_0 + \Omega_t - 1}}. \tag{8}$$

It turns out that this function is significantly lower in a low-density closed Universe than in an open Universe and in a Λ Universe. Curiously, it depends only very weakly on the value of Ω_0 and therefore provides an Ω_0-independent test of this closed model. A precise measurement may be feasible with forthcoming quasar surveys[9)].

The probability for lensing of a source at redshift z_s for $\Omega_0 < 1$ and $\Omega_t + \Omega_0 > 1$ relative to the fiducial case of a standard flat Universe is[10)]

$$P_{\rm lens} = \frac{15}{4}\left[1 - \frac{1}{(1+z_s)^{1/2}}\right]^{-3} \times \int_0^{z_s} \frac{(1+z)^2}{E(z)}\left[\frac{d_A(0,z)d_A(z,z_s)}{d_A(0,z_s)}\right]^2 dz. \tag{9}$$

The current observational constraint is roughly $P_{\rm lens} \lesssim 5$. If Ω_t is chosen so that the CMB comes from the antipode, then $P_{\rm lens} < 2.5$ for $0 < \Omega_0 < 1$. Hence the model is consistent with current data and is likely to remain so.

So far, we have investigated several tests that depend on the geometry. However, each of these also depends on the expansion of the Universe, so no single test can determine the geometry unless the matter density is fully specified. Furthermore, these involve observations at large redshifts where observations are tricky and evolutionary effects may be important.

So how does one determine the geometry of the Universe? CMB temperature maps attainable with forthcoming satellite and interferometry experiments will likely provide the best determination of the geometry of the Universe[11,12)]. Although the detailed shape of the anisotropy spectrum depends on a specific model for structure formation, it has structure (acoustic peaks) on angular scales smaller than that subtended by the horizon at the surface of last scatter. This angle depends primarily on the geometry and only weakly on other undetermined cosmological parameters; in a standard FRW Universe, it is $\theta_{LS} \simeq \Omega^{1/2}\,1^\circ$, where Ω is the *total* density of the Universe. Therefore, measurement of the location of the first acoustic peak provides a reliable determination of the geometry of the Universe[11)]. Furthermore, it can be shown that with forthcoming all-sky CMB maps with sub-degree angular resolution, Ω, may be determined to better than 10% and perhaps as good as 1%.[12)]

Thus, for the first time since the discovery of the expansion raised the issue, the geometry of the Universe may finally be determined. The location of the first acoustic peak will therefore provide a precise test of inflation, which predicts a flat Universe, and will test alternative models such as the low-density closed Universe discussed here. Finally, what

about the homogeneous matter with an energy density which scales as a^{-2}? If this is due to a topologically stabilized scalar-field configuration, as discussed above, then the symmetry-breaking scale must be of order the Planck scale if Ω_t is of order unity. Furthermore, the global symmetry must be *exact*. If confirmed, this model would therefore have significant implications for Planck-scale physics[13].

This work was supported in part by the D.O.E. under contract DEFG02-92-ER 40699 and by NASA under contract NAG5-3091.

REFERENCES

[1] R. L. Davis, Phys. Rev. D 35, 3705 (1987); Gen. Rel. Grav. 19, 331 (1987).
[2] E. W. Kolb, Astrophys. J. 344, 543 (1989).
[3] J. R. Gott III and M. J. Rees, Mon. Mot R. Astr. Soc. 227, 453 (1987).
[4] M. Kamionkowski and N. Toumbas, astro-ph/9601147.
[5] R. L. Davis, Phys. Rev. D 36, 997 (1987).
[6] E.g., M. White and D. Scott, Astrophys. J. 459, 415 (1996); S. M. Carroll, W. H. Press, and E. L. Turner, Ann. Rev. Astron. Astrophys. 30, 499 (1992).
[7] L. M. Krauss and D. N. Schramm, Astrophys. J. Lett. 405, L43 (1993).
[8] C. Alcock and B. Paczyński, Nature 281, 358 (1979).
[9] S. Phillips, Mon. Not. Roy. Astr. Soc. 269, 1077 (1994).
[10] M. Fukugita and E. L. Turner, Mon. Not. R. Astr. Soc. 253, 99 (1991); C. Kochanek, Astrophys. J. 419, 12 (1993).
[11] M. Kamionkowski, D. N. Spergel, and N. Sugiyama, Astrophys. J. Lett. 426, L57 (1994).
[12] G. Jungman, M. Kamionkowski, A. Kosowsky, and D. N. Spergel, Phys. Rev. Lett. 76, 1007 (1996).
[13] M. Kamionkowski and J. March-Russell, Phys. Rev. Lett. 69, 1485 (1992); R. Holman et al., Phys. Rev. Lett. 69, 1489 (1992); R. Kallosh et al., Phys. Rev. D 52, 912 (1995); N. Turok, hep-ph/9511238.

Microwave Background Anisotropies without Inflation

R. Triay
Université de Provence
and
Centre de Physique Théorique (CNRS, UP 7061)
Luminy Case 907, F 13288 Marseille Cedex 9, France

Abstract

Speculations on the Flatness problem and the Horizon problem show that spatially closed world models with a non vanishing cosmological constant are possible solutions, which do not require the Inflation scenario. Consequences on the interpretation of Microwave Background Anisotropies are considered.

1 Introduction

The Inflation scenario [13, 22] is known as the only way to solve the *Horizon problem*, although there is another issue which assumes a positive curvature Universe[11]. Such an alternative [32] has long been contrary to the general consensus, which argued in favor of a zero cosmological constant Λ and a Hubble constant $H_o \approx 50\,\mathrm{km\,s^{-1}/Mpc}$ (probably for ensuring the simplicity of a zero curvature cosmological world model suggested by the Dicke anthropic principle [7]). The *Flatness problem* is a new version of such a speculation which was re-introduced when Inflation came on the scene with the goal of avoiding the *Gauge Monopoles problem*, inherent in the SU(5) approach of grand unification theory. However, such a bet (which sought to unify the strong and the electroweak interactions and to contribute to Cosmology with a solution to the *Antimatter problem*[29, 15]) turned out to be unsuccessful[1] (e.g., the estimated proton mean life-time $> 1.6\,10^{16}$ Gyr[20] exceeds the age of the universe). Nowadays, the end justifying the means, the Inflation scenario is understood as the prenatal phase of the Friedman world model, which provides us with solutions to basics problems of Standard cosmology. However, the short

extragalactic distance scale obtained from recent measurements of the Hubble constant[14, 25, 12], together with the assertion that we live in a critical density universe, do not agree with the estimated ages for metal-poor Galactic globular clusters (e.g., $t_o = 16.5 \pm 2$Gyr [33]). On the other hand, this *Age problem* can be solved with realistic estimates of the density parameter $\Omega_o \approx 0.2$ in a positive curvature Universe [11, 28], which motivates us to investigate the Flatness and the Horizon problems within such a geometry[30, 31, 32].

2 The Flatness problem

A realistic description of the present epoch of the Universe is given by the Friedmann-Lemaitre-Gamow (FLG) model, it accounts for non interacting matter and radiation as the only sources of the gravitational field. The Hubble constant (which provides us with the chronology) is given by

$$H^2 = H_o^2 \left(\lambda_o - k_o a^{-2} + \Omega_o a^{-3} + \alpha_o a^{-4} \right), \tag{1}$$

where $a(t)$ is the (dimensionless) *expansion parameter*, defined so that its present value $a_o = 1$, and the coefficients are the present values of cosmological parameters (which characterize the dynamics of the cosmic evolution), one has : $\lambda = \Lambda/(3H^2)$, $\Omega = \rho/\rho_c$, the reduced curvature $k = K/(H^2)$ (K is the curvature scalar of the comoving space), $\alpha = 8\pi^3 \mathrm{G}(\mathrm{k}T)^4/(45\hbar^3 H^2)$ accounts for the CBR photon (T is the CMB temperature, k is the Boltzmann constant, and $\hbar$ is the Planck constant); the dominant parameter specifies the source which drives the expansion. A limited value domain provides us with the *Standard Big-Bang Universe with an eternal expansion* (e.g., see [3]).

Within the context of the Inflation framework, the Flatness problem tells us that "the standard world model requires stringent initial boundary conditions on the value of the Hubble constant to produce a Universe as flat as one sees today"[13]. Although the extrapolation of the FLG model back to primordial epochs has to be done with caution, it coincides however to Gamow model, which tells us that the present CBR temperature accounts for the Big Bang kinetic impulse $H \sim H_o \sqrt{\alpha_o} a^{-2}$ (the radiation pressure pushes the space out from the singularity), independently of Ω_o (unless a scenario of baryon generation is assumed[1]). The answer to the question of whether the Universe recollapse or go into a curvature-dominated expansion lies in the initial conditions upon the dimensionless parameters α_o, Ω_o and k_o. They account for the amount of massless particles, of massive particles and the geometry of the primordial Universe, the cosmological constant being solely a correction to Newtonian potential[2]. First of all, it is interesting to note that the curvature parameter $k \sim k_o \alpha_o^{-1} a^2$ vanishes when $a \to 0$, which shows that the world model is described asymptotically by the Einstein–de Sitter model, when the spatial curvature $K = k_o H_o^2 a^{-2} \to \pm\infty$ if $k_o \neq 0$; and such a *Dynamical Flatness* is satisfied whatever the present values of the cosmological parameters could be. In order to check whether the initial constraint upon the curvature is peculiar, we can test whether the

[1]It must account for the peculiarly small value for the ratio of the number of baryons to the number of photons, the nature of the Dark matter

[2]The dimensional analysis of Einstein equations shows that Λ can be measured only by large scale observations[27], and does not trace back to the source of the vacuum energy density (a terminology which comes from quantum fields theory). In other words, by choosing adapted units so that the Einstein equations with a non zero Λ reads $R_{\mu\nu} - \frac{1}{2} R g_{\mu\nu} + g_{\mu\nu} = T_{\mu\nu}$, the gravitational units of time is given by $1/\sqrt{\Lambda}$, and of mass by $1/(8\pi G\sqrt{\Lambda})$. Hence, the order of magnitude of the ratio of the gravitational action unit and the quantum action unit ($\hbar$) is of order of 10^{120}, which gives a universal coupling constant $\sim 10^{-60}$. Such a weak value shows that it becomes hopeless to look for a quantum status for Λ.

angle $\beta = \arctan(k_\circ \alpha_\circ^{-1})$, which gives the slope of the function $a^2 \rightarrow k$, is peculiar (independently on the choice of the primordial date). Unfortunately, this angle turns out to be poorly determined ($\beta = 0 \pm 89.99°$) simply because the estimates of cosmological parameters are not enough accurate to date, which shows that the primordial flatness ($\beta \approx 0$) is not justified (!).

The old formulation of the Flatness problem accounts for the Dicke's anthropic considerations [8, 9, 24], which ask "whether it is reasonable that we might have come on the scene just as the expansion, initially driven by the potential energy, becomes curvature dominated". Such a *coincidence* problem can be avoided if the present expansion is so that the dominant parameter is close to its asymptotic value (which is defined when $a \rightarrow +\infty$), which depends strongly on whether the cosmological constant is zero. Indeed, one has :

- if $\Lambda = 0$ then (one has $k_\circ \leq 0$) the expansion reads
  - $H_\infty \sim H_\circ \sqrt{-k_\circ} a^{-1} \left(1 - \frac{1}{2}\Omega_\circ k_\circ^{-1} a^{-1}\right)$ if $k_\circ \neq 0$, and the dominant parameter is
  $$k_\infty \sim -1 + \Omega_\circ |k_\circ|^{-1} a^{-1}, \tag{2}$$
  - $H_\infty \sim H_\circ \sqrt{\Omega_\circ} a^{-3/2} \left(1 + \frac{1}{2}\alpha_\circ \Omega_\circ^{-1} a^{-1}\right)$ if $k_\circ = 0$, and the dominant parameter is
  $$\Omega_\infty \sim 1 - \alpha_\circ \Omega_\circ^{-1} a^{-1}. \tag{3}$$

  Hence, we can see that the (usual) solution $\Omega_\circ \approx 1$ (i.e., $k_\circ \approx 0$) is clearly preferred, since the observations show that it is not a reasonable to assume $\Omega_\circ \approx 0$ (i.e., $k_\circ \approx -1$).

- otherwise ($\Lambda \neq 0$) the expansion is vacuum-dominated
  - $H_\infty \sim H_\circ \sqrt{\lambda_\circ} \left(1 - \frac{1}{2} k_\circ \lambda_\circ^{-1} a^{-2}\right)$, and the dominant parameter is
  $$\lambda_\infty \sim \begin{cases} 1 + k_\circ \lambda_\circ^{-1} a^{-2} & \text{if } k_\circ \neq 0, \\ 1 - \Omega_\circ \lambda_\circ^{-1} a^{-3} & \text{otherwise.} \end{cases}, \tag{4}$$

  Therefore we can note that $\lambda_\circ \approx 1$ (and thus $k_\circ \approx \Omega_\circ > 0$) is a new solution to the Flatness problem.

3 The Horizon problem

Because the origin of large scale structures needs *Seeds* (e.g., simple scalar field fluctuations surviving from earliest epochs, which have been enlarged by Inflation), the Horizon problem regards the status of space-time geometry when the Universe enters into the FLG behavior. Indeed, if such fluctuations are neglected so that the RW-metric holds since the origin of time then it is clear that the *universality of laws of physics* suffices to explain why the CMB photons were emitted from regions at the same temperature regardless of causality requirements[32]. The problem of initial conditions upon the cosmic fluid can be viewed in a different way regarding the compactness of the space, and without specifying the nature of seeds. If the space is infinite then one easily understands that "all the matter has to be created out of any causality in a *same manner*, *every where* and at the *same date*, in order to prevent us from any possible cosmological disaster[3]". On the other hand, if the space is compact then the creation mechanism reduces

[3] *loc.cit.* J.M. Souriau, priv. comm.

to a single primordial event, which makes the irregularities to have the same origin. The CMB black body spectrum (which accounts for a thermodynamical equilibrium at decoupling) and the huge entropy per baryon (e.g., see Misner [19]) suggest that the physics of the cosmic plasma before nucleosynthesis epoch was dominated by *dissipative processes*, which smoothed out the initial irregularities[4]. Hence, the presence of such (irreversible) processes allows one to do not assume a priori that the homogeneity and the isotropy of the cosmic fluid were ensured since the origin of time, but come from evolutionary effects. With this in mind, the FLG geometry can be used for quantifying the efficiency of smoothing mechanisms (with respect to instantaneous homogeneization), which interprets as a *Causality problem*[5]. A possible solution is that the primordial chronology enlarges the particle horizon (by preserving isotropy), although the pereniality of such solutions is not ensured a priori. Positive curvature FLG models provide us with a less stringent solution to the causality problem : the candidate values of cosmological parameters make the size of the last scattering surface smaller than the particle horizon at decoupling (which interprets as a *focusing effect*), although the space where the photon propagate since the recombination era has to become homogeneous and isotropic. The extreme case corresponds to a single decoupling event which can be seen over 4π steradian in the sky, the values of cosmological parameters $(\Omega_\circ, \lambda_\circ)$ which provide us with such a solution are defined by the equation $\tilde{t}_\circ = \pi R_\circ + 2\tilde{t}_r$, where $R_\circ = H_\circ^{-1} k_\circ^{-1/2}$ is the radius of the Universe today, $\tilde{t}_r$ is the conformal date of decoupling and $\tilde{t}_\circ$ is the conformal Age, the corresponding focusing curve is drawn in Fig. 1. Therefore, we understand that if $k_\circ > 0$ then the closer the model to this curve the easier the causality problem vanishes. In particular, the following condition

$$0 \leq \tilde{t}_\circ - \pi R_\circ \leq 2\tilde{t}_r \tag{5}$$

ensures that CMB photons come from a single FLG causal cell. The obvious consequences of the increase of the angular extension are that the level of $\delta T/T$ fluctuations might become substantially lower than the one predicted by assuming a vanishing cosmological constant (such an effect reconciles adiabatic scenarios of galaxies formation with present observations [2]), and the size of spots seen in *COBE* (which extend in linear scale up to 10^3 Mpc in zero curvature world models) could be similar to that of galaxies.

4 Discussion

In addition of speculations above, a spatially closed world model is also favored by fundamental considerations, such as the interpretation of origin of Inertia (determined by the distribution and by the currents of mass-energy in the Universe, see [4]), a Baryon-Symmetric Cosmology (matter and antimatter distributed in two separated hemispheres on the Universe give the lowest annihilation gamma-ray background[11, 6]), which accounts for the zero global electric charge[27]. Observational constraints upon $\lambda_\circ$ have been reviewed [3], which shows that the best upper bound derives from gravitational lens statistics[16, 21, 17]. The most recent estimate gives $\lambda \leq 0.66$ at 95% confidence [18] in flat cosmologies. Hence, one might argue that (a rough extrapolation of) such a result rules out positive curvature world models (although the number of assumptions used in the statistical model is large), but one is forced to find another solution to the Age problem. On the other hand, a less stringent approach which admits a

[4]While the dissipative physics is not yet well understood, such processes are known to facilitate the evolution of thermodynamical systems toward equilibrium.

[5]In other words, the physical processes cannot propagate faster than photon in vacuum.

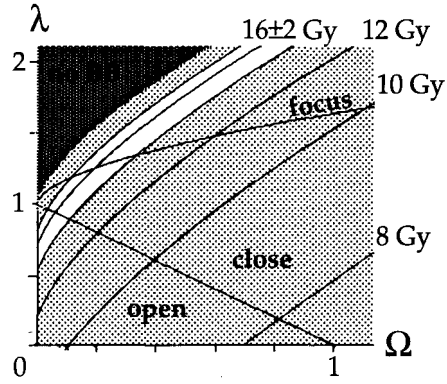

Figure 1: *Candidate World models.* The straight line $\lambda + \Omega = 1$ (zero curvature) disentangle positive (above) from negative curvatures. The white area provides us with an Age $t_o = 16 \pm 2\, h_{87}^{-1}$Gyr ($h_{87} = H_o/87\,\mathrm{km\,s^{-1}/Mpc}$), the curve $t_o = \infty$ is located upward (dark area), the other curves correspond to ages $t_o = 14, 10, 8\, h_{87}^{-1}$Gyr. For the models on the curve "focus", the last scattering surface becomes a single decoupling event (the focussing effect).

relative lens probability $P_{\rm lens} \leq 2$–10 (normalized value to the case $\Omega_o = 1, \lambda_o = 0$) depending on assumptions and data used [3] does not reject (in particular) the candidate world ($\Omega_o \approx 0.2, \lambda_o \approx 1.2$), see Fig. 1. Moreover, this model agrees with constraints on CMB anisotropies $\Omega_o + \lambda_o \leq 1.5$ [34], and provides us with stringent predictions due to the focussing effect, since the acoustic peaks in the angular power spectrum (that occurs around $l \approx 200$ in zero curvature world models) are expected at large angular scales (small l), and might not be visible if the model lies on the curve "focus". However, the pessimistic feature of such a situation is that the sampling of CMB fluctuations over the sky might not be statistically representative of the expected physics at recombination, because of the small area of the last scattering surface.

Acknowledgements. I am grateful to the organizers F. Bouchet and B. Guiderdoni for this enjoyable meeting at Les Arcs.

References

[1] U. Amaldi, W. De Boer, H. Furstenau, 1991, *Phys. Lett. B* **260** 447

[2] A. Blanchard, 1984, *Astr. Astrophys.* **132**, 360

[3] S.M. Carroll, W.H. Press, E.L. Turner, 1992, *Annual Review of Astron and Astrophys.* **30**, 499

[4] I. Ciufolini, J.A. Wheeler, 1995, *Gravitation and Inertia*, (Princeton University Press, Princeton)

[5] P. Coles, G. Ellis, 1994, *Nature* **370**, 609.

[6] F.X. Desert, E. Schatzman, 1986, *Astr. Astrophys.* **158**, 135

[7] R.H. Dicke, 1961, *Nature* **192**, 440.

[8] R.H. Dicke, 1970, *Gravitation and the Universe*, (The Jayne lectures for 1969, American Philosophical Society, Philadelphia, 1970), p. 62.

[9] R.H. Dicke, P.J.E. Peebles, 1979, in *General Relativity: An Einstein Centenary Survey*, ed. S.W. Hawking & W. Israel (Cambridge University Press, London, 1979).

[10] A.D. Dolgov, M.V. Sazhin, Ya.B. Zeldovich, *Basics of Modern Cosmology* (Editions Frontières, 1990).

[11] H.H. Fliche, J.M. Souriau, R. Triay, 1982, *Astr. Astrophys.* **108**, 256

[12] W.L. Freedman, B.F. Madore, J.R. Mould, R. Hill, L. Ferrares, R.C. Kennicutt Jr, A. Saha, P.B. Stetson, J.A. Grahan, H. Ford, J.G. Hoessel, J. Huchra, S.M. Hughes and G.D. Illingworth, 1994 *Nature* **371**, 757.

[13] A.H. Guth, 1981, *Phys. Rev. D* **23,2**, 347

[14] G.H. Jacoby, D. Branch, R. Ciardullo, R.L. Davies, W.E. Harris, M.J. Pierce, C.J. Pritchet,J.L. Tonry, D.L. Welch, 1992 *Pub. Astron. Soc. Pac.* **104**, 599.

[15] E.W. Kolb, M.S Turner, 1983, *Annual Review of Nucl. Part. Sci.* **645**, 645

[16] C.S. Kochakev, 1992, *Astrophys. J.* **384**, 1

[17] C.S. Kochakev, 1993, *Astrophys. J.* **419**, 12

[18] C.S. Kochakev, 1995, *pprint* SISSA astro–ph/9510077

[19] C. Misner, 1967, *Astrophys. J.* **151**, 431

[20] L. Montanet, 1994, *Phys. Rev. D* **50,2**, 81

[21] D. Moaz, HW. Rix, 1993, *Astrophys. J.* **416**, 425

[22] A.D. Linde, 1994, *pprint* hep-th/9410082

[23] P.J.E. Peebles, 1984, *Astrophys. J.* **284**, 439

[24] P.J.E. Peebles, *Principles of Physical Cosmology* (Princeton University Press, Princeton, 1993).

[25] M.J. Pierce, D.L. Welch, R.D. McClure, S. van den bergh, R. Racine, P. B. Stetson, 1994, *Nature* **371**, 385

[26] M.J. Rees, 1984, *J. Astrophys. Astr.* **5**, 331.

[27] J.M. Souriau, 1985, *CRAS (La vie des Sciences)* **2**, 213

[28] J.M. Souriau, R. Triay, 1996 *pprint* cpt-94/P3137

[29] S.M. Steigman, 1976, *Annual Review of Astron. and Astrophys.* **14**, 399

[30] R. Triay, 1995, *pprint* CPT-95/P.3226.

[31] R. Triay, 1995, *pprint* CPT-95/P.3227

[32] R. Triay, 1995, in: *New Trends in Geometrical and Topological Methods – Proceedings 150th anniversary of W. K. Clifford* eds H. Nencka and Ph. Combe (Ed. AMS – Contemporary Mathematics, 1996)

[33] D.A. Van den Bergh in: *The formation and the Evolution of Star Clusters* ed. K. Janes, *Pub. Astron. Soc. Pac. Conf. Ser.* **13**,183 (Astr. Soc. Pacif., San Francisco, 1991).

[34] M. White, D. Scott, 1996, *Astrophys. J.* **459**, 415

[35] S. Weinberg, 1972 *Gravitation and Cosmology* (John Wiley & Sons, eds., New York).

[36] D. Wilkinson, 1990 in: *Physical Cosmology – Proceedings 25th anniversary of the Cosmic Background Radiation Discovery* 97, eds A. Blanchard, L. Celnikier, M. Lachièze-Rey and J. Trân Thanh Vân. (Ed. Frontières, 1991)

NUMERICAL CALCULATIONS OF CMB ANISOTROPIES

Naoshi Sugiyama*
Department of Physics and Research Center for the Early Universe
University of Tokyo, Tokyo 113, Japan

Abstract

New generation satellite experiments will soon provide very high quality data of cosmic microwave background anisotropies. It will become possible to determine cosmological parameters, i.e., density parameter Ω_0, Hubble constant h, baryon density parameter Ω_B etc. to compare these data with theoretical prediction. For this purpose, very precise power spectra from theoretical calculations are needed as templates. Here the accuracy of numerical calculations of evolution of temperature fluctuations is discussed. And the validity of customary assumptions in numerical calculations are checked.

*present address: Department of Physics, Kyoto University, Kyoto 606-01, Japan
e-mail:sugiyama@tap.scphys.kyoto-u.ac.jp

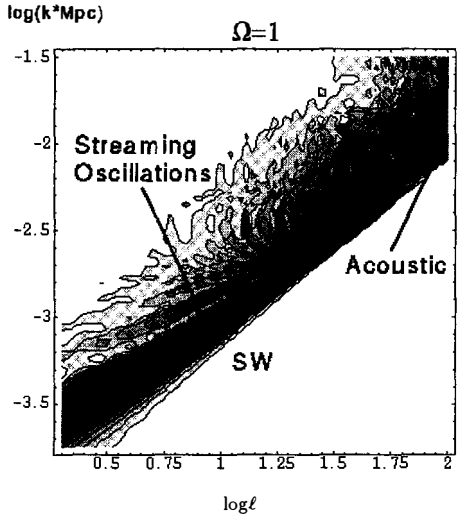

Figure 1: The contribution to the anisotropy per logarithmic k and ℓ interval $k^3|\Theta_\ell(k,\eta_0)|^2\ell/(2\ell+1)$ [4].

1. Introduction

The detection of CMB anisotropies by COBE[1] opened a new era of cosmology. Nowadays, study of CMB anisotropies becomes exact sciences. In particular we are expecting very precise measurements by new satellites, i.e., MAP and COBRAS/SAMBA in the near future. The shape and the amplitude of the power spectrum of CMB anisotropies depend on the cosmological parameter, i.e., density parameter Ω_0, Hubble constant, baryon density parameter Ω_B, number of neutrino families, initial power low index, the nature of perturbations (adiabatic or isocurvature), the nature of dark matter (cold, hot, worm or mixture) and so on. We hope to obtain these information from the measurements of CMB anisotropies. At this stage, one of the most important task for people in the theory side is to calculate the power spectrum of CMB anisotropies as accurate as possible to compare them with actual measurements. Our goal is to obtain so-called C_ℓ with less than 1% errors up to at least $\ell = 1000$. In order to attain this goal, we are organizing COMBA (COsmic Microwave Background Archive) project in February 95. We carefully checked each physical process and computational method. Now we (at least 8 independent Boltzmann codes) are agree with each others within 1% differences up to $\ell = 1000$. Another important topic of this project is how to seed up the code. Readers will find the answer in the Seljek's paper of this proceeding.

In this paper, we briefly describe the conventional method of calculations of CMB anisotropies. Then we discuss about how errors come into calculations, and how we are able to avoid them. This work is mainly based on the reference[2] by Hu, Scott, Sugiyama and White (hereafter HSSW).

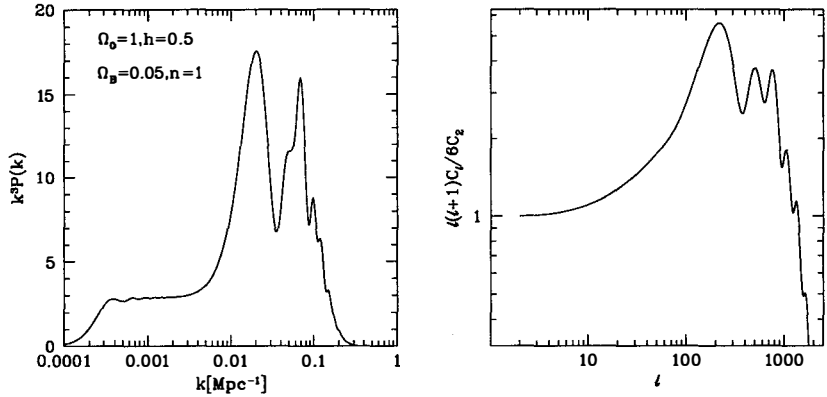

Figure 2: Left panel: Power spectrum of CMB anisotropies $k^3P(k)$ as a function of wave number k. Right panel: Power spectrum of CMB anisotropies $l(l+1)C_l$ as a function of multipole ℓ.

2. Calculations

In this chapter, we explain the standard treatment of evolution of temperature perturbations by Boltzmann equations[3]. First, the temperature fluctuation is expanded in terms of Fourier and multipole components as:

$$\frac{\Delta T}{T} = \int d^3\mathbf{k}\ e^{i\mathbf{k}\cdot\mathbf{x}} \sum_\ell (-i)^\ell \Theta_\ell(k,\eta) P_\ell(\mu)\ ,$$

where $\mathbf{k}$ is the wave number, $k = |\mathbf{k}|$, η is conformal time, μ is direction cosine, and P_ℓ is the Legendre polynomial. Secondary the Boltzmann equations for $\Theta_\ell(k,\eta)$ are solved. For each wave number, we need to calculate the time evolution of coupled equations in ℓ:

$$\frac{d\Theta_\ell}{d\eta} = k\left(\frac{\ell}{2\ell-1}\Theta_{\ell-1} - \frac{\ell+1}{2\ell+3}\Theta_{\ell+1}\right) - n_e\sigma_T a\Theta_\ell\ ,$$

where n_e, σ_T and a are free electron number density, Thomson cross section and scale factor. Eventually we obtain Θ_ℓ at the present epoch η_0. Figure 1 shows $\Theta_\ell(k,\eta_0)$ as function of k and ℓ [4]. As is shown in Figure 2, from $\Theta_\ell(k,\eta_0)$ we can obtain power spectrum $P(k)$ by taking sum in terms of ℓ as $P(k) = \sum_\ell |\Theta_\ell|^2/2\ell+1$ and C_ℓ by integrating in terms of k as:

$$\frac{2\ell+1}{4\pi}C_\ell = \frac{1}{2\pi^2}\int dk k^2 \frac{|\Theta_\ell|^2}{2\ell+1}\ .$$

In our calculations, we consider photons, baryons, dark matter (collisionless particles) and neutrinos. In this paper, we employ cold dark matter (CDM) models with power low index $n = 1$, total density parameter $\Omega_0 = 1$, non dimensional Hubble constant $h = 0.5$ and baryon density parameter $\Omega_B = 0.05$ as a standard.

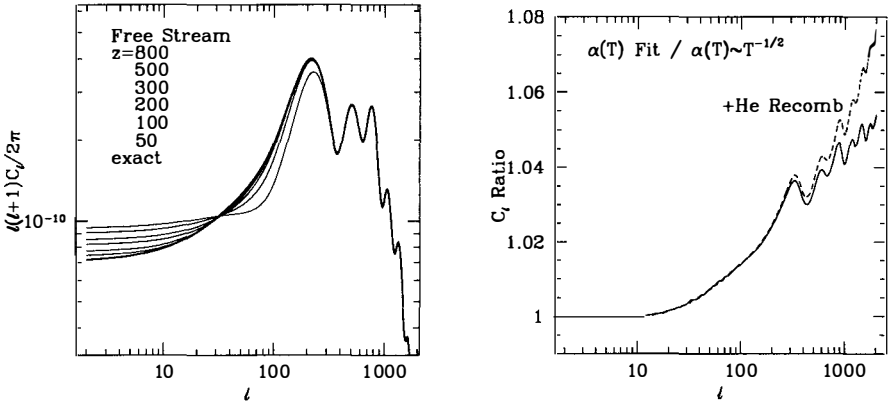

Figure 3: Left panel: Free streaming approximations. Streaming from epochs $z = 50 - 800$ with exact one. Right panel: The effect of different approximations for the physics of recombination. The solid line shows the ratio of C_ℓ using accurate values for the recombination coefficients α relative to a model with using values with scale as $T^{-1/2}$. The dashed curve shows the extra effect on the C_ℓ's of adding the He recombination.

3. Accuracy

First, we discuss about the approximations we often employ in our calculations. More detailed explanations and figures are shown in HSSW.

- Fluid approximation for neutrino: If we treat neutrino as fluid, i.e., ignoring the higher multipole components, we can save our computation time about 20 to 50%. However, this approximation causes 10% error at $\ell = 200$.
- No polarization: If we ignore photon polarization, we can speed up our calculations about $20 - 50\%$. This approximation causes very tiny error at $\ell < 400$ (less than 1%) but causes relatively large error for high ℓ (5% at $\ell = 500$ and 10% at $\ell = 1000$).
- Free streaming approximation: After the recombination (or more precisely, baryon drug) epoch, the coupling between photons and baryons become negligible. If the universe is fully matter dominated, we can employ exact analytic solution of the Boltzmann equations, so-called free streaming solution[5]. We can speed up our calculations factor several. Since this solution is exact, we expect no error comes into the final results. However, if the universe is not completely matter dominated, we have to consider the time variation of the gravitational potential. This time variation causes the integrated Sachs-Wolfe effect[4]. For our fiducial model, the matter radiation equality epoch is $z = 6000$. This is not well before the recombination epoch which is $z \approx 1100$. Even if we switch our calculation from full numerical ones to free streaming solution at $z = 50$, there is 5% error on very small ℓ's (Figure 3). Of course if we take into account integrated Sachs-Wolfe effect in our free streaming solution, we obtain perfect agreement with full numerical calculations.
- Maximum wave number: Higher and higher wave number requires more and more

computational time. Therefore we need to cut wave number at certain maximum value. The criterion we employ is $k_{\max} = 3(\ell_{\max}/c\eta_0)$ where c is speed of light and η_0 is present conformal time. Taking this criterion, we obtain accurate (less than 1% error) C_ℓ up to $\ell_{\max}$.

- Smoothing: Ideally we can obtain very smooth spectrum if we calculate huge number of k's. However it is very time consuming. Very smooth C_ℓ up to $\ell = 1000$ requires more than 5000 k's from minimum k to $k_{\max}$ in log-spacing. If we only calculate 300 k's, the resultant C_ℓ looks miserable. However, we use optimal smoothing method (Wiener filtering) for this highly oscillating data and obtain smooth C_ℓ. This smooth C_ℓ contains less than 1% error compared with full calculations.

- Recombination process:

(a) recombination coefficient α: If we employ crude approximation for the temperature dependence of α, i.e., $\alpha \propto T^{-1/2}$ as Jones and Wyse[6] did, there are 2% error at $\ell = 200$ and 4% error at $\ell = 200$. Better fitting is shown in HSSW.

(b) He recombination: If we ignore He recombination, we have 1% error at $\ell = 1000$ (Figure 3).

(c) Electron temperature: After recombination, electron temperature is not same as photon's one anymore. However this effect is very small because there is almost no interaction between photons and baryons in this stage.

Secondly, we would like to briefly mention about the robustness of the calculations. We believe following secondary fluctuations may modify the primary fluctuations.

- Reionization: If the universe becomes reionized after the recombination, this reionization causes the damping of CMB anisotropies. The damping factor of C_ℓ is $\exp(-2\tau_*)$ where τ_* is the optical depth[7]. The relation between the reionization epoch z_* and τ_* is as following: $z_* = 100\tau_*^{1/3}\Omega_0(0.025/x_e\Omega_B h)^{2/3}$, where x_e is ionizaiton fraction. Even very late reionization $z_* = 4$ causes 1.5% damping at $l > 10$. Moreover if the reionization occurs in the early epoch ($\tau_* \gtrsim 1$), a new peak appears on small ℓ which corresponds to the horizon scale of new last scattering surface.

- Gravitational lensing effect: Bending of light ray by gravitational lensing effect smears C_ℓ. It is very similar to the smearing effect by angular resolution of antenna beam. This causes about 10% effect on very large ℓ ($\ell > 1000$)[8].

- Non linear effect: Nonlinear evolution of density perturbations change the gravitational potential. It is well known that the time varying potential causes temperature fluctuations. This effect is so-called Ress-Sciama effect while the physical mechanism is the same as the integrated Sachs-Wolfe effect. This also causes small error on very large ℓ [9].

- Foreground contamination: The Sunyaev-Zeldovich effect by cluster of galaxies[10] and moving ionized bubble of QSO[11] are possible source of foreground contamination.

Although these secondary fluctuations change primary ones more than 1%, we might have hope to eliminate them by taking into account the correlation with large scale structure.

Moreover, the location of the peaks could be robust because above secondary only change the height of the peaks but the location.

4. Conclusions

For the calculation of CMB anisotropies, we have to solve Boltzmann equations quite accurately. We are now agree with each other within less than 1% error up to $\ell = 1000$ for most of existing codes. There are a lot of efforts on understanding secondary fluctuations. Very soon, we will be able to say 'This is the correct temperature power spectrum. Let's use it to analyze the data'. But don't forget we can reach this agreement by employing the **same physical process**. We have to keep to ask whether we miss some important physical process. Even though it looks negligible, it might cause significant difference on C_ℓ's. For example, no one expected that He recombination causes difference while it is small.

References

1) G.Smoot et al., 1992, ApJ, **396**, L1.
2) W.Hu, D.Scott, N.Sugiyama & M.White (HSSW), 1996, Phys.Rev., D **52**, 5498.
3) for further explanations, see N.Sugiyama & N.Gouda, 1992, Prog.Theor.Phys., **88**, 803.
4) W.Hu & N.Sugiyama, 1995, Phys.Rev., D **51**, 2599.
5) J.R.Bond & G.Efsthatiou, 1987, MNRAS, **226**, 655.
6) B.J.T.Jones & R.F.G.Wyse, 1985, A& A, **149**, 144.
7) see, e.g., N.Sugiyama, J.Silk & N.Vittorio, 1993, ApJ, **419**, L1.
8) U.Seljek, 1996, ApJ, **463**, 1.
9) U.Seljek, 1996, ApJ, in press.
10) J.R.Bond & Myers, 1996, ApJ Suppl. 103 **103**, 63.
11) N.Aghanim et al., 1996, A&A in press.

A FAST METHOD FOR COMPUTING CMB SPECTRA

U. Seljak [1], M. Zaldarriaga [2]
[1] *Harvard Smithsonian Center For Astrophysics, Cambridge, MA 02138 USA*
[2] *Department of Physics, MIT, Cambridge, MA 02139 USA*

Abstract

We developed a new fast and accurate method for calculating linear CMB anisotropies. The method is based on integration over sources along the photon past light cone. The l-th multipole moment of the CMB spectrum C_l is written as a time integral over the product of spherical Bessel function of order l and a source term expressed in terms of photon, baryon and metric perturbations. In this formulation the multipole moments depend only on a small number of variables, which can be evolved in time without expanding the photon distribution function in a large hierarchy. Moreover, the source term is a slowly varying function of wavelength and needs to be evaluated only in a small number of points, while spherical Bessel functions, which are rapidly oscillating, do not depend on the model. This new approach leads to about two orders of magnitude reduction in CPU time when compared to standard methods, while keeping better than 1% accuracy on the CMB spectrum. The method should be especially useful for accurate determinations of cosmological parameters from CMB measurements that will become possible with the next generation of satellite experiments.

1 Introduction

With the new generation of CMB experiments now being developed one hopes to accurately map the CMB sky from arcminute scales to several degree scales. The amount of data thus provided would allow for an unprecedented accuracy in the determination of cosmological parameters. As theoretical modeling shows ([3]), CMB anisotropies are sensitive to most of the cosmological parameters and have a distinctive advantage over other cosmological observations in that they probe the universe in the linear regime. This avoids the complications caused by physical processes in the nonlinear regime and allows to use powerful statistical techniques to search

over the parameter space for the best cosmological model ([3]). A large stumbling block in this program at present is the speed of theoretical model calculations, which are still too slow to allow for a rapid search over the parameter space. This limitation was partially removed by the development of approximation methods ([2], [4]), which can give fast predictions of CMB anisotropy with a 10% accuracy. However, these approximations are not accurate enough to exploit the complete amount of information that will be present in the future CMB maps from MAP and COBRAS/SAMBA satellite missions. Here we overview a new method for computing CMB anisotropies, which is both accurate and fast and can thus be used for precise tests of cosmological models.

2 Integral solution

Boltzmann equation for photons can be formally integrated over conformal time τ to obtain an expression for temperature anisotropy Δ_T,

$$\Delta_T = \int_0^{\tau_0} d\tau e^{ik\mu(\tau-\tau_0)} e^{-\kappa} \{\dot{\kappa} e^{-\kappa} [\Delta_{T0} + i\mu v_b + \frac{1}{2} P_2(\mu)\Pi] + \dot{\phi} - ik\mu\psi\}. \quad (1)$$

Here $\dot{\kappa} = an_e\sigma_T$ is the differential optical depth for Thomson scattering, Δ_{T0} is the photon density perturbation, v_b is the baryon velocity, Π is a combination of photon anisotropic stress and polarization and ϕ, ψ are the scalar metric perturbations. A similar expression can be written for the photon polarization as well as for the tensor contributions to the anisotropy and polarization.

To obtain the anisotropy spectrum one expands the plane wave in radial basis and performs ensemble and angular averaging. This leads to the following expression for the anisotropy spectrum,

$$\begin{aligned} C_l &= (4\pi)^2 \int k^2 dk P_\psi(k) |\Delta_{Tl}(k)|^2 \\ \Delta_{Tl}(k) &= \int_0^{\tau_0} S_T^{(S)}(k,\tau) j_l[k(\tau_0-\tau)] d\tau \\ S_T(k,\tau) &= g\left(\Delta_{T0} + \psi - \frac{\dot{v}_b}{k} - \frac{\Pi}{4} - \frac{3\ddot{\Pi}}{4k^2}\right) \\ &+ e^{-\kappa}(\dot{\phi}+\dot{\psi}) - \dot{g}\left(\frac{v_b}{k} + \frac{3\dot{\Pi}}{4k^2}\right) - \frac{3\ddot{g}\Pi}{4k^2} \end{aligned} \quad (2)$$

Some of the terms in the source function $S_T(\tau)$ are easily recognizable. The first two contributions in the first term are the intrinsic anisotropy and gravitational potential contributions from the last-scattering surface, while the third contribution is part of the velocity term, the other part being the $k^{-1}\dot{g}v_b$ term in the second row. These terms make a dominant contribution to the anisotropy in the standard recombination models. The first term in the second row, $e^{-\kappa}(\dot{\phi}+\dot{\psi})$, is the so-called integrated Sachs-Wolfe term and is important after recombination. It is especially important if matter-radiation equality occurs close to the recombination or in $\Omega_{\mathrm{matter}} \neq 1$ models. In both cases gravitational potential decays with time, which leads to an enhancement of anisotropies on large angular scales. Finally we have the terms caused by photon polarization and anisotropic Thomson scattering, which contribute to Π. These terms affect the anisotropy spectra at the 10% level and are important for accurate model predictions. Moreover, they are the sources for photon polarization. Equation (2) is a generalization of the tight-coupling and instantaneous recombination approximation (Seljak 1994) and reduces to it in the limit where the visibility function is a delta-function and Π can be neglected.

3 Numerical Techniques

In the standard Boltzmann method the photon distribution function is expanded to a high multipole moment and typically one has to evolve in time a coupled system of several thousand differential equations. In the method we present here one requires the source terms $S(k,\tau)$ as a function of time, so that only the photon multipole moments up to $l = 4$ are needed, plus the metric perturbations and baryon velocity. This greatly reduces the number of coupled differential equations that are to be solved. For an accurate evaluation of the lowest multipoles in the integral method one has to extend the hierarchy somewhat beyond $l = 4$, because the lower multipole moments are coupled to the higher multipoles. Because power is only being transferred from lower to higher l it suffices to keep a few moments to achieve a high numerical accuracy of $l < 5$ moments.

Another advantage of the method can be seen in the way the multipole moments are sampled in l. In the standard Boltzmann integration method one solves for the whole photon hierarchy and the resultant Δ_l is automatically obtained for each l up to some $l_{\mathbf{max}}$. The CMB spectra are however very smooth, except for the lowest l, where the discrete nature of the spectrum becomes important. This means that the spectrum need not be sampled for each l and instead it suffices to sparsely sample the spectrum in a number of points and interpolate between them. We choose to compute every 50th C_l beyond $l = 100$ in addition to 15 l modes below $l = 100$, so that a total of 45 l modes are calculated up to $l_{\mathbf{max}} = 1500$. This gives a typical (rms) error of 0.1%, with excursions of up to 0.4%. The number of integrals (equation 2) is thus reduced by 10-50 and the computational time needed for the integrals becomes comparable or smaller than the time needed to solve for the system of differential equations.

After recombination and in the absence of a time changing gravitational potential the source function often becomes negligible. This is the so called free streaming regime, where the photons are freely propagating through the universe. Most of the standard Boltzmann codes use a special free streaming algorithm to map the anisotropies from a given epoch $\tau_{\mathbf{fs}}$ into anisotropies today ([1]). In the method presented here the free streaming regime is only a special case where $S(k,\tau) = 0$ after some time $\tau_{\mathbf{fs}}$. Thus one can stop the integration at the time $\tau_{\mathbf{fs}}$ beyond which the sources are not important and there is no need for a separate algorithm to evolve the anisotropies until today. In reality the source function does not become negligible until very low redshift even in models with no late time decay of gravitational potential, which reduces the applicability of free streaming for high accuracy computations. Nevertheless, for standard CDM the contributions at $z < 10$ are negligible at 1% accuracy and this reduces the computational time in this and similar models by 50%.

The main computational cost of both standard and present method is solving the coupled system of differential equations. The number of k-modes for which the system is solved is the main factor that determines the speed of the method. For results accurate to $l_{\mathbf{max}}$ one has to sample the wavenumbers up to a maximum value $k_{\mathbf{max}} = l_{\mathbf{max}}/\tau_0$. In the standard Boltzmann method one solves for $\Delta_{Tl}(k)$ directly, so this quantity must be sampled densely enough for accurate integration. It is a rapidly oscillating function with a frequency $\Delta k \sim \tau_0^{-1}$. Each oscillation needs to be sampled in at least a few points to assure an accurate integration. To obtain a smooth CMB spectrum one typically requires 6 points over one period, implying $2l_{\mathbf{max}}$ k-mode evaluations. One can see from the decomposition in equation 2 that the rapid oscillations are caused by the oscillations in the spherical Bessel functions, which do not depend on the model, while the source function itself varies much more slowly with a frequency $\Delta k \sim \tau_{\mathbf{rec}}^{-1} \sim 50\tau_0^{-1}$. For accurate sampling of the source one therefore requires 50 times fewer k evaluations and the computational time is correspondingly reduced.

4 Conclusions

The new approach to computing CMB anisotropies has the advantage of being computationally much faster than the standard methods. Speed increases of 10^2 or greater are not only computer time savers, they may allow for the application of accurate methods to the problems that were previously only approachable through approximations or not at all. A case we have in mind are the topological defects, where one cannot assume a phase of a given mode to remain constant in time and so one cannot express the spectrum of CMB directly as an integral over the primordial power spectrum times a transfer function Δ^2_{Tl}. Instead one has to average over many random realizations of the defect network, each of which gives one realization of the spectrum. While such calculations were previously unmanageable, they become quite feasible with the method we presented here. This would then allow the accuracy of the defect model calculations to become comparable to the accuracy in the standard inflationary models. Precision tests that will be possible with the next generation of satellite missions will then be able to extend to such models as well and therefore distinguish between many different scenarios of structure formation.

References

[1] Bond, J. R., & Efstathiou, G. 1987, MNRAS, 226, 655

[2] Hu, W., & Sugiyama, N. 1995a, *Astrophys. J.* **4**, 36,456

[3] Jungman, G., Kamionkowski, M., Kosowsky, A., & Spergel, D. N. 1996, PRL, 76, 1007

[4] Seljak, U. 1994, *Astrophys. J.* **4**, 35,L87

ACCURATE SIMULATIONS OF THE MICROWAVE SKY AT SMALL ANGULAR SCALES

D. Sáez [1] and J. V. Arnau [2]
[1] *Departamento de Astronomía y Astrofísica, Universidad de Valencia, 46100 Burjassot (Valencia) Spain.*
[2] *Departamento de matemática Aplicada, Universidad de Valencia, 46100 Burjassot (Valencia) Spain.*

Abstract

Accurate simulations of the microwave sky are described. The minimal cold dark matter scenario for structure formation is used. Angular scales smaller than those of previous simulations are considered. The spectra obtained from the simulated maps are appropriately compared with the theoretical ones. Various sky coverages and levels of white noise are studied. Preliminary comments about the interest of moderate coverages of the microwave sky (~ 1600 square degrees) are presented.

1 Introduction

Numerical simulations of the microwave sky are expected to be very useful in order to compare theoretical predictions about anisotropies with experimental measurements. In this preliminary paper, some relevant aspects of small angular scale simulations are briefly discussed.

Accurate simulations at small angular scales are presented. The spectra obtained from the simulated maps are compared with those predicted from theory. The method used to do these comparisons is analyzed.

From the C_ℓ quantities corresponding to a theoretical model and the features of a certain experiment, we build up simulated maps. From these maps, the initial spectrum can be partially recovered. The differences between the initial spectrum and the recovered one are shown in some cases.

The experiments considered in our simulations are defined by: (1) an angle, θ_{min}, defining a regular network on the sky. (2) a Gaussian antenna with a full-width at half-maximum angle θ_{FWHM}, (3) a certain sky coverage and, (4) a certain level of white noise.

In all the simulations, the angular spectrum of the CMB anisotropy corresponds to the minimal cold dark matter model for structure formation.

Two cases are analyzed: Simulations with no noise and several coverages, and simulations with small coverages and a certain level of white noise.

2 Simulations

We assume the minimal cold dark matter scenario.

The values of the parameters h and Ω_B are assumed to be $1/2$ and 0.03, respectively.

From COBE [1], [2], [3] and TENERIFE [4] data, the angular power spectrum of the minimal cold dark matter model can be normalized. The C_ℓ coefficients have been taken from [5] and normalized according to the two year COBE data ($Q_{rms-PS} \simeq 18\ \mu K$, [6]).

Our numerical simulations are extended to $40° \times 360°$ regions of the sky. These regions are assumed to be uniformly covered and, consequently, the angle θ_{min} –giving the separation between neighboring points- defines the grid of the simulated maps.

Simulations are based on the expansion:

$$\frac{\delta T}{T}(\theta,\phi) = \sum_{\ell=1}^{\ell_{max}} \sum_{m=-\ell}^{m=+\ell} a_{\ell m} Y_{\ell m}(\theta,\phi), \tag{1}$$

with $\ell_{max} = 1100$. The $a_{\ell m}$ coefficients have been generated as statistically independent random numbers with variance $\langle \mid a_{\ell m} \mid^2 \rangle = C_\ell e^{(-\ell+0.5)^2\sigma^2}$ and zero mean. The quantity $\sigma = 0.425\theta_{FWHM}$ describes the Gaussian beam. The spherical harmonics have been carefully calculated. These simulations include scales smaller than those considered in previous ones (see [7], [8] and [9]). The small θ_{min} and σ values considered in our simulations (see below) require the use of large ℓ values giving information about small angular scales.

In a IBM 30-9021 VF, the CPU cost is $\sim$ 11 hours per simulation. The CPU cost for simulations of the full sky has been estimated to be $\sim$ 50 hours.

3 Extracting the angular power spectrum from a simulated map

Let us begin with some basic definitions and comments: The autocorrelation function can be defined as $C(\theta) = C_{\sigma=0}(\theta)$, where

$$C_\sigma(\theta) = \left\langle (\frac{\delta T}{T})_\sigma(\vec{n}_1)(\frac{\delta T}{T})_\sigma(\vec{n}_2) \right\rangle \ . \tag{2}$$

The angle between the unit vectors $\vec{n}_1$ and $\vec{n}_2$ is θ. The angular brackets stand for a mean on many CMB realizations. Function $C_\sigma(\theta)$ can be expanded in the following form:

$$C_\sigma(\theta) = \frac{1}{4\pi} \sum_{\ell=2}^{\infty} (2\ell+1) C_\ell P_\ell(\cos\theta) e^{(-\ell+0.5)^2\sigma^2}. \tag{3}$$

where the C_ℓ quantities define the power spectrum of the CMB. These quantities have been calculated in many theoretical models of structure formation. From Eq. (2) one easily obtains the relation:

$$C_\ell(\sigma) = e^{(-\ell+0.5)^2\sigma^2} C_\ell = \frac{32\pi^3}{(2\ell+1)^2} \int_0^\pi C(\theta) P_\ell(\cos\theta) \sin\theta d\theta \ . \tag{4}$$

The method used in order to extract the spectrum from a given map of the CMB sky is as follows: First, the autocorrelation function $C(\theta)$ is estimated from Eq. (2). In order to do this, many pairs of directions $(\vec{n}_1, \vec{n}_2)$ forming a given angle θ are randomly placed on the available map to obtain a good average. Afterwards, Eq. (4) is used to get C_ℓ quantities. An accurate determination of $C(\theta)$ requires various full realizations of the CMB sky. If these realizations are not available, there are errors in the resulting autocorrelation function and, consequently, there are errors in the C_ℓ coefficients given by Eq. (4). Since only a realization of the CMB sky is available, there is an unavoidable indetermination in the CMB spectrum (cosmic uncertainty). Unfortunately, a full coverage of our CMB sky is not available. Up to date, only small regions of the sky have been observed (except in the case of large angular scales). Future satellite experiments will give a more complete coverage.

Let us now consider some uncertainties in $C(\theta)$ appearing as a result of the existence of both an angle θ_{min} separating neighboring nodes of the grid and an angle θ_{max} associated to a partial coverage of the sky. In other words, from Eq. (2), the function $C(\theta)$ can be only obtained in a certain interval $(\theta_{min},\theta_{max})$. For angles smaller than θ_{min}, the map have not any information. As a result of partial coverage, the great number of $(\vec{n}_1, \vec{n}_2)$ pairs required by Eq. (2) is only feasible for angles smaller than a certain θ_{max}. This means that the maps have not information for too small ($\theta < \theta_{min}$) and too large ($\theta > \theta_{max}$) angular scales. This discussion holds for both observation maps and simulated ones. Even if the temperatures have been accurately measured in the grid nodes, the integration involved in Eq. (4) can only be extended to the interval $(\theta_{min},\theta_{max})$ –not to the interval $(0,\pi)$– and, consequently the resulting $C_\ell(\sigma)$ quantities are different from the true $C_\ell(\sigma)$ coefficients. This unavoidable problem is a result of intrinsic limitations in the maps and, consequently, we must be cautious with any mathematical method creating (modifying) information outside (inside) the interval $(\theta_{min},\theta_{max})$ in order to look for the true $C_\ell(\sigma)$ quantities.

The spectrum extracted from maps –as described above– is to be compared with a theoretical spectrum estimated as follows: first, Eq. (3) and the C_ℓ coefficients of the assumed model –for $2 \leq \ell \leq 1100$– are used in order to get the function $C_\sigma(\theta)$ in the interval $(0, \pi)$; afterwards, the $C_\ell(\sigma)$ quantities –for $40 \leq \ell \leq 1000$– are obtained from Eq. (4). The integral appearing in this equation is calculated in the interval $(\theta_{min},\theta_{max})$. The resulting spectrum is hereafter called *modified spectrum* to be distinguished from the *true spectrum* corresponding to the theoretical model under consideration.

Results for several values of θ_{min} and θ_{max} are displayed in Fig. 1, where the continuous line corresponds to the true C_ℓ coefficients of the chosen model (see Sec. 2). In this Figure, the value $\theta_{max} = 9°$ is fixed, while the angle θ_{min} takes on the values $2.5'$ (pointed line), $5'$ (dashed line), and $10'$ (pointed-dashed line). From $\ell = 40$ to $\ell = 1000$, the true C_ℓ quantities are different from those obtained from maps. It is not necessary to recover the true C_ℓ quantities from maps. On the contrary, the theoretical modified spectra –corresponding to given values of θ_{min}, θ_{max}, and σ– should be compared with the modified spectra directly extracted from the maps (for the same values of θ_{min}, θ_{max}, and σ).

4 Results

In the simulations considered in this section, the beam size is $\sigma = 4.25'$ ($\theta_{FWHM} = 10'$), and the angles θ_{min} and θ_{max} take on the values $5'$ and $9°$, respectively.

It has been verified that the chosen value of θ_{max} is compatible with the simulation coverages

under consideration.

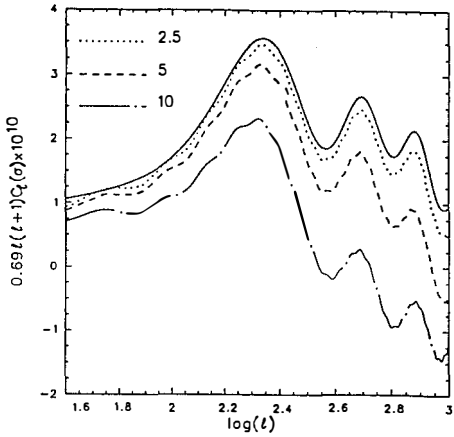

Figure 1. Quantity $0.69\ell(\ell+1)C_\ell(\sigma)\times10^{10}$ as a function of $\log(\ell)$ in various cases. Solid line corresponds to $\sigma = 0, \theta_{min} = 0$ and, $\theta_{max} = \pi$ (true C_ℓ quantities). The remaining curves correspond to $\theta_{max} = 9°$, $\sigma = 0$, and the θ_{min} values –in minutes– displayed inside the panel.

The panels of Fig. 2 display the theoretical modified spectrum (solid line) and the corresponding spectrum obtained from simulations. No white noise has been included. The left and right panels has been obtained from three maps of $40° \times 360°$ (hereafter, C1 coverage) and one map of $40° \times 40°$ (C2 coverage), respectively.

Fig. 2 shows that the simulated spectra essentially oscillate around the modified theoretical one. This is a very good news in order to stablish comparisons with theoretical models (see Sec. 5). Fig. 2 also shows that, for large ℓ values, the curves corresponding to simulations lie slightly below the theoretical ones. This fact suggests the existence of a systematic error for large ℓ values (see Sec. 5 for an interpretation of this fact).

Finally, another simulation has been performed in order to estimate the possible combined effect of uncorrelated noise and partial coverages. It has been verified that this combined effect is negligible for the coverages C1 and C2 and a noise level of 27.3 μK. Since maps involving pure white noise lead to no correlations ($C(\theta) = 0$), only a combination of pure white noise and partial coverage can give nonvanishing C_ℓ coefficients. In order to test the importance of this combined effect, a $40° \times 40°$ map has been built up. This map only involves pure uncorrelated noise at a level of 27.3 μK. The resulting C_ℓ quantities have been extracted as in any other case. The values of $0.69\ell(\ell+1)C_\ell \times 10^{10}$ have appeared to be smaller than 10^{-2} for any scale. These values are much smaller than those of Fig. 2 (order unity), which correspond to cosmological signals. In conclusion, the presence of white noise at a level of 27.3 μK can only be important in the case of coverages much smaller than C2. According to our expectations, it has been verified that the smaller the coverage, the greater the relevance of uncorrelated noise.

5 Discussion

The use of modified spectra (see Sec. 3) allows us to separate the effects of smoothing and pixelization from other effects. The form of the modified spectra depends on θ_{min}, θ_{max} and σ. These spectra are to be compared with those extracted from observations or simulations. The main problems with this comparison are now discussed.

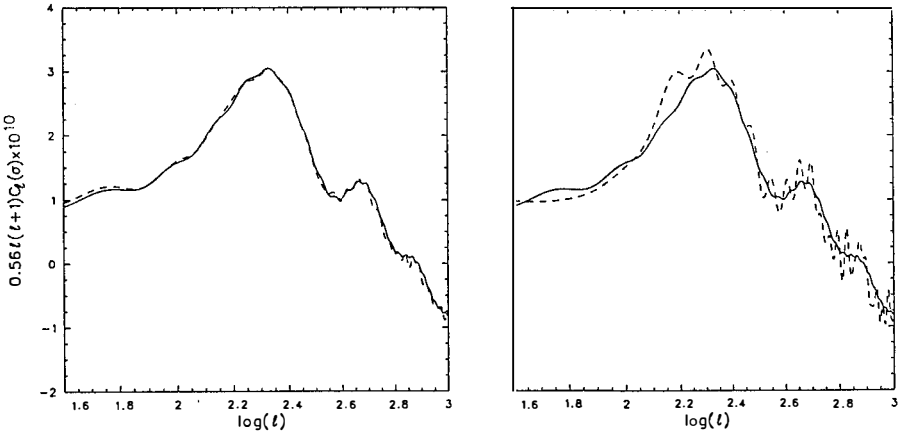

Figure 2. Quantity $0.69\ell(\ell+1)C_\ell(\sigma) \times 10^{10}$ as a function of $\log(\ell)$. The continuous line shows the modified theoretical spectrum and the dashed line exhibits that extracted from simulations. left and right panels correspond to the C1 and C2 coverages defined in the text, respectively.

In order to obtain $C(\theta)$ from a given map, many pairs $(\vec{n}_1, \vec{n}_2)$ are randomly located on the map. Direction $\vec{n}_1$ can be randomly placed on a node of the grid, but then, for a given θ, direction $\vec{n}_2$ does not point towards another node. This mean that the temperature in the direction $\vec{n}_2$ is not known and, consequently, it must be estimated by using interpolations in the grid. This is a mathematical method introducing wrong information. It has been verified that the method is good for angles lying in the interval $(\theta_{min}, \theta_{max})$. The small systematic error described in Sec. 4 seems to appear as a result of the mentioned interpolation. It decreases as θ increases; hence, it is more important for large ℓ values. This error remains small up to $\ell = 1000$ (see Fig. 2). In the case of large θ values, great coverages avoid problems with the location of pairs $(\vec{n}_1, \vec{n}_2)$.

Sky coverage is important. Figure 2 shows the deviations between theoretical and simulated spectra for two coverages. As expected, the greater the coverage, the smaller the deviations [10]. Simulations have showed some relevant features of these deviations. It is noticeable that an important part of the deviations shows an oscillatory character around a curve very close to the theoretical one. It can be seen that even in the case C2, the best fitting to the oscillating values is a curve very close to the theoretical one. This fact enhances the interest of moderated coverages as C2 (right panel of Fig. 2), which lead to a spectrum very similar to that of C1

coverages (left panel of Fig. 2), at least, for $\ell > 200$ and after removing oscillatory deviations. The interest of C2 and similar coverages increases if it is taking into account that maps with these features can be obtained by measuring in selected regions with small contamination.

Uncorrelated noise does not appear to be relevant for the coverages considered in this paper; however, this noise could be important in the case of smaller coverages.

Other admissible normalizations of the C_ℓ coefficients would keep the main results of this paper unaltered. Indeed, these results are independent from normalizations.

Acknowledgements. This work has been supported by the Generalitat Valenciana (project GV-2207/94). Calculations were carried out in a IBM 30-9021 VF at the Centre de Informática de la Universidad de Valencia.

References

[1] Smoot et al., 1992, *Astrophys. J.* **396**, L1

[2] Bennett et al., 1992, *Astrophys. J.* **396**, L7

[3] Wright et al., 1992, *Astrophys. J.* **396**, L13

[4] Hancock et al., 1994, *Nature* **367**, 333

[5] Sugiyama N., 1995, *Astrophys. J. Suppl. Ser.* **100**, 281

[6] Górski et al., 1996, Astro-ph/9601063

[7] Hinsaw G., Bennett C.L., Kogut A., 1995, *Astrophys. J.* **441**, L1

[8] Kogut A., Hinsaw G., Bennett C.L., 1995, *Astrophys. J.* **441**, L5

[9] Jungman G., Kamionkowski M., Kosowsky A., Spergel D.N., 1996, Astro-ph/9512139

[10] Scott D., Srednicki M., White M., 1994, *Astrophys. J.* **421**, L5

STRUCTURE FORMATION IN INFLATIONARY COSMOLOGIES

Andrew R. Liddle
Astronomy Centre, University of Sussex, Falmer, Brighton BN1 9QH, U. K.

Abstract

A brief account is given of large-scale structure modelling based on the assumption that the initial perturbations arise from inflation. A recap is made of the implications of inflation for large-scale structure; under the widely applicable slow-roll paradigm inflation adds precisely two extra parameters to the normal scenarios, which can be taken to be the tilt of the density perturbation spectrum and the amplitude of gravitational waves. Some comments are made about the *COBE* normalization. A short description is given of an analysis combining cosmic microwave background anisotropy data and large-scale structure data to constrain cosmological parameters, and the case of cold dark matter models with a cosmological constant is used as a specific illustration.

1 Introduction

In the medium term, the cosmic microwave background (CMB) shall undoubtedly prove an extremely powerful tool in constraining cosmological parameters. Already, the *COBE* observations of large-angle anisotropies provide the most accurate and unambiguous constraint on the spectra of perturbations in the universe. However, at the present time the best route to constraining cosmological parameters is not through the CMB alone, but from the combination of microwave data with a large number of measures of the power spectrum from large-scale structure observations.

In recent work, my collaborators and I have sought to test a wide parameter space of large-scale structure models, using linear and quasi-linear theory. We have written three papers on this topic, covering cold dark matter (CDM) models in open universes[1)] and in flat universes with a cosmological constant[3)], and the case of a critical density universe[2)] where we also allow a fraction of the dark matter to be hot. The key ingredient of our work is to take the inflationary hypothesis seriously, and to take advantage of the extra parameters that slow-roll inflation lends to large-scale structure modelling.

There isn't space here to give the full details of this work, so instead I'll concentrate on a couple of aspects and illustrate the outcome by showing some results from our investigation of CDM models in flat universes[3)].

2 Inflationary parameters

The simplest approximation for the production of perturbations from inflation, that it gives a scale-invariant density perturbation spectrum and nothing else, is woefully inadequate to describe the output of most inflation models. It is necessary to make a better approximation, which acknowledges that as well as producing density perturbations inflation will produce a spectrum of gravitational waves. Based on the slow-roll approximation, one finds that inflation predicts power-law spectra of both density perturbations and gravitational waves. This gives a total of four parameters, two amplitudes and two spectral indices. This turns out to be an excellent approximation for almost all known inflationary models, and may well be all that is ever needed.

Interestingly, these four parameters are not all independent. The reason is that we have extracted two continuous functions, the spectra, from a single input function, the inflaton potential. The only way you can get two continuous functions from one is if they are related, and at this level of approximation it turns out that one of the four parameters is redundant. This is interesting, because it offers the possibility of a consistency check on the inflationary hypothesis which is *independent* of the choice of inflationary potential.

The three inflationary parameters for large-scale structure are

1. The amplitude of density perturbations, $\delta_{\rm H}$, defined below.
2. The spectral index of the density perturbations n.
3. The relative contribution of gravitational waves to large-angle CMB anisotropies, $R \equiv C_\ell^{\rm GW}/C_\ell^{\rm DP}$, where ℓ could for instance be taken to be 10, the *COBE* pivot scale.

The equation describing the redundancy is

$$R \simeq -2\pi n_{\rm GW}\,, \tag{1}$$

where $n_{\rm GW}$ is the spectral index of the gravitational waves. Although a very distinctive signature of inflation, it seems very unlikely that one will ever be able to carry out this test since $n_{\rm GW}$ is almost certainly impossible to measure. By contrast, one should be extremely optimistic about measuring the non-degenerate parameters n and R.

One sometimes sees the relation $R \simeq 2\pi(1-n)$ quoted as an inflationary signature. This is in fact the prediction of a specific model, the power-law inflation model (which always gives $n < 1$), and is not general enough to describe generic slow-roll inflation, for which n and R enter independently at the same order in the slow-roll expansion. It is quite a useful relation nevertheless, because for $n < 1$ it gives about the largest amount of gravitational waves one finds in any inflation model, and so a good range to consider is R going from 0 up to this value. However, for purposes such as fitting CMB anisotropies, there seems little purpose in adopting such a relation, because simply by including n and R independently one is looking at the generic slow-roll inflation situation. Since one is anyway fitting for a large number of cosmological parameters, the addition of one more can hardly degrade the fit at all and has the enormous benefit of generality.

If one has a particularly complex inflationary potential, one might need more parameters to describe its influence. This can be achieved by a technique known as the slow-roll expansion. Up to a point, having to introduce extra parameters is actually a good thing, because if you feel you need them to describe the data, that means that potentially there is more information, in the form of extra parameters, to be learnt about inflation from the observations. Since there are a lot of parameters anyway, a couple more shouldn't particularly degrade the fit. Equally though, it would be possible to have too much of a good thing and I can't imagine that anyone would be pleased if it was thought that inflation might add say twenty new parameters. Fortunately that will not be the case[1].

3 Cosmological parameters

When one considers short-scale information, such as large-scale structure data, the theoretical prediction depends on the whole range of cosmological parameters, including

1. The Hubble parameter h.
2. The total matter density Ω_0.
3. The cosmological constant Λ.
4. The baryon density $\Omega_{\rm B}$.
5. The hot dark matter (HDM) density Ω_ν. (It is always assumed there'll be some CDM).
6. The effective number (at the photon temperature) of massless species $g_\star$.
7. The redshift of reionization $z_{\rm R}$.

Further complexity can be introduced in many ways, for example by allowing the dark matter to decay, by allowing the HDM to be composed of more than one particle type or by allowing the hot component to violate the usual mass–density relation.

All of these parameters have effects on various kinds of observations, and coupled with the three input parameters from inflation give a fairly large number of parameters to be dealt with. The sort of data a new generation CMB anisotropy satellite might produce could quite conceivably just simultaneously fit all, or a sizeable subset, of them, but present data are a long way off and it is usual to work within some simplifying assumptions. Our analyses have been unusual in that they attempt to retain all the inflationary parameters, as well as a reasonable number of the cosmological ones.

[1]Though it is possible to have models, such as double inflation, that have features so drastic that they can't be described within this perturbative framework at all.

Although the list of cosmological parameters looks intimidating, combining all the options seems very unattractive. Also, various scalings can be utilized, since many changes have an effect very similar to changing the Hubble parameter (the main effect of which is to shift the epoch of matter–radiation equality), which allows many options to be considered at once. The epoch of reionization is only important if one considers intermediate-scale CMB anisotropies.

4 The *COBE* normalization

More than anything else, this section is a request to those carrying out fittings to the *COBE* data to quote the best-fit amplitude of the *matter* power spectrum, as well as radiation anisotropy quantities such as $Q_{\rm rms}$. In general it is far from trivial to get from one to the other. It doesn't really matter in what form this is done, but I'd like to put in a word in favour of a quantity we call $\delta_{\rm H}$.

When the spectrum of density perturbations $\mathcal{P}$ is defined so that the variance is

$$\sigma^2(R) = \int_0^\infty W^2(kR)\,\mathcal{P}(k)\,\frac{{\rm d}k}{k}\,, \tag{2}$$

where $W(kR)$ is whatever window function does the smoothing, then the spectrum can be broken up into pieces as

$$\mathcal{P}(k) = \left(\frac{k}{aH}\right)^4 \delta_{\rm H}^2(k)\,T^2(k,t)\,\frac{g^2(\Omega)}{g^2(\Omega_0)}\,. \tag{3}$$

The final term is the usual growth suppression factor, which can be applied at any epoch provided the Ω at that time is used. This term vanishes if $\Omega = 1$. The transfer function is normalized to unity on large scales. In general it may be time dependent, for example if there is an HDM component, but in a CDM universe it is time independent. The very first term carries the remaining time dependence, that of a critical density CDM universe.

Finally then, $\delta_{\rm H}$ is the initial spectrum of perturbations. It is time-independent, and amounts (when multiplied by the growth suppression term) to a proper definition of what is meant by the perturbation at horizon crossing. In the special case $n = 1$ it is also k-independent. One can specify a fit to the matter power spectrum by giving its value at $k = a_0 H_0$, the present Hubble radius. For the four-year *COBE* data, one finds for CDM models with a cosmological constant[3] that

$$\delta_{\rm H}(a_0 H_0) = 1.94 \times 10^{-5}\,\Omega_0^{-0.785-0.05\ln\Omega_0}\,\exp[f(n)] \tag{4}$$

where

$$f(n) = -0.95(n-1) - 0.169(n-1)^2 \quad \text{No gravitational waves} \tag{5}$$

$$= 1.00(n-1) + 1.97(n-1)^2 \quad \text{Power-law inflation} \tag{6}$$

A similar fitting function can also be found for the open universe case. The joy of this formula is that it says everything about the *COBE* normalization in a single fitting formula. To a good approximation, this fit is *independent* of h, $\Omega_{\rm B}$ and the nature of the dark matter.

5 CDM models with a cosmological constant

Our strategy has been to assemble observational data which can be interpreted in terms of linear and quasi-linear theory. This allows a rapid assessment of which regions in parameter space are

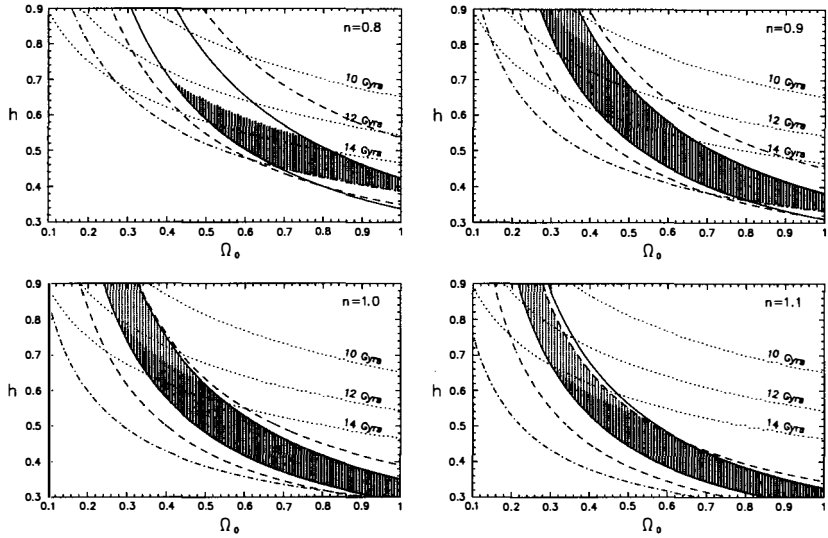

Figure 1: Varying n, but with no gravitational waves, for spatially flat CDM models. All constraints are plotted at 95 per cent confidence, and models are normalized to the 4 year *COBE* data. The constraints are galaxy clustering (solid), cluster abundance (dashed) and DLAS abundance (dot-dashed). Bulk flows and quasar abundance are less constraining. Contours of constant age are shown as dotted lines. The allowed region is shown with two different shadings, both highlighting the parameter space not excluded at more than 95 per cent confidence on any single piece of data. The lighter shading shows models where the optical galaxies have to be antibiased at $8h^{-1}$ Mpc. Finally, the unshaded region in the $n = 0.8$ plot which is allowed by all plotted data is excluded by Doppler/acoustic peak height.

allowed or disallowed. The observations considered are large-angle CMB anisotropies (*COBE*), intermediate angle CMB anisotropies, bulk motions, galaxy clustering and the abundances of galaxy clusters, quasars and damped Lyman alpha systems (DLAS). Extra considerations that can be brought into play are the age of the universe, suppression of intermediate angle anisotropies by reionization and the question of whether (optically identified) galaxies are permitted to be anti-biased.

Figure 1 shows the sort of constraints that can be applied to CDM models in spatially flat universes. These plots show tilt n, but not gravitational waves. There is a sizeable allowed region for each n shown, so observations do not really constrain the inflationary parameters. I'll just make some brief points about these plots.

The age problem is usually cited as motivation for going to cosmological constant models. However, within the region fitting large-scale structure observations, the low density models are actually younger than the high density ones. Of course, as Ω_0 approaches one the required h is alarmingly low, and one might feel inclined to introduce a hot component, which permits larger h with critical density.

In the low density region, optical galaxies typically have to be anti-biased (and of course *IRAS* galaxies more so). This is thought unlikely, though it's not clear exactly what observations this is supposed to be in conflict with. For $n = 0.8$, there is a region which is allowed by all data *except* intermediate-scale CMB anisotropies; in that region of parameter space there isn't

really a Doppler/acoustic peak at all. This is a sign of things to come; intermediate CMB anisotropies have the potential to exclude swathes of parameter space in the future.

6 Conclusions

Cosmologists are beginning to take seriously the possibility that one can determine the whole range of cosmological parameters. Within that context, one appreciates that it is possible to also include information from inflation, and attempt to fit for inflationary parameters at the same time as the cosmological parameters. The most popular inflationary paradigm, the slow-roll approximation, only introduces two extra parameters (n and R) that one didn't have to consider anyway, and there is good reason to be optimistic that one can constrain these.

However, once one takes the extra inflationary input into account, it is clear that present observational data fall some way short of providing any telling constraints. We have found that it is possible to get an adequate fit to present data within almost any context. There are viable regions of parameter space for

- **CDM models[2]:** Requires some or all of low h, high $\Omega_{\rm B}$ or tilt to $n < 1$. Gravitational waves don't help much, but they are not very strongly constrained. It is however very hard to fit the data for $h \geq 0.50$. Adding extra massless species or decaying dark matter will also work though we haven't investigated them in detail ourselves.
- **CHDM models[2]:** The same general picture as CDM models, but allows a higher value of h, at least up to 0.6, provided the amount of hot dark matter is chosen wisely.
- **Low density CDM[1,3]:** Can be made to work either in the open case or in the flat case with a cosmological constant. Observationally, no strong preference between the open and flat cases.

This situation should not remain for long. We stand at a tantalizing time, where observations are just good enough to exclude the more extreme inflationary models. We can look forward in the near future to a time when inflationary and cosmological parameters are extremely well determined, at which point we can expect most inflation models to be ruled out. Or maybe even all!

Acknowledgments: I thank my collaborators on work described herein, namely David Lyth, Dave Roberts, Bob Schaefer, Qaisar Shafi, Pedro Viana and Martin White. I also thank Pedro (again!) for producing the figure. I am supported by the Royal Society and acknowledge use of the Starlink computer system at the University of Sussex.

References

I regret there has been no space here to provide an adequate reference list. Full references can be found in the papers cited here; apologies to the vast number of people who are missing out!

1. A. R. Liddle, D. H. Lyth, D. Roberts and P. T. P. Viana, Mon. Not. Roy. Astr. Soc. **278**, 644 (1996).
2. A. R. Liddle, D. H. Lyth, R. K. Schaefer, Q. Shafi and P. T. P. Viana, Mon. Not. Roy. Astr. Soc., to appear (1996), astro-ph/9511057.
3. A. R. Liddle, D. H. Lyth, P. T. P. Viana and M. White, Mon. Not. Roy. Astr. Soc., to appear (1996), astro-ph/9512102.

COBE–DMR 4–Year PE–Filtered Sky Maps

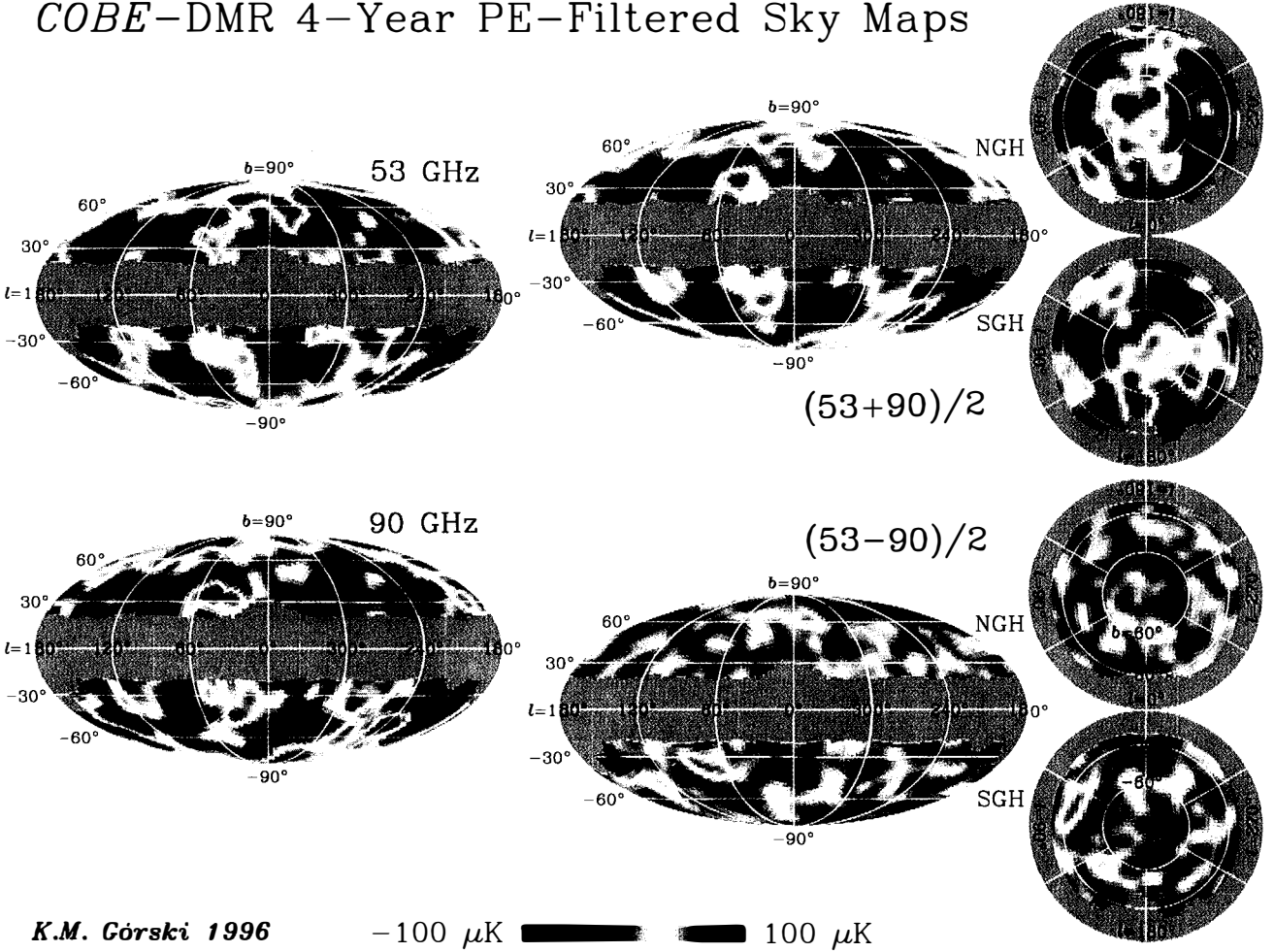

K.M. Górski 1996

–100 μK 100 μK

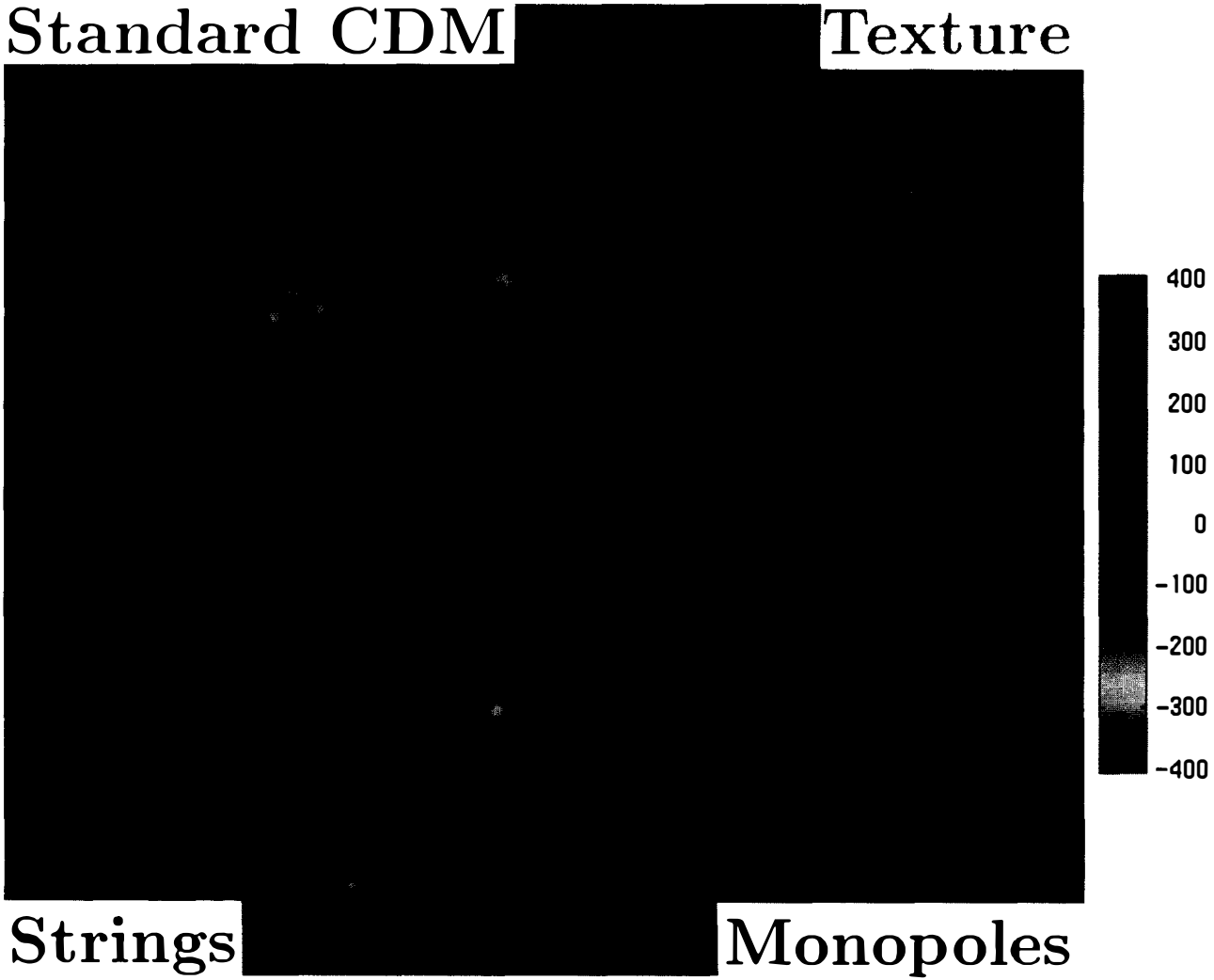

Plate II (figure
Turok's contribution)
degree square patches
microwave sky accord
the four theories disc
here. From top
anticlockwise : sta
CDM, cosmic st
monopoles and texture
colour scale shows
temperature contrast δ
microKelvin, adoptin
COBE normalisation
Coulson et al. (1994)
with a sky rms on 10°
μK. The standard devi
of the string, monopol
texture maps are $\sigma =$ 6
and 63 mK respectively

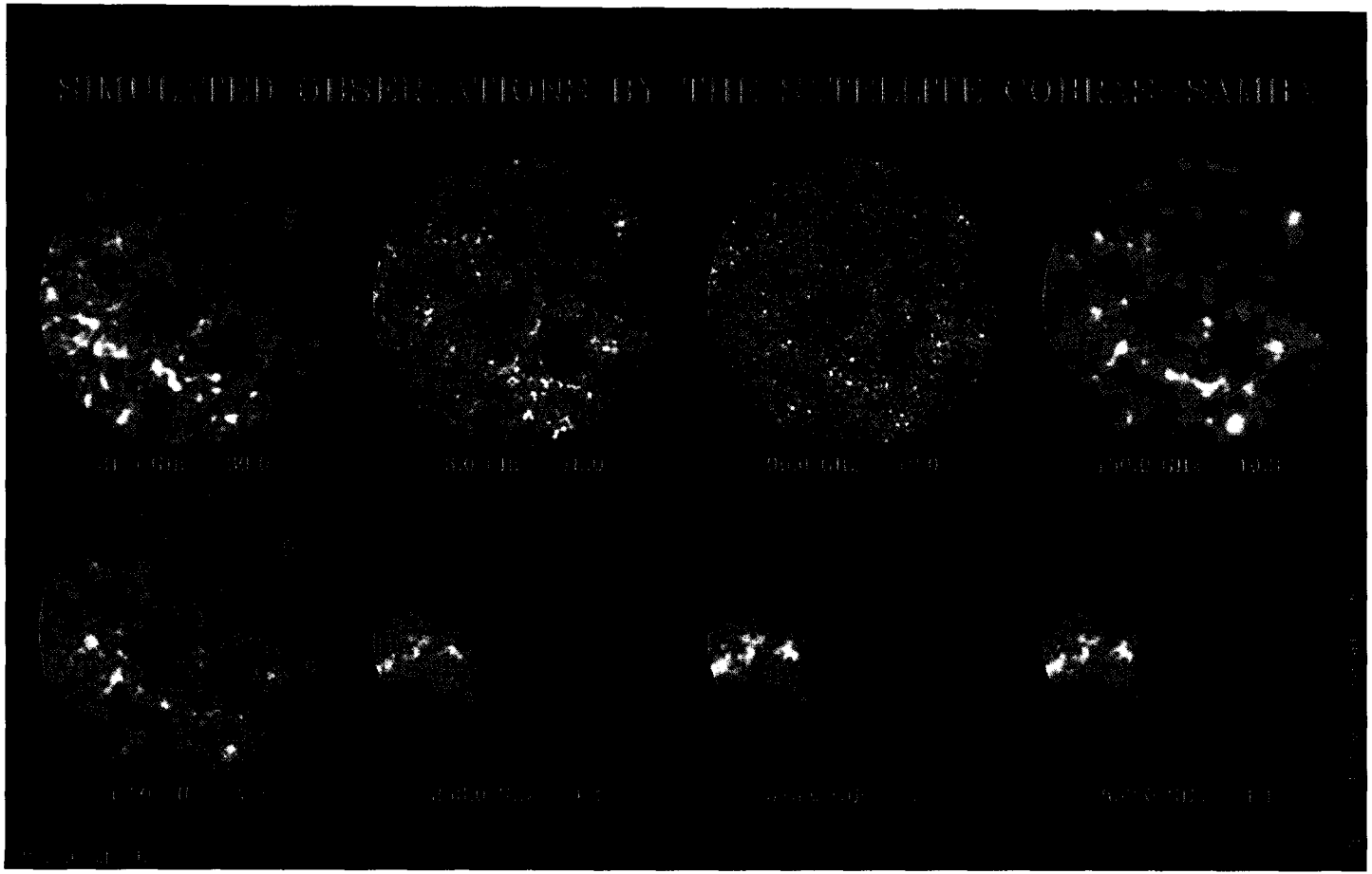

Plate III (in Gispert & Bouchet): Simulated maps of 9 degree diameter, as observed by *COBRAS/SAMBA* . From left to right and from top to bottom are displayed the first three channels of the LFI instrument followed by the *5* channels of the HFI instrument (see Table 1). The *rms* level of the foregrounds corresponds approximately to their median value (cf. BGBP).

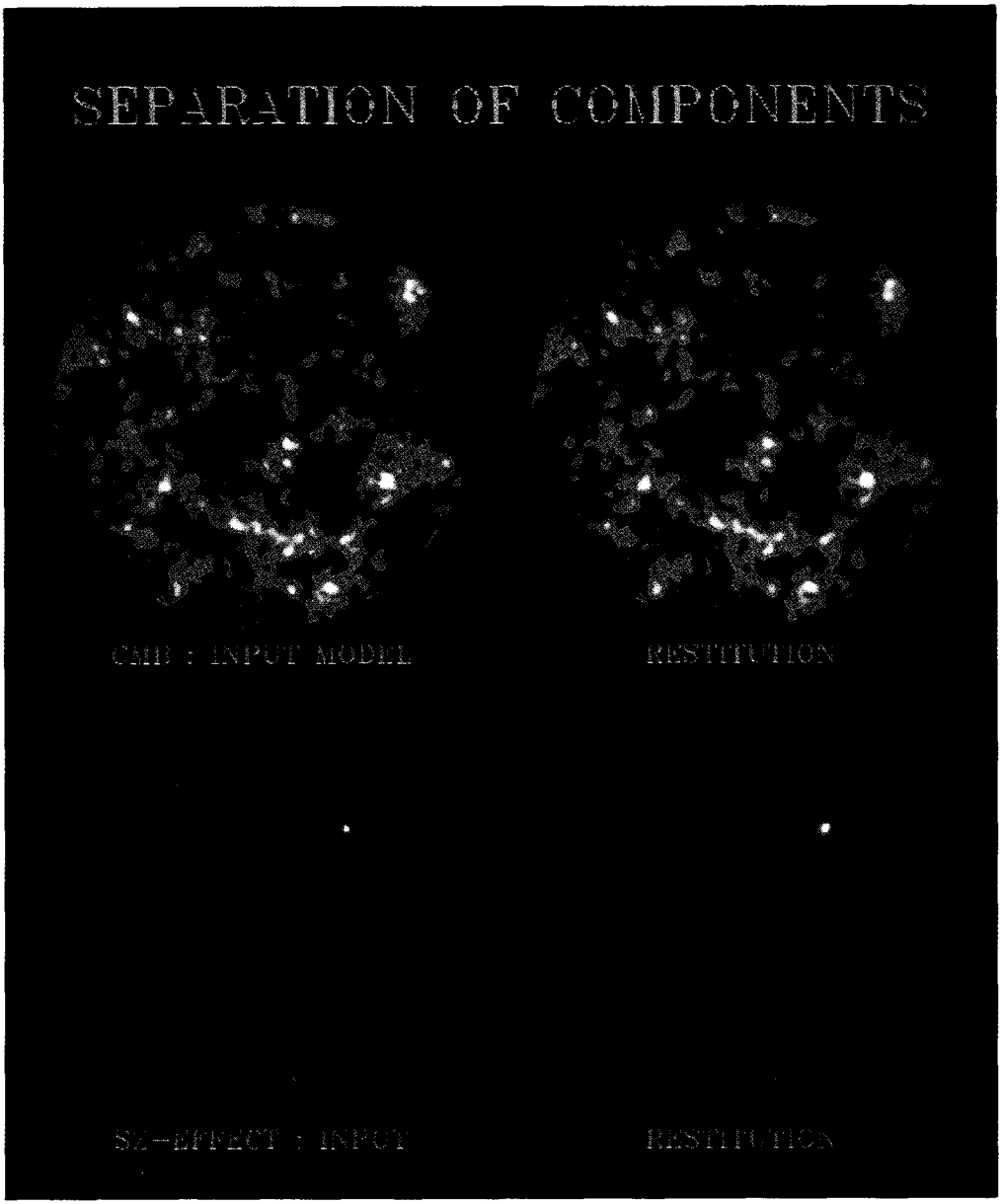

Plate IV (in Gispert & Bouchet): An example of component separation of the "observations" of the color plate III. The left column shows the template maps used in the simulation while the right column shows the recovered maps of the $\Delta T/T$ primary anisotropies (top row) and of the y parameter of the Sunyaev-Zeldovich effect (bottom row).

Open Universes from Bubbles: Introduction & Update

J.D. Cohn [1]
[1] *Dept. of Physics, Univ. of California, and LBNL, Berkeley, USA*

Abstract

This is an introduction to models of open universes originating from bubbles, including a summary of recent theoretical results for the power spectrum.

A flat ($\Omega_{tot} = 1$) universe has long been considered a generic prediction of inflationary [1] models. It has recently been demonstrated that inflation can also produce viable open ($\Omega < 1$) universes [2]. As the data on Ω has not yet converged, further investigation of these models is worthwhile. In the following, why and how bubbles give open universes is reviewed, the main features of the new models are outlined and current results and questions are summarized. Due to space limitations, this is necessarily just an overview, and readers are referred to the cited papers and their references for more in depth discussion and comprehensive referencing.

The basic reason bubbles give an open universe can be illustrated with empty Minkowski space, which does not have a unique coordinate system leading to a metric of the form

$$ds^2 = d\eta^2 - a^2(\eta) d\sigma^2 \,. \tag{1}$$

In empty space ($\rho = 0$), with zero cosmological constant ($\Lambda = 0$), the curvature k obeys

$$H^2 = \left(\frac{\dot{a}(\eta)}{a(\eta)}\right)^2 = \frac{-k}{a^2(\eta)} \,. \tag{2}$$

Consider the two coordinate systems for Minkowski space shown in figure one. On the left, lines of constant time are shown for a coordinate system with metric

$$ds^2 = dt^2 - dx^2 \,, \tag{3}$$

so one can read off that $a(t) = 1$. As a result, for this coordinate system,

$$\left(\frac{\dot{a}(t)}{a(t)}\right)^2 = 0 = -k \,, \tag{4}$$

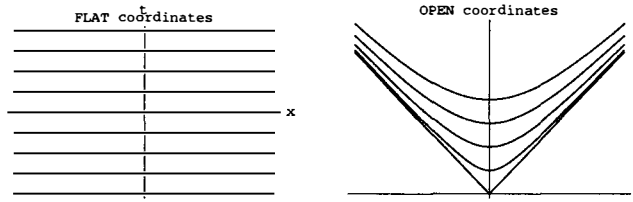

Figure 1: Lines of constant time in two coordinate systems for Minkowski space

the universe has $k = 0$ and is therefore flat.

A second coordinate system (T, χ) is shown on the right. Here, lines of constant time T are shown. In terms of (x, t), we have $T = \sqrt{t^2 - x^2}$, $\tanh \chi = x/t$. The metric becomes

$$ds^2 = dT^2 - T^2 d\chi^2 \,. \tag{5}$$

So in this case, we identify $a(T) = T$. Then,

$$\left(\frac{\dot{a}(T)}{a(T)}\right)^2 = \frac{1}{T^2} = -\frac{k}{T^2} \Rightarrow k = -1 \,, \tag{6}$$

an open universe.

In empty space, there is no reason to prefer either coordinate system. However, if there is matter present, one or the other might be preferred. For example, if the background matter distribution is homogeneous in space only in a particular coordinate system, the metric has the form eqn.(1) only for that choice of coordinates. A bubble is said to create an open universe because inside it the (T, χ) coordinate system is preferred.

To get a bubble, start with a system (here described by a field ϕ) stuck in a false vacuum. A bubble forms when a region of space, the bubble interior, tunnels to the true vacuum. An example of a potential where this could happen is shown on the left of figure two. After

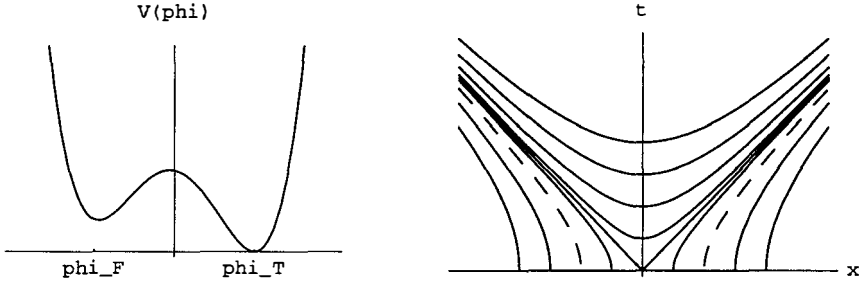

Figure 2: On the left, a potential with a false and true vacuum. On the right, lines of constant ϕ after the bubble nucleates.

tunneling, there is a true vacuum interior, where $\phi = \phi_T$, a bubble (domain) wall, and a false vacuum exterior where $\phi = \phi_F$. The lowest energy solution for tunneling in Minkowski space [3] has spherical $O(4)$ symmetry, $\phi = \phi(x^2 - t^2)$. As the matter (the field ϕ) is constant on

surfaces of constant $t^2 - x^2 = T^2$, it is natural to use the open coordinates [4], where the matter is homogeneous in space.

On the right side of figure two is a spacetime diagram showing lines of constant ϕ. The dashed line is the bubble wall, and the horizontal axis is the nucleation time. As a function of the flat coordinate time t, the bubble wall moves out. Classically the energy difference between the false and true vacua (the latent heat) goes into accelerating the wall outwards. Inside the future light cone of the center of the bubble is a patch with open coordinates. As the light cone is $T = 0$ in this coordinate system, and the bubble wall in this example is exterior to the light cone (approaching it at large times), the bubble wall is "before" $T = 0$.

This picture can be used to generate a candidate for the early universe by making some modifications. Gravity must be included, the field ϕ is taken to be part of the inflationary potential, and the bubble nucleates in a vacuum, the de Sitter vacuum, $\phi \sim const.$ Nucleating a bubble in de Sitter space also means that the global structure of spacetime is more complicated– because the spacetime is expanding in the false vacuum, the future light cone of the bubble does not eventually cover the whole future of the space (see, e.g. [5]). Many of the calculations require normalizing on a Cauchy surface (a spacelike hypersurface which every non-spacelike curve intersects exactly once [6]) and thus use information exterior to the open universe.

The interior of the vacuum bubble has energy density depending on the true vacuum potential, $V(\phi_T)$. If $V(\phi_T) \approx 0$, then after ϕ has tunneled, the universe is effectively empty. All the energy density is in the bubble wall and not in the resulting open universe, which has $\Omega \sim 0$ and stays that way. Under our assumptions, to get a universe with something in it means that $V(\phi_T) \neq 0$. If $V(\phi_T) \neq 0$, then the resulting vacuum is also an expanding de Sitter space, that is, it is still inflating. So one needs a bubble plus inflation before and after nucleation. If one has inflation but no bubble, the amount of inflation providing sufficient homogeneity to agree with observation drives $\Omega \to 1$ (for a nice summary in the context of bubbles, see [7]).

Bucher, Goldhaber and Turok [2] combined bubble formation with inflation to give an open universe. They use four stages, corresponding to potential features sketched in figure 3:

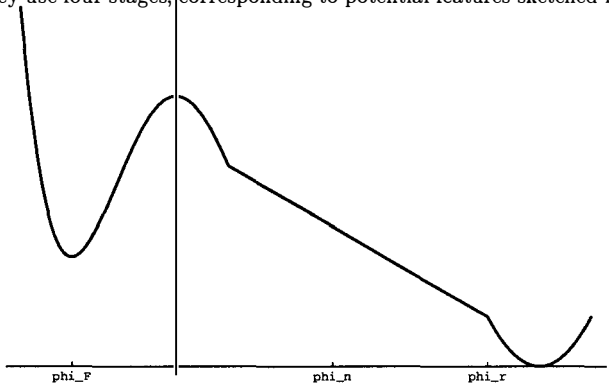

Figure 3: A potential with the features that give a viable open universe inflationary model.

- First, on the far left, the system is trapped in a potential well (at $\phi = \phi_F$), a false vacuum. Inflation occurs, driving the system to the Bunch-Davies vacuum (the natural vacuum here, respecting the symmetries and going over at short distances to the Minkowski space vacuum) and wiping out inhomogeneities.

- Then ϕ tunnels to $\phi \sim \phi_n$, resetting $\Omega \sim 0$;
- Next, on the approximately linear part of the potential, from $\phi \sim \phi_n$ to $\phi \sim \phi_r$, slow roll inflation drives Ω up to a specific value less than or equal to one.
- Finally, on the far right, at $\phi \sim \phi_r$, ϕ decays, leading to the usual reheating after inflation.

The endpoint of the tunneling $\phi \sim \phi_n$ will be called the true vacuum (since $\phi \sim const.$), even though it is also the starting point of the slow roll inflationary stage.

There are constraints on the potential so that this picture is consistent. The potential $V(\phi)$ has to be such that the tunneling rate is rare, so that tunneling from $\phi \sim \phi_F$ only occurs after a long period of inflation has erased initial conditions. The false vacuum well cannot be too flat or ϕ will stochastically go over the barrier rather than tunneling through it (the Hawking-Moss instanton) [8], leading to density perturbations which are too large [9]. The potential $V(\phi)$ must be tuned to within a few percent so that at the end of the slow roll stage $0.1 \leq \Omega \leq 0.9$.

A simple polynomial potential (up to order ϕ^4) does not satisfy these conditions [10], although in principle an effective potential could arise in a supergravity theory with the right features. One can also use more fields, driving inflation by one field while the other one tunnels. Some of the two-field variants of the model lose the ability to predict a definite value of Ω [11], and lead to more questions which have been studied extensively but are outside the scope of this summary.

The density perturbations in these models are a modification of those in $\Omega = 1$ inflationary models. For $\Omega = 1$ inflationary models, inflation drives the universe to the vacuum, and the quantum fluctuations of the inflaton in this vacuum become seeds for structure formation once they re-enter the horizon. In these open universe bubble models, there are vacuum fluctuations (from the false vacuum before tunneling) outside the bubble wall. These evolve through the bubble wall, a time dependent background, to reach the open universe. There is a continuum of these modes and sometimes (depending on properties of the wall and the mass in the false vacuum) a discrete mode. The bubble wall itself also has fluctuations. The calculations incorporate methods for bubbles in Minkowski space [12, 13], and techniques for including gravity as in [14]; see these papers and references therein for background. Various choices for the true and false vacuum masses and the wall profile have been considered.

Calculations so far have been for vacuum fluctuations due to one field, in two field models the second field has been frozen out. Thus one solves

$$\left(\Box - \frac{\delta^2 V(\phi)}{\delta \phi^2}|_{\phi=\phi_{\rm bkgd}} \right) \delta\phi = 0 \tag{7}$$

The gauge invariant gravitational potential produced by the continuous modes has been found assuming a constant value of H in the resulting de Sitter space. The power spectrum has been calculated for a thin wall with arbitrary false vacuum mass $M^2 \geq 2H^2$ and zero radius [15] and nonzero radius [16, 17]. It has also been found for a large false vacuum mass and varying wall profile (with the restriction that the wall is completely exterior to the light cone of the bubble center, the open universe) [16]. In all of these cases, the contribution to the fluctuations is within an envelope between $\coth \pi p/2$ and $\tanh \pi p/2$ times a scale invariant spectrum. (The correspondence with wavelength is $p = k/(H_0\sqrt{1-\Omega_0})$.) Thus, except at very large scales, where cosmic variance interferes with their measurement, these spectra all coincide.

In open de Sitter spacetime, when there is no bubble present, the Bunch Davies vacuum fluctuations of a field of mass $M^2 < 2H^2$ has a continous spectrum of fluctuations plus a discrete mode [18]. This discrete mode was shown to be part of the complete basis of states [18] and is normalizable on a Cauchy surface, but not inside the open universe (which does not

contain a Cauchy surface). In the presence of a bubble, this discrete 'supercurvature' mode with $-1 \leq p^2 \leq 0$ may remain, depending upon the false vacuum mass and the wall profile.

If the field providing density perturbations does not change its mass across the wall (as can happen in two field models), and has $M^2 < 2H^2$, this mode appears [19, 20]. Its contribution to density fluctuations has been found and used to constrain models when combined with the CMB for various cases [19, 20, 21, 22]. It does not seem to give a very strong constraint. However, it has been argued that this state's contribution can be enhanced significantly when the ratio of false to true vacuum energy is large, ruling out some models [22]. There is not yet complete agreement on this. If there is a mass change across the wall [16], an analogue of this state may persist. When matched across the bubble wall, the original vacuum discrete mode does not automatically remain normalizable, but a mode with some other value of $-1 \leq p^2 < 0$ may become normalizable instead. The effects of this new mode have been found in a two field model for a thin wall [16]. This mode disappears if the false vacuum mass is large enough (as argued in [16], the false vacuum mass is necessarily large for most one field models considered so far, so that it does not appear there).

There are also fluctuations of the wall itself, contributing mostly at large scales, and considered in [23, 10, 13, 24, 21, 16]. Requiring these fluctuations to be small constrains models. Schematically, the allowed models have a high barrier between the false and true vacuum, producing a large surface tension and making it energetically unfavorable for the wall to fluctuate.

In summary, the continuum modes reproduce a scale invariant spectrum starting at very large scales. The vacuum supercurvature mode or its analogue (when present) and the wall fluctuation (also a supercurvature mode) have been used so far to constrain possible potentials by requiring that their contribution be small.

Many fits to the data [25] have been made for open universes assuming a scale invariant [26] spectrum, and, except at large scales, the models considered so far also have this spectrum, and so carry over. Many things remain to be done, including adding gravity waves and tilt, and motivating models from particle theory.

Acknowledgement: I thank F. Bouchet for the chance to speak and for organizing the conference, and the participants (D. Bond, P. Ferreira, A. Liddle, N. Turok and M. White in particular) for conversations. I also thank K. Benson, M. Bucher, and V. Periwal for conversations and D. Scott and M. White for comments on the draft. This work was supported in part by the Director, Office of Energy Research, Office of High Energy and Nuclear Physics, Division of High Energy Physics of the U.S. Department of Energy under Contract DE-AC03-76SF00098 and in part by the National Science Foundation under grant PHY-90-21139.

References

[1] A. Guth, Phys. Rev. D23(1981)347; A. Guth and E. Weinberg, Nucl. Phys. B212(1983) 321; Peebles, P.J.E., Ap.J. 284(1984) 439; Turner, M.S., Steigman, G., Krauss, L.M. Phys. Rev. Lett. 52(1984) 2090

[2] M. Bucher, A. Goldhaber, N.Turok, Phys. Rev. D52(1995), 3314

[3] S. Coleman, Phys. Rev. D15(1977)2929; 16(1977)1248(E)

[4] J. R. Gott III, Nature 295 (1982) 304; J.R.Gott and T. Statler, Phys. Lett. 136B(1984)157; S. Coleman and F. DeLuccia, Phys. Rev. D21(1980) 3305

[5] B. Allen, Phys. Rev. D51 (1985) 3136

[6] See, for example, S. Hawking, G.F.R. Ellis, The Large Scale Structure of Spacetime (Cambridge: Cambridge University Press,1973)

[7] J. Garcia-Bellido, Contribution to TAUP'95 Conference proceedings, astro-ph/9511078

[8] S.W.Hawking and I.G.Moss, Phys. Lett. 110B(1982)35

[9] For a discussion and references see A. Linde, Particle Physics and Inflationary Cosmology, Harwood Academic Publishers (1993:USA)

[10] A. Linde, A. Mezhlumian, Phys. Rev. D52 (1995) 6789

[11] A. Linde, Phys. Lett. B351(1995) 99

[12] T. Tanaka, M.Sasaki, K. Yamamoto, Phys. Rev.D49(1994) 1039; M. Sasaki, T. Tanaka, K. Yamamoto, J. Yokoyama, Prog. Theor. Phys. 90(1993) 1019; Phys. Lett. B317(1993) 510; K. Yamamoto, T. Tanaka, M. Sasaki, Phys. Rev. D 51(1995) 2968

[13] T. Hamazaki, M. Sasaki, T. Tanaka, and K. Yamamoto, Phys. Rev. D53(1996) 2045

[14] T. Tanaka and M. Sasaki, Phys. Rev. D50(1994) 6444; Prog. Theor. Phys. 88(1992), 503

[15] M. Bucher, N. Turok, Phys. Rev. D52(1995),5538

[16] K. Yamamoto, M. Sasaki, T. Tanaka, "Quantum fluctuations and CMB anisotropies in one-bubble open inflation models", astro-ph/9605104

[17] J. D. Cohn, "Open universes from finite radius bubbles", astro-ph/9605132

[18] M. Sasaki, T. Tanaka, K. Yamamoto, Phys. Rev. D51(1995)2979

[19] K. Yamamoto, M. Sasaki, T. Tanaka, ApJ. 455 (1995) 412

[20] E.F. Bunn, K. Yamamoto, "Observational Tests of One-Bubble Open Inflationary Cosmological Models", KUNS-1357, CfPA-95-TH-16, ApJ. 464 in press

[21] J. Garcia-Bellido, 'Density Perturbations from Quantum Tunneling in Open Inflation', SUSSEX-AST 95/10-1, astro-ph/9510029

[22] Sasaki and Tanaka, "Can the Simplest Two-Field Model of Open Inflation Survive?", OU-TAP-35, astro-ph/9605104

[23] J. Garriga and A. Vilenkin, Phys. Rev. D44 (1991), 1007; Phys. Rev. D45(1992), 3469

[24] J. Garriga, "Bubble fluctuations in $\Omega < 1$ inflation", gr-qc/9602025

[25] See R. Stompor, these proceedings, and for one recent summary, A. Liddle, D. Lyth, D. Roberts, P. Viana, "Open cold dark matter models", SUSSEX-AST 95/6-2,astro-ph/9506091 and references therein. For tilted open models the COBE four year normalization is in M. White and D. Scott, "The impact of the cosmic microwave background on large scale structure", astro-ph/9601170, to appear in Comm. on Astrophysics, v.8, No.5

[26] D. Lyth, E. Stewart, Phys. Lett. B252 (1990) 336; B. Ratra, P.J.E. Peebles, Phys. Rev. D52 (1995) 1837; Astrophys. J.Lett. 423 (1994) L5 (1995) astro-ph/9508090

COHERENCE AND SAKHAROV OSCILLATIONS IN THE MICROWAVE SKY

A. Albrecht [1]
[1] *Imperial College, London, UK.*

Abstract

I discuss the origin of the "Sakharov oscillations" (or "secondary Doppler peaks") in standard angular power spectra of the Cosmic Microwave Background anisotropies calculated for inflationary models. I argue that these oscillations appear because perturbations from inflation have a set of properties which makes them "passive perturbations". All passive perturbations undergo a period of linear "squeezing" resulting in a dramatic degree of (classical) phase coherence of pressure waves in the photon-baryon fluid. This phase coherence eventually is reflected in oscillatory features in the angular power spectrum of the temperature anisotropies observed today. Perturbations from cosmic defects are "active perturbations" which have sharply contrasting properties. Active perturbations are highly non-linear and the degree of phase coherence in a given model reflects the interplay between competing effects. A large class of active models have *non*-oscillatory angular power spectra, and only an extremely exotic class has the same degree of coherence as is found in all passive models. I discuss the significance of the search for these oscillations (which transcends the testing of any given model) and take a critical look at the degree to which the question of coherence has been treated so far in the literature.

1 Introduction

The Cosmic Microwave Background (CMB) provides us with perhaps the clearest window on the very early universe. Based just on our current understanding, the impact of the next generation of high resolution CMB experiments on theoretical cosmology is guaranteed to be enormous, and full implications of the new data have yet to be determined.

The subject of this paper is the distinctive "Secondary Doppler Peaks" or "Sakharov Oscillations[1]" in the angular power spectra of the microwave anisotropies calculated for inflationary models. I discuss how these features reflect the very specific properties of "passive

perturbations" of which the inflationary models are a subset. The very different nature of the defect based (or "active") models suppresses the tendency to generate Sakharov oscillations, although a different mechanism *can* produce Sakharov oscillations in certain active models.

Section 2 outlines the basic ingredients of a of CMB anisotropy calculation, emphasizing the differences between active and passive models. Section 3 spells out how the Sakharov oscillations appear in passive models. Section 4 describes the basic properties of active models make it hard to produce oscillations in the angular power spectrum, but also points out how some degree of oscillation is still possible. At the end of Section 4 I comment of the degree to which this issue has been addressed quantitatively in the literature. Concluding comments appear in Section 5.

Much of this paper is based on work with my collaborators P. Ferreira, J Magueijo, and D. Coulson, as reported in [2, 3, 4].

2 The evolution of the perturbations

Most models of structure formation consider perturbation which originate at an extremely early time (eg the GUT era or even the Planck era) and which have very small amplitudes (of order 10^{-6}) until well into the matter era. Perturbations of inflationary origin start as short wavelength quantum fluctuations which evolve (during the inflationary period) into classical perturbations on scales of astronomical interest. Defect based models undergo a phase transition (typically at around GUT temperatures, eg $T \approx 10^{16} GeV$) forming defects which generate inhomogeneities on all scales.

For all these models, once the inflationary period and/or phase transition is over, the Universe enters an epoch where all the matter components obey linear equations except for the defects (if they are present). This "Standard Big Bang" epoch can be divided into three distinct periods. The first of these is the "tight coupling" period where radiation and baryonic matter are tightly coupled and behave as a single perfect fluid. When the optical depth grows sufficiently the coupling becomes imperfect and the "damping period" is entered. Finally there is the "free streaming" period, where the CMB photons only interact with the other matter via gravity. While the second and third periods can have a significant impact on the overall shape of the angular power spectrum, all the physics which produces the Sakharov oscillations takes place in the tight coupling regime, which is the focus of the rest of this paper.

Working in in synchronous gauge, and following the conventions and definitions in references [5, 6, 2], the Fourier space perturbation equations are:

$$\dot{\tau}_{00} = \Theta_D + \frac{1}{2\pi G}\left(\frac{\dot{a}}{a}\right)^2 \Omega_r \dot{s}\,[1+R] \tag{1}$$

$$\dot{\delta}_c = 4\pi G \frac{\dot{a}}{a}(\tau_{00} - \Theta_{00}) - \frac{\dot{a}}{a}\left(\frac{3}{2}\Omega_c + 2\,[1+R]\,\Omega_r\right)\delta_c - \frac{\dot{a}}{a} 2\,[1+R]\,\Omega_r s \tag{2}$$

$$\ddot{s} = -\frac{\dot{R}}{1+R}\dot{s} - c_s^2 k^2 (s + \delta_c) \tag{3}$$

Here $\tau_{\mu\nu}$ is the pseudo-stress tensor, $\Theta_D \equiv \partial_i \Theta_{0i}$, $\Theta_{\mu\nu}$ is the defect stress energy, a is the cosmic scale factor, G is Newton's constant, δ_X is the density contrast and Ω_X is the mean energy density over critical density of species X ($X = r$ for relativistic matter, c for cold matter, B for baryonic matter), $s \equiv \frac{3}{4}\delta_r - \delta_c$, $R = \frac{3}{4}\rho_B/\rho_r$, ρ_B and ρ_r are the mean densities in baryonic and

relativistic matter respectively, c_s is the speed of sound and k is the comoving wavenumber. The dot denotes the conformal time derivative ∂_η.

In the inflationary case there are no defects and $\Theta_{\mu\nu} = 0$. With suitable initial conditions these linear equations completely describe the evolution of the perturbations. In the defect case $\Theta_{\mu\nu} \neq 0$, and certain components[1] of $\Theta_{\mu\nu}(\eta)$ are required as input. Cosmic defects are "stiff", which means $\Theta_{\mu\nu}(\eta)$ can be viewed as an external source for these equations. The additional equations from which one determines $\Theta_{\mu\nu}(\eta)$ are highly non-linear, although the solutions tend to have certain scaling properties which allow $\Theta_{\mu\nu}(\eta)$ to be modelled using a variety of techniques [?].

3 The passive case: Squeezing and phase coherence

Quite generically, for wavelengths larger than the Hubble radius ($R_H \equiv a/\dot{a}$), Eqns [1-3] have one decaying and one growing solution. The growing solution reflects the gravitational instability, and, as required of any system which conserves phase space volume, there is a corresponding decaying solution. For example, in the radiation dominated epoch, the two long wavelength solutions for the radiation perturbation δ_r are $\delta_r \propto \eta^2$ and $\delta_r \propto \eta^{-2}$. Over time, R_H grows compared with a comoving wavelength so in the Standard Big Bang epoch a given mode starts with wavelength $\lambda >> R_H$ but eventually crosses into the $\lambda < R_H$ regime. In the period of tight coupling modes with $\lambda < R_H$ undergo oscillatory behavior since the radiation pressure stabilizes the fluid against gravitational collapse. This process of first undergoing unstable behavior which eventually converts to oscillatory behavior is the key to the formation of Sakharov oscillations.

I will now illustrate the process with a simple toy model. The simplest example of growing/decaying behavior is given by the upside down harmonic oscillator ($\ddot{q} = q$) which has the general solution $q = Ae^t + Be^{-t}$). Figure 1 (left panel) shows the trajectories in phase space for this system. As the "particle" rolls down the inverted parabolic potential both q and $\dot{q}$ increase arbitrarily and *any* starting point in phase space evolves arbitrarily close to the $\dot{q} = q$ axis. Any initial region in phase space will become squeezed against this axis and elongated along it, as illustrated by the circle in the figure. This "squeezing[2]" process is generic to any equation which has one growing and one decaying solution, although the simple shape of the squeezed region is specific to models with linear equations.

The right-side-up harmonic oscillator ($\ddot{q} = -q$) serves to illustrate the oscillating regime (when the wavelength is smaller than R_H). The right hand panel in Fig 1 shows the phase space trajectories for the right-side-up harmonic oscillator. The familiar oscillatory behavior describes circles in the $q - \dot{q}$ plane (in polar coordinates the angle corresponds to phase of the oscillation). The linearity ensures that the period of rotation is the same on all trajectories, thus preserving the shapes of any initial region as it rotates around.

The physical system in question (e.g. δ_r) undergoes first squeezing and then oscillatory behavior. During the unstable period the initial phase space distribution (dictated, in the case of an inflationary scenario, by the quantum zero-point fluctuations) is squeezed by many orders of magnitude. The distribution which enters the oscillatory period is thus highly squeezed (much more so than the oblong shape depicted in the right panel of Fig 1). The end result it

[1]Conservation of stress energy allows the equations to be manipulated so that different components of $\Theta_{\mu\nu}$ are required as input (a matter mainly of numerical convenience)[5, 6, 7, 8, 9, 10, 11].

[2]These dynamics are similar to those producing "squeezed states" of light in quantum optics, but the effect discussed here is completely classical. [12]

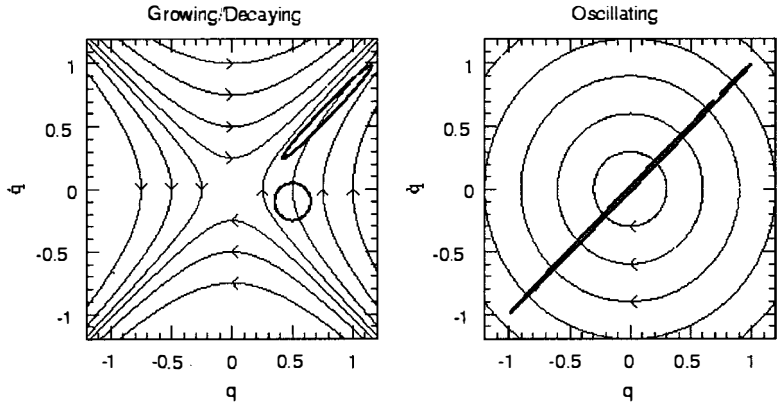

Figure 1: Phase space trajectories for the up-side-down harmonic oscillator (left panel) and right-side-up harmonic oscillator (right panel). These toy models illustrate the growing/decaying regime and oscillating regime (respectively). The growing/decaying regime causes "squeezing", which drives all solutions toward (and outward along) the $q = \ddot{q}$ axis. In a passive model the perturbations first encounter the squeezing regime and thus the phase space distribution which enters oscillatory regime is highly squeezed and a unique temporal phase (up to a shift by π) is specified for the oscillatory regime. The elongated curve on the right panel is the result of squeezing a circle (centered at the origin) by a factor of 100. Typically inflation models will have squeeze factors of 10^{20} or greater.

that the temporal phase of oscillation is rigorously dictated by the period of squeezing which went before.

This effect is illustrated more directly in Fig 2, where different solutions for δ_r are shown. Representative solutions are shown from across the entire ensemble, the growing solution domination guarantees that each one goes through zero at essentially the same time.

Figure 3 shows the ensemble averaged values of δ at a fixed time as a function of wavenumber (the power spectrum). The zeros correspond to modes which have been caught at the "zero-point" of their oscillations. The phase focusing across the entire ensemble guarantees that there will always be some wavenumbers where the power is zero. It is these zeros which are at the root of the oscillations in the angular power spectrum.

An important point is that these zeros are an absolutely fundamental feature in any passive theory. No amount of tinkering with the details can counteract that fact that an extended period of liner evolution will lead to growing mode domination, which in turn fixes the phase of the oscillations in the tight coupling era. If one were to require oscillation in a passive model to be out of phase from the prescribed value, one would imply domination by the decaying mode outside the Hubble radius – in other words a Universe which is not at all Robertson-Walker on scales greater than R_H.

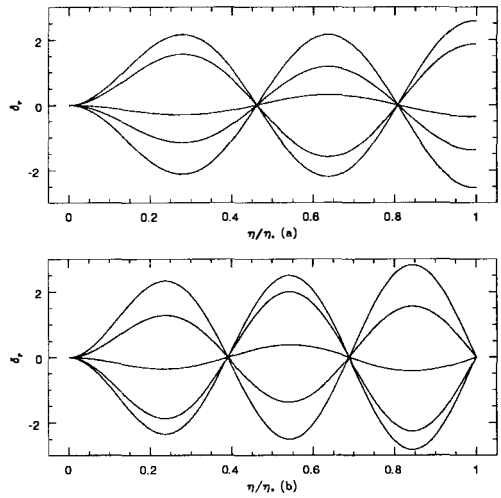

Figure 2: Passive perturbations: Evolution of two different modes during the tight coupling era. While in (a) elements of the ensemble have non-zero values at $\eta_\star$, in (b), *all* members of the ensemble will go to zero at the final time ($\eta_\star$), due to the fixed phase of oscillation set by the domination of the growing solution (or squeezing) which occurs before the onset of the oscillatory phase. The y-axis is in arbitrary units.

4 The active case: Coherence lost

4.1 The nature of the ensemble

As described in Section 2, the active case is very different from the passive case, due to the presence of what is effectively a source term in Eqns [1-3]. One consequence is that the whole notion of the ensemble average is changed. In the passive case any model with Gaussian initial conditions can be solved by solving Eqns [1-3] with the initial values for all quantities given by their initial RMS values. The properties of linearly evolved Gaussian distributions guarantee that this solution will always give the RMS values at any time. Thus the entire ensemble is represented by one solution.

In the active case this is not in general possible. One has to average over an ensemble of possible source histories, which is a much more involved calculation. In [3] we "square" the evolution equations to write the power spectrum as convolution of two-point functions of the sources, but there the added complexity requires the use of the full *un*equal time correlation functions.

4.2 Non-coherence

In general, the source term will "drive" the other matter components, and temporal phase coherence will be only as strong as it is within the ensemble of source terms. An illustration of this appears in Fig 4. In many active models the sources are sufficiently decoherent that no

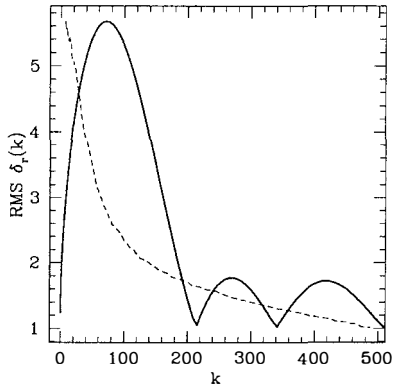

Figure 3: The r.m.s. value of δ_r evaluated at decoupling ($\eta_\star$) for a passive model (solid) and an active model (dashed). This is Fig 2 from ref [2] where the details are presented.

oscillations appear in the power spectrum (see for example the dashed curve in Fig 3).

4.3 Coherence regained

The source evolution is a highly non-linear process, so from the point view of a single wavenumber the source may be viewed as a "random" force term. At first glance it may seem impossible for such random force term could induce *any* temporal coherence, but here is how temporal coherence can occur: The source term only plays a significant role in Eqns [1-3] for a *finite* period of time. This is somewhat apparent in Fig 4. (The y-axis of Fig 4 shows a quantity specially chosen to indicate the significance of the source in Eqns [1-3].) In the limit where this period of significance is short compared to the natural oscillation time of δ_r (and happens at the same time across the entire ensemble) the ensemble of source histories *can* be phase coherent. The tendency for a given active model to produce oscillations in the power spectrum depends on the how "sharply peaked" the significance of the source term is in time.

4.4 Current Status

So far, we are just beginning to learn the degree of coherence which is present in the most popular active models. Much of the work makes use of the "high coherence limit" in which a single solution to Eqns [1-3] is meant to represent the RMS value. This only makes physical sense for the "sharply peaked" sources discussed in the previous subsection[3], but allows one to use code designed for passive perturbations with only minor changes.

The question of coherence has been most aggressively pursued in the cosmic string case[2, 3, 4, 13], and every indication is that cosmic strings give a highly decoherent ensemble. However, there will still be room for some degree of skepticism until the production of gravity waves and small loops is incorporated in some realistic way ([14], see also the methods of[15]). Most of the work on cosmic texture models has not dealt quantitatively with the question of evidence for coherence in the microwave sky although it is pretty clear that textures should have more coherence than the cosmic strings. In [8] the "high coherence" limit was used for calculating the microwave sky, but numerical simulations were used to illustrate some coherent behaviour

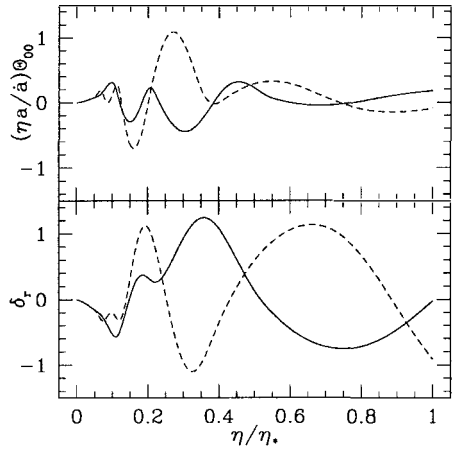

Figure 4: Active perturbations: Evolution of $\delta_r(k)$ and the corresponding source Θ_{00} during the tight coupling era (Θ_D is not shown). Two members of the ensemble are shown, with matching line types. Due to the randomness of the source, the ensemble includes solutions with a wide range of values at η_*. Unlike the inflationary case (Figure 1) the phase of the temporal oscillations is not fixed. The y axis is in arbitrary units, and the source models are the same as for figure 2. The factor $\eta a/\dot{a}$ allows one to judge the relative importance (over time) of the Θ_{00} term in Eqn 2.

in the tight coupling era. In other calculations the high coherence limit has been used for convenience, and these papers have simply not claimed to treat the question of coherence. Recent simulations by Turok [15] are the sort which can in principle address the coherence question for a large number of active models, but the author is not willing to claim conclusive results until a large dynamic range is achieved.

5 Conclusions

The Sakharov oscillations (or secondary Doppler peaks) in the angular power spectrum of CMB anisotropies signify a high degree of coherence in the primordial perturbations. These oscillations are a certain prediction of all passive models (which includes all inflation based models) and can not be adjusted away[3]. As such, this prediction represents probably the most clear-cut opportunity to falsify *all* scenarios in which the perturbations have an inflationary origin. On the other hand the observation of substantial Sakharov oscillations in the data would have an enormous impact on the active models, ruling out all be a very special subset of these. I conclude that the search for Sakharov oscillations in the CMB sky represents an opportunity to gain very deep insights into the origin of the primordial perturbations. Every effort should be made to make sure that the experiments are able to achieve conclusive results

[3]I suppose it might be possible to construct some undulating inflaton potential which gives a non-oscillatory temperature anisotropy spectrum, but then the oscillations would turn up in other observations (such as those of the density field or CMB polarization).

on this matter[16].

Acknowledgements. Special thanks to the organizers for a very productive and enjoyable meeting. I also wish to thank P. Ferreira, J. Magueijo, and D. Coulson for a great collaboration, and also N. Turok for stimulating conversations on the material presented here. This work was supported by the UK Particle Physics and Astronomy Council.

References

[1] See page 280 of Ya. B. Zel'dovich and I. D. Novikov, *"The Structure and Evolution of the Universe"*, publ. Univ. of Chicago Press.

[2] A. Albrecht, D. Coulson, P. Ferreira, and J. Magueijo, *Phys. Rev. Lett.* **76** 1413-1416 (1996).

[3] J.Magueijo, A. Albrecht, D. Coulson, P. Ferreira, *Phys. Rev. Lett*, **76** 2617 (1996), J.Magueijo, A. Albrecht, P. Ferreira, D. Coulson, *Phys . Rev. D*, In Press, (1996)

[4] See also the contributions of P. Ferreira and J. Magueijo in this volume.

[5] S. Veeraraghavan and A. Stebbins, *Astrophys.J.* **365** 37-65 (1990).

[6] U. Pen, D.N. Spergel and N. Turok, *Phys. Rev. D*, **49** 692-729 (1994).

[7] R. Durrer, A. Gangui and M. Sakellariadou, *Phys. Rev. Lett.*, **76** 579 (1996).

[8] R. Crittenden and N. Turok, *Phys. Rev. Lett.*, **75** 2642 (1995).

[9] N. Turok, DAMTP-preprint-96-44, astro-ph/9604173 (1996), N. Turok, DAMTP-preprint-96-69, astro-ph/9607109 (1996).

[10] W. Hu and M. White, IAS preprint astro-ph/9603019 (1996)

[11] W. Hu. D. Spergel, and M. White IAS preprint astro-ph/9605193 (1996)

[12] A. Albrecht, P. Ferreira, M. Joyce, and T. Prokopec, Phys. Rev. D **50** 4807 (1994).

[13] See also the contribution of M. Hindmarsh in this volume.

[14] A. Albrecht and J. Robinson, in preparation (1996)

[15] N. Turok, DAMTP P 96-59, astro-ph/9606087 (1996)

[16] See for example Albrecht and Wandelt Imperial/TP/95-96/23, astro-ph/9602040, J. Magueijo and M. Hobson, DAMTP-96-13, astro-ph/9602023, M. Hobson and J. Mageijo DAMTP 96-01, astro-ph/96030.

MICROWAVE ANISOTROPIES FROM RANDOM SOURCES

Pedro G. Ferreira,
Center for Particle Astrophysics
University of California
Berkeley, CA 94720-7304
USA.

Abstract

I report on recent developments in the theory of cosmic background radiation perturbations. I describe ways of modeling alternatives to the canonical Gaussian theories within the standard framework of cosmological perturbation theory. Some comments are made on using these techniques to resolve the uncertainties in theories of structure formation with topological defects.

The past few years have seen a remarkable development in both the experimental and theoretical understanding of the cosmic backround radiation (CBR). Following the tremendous success of COBE in mapping out the sky to 10° resolution and showing us that, indeed these fluctuations do exist, a flurry of results have come out of groundbased and balloon borne, degree scale experiments. Although it seems premature to make strong claims about the fine features of the current results, it is clear that we are very rapidly progressing to a very detailed knowledge of what the CBR looks like on all scales. Driven by the wealth of experimental data which will be available, theorists have been developing numerical and analytic tools which help us understand what impact these measurements have on our world model.

Almost all efforts have focused on a restricted set of models where perturbations are set up in the initial conditions and are elements of a Gaussian ensemble. A number of groups have developed numerical algorithms for evolving perturbations in radiation in an expanding universe (see Seljak's contribution in this proceeding for an exciting recent development) and it is now possible to calculate the angular power spectrum of the CBR for these models with a precision of smaller than a percent on all scales.

The determination of the statistical properties of the CMB anisotropies involves evolving the linearized Boltzman equation [1]. One can identify various regimes and for the purpose of this proceeding I shall focus on the pre-recombination era where radiation behaves as a tightly coupled fluid with an effective equation of state $P = \frac{1}{3}\rho$. If we make the further simplification of assuming that recombination happens in the radiation era, then it suffices to consider the following set of equations [2]:

$$\begin{aligned} \ddot{h} + \frac{1}{\eta}\dot{h} + \frac{6}{\eta^2}\delta_R &= -8\pi G\mathcal{S}_+ \\ \ddot{\delta}_R + \frac{k^2}{3}\delta_R + \frac{2}{3}\ddot{h} &= 0 \\ \ddot{h}^S + \frac{2}{\eta}\dot{h}^S + 4\tau_{00} &= 8\mathcal{S}^S \end{aligned} \tag{1}$$

where δ_R is the radiation density contrast, we have decomposed the scalar spatial tensors into $A_{ij} = \frac{1}{3}A\delta_{ij} + (\hat{k}_i\hat{k}_j - \delta_{ij})A^S$, η is conformal time and $\tau_{00} = \mathcal{S}_{00} + \frac{3}{4\eta^2}\delta_R - \frac{1}{4\eta}\dot{h}$ is the "pseudo-energy" of the system. $\mathcal{S}_{\mu\nu}$ ($\mathcal{S}_+ = \mathcal{S}_{00} + \mathcal{S}_{ii}$) is the energy-momentum tensor of an external source with its own set of statistical properties; we shall assume that its dominant form of self interaction is non-gravitational. Topological defects are examples of such sources. If we are interested in the angular power spectrum, one must project this set of perturbations forward; for example if one coniders the monopole at last scattering then one obtains

$$C_l = \frac{1}{16}\int_0^\infty k^2 dk < |\delta_R - \frac{2\ddot{h}^S}{k^2}|^2 > j_l^2(k(\eta_0 - \eta_*))$$

The canonical picture of structure formation relies on a few technical assumptions which simplify calculations tremendously. Firstly perturbations are set up in the early universe, deep in the radiation era (at η_i). For example *Inflation* will imprint a set of adiabatic perturbations on superhorizon scales at the Planck time. The subsequent evolution of these perturbations is studied with equations (1) where we set all $\mathcal{S}$'s to 0. Note that this means that all variables, as a function of time, are homogeneous functions of degree one in the initial conditions; heuristically this means that, for example

$$\delta_R(k,\eta) \simeq T_R(k;\eta,\eta_i)\delta_R(k,\eta_i)$$

Secondly the initial set of perturbations is a realization from a Gaussian ensemble with 0 mean, i.e. to describe the statistics of the ensemble *completely* at η_i it suffices to specify $< |\delta_R(k,\eta_i)|^2 >$. These two technical assumptions lead to a remarkably simple algorithm for studying the statistics of perturbations today. One picks as initial conditions the square root of the initial variances of the variables, evolves them forward deterministically using equations (1) and squares the result.

We could however consider a much more general set of perturbations, with non-zero $\mathcal{S}$ and initial conditions with more complex statistics. A restricted set of examples have been studied in this class: if one assumes that the universe underwent a symmetry breaking phase transition, and that the symmetry breaking pattern satisfies a certain set of conditions, than it is possible that topological relics could have formed. For structure formation, the interesting examples are *cosmic strings* and textures. With the aim of going through the same sort of analysis as we have just performed for Gaussian theories let us focus on cosmic strings.

Two important features arise: Firstly, if we assume that universe was homogeneous and isotropic and make the natural assumption that all processes during the phase tranistion were causal, than the initial conditions to equation (1) satisfy a 'causality constraint'. In particular

$\tau_{00} \propto k^2$ on superhorizon scales. Note that this implies a delicate cancellation between the "source" (which, as we shall see, is $\propto k^0$), the other fluids and the gravitational field. Secondly, we must know the statistics of the source. Unlike the case of primordial, Gaussian fluctuations, here we have to describe the time evolving statistics. We must characterize these sources as an ensemble of histories, which satisfy a certain set of properties. In the case of cosmic strings we have

i) $< \mathcal{S} > \simeq 0$

iii) causality enforces the sources to have no correlations on superhorizon scales; this means

$$< \mathcal{S}_{00}(\mathbf{x}, \eta)\mathcal{S}_{00}(\mathbf{x}, \eta) >= 0 \quad \text{if} \quad |\mathbf{x} - \mathbf{x}'| > \eta + \eta'$$

which implies

$$< |\mathcal{S}_{00}(k, \eta)|^2 > \propto k^0 \quad \text{for} \quad k\eta \ll 1.$$

iii) $\mathcal{S}_{00}$ satisfies "active" scaling so that

$$< |\mathcal{S}_{00}(k, \eta)|^2 > \simeq \frac{1}{\eta^{\frac{1}{2}}} f(k\eta)$$

This means that perturbations will be seeded with a constant amplitude at order of the horizon size, inducing "quasi" scale invariance "actively". This condition may not be strictly enforced in certain eras; cosmic strings deviate mildly from it in the radiation/matter transition

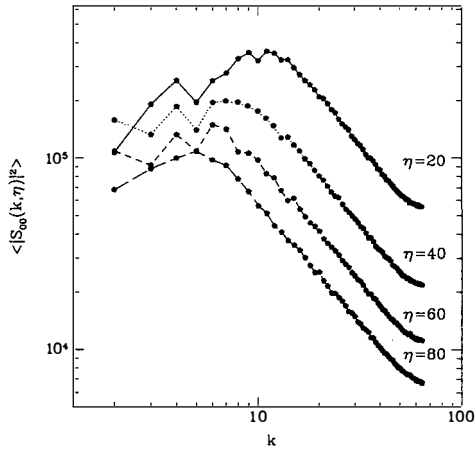

Figure 1: Equal time power spectrum for $\mathcal{S}_+$ for different time steps, from a 3D simulation of a cosmic string network [4]. Note the evidence for scaling and the k^{-1} behaviour, typical of line like configurations, on small scales.

iv)In the case of cosmic strings, the sources are a highly non-linear system, i.e. there is a strong coupling between the evolution of the different modes. As a consequence there is an active randomization of each fourier modes in such a way that, for example

$$< \mathcal{S}_{00}(k, \eta)\mathcal{S}_{00}(k, \eta + \Delta) > \simeq 0 \quad \text{if } \Delta > \eta_c$$

for some coherence time η_c (and the same can be said of other components of $\mathcal{S}$). These features of the unequal time correlation function may have striking observational consequences.

As pointed out in [3] the structure of the secondary peaks will be completely smoothed out if the η_c is small enough and $\mathcal{S}_+$ has enough "power" on small scales.

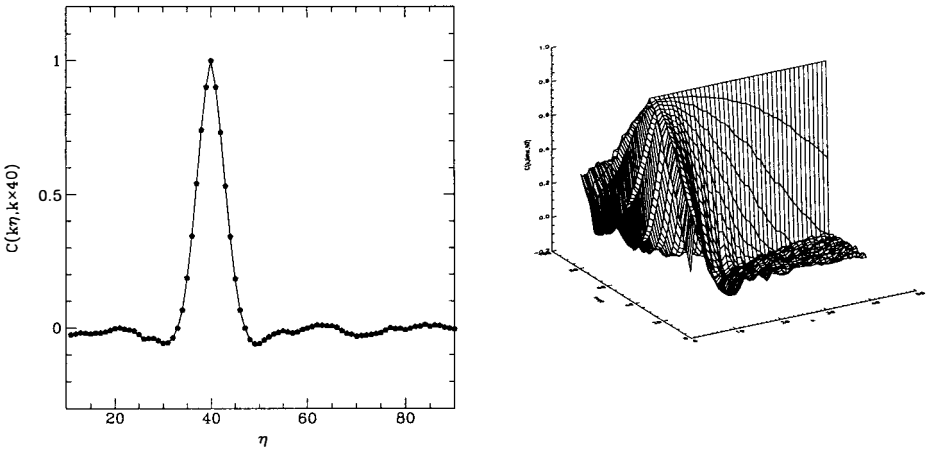

Figure 2: Plots of unequal time correlation function of $\mathcal{S}_{00}$ normalized to unity at equal time, C (see [5, 6]). The right hand side is a surface plot with one of the entries fixed at $\eta = 40$ in box units (note that η_c is scale dependent). The left hand side is a slice through the surface plot (for one mode, $k = 20$)

I should emphazise that this class of perturbations is much more general than the canonical set. To pick a theory one must define the statistics of the initial condition and of the source ensemble. Primoridal Gaussian theories are a sub-class with Gaussian initial conditions and $\mathcal{S}_{\mu\nu} = 0$ which are particularly easy to study.

Having set up the system in this way we can now look at different strategies for studying specific examples in this general class of theories. Again I will focus on cosmic strings. Ideally one should be able to generate an ensemble of evolving networks through some numerical algorithm. These would supply us with $\mathcal{S}_{\mu\nu}$ which would go into eq (1) and generate a set of δ_R and h^S which we could use to reconstruct 2d (or even 3d) realizations of the CMB anisotropy. This technique has the tremendous advantage of supplying us with *all* the information in CMB anisotropies generated by strings, i.e. with a reasonable amount of realizations we can reconstruct the full statistical distribution of anistropies. There are serious practical problems however. Existing high-resolution codes of cosmic string networks have a very limited dynamical range and it is unclear whether one is actually probing the true physical scaling regime of the network. Modified flat-space codes have the advantage of being very fast and have a large dynamic range but it is even less clear whether these numerical systems represent the real world with sufficient accuracy. Also care must be had when evolving the combined system of defects and gravity to ensure that energy-momentum is properly consereved (for a description of the problem see [2]).

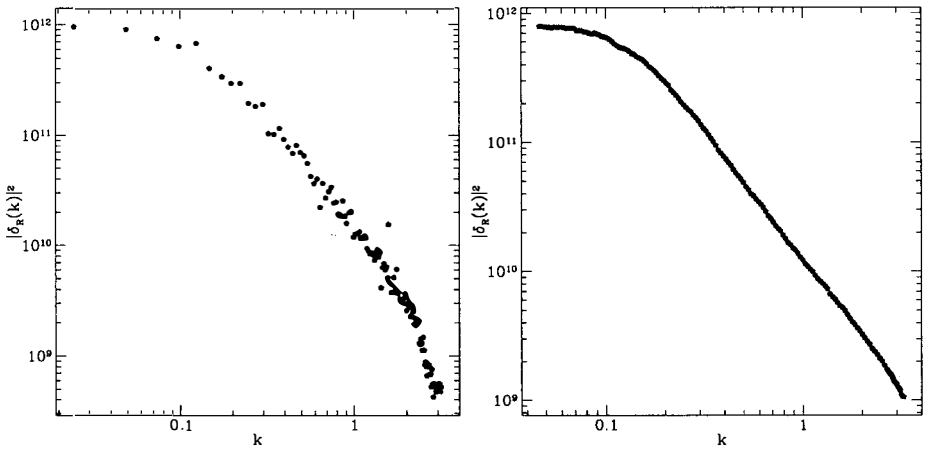

Figure 3: The power spectrum of the δ_R at last scattering using two different techniques: on the left hand side we use a full 3d network code to generate the sources [7]; on the right hand side we use a random number generator to generate a source value at each time step of typical size η_c.

A simplification recently suggested by Turok [7] is to evolve the a defect network and store a small set of one-dimensional fourier transforms (along the main axis, for example), i.e. at each η all we need is (for example)

$$\bar{\mathcal{S}}_+(x,\eta) \equiv \int dydz\mathcal{S}_+(x,y,z,\eta)$$

In this way one reduces considerably the time needed for generating each history and, although one cannot reconstruct 2d (3d) realizations of the anisotropy field, one retains all the statistical information of each mode. Again one is tied down to the accuracy of the code modeling the defect network and it is not possible to vary the phenomenological parameters of the theory and estimate uncertainties in the observables.

One can forgo the use of a defect network if one restricts oneself to estimating the ensemble averaged power-spectrum. It is quadratic in the perturbation variables and therefore quadratic in the sources. If one generates an ensemble of $\mathcal{S}$ histories which have the same two-point correlation properties of the real network then one will obtain the correct averaged power spectrum. Note that this is all we need to estimate the mean of C_l but is not enough enough for the variance of C_l (the "cosmic" variance) which may be significantly different from the Gaussian case. A possible algorithm is the following:

a) evaluate the the statistical properties form a string network simulation
(e.g. $< \mathcal{S}_+(k,\eta)\mathcal{S}_+(k,\eta') >$, $< \mathcal{S}^S(k,\eta)\mathcal{S}^S(k,\eta') >$, $< \mathcal{S}_+(k,\eta)\mathcal{S}^S(k,\eta') >$, etc.)

b) divide the whole time interval over which you are going to evolve Eq. (1) into subintervals of size η_c. An obvious refinement is to choose each time step from a distribution with mean value η_c.

c) use a gaussian number generator to generate realizations of $\mathcal{S}_+$, $\mathcal{S}_{00}$ and $\mathcal{S}^S$ in each subinterval

with the variances from a)
d) feed these histories into Eq. (1).

The tremendous advantage is that one can sidestep the uncertainties in modeling the defect network. By making a realistic guess of the uncertainties in the properties evaluated in a) one can study their impact on the estimate of the angular power spectrum. An example of this has been attempted (although in a different formalism) for cosmic strings in [4, 5]; it was found that current uncertainties lead us to be uncertain about the height of the "Doppler peak" to within a factor of 10, that its position can be estimated to lie between l of 400 and 600 but that one can safely say that there will be little or NO secondary oscillations. One hopes that in this way one can circumvent the uncertainties which have plagued the study the cosmological implications of topological defects during the last 20 years. One important problem that can be addressed has been reiterated by White and Scott [8]; if one accepts the current COBE normalization of these models to be correct then there is serious lack of power on medium to small scales in the matter power spectrum (on sufficiently large scales to be difficult to justify in terms of "bias"). With this method it is possible to assess how serious a problem this is, given the current uncertainites in modeling the defect network.

I have focused on cosmic strings where we have some intuition (and experience) of the behaviour of the sources. However it is possible to consider these sources as a "phenonmenological" ingredient in a theory of structure formation, in the same way that Gaussian initial conditions were postulated before the advent of inflation.

Acknowledgements. This work was done in collaboration with A. Albrecht, D. Coulson and J. Magueijo. I acknowledge useful conversations with R. Durrer, W. Hu, U. Seljak, J. Silk, N. Turok and M. White. I was supported by the Center for Particle Astrophysics, a NSF Science and Technology Center at UC Berkeley, under Cooperative Agreement No. AST 9120005.

References

[1] Wilson M.L. and Silk J. *Astrophys. Jour.* **243** 14 (1981); Bond J.R. and Efstathiou G. *Astrophys. Jour* **285** L45 (1984); Hu W. and Sugiyama N. *Astrophys. Jour* **444** 489 (1985)

[2] Veeraraghavan S. and Stebbins A., *Astrophys. Jour* **365** 37 (1990); Pen U.L., Spergel D.N. and Turok N. *Phys. Rev. D* 692 (1994)

[3] Albrecht A., Coulson D., Ferreira P. and Magueijo J., *Phys. Rev. Lett.* **76** 1413 (1996)

[4] Magueijo J., Albrecht A., Coulson D. and Ferreira P., *Phys. Rev. Lett.* **76** 2617 (1996)

[5] Magueijo J., Albrecht A., Coulson D. and Ferreira P.,

[6] Ferreira P., Albrecht A. and Magueijo J., in preparation astro-ph/9605047, sub. to *Phys. Rev. D*

[7] Turok N., *private communication*

[8] White M. and Scott D. astro-ph/9601170, sub. to *Comm. in Astro.*

The Doppler peaks from a generic defect

João Magueijo
DAMTP and MRAO, University of Cambridge, Cambridge, UK

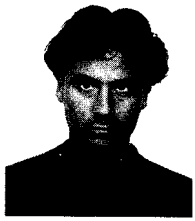

Abstract

We investigate which of the exotic Doppler peak features found for textures and cosmic strings are generic novelties pertaining to defects. We find that the "out of phase" texture signature is an accident. Generic defects, when they generate a secondary peak structure similar to inflation, apply to it an additive shift. It is not necessary for this shift to be "out of phase". We also show which factors are responsible for the absence of secondary oscillations found for cosmic strings. Within this general analysis we finally consider the conditions under which topological defects and inflation can be confused. It is argued that only $\Omega = 1$ inflation and a defect with a horizon size coherence length have a chance to be confused. Any other inflationary or defect model always differ distinctly.

1 Introduction

Recent work has addressed the hitherto virgin ground of Doppler peaks induced by motivated topological defect scenarios. Textures have been studied by [1] and [2] with good qualitative agreement, and cosmic strings were studied in [3, 4, 5]. This work prompts reflection on a more fundamental level. Inflationary perturbations have always been open to the most general class of possibilities. For instance one considered tilt, tensor modes, etc, long before motivated inflationary mechanisms were found to justify them. Defect theories on the contrary have always been tied down to concrete models produced by specific patterns of spontaneous symmetry breaking. Here we shall depart from this (highly positive) trend, and allow ourselves the same speculative freedom inflationary theories enjoy. We shall therefore ask what is a generic defect, and what are the generic Doppler peak features induced by a generic defect.

One metaphysical and one practical motivation assist this project. Firstly one would like to know how much of what has already been found for textures and strings are generic defect novelties. For instance it was found in [1, 2] that texture Doppler peaks appear out of phase with respect to the standard inflationary peaks. Is this a robust defect feature? Or is it an

accident pertaining to textures? In other words, could a generic defect apply an arbitrary shift to the Doppler peaks? This is an important question, as topological defects and standard isocurvature perturbations (like the ones discussed in [6]) are not at all the same thing, a fact often overlooked. Therefore there is no reason why an out of phase signature would have to be associated with defects. A second example is provided by cosmic strings. Despite many uncertainties it has been found that cosmic strings do not have secondary Doppler peaks. This is a rather exotic feature, completely alien to inflationary theories. Is this feature a robust prediction for a large class of defect models? And if so what are the controlling factors responsible for the opposite behaviour of strings and textures in this respect?

A second, perhaps more practical motivation for this type of work lies in the conflict between inflation and defects. Are the inflationary Doppler peaks proof of inflation, or could one in principle cook up a defect which reproduced the inflationary Doppler peaks? Until this question has been answered it is daylight robbery to claim that a measurement of. say, the CDM prediction for the C_ℓ spectrum, would prove inflation.

A detailed and more serious discussion of this problem may be found in [5]. Here we merely highlight the most entertaining aspects of this work.

2 The ontology of defects and inflation

We now focus on the basic assumptions of inflationary and defect theories and isolate the most shocking contrasting properties. We define the concepts of active and passive perturbations, and of coherent and incoherent perturbations. In terms of these concepts inflationary perturbations are passive coherent perturbations. Defect perturbations are active perturbations more or less incoherent depending on the defect.

2.1 Active and passive perturbations, and their different perceptions of causality and scaling

The way in which inflationary and defect perturbations come about is radically different. Inflationary fluctuations were produced at a remote epoch, and were driven far outside the Hubble radius by inflation. The evolution of these fluctuations is linear (until gravitational collapse becomes non-linear at late times), and we call these fluctuations "passive". Also, because all scales observed today have been in causal contact since the onset of inflation, causality does not strongly constrain the fluctuations which result. In contrast, defect fluctuations are continuously seeded by defect evolution, which is a non-linear process. We therefore say these are "active" perturbations. Also, the constraints imposed by causality on defect formation and evolution are much greater than those placed on inflationary perturbations.

2.1.1 Active and passive scaling The notion of scale invariance has different implications in these two types of theory. For instance, a scale invariant gauge-invariant potential Φ with dimensions $L^{3/2}$ has a power spectrum

$$P(\Phi) = \langle |\Phi_{\mathbf{k}}|^2 \rangle \propto k^{-3}$$

in passive theories (the Harrison-Zeldovich spectrum). This results from the fact that the only variable available is k, and so the only spectrum one can write down which has the right dimensions and does not have a scale is the Harrison-Zeldovich spectrum. The situation is

different for active theories, since time is now a variable. The most general counterpart to the Harrison-Zeldovich spectrum is

$$P(\Phi) = \eta^3 F_\Phi(k\eta) \tag{1}$$

where F_Φ is, to begin with, an arbitrary function of $x = k\eta$. All other variables may be written as a product of a power of η, ensuring the right dimensions, and an arbitrary function of x. Inspecting all equations it can be checked that it is possible to do this consistently for all variables. All equations respect scaling in the active sense.

2.1.2 Causality constraints on active perturbations Moreover, active perturbations are constrained by causality, in the form of integral constraints [7, 8]. These consist of energy and momentum conservation laws for fluctuations in an expanding Universe. The integral constraints can be used to find the low k behaviour of the perturbations' power spectrum, assuming their causal generation and evolution [9]. Typically it is found that the causal creation and evolution of defects requires that their energy ρ^s and scalar velocity v^s be white noise at low k, but that the total energy fluctuations' power spectrum is required to go like k^4. To reconcile these two facts one is forced to consider the compensation. This is an underdensity in the matter-radiation energy density with a white noise low k tail, correlated with the defect network so as to cancel the defects' white-noise tail. When one combines the defects energy with the compensation density, one finds that the gravitational potentials they generate also have to be white noise at large scales [5]. Typically the scaling function $F_\Phi(k\eta)$ will start as a constant and decay as a power law for $x = k\eta > x_c$. The value x_c is a sort of coherence wavenumber of the defect. The larger it is the smaller the defect is. For instance $x_c \approx 12$ for cosmic strings (thin, tiny objects), whereas $x_c \approx 5.5$ for textures (round, fat, big things). Sophisticated work on causality [8] has shed light on how small x_c may be before violating causality. The limiting lower bound $x_c \approx 2.7$ has been suggested.

Although we will not here have a chance to dwell on technicalities, it should be stated that the rather general discussion presented above is enough to determine the general form of the potentials for active perturbations. This has been here encoded in the single parameter x_c. We shall see that x_c will determine the Doppler peak position for active perturbations. Doppler peaks are driven by the gravitational potential, so it should not be surprising that the defect length scale propagates into its potential, and from that into the Doppler peaks' position.

2.2 Coherent and incoherent perturbations

Active perturbations may also differ from inflation in the way "chance" comes into the theory. Randomness occurs in inflation only when the initial conditions are set up. Time evolution is linear and deterministic, and may be found by evolving all variables from an initial value equal to the square root of their initial variances. By squaring the result one obtains the variables' variances at any time. Formally this results from unequal time correlators of the form

$$\langle \Phi(\mathbf{k}, \eta)\Phi(\mathbf{k}', \eta')\rangle = \delta(\mathbf{k} - \mathbf{k}')\sigma(\Phi(k, \eta))\sigma(\Phi(k, \eta')), \tag{2}$$

where σ denotes the square root of the power spectrum P. In defect models however, randomness may intervene in the time evolution as well as the initial conditions. Although deterministic in principle, the defect network evolves as a result of a complicated non-linear process. If there is strong non-linearity, a given mode will be "driven" by interactions with the other modes in a way which will force all different-time correlators to zero on a time scale characterized by the "coherence time" $\theta_c(k, \eta)$. Physically this means that one has to perform a new "random"

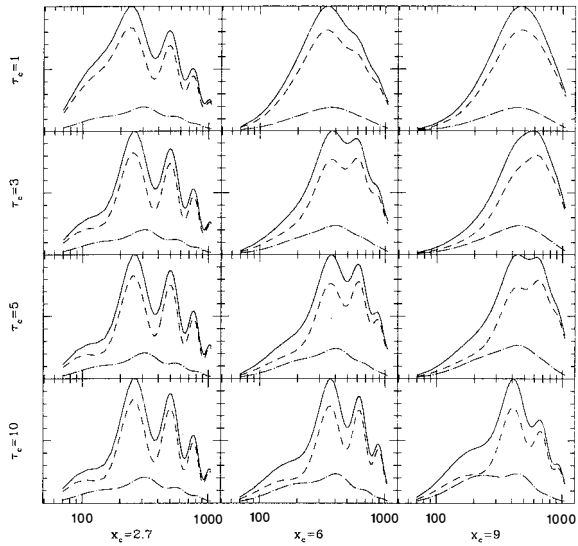

Figure 1: C_l spectra for a grid of models with various values of x_c (related to the defect coherence length) and $\theta_c \approx 2.35\tau_c$ (the defect coherence time). We have included the monopole term (dash) and dipole term (point-dash), Silk damping, and free-streaming. The monopole term is always dominant.

draw after each coherence time in order to construct a defect history [3]. The counterpart to (2) for incoherent perturbations is

$$\langle \Phi(\mathbf{k},\eta)\Phi(\mathbf{k}',\eta')\rangle = \delta(\mathbf{k}-\mathbf{k}')P(\Phi(k,\eta),\eta'-\eta)\ . \tag{3}$$

For $|\eta'-\eta| \equiv |\Delta\eta| > \theta_c(k,\eta)$ we have $P(\Phi(k,\eta),\Delta\eta) = 0$. For $\Delta\eta = 0$, we recover the power spectrum $P(\Phi(k,\eta),0) = P(\Phi(k,\eta))$.

We shall label as coherent and incoherent (2) and (3) respectively. This feature does not affect the Doppler peaks' position but it does affect the structure of secondary oscillations. An incoherent potential will drive the CMB oscillator incoherently, and therefore it may happen that the secondary oscillations get washed out as a result of incoherence.

3 Generic defect Doppler peaks

In Fig. 1 we show a grid of C_ℓ spectra functions of the two parameters introduced above: x_c (related to the defect coherence length) and θ_c (the defect coherence time). For the exact form of the stress energy of these defects we refer the reader to [5].

3.1 The peaks position

In general there may or may not be a system of secondary Doppler peaks. However if they exist, then their position is determined purely by x_c. For $x_c \approx 2.7$ (not impossible, but probably unrealistic because it is very close to the smallest turnover point allowed by causality [8, 10]) the peaks are at the adiabatic positions. As x_c increases from the adiabatic position the peaks are shifted to smaller scales. For $x_c \approx 5.4$ they are out of phase with the adiabatic peaks (as in [1, 2]). For $x_c > 8.5$ the peaks start only in the adiabatic secondary peaks region. For standard values of Ω_b and h these three cases would place the main "Doppler peak" at $l \approx 230$, 350, and 500, respectively. Therefore the placing of the peaks is *not* a generic feature of active fluctuations. Active perturbations simply add an extra parameter on which the Doppler peaks position is strongly dependent. In general we should expect that for the same Ω, Ω_b, and h, active perturbations will apply to the predicted CDM adiabatic peak position a shift of the form

$$l \to l + \frac{\eta_0}{\eta^*}\left(x_c - \frac{\pi\sqrt{3}}{2}\right) \tag{4}$$

where η_0 and η^* are the conformal times nowadays and at recombination. The secondary peaks' separation is not changed, in a first approximation. This is to be contrasted with non-flat inflationary models where $C_l(\Omega = 1)$ is taken into $C_{l\Omega^{-1/2}}$. The defect shift is additive whereas the low-Ω shift is multiplicative, a striking difference that should always allow us to distinguish between low Ω CDM and $\Omega = 1$ high-x_c defects.

3.2 Intensity of secondary oscillations

The strength of the secondary oscillations depends on both x_c and θ_c. For $x_c \approx 2.7$ there are secondary oscillations regardless of the exact θ_c value. This is a confusing defect, as not only does it place the Doppler peaks on the adiabatic position, but also the peak structure is quite insensitive to the defect incoherence. For larger x_c the secondary Doppler peaks survive only if the defect coherence time is much larger than x_c. This condition seems unphysical for large x_c so we expect realistic defects with large x_c not to have secondary oscillations.

This can be understood heuristically. Incoherence tends to erase secondary oscillations. However each mode is active only for a period of scaling time of the order of x_c. If $\theta_c > x_c$ then each mode is coherent for longer than it is active, and so the defect is effectively coherent and the secondary oscillations are preserved. If on the contrary $\theta_c < x_c$ then the defect has time to display its incoherence. Large defects (small x_c) are not active for long enough to display whatever reasonable incoherent properties they may have. Very small defects (large x_c) are active for long enough for their incoherence to be manifest, whatever reasonable coherence time they may have.

To help the reader to connect this general discussion with concrete defect theories. here is a rough guide to the topography of Fig. 1. Current understanding places the cosmic string models on the top right corner of Figure 1 (large x_c, τ_c smaller than 3). They should have a single peak well after the main adiabatic peak. Textures fall somewhere in the middle of the figure (x_c around 6, coherence time not yet measured). Their main peak should be out of phase with the adiabatic peaks. This is an accident related to the x_c value for textures, and not a robust defect feature. Texture secondary oscillations should exist but be softer than predicted by the coherent approximation (used in [1, 2]). How much softer depends on the exact value of the texture's θ_c. If their coherence time is of the same order as strings ($\tau_c \approx 3$) their secondary oscillation will be very soft.

4 Confusing defects and inflation

Given this state of affairs what are the chances of confusing inflation and defect theories? The answer to this question depends on Ω, on the inflation side, and on x_c, on the defect side. We have shown how only $\Omega = 1$ inflation and $x_c \approx 2.7$ (the causal lower bound) have a chance to be confused. Any defect with a larger x_c is bound to cause great disarray in what has come to be expected from Doppler peaks by inflationary trends. Two novelties stand out. First, if defects preserve a structure of secondary peaks, then this tends to be obtained from the inflationary one by an additive shift in l, rather than a multiplicative shift (as it happens for low Ω inflation). Second, defects may erase the secondary peaks.

It remains as an open question the case $\Omega = 1$ inflation vs $x_c = 2.7$ defects. Our work, and also [10] suggests that indeed in this case one may confuse defects and inflation. The work in [6] seems to draw the opposite conclusion. One would hope that this issue is clarified in the not too distant future.

Acknowledgements. I would like to thank Andy Albrecht, Pedro Ferreira and David Coulson for the very enjoyable collaboration leading up to this work. I am indebted to Kim Baskerville for reading this manuscript, and to Anne Davis for partial financial support. I should finally thank Ruth Durrer for ensuring my mental sanity during these Rencontres.

References

[1] R. Crittenden and N. Turok, *Phys. Rev. Lett.*, **75** 2642 (1995).

[2] R. Durrer, A. Gangui and M. Sakellariadou, *Phys. Rev. Lett.*, **76** 579 (1996).

[3] A. Albrecht, D. Coulson, P. Ferreira, and J. Magueijo, *Phys. Rev. Lett.* **76** 1413-1416 (1996).

[4] J.Magueijo, A. Albrecht, D. Coulson, P. Ferreira, *Phys. Rev. Lett*, **76** 2617 (1996).

[5] J.Magueijo, A. Albrecht, P. Ferreira, D.Coulson, astro-ph/9605047, sub. to *Phys. Rev. D*

[6] Hu and White, Acoustic signatures in the cosmic microwave background, IASSNS-96/6, astro-ph/9602019.

[7] J.Traschen, *Phys. Rev. D*, **31** 283-289 (1985); J.Traschen, *Phys. Rev. D*, **29** 1563-1574 (1984).

[8] J. Robinson and B. Wandelt, *Phys.Rev.D* **53** 618 (1996).

[9] L.F.Abbott and J.Traschen, *Astrophys.J.* **302** 39-42 (1986).

[10] N. Turok, Causality and the doppler peaks. astro-ph/9604172.

COSMIC STRINGS AND COHERENCE

M.Hindmarsh [1], M.Sakellariadou [2], G.Vincent [1]
[1] *School of Mathematical and Physical Sciences, University of Sussex, Brighton BN1 9QH, U.K.*
[2] *Département de Physique Théorique, Université de Genève, Quai Ernest-Ansermet 24, CH-1211 Genève 4, Switzerland*

Abstract

Cosmic strings provide a radically different paradigm for the formation of structure to the prevailing inflationary one. They afford some extra technical complications: for example, the calculation of the power spectrum of matter and radiation perturbations requires the knowledge of the history of the evolution of the defects in the form of two-time correlation functions. We describe some numerical simulations of string networks, designed to measure the two-time correlations during their evolution.

1 Introduction

Calculations of the Cosmic Microwave Background (CMB) fluctuations from cosmic strings [1] have proved much harder than their inflationary equivalents. One of the reasons is that the energy-momentum of the defects cannot be considered to be a perfect fluid like most of the rest of the contents of the Universe: instead we have to use numerical simulations to find how important quantities such as the energy density and velocity evolve. The defect energy-momentum is then a source for perturbations in the gravitational field, which must be calculated either using Greens functions [2] or by direct numerical integration [3].

A major problem with using numerical simulations is the lack of dynamic range, even with supercomputers. The largest simulations can only span a ratio of conformal times of about 10, which is not totally satisfactory. For calculating simple quantities such as power spectra an alternative approach is available: to use numerical simulations to construct an accurate model of the appropriate source functions, which are two-time correlation functions of various components of the energy-momentum tensor. Relatively simple Greens functions can then be

used to compute the power spectra of perturbations in perfect fluids, including CDM and tightly coupled photons and baryons.

This talk summarises some work in progress [4] on the properties of cosmic strings as sources of the gravitational perturbations. An issue of interest which we address is that of *coherence*, recently raised in [5], and explored in more detail by the same authors in [6].

2 Perturbations from defects

A simple model serves to illustrate the issues involved. We suppose that the Universe is spatially flat with zero cosmological constant, and consists of Cold Dark Matter (CDM), photons, baryons, and defects, with average densities ρ_c, ρ_γ, ρ_B and ρ_s respectively. The fluid density perturbations are written δ_c, δ_γ, δ_B and the velocity perturbations are $\boldsymbol{v}_c$, $\boldsymbol{v}_\gamma$, $\boldsymbol{v}_B$. The defect energy-momentum tensor is $\Theta_{\mu\nu}$, which is also a small perturbation to the background, and to first order can be considered separately conserved (or *stiff* [2]). We take the synchronous gauge. Before decoupling at a redshift of $z_{\rm rec} \simeq 1100$ (assuming the standard ionization history), the photons and baryons were tightly coupled by Thompson scattering, which forces $\delta_B = \frac{3}{4}\delta_\gamma$ and $\boldsymbol{v}_B = \boldsymbol{v}_\gamma$.

It is very convenient to use an entropy $s = (\frac{3}{4}\delta_\gamma - \delta_c)$, and its time derivative $\dot{s}$, which is equal to the divergence of the radiation peculiar velocity. It is also convenient to introduce the pseudoenergy τ_{00} [2], which is part of an ordinarily conserved energy-momentum pseudotensor:

$$\tau_{00} = \Theta_{00} + \frac{3}{8\pi G}\left(\frac{\dot{a}}{a}\right)^2 (\Omega_c\delta_c + \Omega_\gamma(1+R)\delta_\gamma) + \frac{1}{4\pi G}\left(\frac{\dot{a}}{a}\right)\dot{\delta}_c, \tag{1}$$

where $R = 3\rho_B/4\rho_\gamma$. In the sychronous gauge the pseudo-energy is in fact proportional to the scalar curvature of the constant conformal time slices.

Let us now define the pseudo-energy perturbation

$$\delta_{00} = \frac{8\pi G}{3}\left(\frac{a}{\dot{a}}\right)^2 \tau_{00}. \tag{2}$$

We may use the conservation equations for the defects to write the equations of motion of the fluids as four first-order equations [3]

$$\dot{\delta}_c = \frac{3}{2}\left(\frac{\dot{a}}{a}\right)[\delta_{00} - (\Omega_c + 2\Omega_\gamma(1+R))\delta_c - 2\Omega_\gamma(1+R)s] - \frac{\mathbf{3}}{\mathbf{2}}\left(\frac{\dot{\boldsymbol{a}}}{\boldsymbol{a}}\right)\boldsymbol{\Omega_s\delta_s}, \tag{3}$$

$$\dot{s} = y, \tag{4}$$

$$\dot{\delta}_{00} = \left(\frac{\dot{a}}{a}\right)(1+3w)\delta_{00} + \frac{4}{3}\Omega_\gamma(1+R)y + \boldsymbol{\Omega_s k v_s}, \tag{5}$$

$$\dot{y} = -k^2c_s^2(s+\delta_c) - \left(\frac{\dot{a}}{a}\right)(1-3c_s^2)y, \tag{6}$$

where $w = p/\rho$, the ratio of the total pressure to the total energy density, and $c_s^2 = 1/3(1+R)$.

These equations have the inhomogeneous form $\dot{\Delta}_i = M_i^j\Delta_j + \Sigma_i$, where $\Delta = (\delta_c, s, \delta_{00}, y)^T$, and the source vector, picked out in bold above, is $\Sigma = (-\frac{3}{2}(\dot{a}/a)\Omega_s\delta_s,\ 0,\ \Omega_s k v_s,\ 0)^T$. The solution to these equations with initial condition $\Delta(\eta_i)$ is then

$$\Delta(\eta) = G(\eta, \eta_i)\Delta(\eta_i) + \int_{\eta_i}^{\eta} d\eta' G(\eta, \eta')\Sigma(\eta'), \tag{7}$$

where $G(\eta, \eta')$ is the Green's function. The initial perturbation is $\Delta(\eta_i) = (\delta_c(\eta_i), 0, 0, 0)^T$, corresponding to perturbations which are both adiabatic, in the sense that $s = 0$, and isocurvature,

in the sense that $\tau_{00} = 0$. In the presence of defects, the isocurvature condition forces the initial perturbations in the matter and radiation to *compensate* those of the defects. However, the initial compensation can be ignored, as the initial condition consists only of decaying modes, which is one of the advantages of using this basis for the perturbations [3]. An initial condition consisting purely of adiabatic growing modes would be $\Delta(\eta_i) = (\delta_c(\eta_i), 0, 2\delta_c(\eta_i), 0)^T$.

At time η, the power spectra of the various perturbations are therefore

$$\langle |\Delta_i(\eta)|^2 \rangle = \int_{\eta_i}^{\eta} d\eta_1 \int_{\eta_i}^{\eta} d\eta_2 G_i^j(\eta, \eta_1) G_i^k(\eta, \eta_2) \langle \Sigma_j(\eta_1) \Sigma_k^*(\eta_2) \rangle, \tag{8}$$

(no sum on i). It is clear from this equation that the calculation of the power spectra requires the knowledge of the two-time correlation functions

$$C^{\rho\rho}(\eta_1, \eta_2) = \langle \delta_s(\eta_1) \delta_s^*(\eta_2) \rangle, \quad C^{UU}(\eta_1, \eta_2) = \langle v_s(\eta_1) v_s^*(\eta_2) \rangle, \quad X^{\rho U}(\eta_1, \eta_2) = \langle \delta_s(\eta_1) v_s^*(\eta_2) \rangle, \tag{9}$$

where the angle brackets are to be understood as averages over ensembles of topological defects.

3 Flat space cosmic string simulations

In order to compute the averages in (9) we performed many simulations of networks of string in Minkowski space [7, 8]. It is not at first sight such a good idea to abandon the expanding Universe, but there are arguments which support the procedure. Firstly, a spatially flat FRW cosmology is conformal to Minkowksi space, so one can identify Minkowksi time with conformal time, and Minkowksi space coordinates with comoving space coordinates. Secondly, the string network scale length is significantly smaller than the horizon length, which means that the effects of the expanding background on the dynamics of the string should be small. Thirdly, a string network can be well described by a couple of parameters: the string density and the correlation length of the network [9], which means we can hope to translate Minkowksi space results into FRW results by appropriate scalings. Lastly, the savings in computational resources are immense. The strings can be evolved on a cubic spatial lattice, which means that only integer arithmetic need be used, and that self-intersections are extremely easy to check for.

A vital property possessed by string networks is known as *scaling*. In its simplest form, scaling means that all quantities with dimensions of length are proportional to a fundamental network scale ξ, which is in turn a function of length scales in the network dynamics. In a cosmological setting, the only scale in the equations of motion is the horizon or the conformal time η. Thus $\xi \propto \eta$, where ξ is understood to be a comoving scale. The invariant length density L (which is proportional to the energy density through the string mass per unit length μ) is therefore, on naive dimensional grounds, proportional to ξ^{-2}. In fact, it is convenient to *define* ξ by $\xi = 1/\sqrt{\mathrm{L}}$. The simulations conserve energy and thus invariant length. However, real strings decay into particles and gravitational radiation, so we model this by excluding small loops below a threshold l_c from being counted as string. This threshold may be chosen in many ways: it can be a constant, or it may be a fixed fraction of ξ. However, we find that the remainder ("long" or "infinite" string) always scales towards the end of the simulations, that is, $\xi = x\eta$, although the constant x depends on how the cut-off is chosen.

Scaling has important implications for the correlation functions. For example, the correct scaling behaviour for the power spectrum of the string density is

$$C^{\rho\rho}(\eta, \eta) = \frac{1}{\xi} P^{\rho}(k\xi). \tag{10}$$

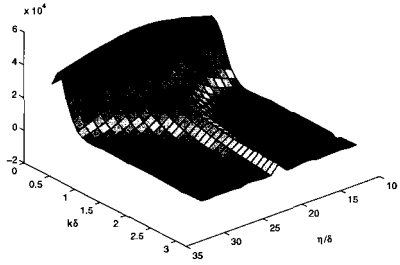

Figure 1: Two-time correlation function $\langle \Theta_{00}(k,\eta)\Theta^*_{00}(k,\eta')\rangle$ for $\eta' = 22\delta$

We can also express the velocity power spectrum in terms of a similar scaling function $P^U(k\eta)$. These forms ensure that the mean square fluctuation in the string density at horizon crossing is constant, when ξ/η is constant. Hence the compensating fluctuations in the matter and radiation are also constant at horizon crossing, which gives a Harrison-Zel'dovich spectrum.

In Figures 1, 2, and 3 the correlation functions (9) measured for strings whose length is above the threshold l_c are displayed. They result from many simulations on $(64\delta)^3$ or $(128\delta)^3$ lattices, where δ is the lattice spacing, with approximately 7500 or 60000 string points. For calculating the two-time correlation functions we typically averaged over 50 simulations.[1] We find that good fits in the important regions where the correlators are large are obtained from the following functions

$$C^{\rho\rho} = \frac{1}{\sqrt{\xi\xi'}}\sqrt{P^\rho(k\xi)P^\rho(k\xi')}\,e^{-\frac{1}{2}\Upsilon^2k^2(1-(k\Delta))(\eta-\eta')^2} \tag{11}$$

$$C^{\rho U} = \frac{1}{\sqrt{\xi\xi'}}\sqrt{P^\rho(k\xi)P^\rho(k\xi')}\,e^{-\frac{1}{2}\Upsilon'^2k^2(\eta-\eta')^2}\left(\frac{\alpha}{k\sqrt{\xi\xi'}} - \Upsilon'^2k(\eta-\eta')\right) \tag{12}$$

$$C^{UU} = \frac{1}{\sqrt{\xi\xi'}}\sqrt{P^U(k\xi)P^U(k\xi')}\,e^{-\frac{1}{2}\Upsilon''^2k^2(\eta-\eta')^2}(1-\Upsilon''^2k^2(\eta-\eta')^2) \tag{13}$$

The values for Υ, Υ' and Υ'' are given in Table 3. Δ is approximately 3δ, which indicates that it is probably a lattice artifact.

Table 1. The values of the parameters for the models in equations (11), (12) and (13), obtained by minimising the χ^2.

l_c	Υ	α	Υ'	Υ''
2δ	0.21 ± 0.05	0.19 ± 0.05	0.42 ± 0.05	0.36 ± 0.07
4δ	0.18 ± 0.05	0.16 ± 0.05	0.42 ± 0.05	0.42 ± 0.06

4 Implications for strings in FRW backgrounds

The effect of the expansion of the Universe in a Friedmann model is to reduce the velocity string segments by Hubble damping, just as for particles. However, as the string moves relativistically,

[1]For more details of the simulations, the reader is referred to [4].

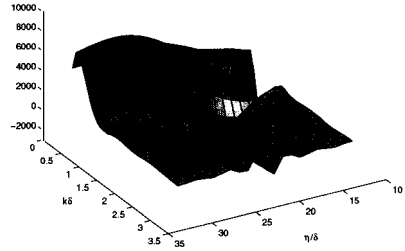

Figure 2: Two-time correlation function $\langle U(k,\eta)\Theta^*_{00}(k,\eta')\rangle$ for $\eta' = 22\delta$

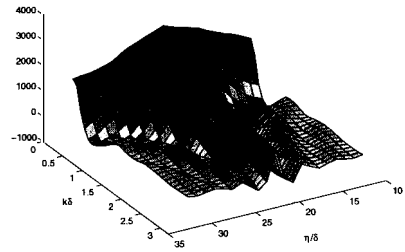

Figure 3: Two-time correlation function $\langle U(k,\eta)U^*(k,\eta')\rangle$ for $\eta' = 22\delta$

the equation of motion becomes non-linear. The conservation equations for Θ_{00} and $U = i\hat{k}_i\Theta_{0i}$ become

$$\dot{\Theta}_{00} + \frac{\dot{a}}{a}(\Theta_{00} + \Theta) + kU = 0, \tag{14}$$

$$\dot{U} + 2\frac{\dot{a}}{a}U + \frac{1}{3}k(\Theta + 2\Theta^{\rm s}) = 0, \tag{15}$$

where $\Theta \equiv \Theta_{ii}$ and $\Theta^{\rm s} \equiv (\hat{k}_i\hat{k}_j - \frac{1}{3}\delta_{ij})\Theta_{ij}$. Both Θ and $\Theta^{\rm s}$ are unconstrained by energy-momentum conservation, and so one could imagine that fluctuations in the pressure could drive extra fluctuations in the energy density through the second term in (14). As the scale of this term is η^{-1} rather than k, this could change the conclusions of the previous section, that the coherence time for a mode of wavenumber k was proportional to k^{-1}. Instead we could have the situation assumed in [5], with coherence time proportional to η. Outside the horizon, this makes a significant difference.

Let us examine how this might work, for superhorizon modes ($k\eta \ll 1$). Firstly, we divide Θ_{00} and Θ into coherent and incoherent parts:

$$\Theta_{00} = \bar{\Theta}_{00} + \Delta_{00}, \qquad \Theta = 3w_s\bar{\Theta}_{00} + r, \tag{16}$$

where r is a random variable, whose fluctuations are limited only by the requirement of scale invariance. Thus

$$\langle r(\eta_1)r^*(\eta_2)\rangle = \frac{1}{\sqrt{\eta_1\eta_2}}R(\eta_1/\eta_2). \tag{17}$$

It is then not hard to show that energy-momentum conservation implies that

$$\langle|\Delta_{00}|^2\rangle \sim \langle|r|^2\rangle.$$

Since $\langle|r|^2\rangle < \langle|\Theta|^2\rangle$, the extra fluctuations in the density induced by the pressure term are controlled by the size of the pressure term. Now, in the Minkowski space simulations, we find that $\langle|\Theta|^2\rangle \sim 0.1\langle|\Theta_{00}|^2\rangle$ for $k\eta \ll 1$, and thus we argue that any extra fluctuations in Friedmann models, with a coherence time set by the horizon η, are likely to be small.

5 Conclusions

We have taken the first steps on the road to calculating the matter and radiation power spectra in the cosmic string scenario, by constructing a realistic model of the important parts of the string energy-momentum tensor which drive the fluid perturbations. We have argued that the Minkowski space simulations we used to construct the model incorporates the essential features of string evolution in an expanding universe, and that corrections due to the expansion are small. This of course should be checked with FRW string codes. Perhaps the most important feature of the string network is its coherence time, the time over which the phases of the Fourier components of the string energy-momentum tensor are correlated. We find that there is no single coherence time for the whole network. Although the fall-off away from the equal-time value is modulated by functions whose dominant behaviour is $\exp(-(\eta_1 - \eta_2)^2/2\eta_c^2)$, and the scale is set by k^{-1} for each mode, η_c is different for different correlation functions.

Acknowledgements. GRV and MBH are supported by PPARC, by studentship number 94313367, Advanced Fellowship number B/93/AF/1642 and grant number GR/K55967. MS is supported by the Tomalla Foundation. Partial support is also obtained from the European Commission under the Human Capital and Mobility programme, contract no. CHRX-CT94-0423.

References

[1] Hindmarsh M. and Kibble T.W.B.. 1995, *Rep. Prog. Phys* **58** 477

[2] Veeraraghavan S. and Stebbins A., 1990, *Astrophys. J.* **365**, 37

[3] Pen U.L., Spergel D.N. and Turok N., 1994, *Phys. Rev.* **D49** 692

[4] Vincent G., Hindmarsh M. and Sakellariadou M., 1996, *Correlations in Cosmic String Networks* `astro-ph/9606137`

[5] Albrecht A., Coulson D., Ferreira P. and Magueijo J., 1996, *Phys. Rev. Lett.* **76** 1413

[6] Magueijo J., Albrecht A., Coulson D. and Ferreira P., 1996, *MRAO-1917* `astro-ph/9605047`

[7] Smith A.G. and Vilenkin A., 1987, *Phys. Rev.* **D36**, 990

[8] Sakellariadou M. and Vilenkin A., 1988, *Phys. Rev.* **D37**, 885

[9] Copeland E.J., Kibble T.W.B. and Austin D., 1992, *Phys. Rev.* **D45** R1000

LARGE ANGULAR SCALE CMB ANISOTROPIES FROM GLOBAL TEXTURE

Ruth Durrer
Université de Genève
Département de Physique Théorique
24, quai E. Ansermet
CH-1211 Genève 4
SUISSE

Abstract

I present a method to calculate the large angular scale CMB anisotropies using gauge–invariant local perturbation variables. The method is applied to structure formation with global texture. Like in inflationary models, a Harrison Zel'dovich spectrum of fluctuations results also in this scenario. I compare the results with previous investigations and a substantial difference in CDM initial conditions is found. This difference actually represents a real difference in the physical models investigated.

1 Introduction

An inflationary period not only solves the standard cosmological horizon and flatness problems, but generically also leads to a Harrison Zel'dovich spectrum of density fluctuations. To obtain small enough fluctuation amplitudes, however, usually requires substantial fine tuning. An alternative mechanism to create fluctuations are topological defects which can form during symmetry breaking phase transitions in the early universe [1]. Depending on the broken symmetry being global or gauged, the defects are called global or local. Defects viable to seed cosmic structure formation are local cosmic strings or global strings, monopoles or texture. They obey (up to possible logarithmic corrections) a scaling relation which ensures that they make up always the same small fraction of the density of the universe. (Local monopoles or domain walls would soon dominate and local textures thin out.) This energy density fraction is of the order of $\epsilon = 4\pi G T_c^2$, where T_c denotes the symmetry breaking temperature. To obtain fluctuation amplitudes of about 10^{-5}, will thus require a symmetry breaking scale $T_c \sim 10^{16} GeV$, i.e. a GUT scale phase transition. As is shown by the numerical simulations presented here, topological defects also lead to a Harrison Zel'dovich spectrum of fluctuations and are thus compatible with the COBE observations.

In the next section, I present the system of equations which we have solved in our simulations. In section 3, I describe our results and compare them with other simulations. It turns out that our results differ from other simulations by nearly a factor of 2. I conclude with a discussion of a possible reason for this discrepancy.

2 Formalism

The scalar field equation of motion is

$$g^{\mu\nu}\nabla_\mu\nabla_\nu\phi + \frac{\partial V}{\partial \phi} = 0 \ , \tag{1}$$

where $g^{\mu\nu}$ denotes the unperturbed Robertson Walker metric and ∇_μ is the covariant derivative with respect to this metric. For our numerical computations, we consider an $O(4)$ model with zero temperature potential $V_0 = \frac{\lambda}{4}(\phi^2 - \eta^2)^2$ for some energy scale η [1, 2]. At low temperatures, (1) can be approximated by a nonlinear σ–model. Setting $\beta = \phi/\eta$ the corresponding equation of motion then reads[2]

$$\Box\beta - (\beta \cdot \Box\beta)\beta = 0 \ , \quad \beta^2 = 1 \ . \tag{2}$$

The numerical solution of this equation on a reasonably large grid requires considerable numerical effort [3, 4].

To describe the motion of photons in the geometry perturbed by such a global scalar field and the induced cold dark matter (CDM) fluctuations one has in principle to solve the Boltzmann equation where the collision term is given by the Compton scattering off the free electrons. However, on large angular scales, $\theta \geq 2^o$, which enter the horizon only after recombination, the scattering term is unimportant and we can neglect it. The first order perturbation equation for the photons in direction γ can then be written as

$$(\partial_t + \gamma^i\partial_i)\chi = 3\gamma^i\partial^j E_{ij} + \gamma^k\gamma^j\epsilon_{kli}\partial_l B_{ij} \equiv S_T(t, \boldsymbol{x}, \boldsymbol{\gamma}) \ . \tag{3}$$

Up to unimportant monopole and dipole terms, χ is the Laplacian of the temperature fluctuation $\chi \approx \nabla^2(\delta T/T)$. E and B denote the electric and magnetic part of the Weyl tensor and

ϵ_{kli} is the totally antisymmetric tensor in three dimensions (see [3]). This equation illustrates once more that photons only couple to the conformally invariant Weyl part of the curvature.

The Weyl tensor is determined by the scalar field and CDM perturbations and thus plays the role of a source term in this equation. In eqn. (3) the contribution from the electric part of the Weyl tensor does not contain tensor perturbations and scalar perturbations do not induce a magnetic gravitational field. If vector perturbations are unimportant, the two terms on the r.h.s of eqn. (3) yield thus a split into scalar and tensor perturbations which is local.

Since the Weyl tensor of Friedmann Lemaître universes vanishes, the r.h.s. of eqn. (3) is manifestly gauge invariant. Hence also the variable χ is gauge invariant.

The general solution to eqn. (3) is given by

$$\chi(t,\boldsymbol{x},\boldsymbol{\gamma}) = \int_{t_i}^{t} S_T(t',\boldsymbol{x}+(t'-t)\boldsymbol{\gamma},\boldsymbol{\gamma})dt' \; + \; \chi(t_i,\boldsymbol{x}+(t_i-t)\boldsymbol{\gamma},\boldsymbol{\gamma}) \; , \tag{4}$$

where S_T is the source term on the r.h.s. of eqn. (3). Let us compare this result with the more familiar one, where one calculates $\delta T/T$ by integrating photon geodesics (which is of course equivalent to solving the Liouville equation). For simplicity, we specialize to the case of pure scalar perturbations (the expressions for vector and tensor perturbations given in [5] can be compared with eqn. (4) in the same manner.) For scalar perturbations, integration of photon geodesics yields [5]

$$\frac{\delta T}{T}(t_f,\boldsymbol{x}_f,\boldsymbol{\gamma}) = -[\frac{1}{4}D_g^{(r)} - \boldsymbol{V}\cdot\boldsymbol{\gamma} + (\Psi - \Phi)]\Big|_i^f + \int_i^f (\dot{\Psi}-\dot{\Phi})d\lambda \; . \tag{5}$$

Here Ψ and Φ denote the Bardeen potentials as defined, e.g., in [6, 5]. On super horizon scales (which are the important scales for the Sachs–Wolfe contribution) $V_i\cdot\gamma^i$ can be neglected. Furthermore, the contributions of the square bracket of eqn. (5) from the final time $t=t_f$, only lead to uninteresting monopole and dipole terms. Using the expression for the Weyl tensor in terms of Φ and Ψ leads after an integration by parts to

$$\frac{\delta T}{T}(t,\boldsymbol{x},\boldsymbol{\gamma}) = \frac{1}{4}D_g^{(r)}(t_i,\boldsymbol{x}_i) + 3\int_i^f \nabla^{-2}\partial^j E_{ij}\gamma^i dt \tag{6}$$

Comparing this result with eqn. (4), we find

$$\chi(t_i,\boldsymbol{x}_i,\boldsymbol{\gamma}) = \frac{1}{4}\nabla^2 D_g^{(r)}(t_i,\boldsymbol{x}_i) = \frac{1}{4}\nabla^2 D_g^{(r)}(t_i,\boldsymbol{x}-\boldsymbol{\gamma}(t-t_i)). \tag{7}$$

We now want to investigate this initial value and decompose eqn. (6) into terms due to CDM and terms coming from the seeds, the scalar field. We assume that dark matter and radiation perturbations are adiabatic on *superhorizon scales*, $D_g^{(r)} = (4/3)D_g^{(c)}$. We can then derive from equations (2.36, 2.37, 2.45, 2.46, 2.47) in [5]

$$\frac{1}{4}D_g^{(r)} = \frac{5}{3}\Phi_C + \frac{2}{3}\dot{\Phi}_C/(\dot{a}/a) + \Phi_S$$

on super–horizon scales. Here the Bardeen potentials are split into parts due to cold dark matter (C) and the scalar field (s) respectively. For cold dark matter $\Psi_C = -\Phi_C$. Using this, we can bring eqn. (4) into the form

$$\begin{aligned}\frac{\delta T}{T}(t_f,\boldsymbol{x}_f,\boldsymbol{\gamma}) \;\; &= \;\; \frac{1}{3}\Psi_C(t_i,\boldsymbol{x}_i) - \frac{2}{3}\dot{\Psi}_C/(\dot{a}/a)(t_i,\boldsymbol{x}_i) + 2\int_i^f \dot{\Psi}_C dt \\ &\quad + \Phi_S(t_i,\boldsymbol{x}_i) - \int_i^f \nabla^{-2}S_{TS}(t,\boldsymbol{x}_f-(t_f-t)\boldsymbol{\gamma},\boldsymbol{\gamma})dt \; ,\end{aligned} \tag{8}$$

where S_{TS} denote the portion of the source term due to the scalar field only.

From an analysis analogous to the one presented here for scalar perturbations, one can conclude that initial contributions to $\delta T/T$ from vector perturbations can be neglected on super–horizon scales and that those for tensor perturbations vanish. eqn. (8) is thus the general solution on superhorizon scales, $\lambda >> t_i$ for our adiabatic model (including vector and tensor perturbations of the seeds).

For pure CDM, $\Phi_C = -\Psi_C =$ constant, and $\Phi_S = S_{TS} = 0$ one easily recovers the well-known result

$$\frac{\delta T}{T}(t, \boldsymbol{x}, \boldsymbol{\gamma}) = \frac{1}{3}\Psi_C(t_i, \boldsymbol{x} - \boldsymbol{\gamma}(t - t_i)) \; .$$

The Bardeen potential $\Psi_C = -\Phi_C$ is determined by the CDM density perturbation whose evolution equation is given by [7]

$$\ddot{D} + (\frac{\dot{a}}{a})\dot{D} - 4\pi G a^2 \rho_C D = 8\pi G \dot{\phi}^2 = \mathcal{S} \; . \tag{9}$$

During the radiation dominated era $8\pi G\rho_R D_R$ in principle has to be included in eqn. (9). But since radiation perturbations cannot grow substantially on sub-horizon scales, and since dark matter fluctuations do not grow in a radiation dominated universe [8], their influence is not important on scales which enter the horizon only in the matter dominated epoch. (We have checked this and found differences of up to 20% on small scales and much less on large scales.)

To determine the CDM initial conditions, we use that the time dependence of $\mathcal{S}$ on super horizon scales is given by $\mathcal{S} \propto 1/\sqrt{t}$. We then can solve (9) exactly on super horizon scales, which leads to the initial conditions

$$D(t_i) = -4/9 t_i^2 \mathcal{S} \quad , \quad \dot{D}(t_i) = -2/3 t_i \mathcal{S} \; .$$

This initial conditions yield about a factor of two larger CDM perturbations than the approach presented in [4].

3 Results and Discussion

The cosmic microwave background (CMB) perturbation spectrum resulting from our simulations is presented in Fig. 1.

Even though this is not obvious, the CMB power spectrum fits very well a cold dark matter induced spectrum of anisotropies for which

$$C_\ell = C_2 \frac{\Gamma(l + (n-1)/2)\Gamma((9-n)/2)}{\Gamma(l + (5-n)/2)\Gamma((n+3)/2)} \tag{10}$$

with $n = 0.9 \pm 0.25$. The minimal χ^2 is 0.56 (see Fig. 1 and for more details [3]).

To reproduce the COBE amplitude $Q_{COBE} = (20 \pm 5)\mu K$ [9], we have to normalize the spectrum by choosing the phase transition scale η according to

$$\epsilon = 4\pi G \eta^2 = (0.8 \pm 0.4) 10^{-5} \; . \tag{11}$$

This value is about a factor of 2 smaller than the result obtained in [10, 4]. Unfortunately I do not fully understand why this is so. One part of the answer lies in the dark matter fluctuations. As already mentioned our choice of initial conditions leads to about a factor 2 larger CDM fluctuations. Even though the CDM contributions to the power spectrum themselves are only

about 20% of the total, they add in phase to the scalar field contributions, and the average over ℓ of $\ell(\ell+1)c_\ell$ drops by about a factor of two if we neglect CDM (see Fig. 2):

$$\langle \ell(\ell+1)c_\ell \rangle_{scal} = 8\epsilon^2 \;\; ; \;\; \langle \ell(\ell+1)c_\ell \rangle_{tot} = 15\epsilon^2 \; .$$

Therefore, if the dark matter perturbations are significantly smaller, this can lead to an increase in ϵ by about a factor 1.4.

This does not account for the full factor 2 in the difference of our results. However taken into account the level of complication of the simulations and the completely different approaches to calculate the CMB power spectra an agreement within 50% is a first result to build upon.

Let me finally discuss the difference in the dark matter initial conditions:

The way we define our initial conditions, all components in the total energy momentum tensor can have small white noise perturbations about an average Friedmann universe energy momentum tensor. We do not require that at some initial time, t_i (the time of the phase transition) the universe was exactly Friedmann and all perturbations vanish at t_i. In that sense we free ourselves from the original GUT inspired version of the texture scenario and just assume that the perturbations in the energy momentum tensor can by described effectively by causally evolving scalar field degrees of freedom, a self ordering process. The white noise spectrum on superhorizon scale is dictated by causality.

On the other hand, in [4], the universe is assumed perfect Friedmann before t_i and therefore a so called 'pseudo energy' is required to vanish identically on superhorizon scales.

We however believe that this approach leads to too small CDM fluctuations and hence to a high bias factor incompatible with observations (compare [4] and [3]).

Acknowledgment

Most of the numerical work has been performed in collaboration with Z.H. Zhou. I thank Neil Turok for valuable discussions. This work was supported by the Swiss National Science Foundation.

References

[1] T.W.B. Kibble, *J. Phys.* **A9**, 1387 (1976).

[2] R. Durrer in: *Formation and Interactions of Topological Defects*, eds. A.C. Davis. R. Brandenberger and T.B.W. Kibble, *NATO ASI Series B 349*, 255 (1995).

[3] R. Durrer and Z.H. Zhou *Phys. Rev.* **D53**, 1 (1996).

[4] U.-L. Pen, D.N. Spergel and N. Turok, *Phys. Rev.* **D49**, 692 (1994).

[5] R. Durrer, *Fundamentals in Cosmic Physics*, **15**, 209 (1994).

[6] H. Kodama and M. Sasaki, *Prog. Theor. Phys. Suppl.* **78**, 1 (1984).

[7] R. Durrer, *Phys. Rev.* **D42**, 2533 (1990).

[8] P. Mészáros, *Astron. Astrophys.* **37**, 225 (1974).

[9] K.M. Gorski et al. *Ap. J.* **430**, L85, K.M. Gorski, ibid. L89 (1994).

[10] D. Bennett and S.H. Rhie, *Astrophys. J.* **406**, L7 (1993).

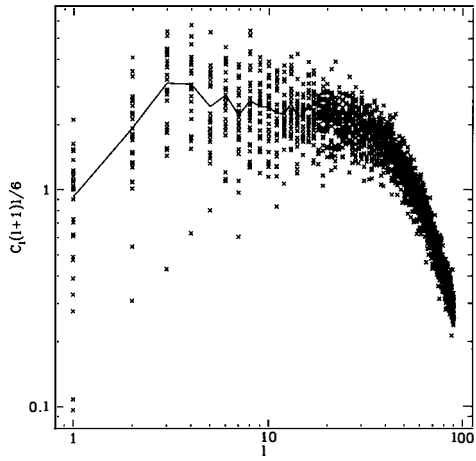

Figure 1: The values $\ell(\ell+1)C_\ell/6$ for 27 observers are plotted for $\epsilon = 1$. The crosses are the individual observers and the solid line indicates the average. The sharp drop after $\ell \sim 30$ is due to finite resolution (our dynamical range is approximately 25).

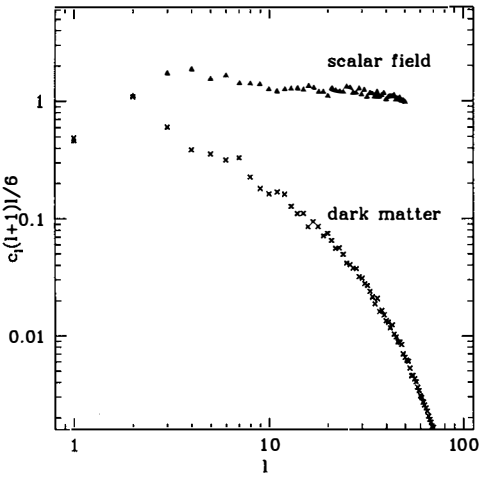

Figure 2: The same quantity as above (for only one observer) is shown where for the triangles only the scalar field contribution is taken into account and crosses represent the CDM contribution alone. Even though the CDM contribution alone amounts only to about 20% ; the pure scalar field $c_l's$ are nearly a factor 2 lower than the full result (see Fig. 1 and text). The CDM contribution is clearly not scale invariant. It shows a $n = 0$, white noise spectrum (see [3]).

NON–GAUSSIAN FLUCTUATIONS FROM TEXTURES

Alejandro Gangui
ICTP – International Center for Theoretical Physics,
P. O. Box 586, 34100 Trieste, Italy.
and
SISSA – International School for Advanced Studies,
Via Beirut 4, 34013 Trieste, Italy.

Abstract

One of the most powerful tools to probe the existence of cosmic defects in the early universe is through the Cosmic Microwave Background (CMB) radiation. It is well known that computations with causal sources are more involved than the adiabatic counterparts based on inflation, and this fact has in part hampered the development of fine detailed predictions. Analytical modeling, while necessarily limited in power, may tell us the overall characteristics of CMB from defects and hint at new features. We apply an analytical model for textures to the study of non–Gaussian features of the CMB sky and compare our predictions with the four–year *COBE*-DMR data.

1 Introduction

It has by now become clear that one of the most promising ways to learn about the early universe is through the Cosmic Microwave Background (CMB) radiation. With the prospective launch of future missions. like MAP and COBRAS/SAMBA[1], one can hope that many of the so far elusive cosmological parameters will be pinned down with unprecedent precision. The four–year *COBE* plus other large–scale structure data have placed strong constraints on current models of structure formation. However the remaining window is still too large and many (widely) different cosmological models pass the test. This is actually the case with cosmic defect theories, on the one hand and inflation–based adiabatic models on the other.

The search for the so–called Doppler peaks (or Sakharov peaks if you like) seems to be among the first goals for next generation detectors, the aim being in trying to discriminate among, say, standard adiabatic CDM models[1)], cosmic strings[2)] and textures[3)]. Whereas the generation of CMB anisotropies seems to be fully understood within adiabatic models [refer to Hu's contribution to these proceedings], the same does not happen for the latter models, where the non–linear evolution of the defects and their active role in seeding anisotropies in the CMB makes the analysis far more involved [see Durrer's contribution]. Moreover, causal sources can produce spectra mimicking the outcome of inflationary models[4)], hence increasing the uncertainty and calling for fast and accurate methods for computing the theoretical predictions [Seljak's contribution], and refined experiments to confront these competing theories.

Other means of narrowing somewhat the window regards the recognition that the CMB radiation carries valuable information of the processes that generated the anisotropies, all along the path of the photons from the last scattering surface to our present detectors: should future experiments find (with high confidence level) a departure of the statistics of the anisotropies from Gaussianity, it would disfavor the standard inflaton field quantum fluctuation origin of the cosmological perturbations. It then follows that it is interesting to calculate what predictions cosmic defects make regarding non–Gaussian features in the CMB sky. It is the aim of this short contribution to report on some work done on the CMB three–point correlation function predicted by textures within a simple analytical model.

2 The model

Magueijo[5)] recently proposed a simple analytical model for the computation of the $\mathcal{C}_\ell$'s from textures. The model exploits the fact that in this scenario the microwave sky will show evidence of spots due to perturbations in the effective temperature of the photons resulting from the non–linear dynamics of concentrations of energy–gradients of the texture field. The model of course does not aim to replace the full range numerical simulations but just to show overall features predicted by textures in the CMB anisotropies. In fact the model leaves free a couple of parameters that are fed in from numerical simulations, like the number density of spots, ν, the scaling size, d_s, and the brightness factor of the particular spot, a_k, telling us about its temperature relative to the mean sky temperature.

Texture configurations giving rise to spots in the CMB are assumed to arise with a constant probability per Hubble volume and Hubble time. In an expanding universe one may compute the surface probability density of spots

$$dP = N(y)dyd\Omega, \quad \text{with} \quad N(y) = -\frac{8\nu\ln(2)}{3}\left(2^{y/3}-1\right)^2, \tag{1}$$

[1]The best place to learn about these missions and to follow the developments are, respectively, the sites http://map.gsfc.nasa.gov/ and http://astro.estec.esa.nl/SA-general/Projects/Cobras/cobras.html

where Ω stands for a solid angle on the two–sphere and the time variable $y(t) \equiv \log_2(t_0/t)$ measures how many times the Hubble radius has doubled since proper time t up to now[2].

In the present context the anisotropies arise from the superposition of the contribution coming from all the individual spots S_k produced from $y_{\rm ls}$ up to now, and so, $\Delta T/T = \sum_k a_k S_k(\theta_k, y)$, where the random variable a_k stands for the brightness of the hot/cold k-th spot with characteristic values to be extracted from numerical simulations[6]. $S_k(\theta_k, y)$ is the characteristic shape of the spots produced at time y, where θ_k is the angle in the sky measured with respect to the center of the spot. A spot appearing at time y has typically a size $\theta^s(y) \simeq d_s\ \theta^{\rm hor}(y)$, with $\theta^{\rm hor}(y)$ the angular size of the horizon at y, and where it follows that $\theta^s(y) = \arcsin\left(\frac{0.5 d_s}{2^{y/3}-1}\right)$. Textures are essentially causal seeds and therefore the spots induced by their dynamics cannot exceed the size of the horizon at the time of formation, hence $d_s \leq 1$. Furthermore the scaling hypothesis implies that the profiles satisfy $S_k(\theta_k, y) = S(\theta_k/\theta^s(y))$. From all this it follows a useful expression for the multipole coefficients, $a_\ell^n = \sum_k a_k S_k^\ell(y) Y_\ell^{m*}(\hat{\gamma}_k)$, with $S_k^\ell(y)$ the Legendre transform of the spot profiles.

At this point the $\mathcal{C}_\ell$'s are easily calculated[5]. As we are mainly concerned with the three–point function we go on and compute the angular bispectrum predicted within this analytical model, which we find to be

$$\langle a_{\ell_1}^{m_1} a_{\ell_2}^{m_2} a_{\ell_3}^{m_3} \rangle = \langle a^3 \rangle \int dy N(y) S^{\ell_1}(y) S^{\ell_2}(y) S^{\ell_3}(y) \int d\Omega_{\hat{\gamma}} Y_{\ell_1}^{m_1}(\hat{\gamma}) Y_{\ell_2}^{m_2}(\hat{\gamma}) Y_{\ell_3}^{m_3}(\hat{\gamma}). \qquad (2)$$

$\langle a^3 \rangle$ is the mean cubic value of the spot brightness.

Having the expression for the bispectrum we may just plug it in the formulae for the full mean three–point temperature correlation function[7]. To make contact with experiments however we restrict ourselves to the collapsed case where two out of the three legs of the three–point function *collapse* and only one angle, say α, survives (this is in fact one of the cases analyzed for the four–year *COBE*–DMR data[8]).

The collapsed three–point function thus calculated, $\langle C_3(\alpha) \rangle$, corresponds to the mean value expected in an ensemble of realizations. However, as we can observe just one particular realization, we have to take into account the spread of the distribution of the three–point function values when comparing a model prediction with the observational results. This is the well–known cosmic variance problem. We can estimate the range of expected values about the mean by the *rms* dispersion $\sigma_{CV}^2(\alpha) \equiv \langle C_3^2(\alpha) \rangle - \langle C_3(\alpha) \rangle^2$. We will estimate the range for the amplitude of the three–point correlation function predicted by the model by $\langle C_3(\alpha) \rangle \pm \sigma_{CV}(\alpha)$.

It has been shown[6] that spots generated from random field configurations of concentrations of energy gradients lead to peak anisotropies 20 to 40 % smaller than those predicted by the spherically symmetric self–similar texture solution. These studies also suggest an asymmetry between maxima $\langle a_{\rm max} \rangle$ and minima $\langle a_{\rm min} \rangle$ of the peaks as being due to the fact that, for unwinding events, the minima are generated earlier in the evolution (photons climbing out of the collapsing texture) than the maxima (photons falling in the collapsing texture), and thus the field correlations are stronger for the maxima, which enhance the anisotropies.

3 Results

Let us now compute the predictions on the CMB non–Gaussian features derived from the present analytical texture model. One needs to have the distribution of the spot brightness $\{a_k\}$ in order to compute the mean values $\langle a^n \rangle$. It is enough for our present purposes to take for all hot spots the same $a_h > 0$ and for all the cold spots the same $a_c < 0$. Then the $\langle a^n \rangle$ needed

[2] e.g., for a redshift $z_{\rm ls} \sim 1400$ at last scattering we have $y_{\rm ls} \simeq \log_2[(1400)^{3/2}] \simeq 16$.

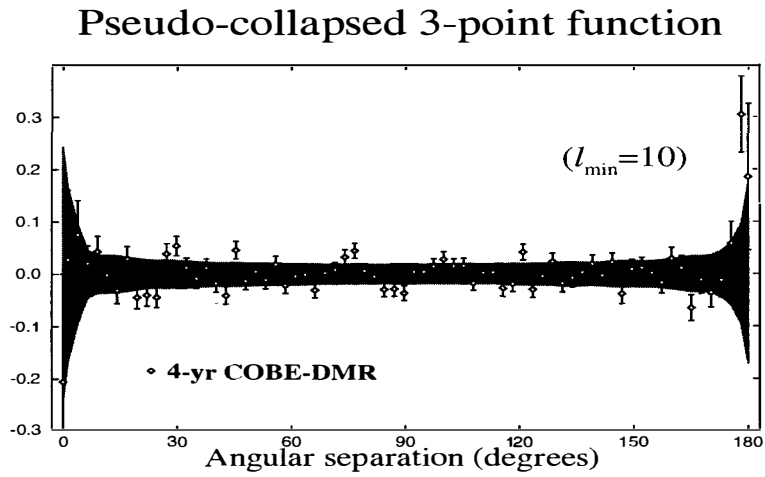

Figure 1: The 'pseudo–collapsed' three–point function (in units of $10^4 \mu K^3$) as computed from the analysis of the four–year *COBE*–DMR data [data courtesy of G. Hinshaw and the *COBE* team]. The points plotted are the analogue of our $\langle C_3(\alpha) \rangle$. Error bars represent instrument noise while the grey band represents the rms range of fluctuations due to a superposition of instrument noise and cosmic variance.

can readily be obtained in terms of $\langle a^2 \rangle$ and $x \equiv \langle a \rangle / \langle |a| \rangle$. We fix $\langle a^2 \rangle$ from the amplitude of the anisotropies according to four–year *COBE*–DMR[8]. The other parameter, x, that measures the possible *asymmetry* between hot and cold spots, we leave as a free parameter.

We consider the *COBE*–DMR window function and, in order to take into account the partial sky coverage due to the cut in the maps at Galactic latitudes $|b| < 20°$, we multiply σ_{CV} by a factor ~ 1.5 in the numerical results (sample variance)[3]. Let us now compare with the data: Subtracting the dipole and for all reasonable values of the asymmetry parameter x, the data falls well within the $\langle C_3(\alpha) \rangle \pm \sigma_{CV}(\alpha)$ band, and thus there is good agreement with the observations. However, the band for Gaussian distributed fluctuations (e.g., as predicted by inflation) also encompasses the data well enough, and it is in turn included inside the texture predicted band. The fact that the range of expected values for the three–point correlation function predicted by inflation is included into that predicted by textures for all the angles, and that the data points fall within them, makes it impossible to draw conclusions favoring one of the models.

It is well known that the largest contribution to the cosmic variance comes from the small values of ℓ. Thus, no doubt the situation may improve if one subtracts the lower order multipoles contribution, as in a $\ell_{min} = 10$ analysis[9]. In Figure 1 we show the analysis of the four–year *COBE*–DMR data evaluated from the 53 + 90 GHz combined map, containing power from the $\ell = 10$ moment and up. It is apparent that the fluctuations about zero correlation (i.e., no

[3]In the analysis of the data, the method used for computing the uncertainty is to generate 2000 random skies with HZ signal + noise, then to compute the three–point function of each realization *on the cut sky* after subtracting a best–fit multipole. Hence, the result automatically includes sample variance.

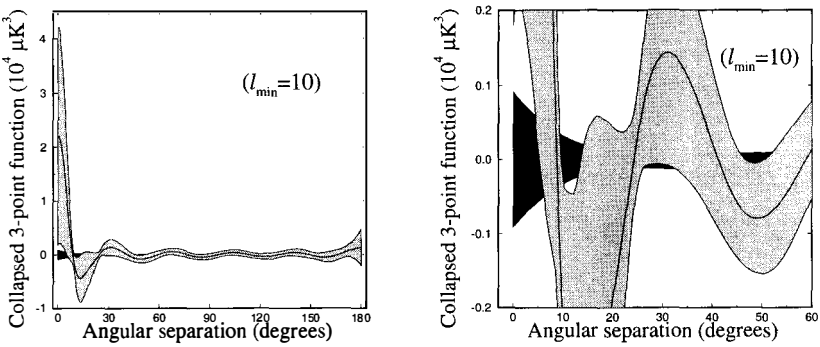

Figure 2: Expected range of values for the three–point correlation function for the texture model with asymmetry parameter $x = 0.4$ (grey band). Also shown is the expected range for inflationary models (black band). Both bands include the $\sim 50\%$ increase in σ_{CV} due to the sample variance. All multipoles up to $\ell = 9$ have been subtracted. The right panel shows a zoomed fraction of the same plot.

signal) are too large for the instrument noise to be the only responsible. These are however consistent with the range of fluctuations expected from a Gaussian process (grey band).

What we want to see now is whether our analytical texture model for the three–point function[10] can do better when compared with the data. Figure 2 shows the collapsed three–point function $\langle C_3(\alpha)\rangle$ (solid line) and the grey band indicates the *rms* range of fluctuations expected from the cosmic variance. Also shown is a black band with the expected range for inflationary models (no instrument noise included). The bands do not superpose each other for some ranges of values of the separation angle for the value of $x = 0.4$ considered, what means that measurements in that ranges can distinguish among the models. The value of the parameter x considered is quite in excess of that suggested by simulations[6], but was chosen to show an example with a noticeable effect.

In Figure 3 we show the result of combining the previous figures, confronting the actual data with the curves predicted by the texture model. From these figures one may see qualitatively by eye that (for some ranges of the angular separation better than for others, of course) the data seems to follow 'approximately' the trend of the texture curves. While many of the data points fell outside the Gaussian band (Figure 1), most of them are now inside the grey band in Figure 3 (left panel). Moreover, while we vary the x values from 0.4 down to 0.1 (the actual value suggested by texture simulations) we see that more and more points (with error bars) get inside (or touch) the grey band. Can this be just by chance? Or is it there something worth of further study? In order to answer these questions one ought to quantify more the analysis by using a χ^2 statistics for the model and data, and comparing it to the Gaussian case, e.g.[11]

$$\chi^2 = \sum_{\alpha\beta} (D_\alpha - \langle C_3\rangle_\alpha)(\mathrm{M}^{-1})_{\alpha\beta}(D_\beta - \langle C_3\rangle_\beta), \qquad (3)$$

with D_α the *COBE*–DMR three–point function and M is the covariance matrix of the analytical model. It might be that the data picks out a preferred value for the asymmetry parameter x. Work in this direction is currently under way.

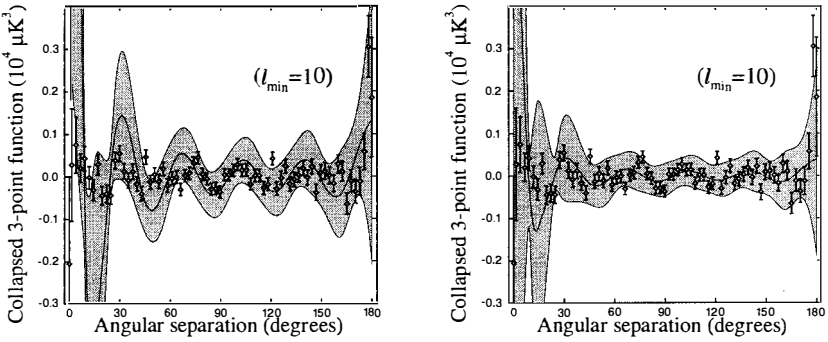

Figure 3: Combined four-year *COBE*–DMR data and collapsed three–point correlation function predicted by the analytical texture model (as in previous figures). Left panel: for a somewhat exaggerated value of the asymmetry parameter $x = 0.4$. Right panel: for the value $x \sim 0.1$ suggested by texture simulations.

Acknowledgments: I thank Gary Hinshaw and the *COBE* team for providing the 4-yr data, and especially Gary for useful correspondence. I also thank Silvia Mollerach for her collaboration on the work described herein, Ruth Durrer, Andrew Liddle and Neil Turok for useful conversations during the workshop, and the organizers for making this such a stimulating meeting. I acknowledge partial funding from The British Council/Fundación Antorchas.

References

1. W. Hu, N. Sugiyama and J. Silk, astro-ph/9604166.
2. A. Albrecht, D. Coulson, P. Ferreira and J. Magueijo, Phys. Rev. Lett. **76**, 1413 (1996); see also Hobson's contribution to these proceedings.
3. R. G. Crittenden and N. Turok, Phys. Rev. Lett. **75**, 2642 (1995); R. Durrer, A. Gangui and M. Sakellariadou, Phys. Rev. Lett. **76**, 579 (1996).
4. N. Turok, astro-ph/9604172.
5. J. Magueijo, Phys. Rev. D **52**, 689 (1995).
6. J. Borrill, E. Copeland, A. Liddle, A. Stebbins and S. Veeraraghavan, Phys. Rev. D. **50**, 2469 (1994).
7. A. Gangui, F. Lucchin, S. Matarrese and S. Mollerach, Astrophys. J. **430**, 447 (1994).
8. E. W. Wright, C. L. Bennett, K. M. Górski, G. Hinshaw and G. F. Smoot, astro-ph/9601059.
9. G. Hinshaw, A. J. Banday, C. L. Bennett, K. M. Górski and A. Kogut, Astrophys. J. **446**, L67 (1995).
10. A. Gangui and S. Mollerach, astro-ph/9601069.
11. A. Kogut, A. J. Banday, C. L. Bennett, K. Górski, G. Hinshaw, G. F. Smoot and E. L. Wright, astro-ph/9601062.

DOPPLER PEAKS AS A TEST FOR TOPOLOGICAL DEFECTS

Mairi Sakellariadou
Département de Physique Théorique, Université de Genève
24 quai Ernest-Ansermet, CH-1211 Genève 4, Switzerland

Abstract

Doppler peaks in the cosmic microwave background may allow us to distinguish among the classes of theories to explain structure formation. We consider density perturbations seeded by global textures in a universe dominated by cold dark matter. We calculate the height and the position of the primary peak and obtain a different signature than the one resulting from initial perturbations due to amplification of quantum fluctuations of a scalar field during a generic inflationary era.

1. Introduction

Among the main, still open problems in modern cosmology, remains the origin of the observed structure in the universe. Based on all present indications, we believe that the large-scale structure was produced by gravitational instability from small primordial fluctuations in the energy density, generated during the early stages of the universe. Within this framework, there are two families of models to explain the origin of the primordial density perturbations. They can be due to quantum fluctuations of a scalar field during an inflationary era, leading to an approximately scale-invariant Harrison-Zel'dovich spectrum of density fluctuations, which are generated through a linear mechanism, with a Gaussian distribution of amplitudes on scales which are cosmological today. Since inflationary models are plagued with problems, one should also explore the alternative scenario, according to which perturbations may be seeded by topological defects contained in the disordered phase and formed during a symmetry breaking phase transition in the early universe. As the field distribution orders itself, via a non-linear process, it generates an approximately scale-invariant Harrison-Zel'dovich initial spectrum of density perturbations of constant amplitude on each scale at horizon crossing at all times. Depending on the nature of the broken symmetry, topological defects can either be local or global, while their classification depends on the number of components of an order parameter ϕ which breaks the symmetry group. Among the various topological defects, global monopoles, global textures and both global or local cosmic strings, are the viable candidates. Since the initial density fluctuations have tiny amplitudes, their evolution at early times can be studied using linear cosmological perturbation theory.

Either of these two families of models predicts precise fingerprints in the cosmic microwave background (CMB) anisotropies, which can be used to differentiate among these models using a purely linear analysis. The CMB fluctuation spectrum is usually parametrized in terms of multiple moments C_ℓ, defined as the coefficients in the expansion of the temperature autocorrelation function

$$\left\langle \frac{\delta T}{T}(\mathbf{n}) \frac{\delta T}{T}(\mathbf{n}') \right\rangle \Big|_{(\mathbf{n}\cdot\mathbf{n}'=\cos\vartheta)} = \frac{1}{4\pi} \sum_\ell (2\ell+1)\, C_\ell P_\ell(\cos\vartheta)\,, \tag{1}$$

which compares points in the sky separated by an angle ϑ. The value of C_ℓ is determined by fluctuations on angular scales of order π/ℓ. One usually plots $\ell(\ell+1)C_\ell$ versus ℓ, which is the power per logarithmic interval in ℓ, giving the spectrum of anisotropies observed today.

The main physical mechanisms which contribute to the redshift of photons propagating in a perturbed Friedmann geometry, for scalar perturbations, are due to: (i) fluctuations

in the gravitational potential on the last-scattering surface (Sachs-Wolfe effect) acting on large angular scales; (ii) acoustic waves in the baryon-radiation fluid prior to recombination (Doppler peaks or Sacharov peaks) acting on angular scales $0.1^\circ \lesssim \theta \lesssim 2^\circ$; (iii) suppression of CMB anisotropies due to the finite thickness of the recombination shell, as well as to photon diffusion during recombination (Silk damping) acting on the smallest angular scales.

Both generic inflationary models and topological defect scenarios predict an approximately scale-invariant spectrum of density perturbations on large angular scales ($\ell \lesssim 50$), thus the COBE-DMR data provide mainly a normalization for the different models. Cosmic microwave background anisotropies on intermediate and small angular scales are very important. If the two classes of theories predict different characteristics for the Doppler peaks, we can discriminate among them. In the nearby future, a number of sophisticated experiments will scrutinize various regions of the sky trying to reveal the characteristics of the relic radiation. Here, we summarize a study of the Doppler contribution from textures[1], in a universe dominated by cold dark matter (CDM). Since our results depend basically on the form of the time-dependence of the source term on large scales, which is the same for all global defects, we expect our conclusions to hold for all kinds of global topological defects.

2. Doppler peaks in the angular power spectrum of CMB

Gauge-invariant linear perturbation analysis shows that the Doppler contribution to the CMB anisotropies is approximately[2]

$$\left[\frac{\delta T}{T}(\mathbf{x},\mathbf{n})\right]^{\text{Doppler}} \approx \frac{1}{4} D_r(\mathbf{x}_{\text{rec}}, t_{\text{rec}}) + \mathbf{V}(\mathbf{x}_{\text{rec}}, t_{\text{rec}}) \cdot \mathbf{n} \,, \tag{2}$$

where $\mathbf{V}$ denotes the peculiar velocity of the baryon fluid with respect to the overall Friedmann expansion, D_r is a gauge-invariant variable which describes the density fluctuation in the coupled baryon radiation fluid and $\mathbf{x}_{\text{rec}} = \mathbf{x} - \mathbf{n}\, t_0$ ($\mathbf{n}$ denotes a direction in the sky, t is the conformal time, with t_0, t_{rec} the present time and the time of recombination respectively). We employ gauge-invariant linear perturbation theory, since it is not plagued by gauge modes and leads to rather simple equations for the perturbation variables. Here, we neglect the integrated Sachs-Wolfe (ISW) effect, the Silk damping of perturbations and the contribution of neutrino fluctuations. Also, the Doppler contribution to the CMB anisotropies must in principle be added to the SW term, which however decays as l^{-2} on sub-horizon scales. Our approximations lead to an error of less than about 30% in the amplitude of the first Doppler peak and overestimate the value ℓ of its position by less than 10%. We will include these terms in a future work[3].

We study a two-component fluid system: baryons plus radiation, which prior to recombination are tightly coupled, and CDM. The evolution for the perturbation variables D (density perturbation) and V (velocity perturbation), in a flat background is given by[4]

$$
\begin{aligned}
&V_{\rm r}' + \frac{a'}{a} V_{\rm r} = k\,\Psi + k \frac{c_{\rm s}^2}{1+w} D_{\rm r}\ , \\
&V_{\rm c}' + \frac{a'}{a} V_{\rm c} = k\,\Psi\ , \\
&D_{\rm r}' - 3w\frac{a'}{a} D_{\rm r} = (1+w)\left[3\frac{a'}{a}\Psi - 3\Phi' - kV_{\rm r} - \frac{9}{2}\left(\frac{a'}{a}\right)^2 k^{-1}\left(1+\frac{w\rho_{\rm r}}{\rho}\right) V_{\rm r}\right]\ , \\
&D_{\rm c}' = 3\frac{a'}{a}\Psi - 3\Phi' - kV_{\rm c} - \frac{9}{2}\left(\frac{a'}{a}\right)^2 k^{-1}\left(1+\frac{w\rho_{\rm r}}{\rho}\right) V_{\rm c}\ ,
\end{aligned}
\tag{3}
$$

where subscripts "r" and "c" denote the baryon-radiation plasma and CDM, respectively; $w = p_{\rm r}/\rho_{\rm r}$, $c_{\rm s}^2 = p_{\rm r}'/\rho_{\rm r}'$ and $\rho = \rho_{\rm r} + \rho_{\rm c}$. Φ and Ψ are gauge-invariant quantities describing the geometrical perturbations, through which the seeds enter the system. The potentials Φ and Ψ can be split into a part coming from standard matter and radiation, and a part due to the seed, which for us are global textures (π_3–defects), *i.e.*, $\Psi = \Psi_{\rm (c,r)} + \Psi_{\rm seed}$, where $\Psi_{\rm seed}$ abd $\Phi_{\rm seed}$ are determined by the energy momentum tensor of the seeds. The above system for the evolution of perturbation variables, can be written[2] as a system of two second order equations for $D_{\rm r}$ and $D_{\rm c}$ where in the r.h.s. is the source term S, in general given by $S = 4\pi G a^2(\rho + 3p)^{\rm seed}$. In our case, where the seed is described by a global scalar field ϕ, we have $S = 8\pi G(\phi')^2$. From numerical simulations one finds that the average of $|\phi'|^2$ over a shell of radius k, can be modeled by[5]

$$
\langle|\phi'|^2\rangle(k,t) = \frac{1}{2} A \eta^2 t^{-1/2}[1 + \alpha(kt) + \beta(kt)^2]^{-1}, \tag{4}
$$

with η denoting the symmetry breaking scale of the phase transition leading to texture formation. The parameters in this fit are $A_{\rm m} \sim 2.8$, $\alpha_{\rm m} \sim -0.43/(2\pi)$ and $\beta_{\rm m} \sim 0.43/(2\pi)^2$ in the matter dominated era (MDE) and $A_{\rm r} \sim 3.8$, $\alpha_{\rm r} \sim -0.31/(2\pi)$ and $\beta_{\rm r} \sim 0.31/(2\pi)^2$ in the radiation dominated era (RDE). On super-horizon scales, where the source term is important, this fit is accurate to about 10%. On small scales the accuracy reduces by a factor of 2. By using this fit in the calculation of $D_{\rm r}$ and $D_{\rm c}$, we actually neglect the time evolution of phases of $(\phi')^2$; the incoherent evolution of these phases may smear out subsequent Doppler peaks[6], but will not affect substantially the height of the first peak. Preliminary results[3] support the validity of a "soft" coherence assumption.

To calculate the Doppler contribution to the C_ℓ's, one should know $D_{\rm r}$ and $D_{\rm r}'$, which are found by solving the system of second-order equations for the perturbation variables, with

initial conditions: for a given scale k, we chose the initial time such that the perturbation is super-horizon and the universe is in the RDE. In this limit the evolution equations reduce to

$$D_{\rm r}'' - \frac{2}{t^2} D_{\rm r} = \frac{4}{3}\frac{A\epsilon}{\sqrt{t}} \quad ; \quad D_{\rm c}'' + \frac{3}{t} D_{\rm c}' - \frac{3}{2t} D_{\rm r}' - \frac{3}{2t^2} D_{\rm r} = \frac{A\epsilon}{\sqrt{t}} \,, \tag{5}$$

with particular solutions $D_{\rm r} = -\frac{16}{15}\epsilon A t^{3/2}$ and $D_{\rm c} = -\frac{4}{7}\epsilon A t^{3/2}$, where we have introduced $\epsilon \equiv 4\pi G \eta^2$, the only free parameter in the model. We consider perturbations seeded by the texture field, so it is incorrect to add a homogeneous growing mode to the above solutions.

The Doppler contribution to the CMB anisotropies is obtained using

$$C_\ell = \frac{2}{\pi} \int {\rm d}k \left[\frac{k^2}{16} \left| D_{\rm r}(k, t_{\rm rec}) \right|^2 j_\ell^2(kt_0) + \frac{1}{(1+w)^2} \left| D_{\rm r}'(k, t_{\rm rec}) \right|^2 (j_\ell'(kt_0))^2 \right] , \tag{6}$$

where j_ℓ is the spherical Bessel function of order ℓ, and j_ℓ' its first derivative. The angular power spectrum, shown in the figure, yields the Doppler peaks.

3. Conclusions

The angular power spectrum for the Doppler contribution to the CMB anisotropies, for perturbations induced by global textures and cold dark matter, show for $\ell < 1000$, the appearance of three peaks. In the figure we show separately the contribution of $D_{\rm r}$ (upper dotted line), $D_{\rm r}'$ (lower dotted line), as well as their sum (solid line).

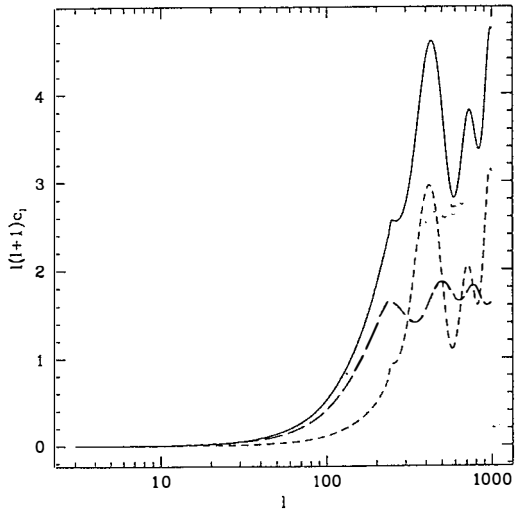

Fig. The angular power spectrum for the Doppler contribution to the CMB anisotropies is shown in units of ϵ. We choose the cosmological parameters $h = 1/2$, $\Omega_B = 0.05$ and $z_{rec} = 1100$.

The integrated SW effect, which has been neglected here, will shift the position of the first peak to somewhat larger scales, lowering $\ell_{\rm peak}$ by (5 – 10)% and possibly increasing its amplitude slightly (by less than 30%). So, the primary peak, located in the figure at $\ell \sim 400$, will be shifted to $\ell \sim 360$, meaning that its position is displaced by $\Delta\ell \sim 150$ towards smaller angular scales than in standard inflationary models[7]. Silk damping, which we have not taken into account here, will decrease the relative amplitude of the third peak with respect to the second one; however it will not affect substantially the height of the first peak. As our figure shows, the amplitude of the first Doppler peak is $\ell(\ell+1)C_\ell|_{\rm Doppler} = 4.6\epsilon^2$. We actually must compare the amplitude for the Doppler peak with the level of the SW plateau, which however is uncertain within a factor of 2, leading to a factor 4 uncertainty in the SW contribution to the power spectrum. More precisely, the results are $\ell(\ell+1)C_\ell|_{\rm sw} \sim 2\epsilon^2$ and $\ell(\ell+1)C_\ell|_{\rm sw} \sim 8\epsilon^2$. According to the first two groups[8),9)], the Doppler peak is a factor of $\sim$ 3.3 times higher than the SW plateau, whereas it is only about 1.5 times higher if the second result[5)] is assumed. Improved numerical simulations or analytical approximations are needed to resolve this discrepancy. As our study shows, the Doppler contribution from global defects is smaller than for generic inflationary models. We therefore conclude that if the existence of Doppler peaks is indeed confirmed and if the primary peak is positioned at $\ell < 300$, global topological defects are most probably ruled out. However, if the first Doppler peak is positioned at $\ell \sim 360$ and if its amplitude is lower that the one predicted for standard inflationary models, global topological defects are strongly favored. This problem has also been studied by[10)].

References

* This work was done in collaboration with Ruth Durrer and Alejandro Gangui.
1) Turok N., 1989, *Phys. Rev. Lett.* **63**, 2625.
2) Durrer R., Gangui A., and Sakellariadou M., 1996, *Phys. Rev. Lett.* **76**, 579.
3) Durrer R., and Sakellariadou M., 1996 (in preparation).
4) Kodama H., and Sasaki M., 1984, *Prog. Theor. Phys. Suppl.* **78**, 1.
5) Durrer R., and Zhou Z.H, 1996, *Phys. Rev.* D (to be published).
6) Albrecht A., *et al*, Report No. astro-ph/9505030 (to be published).
7) Steinhard P.J., 1993, *Class. Quantum Gravity* **10**, S33.
8) Bennett D., and Rhie S.H., 1993, *Astrophys. J.* **406**, L7.
9) Pen U.-L., Spergel D.N., and Turok N., 1994, *Phys. Rev.* D **49**, 692.
10) Crittenden R.G., and Turok N., 1995, *Phys. Rev. Lett.* **75**, 2642.

CONSEQUENCES OF COSMIC MICROWAVE BACKGROUND ANISOTROPY MEASUREMENTS FOR INFLATIONARY COSMOLOGY

George Efstathiou
Astrophysics, University of Oxford, England.

Abstract

Inflationary cosmology can explain many of the key features of our Universe, such as the observed large-scale homogeneity and isotropy. However, there is as yet no consensus on whether inflation ever ocurred, nor on the detailed mechanism of inflation. In this article, I review the prospects for constraining inflationary models from observations of cosmic microwave background (CMB) anisotropies. CMB observations with an angular resolution of better than $30'$ are essential if the parameters of inflationary models are to be disentangled from small variations in other cosmological parameters. Fortunately, such observations are planned with next generation of CMB satellites - MAP and COBRAS/SAMBA. These satellites promise the simultaneous measurement of spectral parameters that can test inflationary models and fundamental cosmological parameters such as the Hubble constant and baryon density to accuracies far beyond those achievable by conventional astronomical techniques. Observations of the CMB therefore promise to revolutionize cosmology over the next decade.

1 Introduction

The theory of inflation[1]–[4] has had a dramatic impact on cosmology. It solves some of the most fundamental of cosmological problems, such as the homogeneity and near spatial flatness of our Universe, and the origin of the small irregularities required to explain present day structure. Although the theory is elegant and seems compelling to many people, there is little direct observational evidence that inflation ever took place. Furthermore, we lack a compelling high-energy physics model for inflation, with the result that the mechanism of inflation is almost entirely ad-hoc. It is therefore possible for theorists to construct models which, as we will see below, can easily be tuned to give different observational predictions.

Observations of the microwave background probably offer the best prospects for testing inflationary cosmology[5]-[7]. In this article, I will describe how the microwave background anisotropies can be used to test some of the fine details of inflationary models. For example, accurate determinations of the spectral indices of the fluctuation spectra and the measurement of a gravitational wave contribution to the temperature anisotropies can constrain inflationary models and so provide information on the relevant high energy physics. Where numerical examples are required, I will assume that inflation is driven by a single scalar field ϕ evolving in a potential $V(\phi)$. It is possible to construct more complicated models[8]-[9] involving, for example, multiple scalar fields. The full range of observational predictions is therefore even wider than those presented here.

The following are often cited predictions of inflationary models:

[1] Inflation predicts a spatially flat Universe with a nearly critical density parameter, $\Omega = 1 \pm \epsilon$, $\epsilon \lesssim 10^{-4}$.

[2] Curvature (adiabatic) fluctuations are generated during inflation that obey Gaussian statistics.

[3] Inflation produces a power-law spectrum of density (scalar) perturbations, $|\delta_k|^2 \propto k_s^n$, with a scale-invariant spectrum $n_s = 1$.

[4] Inflation can produce a scale-invariant spectrum of tensor (gravitational wave) perturbations in addition to scale-invariant scalar perturbations.

In fact, inflationary models can be constructed that violate all of the above predictions, and nearly all models will violate the last two points to some small degree. For example, point [1] does not apply if the cosmological constant Λ is non-zero, in which case simple models of inflation lead[10] to a spatially flat universe with density parameter $\Omega_0 = (1 - \Lambda/3H_0^2)$. Even if the cosmological constant is zero, it is possible to construct 'double inflation' models that lead to open universes[11]. Point [2] is one of the more robust predictions of inflationary models, but even here it is possible to construct models with multiple scalar fields that generate a component of isocurvature perturbations[8] and even non-Gaussian fluctuations[12].

The Hamilton-Jacobi formulation gives the following equation[12] relating the Hubble parameter during inflation to the potential $V(\phi)$

$$H^2 = \frac{8\pi}{3m_p^2}\left[\frac{1}{2}\left(\frac{m_p^2}{4\pi}\frac{\partial H}{\partial \phi}\right)^2 + V(\phi)\right], \tag{1}$$

where m_p is the Planck mass. It is useful to define a 'deceleration' parameter q,

$$(1+q) = \frac{m_p^2}{4\pi}\left(\frac{\partial \ln H}{\partial \phi}\right)^2. \tag{2}$$

The parameter q thus measures the departure from pure exponential expansion during inflation (for which $q = -1$). In the 'slow rollover' approximation, $q \approx -1$ and the first term in brackets in equation (1) can be neglected giving the familiar result $H^2 \approx 8\pi V/(3m_p^2)$.

The amplitudes of the post-inflation scalar and tensor fluctuation spectra, P_S and P_T, can be calculated in terms of q and H giving[8]

$$P_S = \frac{1}{1+q}\frac{H^2(\tau_k)}{\pi m_p^2} e^{2u_s}, \tag{3}$$

$$P_T = \frac{8H^2(\tau_k)}{\pi m_p^2} e^{2u_t}, \tag{4}$$

where τ_k is the conformal time when a comoving wavenumber k crosses the Hubble radius $k = Ha$. The parameters u_s and u_t are small for power-law like potentials. The precise definitions of these spectra are rather technical and will not be given here (see ref [8]). The

key point for our purposes is that these spectra are linearly related to the power spectra of the scalar and tensor components of the CMB anisotropies (see equations (11) and (12) below). The logarithmic derivatives of the spectra P_S and P_T with respect to wavenumber k define scalar (n_s) and tensor (n_t) spectral indices,

$$n_s = 1 + 2\left(1 + \tfrac{1}{q}\right) - \tfrac{1}{q}\tfrac{m_p^2}{2\pi}\tfrac{\partial^2 \ln H}{\partial \phi^2} + \epsilon_s, \tag{5}$$

$$n_t = 2\left(1 + \tfrac{1}{q}\right) + \epsilon_t, \tag{6}$$

where the terms ϵ_s and ϵ_t are small corrections arising from derivatives of u_s and u_t. In a realistic model of inflation, the potential $V(\phi)$ cannot be perfectly flat but must steepen if inflationary is to end and normal power-law expansion is to begin. Thus, in realistic models we expect $q > -1$, and so we would expect to see departures from pure scale-invariant spectra (for which $n_s = 1$, $n_t = 0$).

In the next section, we relate these results to the power spectra of the CMB anisotropies. In principle, observations of the CMB can constrain the amplitudes and shapes of the scalar and tensor power spectra and so constrain the parameters of inflationary models. However, there are several complications in such an analaysis, some of which are described in Section 3. Nevertheless, in Section 4 I argue that high resolution CMB measurements, especially those expected from new satellites, should so severely constrain the parameters of inflationary models as to decouple post-recombination evolution (galaxy formation, large-scale structure *etc*) from any residual uncertainties in the physics of the early universe.

2 CMB Anisotropies: Theory

2.1 Scalar and tensor modes

The CMB temperature anisotropies $\Delta T/T$ on the plane of the sky can be expanded in a series of spherical harmonics

$$\frac{\Delta T}{T} = \sum_{\ell,m} a_\ell^m Y_\ell^m(\theta, \phi). \tag{7}$$

If we have complete sky coverage and the fluctuations are Gaussian, then each a_ℓ^m coefficient in (7) is statistically independent with variance,

$$C_\ell = \langle |a_\ell^m|^2 \rangle. \tag{8}$$

The coefficients C_ℓ define the power spectrum of the temperature anisotropies. The scalar and tensor perturbations generated during inflation will make statistically independent contributions to the temperature power spectrum, so we can write $C_\ell = C_\ell^S + C_\ell^T$, where the superscripts S and T denote the perturbation mode. Figure 1, shows theoretical predictions for C_ℓ^S and C_ℓ^T for a scale-invariant cold dark matter (CDM) model with the following parameters $\Omega_0 = 1$, $\Omega_\Lambda = \Lambda/(3H_0^2) = 0$, $\Omega_b = 0.05$, $h = 0.5$ (where Ω_b is the baryon contribution to the density parameter and h is Hubble's constant in units of 100 $\mathrm{kms^{-1}Mpc^{-1}}$). The scalar power spectrum in Figure 1 has been matched approximately to the 4-year COBE measurements at multipoles $2 < \ell \lesssim 20$ and the tensor power spectrum has been normalized arbitrarily so that the quadrupole amplitudes of the two modes are equal ($C_2^T = C_2^S$).

The general shapes of these power spectra are easy to understand. At low multipoles, scale-invariant perturbations lead to nearly scale-invariant temperature anisotropies on the sky, $C_\ell \propto \ell^{-2}$, hence the scalar and tensor curves in Figure 1 look approximately flat at $\ell \lesssim 50$.

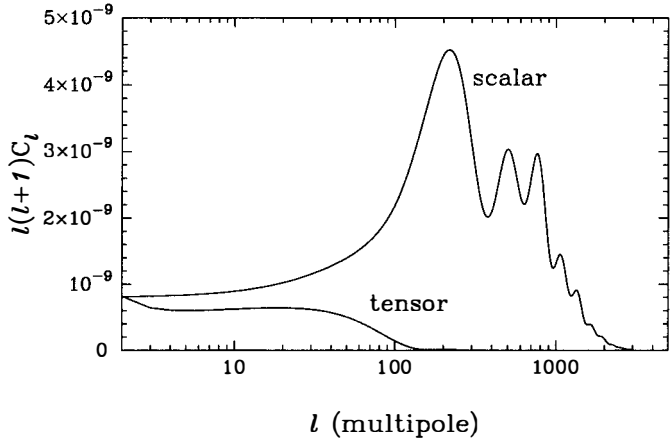

Figure 1. Power spectra of the temperature anisotropies arising from scalar and tensor perturbations in a scale-invariant CDM model with parameters $\Omega = 1$, $\Lambda = 0$, $\Omega_b = 0.05$ and $h = 0.5$.

In this regime, the scalar anisotropies arise from the Sachs-Wolfe effect[13] from which we can derive the following expression[14] for the power spectrum for an arbitrary spectral-index n_s,

$$C_\ell^S = C_2^S \frac{\Gamma\left(\frac{9-n_s}{2}\right)}{\Gamma\left(\frac{3+n_s}{2}\right)} \frac{\Gamma\left(\ell+\left(\frac{n_s-1}{2}\right)\right)}{\Gamma\left(\ell+\left(\frac{5-n_s}{2}\right)\right)}. \tag{9}$$

The tensor component at low multipoles is given by,

$$C_\ell^T \approx 4\pi^2 \frac{(\ell+2)!}{(\ell-2)!} \int \frac{dk}{k} P_T(k) I_\ell^2, \qquad I_\ell = \int_0^{k\tau_0} d(k\tau) \frac{j_2(k\tau)}{k\tau} \frac{j_\ell(k(\tau_0-\tau))}{[k(\tau_0-\tau)]^2}, \tag{10}$$

where τ_0 is the conformal time at the present day and the j_ℓ are spherical Bessel functions. The amplitudes C_2^S and C_2^T are related to the amplitudes of equations (3) and (4) according to[6]

$$C_2^S \approx 0.017 P_S, \tag{11}$$

$$C_2^T \approx 0.029 P_T. \tag{12}$$

At multipoles $\ell \gtrsim 50$, the tensor component of the CMB power spectrum declines sharply. Semi-analytical calculations of the gravitational wave spectrum may be found in references [15] –[17]. The important point to note is that if the fluctuations are nearly scale-invariant, then the CMB power spectrum will contain very little information on gravitational waves at multipoles $\ell \gtrsim 50$. We will see in the next section that this imposes a fundamental limit on our ability to test inflationary models from observations of the CMB.

In contrast to C_ℓ^T, the power spectrum of the scalar mode rises at multipoles $\ell \sim 100$, corresponding roughly to the angular size of the Hubble radius at the redshift, z_R, of recombination ($\ell \sim \pi(z_R/\Omega_0)^{1/2}$). At higher multipoles, the power spectrum displays a characteristic pattern of regulary spaced 'Doppler peaks', which are the result of acoustic oscillations of the baryon-photon fluid prior to recombination[14,18,19]. The shape of C_ℓ^S at high multipoles is thus sensitive to parameters which determine the effective sound speed prior to recombination (principally

$\Omega_b h^2$), to the geometry of the Universe via the angle-length relation (relating physical scales at the time of recombination to angular scales on the sky), as well as the amplitudes and shapes of the inflation generated power spectra.

In summary, measurements of the CMB temperature power spectrum can provide us with a set of about 2000 C_ℓ coefficients from which we are invited to extract fundamental cosmological parameters, including the amplitudes and spectral indices of the perturbation spectra. Since inflationary models generally predict Gaussian fluctuations, the C_ℓ coefficients completely define the statistics of the background anisotropies and there is no further information that can be extracted from higher order statistics [1]. It is clear, however, from inspection of Figure 1 that a typical inflationary power spectrum can be specified by many fewer than 2000 numbers. The C_ℓ curves are smooth and could be specified to high accuracy by perhaps 20 or so numbers, *i.e.* of the same order as the number of cosmological parameters required to define a theoretical model. It is therefore not obvious that CMB measurements alone can eliminate the degeneracies between the cosmological parameters and so constrain inflationary models. Evidently a detailed calculation is necessary. This important point is discussed in further detail in Section 4.

2.2 Consistency relations

Under certain conditions, the amplitudes and spectral indices of the CMB power spectra predicted by inflationary models obey certain consistency relations. For example, if the acceleration rate during inflation is uniform ($\partial^2 \ln H/\partial\phi^2 = 0$), then[5]-[7]

$$n_t = -\tfrac{1}{4}\tfrac{P_T}{P_S}, \tag{13}$$

$$n_s = (1 + n_t), \tag{14}$$

$$\frac{C_2^T}{C_2^S} = -7n_t = 7(1 - n_s). \tag{15}$$

These equations are exact for power-law inflation in which the scale factor varies as $R(t) \propto t^p$. For many models, equations (13)-(15) define a useful set of 'zeroth-order' relations to which we can add corrections terms dependent on the variation of the acceleration rate during inflation. For example, if the potential is a power-law

$$V(\phi) = A\phi^\beta, \tag{16}$$

then,

$$n_t \approx -\tfrac{m_P^2}{8\pi}\tfrac{\beta^2}{\phi_I^2} \approx -\tfrac{\beta}{100}, \tag{17}$$

$$n_s - 1 \approx -\tfrac{m_P^2}{8\pi}\tfrac{\beta^2}{\phi_I^2} - \tfrac{m_P^2}{4\pi}\tfrac{\beta}{\phi_I^2} \approx -\tfrac{\beta}{100} - \tfrac{1}{50}, \tag{18}$$

$$\frac{C_2^T}{C_2^S} \approx \frac{7\beta}{100}, \tag{19}$$

where $\phi_I = (N\beta/4\pi)^{1/2} m_p$ is the relevant value of the inflaton field and N is the number of e-foldings between the time a perturbation mode is stretched beyond the Hubble distance and

[1] Further information is, however, contained in the polarization pattern[14,20]

the time that inflation ends (typically $N \sim 50-60$). These equations are identical to the zeroth order relations given above except for the small correction of $1/50$ to the scalar spectral index which arises from the term proportional to $\partial^2 \ln H/\partial\phi^2$ in equation (5).

Although the zeroth-order relations (13)-(15) are a useful starting point for the analysis of power-law like potentials, there is a particular class of model, in which inflation occurs at an inflection point in the potential, for which they do not apply. An example is 'natural' inflation[21], where the potential has the form

$$V(\phi) = V_0 \sin^2\left(\frac{\phi}{2f}\right). \tag{20}$$

In this type of model, inflation must begin with $V(\phi)$ very close to its maximum value (*i.e.* $\phi/f \approx \pi$) if the universe is to inflate by a large enough factor. In this case, the 'deceleration' parameter is exponentially close to -1 and so the tensor amplitude and tensor spectral index are exponentially suppressed. However, the scalar spectral index is

$$n_s - 1 = -\frac{m_p^2}{8\pi f^2}, \tag{21}$$

and so depends on the value of the symmetry breaking scale f. Similar behaviour arises in the supergravity inflation model of Ross and Sarkar[22].

In summary, inflationary models (at least those involving a single scalar field) can be grouped roughly into two categories: those in which the zeroth order relations (13)-(15) provide a useful approximation, and those in which the tensor amplitude and spectral index are exponentially suppressed. In the former case, deviations from the zeroth order relations tell us about the rate of acceleration during inflation.

It is worth mentioning two other approaches to testing inflationary models. In the first, observations of the CMB anisotropies are used to constrain the inflaton potential and its derivatives evaluated at a value ϕ_I[23]–[25]. Such an expansion is reasonable for power-law like potentials since all observable spatial modes cross the Hubble radius when the inflaton field is within a small range of the value ϕ_I . A very useful review of this approach is given by Lidsey *et al* [7]. The second involves the analysis of differences between the Doppler peak structure of isocurvature and adiabatic modes. This approach is discussed by *e.g.* Hu, Spergel and White[26].

3 CMB Anisotropies: Practice

Whether we attempt to apply consistency relations such as those described in the previous section, or to reconstruct an inflationary potential, there will be practical limitations imposed on such tests by realistic observations of the CMB. For example, even if we ignore complications such as contaminating foregrounds and instrumental noise, there will be fundamental limitations imposed by the fact that we observe only one realization of the sky (cosmic variance) and by deviations from the simple Sachs-Wolfe type formulae (9) and (10) that couple inflationary parameters to other cosmological parameters such as H_0 and Ω_b. Some consequences of these effects are described in this section.

3.1 Cosmic variance

In a Gaussian theory, each of the a_ℓ^m coefficients in equation (7) is statistically independent and Gaussian distrubuted. Thus each coefficient of the power spectrum will be χ^2 distributed with

$(2\ell+1)$ degrees of freedom. More generally, the fractional (1σ) error of a C_ℓ coefficient can be written as the sum of two terms[27]–[28]

$$\frac{\Delta C_\ell}{C_\ell} \approx \left[\frac{2}{(2\ell+1)f_{sky}}\right]^{1/2}\left[1+\frac{1}{wC_\ell}\exp(\ell^2\sigma_b^2)\right]. \tag{22}$$

The first term is independent of the experimental apparatus and depends only the fraction of sky surveyed, $f_{\rm sky}$. The parameters of the experiment are contained in the second term, where σ_b is the Gaussian beam width, $w^{-1}=(\sigma_{pix}\theta_{fwhm})^2$, $\sigma_b = 0.425\theta_{fwhm}$ and σ_{pix} is the sensitivity per $\theta_{fwhm}\times\theta_{fwhm}$ pixel.

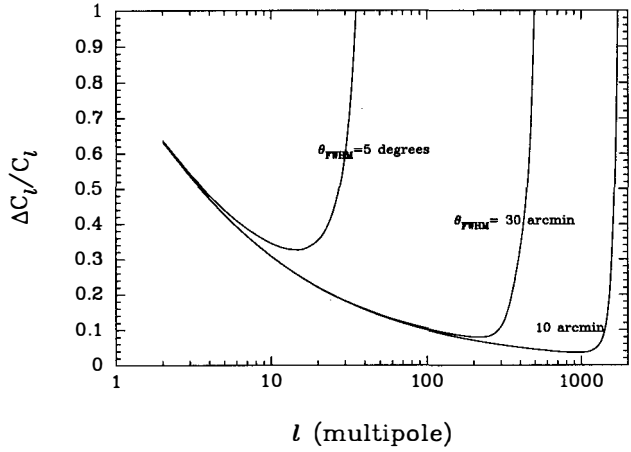

Figure 2. Fractional error in C_ℓ for experiments with angular resolutions (θ_{fwhm}) and pixel sensitivies (σ_{pix}) of: $\theta_{fwhm}=5°$, $\sigma_{pix}=1\times10^{-5}$; $\theta_{fwhm}=30'$, $\sigma_{pix}=1\times10^{-5}$; $\theta_{fwhm}=10'$, $\sigma_{pix}=2\times10^{-6}$. We have assumed the scalar power spectrum plotted in Figure 1 and $f_{sky}=1$ in computing these curves.

Figure 2 shows equation (22) plotted for various experimental configurations: a low resolution experiment with $\theta_{fwhm}=5°$ and two much high resolution experiments with parameters similar to those of proposed CMB satellites (see Section 4). This figure illustrates the following points:

- Cosmic variance sets fundamental limits on the accuracy with which we can estimate theoretical parameters that determine the form of C_ℓ. Since the errors on C_ℓ decline with increasing ℓ, cosmic variance is particularly important for theoretical quantities that are related only to low multipoles.
- The errors on C_ℓ are much more sensitive to the angular resolution of an experiment than to its sensitivity.
- An experiment with an angular resolution of $\theta_{fwhm}\approx 10'$ can determine multipoles up to $\ell\sim 2000$. Since the power spectrum from primary anisotropy declines rapidly at higher multipoles (Figure 1), we learn little more about the very early universe by going to much higher angular resolutions.

Knox and Turner[29] and Knox[27] have considered the limitations imposed by cosmic variance in extracting information on the tensor component of the CMB anisotropies. Cosmic variance is particularly important in this case because the tensor mode, even if present, is unlikely to

make a significant contribution to the anisotropies at $\ell \gtrsim 100$. These authors conclude that the true value of the ratio $r = C_2^T/C_2^S$ must exceed $r \sim 0.14$ if the amplitude of the tensor component is to be distinguished from zero at the 95% confidence level, assuming that all other parameters that can affect the CMB anisotropies are known exactly. Evidently cosmic variance sets fundamental limits on our ability to test inflationary models, but as we will now describe, degeneracies with other cosmological parameters must be taken into account in assessing the accuracy with which inflationary models can be constrained by CMB observations.

3.2 Cosmic confusion

Analyses of the 4-year COBE maps already set tight limits of $n \approx 1.2 \pm 0.3$ on the spectral index of the fluctuation spectrum[30]–[31]. The COBE observations are thus consistent with the near scale-invariant spectrum expected in inflationary models. This is an important result, but it does yet strongly constrain the dynamics of inflation. As discussed in Section (2.1), the constancy of H during inflation implies small deviations from a scale-invariant spectrum; for example $n_s = 0.94$ for a quartic potential $V(\phi) \propto \phi^4$. It is therefore likely that we will need to measure spectral indices to very high accuracy (much better that ± 0.1) if we are to detect any significant departure from a scale-invariant spectrum. However, at this level of accuracy, we must address the possibility of 'cosmic confusion'[32], *i.e.* that models with different cosmological parameters can produce nearly identical CMB power spectra. For example, it is possible to mask a slight change in the scalar spectral index by changing other cosmological parameters such as the cosmological constant, baryon density and ionization history. This is illustrated in Figure 3, which shows CMB power spectra for two CDM models with slightly different values of n_s, Ω_b and h. The models are almost indistinguishable at multipoles $\ell \lesssim 300$. The lower panel shows that the differences in the power spectra are smaller than the cosmic variance limits up

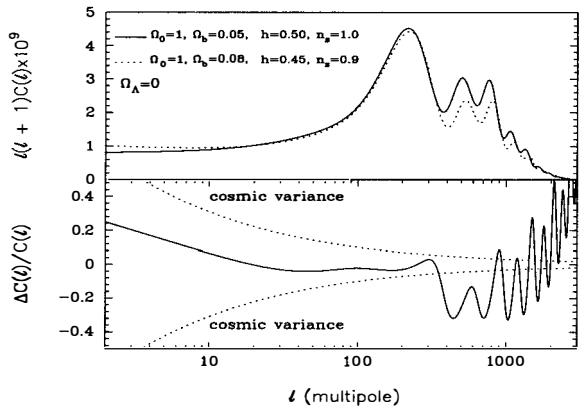

Figure 3. An example of cosmic confusion. The upper panel shows the temperature power spectra of two CDM models with slightly different spectral indices, Ω_b and Hubble constants. Tensor modes are ignored. The solid line in the lower panel shows the fractional difference between these two power spectra. The dotted lines shows the 1σ errors arising from cosmic variance for an 'ideal' experiment ($f_{sky} = 1$, $w^{-1} = 0$.)

to the first Doppler peak. To distinguish between these models, which within the context of the inflationary paradigm have a relatively large difference in their spectral indices, we would need to break the degeneracies between the cosmological parameters defining the models. This might be achievable by observing the CMB anisotropies at high angular resolution so measuring the Doppler peak structure at mutipoles $\ell \gtrsim 300$ where the spectra in Figure 3 differ (see Section 4), or by determine parameter combinations such as $\Omega_b h^2$ to exquisite precision using other techniques (*e.g.* primordial nucleosynthesis[33]).

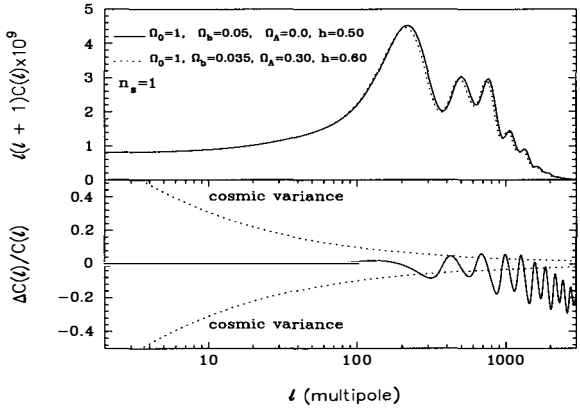

Figure 4. Another example of cosmic confusion showing two models with different Ω_Λ, Ω_b and h which have very similar CMB power spectra.

Another example of 'cosmic confusion' is shown in Figure 4. Here, the Doppler peak structure of the two models is almost identical and it would require a high precision experiment, capable of measuring the CMB power spectrum to multipoles of $\ell \gtrsim 1000$, to distinguish between these models.

4 CMB Constraints on Inflation

Fortunately, the prospects for measuring the CMB anisotropies at high sensitivity and angular resolution over the next decade seem excellent. In particular, the NASA MAP[34] and ESA COBRAS/SAMBA[35] satellites promise near cosmic variance limited measurements of the CMB power spectrum at angular resolutions of $\sim 20'$ ($\ell \sim 500$) and $\sim 4'$ ($\ell \sim 2000$) respectively. In this section, I do not attempt a detailed analysis of these satellites (which will be reported elsewhere[36]) but simply sketch what can be achieved by 'ideal' experiments ($w^{-1} = 0$) which measure the CMB power spectrum to the cosmic variance limits over the multipole ranges $2 \leq \ell \leq 500$ and $2 \leq \ell \leq 2000$. I stress that this example has been chosen to demonstrate the effects of cosmic variance and cosmic confusion and should not be taken as indicative of the relative performance of MAP and COBRAS/SAMBA.

As a target model, I have adopted the standard CDM model with $\Omega_0 = 1$, $\Omega_b = 0.05$, $\Omega_\Lambda = 0$, $h = 0.5$, $n_s = 1$, $n_t = 0$ and varied the tensor-to-scalar ratio $r = C_2^T/C_2^S$ while keeping the other parameters fixed. I then apply the covariance matrix approach[28] to compute the accuracies with which the cosmological parameters can be determined. Nine parameters have been adopted in this analysis: Q, the amplitude of the scalar component of the spectrum;

$r = C_2^T/C_2^S$; the spectral indices n_s and n_t; the cosmological densities Ω_0, Ω_b, Ω_Λ; the Hubble parameter h and the residual optical depth τ arising from reionization of the inter-galactic medium. Derivatives of the power spectra with respect to the nine parameters α_i, $\partial C_\ell/\partial\alpha_i$ have been computed from accurate numerical computations of C_ℓ, except for the derivative with respect to Ω_0, where we have adopted the $\ell\Omega_0^{1/2}$ scaling as in ref [28] (*i.e.* we assume that the CMB power spectrum in a low density universe is identical in shape to that of an $\Omega_0 = 1$ universe but shifted to higher multipoles).

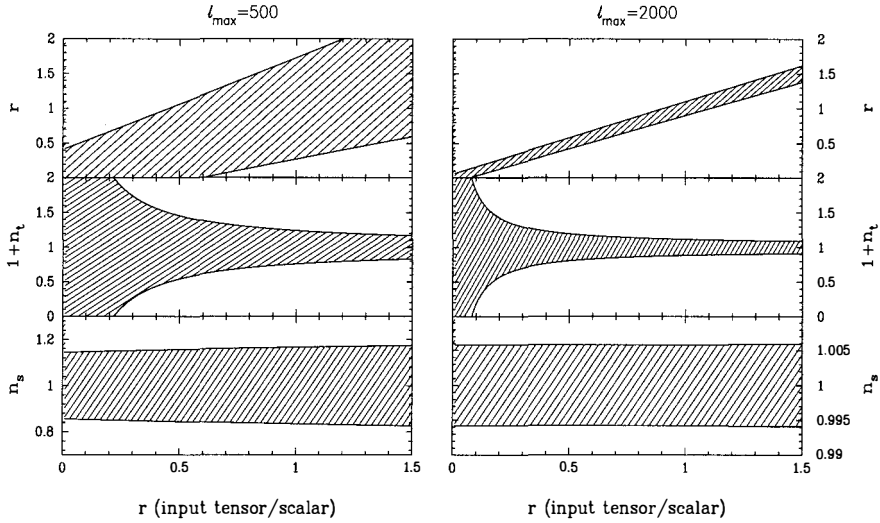

Figure 5. The 1σ ranges on the tensor-to-scalar ratio r, tensor spectral index n_t and scalar spectral index n_s as a function of the input value of r for a standard CDM model with parameters as given in the text. The errors on these parameters have been marginalized over uncertainties in the other parameters defining the models. The figures to the left are for an ideal experiment sampling multipoles $2 \leq \ell \leq 500$ and the figures to the right are for a wider range $2 \leq \ell \leq 2000$.

Some results from this analysis are shown in Figure 5. These figures show the 1σ errors on r, n_s and n_t marginalized over the errors in the other cosmological parameters; *i.e.* for each parameter plotted in Figure 5, we make no prior assumptions about the values of any other cosmological parameter. The results are striking: an ideal experiment sampling multipoles $\ell \leq 500$ can measure the scalar spectral index n_s to an accuracy of about ± 0.15, an improvement over COBE, but well below the precision required to test inflationary models. Furthermore, such an experiment is incapable of unambigously detecting a tensor mode contribution to the CMB anisotropies at the 2σ level for any input value of r plotted in the Figure. In contrast, an ideal experiment sampling multipoles $\ell \leq 2000$ can determine n_s to an accuracy of ± 0.005, n_t to an accuracy of $\pm 0.05(1.5 + r)/r$ and the ratio r to an accuracy of about ± 0.07. These errors on n_t and r are close to the theoretical limits determined by Knox[27] and for a simple reason – by measuring the power spectrum to $\ell \sim 2000$ the degeneracies between most of the cosmological parameters are lifted. For example, Ω_0, Ω_b, h can each be determined to a precision of better than 1% and so the uncertainties in the spectral parameters n_s, n_t and r become decoupled

from those of other parameters. Future observations of the CMB should therefore be capable of testing inflationary models to high precision and of simultaneously constraining fundamental parameters such as Ω_0, Ω_b and the Hubble constant to precisions far in excess of those achievable by conventional astronomical techniques.

In summary, the accuracy with which we can test inflationary models via CMB observations depends critically on our ability to disentangle small variations in the quantities r, n_s and n_t from variations in other parameters. Measurements of C_ℓ to $\ell_{max} \sim 500$ thus provide poor constraints on r, n_t and n_s in the absence of prior constraints on other cosmological parameters. However, the degeneracies with other cosmological parameters can be removed by measuring C_ℓ to higher values of ℓ, and we can achieve errors close to the theoretical limits for $\ell_{max} \sim 2000$.

The examples presented here are idealized, and at least the following problems require further investigation before we can assess the precise limits that can be placed on inflationary models.

- How sensitive are the errors on r, n_t and n_s to prior constraints on other cosmological parameters? Do we really need to sample multipoles $\ell \sim 2000$, or can we set useful limits on inflationary models with lower resolution CMB experiments together with other constraints on cosmological parameters?
- How sensitive are the errors on r, n_t and n_s to variations of n_s and n_t with wavenumber (*i.e.* 'runs' in the spectral indices[37])? The point here is that most of the information about cosmological parameters comes from the Doppler peak structure in C_ℓ at multipoles $\ell \gtrsim 300$, whereas any tensor mode contribution is localised at $\ell \lesssim 100$. An abrupt change in the spectrum at $\ell \sim 100$ could therefore exacerbate the cosmic confusion problem.
- What are the effects on cosmological parameter estimation of systematic errors on the CMB power spectrum arising, for example, from Galactic emission and point sources? In particular, how important are such effects at multipoles $\ell \gtrsim 1000$?
- What are the effects of distortions to the linear theory CMB power spectra caused, for example, by gravitational lensing?

Although no self-contained analysis of parameter estimation incorporating all of these effects has yet been done, other work[35,38,39] suggests that they will not cause significant changes to the conclusions presented here, provided the primordial power spectra are well approximated by power laws. In this event, observations of the CMB should determine all of the parameters required to specify a theory of structure formation, so decoupling post-recombination astrophysics from remaining uncertainties in the evolution of the early Universe.

Acknowledgements Most of the CMB power spectra in this paper were computed using the code described in ref [40]. I thank the UK Particle and Astrophysics Reseach Council for the award of a Senior Fellowship.

REFERENCES

[1] Guth A.H., 1981, Phy. Rev. D**23**, 347.
[2] Albrecht A. and Steinhardt P.J., 1982, Phys. Rev. Lett., **48**, 1220.
[3] Linde A.D., 1982, Phys. Lett. **B108**, 389.
[4] Linde A.D., 1990, *Particle Physics and Inflationary Cosmology*, Harwood Academic Publishers, Chur, Switzerland.
[5] Bond J.R., 1996, in *Cosmology and Large Scale Structure*, Les Houches Lectures, ed. R. Schaeffer, Elsevier Science Publishers, Netherlends.

[6] Steinhardt P.J., 1996, SUSY-95, eds I. Antoniadis and H. Videau, Editiones Frontieres, Gif sur Yvetter, France, p549.
[7] Lidsey J.E., Liddle A.R., Kolb E.W., Copeland E.J., Barreiro T. and Abney M., 1996, Rev. Mod. Phys., in press.
[8] Kofman L.A. and Linde A.D., 1987, Nucl. Phys. **B282**, 555.
[9] Salopek D.S., Bond J.R. and Bardeen J.M., 1989, Phys. Rev. D**40**, 1753.
[10] Peebles P.J.E., 1984, ApJ, **284**, 439.
[11] Bucher M.A., Goldhaber A.S. and Turok, N., 1995, Phys. Rev. D**52**, 3314.
[12] Salopek D.S. and Bond J.R., 1990, Phys. Rev. D**42**, 3936.
[13] Sachs R.K. and Wolfe A.M., 1967, ApJ, **147**, 73.
[14] Bond J.R. and Efstathiou G., 1987, MNRAS, **226**, 655.
[15] Abbott L.F. and Wise M.B., 1984, Nucl. Phys. **B244**, 541.
[16] Starobinsky A.A., 1985, Sov. Astron. Lett. **11**, 133.
[17] Allen B. and Koranda S., 1994, Phys. Rev. D**50**, 3713.
[18] Doroshkevich A.G., Zeldovich Ya.B. and Sunyaev R.A., 1978, Sov. Astron. **22**, 523.
[19] Hu W. and Sugiyama N., 1995, Phys. Rev D**51**, 2599.
[20] Seljak, U., 1996, preprint, astro-ph/9608131.
[21] Adams F.C., Bond J.R., Freese K., Frieman J.A. and Olinto A.V., 1993, Phys. Rev. D**47**, 426.
[22] Ross G.G. and Sarkar S., 1996, Nucl. Phys. **B461** 597.
[23] Turner M.S., 1993, Phys. Rev. D**48**, 3502.
[24] Copeland E.J., Kolb E.W., Liddle A.R. and Lidsey J.E., 1993, Phys. Rev. D**48**, 2529.
[25] Copeland E.J., Kolb E.W., Liddle A.R. and Lidsey J.E., 1994, Phys. Rev. D**49**, 1840.
[26] Hu W., Spergel D.N. and White M., 1996, preprint, astro-ph9605193.
[27] Knox L., 1995, Phys. Rev. D**52**, 4307.
[28] Jungman, G.,Kamionkowski M., Kosowsky A., and Spergel D.N., 1996, Phys. Rev. D**54**, 1332.
[29] Knox L. and Turner M.S., 1994, Phys. Rev. Lett. **73**, 3347.
[30] Wright E.L., Bennet C.L., Gorski K., Hinshaw G. and Smoot G.F., 1996, ApJ, **464**, L21.
[31] Bennet C.L. *et al* , 1996, ApJ, **464**, L5.
[32] Bond J.R., Crittenden R., Davis R.L., Efstathiou G., Steinhardt P.J., 1994, PRL, **72**, 13.
[33] Walker T.P. *et al* , 1991, ApJ, **376**, 51.
[34] Bennet C. *et al* , 1996, NASA Midex proposal.
[35] Bersanelli M. *et al* , 1996, ESA Phase A report D/SCI(96)3.
[36] Bond J.R., Efstathiou G. and Tegmark M., in preparation.
[37] Kosowsky A. and Turner M.S., 1995, Phys. Rev. D**52** R1739.
[38] Seljak U. 1996, ApJ, **463**, 1.
[39] Tegmark M. and Efstathiou G., 1996, MNRAS, **281**, 1297.
[40] Seljak U. and Zaldarriaga M., 1996, ApJ., **469**, 437.

MICROWAVE ANISOTROPIES FROM COSMIC DEFECTS

Neil Turok
Cambridge University, Cambridge UK.

Abstract

A high resolution map the cosmic microwave sky offers a unique opportunity of searching for the macroscopic topological defects predicted by many theories of high energy physics. This talk summarises the theoretical reasons for taking the existence of cosmic defects seriously, both from a fundamental physics viewpoint and because they give us theories of cosmic structure formation which are viable alternatives to quantum inflationary perturbations. I also describe recent work on defect signatures in the microwave sky, namely the shift of the Doppler peaks to smaller angular scales, the issue of the smearing of these peaks by decoherence of the source, and the distinctive pattern of hot spots produced by the monopole and texture theories on subdegree scales.

1 Why are Cosmic Defects Interesting?

There are two very good reasons for being interested in cosmic defects [1].

The first is from fundamental theory. The ideas of symmetry and symmetry breaking are central both in the standard model of high energy physics, and in unified theories which attempt to go beyond it. All such attempts incorporate the standard model in a simpler, and more symmetrical theory. And it is inconceivable that such a deeper underlying symmetry does not exist - the highly regular pattern of particles and charges in the standard model simply cannot be accidents. There are probably several types of additional symmetries - supersymmetry, unified gauge symmetry, some sort of family symmetry, are all ideas which most theorists believe will eventually be confirmed in nature.

If there are higher symmetries, they must be broken so that they are not manifest in our low energy world. Spontaneous symmetry breaking is the only manner we know of in which an underlying symmetry avoids becoming explicit. And spontaneous symmetry breaking inevitably

produces defects. In fact the process of spontaneous symmetry breaking occurs all around us in nature, from the breakdown of translational/rotational symmetry when water freezes to the veritable zoo of defects formed in superfluid Helium three, or in liquid crystals. It is no exaggeration to say that spontaneous symmetry breaking is a cornerstone of modern theoretical physics.

Here there are also some very general theorems. The simplest is that the breaking of a discrete symmetry produces domain walls - this happens in the Ising model for example, where the proliferation of the domain walls is responsible for the observed phase transition. The breaking of an abelian ($U(1)$) continuous symmetry produces vortex strings, as observed in liquid Helium or in superconductors, and the complete breaking of a nonabelian symmetry like $SU(2)$ produces texture, examples of which occur in two places in standard model physics. The Skyrme model of nuclear matter represents the nucleons as texture defects, and in the standard electroweak theory, the number of defects present in the classical vacuum corresponds to the baryon number of the universe. Partially broken symmetries are also interesting - if one starts with a simple grand unified gauge group, and breaks down to the standard model, the existence of the unbroken $U(1)$ symmetry of electromagnetism guarantees that magnetic monopole defects will form. Likewise if one breaks to a subgroup with a discrete factor, one inevitably forms cosmic strings.

I do not believe it overstates things to say that if current ideas about unified theories are correct, cosmic defects almost certainly exist. This view is strengthened by the recent theoretical developments involving duality in supersymmetric theories, in which the magnetic monopole defects play a central role.

The second reason for considering cosmic defects is because they provide an alternative theory of structure formation, which can be very usefully compared with the more popular inflationary mechanism. If there had not been an alternative theory to inflation, it might have been already accepted as proven, because of the qualitative successes it has had in matching the observations. The fact that cosmic defects have had similar qualitative successes has shown that those successes are actually a result of far milder theoretical assumptions, like approximate scale invariance, and the growth of perturbations under gravity, which both theories have in common. It has also helped focus work on tests which *are* sensitive to the finer details of the theories. So the defect theories are useful as a 'foil' to inflation.

I would admit that inflation is clearly a grander, more ambitious theory of structure formation, and there are good reasons why most workers focus on it. After all it 'explains' the structure of the smooth background universe, as well as the perturbations. The notion that the large scale structure emerged via quantum mechanics is also attractive. From a pragmatic point of view, inflation is by far the easiest theory to work with, and to tune to new observations. For example the predictions for cosmic microwave anisotropies are now routinely calculated to accuracies of a per cent or so. These are all good reasons to work on inflation. The bad side of inflation, however, is its enormous adjustablility - I for one don't believe there is a single honest-to-god prediction of inflationary theory. All the 'predictions' are actually a result of preconceptions as to what a 'typical' scalar field potential looks like - if it is monomial or polynomial, sinusoidal, exponential, or whatever. I think one has to admit we have very little idea what a 'generic' Planck-scale scalar field potential should look like.

Structure formation from defects is cleaner in this respect. There is a discrete set of possible patterns of symmetry breaking, and in general the predictions are completely independent of the details of the scalar field potential. They would hold even if there were no fundamental scalars, if fermion condensates broke the symmetry for example. And we are reasonably sure that spontaneous symmetry breaking actually happened in the early universe. Furthermore, cosmic defects offer us a unique probe of the pattern of symmetry breaking at very high

energies, one of nature's deepest questions. For this reason, they are well worth looking for quite independently of whether they played a role in structure formation. In contrast, inflationary theories offer the chance of measuring a small piece of the inflaton scalar potential, a very limited piece of information about the underlying theory which would be unlikely to have much theoretical consequence. So cosmic defects should at the very least be considered as an 'honorable opposition' to the inflationary hypothesis!

The key differences between the inflationary and defect theories are summarised below:

Inflation	**Defects**
Quantum	Classical
Linear $\Rightarrow$ Gaussian	NonLinear $\Rightarrow$ NonGaussian
Coherent Perturbations	Incoherent Perturbations
Causally Unconstrained	Causally Constrained
More adjustable	Less adjustable

Perhaps the most fundamental difference between the two sets of theories is that whereas the inflationary mechanism involves only linear physics (at least in the simplest case), the defect theories are intrinsically nonlinear. This has the important consequence that the fluctuations induced obey Gaussian statistics whereas the defect theories are non-Gaussian - many-σ fluctuations occur much more frequently. The nonlinearity also has the consequence that the perturbations from defects are 'incoherent', as I shall discuss later.

Another basic difference is that in the inflationary mechanism there is an epoch preceding the hot big bang, during which the perturbations are set up. From the standard hot big bang viewpoint, these perturbations appear to be 'acausal', since they involve correlations on scales beyond the standard hot big bang horizon scale. In contrast, in the defect theories, one assumes that the universe began perfectly homogeneous, either as a result of inflation or just special initial conditions. The perturbations are set up subsequently, as a result of completely causal physics. Again, this is only possible because of the nonlinearity of the defect ordering process.

Finally, the inflationary predictions are far more adjustable than the defect induced ones, as mentioned above.

2 Large Scale Structure: the Matter distribution

Neither theory has a spectacular record in quantitatively matching the COBE amplitude to observations of the mass fluctuations on smaller scales, although both come within factors of a few. Early work showed [6] that if one normalises to the COBE amplitude on large scales, the rms mass perturbations on the scale of galaxy separations are substantially smaller than those from standard cold dark matter (i.e. the simplest inflationary model).

As Figure 1 shows, in a critical density, $\Lambda = 0$ universe this is a 'good thing' on smaller scales ($\lambda \sim 10h^{-1}$ Mpc), where the simplest inflationary theory vastly overestimates the power. (I have adopted a Hubble constant $h = 0.7$ in this Figure, more in line with recent data, which increases the growth of perturbations, exacerbating the inflationary theory's problems, and improves the defect theory). The numerical curves are recent results of Pen and myself using very large scale (512^3) texture simulations, which show somewhat more large scale power than in ref. [6]. On larger scales, where the observations of the mass fluctuations are very much more uncertain, the texture theory still looks bad, having much less power than the phenomenological spectrum advocated by Peacock and Dodds [8]. It should however be kept in mind that the latter is based on an inference of the underlying mass perturbations from observations of galaxy clustering, and there are large uncertainties in this.

Figure 2 shows that in a low Ω universe, the shape of the defect power spectrum matches the phenomenological curve much better. However, in this plot the defect power spectrum has been multiplied by a factor of $(2.5)^2$, which one would have to attribute to a 'bias' of the galaxy correlations relative to the mass. There is therefore a problem of a large bias factor needed, even in a low Ω universe. Below, I will argue that if one is willing to tune the theory, one can in effect dial the COBE amplitude downwards relative to the mass power spectrum on observed scales, in the same way that 'tilt', Λ and mixed dark matter are used in inflationary models to suppress the mass fluctuation. One could then have an open universe theory with defect-induced perturbations and a 'bias' factor close to unity.

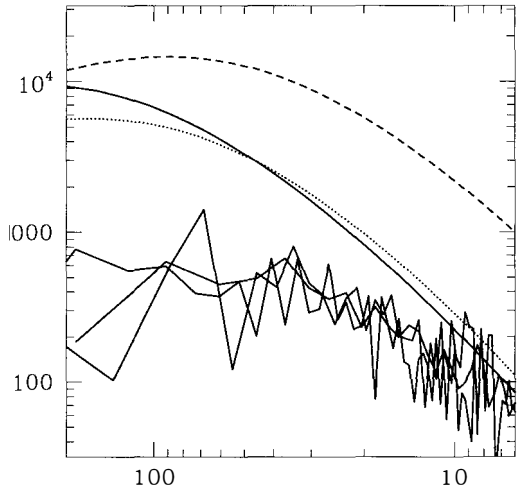

Figure 1: The power spectrum of dark matter perturbations P_k is plotted against wavelength $\lambda = (2\pi/k)$ measured in h^{-1} Mpc, as computed in a critical density, $\Lambda = 0$ universe with $h = 0.7$. A phenomenological fit to galaxy clustering data by Peacock and Dodds is shown as a solid curve. The jagged curves below are the preliminary results of a new set of 512^3 simulations of cosmic texture by Pen and the author. The upper dashed curve is the prediction of the simplest inflationary model, standard CDM, the dotted curve is the prediction of a 'tilted' CDM model with primordial spectral index 0.8 instead of unity. All theories are normalised to COBE - note that on scales of 10 h^{-1} Mpc, where observations are firmest (e.g. cluster abundances), the simplest texture theory does significantly better than the simplest inflationary theory.

There is a second observational fact which also seems to disfavour the defect models, namely that the counts in cells in the galaxy distribution on large scales (cubes of 10, 20, 40 h^{-1} Mpc) seem consistent with the hypothesis of Gaussian initial conditions and gravitational clustering (there is a well known prediction for the relation between the skewness and the variance for example).

Here it should be remembered that the nonGaussianity in the defect-induced matter perturbations is not very large. If the nonGaussianity induced by gravitational clustering is much larger (as would almost be the case in the low Ω example discussed above) than the 'primordial'

nonGaussianity, it would be very hard to distinguish the theory from a Gaussian one by this test [2]. I also want to mention a possible way of 'tuning' of the global defect theories, which is worth

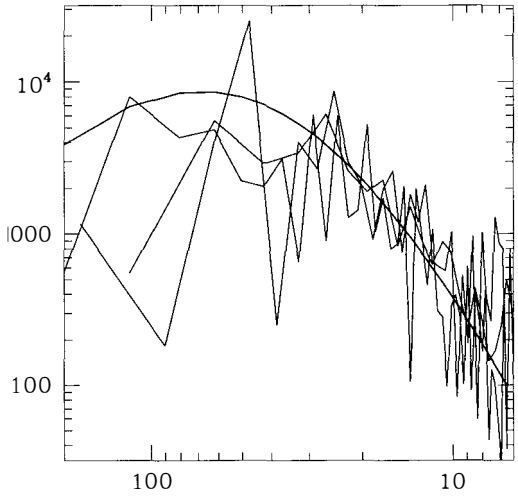

Figure 2: As in Figure 1, but for an $\Omega = 0.4$ universe again with $h = 0.7$. The texture results have now been multiplied by a factor of $(2.5)^2$, in order to match the amplitude of the phenomenological fit. This could be justified by either a high bias of galaxy correlations relative to the mass correlations, or by appealing to a 'tilt' mechanism as described in the text.

exploring [3]. As in pion physics, one can imagine that the Goldstone bosons do possess a a small mass, and that this is within the interval $t_o^{-1} < m_{GB} < t_{eq}^{-1}$. This would effectively 'switch off' the defects some time between matter-radiation equality and the present, thus suppressing the COBE-scale anisotropy relative to the observable matter perturbations. Introducing such a very small mass would normally be regarded as extreme fine tuning, but exponentially light 'almost-Goldstone' bosons do seem to occur quite naturally in certain compactified versions of string theory [4], and these could meet the requirements. It will be interesting to see whether with this additional tuning the global defect theories can fit the current data as well as the inflationary ones.

In summary, cosmic defect induced perturbations certainly do not provide a compelling fit to observations of the galaxy distribution. But neither is there a compelling discrepancy. Luckily for us, there is a far cleaner observational test for cosmic defects, namely observations of the microwave sky.

3 How Can We Find Them?

If, as argued above, it is likely that macroscopic cosmic defects do exist, how do we find them? Obviously, our best chance is in examining our entire 'past light cone', covering an entire horizon volume in the universe. The cosmic microwave background gives us the opportunity to do just that. There have been very exciting developments in our understanding of defect induced CMB anisotropies over the last year or so, throwing up three signatures which qualitatively distinguish defect-induced anisotropies from their inflationary counterparts. All of these rely on the sub-degree scale anisotropies due to perturbations in the photon-baryon fluid on the surface of last scattering. They are: a) Hot spots for monopoles and textures, b) A shift in the angular power spectrum to higher l, particularly pronounced for cosmic strings, and c) A smearing of the pattern of 'Doppler peaks', caused by the decoherent nature of the defect-induced perturbations. I shall deal with these in turn.

3.1 Defect Sky Maps

A great deal of effort has been made over the last few years to compute the predictions of cosmic defects for the microwave sky. The pattern of fluctuations on COBE scales was computed over two years ago, for global defects like monopoles and textures[5],[6], and more recently for cosmic strings [7]. The results show that with COBE's poor angular resolution the characteristic defect induced patterns of anisotropies are very difficult to distinguish from inflationary predictions. On smaller angular scales, however, the results become progressively more interesting.

As first realised for cosmic strings [9, 10], the time dependent spacetime metric around evolving cosmic defects causes a gravitational redshifting or blueshifting of the photons travelling to us from the surface of 'last scattering' (Figure 3). In the case of cosmic strings, linear discontinuities are produced, a really distinctive signal. Unfortunately, at least in the case of standard recombination, on the angular scales which will be probed by the current generation of CMB experiments, and the two forthcoming satellites, the string-induced discontinuities are likely to be masked by the 'intrinsic' and 'Doppler' anisotropies. Seeing them will probably require large sky coverage, and arc minute resolution. Nevertheless this is an extremely powerful signature, and well worth looking for.

For global monopoles and textures, the signatures from the time-dependent potential effect are easier to observe at degree scale resolution. A very characteristic pattern of a cold spot with a hot spot on each side is produced by monopoles [11], and for textures, isolated hot and cold spots are produced [12],[11], [13]. These latter patterns are visible on scales of order a degree or so, but finding one such defect-induced event requires a great deal of sky coverage (many thousands of square degrees). It was also found in [11] that the non-Gaussianity of the pattern was only mild, and that even in the absence of instrument noise or other foregrounds, quite a subtle statistical analysis was needed to discriminate between the defect induced skies and inflationary equivalents. These papers considered a reionised universe, mainly for technical facility. Over the last year, there has been intense interest in the case of standard recombination, which is far more interesting because the small scale structure in the anisotropy is not smeared out.

In a universe with standard recombination, the CMB anisotropy on the sky in a direction $\mathbf{n}$ is given to a good approximation by

$$\frac{\delta T}{T}(\mathbf{n}) = \frac{1}{4}\delta_R(i) - \mathbf{n}\cdot\mathbf{v_R}(i) - \frac{1}{2}\int_i^f d\tau \dot{h}_{ij}\mathbf{n}^i\mathbf{n}^j \qquad (1)$$

where δ_R is the 'intrinsic' perturbation in the photon density and and v_R the velocity of the photon-baryon fluid on the 'surface of last scattering' (a spherical shell at fixed conformal time).

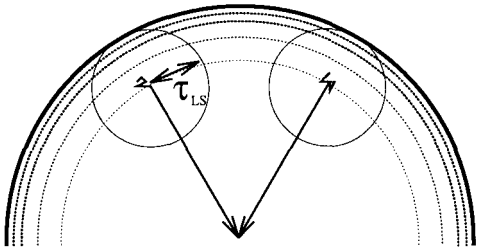

Figure 3: Looking back towards the big bang with microwave photons. Tracing photons back along a line of sight, one eventually comes to the surface of last scattering. The horizon scale at this time, τ_{LS} subtends a scale of 1.1 degrees in a flat universe. Above this scale, the defect induced anisotropies are dominated by the line of sight term produced by a time varying gravitational potential - but on scales down to an arc minute the intrinsic and Doppler effects dominate.

The final term is the line of sight integral over the time dependent metric perturbation, the Sachs-Wolfe integral.

Recent work on defect induced CMB anisotropies has focussed on the first two surface terms. These represent the intrinsic temperature and velocity perturbations in the photon-baryon fluid, and at least with standard recombination, they dominate over the last, time-dependent gravitational potential term, on sub-degree scales. Basically these terms represent what one sees if one carves a spherical shell through the universe, catching the photon-baryon fluid at a fixed moment in cosmic time around the epoch of 'last scattering'. The acoustic perturbations are driven by the cosmic defects' gravitational fields, and one can expect some of the structure of the defects to be represented in the corresponding aniostopy pattern.

Figure 4 (color plate 2) shows examples of ten degree square CMB anisotropy maps, obtained through large scale computer simulations of cosmic string, global monopoles and textures. (The colour version is included in the preprint version of this article available on the bulletin board astro-ph.) These maps include only the 'Doppler' and 'intrinsic' surface terms in equation (1), but as argued in [14] these terms dominate on the subdegree scales where the most striking features are visible. The fourth map shows an inflationary ('standard CDM') map, including the last term in (1), and therefore having more long wavelenth power than the other maps. All maps were computed assuming a critical density, zero Λ universe.

There are two ways in which the theories are manifestly different. First, the *scale* of the structure in the maps increases as one goes from strings to monopoles, textures and standard inflation. Second, the texture and monopole maps show clear 'hot spots' in excess of 5 or 6 σ, which would be highly improbable in a Gaussian theory. The fact that extreme 'hot spots', and no 'cold spots' are seen is a result of the defects being localised positive concentrations of energy, which attract the photon-baryon fluid and cause a rise in the local density and temperature. One would expect localised defects, like unwinding textures or annihilating monopole-antimonopole pairs, to do so more effectively than extended objects like strings, and the simulations bear this out. Likewise, even though there is actually more power in the Doppler term than the intrinsic term, the former is more spread out and Gaussian - it is really the 'intrinsic' term which is responsible for the very high peaks. Note that even though the string map does show some hot and cold spots, since the scale of the structure in the map is smaller, one has in effect have many more independent samples and the chance of a large fluctuation is increased. A quantitative measure of the nonGaussianity of the maps is provided by Figure 5. This shows

the differential number of maxima (and minima) in the maps between ν and $\nu+d\nu$ (and between $-\nu$ and $-(\nu + d\nu)$) standard deviations. For Gaussian noise, these two curves are identical, so the difference provides a measure of the nonGaussianity. These curves are also presented in 'experimental' units - the number of maxima/minima per square degree is the integral under this curve. For example, to see a 5 sigma monopole event one needs to survey of order 100 square degrees, but a 5 sigma texture event requires of order 250 square degrees.

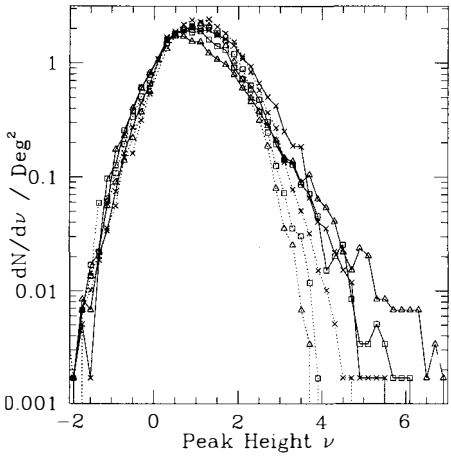

Figure 4: The differential number of maxima and minima of the temperature maps in a given range of $(\delta T/T) = \nu\sigma$, measured in units of the standard deviation σ. The solid lines, linking crosses, triangles and boxes respectively, show the results for maxima for cosmic strings, monopoles and textures. The dashed lines show the number of minima plotted against the *negative* of the height in the same theories. In a Gaussian theory, the curves for maxima and minima are identical, and are computable from the angular power spectra. The curves shown for minima resemble those for a Gaussian random field, whilst the curves for maxima are clearly nonGaussian, most markedly so for monopoles and textures.

These signatures offer a clear signal which experiments such as the Cambridge/Tenerife VSA experiment, and the MAP/COBRAS-SAMBA satellite can go after, and finding them should be quite straightforward [15]. It is also worth noting that the curves in Figure 5 are independent of the COBE normalisation, so if there is a tilt in the Goldstone boson potential as discussed above, suppressing the COBE scale fluctuations, this curve is unaffected. Of course there is however an increase in the *amplitude* of the fluctuations on degree and sub-degree scales.

4 The Location of The Doppler Peaks

Model calculations for cosmic texture first revealed [16],[17],[18] a qualitative difference between the angular power spectra from defects and those from inflation, namely a shift in the primary Doppler peak from $l \sim 220$ to $l \sim 350$. This shift has a nice explanation, which hinges on one of the basic distinctions between the theories discussed above, namely the 'causally constrained' nature of the defect perturbations.

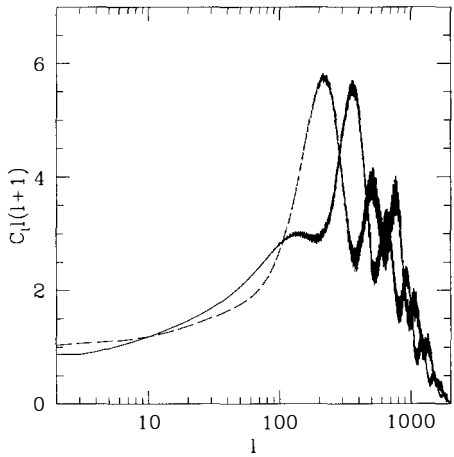

Figure 5: The angular power spectrum of anisotropies, C_l, is plotted versus multipole index l. The dashed curve shows the simplest inflationary theory: the solid curve shows the coherent model calculation of Crittenden and Turok for the cosmic texture theory. The largest Doppler peak is shifted to higher l. The most uncertain part of these model calculations was the matching to the COBE amplitude, so the low l part of the texture curve should be treated with caution.

In the inflationary case, adiabatic perturbations exist outside the Hubble radius. As they approach horizon crossing, the amplitude of the perturbations grow. After horizon crossing, the dark matter perturbations continue to grow, but the photon-baryon fluid instead begins to oscillate. The modes which reach their first maximum at recombination have a value of $k\tau_{rec} \sim 5$, where k is comoving wavenumber and τ_{rec} is the conformal time. These modes subtend an angular scale corresponding to a multipole moment $l \sim k\tau_o \sim 50k\tau_{rec} \sim 250$. Higher peaks occur at shifts of $\Delta l \sim 280n$, $n = 1, 2, ...$ upwards, corresponidng to modes which reached their second, third, ... maximum in amplitude at recombination.

For defects, the story is a bit more complicated. By assumption the universe is taken to be smooth on scales larger than the horizon. So a positive fluctuation in the defect energy is compensated by a negative fluctuation in the density of photons, baryons, and dark matter. The latter are all of the same sign if one assumes as usual that the photon-baryon and photon-dark matter ratios are fixed by microphysics (i.e. the perturbations are 'adiabatic'). As a given scale crosses the horizon, the gravitational field induced by the defects drives the photon-baryon fluid and dark matter densities in the same sign as the defect fluctuation, due to the attractive nature of gravity. This means that the photon-baryon fluid perturbation must change sign, as it goes from 'compensating' to being 'driven' by the defects' gravitational field. The first maximum in the amplitude of the photon-baryon fluid occurs before this sign change, at $k\tau \sim 2$ rather than 5. It is barely visible in plots of the angular power spectrum (it is enhanced in Figure 6 by the vector and tensor contributions). The main peak, which id really 'driven' by the defect stress energy, is 'delayed', by the sign change, and occurs at $k\tau_{rec} \sim 7$, or $l \sim 350$, for textures.

Figure 7 shows the angular power spectra determined from simulated sky maps such as

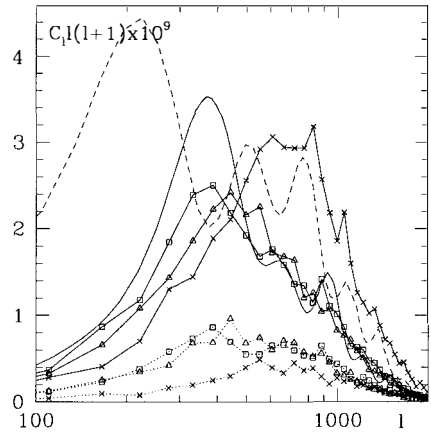

Figure 6: CMB anisotropy power spectra for the intrinsic and Doppler terms as measured in computer simulations (Turok 1996). The dashed curve shows the simplest inflationary model for reference, which includes in addition the Sachs Wolfe integral. The solid curve shows the prediction of the model in Figure 6 for the same quantity as measured in the simulations. There is a progressive shift to the right in the main Doppler peak, from textures to monopoles to cosmic string.

shown in Figure 4 (color plate 2). The rightward shift of the main peak is stronger for monopoles, and strongest for cosmic string. The string result is consistent with that based on earlier model string calculations by Albrecht, Magueijo and collaborators [18].

5 Decoherence and Smearing of the Doppler Peaks

Recent work [18, 19, 20] has emphasised a second, qualitative difference between the cosmic defect theories and inflation. Namely that perturbation modes of a given wavenumber k do not all follow the same time evolution, and are not simply determined by their own initial conditions. The mode-mode coupling is crucial to the defect ordering process, and produces an ensemble of possible evolutions for modes of equal k. This has important consequences for the structure of the Doppler peaks in the microwave anisotropy. there is an ensemble of possible histories for perturbation modes of a given wavenumber. Note that this is a completely different effect from nonGaussianity, but it is also a consequence of the nolinearity orf the theory. In a 'coherent' theory two point correlators factorise: perturbation variables $A_{\mathbf{k}}(\tau)$ and $B_{\mathbf{k}'}(\tau')$, where $\mathbf{k}$ and $\mathbf{k}'$ are the corresponding wavevectors and τ, τ' the conformal times, obey

$$\langle A_{\mathbf{k}}(\tau) B_{\mathbf{k}'}(\tau') \rangle = \delta_{\mathbf{k}+\mathbf{k}'} a(k,\tau) b(k,\tau')$$

which is to say it factorises. In such a theory, one does not need to evolve an ensemble of universes, just to compute the functions $a(k,\tau)$ and $b(k,\tau')$, equivalent to evolving just one Foruier mode of each k.

For oscillatory quantities, like the photon-baryon density before decoupling, factorisation has the dramatic consequence that the fixed time three dimensional power spectrum has *zeros* - corresponding to modes which happen to be zero at that instant. In effect, the location of the zeros would tell us the time back to the big bang. Unfortunately, there is no method is known of measuring the three dimensional power spectrum in such a quantity. The best we have is a two dimensional power spectrum, namely the angular power spectrum of anisotropies on the microwave sky. This is basically an integral of the three dimensional power spectrum, and the zeros are smeared out. But the oscillations are generally still clearly visible (Figure 6).

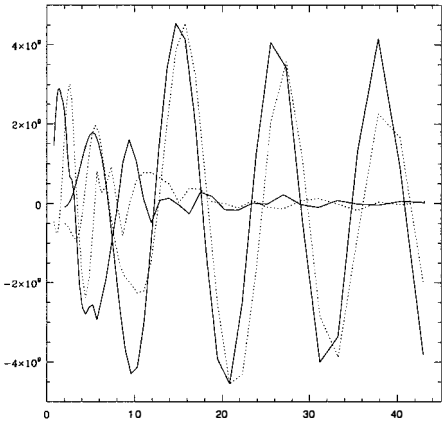

Figure 7: An illustration of decoherence - the history of two Fourier modes of the same wavenumber k is shown as a function of $k\tau$ from a cosmic texture simulation. One mode is shown with dashed lines, the other with solid lines. The curves which die out after $k\tau \sim 10$ are those for the perturbation source $\rho + 3P$. The oscillating curves are those for the perturbations to the photon-baryon fluid.

In defect theories, there is no such factorisation, and one expects the correlations to decay more strongly away from $\tau = \tau'$ than they would in the factorised product. The Fourier modes of given k in effect 'lose memory' of their initial conditions. All have different interactions with the other k modes, and so evolve differently. This is illustrated in Figure 8, which shows two different Fourier modes of the same wavenumber in a cosmic texture simulation. The Figure shows the time evolution of the source for isotropic perturbations, $\rho + 3P$, which is large at early times and decays away after horizon crossing ($k\tau \sim 5 - 10$). The two Fourier modes ave very different source evolutions. The Figure also shows the evolution of the radiation density perturbation δ_R, driven by this source. Note that in this example, even though the sources behave quite differently, the radiation oscillations are quite close to being in phase. In fact, the texture theory seems to show only modest 'decoherence' [16] - the expectation is that the cosmic string theory will show a stronger effect [19], although there is as yet no realistic calculation of this.

The consequence of 'decoherence' is to smear out the Doppler peaks in the angular power spectrum of anisotropies [18]. At the instant of recombination, when one looks at modes of a given wavelength, they will be at a variety of phases in their oscillations. They will not all

be 'in phase'. Adding them up has the effect of smearing out the oscillations. An analysis of the observational strategy needed to look for this smearing effect has appeared [21]. If we do see such a smearing, we will be able to conclude with some certainty that the mechanism for structure formation involved nonlinear rather than linear physics, a quite fundamental advance.

6 Summary: Future Directions

The cosmic defect theories teach us that there is more than one way to make structure in the universe. Whilst calculations are difficult, advances in computational power have brought accurate predictions within reach, although with some effort. The theories are in principle highly predictive, and offer exciting distinctive signatures which will soon be accessible to observations.

It was fascinating at the joint session of this meeting with the Electroweak Physics meeting to see the contrast in styles. The mapping of CMB anisotropies is a very young branch of experimental physics - particle accelerators like the LHC are at the forefront of a much more mature endeavour. Both share a similar goal, however, namely pushing our knowledge of the fundamental physics underlying the universe beyond the standard model. I think we should look at the MAP and COBRAS-SAMBA satellites, and their successors as the 'CERNs' of the future.

Acknowledgements. I thank the organisers of this excellent meeting for bringing together such a broad cross section of experimental and theoretical workers in this field, and allowing us the time to interact so usefully. I also thank my collaborators on defect-induced CMB anisotropies, C. Barnes, D. Coulson, R.G. Crittenden, P. Ferreira, U-L. Pen, D. N. Spergel. I also thank Cambridge University and PPARC (UK) for grant support.

References

[1] For a review see A. Vilenkin and E.P.S. Shellard, *Cosmic Strings and other Topological Defects*, Cambridge University Press (1994).

[2] A. Gooding, J.R. Gott, C. Park, D. Spergel and N. Turok, Ap. J. **393** (1992) 42.

[3] N. Turok, in preparation, 1996.

[4] N. Turok, Physical Review Letters **76**, 1015 (1996).

[5] D.P. Bennett and S.H. Rhie, Ap. J. **406**, L7 (1993).

[6] U. Pen, D. Spergel and N. Turok, Phys. Rev. **D49**, 692 (1994).

[7] B. Allen, R. Caldwell, E.P.S. Shellard, A. Stebbins and S. Veeraraghavan, submitted to Phys. Rev. Lett. (1996).

[8] J. A. Peacock and S.J. Dodds, MNRAS **267**, 1020 (1994).

[9] N. Kaiser and A. Stebbins, Nature, **310**, 391 (1984).

[10] F. Bouchet, D.P. Bennett and A. Stebbins, 1988, Nature **335**, 410.

[11] D. Coulson, P. Ferreira, P. Graham and N. Turok, Nature **368**, 27 (1994).

[12] N. Turok and D. Spergel, Phys. Rev. Lett. **64** (1990) 2736.

[13] J. Borrill, E.J. Copeland, A. Liddle, A. Stebbins and S. Veeragahavan, Phys. Rev. **D50**, 2469 (1994).

[14] N. Turok, DAMTP preprint 96-59, astro-ph/9606087, Ap. J. Lett, in press (1996).

[15] K. Maisinger, M. Hobson, A. Lasenby and N. Turok, MRAO preprint in preparation (1996).

[16] R. Crittenden and N. Turok, 1995, Physical Review Letters **75**, 2642.

[17] R. Durrer, A. Gangui and M. Sakellariadou, 1996, Phys. Rev. Lett. **76**, 579.

[18] A. Albrecht, D. Coulson, P. Ferreira and J. Magueijo, 1996, Phys. Rev. Lett. **76**, 1413.

[19] J. Magueijo, A. Albrecht, D. Coulson and P. Ferreira, 1996, Phys. Rev. Lett. **76**, 2617; preprint MRAO-1917,DAMTP-96-26, Imperial/TP/95-96/47,CfPA-96-th-11, astro-ph/9605047.

[20] N. Turok, Physical Review **D54**, 3686 (1996).

[21] J. Magueijo and M. Hobson, preprint DAMTP-96-11, MRAO-1900, astro-ph/9602023.

MEASURING THE CURVATURE OF THE UNIVERSE

Wayne Hu[1] & Martin White[2]
[1]*Institute for Advanced Study, Princeton NJ 08540*
[2]*Enrico Fermi Institute, 5640 S. Ellis Ave, Chicago IL 60637*

Abstract

We discuss how the curvature of the universe can be robustly measured employing only the gross features of the CMB anisotropy spectrum. Though the position of the first peak is not robust, uncertainties in the model for structure formation can be removed by using the spacing of the acoustic peaks and the location of the damping tail. Combined these provide important consistency tests that can be used to discriminate against a truly exotic model.

If we knew the model of structure formation exactly, we could determine many cosmological parameters, including the curvature of the universe, to several percent accuracy (for a review see [1] and references therein) from features in the CMB anisotropy power spectrum. The question arises: how is our ability to measure them degraded as we relax our assumptions about the underlying model. Once we understand which features are model independent (and why), we can go on to study the process of structure formation from those which are model *dependent.* For concreteness, we will focus here on one step of this program [2]: measuring the spatial curvature of the universe, i.e. $\Omega_{\rm tot} = \Omega_0 + \Omega_\Lambda$. The complementary approach of first verifying the model and then measuring the cosmological parameters is taken in a companion piece [3].

Let us assume that we understand the "big picture", i.e. that gravitational instability enhances initially small fluctuations, and that the CMB is coupled to the baryon-electron plasma before recombination. Can we build a measurement of the curvature from such minimal assumptions? Are there sufficient cross checks such that we can have confidence in the measurement? The answers to these questions lie in the acoustic signature of the small angle CMB anisotropy spectrum.

Our "big picture" leaves several questions unanswered:

1. What is the fundamental nature of the fluctuations?

- do curvature perturbations exist outside the horizon as in the inflationary model or are the perturbations initially isocurvature as in a defect model (see also [2, 3]).

2. What is the matter content of the universe?
   - does the baryon-photon ratio ($\Omega_b h^2$) follow the big bang nucleosynthesis (BBN) prediction?
   - what is the matter-radiation ratio ($\Omega_0 h^2$ or more generally, the equality epoch z_{eq})?
3. Does the thermal history of the universe follow the prediction of standard recombination at $z_* \sim 10^3$?

These questions and their consequence for the curvature measurement can be addressed by examining the gross properties of the CMB spectrum taken as a whole. The fine details, so useful for making precision measurements in a fixed model, are too model-dependent to serve us here.

Under our minimal assumptions, we have two striking features (1) the acoustic peaks: their positions, position ratios, spacings and relative heights; and (2) the damping tail: its position, position relative to the peaks and shape. The acoustic peaks probe the sound horizon at last scattering; the damping tail probes the photon diffusion scale at that epoch. Both reflect the curvature of the universe in the projection from physical scale at last scattering to angular scale on the sky. We shall show that these features have complementary strengths and weaknesses in guarding against model uncertainties. Combined they can be proof against any one of a host of exotic possibilities.

To set the stage for this discussion, let us briefly review the angular size distance test for curvature in the universe as it relates to the CMB spectrum. A feature in the temperature fluctuations on the last scattering surface, corresponding to wavenumber $k_{\rm feature}$, is viewed as an anisotropy on the sky at the multipole moment of a spherical harmonic decomposition $\ell_{\rm feature} = k_{\rm feature} D$, where D is the comoving angular size distance and is dependent strongly on the curvature of the universe:

$$D = |K|^{-1/2} \sinh[|K|^{1/2}(\eta_0 - \eta_*)], \tag{1}$$

where $\eta_0 - \eta_*$ is the conformal distance to the last scattering surface and the curvature $K = -H_0^2(1 - \Omega_{\rm tot})$ (for $K > 0$ replace $\sinh \to \sin$). Here the Hubble constant is $H_0 = 100h$ km s^{-1} Mpc^{-1}. Since the projection depends sensitively on $\Omega_K = 1 - \Omega_{\rm tot}$, any feature in the CMB at last scattering may serve in the angular size distance test for curvature in the universe (see Fig. 1). Let us now turn to the two acoustic features, the peak spacings and damping tail location, that best suit this purpose.

Before recombination, the photons and baryons are tightly coupled into a single fluid by Compton scattering. Acoustic oscillations are stimulated as the gravitational compression or rarefaction of the fluid is halted and turned around by photon pressure as the Jeans length (or sound horizon) passes the wavelength. Because gravity is impotent under the Jeans length, typically its effects subsequently die away leaving the fluid to oscillate at its natural frequency thereafter.

As discussed further in [2, 3], the nature of the fluctuations basically determines whether the photon-baryon fluid is undergoing a compression or rarefaction at Jeans crossing which affects the acoustic phase (see Fig. 1b). For either case, the spacing of the peaks reflects the natural frequency of the oscillator. More specifically, in the radiation-dominated era the oscillator equation for the effective temperature fluctuation T of the CMB becomes $T'' + c_s^2 T = 2\Psi''$, where Ψ is the Newtonian potential, c_s is the sound speed, and primes are derivatives with respect

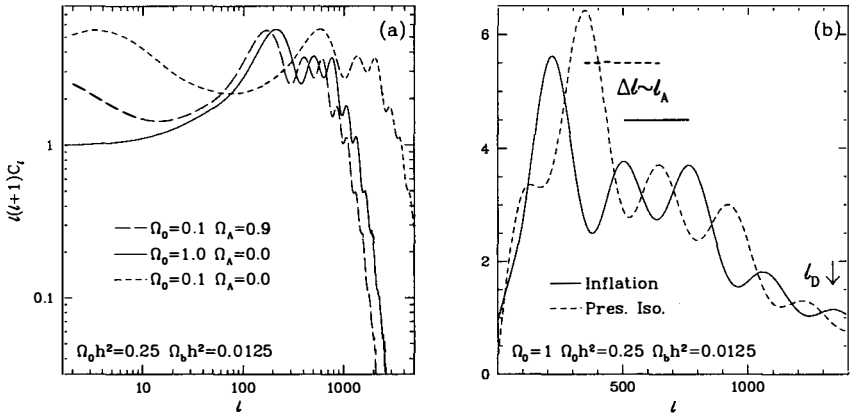

Figure 1: (a) Angular size distance. For an inflationary model, features at last scattering such as the peaks and damping tail are fixed in real space by $\Omega_0 h^2$ and $\Omega_b h^2$, providing in the anisotropy power spectrum $\ell(\ell+1)C_\ell$ standard rulers for the angular size distance test. The cosmological constant Ω_Λ yields a minor effect compared with the curvature $1-\Omega_0-\Omega_\Lambda$. (b) In a broad class of models, the peak spacing $\Delta\ell$ and damping tail location ℓ_D depend only on the background parameters and provide rulers that are robust to model changes. The inflationary model is here compared with the pressure scaling model [7].

to $k\eta$, where $\eta = \int dt/a$ is the conformal time. From the Poisson equation, $|\Psi| \sim (k\eta)^{-2}\delta\rho/\rho$. Since in the radiation-dominated era, the density fluctuation $\delta\rho/\rho = \mathcal{O}(T)$ typically, Ψ is usually negligible well inside the horizon. More generally, if Ψ'' is small or slowly-varying then the solution is an oscillation at the frequency $\omega = kc_s$, possibly with a zero point offset. On the last scattering surface, the acoustic peaks will be spaced by

$$k_{m+1} - k_m = k_A = \pi/r_s, \qquad \Delta\ell = \ell_A = k_A D, \tag{2}$$

where $r_s = \int c_s d\eta$ is the sound horizon at last scattering. To summarize: while the phase and first peak bear the mark of the model-dependent driving force, the spacing of the higher peaks reflects the model-independent natural frequency, set by the sound horizon at last scattering.

If the sound horizon at last scattering is a known quantity, then the peak spacing provides a sensitive angular size distance test of the curvature that is relatively robust to the nature of the fluctuations. In Fig. 2, we show that the peak spacings for the inflationary, texture [5], hot dark matter [4], axionic [6], and pressure scaling [7] isocurvature models are to good approximation related by Eq. (2) to the sound horizon scale.

There are two possible drawbacks to this method of measuring the curvature. The first is that the sound horizon at last scattering depends on the baryon content $\Omega_b h^2$, the matter-radiation ratio $\Omega_0 h^2$ and the thermal history. In Fig. 3a, we show that an uncertain baryon content does not pose an obstacle nor do reasonable values of the Hubble constant $0.4 < h < 0.8$. We shall return to comment on the thermal history below. The second drawback is that for a precise measurement, gravitational forcing effects must be negligible so that the peak spacing reflects the natural frequency of the oscillator. In some models, this may not occur until the higher peaks where damping and secondary effects may make the signal difficult to observe

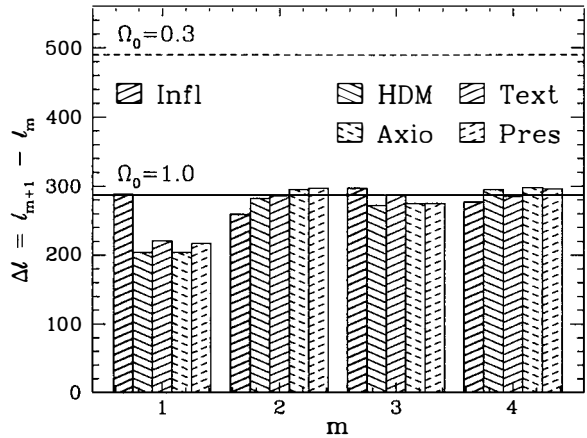

Figure 2: The peak spacing, especially between higher peaks, is mainly dependent on the sound horizon at last scattering (projected on the sky) yielding a robust feature for the angular size distance test. Here five $\Omega_0 = 1$ models (see text; $\Omega_0 h^2 = 0.25$, $\Omega_b h^2 = 0.0125$ and $\Omega_\Lambda = 0$) are compared with the simple prediction $\Delta\ell = \ell_A$ (solid line).

(compare the 1st-2nd peak spacing with the higher ones in Fig. 2).

The location of the damping tail in the CMB spectrum provides yet another angular size distance test of the curvature [2, 8]. The damping is a function of the duration of recombination, or the thickness of the last scattering surface. As the universe recombines, the coupling between the photons and the baryons decreases and the distance that photons can travel before scattering increases. Acoustic oscillations are destroyed as the photons random walk through the electron-baryon fluid. The random walk distance, approximately the geometric mean of the horizon and Compton mean free path, sets the scale of this feature in the CMB.

The benefit of this test is that it is entirely independent of the nature of the fluctuations (see Fig. 1b). As long as the baryon fluctuations are linear, the random walk scale depends only on the background baryon density, ionization fraction, and expansion rate, not on the fluctuations themselves. The main drawback is that it is difficult to measure accurately. The signature of diffusion damping is a sharp exponential cutoff in ℓ at the diffusion scale (see Fig. 1a). Although this exponential shape is essentially unique, secondary effects such as gravitational redshifts between last scattering and the present (ISW effect) can quickly overwhelm the signal making it difficult to measure. How much these factors will degrade the measurement of the curvature will vary from model to model. In inflationary models, both this effect and various other secondary anisotropies are small enough that ℓ_D should be measurable [8].

Another concern is that the damping scale is quite sensitive to the background baryon content, expansion rate and thermal history. In Fig. 3b, we show that for reasonable values of $\Omega_b h^2$ and h this will not prevent us from distinguishing between $\Omega_0 \approx 0.3$ and 1.0 models.

Interestingly the benefits and drawbacks of the peak spacing and damping tail tests are complementary. The peak spacing is easily measured and relatively robust to changes in the other background parameters, but not fully immune to radical behavior in the model for the gravitational fluctuations. The damping tail is immune to such effects but is more difficult to

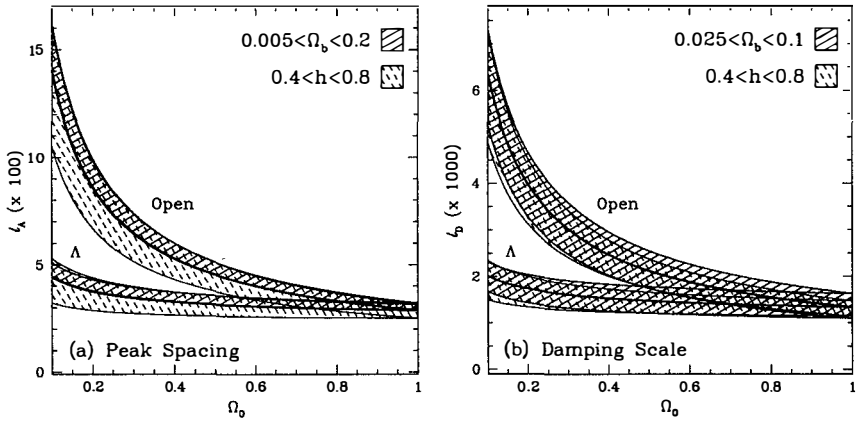

Figure 3: (a) Peak spacing as a function of Ω_0 in a flat cosmological constant ($\Omega_K = 0$) and open model ($\Omega_\Lambda = 0$). Uncertainties in $\Omega_b h^2$ and h have little effect on the ability to distinguish an open from a flat model. (b) Damping tail as a function of Ω_0. The damping tail is more dependent on $\Omega_b h^2$ than the peak spacing but still provides interesting constraints.

measure and suffers more from uncertainties in the other background parameters.

Ideally, we would like to measure both quantities. By combining these two tests, we have an important consistency check on the underlying assumptions of the model and a discriminator against truly exotic models. For example, the baryon content $\Omega_b h^2$ could be far from the BBN value or recombination could be delayed by early energy injection from decaying particles or non-linear structure formation.[1] Since these exotic possibilities affect the two scales differently, a useful discriminator is the ratio of the two scales ℓ_D/ℓ_A (see Fig. 4). If this ratio is anomalous, it is a clear indication that one of the fundamental assumptions is invalid. If one knew from external information which assumption that is (e.g. baryon content, radiation content, thermal history, etc.) then accurate measurements of the curvature could again be made.

The full acoustic signature in the CMB provides additional consistency checks. The Compton drag of the baryons on the photons tends to enhance the fluctuations inside gravitational potential wells. For the acoustic oscillations, this implies that compressional phases will be enhanced over rarefaction phases leading to an alternating series of relative peak heights (see Fig. 1b). If the baryon content is far lower than the BBN value, then this effect is too weak to modulate the peak heights. If it is far higher then it is so strong that the rarefaction phases will not appear as peaks in the anisotropy at all [2]. This could also occur if recombination is delayed such that the ratio of baryon to photon densities is higher at last scattering. Since the modulation of the peaks is a unique signature of baryons at last scattering, its detection would provide an important consistency check on the assumptions underlying the curvature measurement.

In summary, the acoustic signature in the CMB anisotropy spectrum provides a sufficient number of features such that a curvature measurement which is essentially robust to the nature of the fluctuations, the other background parameters, and thermal history may be constructed.

[1]Late reionization does not interfere with these tests since it mainly suppresses power uniformly on small scales without changing the peak spacing or damping tail location.

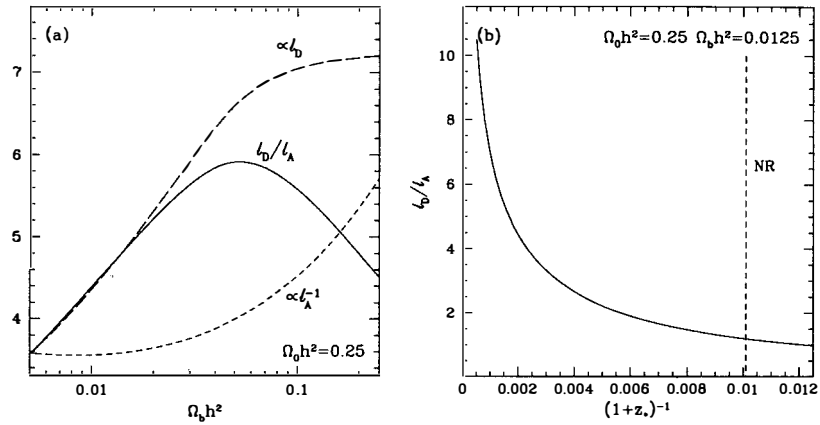

Figure 4: Discriminating exotic cases. (a) If the baryon content is far from the BBN value, it will be reflected in the ratio of the damping scale to peak spacing ℓ_D/ℓ_A, which gives roughly the number of observable peaks. (b) Likewise, ℓ_D/ℓ_A will also detect any delay in recombination. For simplicity, we have here assumed that the universe recombines instantaneously at z_*. A realistic recombination scenario will lower ℓ_D/ℓ_A. If recombination occurs late, the model becomes identical to the no-recombination (NR) scenario in its prediction for the CMB.

The full battery of tests will require complete information on the acoustic signal – from the first peak all the way through to the damping tail.

Acknowledgements. We would like to thank F. Bouchet and all of the organizers for a pleasant and productive meeting. W.H. was supported by the NSF and WM Keck Foundation.

References

[1] W. Hu, N. Sugiyama, J. Silk, 1996, *preprint*, astro-ph/9604166

[2] W. Hu, M. White, 1996, *Astrophys. J.* in press, astro-ph/9602019

[3] M. White, W. Hu, 1996, *these proceedings*

[4] A.A. de Laix, R.J. Scherrer, 1996, *Astrophys. J.* **464** 539

[5] R.G. Crittenden, N.G. Turok, 1995, *Phys. Rev. Lett.* **75** 2642

[6] M. Kawasaki, N. Sugiyama, T. Yanagida, 1995, *preprint*, hep-ph/9512368

[7] W. Hu, D.N. Spergel, M. White, 1996, *preprint*, astro-ph/9605193

[8] W. Hu, M. White, 1996, *Astron. & Astrophys.* in press, astro-ph/9507060

TESTING INFLATION WITH SMALL SCALE CMB ANISOTROPIES

Martin White[1] & Wayne Hu[2]
[1]*Enrico Fermi Institute, 5640 S. Ellis Ave, Chicago, IL 60637*
[2]*Institute for Advanced Study, Princeton, NJ 08540*

Abstract

We discuss ability of the harmonic pattern of peaks in the CMB angular power spectrum to test inflation. By studying robust features of alternate models, which must all be isocurvature in nature, we reveal signatures unique to inflation. Inflation thus could be validated by the next generation of experiments.

Inflation is the front running candidate for generating fluctuations in the early universe: the density perturbations which are the precursors of galaxies and cosmic microwave background (CMB) anisotropies today. By "inflation" here we simply mean the idea that the universe underwent a period of vacuum driven superluminal expansion during its early evolution, which provides a mechanism of connecting, at early times, parts of the universe which are currently space-like separated. It has been argued that inflation is the unique *causal* mechanism for generating correlated curvature perturbations on scales larger than the horizon [1, 2]. If there are unique consequences of such super-horizon curvature perturbations, their observation would provide strong evidence for inflation.

Here we probe the nature of the fluctuations through CMB anisotropy observations of the acoustic signatures in the spectrum. Many of the relevant technical details as well as more subtle examples can be found in [2]. As a working hypothesis, we shall assume that the CMB spectrum exhibits a significant harmonic signature: a series of peaks in the power spectrum when plotted against multipole number ℓ (see Fig. 1a; for reviews of the underlying physics of these peaks see [5, 6]). Such a signature is expected in inflationary models and is characterized by the locations and relative heights of the peaks as well as the position of the damping tail.

The possibility of distinguishing some specific defect models from inflation based on the structure of the power spectrum below 0.5 has recently been emphasized [3, 4]. By characterizing the features of such alternate models and revealing signatures unique to inflation [2], we

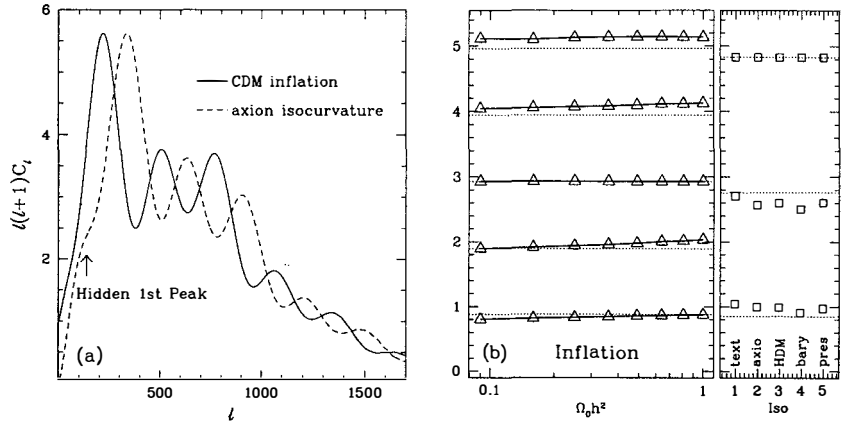

Figure 1: (a) The angular power spectrum of a "standard" inflationary CDM model with $\Omega_0 = 1$, $h = 0.5$ and $\Omega_b = 0.05$ (solid) compared with an axionic isocurvature model (dashed) of the same parameters. Note the peaks are offset from the inflationary prediction, and the first "peak" is more of a shoulder in this model. (b) The *relative* positions of the peaks in the angular power spectrum $\ell_1 : \ell_2 : \ell_3 \cdots$ for the inflationary (left panel, points) and 5 isocurvature models (right panel, points, see text). The series are normalized at ℓ_3 to the idealized inflationary and isocurvature series respectively (dotted lines). Test cases illustrate that the two cases remain quite distinct, especially in the ratio of the first to the third peak and to the peak spacing.

provide the extra ingredients necessary to allow a test of the inflationary paradigm. Another means of testing inflation is the consistency relation between the ratio of tensor and scalar modes and the tensor spectral index [7, 8]. However this test requires a large tensor signal [8] or it will be lost in the cosmic variance.

In Fig. 1a (solid lines), we show the angular power spectrum of CMB anisotropies for a standard cold dark matter (CDM) inflationary model, as a function of multipole number $\ell \sim \theta^{-1}$. Let us review the physics behind the features in the spectrum below 0°.5 ($\ell \gtrsim 200$). Consider the universe just before it cooled enough to allow protons to capture electrons. At these early times, the photons and baryon-electron plasma are tightly coupled by Compton scattering and electromagnetic interactions. These components thus behaved as a single 'photon-baryon fluid' with the photons providing the pressure and the baryons providing inertia. In the presence of a gravitational potential, forced acoustic oscillations in the photon-baryon fluid arise. The energy density, or brightness, fluctuations in the photons are seen by the observers as temperature anisotropies on the CMB sky. Specifically, if Θ_0 is the temperature fluctuation $\Delta T/T$ in normal mode k, the oscillator equation is

$$\frac{d}{d\eta}\left[m_{\rm eff}\frac{d\Theta_0}{d\eta}\right] + \frac{k^2}{3}\Theta_0 = -F[\Phi, \Psi, R] \tag{1}$$

with

$$F[\Phi, \Psi, R] = \frac{k^2}{3} m_{\rm eff}\Psi + \frac{d}{d\eta}\left[m_{\rm eff}\frac{d\Phi}{d\eta}\right], \tag{2}$$

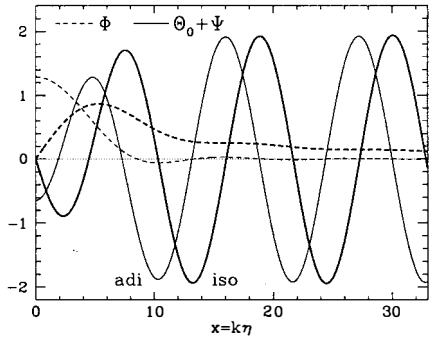

Figure 2: The self-gravity of the photon-baryon fluid drives a cosine oscillation for adiabatic initial conditions (thin lines) and a sine oscillation (thick lines) for isocurvature initial conditions. The dashed lines show the full potential, the solid lines the effective temperature.

where $m_{\rm eff} = 1 + R$, $R = 3\rho_b/4\rho_\gamma$ is the baryon-to-photon momentum density ratio, $\eta = \int dt/a$ is conformal time, Φ is the Newtonian curvature perturbation, and $\Psi \approx -\Phi$ is the gravitational potential [2, 5].

In an inflationary model, the curvature or potential fluctuations are created at very early times and remain constant until the fluctuation crosses the sound horizon. Inside the sound horizon the pressure becomes important and the potential begins to decay (see Fig. 2). As a function of time, this force excites a cosine[1] mode of the acoustic oscillation with peaks at $x/\sqrt{3} \simeq \pi, 2\pi, 3\pi, \cdots$. The first feature represents a compression of the fluid inside the potential well as will become important in the discussion below. Furthermore, the harmonic series of acoustic peak location $\ell_1 : \ell_2 : \ell_3$ approximately follows the cosine series of extrema $1 : 2 : 3 \cdots$. There are two concerns that need to be addressed for this potential test of inflation. How robust is the harmonic prediction in the general class of inflationary models? Can any other model mimic the inflationary series?

The peak ratios are not affected by the presence of spatial curvature or a cosmological constant in the universe [2]. However it is possible to distort the shape of the first peak by non-trivial evolution of the metric fluctuations after last scattering. For example, the magnitude of the scalar effect increases with the influence of the radiation on the gravitational potentials, e.g. by a decrease in the matter content $\Omega_0 h^2$. Tensor fluctuations could distort the first peak and spectral tilt shift the series only if they are very large. That possibility is inconsistent with the observed power at degree scales.[2] The damping of power in the oscillations at small scales due to photon diffusion cuts off the spectrum of peaks and could also confuse a measurement of their location. In Fig. 1b, we plot the ratio of peak locations as a function of $\Omega_0 h^2$. Although the first peak is indeed slightly low in the low $\Omega_0 h^2$ models the harmonic series is still clearly discernible in the regular spacing of the higher peaks. Two numbers serve to quantify the spectrum: the ratio of third to first peak location $\ell_3/\ell_1 \approx 3.3 - 3.7$ and the first peak location

[1]The inflationary series only reaches a cosine asymptotically at high peak number: $0.88 : 1.89 : 2.93 : \cdots$. Likewise the most natural isocurvature series starts at $0.85 : 2.76 : 4.83 : \cdots$ [2].

[2]If degree scale power is present, $n \geq 0.5$, the peaks and positions are not obscured by tilt.

to the spacing between the peaks $\ell_1/\Delta\ell \approx 0.7-0.9$. Ratios in this range are a robust prediction of inflation with reasonable baryon content.[3]

Is the cosine harmonic series a *unique* prediction of inflation? Causality requires that all other models form significant curvature perturbations near or after horizon crossing.[4] We call these *isocurvature* models. The axionic isocurvature model of Fig. 1a (dashed lines) is representative [9]. Since curvature fluctuations start out small and grow until horizon crossing, the peak locations are phase shifted with respect to the inflationary prediction (see Fig. 2).

In typical models, including the baryon isocurvature [5], texture [3], axionic isocurvature [9], hot dark matter isocurvature [10], and pressure scaling [11] models, the peaks approximately form a sine series $1:3:5\cdots$ (see Fig. 1b). The origin of this sine series signal is described in [2] where it is shown acoustic oscillations are driven as the fluctuation passes the sound horizon by the fluid's own self gravity. The first "peak" is a rarefaction, which is a continuation of the super-horzon scale behaviour of the isocurvature model. This is robust due to causal constraints as we shall see below and also implies that the first peak can be quite small. Thereafter, the photon pressure becomes important and the fluid collapses into the potential, becoming more dense and boosting Φ (see Fig. 2). This enhances the second peak. The tendency to first fight and then help the driving potential is generic. Because this is a resonant process, in most cases it dominates over other truly external effects. In particular, all models in which fluctuations are generated causally by pressure perturbations that are constrained to produce nearly scale invariant CMB anisotropies will be dominated by this effect in their acoustic signature [11].

However since we wish to test inflation against all possible alternatives, let us now turn to the broader class of isocurvature models. Isocurvature models with more radical source behavior may introduce some other phase shift with respect to the inflationary prediction. Might this allow an isocurvature scenario to mimic the inflationary prediction? Two possibilities arise. If the first isocurvature feature, which is intrinsically low in amplitude, is hidden, e.g. by external metric fluctuations such as tensor and vector contributions between last scattering and the present, the series becomes approximately $3:5:7$. Might this be mistaken for an inflationary spectrum, shifted to smaller angles by the curvature of the universe? The spectra remain distinct since the spacing between the peaks $\Delta\ell$ is model-independent: it reflects the natural period of the oscillator. The ratio of the first peak position to peak spacing $\ell_1/\Delta\ell$ is thus larger by a factor of 1.5 in this case if $\Omega_0 h^2$ is fixed. In [2], we treat the ambiguity that arises if this and other background quantities are unknown. More generally, any isocurvature model that either introduces a pure phase shift or generates acoustic oscillations only well inside the causal horizon can be distinguished by this test. Of course, isocurvature models need not exhibit a simple regularly-spaced series of peaks [2, 4], but these alternatives could not mimic inflation.

The remaining possibility is that an isocurvature model might be tuned so that its phase shift precisely matches the inflationary prediction. Heuristically, this moves the whole isocurvature spectrum in Fig. 1 toward *smaller* angles. We shall see that causality forbids us to make the shift in the opposite direction. As Fig. 1a implies, the relative peak heights can distinguish this possibility from the inflationary case.

The important distinction comes from the process of compensation, required by causality. During the evolution of the universe, the dominant dynamical component counters any change in the curvature introduced by an arbitrary source [2]. Producing a positive curvature perturbation locally stretches space. The density of the dominant dynamical component is thus reduced in this region, and hence its energy density is also reduced. This energy density however

[3] If *both* the baryon content $\Omega_b h^2 \gtrsim 0.03$ and the CDM content $\Omega_0 h^2 \gtrsim 0.6$ are anomalously high then the second peak (r) will be hidden by the baryon inertia [2].

[4] This does not preclude the possibility of white noise curvature perturbations at low k generated by pressure perturbations. See [2, 11] for more discussion.

contributes to the curvature of space, thus this reduction serves to offset the increased curvature from the source. Heuristically, curvature perturbations form only through the motion of matter (see [11] for more details), which causality forbids above the horizon.

In the standard scenario, the universe is radiation dominated when the smallest scales enter the horizon (see [2] for exotic models). Thus near or above the horizon, the photons resist any change in curvature introduced by the source. Breaking Φ into pieces generated by the photon-baryon fluid (γb) and an external source (s), we find in this limit [2]

$$x^2\Phi''_{\gamma b} + 4x\Phi'_{\gamma b} = -x^2\Phi''_s - 4x\Phi'_s, \tag{3}$$

where primes denote derivatives with respect to $x = k\eta$.

Thus the first peak in an isocurvature model, if it is sufficiently close to the horizon to be confused with the inflationary prediction and follows the cosine series defined by the higher peaks, must have photon-baryon fluctuations anti-correlated with the source. The first peak in the rms temperature thus represents the rarefaction (r) stage when the source is overdense rather than a compression (c) phase as in the inflationary prediction. The peaks in the inflationary spectrum obey a c-r-c pattern while the isocurvature model displays a r-c-r pattern. Though compressions and rarefactions have the same amount of power (squared fluctuation), an additional effect allows us to distinguish the two: baryons provide extra inertia to the photons to which they are tightly coupled by Compton scattering (the $m_{\rm eff}$ terms in Eq. 1). If overdense regions represent gravitational wells,[5] this inertia enhances compressions at the expense of rarefactions leading to an alternating series of peaks in the rms [5]. For reasonable baryon content, the *even* peaks of an isocurvature model are enhanced by the baryon content whereas the *odd* peaks are enhanced under the inflationary paradigm (see Fig. 1a). This non-monotonic modulation of the peaks is not likely to occur in the initial spectrum of fluctuations. The oscillations could be driven at exactly the (evolving) natural frequency of the oscillator in such a way as to counteract this shift, but such a long duration tuned driving seems contrived.

There is one important point to bear in mind. Since photon diffusion damps power on small scales, the 2nd compression (3rd peak) in an inflationary model may not be *higher* than the 1st rarefaction (2nd peak). even though it is enhanced (see e.g. Fig. 1a). However it will still be anomalously high compared to a rarefaction peak, which would be both suppressed by the baryons and damped by diffusion. Since the damping is well understood this poses no problem in principle [2].

Diffusion damping also supplies an important consistency test. The physical scale depends only on the background cosmology and not on the model for structure formation (see Fig. 1a and [5, 2]). This fixed scale provides another measure of the phase shift introduced by isocurvature models. For example, if the first isocurvature peak in Fig. 1a is hidden, the ratio of peak to damping scale increases by a factor of 1.5 over the inflationary models. We also consider in [2] how the damping scale may be used to test against exotic background parameters and thermal histories.

In summary, the ratio of peak locations is a robust prediction of inflation. If acoustic oscillations are observed in the CMB, and the ratio of the 3rd to 1st peak is not in the range $3.3 - 3.7$ or the 1st peak to peak-spacing in the range $0.7 - 0.9$ then either inflation does not provide the main source of perturbations in the early universe or big bang nucleosynthesis grossly misestimates the baryon fraction. The ranges can be tightened if $\Omega_0 h^2$ is known. If the spatial curvature of the universe vanishes, these tests require CMB measurements from $10 - 30$ arcminutes. Even if the location of the first peak is ambiguous, as might be the case

[5]Neil Turok (private communication) has shown that for a particular choice of stress-energy tensor, with an anisotropic stress large compared with the density, it is possible to have *under*densities associated with potential wells. If such a model also has peaks π out of phase with the cosine mode it could mimic an inflationary spectrum.

in some isocurvature models, these tests distinguish them from inflation. Isocurvature models thus require fine tuning to reproduce this spectrum. To close this loophole, the relative peak heights can be observed. If the location of the peaks follows the inflationary prediction, the enhancement of odd peaks is a unique prediction of inflation.[6]

The true discriminatory power of the CMB manifests itself in the spectrum as a whole, from degree scales into the damping region. In particular, we emphasize the acoustic *pattern* which arises from forced oscillations of the photon-baryon fluid before recombination, including the model-independent nature of the damping tail. The tests we describe rely on the gross features of the angular power spectrum and so could be performed with the upcoming generation of array receivers and interferometers.

Acknowledgements. We acknowledge useful conversations with J. Bahcall, P. Ferreira, A. Kosowsky, J. Magueijo, A. Stebbins and M. Turner. We thank R. Crittenden, A. de Laix, and N. Sugiyama for supplying isocurvature power spectra. W.H. was supported by the NSF and WM Keck Foundation. We would also like to thank F. Bouchet and all the organizers for a pleasant and productive conference.

References

[1] Y. Hu, M.S. Turner, E.J. Weinberg, 1994, *Phys. Rev.* **D49** 3830; A.R. Liddle, 1995, *Phys. Rev.* **D51** 5347

[2] W. Hu, M. White, *Astrophys. J.* in press, astro-ph/9602019

[3] R.G. Crittenden, N.G. Turok, 1995, *Phys. Rev. Lett.* **75** 2642

[4] A. Albrecht, D. Coulson, P. Ferreira, J. Magueijo, 1995, *Phys. Rev. Lett.* **76** 1413

[5] W. Hu, N. Sugiyama, 1995, *Astrophys J.* **444** 489; W. Hu, N. Sugiyama, 1995, *Phys. Rev.* **D51** 2599; W. Hu, N. Sugiyama, 1995, *Astrophys. J.*, in press, astro-ph/9510117

[6] U. Seljak, 1994, *Astrophys. J.* **435** L87; D. Scott, M. White, 1995, *General Relativity & Gravitation* **27** 1023; D. Scott, J. Silk, M. White, 1995, *Science* **268** 829

[7] R. Davis, *et al.* 1992, *Phys. Rev. Lett.* **69** 1856; (erratum **70**,1733).

[8] M. White, L.M. Krauss, J. Silk, 1993, *Astrophys. J.* **418** 535; L. Knox, M.S. Turner, 1994, *Phys. Rev. Lett.* **73** 3347

[9] M. Kawasaki, N. Sugiyama, T. Yanagida, 1995, *preprint*, hep-ph/9512368

[10] A.A. de Laix, R.J. Scherrer, 1995, *Astrophys. J.*, **464** 539

[11] W. Hu, D.N. Spergel, M. White, 1996, *preprint*, astro-ph/9605193

[6] This is strictly only true if the photon energy density is significant when the relevant scales enter the horizon and gravitational potential wells are associated with *over*dense regions.

PROBING THE GEOMETRY OF THE UNIVERSE WITH CMB TEMPERATURE PEAKS

J. L. Sanz [1], R. B. Barreiro [1,2], E. Martínez-González [1], L. Cayón [2,3], J. Silk [3]
[1] *Instituto de Física de Cantabria, CSIC-Universidad de Cantabria, Facultad de Ciencias, Avda. Los Castros s/n, 39005 Santander, Spain.*
[2] *Dpto. de Física Moderna, Universidad de Cantabria, Facultad de Ciencias, Avda. Los Castros s/n, 39005 Santander, Spain.*
[3] *Astronomy Department and Center for Particle Astrophysics, University of California, Berkeley, CA 94720, USA.*

Abstract

We discuss some discriminators for CDM models based on statistical properties of the CMB: number of peaks, Gaussian curvature and eccentricity distributions above a certain threshold. For temperature anisotropies represented by a 2D Gaussian random field, all these quantities can be obtained as functions of two spectral parameters. Angular resolutions ranging from 7′.5 to 30′ are considered, covering the most sensitive values of the COBRAS-SAMBA experiment. We find that the number of peaks and Gaussian curvature distribution are valid discriminators of the geometry of the universe, whereas the eccentricity distribution is very insensitive to it.

1 Peaks at 2D Gaussian random fields

The texture of the CMB offers a useful alternative in the study of the CMB anisotropies, usually faced through the computation of the radiation power spectrum. In our analysis of the temperature anisotropies, we assume that those are described by a two-dimensional Gaussian random field. We shall consider the peaks of the field above a certain threshold $\nu = (\Delta T)/(\Delta T)_{rms}$. In this way, once the threshold is fixed, all the calculated quantities will be normalization independent.

Let us define the curvature radii as: $R_1 = [-\Delta_1''(max)/2]^{-1/2}$ and $R_2 = [-\Delta_2''(max)/2]^{-1/2}$, where Δ is the temperature field normalized to the rms-fluctuations and Δ_i'' its second derivative

along the principal direction i. Since these derivatives take part in the local description of maxima, we can associate to each maximum the invariant quantities:

$$\kappa = \frac{1}{R_1 R_2}, \quad \epsilon = \left[1 - \left(\frac{R_2}{R_1}\right)^2\right]^{1/2}. \tag{1}$$

being κ the Gaussian curvature and ϵ the eccentricity. Bond and Efstathiou (1987) have studied the number density of peaks of a 2D homogeneous and isotropic Gaussian random field. After some straightforward calculation, it is possible to get the mean number of maxima (over the celestial sphere) $N(\kappa, \epsilon, \nu) d\kappa\, d\epsilon\, d\nu$ with Gaussian curvature, eccentricity and threshold between $(\kappa, \kappa + d\kappa)$, $(\epsilon, \epsilon + d\epsilon)$ and $(\nu, \nu + d\nu)$, respectively. This quantity N is given in terms of two parameters γ and θ_*, related to the radiation power spectrum, as defined by Bond and Efstathiou.

We shall apply this technique to flat and open CDM models ($\Omega = 1, 0.3, 0.1$, $\Omega_b = 0.05$, $h = 0.5$) with adiabatic fluctuations and a Harrison-Zel'dovich primordial spectrum, kindly provided by N. Sugiyama. We shall analize 2D maps with angular resolution $FWHM(') = 7.5, 10.5, 18$ and 30, which correspond to the most sensitive radiometers and bolometers borne by the COBRAS-SAMBA mission.

2 Number of peaks

We have represented in Figure 1 the number of peaks above the threshold ν, $N(> \nu)$, for different angular resolutions and $\Omega = 0.1, 0.3, 1$. It can be seen, that decreasing either the Ω parameter or the angular resolution, increases the number of peaks, except for $FWHM = 30'$ where the number is larger for $\Omega = 0.3$.

Table 1. Number of peaks above the threshold ν

		$\nu = 3$			$\nu = 3.5$			$\nu = 4$	
FWHM	$\Omega = 0.1$	$\Omega = 0.3$	$\Omega = 1$	$\Omega = 0.1$	$\Omega = 0.3$	$\Omega = 1$	$\Omega = 0.1$	$\Omega = 0.3$	$\Omega = 1$
$7'.5$	4205	2699	1572	936	591	339	161	100	57
$10'.5$	2579	1730	1106	573	382	239	99	66	40
$18'$	931	825	531	205	184	116	35	32	20
$30'$	302	337	245	66	74	54	11	13	9

It is worth remarking that for the angular resolution of $7'.5$, the number of peaks above the threshold $\nu = 3$ for $\Omega = 0.1$ is approximately 3 times the value for $\Omega = 1$ (i.e. 4205 as compared to 1572 peaks for the open and flat cases, respectively). All the studied cases produce a null result,using a KS test, for the flat and open models, what would allow us to distinguish between them. In Table 1, the number of peaks above the thresholds $\nu = 3, 3.5, 4$, for different Ω's and angular resolutions, are given.

3 The distribution of Gaussian curvature and eccentricities

The distribution of peaks above the threshold ν with Gaussian curvature between $(\kappa, \kappa + d\kappa)$ is plotted in Figure 2 for different values of Ω and threshold $\nu = 3$. Different angular resolutions

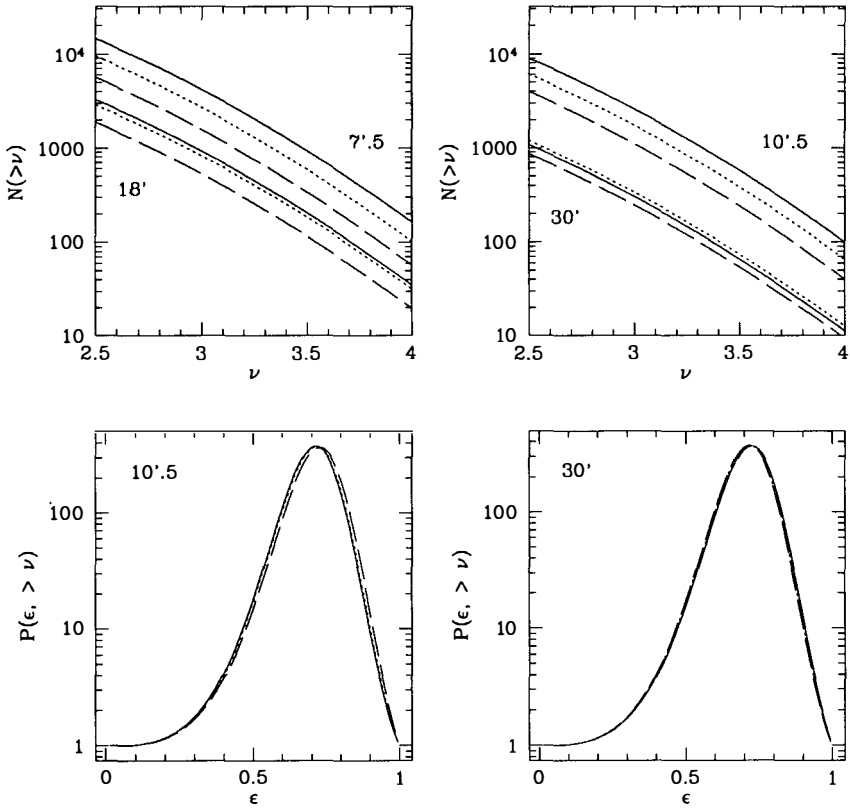

Figure 1: In the two upper figures, we represent the number of peaks above a threshold ν versus that threshold, for different angular resolutions. Each set of three different lines corresponds to a value of the angular resolution. In the lower figures, the cumulative p.d.f. $p(\epsilon, > \nu)$ for a threshold $\nu = 3$ and different angular resolutions is plotted. In all the plots, the solid and dotted lines correspond to open universes (Ω =0.1 and 0.3, respectively) and the dashed one to a flat universe.

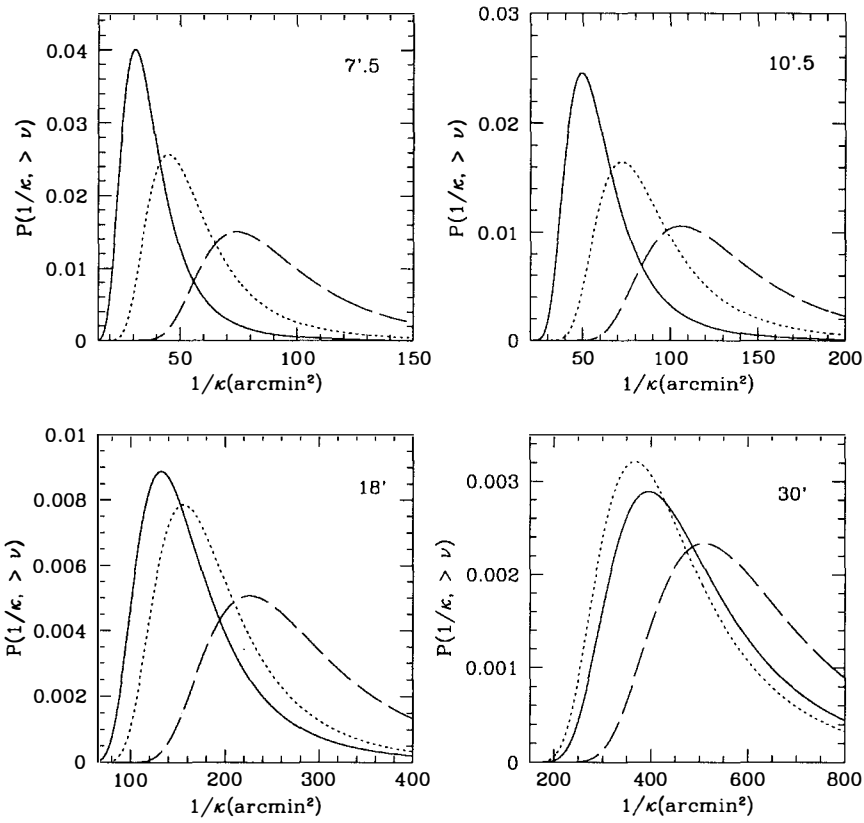

Figure 2: **Distribution of the inverse of the Gaussian curvature of the peaks above a threshold $\nu = 3$ for different angular resolutions. The solid, dotted and dashed lines correspond to $\Omega = 0.1, 0.3, 1$, respectively.**

are also considered. We can clearly distinguish the curves corresponding to different models in all the cases. In fact, a KS-test yields a quantitative null result for the hypothesis that the flat and low-Ω open models derive from the same population.

We have also studied the distribution of peaks above the threshold ν with eccentricity between $(\epsilon, \epsilon + d\epsilon)$. The main conclusion is that the eccentricity p.d.f. is not a good test to distinguish between flat and open models (see figure 1). However, it is interesting to remark that the eccentricity p.d.f. could be useful as a gaussianity discriminator.

4 Conclusions

We have studied the distribution of peaks above a threshold ν through the mean number and a couple of local quantities: Gaussian curvature and eccentricity. We have calculated these quantities for standard CDM models (with a Harrison-Zel'dovich primordial spectrum) and considered a 2D map covering the whole sky, with angular resolutions FWHM($'$) $= 7.5, 10.5, 18, 30$. The main conclusions are that the number of peaks and the Gaussian curvature p.d.f. are good discriminators between flat and open models, whereas the eccentricity p.d.f. cannot be used to distinguish between them.

EMG and JLS acknowledge financial support from the Spanish DGICYT, project PB92-0434-C02-02. RBB acknowledges a Spanish M.E.C. Ph.D. scholarship. We also acknowledge financial support from the PECO contract of the EU ERBCIPDCT 940019.

IMPACT OF ANISOTROPY AND POLARIZATION MEASUREMENTS ON PARTICLE PHYSICS

M.V.Sazhin, V.V.Shulga
Sternberg Astronomical Institute, 119899 Moscow, Russia,
E-mail: sazhin@sai.msu.su

Here we discuss the contribution of scalar perturbation and the gravitational waves contribution in anisotropy. The separation of these contributions is one of the important aim of the future measurements. One of possible tool to separate these contributions is polarization measurements. The impact of anisotropy and polarization measurements on particle physics is discussed. Upper limit on the slow rolling of inflation potential is discussed.

During recent decades, cosmology has been in a period of intensive development, including the understanding of the large scale structure of the Universe, the discovery and investigation of the CMBR, the revealing of early epochs in the history of our Universe, and understanding of some fundamental cosmological problems (at least at a qualitative level). This last factor is closely connected with modern cosmology and particle physics. This part of cosmology is very popular among both cosmologists and physicists dealing with consequences of high energy physics. Sometimes they call the early Universe "the poor man's accelerator" [1].

Large impact on the last is coming and will come in future from the anisotropy investigation of the CMBR. The discovery of the CMBR [2] or the first multipole harmonic - monopole (3 K) proved the theory of the hot Universe and establish one of most firm component of the observational basis of modern cosmology. Each consequent step requested large efforts of experimentalists. The measurements of dipole amplitude [3] (3 mK) requested 1000 times of radiometers improvement in comparison with measurements of monopole amplitude. The discovery of dipole component of the CMBR allows to establish the most universal reference frame connected with the CMBR. The measurement of large scale and intermediate scale anisotropy [4] ($30\mu K$-$80\mu K$) requested 100 times of sensitivity arising, but it allows to establish the normalization of spectrum of primordial density fluctuations. Next natural step - polarization measurements - will request the enormous arising of sensitivity again.

Before proceeding the discussion of polarization and scientific aims of polarization measurements, let us stress on the different types of perturbations which can contribute into anisotropy.

At the inflation epoch two types of gravitational perturbations are generated: scalar perturbations (below SP) (see for instance in [5]) and tensor perturbations (or gravitational waves, below GW) (see in and reference therein [6]). The fluctuations which cause the large scale anisotropy are defined by super high energy physics namely the Grand Unification Theory (below GUT) as it was clarified by the theory of inflation. The amplitudes of SP and GW are defined by the different parameters of GUT. So, it is very important to distinguish between the contribution of SP and GW into anisotropy to have more information about the physics of the early Universe.

For generation of polarization three conditions are necessary :

- anisotropy of the CMBR at the moment of scattering
- dense plasma which can provide with big number of scattered events
- the expansion of the Universe and the rapid decreasing of the density of free electrons to make the probability of the second scattering negligible.

Therefore, the polarization of the CMBR must be created during recombination. Generation of polarization of the CMBR is considered in many papers [7].

In the table the expected degree of polarization is shown. The spectral index of primordial fluctuation is $n = 1$. In the first column the $FWHM$ of an antennae in the second column is expected polarization generated by scalar perturbation and in third column the expected degree of polarization generated by cosmological gravitational waves is listed.

Table.

$FWHM$	scalar perturbation	gravitational waves
2°	$0.4\mu K$	$0.26\mu K$
3°	$0.1\mu K$	$0.17\mu K$
5°	$37\,nK$	$0.13\mu K$
7°	$19\,nK$	$0.13\mu K$

Some comments are necessary. The degree of polarization is r.m.s. and polarization generated by gravitational waves was calculated in supposition that observed amplitude of anisotropy is generated by gravitational waves only. The difference between observed and calculated amplitude will indicate the contribution of gravitational waves.

One can expect also the larger amplitude of polarization (up to $3\mu K$) into hot and cold spots of distribution of $\delta T/T$ [8].

Other method of estimation of gravitational waves contribution was proposed by [9] and [10]. This method is based on comparison of low multipole amplitude of $\delta T/T$ with intermediate scale anisotropy (with amplitude of Doppler peak). Gravitational waves contribute only in low multipole harmonics ($l_{max} \sim 30$). They contribution into intermediate scale harmonics ($l \sim 100 - 200$) is negligible. Therefore one can compare the predicted amplitude of Doppler peak with amplitude of low multipoles via next procedure:

$$A^2 S_{low} + B^2 T_{low} = R_{low} \tag{1}$$

$$A^2 S_{peak} + B^2 T_{peak} = R_{peak} \tag{2}$$

Here A and B are scalar and tensor amplitudes in definition of Starobinsky and S_{low}, T_{low} are conversion of multipole coefficients with window function of low harmonic experiment, and S_{peak} T_{peak} are conversions of intermediate scale experiment. R_{low} R_{peak} are r.m.s. values of these experiments. One can resolve this set of linear equations and find the amplitudes A and B.

This comparison was done in [10] in which they found that in the case of independent inflation and present Hubble constant $H = 50km/sec/Mpc$ the ratio of squares of gravitational amplitude over scalar amplitude is less then 0.02. Detailed discussion see in this paper.

This method looks very attractive while the polarization is not observed yet. Any case some remarks are necessary. First of all the amplitude of Doppler peak depends both of amplitude of scalar perturbation and cosmological model (global cosmological parameters). Therefore to use this method one must to measure intermediate scale anisotropy as exact as possible to avoid the uncertainties with cosmological parameters. Second is the uncertainty connected with unique realization of our Universe. As for as there is "cosmic variance" of multipole harmonics one must also analyze the variance of low multipole to estimate correctly S and T from these equations.

We will deal with value

$$\frac{A^2}{B^2} \leq 0.02 \tag{3}$$

to estimate some parameters of inflation.

The impact of anisotropy measurements was considered in [11] and in [12]. In [11] some specific model was considered and the estimation of an inflation parameter was obtained

$$m_{scale} \simeq 10^{16} GeV. \tag{4}$$

More general consideration was done in [12]. Let us rewrite above mentioned upper limit in terms of [12]. In this paper was considered and indicated that the reconstruction of inflation potential is possible in narrow interval $\varphi \in \{2.7 - 3\}m_{pl}$. In this narrow interval one can reconstruct $V(\varphi)$, $\dot{V}(\varphi)$, and $\ddot{V}(\varphi)$. It is not abundance of information, but it is very important information about the high energy physics.

The parameters of inflation were introduced which characterize the evolution of scalar field during inflation. They are

$$\epsilon = \frac{3\dot{\phi}^2}{2}\{V(\phi) + \frac{\dot{\phi}^2}{2}\}^{-1} \tag{5}$$

$$\eta = -\frac{\ddot{\phi}}{H\dot{\phi}} \tag{6}$$

They both characterize slow rolling condition during inflation. Here dot represents differentiation with respect to time. The same values one can rewrite in terms of differentiation with respect to ϕ which is more convenient. In this case both equations will be

$$\epsilon = 3 \cdot \{1 - \frac{8\pi}{3m_{pl}^2}\frac{V(\phi)}{H^2}\} \tag{7}$$

$$\eta = \frac{3m_{pl}^2}{4\pi}(\frac{H''}{H})^2 \tag{8}$$

Here prime means differentiation with respect to ϕ.

Scalar and tensor amplitudes are

$$A^2 = 32\pi^5\frac{H^4}{m_{pl}^4 H'^2} \tag{9}$$

$$B^2 = 16\pi\frac{H^2}{m_{pl}^2} \tag{10}$$

It means that one can obtain the equation

$$\frac{B^2}{A^2} = \frac{2}{\pi^3}\epsilon \tag{11}$$

or the upper limit for one parameter of slow rolling condition is

$$\epsilon \leq 0.3 \tag{12}$$

The upper limit for η is not significant yet.

The above upper limit for ϵ is very important from the point of view of inflation theory. It means that basic supposition is valid. It becomes more transparent in terms of relation of kinetic energy of scalar field which drive inflation with potential energy of this field. One can write the equations for normalized potential energy of inflation field and for normalized kinetic energy as

$$E_{pot} = \frac{4\pi}{3m_{pl}^2}V(\phi) \tag{13}$$

$$E_{kin} = \frac{4\pi}{6m_{pl}^2}\dot{\phi}^2 \tag{14}$$

One can write the upper limit for potential energy in terms of

$$1 - \frac{2E_{pot}}{H^2} \leq 0.1 \tag{15}$$

But as far as the equation $\frac{1}{2}H^2 = E_{kin} + E_{pot}$ is exact one can say that the contribution of kinetic energy of scalar field is as small as $\leq 10\%$ of potential energy in driving inflation.

Instead of these very optimistic conclusions one have to claim that polarization measurements will be ultimate referees of gravitational waves contribution into anisotropy which is independent of cosmological models and global cosmological parameters. The observation of polarization will allow to determine part of shape of inflation potential. The consequent observation of gravitational waves in whole frequency range will allow to reconstruct the complete shape of potential and to investigate the physics in the energy range of the order of 10^{16} GeV.

This work was supported in part by ISF grants NDH000 and NDH300 and center for cosmoparticle physics "Cosmion".

References

[1] Dolgov, A.D., Sazhin, M.V. & Zeldovich, Ya.B., Basic of Modern Cosmology (1990) Editions Frontiers.

[2] Penzias A.A, Wilson R.W. Astrophys.J., **142**, P.419, 1965.

[3] Smoot G.F., Gorenstein M.V., Muller R.A. Phys. Rev. Lett., **39**, P.898, 1977.

[4] Strukov,I.A., Brukhanov,A.A., Skulachev,D.P., Sazhin,M.V., Pis'ma v Astron. Zh., **18** P.387, 1992; (Sov.Astron.Lett.,**18**, p.153,(1992)); Smoot, G. et al., Astrophys. J., **396** P.L1, 1992; Hancock S., Davies R.D., Lasenby A.N. et al., Nature, **367**, P.333 1994; Meinhold P. et al., Astrophys. J. Lett., **409**, P.L1, 1993 Netterfield C.B. et al., preprint astro-ph 9601197, 1996.

[5] Inflationary cosmology (1986),Ed.Abbott,L.F. and So-Young Pi, World Sci.

[6] Starobinsky A.A. JETP Lett., **30**, P.719, 1989; Rubakov, V., et all., Phys. Lett., **B115**, P.189, 1982; Fabbri R., Pollock M.D., Phys. Lett., **B125**, P.445, 1983 Starobinsky A.A. Sov. Astron. Lett., **11**, P.133, 1985; Souradeep T., Sahni V., Mod. Phys. Lett., **7**, P.3541, 1992; Allen B., Korand S., Preprint WICS-MILW, N 94-TH-11, 1994

[7] Basko M.M., Polnarev A.G., Mon. Not. R. Astron. Soc., **191**, P.L47, 1980; Sazhin M.V. in: Modern theoretical and experimental problems of General Relativity and Gravitation. MGPI Publ., P.88 , 1984(russian); Polnarev A.G., Astron. Zh., **62**, P.1041, 1985(russian); Harrari D.D., Zaldariaga M., Phys. Lett. **B315**, P.96, 1993; Crittenden R., Davies R.L., Steinhard P.J., Astrophys.J.,**417**, P.L13, 1993; Sazhin M.V., Benitez N., Astro. Lett. and Comm., **32**, P.105, 1995; Gibilisco M., Int. J. of Modern Phys., **10**, P.3605, 1995;

[8] Sazhin M.V., Toporensky A.V. Astronomy Lett. 1996 (in press)

[9] Dodelson S., Knox L., Kolb E.W., Phys. Rev. Lett., **72**, P.3444, 1994

[10] Markevich A.V., Starobinsky A.A., Astronomy Lett., 1996, (in press)

[11] Strukov I.A. et al., Phys. Lett. **B315**, P.198, 1993.

[12] Copeland E.J. et al., Phys. Rev. **D48**, P.2529, 1993.

PART IV

THEORY AND OBSERVATIONAL STATUS OF FOREGROUNDS

MOLECULAR SECONDARY ANISOTROPIES

Roberto Maoli
DEMIRM-Observatoire de Paris, France.

Abstract

We describe a new kind of secondary anisotropies: the primordial lines that can be produced by the resonant elastic scattering of the CBR photons by an high redshift molecular medium. LiH molecule is the best candidate for an effective interaction. We calculate the principal characteristics of the signal emitted by a primordial cloud during its different phases of evolution. The molecular secondary anisotropies probably are the only CBR distorsions associated with perturbations in their linear evolution phase and the strongest one emitted by collapsing primordial clouds before the cosmological medium was reionized and the Sunyaev-Zeldivich effect became predominant.

1 Introduction

Speaking of secondary anisotropies of the Cosmic Background Radiation means to consider the interaction between the CBR photons and the cosmological medium in the post–recombination Universe.
After $z = 1000$, there are not enough free electrons to produce a strong interaction between photons and matter. In this epoch only Rees-Sciama effect is able to produce a spatial anisotropy in the photon distribution. However, at least in the standard model that is if $\Omega = 1$, this effect can be produced only during the non linear evolution of density perturbations and very huge masses must be involved (as is natural, being gravitational force responsible for).
As far as concern the Vishniac effect, the Sunyaev-Zeldovich effect and the thermic emission of dust in primordial galaxies, all these kinds of proposed secondary anisotropies need the presence of an heating source to ionize the matter or to heat the dust. Unless supposing an early reionization of the Universe, these anisotropies are produced in a quite recent epoch, after a first generation of stars or at least when structures at some typical scale were completely formed.

The molecular secondary anisotropies could probably produce the only signal associated with perturbations during their linear evolution, a very small signal indeed, and they compete with the Rees–Sciama effect for the successive epoch of perturbation evolution.
In some ways, they are in alternative with the S-Z effect: in a cold cosmological medium we have to look for primordial molecular anisotropies, while in a heated medium, molecules are dissociated, free electrons are produced and the S-Z effect becomes the most important CBR secondary anisotropy.

2 Interaction between the molecular medium and CBR

Molecules are one of the component of the cosmological medium, they form at $z = 200 \div 400$ when the temperature of the Universe has decreased enough to make the photodissociation processes ineffective [1] [5] [9]. Molecules are formed by the elements produced by the primordial nucleosynthesis. They are normally diatomic because of the absence of dust and the low density of the primordial medium that don't allow for three bodies processes. As a consequence, the molecular species are not the same we find in the interstellar medium. H_2, H_2^+, HD, HD^+, HeH^+, LiH and LiH^+ are the main components of the primordial molecular medium.
Being this medium non collisional and in equilibrium with the radiation, absorption and emission processes are ineffective and resonant elastic scattering must be considered as the most efficient in coupling matter and radiation [2] [7].
In this process, a photon is absorbed by a molecule at a frequency ν_{ij} corresponding to a rotational or ro–vibrational transition of the molecule and reemitted at the same frequency. The cross section for this process is given by equation:

$$\sigma_{res} = \frac{g_j}{g_i} \frac{\lambda_{ij}^3 A_{ji}}{4c} \frac{\nu_{ij}}{\Delta\nu} = \frac{16\pi^4}{3hc} \left|\vec{d}\right|^2 \frac{(J+1)^2}{J(2J+3)} \frac{\nu_{ij}}{\Delta\nu} = 3.37 \cdot 10^{-19} \left|\vec{d}\right|^2 \frac{\nu_{ij}}{\Delta\nu} \qquad (1)$$

where g_i and g_j are the statistical weights of the starting level i and the resonant level j, λ_{ij} and ν_{ij} are the wavelength and the frequency of the transition, $\Delta\nu$ is the broadening of the line (Doppler broadening in the non collisional primordial medium), $\vec{d}$ is the dipole moment of the molecule and the second equality is effective for resonant scattering between two rotational levels with angular moment J and $J+1$.
Substituting the numerical values for the Plank constant and the velocity of light and neglecting the J-term (whose value is between 0.5 and 1) we obtain the last equality where the dipole moment is in Debye. This cross section has to be compared with the Thomson one ($\sigma_T = 6.652 \cdot 10^{-25}\ cm^2$). For dipole moments of order of unity and typical line widths $\frac{\Delta\nu}{\nu} = 10^{-4} \div 10^{-6}$, the molecular resonant scattering is $10^{10} \div 10^{12}$ times more efficient than Thomson scattering. This explains why the coupling with the molecular medium can be stronger than the coupling with the electrons in spite of the low abundance of primordial molecules. LiH is the best candidate for an effective interaction with CBR, due to its high dipole moment (5.88 Debye).
Being the resonant scattering an elastic process, it can result in a CBR primary anisotropy attenuation and secondary anisotropy production, exactly as in the case of an early reionisation of the Universe. Nevertheless the strong dependance of the resonant scattering cross section from the frequency gives a peculiar behaviour comparing with the effects of Thomson scattering in a ionized medium.
As regards the primary anisotropy attenuation, resonant molecular scattering is efficient only if CBR photons fulfil the resonance condition:

$$\nu_{obs} = \frac{\nu_{ij}}{1+z} \qquad (2)$$

where ν_{ij} is the frequency of all the molecular transitions (rotational and vibrational) and ν_{obs} is the observational frequency at redshift zero. The total optical depth, responsible for the attenuation, is the result of all the contributions of scattering molecules in the i state that are at different redshifts according to the previous condition. The redshifts fulfilling the resonance condition are function of the observational frequency, therefore the attenuation is frequency dependent too (see [7] for more details).

3 Primordial cloud signal

If the scattering source has a non zero component of the peculiar velocity along the line of sight, the elastic scattering is no more isotropic in the observer frame and molecular secondary anisotropies are produced [6]. Also in this case, the strong frequency dependance of the cross section is responsible for the differences from the secondary anisotropies produced by the Thomson scattering in an early reionised Universe. We have molecular lines instead of fluctuations of the cosmic black body temperature. These primordial lines will result in a typical molecular spectrum in emission or absorption depending on the peculiar velocity direction.
In the case of LiH, the frequencies of the first resonant rotational lines are given by $\frac{\nu_{ij}}{(1+z)_c}$ where $\nu_{01} = 443.953$, $\nu_{12} = 887.295$, $\nu_{23} = 1329.415$, $\nu_{34} = 1769.711$ and $\nu_{45} = 2207.585\ GHz$.

3.1 Molecular line intensity

The signal produced by a moving source is given by the formula:

$$\frac{\Delta I}{I_{CBR}} = \left(1 - \exp^{-\tau_{ij}}\right) \beta_{pec} \cos\theta \, (2 - \alpha_N) \tag{3}$$

where β_{pec} is the peculiar velocity normalized to the speed of light, $\cos\theta$ gives the projection along the line of sight ($\theta = 0$ for clouds moving towards the observer), α_N is the spectral index for the photon number $\left(\alpha_N = \frac{\nu}{N}\frac{\partial N}{\partial \nu}\right)$ and τ_{ij} is the optical depth given by equation:

$$\tau_{ij} = \int_{cloud} \sigma_{res,ij}\, n_i \, cdt \tag{4}$$

where n_i is the numerical density of the molecule in the state i.
The meaning of equation 3 is easy: the first factor is the number of scattered photons, the last one is the result of two different effects:
i) scattering of photons is not isotropic in the observer frame
ii) scattered photons are observed at a frequency $\nu_{obs} = \frac{\nu_{ij}}{(1+z)_c}(1 + \beta_{pec}\cos\theta)$, but they come on average from the black body distribution at frequency $\frac{\nu_{ij}}{(1+z)_c}$.
Both these effects are proportional to the projection of the peculiar velocity along the line of sight and this explains the second factor in equation 3.
Being the $(2 - \alpha_N)$ factor always positive, the sign of $\frac{\Delta I}{I}$ depends only on the sign of $\cos\theta$; we will have emission lines for approaching clouds and absorption lines for departing clouds.

3.2 Molecular line width

The processes responsible for the line width of the resonant lines are different for different phases of evolution of the primordial clouds.

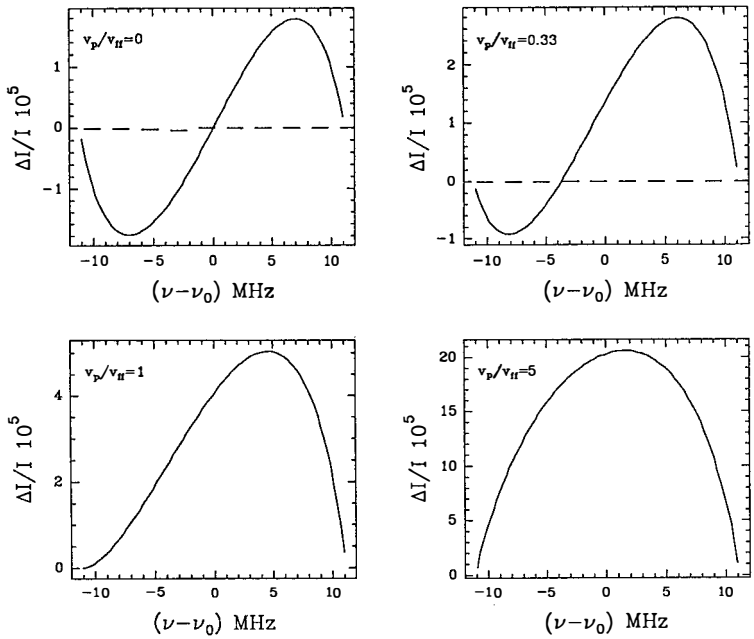

Figure 1: Shape of the molecular lines as a function of the rate between the peculiar and the infall velocities.

3.2.1 Linear evolution: The perturbations follows the expansion of the Universe and for the same rotational line the resonance condition 2 is fulfilled at different observational frequencies for different parts of the primordial cloud. The line width depends on the extension in redshift of the perturbation, that is it depends on its mass through equation:

$$\frac{\Delta\nu}{\nu} = D\frac{H_0}{c}(1+z)\sqrt{1+\Omega z} = 6.35\cdot 10^{-4}\,\Omega^{-1/3}h^{1/3}m_{12}^{1/3}\sqrt{1+\Omega z} \qquad (5)$$

where $m_{12} = \frac{M}{10^{12}M_\odot}$.

The intensity is mass independent and is proportional to $\frac{(1+z)^{3/2}}{\sqrt{1+\Omega z}}$ if we neglect the variation of the population of the rotational levels with redshift and if we assume $v_{pec} \propto (1+z)^{-1/2}$. Rotational lines of high J are stronger at higher redshifts, the fondamental one becoming the strongest one for $z \lesssim 7$.

During the phase of linear evolution the molecular lines are very weak and broad.

3.2.2 Turn-around: When the cloud stops following the expansion of the Universe, all the scattered photons contribute to the signal at the same frequency. The line width is due to the thermal broadening. For a Maxwellian distribution of the velocities it is given by equation:

$$\frac{\Delta\nu}{\nu} = \frac{2}{c}\sqrt{\frac{2\ln 2k_BT}{m_a}} = 7.16\cdot 10^{-7}\sqrt{\frac{T}{A}} = 2.541\cdot 10^{-7}\sqrt{T} \qquad (6)$$

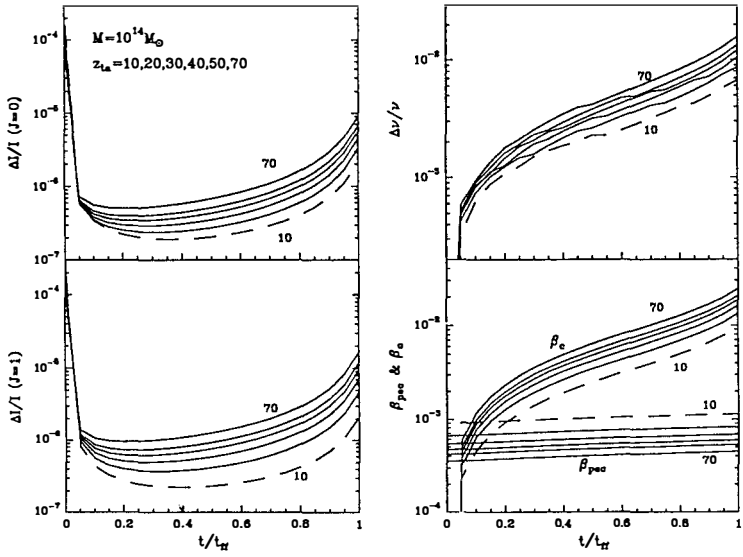

Figure 2: The differential intensities of the first two resonant rotational lines of LiH, the line width and the infall and peculiar velocities for a primordial cloud of $10^{14}\,M_{\odot}$.

where m_a and A are the atomic mass and the atomic number of the molecule, T is the matter temperature and the last equality is effective for LiH.
Sources at turn–around produce the strongest and thinnest molecular lines.

3.2.3 Non–linear collapse: During the non–linear collapse two different velocities have to be considered: the peculiar velocity β_p of the cloud and its infall velocity β_c. Using a simple model of spherical collapse, only a strip of the cloud having the same projection of the infall velocity along the line of sight will contribute at the same observational frequency.
The line width is roughly twice the maximal infall velocity:

$$\frac{\Delta\nu}{\nu} \approx 2\beta_{c,max} \tag{7}$$

and the lineshape depends on the ratio between the peculiar and the infall velocity (see figure 1): if the first one is negligible, we have a double peak line. This is the only signal emitted by a no moving primordial cloud and is the consequence of the strong frequency dependence of the resonant scattering cross section; in the same situation the Thomson scattering will not produce any signal. The double peak feature progressively desappears when the peculiar velocity becomes more important.

4 Results and discussion

In figure 2, we reported the line intensity for the first two LiH rotational lines, the line width and the peculiar and infall velocity for a perturbation of $10^{14}\,M_{\odot}$ as a function of the collapse

phase, starting from the turn–around to a free-fall time ($t/t_{ff} = 1$). We took $\Omega = 1$, $\Omega_{bar} = 0.1$, $h = 0.75$ and we considered different values of the turn–around redshift for the perturbation. We choose for the fractional abundance of LiH a value $\frac{n_{LiH}}{n_H} = 10^{-12}$. In this case the cloud is always optically thin and we can easily obtain the intensity for other LiH abundances, being the signal proportional to it.

Indeed the LiH abundance is rather controverse, resulting from the uncertainties about the primordial abundance of lithium (ranging between $2 \cdot 10^{-10}$ and 10^{-9}) and about the lithium conversion rate to LiH (ranging between 1 and 10^{-3}) [2] [4] [5] [8] [9]. Recently, Dalgarno and collaborators [10] proposed a very low value for the lithium conversion ($\frac{n_{LiH}}{n_{Li}} \approx 2 \div 3 \cdot 10^{-7}$). In this case LiH molecule would not be any more the best candidate for the production of molecular secondary anisotropies and other molecules as for example H_2 or perhaps H_2D^+ should be considered [3].

Referring to figure 2, the differential signal $\frac{\Delta I}{I}$ is as high as $2 - 3\,10^{-4}$ at the turn–around, with $\frac{\Delta\nu}{\nu} \approx 1 - 4\,10^{-6}$. At the beginning of the collapse the signal decreases due to the spread in frequency of the contribution of the scattering molecules; in a more advanced phase $\frac{\Delta I}{I}$ starts to increase again, taking advantage of the rise of the column density. Depending on the value of the turn–around redshift, the differential intensity ranges from $2 \cdot 10^{-6}$ to $2 \cdot 10^{-5}$ and $\frac{\Delta\nu}{\nu}$ from $6 \cdot 10^{-3}$ to $2 \cdot 10^{-2}$.

In an advanced phase of the collapse the infall velocity is greater than the peculiar velocity and the molecular line is characterized by a double peak. The passage in the regime with $\beta_c > \beta_p$ is a function of M and z_{ta}, occurring earlier for perturbations of higher mass, collapsing at higher redshifts.

These results indicate that search for primordial molecular lines can be one of the best tools to investigate proto–structure evolution as far as the primordial medium is cold. Then, any heating of the medium dissociates the molecules, creates free electrons and makes the S–Z effect the dominant process in producing secondary anisotropies.

Acknowledgements. I am grateful to P. Encrenaz, F. Melchiorri and M. Signore for stimulating and fruitful discussions and I thank Italian CNR for financial support.

References

[1] Dalgarno A., Lepp S., 1987, in *Astrochemistry* p. 109, eds Vardya & Tarafdar

[2] Dubrovich V.K., 1977, *Sov. Astron. Lett.* **3**, 128

[3] Dubrovich V.K., 1993, *Sov. Astron. Lett.* **19**, 132

[4] Khersonskii V.K., Lipovka A.A., 1993, *Astrofizicheskie Issledovaniya* **36**, 88

[5] Lepp S., Shull M.J., 1984, *Astrophys. J.* **280**, 465

[6] Maoli R., Ferrucci V., Melchiorri F., Signore M., Tosti D., 1996, *Astrophys. J.* **457**, 1

[7] Maoli R., Melchiorri F., Tosti D., 1994, *Astrophys. J.* **425**, 372

[8] Palla F., Galli D., Silk J., 1995, *Astrophys. J.* **451**, 44

[9] Puy D., Alecian G., Le Bourlot J., Leorat J., Pineau des Forets G., 1993, *Astr. Astrophys.* **267**, 337

[10] Stancil P.C., Lepp S., Dalgarno A., 1996, *Astrophys. J.* **458**, 401

COMPARISON OF *COBE* DMR AND *ROSAT* ALL-SKY SURVEY DATA

Rüdiger Kneissl
Max-Planck-Institut für Astrophysik, Garching bei München, Germany

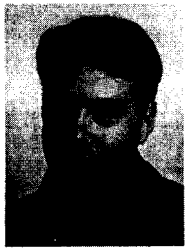

Abstract

Statistical comparisons of microwave maps in the GHz range and X-ray maps at around 1 keV are an interesting probe to constrain different astrophysical phenomena. Possible correlations on various angular scales and with different frequency (energy) dependences, although not expected at present day experimental sensitivity, could in principle be due to galactic emission/absorption, the Sunyaev-Zel'dovich effect, the Integrated Sachs-Wolfe effect in cosmological models with a cosmological constant or low density, or X-ray luminous radio sources such as radio-loud AGNs. I report on work cross-correlating the COBE DMR and ROSAT All-Sky Survey in a selected area of the sky. This area ($+40° < b$, $70° < l < 250°$) is the best presently available data set probing the medium-hard extragalactic X-ray background around 1 keV. No significant correlation on astrophysically relevant scales has been found in this analysis, but it will be possible to infer constraints from the limits.

1 Introduction

Statistical comparison between experiments probing different astrophysical backgrounds are motivated by physical effects leading to possible correlations. These effects, galactic emission or absorption in X-rays, Sunyaev-Zel'dovich effect (SZ) in hot plasmas such as galaxy clusters or group halos, point sources, and the Integrated Sachs-Wolfe effect (ISW), are astrophysically interesting (see also Table 1) and test sources of possible confusion for the measurement of the cosmic microwave (CMB) and X-ray (XRB) backgrounds.
Comparisons between CMB and XRB observations were first carried out by Boughn & Jahoda [1] comparing the 19 GHz map with HEAO-1 A2 (~10 keV, 3° resolution), and they found no significant correlation based on Monte Carlo simulations for noise properties. Bennett et al. [2] cross-correlating the 1 yr DMR data to HEAO-1 found no significant correlation for $|b| > 30°$ and the LMC masked. In the latest analysis by Banday et al. [3] an expansion in orthogonal functions on a cut sky and a likelihood analysis for the coupling constant between the 4 year DMR and HEAO-1 data was used. Again no significant correlation was found, when applying a specially designed Galactic cut based on correlations obtained from the Dirbe 140 μm map and masking the LMC.
The present analysis uses another X-ray data set, the ROSAT [4] PSPC [5] All-sky Survey (RASS) which measures the sky in the soft X-rays from 0.1 – 2 keV with an angular resolution of ~10 arcmin. These data have not previously been used for this kind of analysis and are particularly sensitive to galaxy clusters even in the diffuse XRB component, as has been shown by Soltan et al. [9]. They find an extended X-ray component around clusters. The present work is also motivated towards constraining a possible extended gas halo.

2 The COBE and ROSAT data

A full description of the COBE DMR data and the 4 year results can be found in the contribution by G.F. Smoot [6] and references therein.
For our analysis we used various maps of the COBE DMR data. The final analysis uses the 4 year data, although consistency tests with the 1 year and 2 year data were performed. From the different channels we constructed inverse noise weighted A+B sum maps. The same procedure was used for combining the different frequency channels (31.5, 53 & 90 GHz), which were converted from antenna to Planck temperatures. The standard frequency combination for this analysis is the 53+90 GHz map, having low noise and little galactic contribution [7], but the individual frequency maps and the linearly combined and subtracted galaxy reduced maps were used for comparison.
The RASS R6 energy band, 0.73 – 1.56 keV with maximum response around 1.1 keV, is regarded as the best probe for the diffuse cosmological XRB because the content of foreground, non-cosmic photons, and contamination by charged particles is minimized. In spite of the careful corrections for exposure and elimination of non-cosmic backgrounds [8] the final count rate distribution is not completely free from residual contamination. To test for spectral dependence we compared to the neighbouring partly overlapping band R5 (maximum response around 0.9 keV), which is low in non-cosmic photons and in contamination by charged particles, but contains increased galactic foreground. The maps supplied for this work were binned as 0.7° x 0.7°, with point sources left in to compare to the complete integrated flux. The mean intensity of the XRB in the R6 is $\sim 80 \times 10^{-6}$ cts s^{-1} arcmin^{-2} with a fluctuation level of $\sim 7 \times 10^{-6}$ cts s^{-1} arcmin^{-2} at the COBE pixelization level 6 (2°.6 x 2°.6). Even the high energy R6 band

is, in large regions of the sky, dominated by galactic emission. The chosen area ($+40° < b$, $70° < l < 250°$) is the largest simply connected patch probing dominantly the XRB. Properties of the XRB in this field have been studied in a series of papers ([9],[10],[11]).

3 Correlation Method

Due to the small size ($\sim 8\%$ of the sky) and the peculiar geometry of the patch a local statistical measure, the 2-point cross-correlation function, is preferred. The form of the correlation function used in this analysis is the Pearson product moment correlation coefficient

$$C(\alpha) = \frac{< X_i T_j >_\alpha - < X_i >_\alpha < T_j >_\alpha}{\sqrt{< X_i^2 >_\alpha - < X_i >_\alpha^2} \sqrt{< T_j^2 >_\alpha - < T_j >_\alpha^2}} \quad (1)$$

in an unweighted scheme. Inverse noise variance weighting has also been applied and was found to give similar results. The average is taken over all pixel pairs $\{ij\}$ with separation α in the patch. The subscript α denotes that all the terms are evaluated separately for each angular bin. To determine the uncertainties, which are assumed to be dominated by the DMR noise on small scales and the cosmic variance of the CMB structure on large scales, different techniques were applied. These are a simple rotation method using random samples, and simulation of DMR maps. The CMB structure is taken to be a random Gaussian field with a power law ($Q_{rms-PS} = 15.3\ \mu$K, n = 1.2) power spectrum [12] convolved with the DMR filter function [13] and the DMR noise to be Gaussian pixel noise distributed according to the coverage.

4 Results

Correlating the raw data yields a marginally significant positive correlation on large angular scales, which appeared to be independent of different procedures that had been applied. Different source exclusion thresholds in the ROSAT maps ranging from 0.3 - 1 cts s^{-1} were compared. By far the strongest source in the field with 5.3 cts s^{-1} in the R6 is MKN 421, a BL Lac object at $z \sim 0.031$, which had to be removed, because it clearly produces positive correlation on the beam scale. Otherwise the different thresholds affect the results only marginally. Different sampling tests were undertaken also showing stability of the result against small scale features such as point sources and noise. The maps were smoothed on various angular scales including smoothing of the ROSAT maps with the actual DMR beam [13], and Gaussian smoothing of both maps out to 20° with the effect of smoothing the correlation function, but not significantly changing the correlated signal. Correlating to noise maps revealed no correlated noise feature. The energy dependence in X-rays is found to be consistent with a galactic signal increasing from hard to soft energies. The frequency dependence in microwaves is unclear. There is a clear signal in both the 53 and 90 GHz channels and no signal at 31.5 GHz.
To determine the angular scale of the correlated signal, gradients were removed from the field. This was done in fitting dipoles onto the field in both maps and subtracting them. As a result the signal vanished. The multipoles on the sky dominating these gradients turn out to be of low order (Figure 1). The best fit DMR residual dipole, which would introduce substantial correlation of no physical significance had been removed in addition to the standard removed dipole. The gradient in the ROSAT field is produced by a whole map dipole which has the following galactic signatures, the positive pole lying near the galactic center, and increasing relative amplitude from the hard to the soft energies, also in comparison to R7 and R4. The

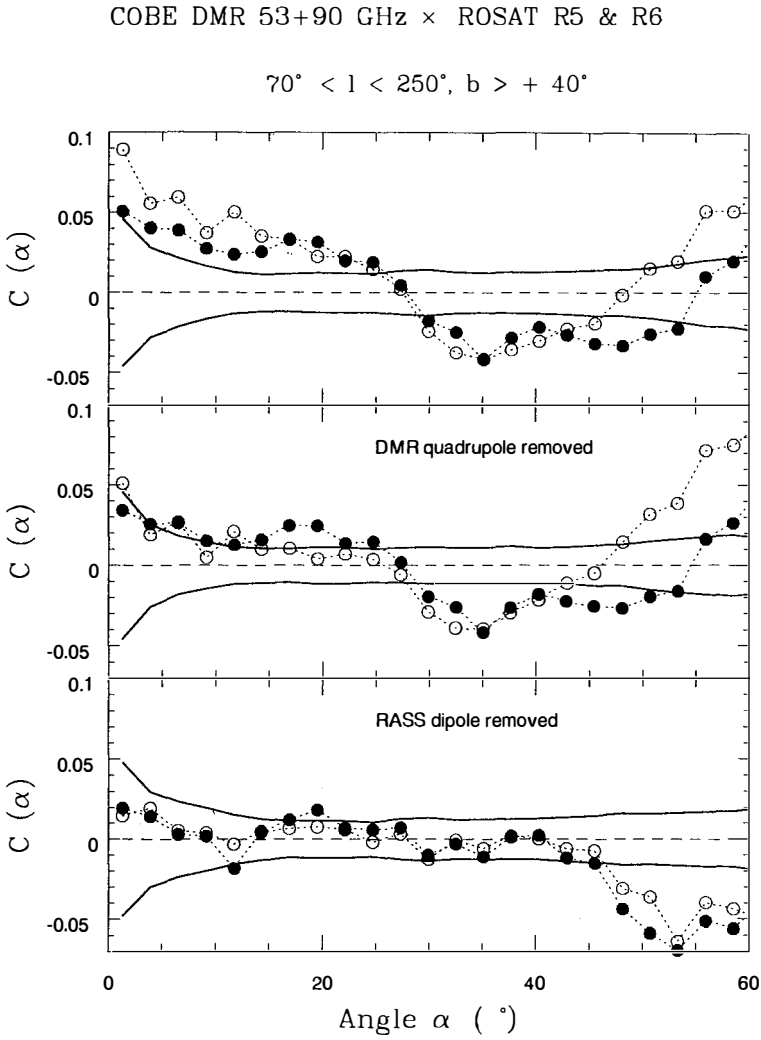

Figure 1: Cross-correlation function between the COBE DMR 53+90 GHz (A+B)/2 and the ROSAT All-sky survey energy bands R5 (softer band, open circles) and R6 (harder band, full circles) in a ROSAT selected area ($+40° < b$, $70° < l < 250°$). The effect of lowering the zero-lag amplitude by subtracting either a best fit quadrupole from the Galactic cut DMR map or a best fit dipole which has Galactic signature from the full ROSAT map can be seen. The 1-σ error bands are taken from DMR simulations correlated to R6.

gradient in the COBE field is dominated by a quadrupole fitted to the COBE cut sky, a combination of the cosmic and the Galactic quadrupole. In the field the cosmic quadrupole seems to dominate, not inconsistent with the COBE frequency dependence of the correlated signal.

5 Discussion

The conclusion of this work is that no significant correlation on scales from 7° to 60° has been found between the COBE DMR and the ROSAT All-Sky Survey in the area investigated. A possible correlation on larger scales can not be distinguished from chance alignment, because the corresponding multipole terms are different and the frequency and energy dependences are not conclusive for a single physical mechanism. The full description of this work, also including the analysis of larger areas of the sky, as well as results on a ROSAT dipole determination and limits on the correlation coefficient with a discussion of the possible mechanisms, can be found in a paper by our collaboration [14].
Different effects resulting in a possible, although not at present expected, angular correlation between microwave and X-ray experiments are known or have been suggested recently.

EFFECT / SOURCE	*SIGN*	*ANGULAR SCALE*	*FREQU. DEP.* microwave	*ENERGY DEP.* X-ray	*AUTHOR*
Galaxy geometrical ?	+ (−) X-abs.	large	$\beta_{synch,ff,dust}$	thermal 0.3 keV	
SZ thermal (**clusters** / super-)	−	(< 10' clust.) (< 5° c-corr)	y - dist.	thermal 10 keV	
SZ thermal local group **halo**	−	large	y - dist.	thermal 1 keV	[15]
X-ray/radio point **sources**	+	small	flat, $\alpha < 0.5$ $(10 - 100\,GHz)$	$\gamma \approx 2 - 2.5$ $I = I_0(E/E_0)^{-\gamma}$	[16]
ISW / RS in Λ / open universe	+	large $\ell \approx 10$	Planck	$\gamma \approx 2 - 2.5$ $I = I_0(E/E_0)^{-\gamma}$	[17], [18]

Table 1: Overview of different effects introducing possible correlations between microwave and X-ray data

At the present state of observations, and with the available data, no astrophysically interesting correlation could be found. Still interesting limits can be drawn from this analysis, although no direct quantification of the effects. The current X-ray observations have much higher angular resolution and better signal to noise ratio than CMB measurements. But as these data were taken in the soft X-rays (< 2 keV) they show predominantly a galactic signal limiting a comparison with the XRB to small patches of the sky. This situation is going to change dramatically in the future. With the European CMB mission COBRAS/SAMBA and the German X-ray satellite ABRIXAS, two all sky data sets will be available that have wide angular and spectral coverage and high angular and spectral resolution. COBRAS/SAMBA [19],[20] will have 9 frequency channels from 31 to 857 GHz with an angular resolution of ∼ 10 arcmin and a best sensitivity of 10^{-6} per resolution element. ABRIXAS [21] will cover the energy range from 0.5 to 10 keV with a sensitivity of 1.6 cts s^{-1} for the XRB, a spectral resolu-

tion of 150 eV and an angular resolution of 1 arcmin. With these data sets a detailed statistical analysis for all the effects discussed above will be feasible, including the direct comparison of radio loud, X-ray luminous point sources and distant galaxy clusters.

Acknowledgements. I thank my collaborators from the ROSAT team, R. Egger, G. Hasinger and J. Trümper. The ROSAT project has been supported by the Bundesministerium für Forschung und Technologie (BMTF/DARA) and by the Max-Planck-Society. The COBE datasets were developed by the NASA Goddard Space Flight Center under the guidance of the COBE Science Working Group and were provided by the NSSDC.

References

[1] Boughn S.P., Jahoda K., 1993, *Astrophys. J.* **412**, L1

[2] Bennett C.L., et al., 1993, *Astrophys. J.* **414**, L77

[3] Banday A.J., et al., 1996, *Astrophys. J. (Lett.)* in press, *astro-ph/9601064*

[4] Trümper J., 1983, Adv. Space Res. 4, (4)241

[5] Pfeffermann E. et al., 1986, Proc. SPIE 733, 519

[6] Smoot G.F., *these Proceedings*

[7] Kogut A., et al., 1996, *Astrophys. J. (Lett.)* in press, *astro-ph/9601060*

[8] Snowden S.L., et al., 1995, *Astrophys. J.* **454**, 643

[9] Soltan A.M., et al., 1996, *Astr. Astrophys.* **305**, 17

[10] Miyaji T., et al., 1996, *Astr. Astrophys.* in press, *astro-ph/9601173*

[11] Soltan A.M., et al., 1996, *Astr. Astrophys.* submitted

[12] Górski K., et al., 1996, *Astrophys. J. (Lett.)* in press, *astro-ph/9601063*

[13] Kneissl R., Smoot G.F., 1993, COBE Note 5053

[14] Kneissl R., Egger R., Hasinger G., Soltan A.M., Trümper J., 1996, *Astr. Astrophys.* submitted

[15] Suto Y., et al., 1996, *Astrophys. J.* **461**, L33

[16] Franceschini A., *personal remark*

[17] Crittenden R.G., Turok N., 1996, *Phys. Rev. Lett.* **76**, 575

[18] Kamionkowski M., 1996, *Phys. Rev. Lett. (Comment)* submitted, *astro-ph/9602150*

[19] Tauber J., *these Proceedings*

[20] Bouchet F., *these Proceedings*

[21] Friedrich P. et al., 1996, in *Proceedings of the International Conference on X-ray Astronomy and Astrophysics, "Röntgenstrahlung from the Universe"* p. 681, eds Zimmermann H.U., Trümper J.E. & Yorke H., MPE Report 263

THE SUNYAEV-ZELDOVICH EFFECT AT 1 AND 2 MM TOWARDS ROSAT CLUSTERS

P. Andreani[1], G. Dall'Oglio[2], L. Pizzo[2], L. Martinis[3], P. Shaver[4], H. Böhringer[5], R. Lemke[6], L.-Å. Nyman[6], R. Booth[7], N. Whyborn[8]
[1]*Dip. di Astronomia, Univ. di Padova, Italy*
[2]*Dip. di Fisica, III Univ. Roma, Italy*
[3]*ENEA TIB, Frascati, Italy*
[4]*ESO Garching, Germany*
[5]*MPE Garching, Germany*
[6]*ESO La Silla, Chile*
[7]*ONSALA Observatory, Sweden*
[8]*SRON, Groningen, The Netherlands*

Abstract

An observing campaign was devoted to the search for the Sunyaev-Zeldovich (S-Z) effect towards X-ray ROSAT Clusters in the millimetric spectral domain. A double channel (1.2 and 2 *mm*) photometer was installed at the focus of the 15m Swedish ESO Submillimeter Telescope (SEST) in Chile in september 1994 and 1995 and observations of the targets S1077, A2744, S295 and RXJ0658-5557 were gathered. Detections were found for A2744 at 1 *mm* and in both channels (at 1.2 and 2 *mm*) towards RXJ0658-5557. For the first time there is evidence for the S-Z enhancement and both the latter and the decrement were detected on the same source. We discuss astrophysical and systematic effects which could give origin to these signals.

1 Introduction

The S-Z effect is one of the major sources of secondary anisotropies of the Cosmic Microwave Background (CMB), arising from (inverse) Compton scattering of the microwave photons by hot electrons in clusters of galaxies. This effect generates a peculiar signal with a decrement at wavelengths longer than 1.4*mm* and an enhancement at shorter ones relative to the CMB planckian value.

The original computation by Sunyaev and Zeldovich [1-3] of the the net transfer of energy from the hot e^- to the microwave photons predicts a signal for the relative temperature change:

$$(\frac{\Delta T}{T})_{therm} = y\,(x\,\frac{e^x+1}{e^x-1} - 4). \quad (1)$$

where T is the CMB temperature, $x = h\nu/kT$ and $y = \int (kT_e/mc^2)\, n_e \sigma_T d\ell$ is the comptonization parameter, n_e, T_e being the electron density and temperature. Equation 1 is an approximated solution of the full kinetic equation for the change of the photon distribution due to scattering. A more accurate solution gives rise to corrections which are not negligible at high frequencies [4].

If the cluster has a peculiar velocity relative to the frame where the CMB is isotropic an additional *kinematic* effect should be measured. The motion of the gas cloud will induce a Doppler change whose relative amplitude, $(\frac{\Delta T}{T})_{kin}$, does not depend on the frequency but only on the peculiar velocity, v_r, and cloud optical depth for Thomson scattering, τ,: $(\frac{\Delta T}{T})_{kin} = -\frac{v_r}{c}\tau$ (where the minus sign refers to a cluster receding from the observer). Since both effects are very small the net relative temperature change is the sum of the two: $(\frac{\Delta T}{T})_{SZ} = (\frac{\Delta T}{T})_{therm} + (\frac{\Delta T}{T})_{kin}$.

There is considerable interest in the detection of this effect also because of its potential in determining the distance of clusters, their peculiar velocities and in studying the intracluster medium [1-3]. Most of the observations carried out so far (e.g. [5]) were taken in the Rayleigh - Jeans (R-J) part of the spectrum, where the scattering leads to an intensity decrement. The more recent radio observations agree in finding this decrement at centimeter wavelengths towards A2218, A665, 0016+16, A773, A401, A478, A2142, A2256 [6-9] and Coma [10] and at $2.2mm$ towards A2163 ([11] and Lange, these proceedings).

Measurements near the planckian peak and on the Wien side have several advantages: (a) the intensity enhancement relative to the planckian value is larger than the magnitude of the R-J decrement; (b) the simultaneous detection of the enhancement (positive) and decrement (negative) on the same cluster provides an unambiguous signature of their presence and minimize systematic errors and spurious signals; (c) sources in the cluster are expected to give a negligible contribution at high frequency, while radio observations are plagued by the possible radio emission from sources within the clusters; (d) because of the large bandwidth the sensitivity of bolometer systems is excellent.

2 The Instrument

A double channel photometer was built and devoted to the search for the enhancement and decrement of the S-Z effect. The system works, in fact, simultaneously at 1.2 *mm* and 2 *mm* using two bolometers cooled at 0.3 K by means of a ^{3}He refrigerator. The $2mm$ band includes the peak brightness of the decrement in the S-Z thermal effect, while the $1.2mm$ bandwidth is a compromise between the maximum value of the enhancement in the S-Z and the atmospheric transmission. The collecting optics, cooled at 0.3 K, define a field of view in the sky of 44″ at both frequencies. The beam separation in the sky was limited by the antenna chopping system and was set to the maximum chopping amplitude: 135″.

This photometer was built to feed the O.A.S.I. (Osservatorio Antartico Submillimetrico Infrarosso) telescope installed at the Italian base in Antarctica [12] and was adapted to the focus of the SEST and its performance was tested during an observing run in September 1994. Details of the instrument can be found in [13].

Responsivities, beam shapes and widths were measured with planets and the main figures measured at the focus are listed in table 1. Sensitivities are also given in terms of relative change of the thermodynamic temperatures in one second integration time.

Table 1. Performances of the photometer at focus

λ_c (μm)	$\Delta\lambda$ (μm)	FWHM (′)	noise (nV/$\sqrt{Hz}$)	Responsivities ($\mu V/K$)	N.E.T. (mK/s)	$(\frac{\Delta T}{T})_{therm}$ (1s)
1200	360	44	45	3.0	7.5	0.010
2000	580	46	31	1.4	10.7	0.007

3 Observations

The targets were selected because of their high X-ray luminosity in the ROSAT band (0.5÷2.4 keV) $\sim 2 - 5\ 10^{45}$ erg/s and because of their high redshift (0.3-0.42). The apparent size of the core radius, being small, well matches the beam size: for a core radius of 250÷400 kpc in standard cosmologies the apparent size is (40÷60)″. However, a chop throw of 135″ means that at the reference beam position the ratio between the electron density, $n_e(\theta = 135'')$, to its central value, $n_e(\theta = 0)$, is 0.25 - 0.35, i.e. 20 - 30 % of the signal could be lost because of the limited chop throw.

The present paper deals with observations of A2744 and RXJ0658-5557 carried out in four different nights during september 1-5 1995. A total integration time of 10800s and 12400s were spent on A2744 and RXJ0658-5557 respectively, and the same integration time was spent on a blank sky located 15m ahead in right ascension with respect to the source position. During the observations the sky opacity was very low ($\tau_{1mm} < 0.1$ with an average value of $< \tau_{1mm} >= 0.07$, $\tau_{2mm} < 0.05$ with an average value of $< \tau_{2mm} >= 0.03$) and the sky emission very stable thus producing a very low sky-noise.

In order to get rid of the major sources of noise in this kind of experiment, fluctuations in the atmospheric emission and systematics from the antenna, the observing strategy makes use of two combined procedures: the common three-beam technique, beam-switching + nodding, which gets rid of the linear spatial and temporal variations in the atmospheric emission, and the observations of blank sky regions located at right ascension position of 15m ahead with respect to the location of the source. This latter implies that for each 10m integration ON the source (10m integration + overheads give a total tracking time of 15m) a similar integration is performed on blank sky. The comparison between the two signals is a measurement of the systematics introduced by the antenna. In fact, the instrument tracks the same sky position twice with respect to the local environment, once ON the source and the other on the blank sky (position OFF). The choice of 600s of integration ON and OFF the source is a compromise between the minimization of the time wasted on overheads and the need of minimizing the atmospheric variations between one observation and the other.

The data analysis procedure is described in detail elsewhere[14]. Briefly, data on each sky position (on the source and on the blank sky) consist of differential measurements of the antenna temperature, ΔT_{ant}, with integration chunks lasting 3 x 200s. 200s data are averaged and a variance is assigned for each of this *"scan"*.

Weighted means are computed over the 600s integration when the antenna tracked the source (hereafter called ΔT_{ON}) and when the antenna tracked the blank sky (hereafter called ΔT_{OFF}). Cluster signals are then estimated from the subtraction: $\Delta T_{SZ} = \Delta T_{ON} - \Delta T_{OFF}$ and the

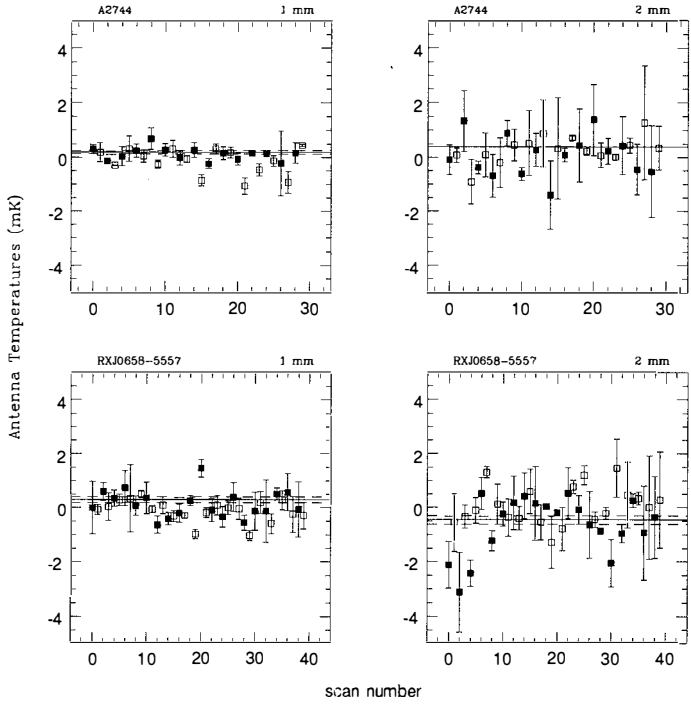

Figure 1: Differential antenna temperatures at 1 and 2 *mm* for A2744 and RXJ0658-5557. Filled squares refer to data ON the source, while empty squares to blank sky regions located 15m ahead in R.A. with respect to the source position. The cluster signals are estimated by subtracting $\Delta T_{SZ} = \Delta T_{ON} - \Delta T_{OFF}$. The maximum likelihood values of these differences is shown as a solid line while the dashed lines correspond to 70% confidence interval. For the 2 *mm* signal of A2744 only the 3σ upper limit is reported.

quadratic sum of the two standard deviations are used to estimate errors: $\sigma^2_{SZ} = \sigma^2_{ON} + \sigma^2_{OFF}$. Figure 1 ($a,b,c,d$) shows the values ON (filled squares) and OFF (empty squares) of the antenna temperatures of the two clusters and for both channels. The solid lines represent the maximum likelihood estimates of the ΔT_{SZ}, while the dotted lines correspond to the 70% confidence range. This was found by computing the values of the signal where the likelihood drops by a factor of 1.71 from its maximum. From the figure one can infer that a 3σ detection can be claimed in both channels for RXJ0658-5557: $\Delta T_{1mm} = 0.3$ mK, $\Delta T_{2mm} = -0.46$ mK, while a signal of $\Delta T_{1mm} = 0.18$ mK, is present only at 1*mm* for A2744.

To check whether these detections were spurious additional measurements were carried out to test the behaviour of (a) the photometer + the electronic chain and (b) the antenna systematics. The *same* observing strategy (on the source and on the blank sky) was applied in two cases: (a) blocking the photometer entrance window and (b) following an empty sky region for integration times comparable with those used for the observations of the sources.

No signals are detected at a level of 0.1 mK (3σ) so that we believe that the adopted observing strategy gets rid of most of the unknown systematics (however one must note that if during the observation of the sources the antenna, because of a loss of synchronization, did not track *precisely* the same paths relative to the local environment, when looking at the source and at the blank sky some, very small spurious signals can survive).

4 Discussion

If the detected signals are due to clusters several questions are raised. We briefly discuss here only the case of RXJ0658-5557.

Let us assume that the decrement seen at $2mm$ is due to the SZ effect. From this value the *expected* $1mm$ signal for the thermal effect can be easily computed by convolving eq.1 with the beam shape, the optics transmission and the atmospheric spectrum. However, the difference with the observed value is larger than a factor of 2 and this can be explained either with a large peculiar velocity of the cluster, of the order of -1000 km/s, or with a source contaminating mainly the $1mm$ channel. To our knowledge there is no determination of the peculiar velocity from optical data and we are not able to verify the first hypothesis. The latter can be checked in several ways.

(1) No sources in the IRAS Faint Source Catalogue or in the 5GHz NRAO survey are present at the position of the main beam and/or of the reference beams.

(2) If we scale the $60\mu m$ IRAS flux limit of 240 mJy at $1.2mm$ by using the average flux of nearby spirals [15], we find that a normal spiral would give rise to a signal not larger than 0.02 mK in antenna temperature.

(3) If we assume a contribution of many unresolved sources fluctuating in the beam and take the estimation made by Franceschini et al. ([16]), the expected signal will be not larger than 0.02 mK.

(4) Irregular emission from the Galactic cirrus can also give origin to a signal at these wavelengths. If we take the estimation by Gautier et al. ([17]) and extrapolate the $100\mu m$ flux at 1.2 mm using the average Galactic spectrum a maximum signal of 0.02 mK is found.

(5) If part of the signal is due to CMB anisotropies at these scales, it will be hard to disentangle them from the S-Z kinematic effect since this latter has a spectrum identical to that of the anisotropies (see e.g. [18]).

We conclude that it is very likely that part of the signal at 1.2 mm is due to one or more sources but at present it is hard to identify it. This point however deserves further investigations and it will be the goal of future research.

The authors are indebted to the ESO/SEST teams at La Silla and in particular to Peter de Bruin, Peter Sinclair, Nicolas Haddad and Cathy Horellou. This work has been partially supported by the P.N.R.A. (Programma Nazionale di Ricerche in Antartide). P.A. warmly thanks ESO for hospitality during 1995, when part of this work was carried out.

References

[1] Zeldovich Ya.B. & Sunyaev R.A., 1969, *Astrop. & Spa.Sci.* 4, 301

[2] Sunyaev R.A. & Zeldovich Ya.B. 1972, *Comm.Astr.Spa.Phys.* 4, 173

[3] Sunyaev R.A. & Zeldovich Ya.B. 1981, *Astrop.Spa.Sci.Rev.* 1, 11

[4] Rephaeli Y., 1995, *Ann. Rev. Astr. Ap.* 33, 541

[5] Birkinshaw M.: 1990, "Observations of the Sunyaev-Zeldovich effect", in *The Cosmic Microwave Background: 25 Years Later* eds N. Mandolesi & N. Vittorio, pp 77-94, Kluwer Academic Publisher, Dordrecht (the Netherlands)

[6] Birkinshaw M.: 1991, in *Physical Cosmology*, ed. A.Blanchard et al. (Gif-sur-Yvette: Editions Frontiéres), p. 177

[7] Klein U., Rephaeli Y., Schlickeiser R., Wielebinski R.: 1991, *A&A* 244, 43

[8] Jones M. et al.: 1993 *Nature* 365, 322

[9] Grainge K. et al.: 1993, *MNRAS* 265, L57

[10] Herbig T., Lawrence C.R., Readhead A.C.S. and Gulkis S. 1995 *ApJ* 449, L5

[11] Wilbanks T.M. et al.: 1994, *ApJ* 427, L75

[12] Dall'Oglio et al., 1992, *Exp. Astron.* 2, 256

[13] Pizzo L., Andreani P., Dall'Oglio G., Lemke R., Otàrola A., Whyborn N., 1995a, *Exp. Astron.* 6, 249

[14] Andreani P., Pizzo L., Dall'Oglio G., Whyborn N., Böhringer H., Shaver P., Lemke R., Otàrola A., Nyman L.-Å. , Booth R. 1996, *ApJ* , march 10th

[15] Andreani P. & Franceschini A., submitted to *MNRAS*

[16] Franceschini A. et al. 1991, *A&AS* 89, 285-310

[17] Gautier T.N., Boulanger F., Perault M., Puget J.L. 1992 *AJ* 103, 1313

[18] Haehnelt M. & Tegmark M., 1996, *MNRAS* 279, 545

SUNYAEV-ZEL'DOVICH OBSERVATIONS WITH THE RYLE TELESCOPE

Richard Saunders
Mullard Radio Astronomy Observatory, Cavendish Laboratory, Madingley Road, Cambridge CB3 0HE, UK.

Abstract

The Ryle Telescope has been used to provide images at 15 GHz of the Sunyaev-Zel'dovich decrements towards a dozen clusters in an X-ray luminosity-limited sample. So far, X-ray data have allowed H_0 estimates towards two of these, both giving "low" values that are self-consistent, though it is essential to obtain many more estimates to reduce the effects of cluster projection. We have also discovered a decrement towards the $z = 3.8$ quasar pair PC1643+4631A&B (198" separation); substantial X-ray, optical and infrared follow-up show that the cluster responsible is either at $z > 1$ or very underluminous and that very significant gravitational lensing must be occuring.

1 Introduction

The Ryle Telescope (RT) is being used to carry out a major programme of observations of Sunyaev-Zel'dovich (S-Z) decrements [1] towards clusters of galaxies. This interferometer array consists of 8, 13-m diameter dishes, currently operating at 15 GHz with a 50-K system temperature, and a 350-MHz bandwidth correlator. Interferometers have certain advantages over switched-beam instruments for observations of CMB anisotropy, such as the filtering-out of much of the atmospheric noise, the lack of need for highly stable amplifiers because only correlated power is measured, and the fact that contaminating radiosources can be recognised and subtracted using the longer baselines at the same time and at the same frequency as the S-Z signal is measured — see e.g. [2, 3, 4] ad infinitum. The RT itself has two features that make it particularly suitable for S-Z work. First, its dishes are small: observations at cm-wavelengths are required to make the source contamination manageable, and the angular scales of S-Z decrements thus imply small baselines. Second, the achievement of very long integrations without

systematic offsets was a critical goal throughout all stages of the signal-processing design and construction.

Our main S-Z programme is targetting an unbiased sample of ROSAT-selected clusters with X-ray luminosities $> 10^{37}$ W (0.5-2.5 keV) and with source contamination at 15 GHz of less than 5 mJy. To date we have successful observations of a dozen clusters (see e.g. [5, 6]). I would like to stress that there are of course firm S-Z detections from other instruments, including the OVRO 40-m (e.g. [7]), the OVRO 5-m [8], the OVRO interferometer [9] and SUZIE [10]. There is agreement in observation from a range of techniques, and the business of S-Z observation has moved on from its checkered history to a stage at which observation, though still challenging, is secure.

2 Measuring H_0

A key feature of S-Z astronomy is that, for a given integral of pressure $\int nTdl$ along the line-of-sight through the cluster, the decrement is independent of redshift z. Given that the X-ray surface brightness is a line integral involving n^2 rather than n, combination of X-ray image, S-Z image and T (from X-ray spectroscopy) gives the line-of-sight depth through the cluster. If one can turn this length into one in the plane of the sky, then, knowing z and the angular size, one has a determination of H_0. The effect of the uncertainty in the change of view from the 90-degree turn is reduced if a suitable sample of clusters is used; the best estimate of H_0 is then the geometric mean of the estimates for each cluster. This is one reason why our S-Z programme concentrates on clusters selected by X-ray luminosity.

In practice, we fit a King profile for n to the X-ray image to give a best-fit gas distribution, simulate the visibilities the RT would measure from this distribution as a function of H_0, and compute the likelihood function for H_0 . Details of the method are given in [11], which describes its application to A2218.

A2218 seemed to us a sensible choice as our first target for this type of analysis. It is almost circular in projection, so that there is reason to assume its size may be similar along the line-of-sight. It contains no cooling flow. Indeed, on the scales to which the RT is sensitive, it is isothermal and is fitted well by a King distribution. We obtained a value for H_0 of 38^{+18}_{-16} km s^{-1} Mpc^{-1}. The individual errors (see below) have been combined in quadrature.

We have applied these methods to another cluster in our sample, A1413 at $z = 0.143$. Its S-Z decrement and other properties are described in [12]. It differs from A2218 in two ways. It has a cooling flow. And it is elliptical in projection, with an axial ratio of 1.3. We are engaged in developing more-sophisticated methods for handling such clusters, but I report here the result of what I emphasise is our first attempt (see [13]) to measure H_0 from A1413. The error budget is as follows (all errors are 1-σ). There is an error in H_0 of 5% from the 3C48/3C286 calibrators (including variability), 25% from RT noise, 10% from source subtraction, 12% from the ASCA estimate of T, and perhaps 4% from a kinetic S-Z contribution. We allow the line-of-sight length to vary between the extreme projected values. Finally there is the issue of gas clumping: the cooling flow implies clumping, and simulations by Steve Allen (private communication) imply the gas temperature may be underestimated by as much as 1 keV, corresponding to an underestimate of H_0 by up to 10%. With all errors combined in quadrature, we find from A1413 that H_0=47^{+20}_{-15} km s^{-1} Mpc^{-1}. It is worth noting that both A2218 and A1413 (despite its cooling flow) have "well-behaved" X-ray properties on the relevant angular scales.

We have not so far been able to make H_0 determinations for other clusters in our sample because of the lack of available X-ray observations, though this situation is fortunately changing. Our best estimate of H_0 is thus the geometric mean of the values for the two clusters. It will

come as no surprise to many (see [14]) that this is 42.

3 Finding distant clusters

The redshift-independence of S-Z has an even more direct implication: if they exist, one should indeed be able to detect clusters that are too distant to be seen optically or in X-rays. Sunyaev (see e.g.[15]) has long emphasised that deep observation of a patch of sky should reveal an "integrated" S-Z effect from distant clusters. The observational difficulty is that there are no telescopes with the requisite combination of sensitivity and field of view to have a significant chance of detecting a (proto-) cluster in one pointing. We therefore have used the RT to look in the directions of three radio-quiet quasars which, for different reasons, we judged may lie in clusters. We found a decrement towards one of these systems, the quasar pair PC1643+4631A&B which have redshifts of 3.79 and 3.83 and lie 198" apart (see [16]). The 6-σ detection is shown in Fig. 1. The signal is consistently present in different phase and primary-beam pointings and in time-splits of the data, and checks reveal no correlator offsets.

What kind of system might produce this decrement? Such an S-Z signal from the RT gives a *lower* limit to the line integral of pressure through the (proto-) cluster. This is because the least-massive system that can produce such an S-Z effect is one which just fills the synthesised beam: if the cluster is smaller than the beam, there is beam dilution and the "true" S-Z effect and hence cluster mass increase; if the cluster is bigger than the beam, the cluster tends to be resolved out and *again* the "true" S-Z effect and cluster mass increase. Now, if the cluster has $T \sim 5$ keV (like the clusters we know about), then, given the relation between angular size and z, a baryon mass of 10^{14} $M_\odot$ within a 1-Mpc radius at $z \sim 1$ is the way to produce the S-Z effect that requires the least mass. Given a ratio of total mass to baryon mass of 10, the cluster mass is at least 10^{15} $M_\odot$.

The next question: is there evidence to support the notion that the massive cluster *is* distant? Evidence so far comes from two fronts. First, PC1643+4631A&B lies on the edge of a pointed ROSAT PSPC field; the upper limit to its X-ray flux corresponds to a luminosity of 7×10^{37} W (similar to the luminosities of nearby clusters in which we see S-Z decrements) at $z > 1$. Second, we have obtained deep R, J and K images of the field with the WHT and UKIRT; there is nothing near the decrement that looks like a cluster at $z < 1$.

It thus appears that, if the cluster is like known luminous clusters, it must lie at $z > 1$ and may be an embarrassment to our standard view of structure formation. Or it may be that the cluster is nearer, in which case it contains far fewer luminous galaxies than known clusters, has gas more rarefied than known clusters (to reduce the X-ray luminosity), yet has a higher gas temperature (to maintain the S-Z).

A system of 10^{15} $M_\odot$ will gravitationally lens objects behind it. We have carried out simple modelling of the lensing, assuming (and this is not critical) that the lens lies at $z = 1$ and that the gas fits the standard β-model. With a total mass of 1.2×10^{15} $M_\odot$ within 1 Mpc of the centre, the source (true) positions of quasars A and B almost coincide, despite their observed positions being 3' apart. A tiny adjustment to the gas distribution model would make the source positions coincident. If A and B really are two images of one quasar, then their spectra should be identical — with two exceptions. Absorption/scattering may be different along the two paths from source to image, and the travel time is likely $\sim 10^3$ years different so that source variability will affect the images. We have obtained high quality optical spectra of A and B: they are remarkably similar, though there are narrow absorption features in them that have the same one-percent redshift difference. We are currently considering a model in which the absorbing gas is in the broad-line region, and that the broad-line velocities we see have not

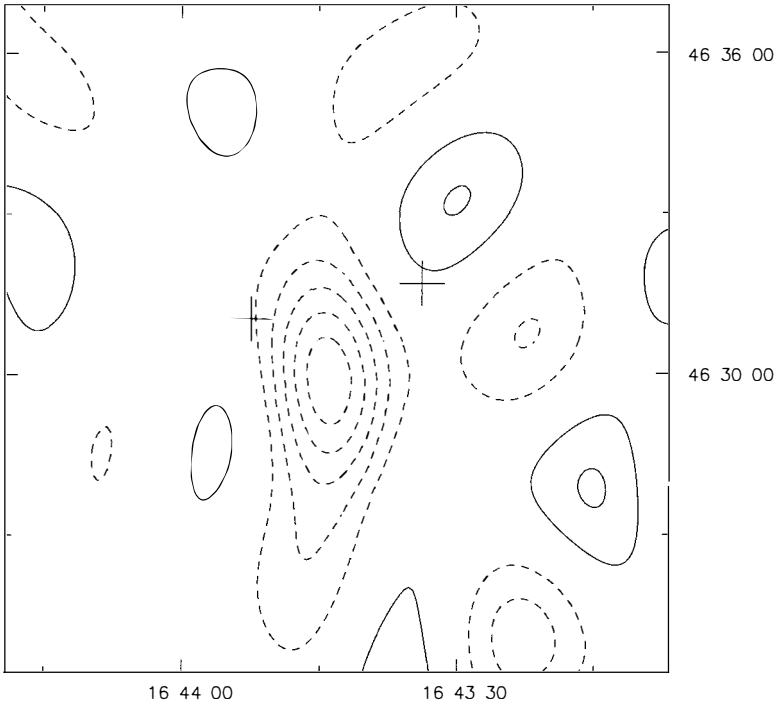

Figure 1: PC16433+4631: CLEANed map of the 0.65–1.25 kλ baseline data after source subtraction. The '+' crosses indicate the positions of quasars A (right) and B (left). Contour levels are -325 to $+130\mu$Jy in steps of 65 μJy; dashed contours are negative. The final map is not corrected for primary-beam attenuation, so the noise level is uniform across the map. Coordinates are B1950.

only a Keplerian component but also a bulk one that changes with time.

Acknowledgements. Thanks are due to Mike Jones, Jo Baker, Malcolm Bremer, Andy Bunker, Garret Cotter, Steve Eales, Alastair Edge, Keith Grainge, Toby Haynes, Mark Lacy, Guy Pooley and Steve Rawlings, and to the technicians and engineers on the Ryle Telescope project, for a superb collaborative effort. The RT is funded in part by PPARC.

References

[1] Sunyaev, R., Zel'dovich, Ya. B., 1972, *Comm. Astrophys. Sp. Phys.*, **4**, 173

[2] Saunders, R., 1986, in Swings, J-P., ed, *Highlights of Astronomy*, **7**, Dordrecht: Reidel

[3] Jones, M., et al, 1993, *Nature* **365**, 320

[4] Church S.E., 1995, *MNRAS* **272**, 551

[5] Grainge, K., Jones, M., Pooley, G., Saunders, R., Edge, A., 1993, *MNRAS* **265**, L57

[6] Saunders, R., 1995, *Astrophys. Lett. Commun.*, **32**, 339

[7] Birkinshaw, M., Gull, S. F., Hardebeck, H., 1984, *Nature* **309**, 34

[8] Herbig, T., Lawrence, C. R., Readhead, A. C. S., Gulkis, S., 1995, *Astrophys. J.* **449**, L5

[9] Carlstrom, J. E., Joy, M., Grego, L., 1996, *Astrophys. J.* **456**, L75

[10] Wilbanks, T. M., Ade, P. A. R., Fischer, M. L., Holzapfel, W. L., Lange, A. E., 1994, *Astrophys. J.* **427**, L75

[11] Jones, M., !995, *Astrophys. Lett. Commun.*, **32**, 347

[12] Grainge, K., Jones, M., Pooley, G., Saunders, R., Baker, J., Haynes, T., Edge, A., 1996, *MNRAS* **278**, L17

[13] Grainge, K., 1996, PhD thesis, Cambridge University

[14] Adams, D., 1980, in *The Restaurant At The End Of The Universe*, London: Pan Books

[15] Markevitch, M., Blumenthal, G. R., Forman, W., Jones, C., Sunyaev, R., 1994, *Astrophys. J.* **426**, 1

[16] Schneider, D. P., Schmidt, M., Gunn, J. E., 1994, *Astron. J.* **107**, 1245

THE EFFECT OF ELECTRON TEMPERATURE ON THE SHAPE OF S.Z. SPECTRA

M. Giard and E. Pointecouteau
CESR/CNRS, BP 4346
F31029 Toulouse cedex, France

Abstract

The effect of middly relativistic electrons, $\frac{v}{c} > 0.1$, is not correctly taken into account in the usual expression the Sunyaev-Zel'dovitch spectral distorsion of the cosmic microwave background through hot gas $T_e > 5$ keV. We show how to obtain exact spectra, using a Monte-Carlo integration of the inverse Compton scatterings. Use of the exact spectrum is necessary to correctly derive the Compton parameter and the peculiar velocity of galaxy clusters from millimetric data. The exact calculation shows a submilimeter excess which increases with the electron temperature. This excess can be used to derived the electron temperature from future sensitive millimeter/submillimeter data, independently of any Xray measurements.

1 Inverse compton scattering of CMB photons by middly relativistic electrons

The general transfer equation of the CMB radiation through a hot electron gas is obtained from the Boltzman equation for compton scattering ([4]), under the assumption that the photon energy, $10^{-3}eV$, is much smaller than the electron energy, $> 10^3 eV$:

$$\frac{dI_\nu(\nu)}{ds} = \int\int n_e p(\beta) \frac{d\sigma}{d\Omega} (I_\nu(\nu_1) - I_\nu(\nu)) d\Omega d\beta. \quad (1)$$

where ν (respectively ν_1) is the photon energy before (respectively after) the scattering, $I_\nu(\nu)$ is the CMB spectral distribution, n_e is the electron density, $\beta = \frac{v}{c}$ is the electron velocity,

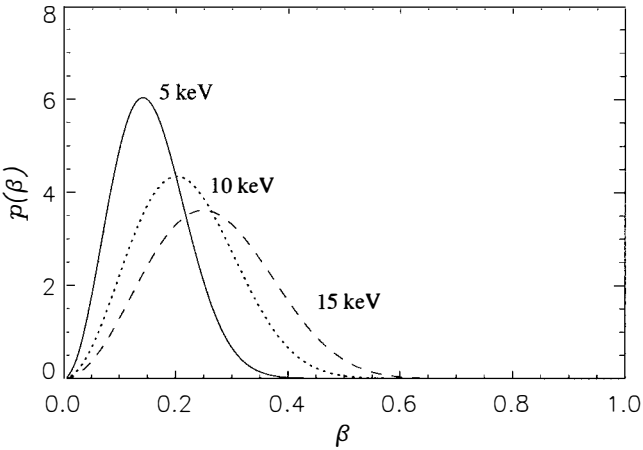

Figure 1: Velocity distribution of thermal electrons for $T_e = 5$, 10 and 15 keV.

Ω is the solid angle, $\frac{d\sigma}{d\Omega}$ is the scattering differential cross section, $p(\beta)$ is the thermal velocity distribution of the electrons and n_e is the electron density.
The usual analytical expression of SZ spectra is the solution of the Kompaneets equation (see [2]):

$$\frac{dI_\nu}{ds} = \sigma_T n_e \frac{kT_e}{m_e c^2} I_\nu f(x) \tag{2}$$

where $x = \frac{h\nu}{kT_{CMB}}$ is the reduced frequency, $\sigma_T = \frac{8\pi}{3} r_e^2$ is the Thompson scattering cross-section and T_e is the electron temperature. Expression (2) can be obtained by a second order expansion of (1) in $\nu_1 - \nu$, and averaging over a thermal electron velocity distribution. However, the photon frequency shift, which shows a first order dependency in β, can be large in the hot intra-cluster gas:

$$\frac{\nu_1}{\nu} \simeq \frac{1 - \beta cos\theta}{1 - \beta cos\theta_1}. \tag{3}$$

θ (respectively θ_1) is the electron/photon angle before (respectively after) the scattering. We have plotted in Fig. 1 the distributions of β for a thermal gas at 5, 10 and 15 keV. These distributions show that large β (and thus frequency shifts) occur frequently, demonstrating the limit of the validity of the usual approximation.

A correct evaluation of S.Z. spectra has to integrate Equ. (1) over all possible scattering events. A semi-analytical devellopement has been perfomed in [3]. However, this integration can be performed by a simple Monte Carlo simulation, if one uses the correct expression of the differential cross section:

$$\frac{d\sigma}{d\Omega} = \frac{r_e^2}{2} \frac{1 - \beta cos\theta}{\gamma^2 (1 - \beta cos\theta_1)^2} (1 + (1 - \frac{1 - cos\alpha}{\gamma^2 (1 - \beta cos\theta)(1 - \beta cos\theta_1)})^2). \tag{4}$$

where α is the photon deflection angle and $\gamma = 1/\sqrt{1 - \beta^2}$.

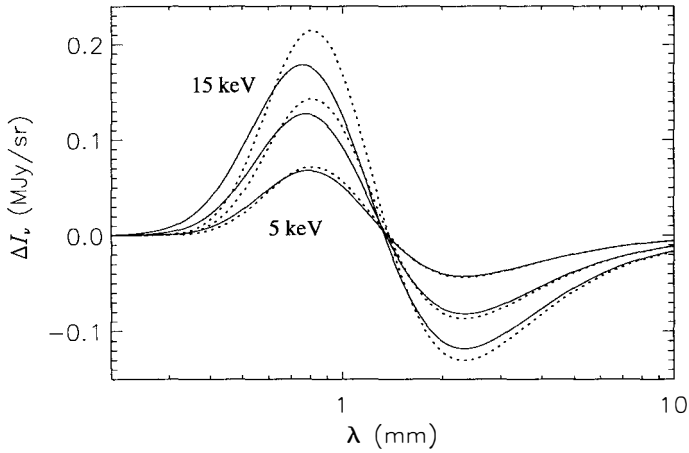

Figure 2: Full line: exact S.Z. spectra obtained by Monte-Carlo simulations for $T_e = 5$, 10 and 15 keV. Dotted line: Solution of the Kompaneets equation. The value of the Compton optical depth for all spectra is $\tau = 3\ 10^{-3}$.

The resulting spectra obtained for an average of 10^6 electron scatterings are shown in Fig. 2 (full line), and compared with the solution of the Kompaneets equation (dotted line). The most significant features that appear in the exact spectra are: (1) The reduction of the amplitude of the SZ effect, which is balanced by (2) the increase of the submillimeter wing of the profile. This is due to the large photon frequency shifts, that have been underestimated in the evaluation of the Kompaneets solution.

In [3], Rephaeli has clearly demonstrated how the use of the Kompaneets solution could lead to large errors, $\Delta v \simeq 500$ km/s to 1000 km/s, in the determination of the cluster peculiar velocity from millimeter measurements at the frequency where the thermal effect is null. Actually, in the case of rich clusters, the effect of the Kompaneets approximation is comparable to a cinetic effect of order 500 km/s. We show in Fig. 3 how a 500 km/s cinetic effect, added to the Kompaneets approximation of the thermal effect, can mimic the exact thermal profile at 10 Kev, particularly if the measurements are limited to millimeter wavelengths. The error bars in Fig. 3 are drawn for the expected sensitivities of the COBRA/SAMBA survey.

2 Determination of the electronic temperature from submillimeter measurements

The point that we want to emphasize here, is that the submillimeter wing of the thermal SZ effect (see Fig. 3) may be used to estimate the temperature of the intra-cluster gas from future sensitive measurements, independently of any Xray data. It is expected that COBRA/SAMBA will be able to detect distant clusters, $z > 1$, unreachable to the sensitivity of future Xray telescopes. This is illustrated in Fig. 4 reprinted from the COBRA/SAMBA red book [1]. A simple simulation of the COBRA/SAMBA observations in the four wavelength bands at 0.55,

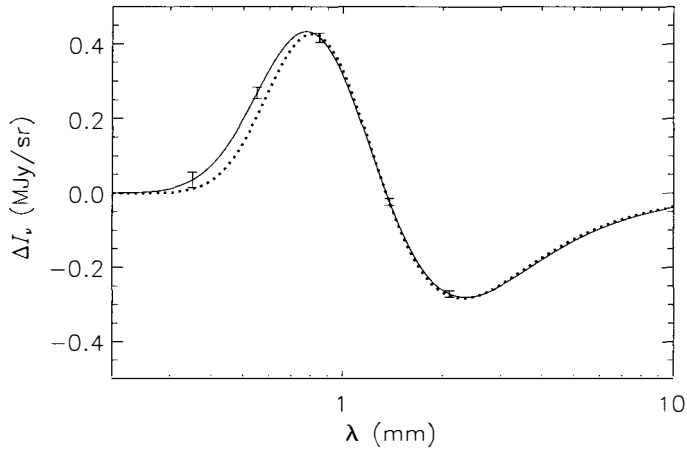

Figure 3: full line: exact S.Z. thermal spectra ($y = 2\ 10^{-4}$, $T_e = 10$ keV). dotted line: Kompaneets thermal approximation ($y = 1.8\ 10^{-4}, T_e = 10$ keV) plus 500 km/s cinetic effect. The bars show the wavelengths and sensitivities of the COBRA/SAMBA mission (high frequency instrument only).

0.85, 1.38 and 2.0 mm, with the expected sensitivities (respectively 0.015, 0.012, 0.034 and 0.0016 MJy/sr), shows that we will be able to restore the gaz temperature with a precision of 2.8 keV in the case of a massive nearby clusters: $y = 310^{-4}, T_e = 10keV$, no beam dilution. Actually, this determination is highly hampered by the low sensitivity of the COBRA/SAMBA submillimeter channel ($\lambda = 0.55mm$), and the dilution of the cluster flux in the beam: 5 arcmin in the submillimeter range.

However, due to the COBRA/SAMBA scanning strategy, a fraction of the sky will be observed with a 10 times better sensitivity. In this region the temperature determination will be possible without any Xray data for clusters down to $y = 2\ 10^{-5}$. Another way to avoid the COBRA/SAMBA sensitivity problem, is to combine sensitive high resolution submillimeter data obtained with the FIRST telescope bolometric instrument, with the very sensitive millimeter COBRA/SAMBA measurements. The FIRST angular resolution, $\simeq 1$ arcmin, will be well adapted to the detection of distant clusters. Moreover, at equal geometrical dilution, the FIRST sensitivity will be at least one decade better than the COBRA/SAMBA full mission sensitivity This is simply because, FIRST being a pointed observatory, the target integration time can be a few decades larger than for COBRA/SAMBA (a few 1000 secondes possible, compared to 5 secondes in the 5 arcmin COBRA/SAMBA beam).

With such capabilities, the FIRST - COBRA/SAMBA combination, planned to fly at the begining of the next century, will be a unique opportunity to observe the very distant universe, study the formation and evolution of clusters of galaxies, and probe the super-structures that they may form.

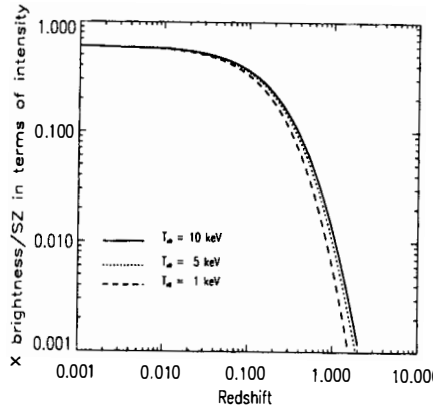

Figure 4: Ratio of Xray to SZ brightnesses for different temperatures. Reproduced from the COBRA/SAMBA 'red book' [1]

References

[1] 1996, COBRA/SAMBA 'red book', ESA report.

[2] Kompaneets, A.S., 1957, *Sov. Phys. -JETP, 4, 730*

[3] Rephaeli, Y., 1995, *Astrophys. J.* **445**, 33

[4] Ribicki, G.B., and Lightman, A.P., 1979, in *Radiative processes in astrophysics*, p. 213, eds. Wiley-interscience.

The Sunyaev-Zel'dovich Effect as a Probe of Ω_o

Domingos Barbosa [1,2], James G. Bartlett [1], Alain Blanchard [1], Jamila Oukbir [3]
[1] *Observatoire Astronomique, 11, rue de l'Université, 67000 Strasbourg, France.*
[2] *Centro de Astrofísica da U.P., Rua do Campo Alegre 823, 4150 Porto, Portugal.*
[3] *SAp, CE-Saclay, 91191 Gif-sur-Yvette Cedex, France.*

Abstract

We examine how the Sunyaev-Zel'dovich (SZ) effect of clusters can probe Ω_o. Using self-consistent models of X-ray clusters in the context of hierarchical models of structure formation, we show that both the mean Compton y parameter and the number of clusters observed via the SZ effect strongly depend on Ω_o. These quantities are higher in open cosmological models due to the earlier epoch of structure formation. Specifically, we compare two models which are able to reproduce the present abundance of X-ray clusters, one for $\Omega_o = 0.2$ and the other $\Omega = 1$. For $\Omega_o = 0.2$, $< y >$ exceeds the current FIRAS limit of 1.5×10^{-5}. Also, the SZ redshift source distribution considerably differs in the two cosmological models. Thus, these results show that both an improvement in our knowledge of CMB spectral distortions and the realization of millimeter surveys to look for SZ sources over a large area of the sky should produce interesting constraints on Ω_o and on the evolution of the baryonic fraction of virialized structures.

[1] *email : barbosa@wirtz.u-strasbg.fr*

1 Introduction

In open cosmological models, structure formation starts earlier, with its rate approaching a constant for redshifts $z_f \sim 1/\Omega_o - 1$. Thus, the structure observed today already existed at z_f. An interesting feature is that structure formation rates are independent of the specified spectrum [12]. So, cluster distribution functions should present this caracteristic Ω_o dependence. Clusters of galaxies are known to have hot intra-cluster gas which emits in X-rays and is the main reservoir of the baryons that fell into the cluster potential wells. This gas will produce a unique spectral distortion in the CMB spectrum by its interaction with CMB photons by inverse Compton scattering [18].
The change, for a given frequency and for a given line of sight, in the sky brightness relative to the CMB intensity, which we will call the SZ surface brightness of a source, is given by $S_\nu = y j_\nu(x)$, where $j_\nu(x)$ describes the frequency dependence and the Compton y parameter measures the distortion magnitude. It has been shown that the integrated SZ surface brightness of a source (the total increment or decrement in the normal CMB flux) depends linearly on the total hot gas content of the cluster and therefore only on their baryonic fraction [2] and not on the spatial distribution of the cluster hot gas :

$$S_\nu = (8\,\mathrm{mJy}\,h^{8/3}) f_\nu(x) f_B \Omega_o^{1/3} M_{15}^{5/3} [\frac{\Delta(z)}{178}]^{1/3} (1+z) D^{-2}(z), \tag{1}$$

where f_B, z, and M_{15} are the baryonic fraction, redshift and mass of the cluster. D_a and $f_\nu(x)$ are respectively the dimensionless parts of the angular distance and of the characteristic SZ frequency function. We have assumed h=0.5 in all subsequent calculations.

2 X-ray Data and the Compton y parameter

In hierarchical models like the cold dark matter (CDM) family of models of structure formation, it is natural to adopt the Press and Schechter (PS) mass function [17] :

$$\frac{dn}{d\ln M} d\ln M = \sqrt{\frac{2}{\pi}} \frac{\rho}{M} \nu(M,z) \Big(- \frac{d\ln\sigma}{d\ln M} \Big) e^{-\nu^2/2} d\ln M, \tag{2}$$

where ρ is the the present mass density of the Universe, $\nu = \delta_c D_g(z)/\sigma(M)$, where $\delta_c D_g(z)$ and $\sigma(M)$ are, respectively, the linear density contrast for collapse at an epoch z and the amplitude of the mass fluctuations. The mass variance σ(M) is expressed in the Fourier plane by :

$$\sigma(M) = \frac{1}{2\pi^2} \int_0^\infty P(k) W_F^2(kR) k^2 dk. \tag{3}$$

Here, W_F is some window function and M is the mass contained in a sphere of radius R. In the case of a CDM-like perturbation spectrum, the original primordial power-law spectrum (P_p) is modified by the presence of cold, non-baryonic dark matter, among other factors. The change in the spectrum is contained in the CDM transfer function, for which $P(k) = T^2 P_p(k)$, where $P_p \propto k$ just describes the scalar invariant primordial perturbations. A good fitting formula to T(k) is provided by equation(4), where its shape is controled only by the so called Γ factor [3] :

$$T(q) = \frac{log(1+2.34q)}{(2.34q)} \left[1 + 3.89q + (16.1q)^2 + (5.46q)^3 + (6.71q)^4\right]^{-1/4}, \tag{4}$$

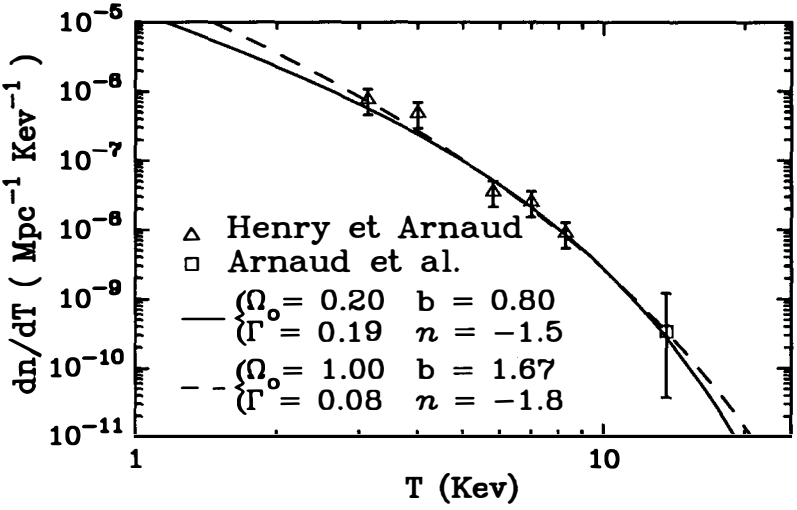

Figure 1: The temperature function for the two models; in both cases we have assumed $h = 0.5$. For each Ω_o, the curves correspond to the best χ^2 fits to b and Γ. The local power spectrum index is given by n.

where $q = k/(h\Gamma)$. In the CDM family, Γ is usually identified as Ωh, but here is considered as a free parameter. Also, for the spectrum normalization, we take the bias $b = 1/\sigma(M)$ at $8h^{-1}$ Mpc .

Because clusters are virialized structures, the mass-temperature relation derived in the framework of the spherical collapse model, $T \propto M^{2/3}(1+z)$ [7], together with the mass function yields the temperature function dn/dT. To compare the X-ray data [12], [9], to the theoretical temperature functions for different cosmological models, a χ^2 fit was performed assuming as free parameters the normalization b and the shape of the power spectrum Γ.

Figure 1 shows the temperature function dn/dT, with the best χ^2 fits to the data for the $\Omega_o = 1$ and $\Omega_o = 0.2$ cosmological models analysed here. An analogue method was used by Oukbir et al. [13], [14] who made a similar χ^2 fit to X-ray data, considering the perturbation spectrum around cluster scales as a power law. They chose as free parameters b and the local power spectral index n. The values found by both analyses agree very well, with the $b - \Gamma$ fit indicating the same local spectrum index found by Oukbir et al.

The mean global Compton distortion, $< y >$, will be the sum of all single distortions produced by each cluster. Naturaly, it will be defined as an integral over the entire mass distribution function (in this case the PS mass function) :

$$< y >= f_B \int dz \frac{dt}{dz} c\sigma_T (1+z)^3 \int d\ln M \frac{dn}{d\ln M} \frac{\chi M}{m_p} \frac{kT(M,z)}{m_e c^2}, \qquad (5)$$

where χ is the number of electrons per baryon. For f_B, X-ray observations indicate values as high as $0.05h^{-3/2}$ [6], [8], [19], which agree with nucleosynthesis for $\Omega_o = 0.2 - 0.3$, but are inconsistent for $\Omega_o = 1$ [20]. Also, note that gas in low mass structures is able to cool in less than one Hubble time, so the mass integral in equation(5) has a low mass cut-off. This cut-off is $10^{12} M_\odot$ and is almost independent of redshift [5]. Typically, at redhifts higher than

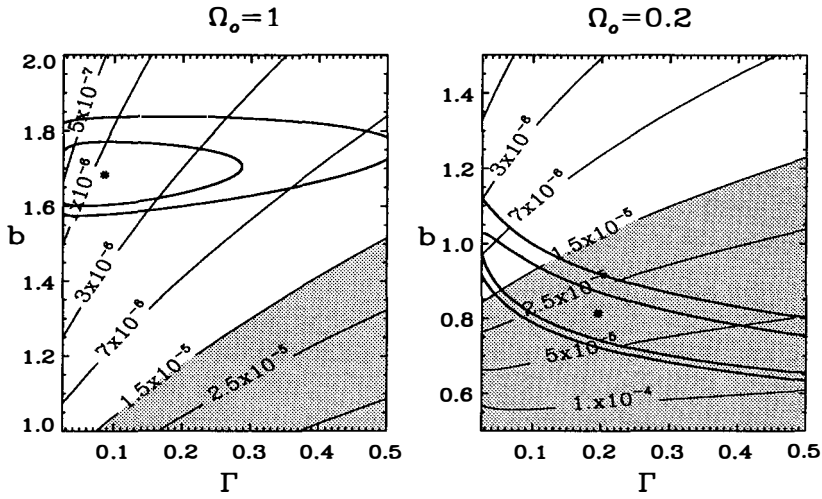

Figure 2: $b - \Gamma$ plane. Thin lines represent y isocontours. The gray zone is the forbidden region : $< y >$ is higher than the current FIRAS limit of 1.5×10^{-5}. Thick contours represent the 1σ and the 2σ contours of the χ^2 fit to temperature function data if errors were gaussian. Asterisks are the best fit values. Note the change in the bias scale between the two panels.

$z \sim 5$, Compton cooling is efficient, so gas within the structures will cool and, consequently, the contribution at these high redshifts to $< y >$ will be small.

Figure 2 shows X-ray and $< y >$ constraints in the $b - \Gamma$ plane. The ellipses (thicker contours) represent the 1σ and 2σ contours of the χ^2 fits. The bias is quite well constrained, unlike Γ. This is not surprising, because b is defined at the cluster scale, while Γ is a shape parameter linking all scales. The best fit values for Γ are quite different from the value of ~ 0.25 founded by the galaxy distribution [16] but still largely compatible within the 1σ confidence level. It is clear that for $\Omega_o = 0.2$, only a small region of the $b - \Gamma$ region allowed by X-ray data does not violate the FIRAS limit of 1.5×10^{-5} [15]. Further improvement in the limit on $< y >$ (a factor of 2) could provide stronger constraints on this model.

3 Source Counts

Integrating the PS mass function, we can study the redshift distribution function of sources brighter on the sky than a certain threshold, $dN/d\Omega/dz(> S_\nu)$, and the the corresponding SZ source counts. The source counts are expressed by :

$$\frac{dN}{d\Omega}(> S_\nu) = \int dz \frac{dV}{dz d\Omega} \int_{M_{min}(S_\nu, z)} dM \frac{dn}{dM}, \tag{6}$$

where M_{min} is given by equation(1). Figure 3 presents the calculated redshift distribution and SZ source counts at 0.75 mm. The panel on the left shows how different the redshift distribution of the two cosmological models can be : in an open universe, the long high-redshift tail reveals the geometrical effects in the rate of structure formation absent in the flat model. This effect

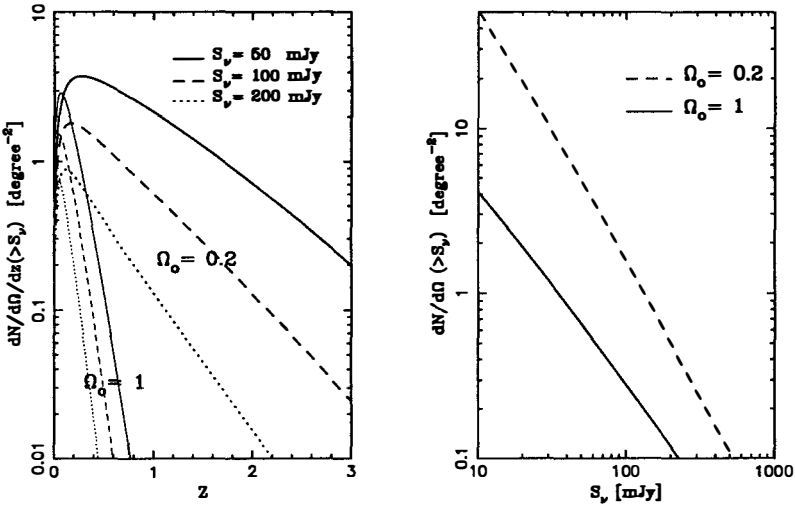

Figure 3: The SZ source counts and the redshift distribution for several S_ν. The parameters b and Γ used are the best fit values to dn/dT. The calculation is for a wavelength of 0.75 mm.

is independent of cluster evolution and it is also visble in X-ray redshift temperature function analysis, [11],[13]. The righthand panel shows the SZ source counts. A difference of 10 is visible at 50 mJy, the expected threshold for COBRAS/SAMBA. If we use a more conservative Γ value of 0.25, the difference in the two distributions is still higher than a factor of 4, thus showing the Ω_o effects.

4 Conclusion

Unlike X-rays, the SZ effect is insensitive to the radial distribution of hot gas in clusters; it depends only on the cluster baryonic fraction. Thus, the Sunyaev-Zel'dovich effect is a good probe of the Universe's geometry. Both the $< y >$ and the SZ source counts show large differences between the flat and open cosmological models considered here. It is clear that an $\Omega = 0.2$ universe which reproduces the temperature cluster function is left with a small region in the $b - \Gamma$ plane. This suggests that an improvement in the limit on $< y >$ should be very constraining for open models. The redshfit distribution of SZ sources is an elegant method of probing Ω_o, due to its independence on the normalisation of the perturbation spectrum. Also, as first pointed out by Korolev et al. [10], cluster source counts should also be a good probe of Ω_o, even if they are more sensitive to evolution than the SZ redshift distribution $dN/d\Omega dz$. In fact, the construction of a catalogue of SZ sources could reveal the Ω_o geometrical effects as presented in Figure 3.

Acknowledgements. D.B is supported by the Praxis XXI CIENCIA-BD/2790/93 grant attributed by JNICT, Portugal.

References

[1] Arnaud M. et al., 1992, *Astrophys. J.* **390**, 345

[2] Barbosa D., Bartlett J.G., Blanchard A., Oukbir J., 1996, *Astr. Astrophys.*, in press

[3] Bardeen J.M., Bond J.R., Kaiser N. and Szalay A.S., 1986, *Astrophys. J.* **304**, 15

[4] Bartlett J.G., Silk J., 1994, *Astrophys. J.* **423**, 12

[5] Blanchard A., Valls-Gabaud D., Mamon G., 1992, *Astr. Astrophys.* **264**, 365

[6] David L.P., Jones C., Forman W., 1995, *Astrophys. J.* **445**, 578

[7] Evrard A.E., 1990, in M. Fitchett, & W.Oegerle (eds) *Clusters of Galaxies,* Cambridge University Press

[8] Evrard A.E., 1996, *Strasbourg-Berkeley Workshop The role of baryons in Cosmology*

[9] Henry J.P., Arnaud K.A., 1991, *Astrophys. J.* **372**, 410

[10] Korolev V.A., Sunyaev R.A., Yakubtsev L.A., 1986, Soviet Astron. Lett. 12, 141

[11] Oukbir J., 1994, *PhD thesis, Université Paris VII*

[12] Oukbir J., Blanchard A., 1992, *Astr. Astrophys.* **262**, L21

[13] Oukbir J., Blanchard A., 1996, *Astr. Astrophys.*, in press

[14] Oukbir J., Bartlett J.G. and Blanchard A., 1996, *Astr. Astrophys.*, submited

[15] Fixsen D.J., Cheng E.S.,Gales J.M., Mather J.C., Shafer R.A. and Wright E.L., 1996, *Astrophys. J.*, in press

[16] Peacock J.A., Dodds S.J., 1994, *MNRAS* **267**, 1020

[17] Press W.H., Schechter P., 1974, *Astrophys. J.* **187**, 425

[18] Sunyaev R.A. and Zel'dovich Ya. B., 1972, *Comm. Astrophys. Space Phys.* 4, 173

[19] White D.A., Fabian A.C., 1995, *MNRAS* **273**, 72

[20] White S.D.M., Navarro J.F., Evrard A. and Frenk C.S., 1993, *Nature* **366**, 429

EVOLUTION OF CLUSTERS OF GALAXIES

S. Colafrancesco [1], N. Vittorio [2] and P. Mazzotta [2]
[1] *Osservatorio Astronomico di Roma, Monteporzio, Italy.*
[2] *II Università di Roma "Tor Vergata", Roma, Italy.*

Abstract

In this paper we discuss theoretical predictions for the local abundance of galaxy clusters and their evolution. We also discuss the constraints set by two different databases: the X-Ray luminosity function (XRLF) and the temperature function (TF).

1 Introduction

Clusters of galaxies provide good tools for testing structure formation scenarios. In particular the Press & Schechter (hereafter P&S) theory [1] allows to predict the abundance and evolution of clusters in a simple and semi-analitycal way, which relates these observables to the linear theory of density fluctuations. It turns out that the theoretical predictions with density flutuations normalized to COBE/DMR are in general not consistent with the available data: these are the local X-ray luminosity function (XRLF) [2] and the temperature function (TF) [3,4]. The usual procedure is then to tune the normalization of the density fluctuation field to fit locally these observables, and then to make predictions for other observables such as cluster number counts or the Comptonization parameter (see *e.g.* [5,6]). The fit to the XRLF or to the TF yields in general different amplitudes and shapes for the local mass function (MF), and this implies differences in the predictions of observables, in particular regarding their evolution. It should be noted that predictions of the cluster XRLF heavily rely on assumptions about the gas distribution and evolution. On the contrary the IC gas temperature depend only upon the potential well of the cluster, usually assumed spherically simmetric and virialized.

In this contribution, we discuss the constraints posed by the local database on the cluster abundance as predicted in different models for structure formation. Based on this, we also discuss cluster evolution in flat and low density cosmological models.

2 The local abundance

The mass and redshift distribution of clusters, $N(M,z)$, can be determined from the P&S theory:

$$N(M,z) = \mathcal{I}\frac{\rho}{M}\frac{\delta_v}{\sigma^2}\frac{d\sigma}{dM}\frac{1}{\sqrt{2\pi}}\exp[-\delta_v^2/2\sigma^2]\,, \tag{1}$$

where ρ is the comoving background density, $\mathcal{I} = 2$ (see [7] for a theoretical derivation), M is the total cluster mass, $\sigma(M,z)$ is the *rms* of the linear density fluctuation field at z, smoothed over the region containing M, and δ_v is the linear density contrast of a perturbation that virializes at z. The variance of density fluctuations of mass M is normalized in order to have $\sigma(8\ h^{-1}\ \mathrm{Mpc}, 0) = b^{-1}$. Thus, $N(M,z)$ depends on the product $\delta_v b$, and not separately on δ_v and b.

2.1 Properties and Evolution of Intracluster Gas

There are various open issues pertaining to the formation of the hot gaseous cores of clusters. For our purposes here we can adopt the following simplified approach: shortly after a cluster forms and virializes, a gaseous core forms (probably as a result of tidal galactic interactions and other gas stripping processes) with the hot gas in hydrostatic equilibrium in the potential well of the cluster. To avoid introducing a large number of free parameters, we will simply scale the gas properties to those of the cluster. The gas mass is taken to be a fraction f of the total cluster mass, and the gas density profile is assumed to have the commonly adopted form $n(r) = n_0[1 + (r/r_c)^2]^{-3\beta/2}$, where n_0 is the central electron density and r_c is a core radius. Here we use the value $\beta = 2/3$ which is particularly convenient in analytic calculations. The radial extent of a cluster is taken as $R = pr_c$. The mass within the outer radius $R(p)$ is $M(p) = 3M_0[p - tg^{-1}p]$, where $M_0 = (4\pi/3)r_c^3\rho_0$, and ρ_0 is the central total mass density of the cluster. Assuming that cluster collapse is self-similar, we can infer the mass and redshift dependence of r_c from scaling laws:

$$r_c(\Omega_0, M, z) = \frac{1.29\ h^{-1}\ \mathrm{Mpc}}{p}\left[\frac{M}{10^{15}\,\mathrm{h^{-1}\ M_\odot}}\cdot\frac{1}{\Omega_0\Delta(\Omega_0,z)}\right]^{1/3}\frac{1}{1+z}\,. \tag{2}$$

where Δ is the cluster density contrast at virialization. Hereafter we fix $p = 10$ to recover values of the IC gas core radii consistent with observations: for a local cluster of $10^{15}\,\mathrm{h^{-1}\ M_\odot}$ we get $r_c = 0.12$ and $0.16\ h^{-1}$ Mpc for $\Omega_0 = 1$ and $\Omega_0 = 0.2$, respectively. The gas is assumed isothermal at the virial temperature $T \propto M/R$. This gives

$$T = 6.7\cdot 10^7(1+z)\left(\frac{M}{10^{15}M_\odot h^{-1}}\right)^{2/3} K. \tag{3}$$

for a flat universe. Although it is known that the gas mass fraction depends on z and M, little is currently known on the exact form of these dependences. We adopt the simple parametrization (described in detail in [8]) which is based on the results of analyses of the *Einstein* Medium Sensitivity Survey (EMSS) data [9,10] which seem to indicate a decrease in the number of bright clusters with redshift, and an analysis of a local cluster sample (see [8,11] for details)

$$f = f_o\left(\frac{M}{10^{15}\,\mathrm{h^{-1}\ M_\odot}}\right)^{\eta}\left(\frac{t}{t_o}\right)^{\xi}. \tag{4}$$

Here t_o is the age of the universe, and the normalization to $f_o \simeq 0.1$, is based on a local, rich cluster sample. Values of $\eta = 0.2$ and $\xi = 1.2 \div 1.8$ are found for flat and low density CDM

models, respectively. Hence, X-ray cluster bolometric luminosities are predicted to scale as:

$$L \approx (2 \cdot 10^{45} erg/s)\left(\frac{kT}{keV}\right)^{1/2}\left(\frac{f}{0.1}\Omega_o\frac{\Delta}{400}\right)^2\left(\frac{r_c}{0.15\ h^{-1}\ \mathrm{Mpc}}\right)^3(1+z)^6 h \qquad (5)$$

Using eqs. (1), (3) and (5) we can derive the XRLF, $N(L,z) = N(M,z)dM/dL$, and the TF, $N(kT,z) = N(M,z)dM/dkT$. A χ^2 analysis provides the values of the parameters ($\delta_v b$ and h) that best fit the corresponding observables (see Table 1).

Table 1. Fitting parameters for the XRLF (col. 3,4) and for the TF (col. 5,6).

Model	Ω_0	n	h	$b\delta_v$	h	$b\delta_v$
SCDM	1	1	0.5	2.5	0.5	1.8
OCDM	0.2	1	0.5	1.4	1	1.25
CDM+Λ	0.2	1	0.5	1.3	1.	1.15
BDM	0.1	-1	0.5	0.7	1.	0.7

3 Cluster Evolution

Because of their definition, the redshift evolution of the XRLF and TF is determined from the redshift evolution of the cluster mass function, $N(M,z)$, and of the Jacobians, dM/dL and dM/dT. The time derivative of the mass function takes the form of a kinetic equation:

$$\frac{dN}{dt} = N\left(\frac{1}{\tau_+} - \frac{1}{\tau_-}\right) \qquad (6)$$

where $\tau_- = D/\dot{D}$ and $\tau_+ = \tau_-\sigma^2(M,z)/\delta_v^2$. For power law spectra [*i.e.* , $P(k) = Ak^n$] we can

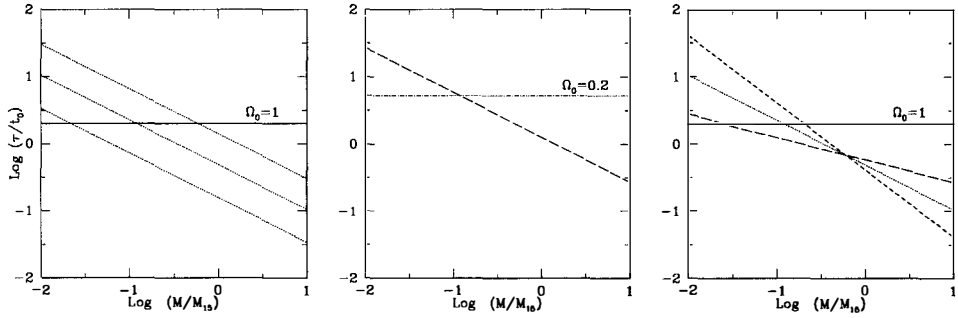

Figure 1: The time scales τ_+ and τ_- as a function of the mass for flat (panel a and c) and open (panel b) cosmologies at $z = 0$. The horizontal lines correspond to τ_-. The three dotted curves in panel a) represent, from the top, τ_+ for ($n = -1$, $b\delta_c = 1$), ($n = -1$, $b\delta_c = 1.7$), ($n = -1$, $b\delta_c = 3$), respectively. In panel b) we show τ_- (horizontal line) and $\tau_=$ for $\Omega_0 = 0.2$ and $n = -1$, $b\delta_c = 1$. In panel c) we show τ_- (horizontal line) and τ_+ for ($n = 0$, $b\delta_c = 1.7$: short dashes), ($n = -2$, $b\delta_c = 1.7$: long dashes) together with ($n = -1$, $b\delta_c = 1.7$: dotted line).

write

$$\frac{dlnN}{dlnt} = \frac{D}{\dot{D}}\left[\frac{(b\delta_v)^2}{D^2}\left(\frac{M}{M_{*0}}\right)^{2a} - 1\right] \qquad (7)$$

where $a = (n+3)/6$ and M_{*0} is the mass contained in a sphere of 8 h^{-1} Mpc of radius.

So the MF evolution is determined by: i) the structure formation scenario, through the growing factor D, and the mass variance, $\sigma(M,z)$; ii) the normalization to the local data, which determines $\delta_v b$. In particular, the evolution is positive for $M > \hat{M} = M_{*0}(D/b\delta_v)^{1/a}$ and negative for $M < \hat{M}$. Note that $\hat{M}$ depends, for a given cosmological model, only on $b\delta_v$ (see Fig.1).

Moreover, it is easy to show (see also [11]) that in this simple case:

$$\frac{dlnN}{dlnt} = -\frac{t}{\tau_-}\left[1 + \frac{1}{D^2 a}\left(2 - a + \frac{dlnN}{dlnM}\right)_{t=t_o}\right] \tag{8}$$

which further shows the link between the evolution of the cluster MF and its shape in the local frame.

The evolution of the XRLF and of the TF depends also on the evolution of the Jacobians dM/dL and dM/dT. In fact, we can write:

$$\frac{dN(L,z)}{dt} = N(L,z)\left(\frac{1}{\tau_+} - \frac{1}{\tau_-} - \frac{1}{\tau_L}\right) \; ; \quad \frac{dN(T,z)}{dt} = N(T,z)\left(\frac{1}{\tau_+} - \frac{1}{\tau_-} - \frac{1}{\tau_T}\right) \tag{9}$$

where

$$\tau_L = \frac{t}{(dlnL/dlnt)} \; ; \quad \tau_T = \frac{t}{(dlnT/dlnt)} \tag{10}$$

Thus, the balance among these different time scales determines both the local normalization

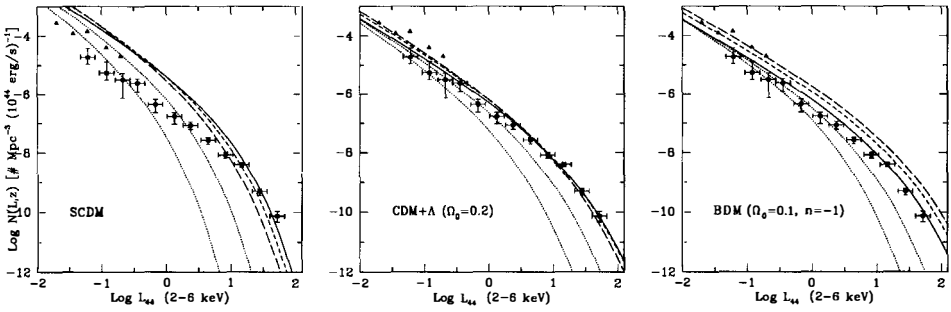

Figure 2: The best fits for the local XRLF (continuous curves) and its evolution in SCDM (panel a), open CDM (panel b) and in BDM (panel c) models. Dotted lines refer to IC gas evolution at $z = 0.5, 1$ (from the top) while the dashed curves refer to the same redshifts (small dashes: $z = 0.5$; long dashes: $z = 1$) but with no IC gas evolution.

and the evolution of $N(L,z)$ and $N(T,z)$. The evolution of the XRLF and of TF is shown in Figs 2 and 3 for different models, at different redshifts. In the calculations we use the best fit values listed in Table 1.

4 Discussion

Measurements of cluster X-ray luminosities and temperatures at intermediate redshifts $z \sim 0.3 \div 0.5$ are extremely important to understand the structure and the evolution of cluster

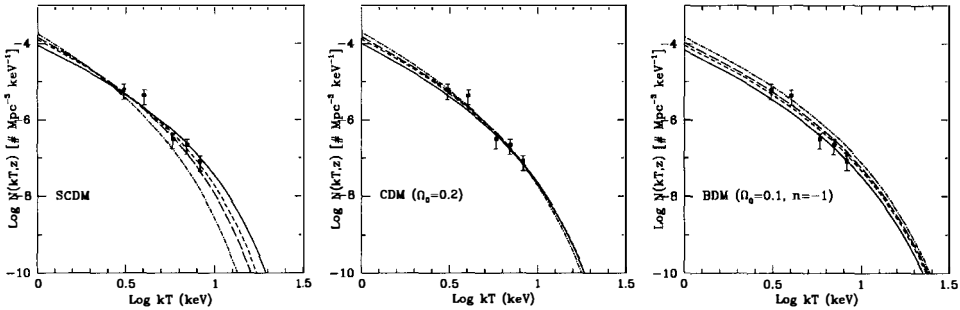

Figure 3: The TF for different flat and low density models (as labelled in each panel) at different redshifts: $z = 0$ (continuous lines), $z = 0.3$ (dotted line), $z = 0.5$ (dashed lines) and $z = 1$ (dot-dashed lines).

potential wells and to constraint the physical status of the intergalactic medium. In fact, statistically reliable measurements of $N(L, z)$ even at moderate redshifts $z \approx 0.3 \div 0.5$ will set strong constraints on the IGM evolution. These in turn can be used to set reliable limits to the Comptonization parameter or to the cluster number counts (see [5,6]).

However, the attempt to derive constrains to the global cosmological parameters, like Ω_0, from the evolution of $N(T, z)$ seems a rather complicated issue as the degree of evolution of $N(T, z)$, intrinsically smaller than the XRLF one at least for the scenarios we consider, is still hidden by the uncertainties in the present data (see Fig.3). Moreover, there are also theoretical aspects that shadow this analysis. The possibility suggested by some authors [12,13,14] to discriminate between low density and high density cosmologies using the evolution of $N(T, z)$ relies on the choice of the fitting parameters for the local distribution. Using power-law spectra with very negative spectral indexes $n \lesssim -1.5$, determines $b\delta_v \gtrsim 1.5$: this yields a strong positive evolution. For $n \gtrsim -1$, $b\delta_v \lesssim 1$: this yields a negative evolution, quite independently from the value of Ω_0. Then the TF evolution is mainly determined, as shown in Sect.3, by the choice of the model power spectrum, which yields specific values for $\delta_v b$. Thus, the possibility to use the TF at $z \gtrsim 0.3$, from the present (ASCA) or next coming (SAX) X-ray satellites with a broad energy band and sufficient spectral and spatial resolutions, to discriminate among different cosmological scenarios is at most model dependent.

An alternative strategy is to design very detailed observations of a limited sample of clusters – with a good luminosity coverage – at moderate redshifts ($z \approx 0.3$) in order to put strong limits to the amount of luminosity evolution and to the distribution and structure of the IGM in distant clusters. Future, high spatial and spectral resolution, large covering areas X-ray missions could be able to disentengle the history of the IGM from the geometry of the universe.

References

[1] Press,W.H. & Schechter, P. 1974, *Ap. J.* 187 425

[2] Kowalski *et al.* 1984, *Ap. J. Supp.* 56 403

[3] Henry, J.P. & Arnaud, K. 1991, *Ap. J.* 372 410

[4] Edge, A. *et al.* 1990, *MNRAS* **245**, 559

[5] Colafrancesco, S., Mazzotta, P., Rephaeli, Y. & Vittorio, N. 1996, *Ap. J. in press*

[6] Vittorio, N., Colafrancesco, S., Mazzotta, P. & Rephaeli, Y. 1996, *These Proceedings*

[7] Bond, R., Cole, S., Efstathiou, G. & Kaiser, N. 1993, *Ap. J.* 379 440

[8] Colafrancesco, S. & Vittorio, N. 1994, *Ap. J.* 422 443

[9] Gioia, I. *et al.* 1990, *Ap. J. Supp.* 72 567

[10] Henry, J.P. *et al.* 1992, *Ap. J.* 386 408

[11] Colafrancesco, S., Mazzotta, P. & Vittorio, N. 1996, *preprint*

[12] Hattori, M. & Matsuzawa, H. 1995, *Astron. Astrophys.* 300 637

[13] Barbosa, D., Bartlett, Blanchard, A. & Oukbir, J. 1996, *Astron. Astrophys. in press*

[14] Eke, V.R., Cole, S. & Frenk, C.S. 1996, *preprint*

INTRACLUSTER COMPTONIZATION OF THE CMB IN CDM COSMOLOGIES

N. Vittorio [1], S. Colafrancesco [2], P.Mazzotta[1] and Y. Rephaeli [3]
[1] *II Università di Roma "Tor Vergata", Roma, Italy.*
[2] *Osservatorio Astronomico di Roma, Monteporzio, Italy.*
[3] *Tel Aviv University*

Abstract

We present calculations of the mean sky-averaged Comptonization parameter describing the scattering of the CMB by hot gas in clusters of galaxies, in an array of flat and open CDM cosmologies. The models are globally normalized to fit cluster X-ray data, and the intracluster gas is assumed to have evolved in a manner consistent with current observations. We also discuss the rms temperature fluctuations induced by a population of evolving clusters. Finally, we predict the number counts of clusters across which a net flux (with respect to the CMB) higher than some limiting value can be detected. Such number counts are specifically predicted for the COBRAS/SAMBA mission.

1 Introduction

Compton scattering of the cosmic microwave background (CMB) radiation by hot gas in clusters of galaxies – the Sunyaev-Zeldovich [1] (hereafter S-Z) effect – affects both the spectrum and the angular distribution of the radiation. When the intensity (or temperature) is differentially measured, the radiation will appear anisotropic, on characteristic angular scales of several arcminutes, reflecting the typical sizes of clusters that contribute most to the anisotropy. This cluster-induced anisotropy can be an important component of the full anisotropy on such scales, as has been shown in many studies (see [2] and references therein). The spectral change of the CMB across each cluster translates into a superposed average change of the spectrum across the sky. This parameter is of prime interest in the characterization of spectral deviations from a pure blackbody spectrum. Currently, the COBE/FIRAS database provides the best measure of such non-Planckian distortions by constraining the degree of Comptonization to

be $y \leq 1.5 \times 10^{-5}$ at the 90% statistical significance level [3]. The significance of this value stems from the fact that it limits the cumulative effects of energy release processes in the early universe (at $z \lesssim 3 \times 10^6$), and the superposed effects of hot intergalactic (IG) and intracluster (IC) gas [4]. The COBRAS/SAMBA mission (hereafter C/S), has been selected as the next Medium-Sized Mission of the ESA Horizon 2000 Program. The 140, 222 and 400 GHz channels of the High Frequency Instrument (HFI) are particularly relevant for measurement of the S-Z effect in clusters. The first frequency is on the Rayleigh-Jeans (R-J) side, where the intensity change (across a cluster) is negative; the second is near the crossover frequency (where the thermal effect vanishes), and the third is on the Wien side, where the effect is positive (for a discussion of the significance of high-frequency measurements, see [2]). The sensitivity and angular resolution of the C/S mission are very suitable for a survey of a large number of clusters.

The purpose of this paper is to review the theoretical predictions for the mean Comptonization parameter and the rms temperature anisotropy due to a population of evolving clusters. We also present predictions for the cluster number counts in the sub-mm region. We limit ourselves to CDM cosmologies: the standard (SCDM) flat model, an open (OCDM) model with $\Omega_o = 0.2$ and a low density, vacuum dominated model (ΛCDM) with $\Omega_0 = 0.2$ and $\Omega_\Lambda = 0.8$.

2 Cluster Comptonization

2.1 Basic Assumptions

The main assumptions behind the calculations we present here are the following:
i) The intracluster (IC) gas mass is assumed to be a fraction, f, of the cluster virial mass. f is supposed to be a power law of the cluster mass and of the cosmic time, with power indeces obtained by fitting the EMSS and a local cluster sample (see [5,6,7] and references therein).
ii) The 3D, IC gas distribution is described by a β-profile (with $\beta = 2/3$), truncated at $p = 10$ times the core radius

$$r_c(\Omega_0, M, z) = \frac{1.29\ h^{-1}\ \mathrm{Mpc}}{p}\left[\frac{M}{10^{15}\,\mathrm{h}^{-1}\ \mathrm{M}_\odot}\cdot\frac{1}{\Omega_0\Delta(\Omega_0, z)}\right]^{1/3}\frac{1}{1+z}\,. \qquad (1)$$

where Δ is the non linear density contrast of a cluster that virializes at redshift z.

iii) the IC gas is assumed to be isothermal and in hydrostatic equilibrium in the spherical symmetric potential well of a virialized cluster. This fixes the IC gas temperature: $T = 6.7 \cdot 10^7(1+z)(M/10^{15}M_\odot h^{-1})^{2/3}\,K$. for a flat universe.
iv) the cluster mass function, $N(M, z)$, is given by the Press & Schecter [8] formalism, and it is normalized to fit the local X-Ray luminosity function [7]. Values of the fitting parameters are given in [6] (see also [5] for more details).

2.2 Sky averaged y

The mean Comptonization parameter averaged over the cluster ensemble and over the sky is

$$\overline{y} = \int \frac{dV}{dz}dz \int N(M, z) y_o(M, z)\overline{\zeta(M, z)}dM\,. \qquad (2)$$

Here $y_o(M, z) \equiv (2tg^{-1}p)(kT/m_ec^2)\sigma_T n_o r_c$ is the value of the Comptonization parameter along a los, $\hat{\gamma}_l$, through the center of the cluster, and $\overline{\zeta(M, z)} = (\theta_c^2/2tg^{-1}p)(p - tg^{-1}p)$ is the mean

over the sky of the cluster angular profile

$$\zeta(\theta, M, z) = \frac{1}{tg^{-1}p} \cdot \frac{1}{\sqrt{1+(\theta/\theta_c)^2}} tg^{-1} p \frac{\sqrt{1-(\theta/p\theta_c)^2}}{\sqrt{1+(\theta/\theta_c)^2}} \tag{3}$$

which is obtained by integrating the truncated 3D β-profile along different los's. Here $\theta_c = r_c/D_A$ is the angle subtended by the core radius of a cluster, and D_A is the angular diameter distance. The mass integral is performed from $10^{13} M_\odot$ up to, formally, infinity. The central density of the cluster is $n_o = f(1+X)\rho_o/2m_p$ (where $X = 0.69$ and m_p is the proton mass).

In Table 1 we list values of $\overline{y}$ for the CDM models we consider. The values of $\overline{y}$ are well below the FIRAS upper limit.

Table 1. Average Comptonization and cluster number couts in CDM models.

Model	Ω_0	h	$\overline{y}/10^{-6}$	$N(>F_\nu)/10^3$	$N(>2F_\nu)/10^3$	$C^{1/2}(0,1.9')/10^{-6}$
SCDM	1	0.5	0.35	5.0	1.1	1.58
OCDM	0.2	0.5	0.20	5.5	1.6	1.92
OCDM	0.2	0.7	0.12	2.2	0.5	1.06
CDM+Λ	0.2	0.5	0.27	7.1	2.1	2.24
CDM+Λ	0.2	0.7	0.18	3.2	0.8	1.33

2.3 Temperature anisotropies

Compton scattering of the CMB by IC gas results in an intensity change across the cluster:

$$\Delta I = \frac{2(kT_{CMB})^3}{(hc)^2} y_c g(x), \tag{4}$$

where T_{CMB} is the CMB temperature, $x = h\nu/kT_{CMB}$, and $g(x) = [x^4 e^x/(e^x-1)^2]s(x)$ is a spectral function, with $s(x) = [x\coth(x/2) - 4]$. In the R-J side of the spectrum this yields: $\Delta I/I = \Delta T/T = -2y_c$. Therefore, the CMB temperature change across a single cluster is

$$\Delta(\hat{\gamma}) \equiv \frac{\Delta T}{T}(\hat{\gamma}) = \Delta_o \cdot \zeta(|\hat{\gamma} - \hat{\theta}|, M, z) \tag{5}$$

where $\Delta_o = -(4tg^{-1}p)(kT/m_e c^2)\sigma_T n_o r_c$. The power spectrum of the process $\Delta(\hat{\gamma})$ can be written as (see [7] and reference therein):

$$P(q) = \int r^2 \frac{dr}{dz} dz \int dM N(M,z) \Delta_o^2(M,z) |\tilde{\zeta}[\vec{q}, M, z]|^2 \tag{6}$$

where $\tilde{\zeta}$ is the the Fourier transform of the cluster angular profile. The angular correlation function of the cluster induced anisotropy pattern is

$$C(\alpha, \sigma_b) = \frac{1}{2\pi} \int_o^\infty dq\ qP(q) J_o(q\alpha) \exp(-q^2\sigma_b^2) \tag{7}$$

where σ_b is the dispersion of a Gaussian approximating the angular response of the receiver. The full expressions for $P(q)$ and $C(\alpha, \sigma_b)$ should, in principle, include the effects of spatial correlations between clusters. These effects are ignored here, based on our estimation that they are small (see [9] and references therein) We give in Table 1 values of $C(0, 1'.9)$, for the C/S 400 GHz channel with angular resolution FWHM $= 1'.9 \cdot 2\sqrt{2ln2}$. In Fig.1 we plot the rms, single subtracted, CMB anisotropy as a function of the angular scales, for $\sigma_b = 1.9'$. A population of evolving clusters provides a rms signal of few $\times 10^{-6}$ on the C/S 400 GHz map.

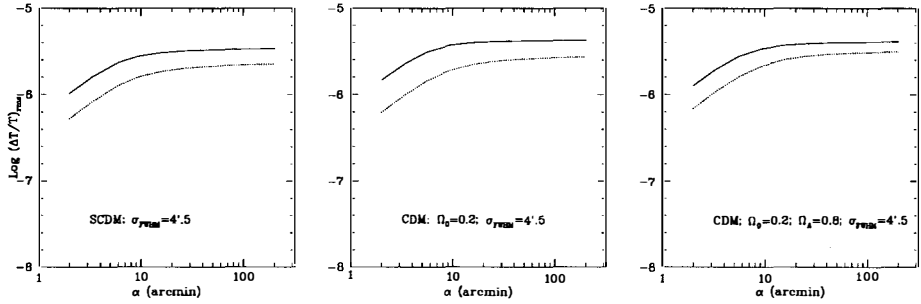

Figure 1: The rms temerature anisotropy induced by galaxy clusters in CDM scenarios as a function of the beamswitching angle α. Continuous curves refer to the case without IC gas evolution.

3 Cluster Counts

With respect to the incident radiation field, the change of the CMB intensity across a cluster can be viewed as a net flux emanating from the cluster. The flux is negative below the crossover frequency and positive above this characteristic frequency ($\simeq$ 217 GHz in the nonrelativistic limit). The differential flux measured at a given frequency from the cluster is

$$\overline{\Delta F}_\nu = \frac{2(kT_{CMB})^3}{(hc)^2}\overline{g}(x)y_o(M,z)\Xi(M,z)\,, \tag{8}$$

where Ξ is the beam convolved cluster angular profile and $\overline{g}(x)$ is the spectral function averaged over the passband of the channel with central frequency ν. We take the spectral response to be uniform with widths $\Delta\nu/\nu = \Delta x/x = 0.7$ at 400 GHz. Thus, the predicted number of clusters with a net flux $> \overline{\Delta F_\nu}$ is (see Fig.2)

$$N(>\overline{\Delta F_\nu}) = \int \frac{dV}{dz}dz \int_{\overline{M}} dM N(M,z)\,, \tag{9}$$

The lower integration bound, $\overline{M}$, is set from the requirement that the source flux is $> \overline{\Delta F_\nu}$.

The receivers of the C/S HFI are bolometers with a Noise Equivalent Power (NEP) of $\approx 10^{-17}\ WHz^{-1/2}$. The limiting flux is expected to be $\overline{F}_\nu^{noise} \approx NEP/\Delta\nu\sqrt{t}A\epsilon$, where t is the integration time in seconds, A is the effective mirror area in squared meters, and ϵ is the total (optical and electric) efficiency of the system. For C/S, NEP values of $2.7 \times 10^{-17}\ WHz^{-1/2}$ are expected at 400 GHz. The C/S telescope has an effective diameter $\approx$ 1 meter, and total efficiency of $\approx$ 0.30, so that with an integration time of one year we have $\overline{F}_\nu^{noise} \approx$ 20 mJy at 400 GHz. In Table 1 we also give the number of clusters with flux greater than $\overline{F}_\nu^{noise}$ and $2\overline{F}_\nu^{noise}$, corresponding to 1 and 2 sigma detections.

Note that these numbers are obtained by requiring that the flux collected by the receiver from the center of the cluster is greater than the limiting flux. This estimate could be conservative for extended clusters if the flux emanating from the central region is under the detection limit. However, a further smoothing of the observed map could help in extracting additional clusters out of the noise (the noise of the smoothed map is lower by the factor $\theta_{smooth}/\theta_{obs}$, where θ_{smooth} and θ_{obs} are the resolutions of the smoothed and observed maps, respectively). This is reflected in Figs. 2a and 2b, where we show the cluster number counts expected after

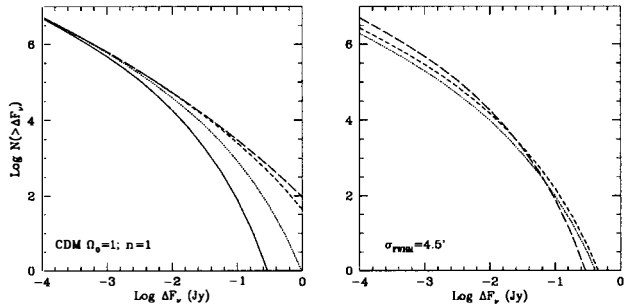

Figure 2: Cluster counts for the C/S 400 GHz channel in a flat CDM model (panel a) for different angular resolutions (continuous, dotted, short-dashed and long-dashed lines for 4.5′, 10′, 30′ and 60′, respectively) with IC gas evolution, and for different cosmological models (panel b; dotted, short-dashed and long-dashed lines for open CDM, CDM+Λ and standard CDM respectively).

smoothing the original map. The noise level of the smoothed maps at 400 GHz is 10.3, 3 and 1.5 mJy for final resolutions of 10, 30 and 60 arc-minutes, respectively. Correspondingly, the number of clusters that can be detected increases.

Most of the detected clusters are expected to be contained just in one pixel of the mm and sub-mm maps, and so it will be difficult to clearly identify clusters under these circumstances. It is therefore important to determine also the distribution of angular sizes of clusters whose fluxes are higher than the above limiting values. This is accomplished by calculating the distribution

$$N(\theta_{FWHM}, z) = N(M, z)\frac{dM}{d\theta_c}\frac{d\theta_c}{d\theta_{FWHM}} \tag{10}$$

where θ_{FWHM} is the FWHM of the beam convolved cluster profile. In Fig.3 we show the quantity $\mathcal{N}(>\theta_{FWHM}) = \int_{\theta_{FWHM}}^{\infty} d\theta'_{FWHM} \int dz N(\theta'_{FWHM}, z)$, where the double integral is performed so that a cluster with a flux $> \overline{F_\nu^{noise}}$ has a FWHM angular size larger than $\overline{\theta}_{FWHM}$.

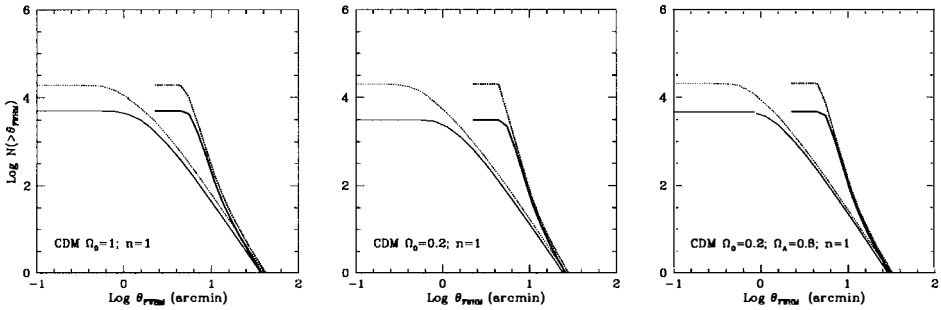

Figure 3: The distribution $\mathcal{N}(>\theta_{FWHM})$ for clusters above the limiting flux for the C/S 400 GHz channels are shown for flat and open CDM models. Thin lines, with (continuous) and without (dotted) IC gas evolution, refer to the distribution of intrinsic dimension. Thick lines, with (continuous) and without (dotted) IC gas evolution, refer to 4.5 arcmin smoothing of the C/S maps.

4 Discussion.

The approach described here is phenomenological, as it is based on the normalization of the predicted cluster number counts so they reproduce the locally observed distribution. We consider our normalization to the XRLF to be quite robust, in the sense that a statistically significant fit to the data is obtained over a range of X-ray luminosities from $\sim 10^{43}$ to $\gtrsim 10^{45}$ erg s^{-1}.

A comparison of the number counts (for a given value of h) for flat and low density CDM cosmologies shows that the counts increase with decreasing Ω_0. This increase is larger when the IC gas is not supposed to evolve. Note that the strong dependence of the counts on the assumed value of the Hubble constant complicate somehow the comparison between flat and open cosmologies: low density, either open or flat, CDM models with $h \simeq 0.6$ predict the same cluster counts of the SCDM model with $h = 0.5$.

It should also be noted that, from one hand, our scaling of the gas fraction to a value of 10% in a rich, local cluster may be conservatively low, judging by some observational indications of a value of up to 30% [10]. Increasing f produce a substantial increase of the predicted cluster counts. On the other hand, the number counts shown in Table 1 are optimistic in several ways. First, sky confusion was not taken into account; its inclusion will obviously reduce our predicted numbers in a way which will largely depend on the degree of sensitivity in modeling emission from Galactic dust and far-IR emission from other galaxies. The Galactic disk region will reduce useful sky coverage to $\approx$ 80%. The integrated emission from galaxies is not known, but in some models with strong luminosity or density evolution the predicted intensity levels (e.g., [11,4]) may well exceed those corresponding to Comptonization. A quantitative comparison is not warranted at this stage because of the high degree of uncertainty in these models. In the analysis of actual data it will likely be possible to separate out the S-Z component based on its unique spectral shape and its larger characteristic spatial scales. For now, we include in Table 1 the numbers of clusters with $\overline{\Delta F}_\nu > 2\overline{F}_\nu^{noise}$. From these we can predict that if sky-confusion is minimal, then a full sky map – which can be generated by C/S at 400 GHz (*i.e.* , with a resolution of 1.9′) after one year of operation – should include as many as $\approx 10^3$ clusters detected at the 2σ statistical significance level.

References

[1] Sunyaev, R.A. & Zel'dovich, Y.B. 1970, *Astrophys. Sp. Sci*, **7**, 4

[2] Rephaeli, Y. 1995, *Ann. Rev. Astr. Astrophys.* **33**, 541

[3] Fixsen, D.J. *et al.* 1996, *preprint*

[4] Wright, E.L. *et al.* 1994, *Ap. J.* 420 450

[5] Colafrancesco, S., Mazzotta, P., Rephaeli, Y. & Vittorio, N. 1996, *Ap. J. in press*

[6] Colafrancesco, S., Vittorio, N. & Mazzotta, P., 1996, these Proceedings

[7] Colafrancesco, S. & Vittorio, N. 1994, *Ap. J.* 422 443

[8] Press, W.H. & Schechter, P. 1974, *Ap. J.* 187 425

[9] Colafrancesco, S., Mazzotta, P., Rephaeli, Y. & Vittorio, N. 1994, *Ap. J.*

[10] White, S.D.M. *et al.* 1993, *Nature* **366**, 429

[11] Beichman, C.A. & Helou, G. 1991, *Ap. J. Lett.* 370 1

$\Delta T/T$ AND INHOMOGENEOUS REIONIZATION

N. Aghanim , J.L. Puget and R. Gispert
Institut d'Astrophysique Spatiale, Orsay, France.

Abstract

We discuss the photoionization of the intergalactic medium by early formed quasars and propose a mechanism which could generate measurable temperature fluctuations of the cosmic microwave background (CMB). Early quasars produce individual ionized bubbles. We evaluate both thermal and kinetic (first-order Doppler) Sunyaev-Zeldovich (SZ) effects associated with those ionized regions. Whereas the former is negligible, the latter generates detectable secondary small and medium scale CMB anisotropies. We find that this effect could produce measurable individual sources with temperatue fluctuations $\delta_T \simeq 10^{-6}$ to $\simeq 10^{-4}$ on scales up to 1°, introducing a non gaussian signature in the statistics of the primordial anisotropies.

1 Introduction

Reionization must have occure between recombination ($z \simeq 1000$) and the present time [5]. Hereafter, we assume that it is due to sources including early formed quasars ($6 < z < 10$). The main effect of the reionization is to wash out some of the temperature fluctuations of the CMB on small scales which undergo Thomson scattering on the reionized IGM. We present here a new kind of detectable secondary fluctuations that might appear induced by the kinetic Sunyaev-Zeldovich (SZ) effect [7] in the context of an inhomogeneous reionization by early quasars. At times preceding the full reionization, quasars ionize the gas around themselves producing ionized bubbles which are moving together with the quasars in the large scale gravitational potential wells. An effect equivalent to the SZ kinetic effect for rich clusters creates relative temperature fluctuations which are proportional to the product of the Thomson optical depth of the ionized bubble τ by the ratio of the quasar radial velocity to the velocity of light (v_r/c). Contrary to clusters , the corresponding thermal SZ effect is negligible in our case.

The present work has no strong dependence on quasar formation theory, the presence of any high luminosity ionizing point sources will have the same kind of effect on the CMB, as long as it can roughly account for the total reionization of the universe at the present time.

Hereafter, we neglect the contributions other than those induced by hydrogen and helium, and assume an isotropic emission inducing a spherical bubble. Other possible geometrical effects are neglected.

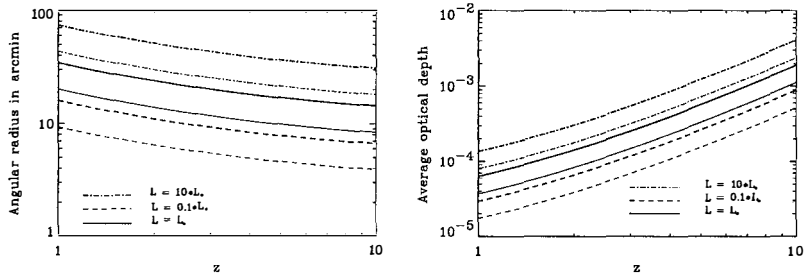

Figure 1: *Left: Angular radius Right: optical depth of an ionized bubble as functions of the redshift for three values of the quasar luminosity. The series of thin lines are obtained with quasar lifetime* $t_q = 10^7$ *yrs and the thick ones with* $t_q = 5\,10^7$ *yrs.*

2 Temperature of the bubble

If the intergalactic matter around the quasar is ionized by the emitted radiation, the ionization of a hydrogen atom produces a photoelectron with an average kinetic energy defined by $\overline{E_c} = \overline{E_{UV}} - 13.6\,\mathrm{eV}$, where $\overline{E_{UV}}$ is the average energy of the ionizing photon. Electrons and protons rapidly thermalize owing to the short time scale of the Coulomb interactions, therefore, the temperature of the plasma is given by $T = \overline{E_c}/3k_b$ as long as the cooling by recombination is negligible (k_b is the Boltzmann constant).

We compute the average energy of the ionizing photon $\overline{E_{UV}} = h_{pl}\overline{\nu}$ using a power law spectrum for the quasar $L \propto \nu^{-1.5}$ ($\lambda < 1216\,\mathring{A}$) [2], where L is the luminosity of the quasar and ν the frequency, and assuming that every photon is absorbed sooner or later. We find a temperature $T \approx 10^5$ K. In the bubble, the gas is fully ionized, therefore there is no collisional cooling. We find that the bremsstrahlung cooling time is longer than the age of the universe. Likewise, we investigate the effect of the inverse Compton cooling and find that it becomes important for redshifts greater than $10\,h^{2/5}$ (cooling time equal to the age of the universe), which gives $z \simeq 8$ for $h = 0.5$. In this case, we check that the temperature of the bubble decreases by a factor 2 at $z = 10$. The Compton cooling does not change drastically the temperature. The exact temperature is not critical, therefore, we assume that it remains constant at $T \approx 10^5$ K. This approximation breaks down for redshifts significantly larger than 10.

3 Radius

Let us assume that a quasar turns on at a redshift z_{on} and turns off at z_{off}, in the assumption of a lifetime t_q short compared to the expansion time, we have $1 + z_{on} \approx 1 + z_{off}$. The proper radius R of an ionized bubble at a given time t (when it has not reached the stationary Strömgren sphere state) is computed by writing that every UV photon emitted by the quasar is absorbed through the photoionization of a neutral atom. The main quantity that rules the size of the bubble is the total number of ionizing photons emitted by a quasar during its lifetime. It is proportional to the product Lt_q.

The proper radius R will reach a maximum value at the redshift z_{off} and then it undergoes the average Hubble expansion. At a given redshift z smaller than z_{off}, the expansion leads to the following relation:

$$R(l_Q, z) \;=\; R_c l_Q^{1/3}(1+z)^{-1}. \qquad (1)$$

where $R_c = 10 \left(\frac{\Omega_b h^2}{0.015}\right)^{-1/3} \left(\frac{\Omega_0}{1}\right)^{-1/6}$ Mpc is a characteristic radius for $t_q = 10^8$ yrs associated with a characteristic luminosity, L_c^* and $l_Q = L/L_c^*$. The comparison between the proper and the Strömgren radii shows that recombinations can be neglected. Figure 1, left, show the angular scale of the bubble versus the redshift different values of t_q and L.

4 Optical depth

Using the proper radius of the ionized sphere, we compute the average Thomson optical depth over the spherical ionized bubble, it is given by:

$$\tau_a = \frac{2}{3}\tau_c l_Q^{1/3}(1+z)^2 \tag{2}$$

where $\tau_c = \sigma_T n_{e0} R_c$ the characteristic optical depth and n_{e0} the electronic density at present time. Figure 1, right, shows the dependence of the bubble optical depth with both the lifetime of the quasar and its luminosity, as a function of the redshift. We note that typical optical depths of 10^{-3} (comparable to those of rich clusters) are reached for our redshift range of interest.

5 Sunyaev-Zeldovich effects

Thermal Sunyaev-Zeldovich effect

Compton scattering of the CMB radiation on hot free electrons imprints on the incident photon spectrum a signature known as the thermal SZ effect [7] by redistributing the photons in the spectrum with a shift towards higher frequencies. For an isothermal sphere, the comptonization parameter, y, which characterizes the SZ distortion is given by: $y = \frac{k_b T_e}{m_e c^2}\tau$, where T_e is the electronic temperature and $m_e c^2$ is the electron rest mass.

Kinematic Sunyaev-Zeldovich effect

The significance of the so called kinetic effect has been given in [7]. The motion of a cluster with respect to the background leads (due to the Doppler effect) to an additional change of the radiation temperature in its direction, because of the finite optical depth associated to the bubble. The spectrum of the distortion is indistinguishable from a primordial anisotropy spectrum which is equivalent to a simple temperature change. The observed radiation temperature is changed by $\delta_T = \Delta T/T = -(v_r/c)\tau$, in a direction crossing the bubble where τ is the Thomson optical depth and v_r is the radial component of the bubble peculiar velocity (a positive one corresponds to a recession velocity).

We will assume that the bubbles produced by quasars are random substructures in the linear potential of large scale structures and thus in motion with them. The distribution of their radial velocities is therefore given by the large scale velocity field gaussian distribution with a velocity dispersion $\sigma_v(z)$. We take a semi empirical approach using the z dependence given by the linear theory and a conservative value of $\sigma_{0v} = 300$ km/s [4]. The average anisotropy associated with an ionized bubble is given by: $\delta_T = -(v_r/c)\tau_a$ We find that the thermal effect is negligible compared with the kinetic effect for the ionized bubbles. This is opposite to what happens for clusters, because the intracluster gas is much hotter ($\approx 10^8$ K).

6 Generalization to quasars distribution

The distribution of ionized bubbles is derived from the quasars luminosity function $\Phi(L, z)$ which gives for a redshift z the comoving space density of quasars as a function of the luminosity. The

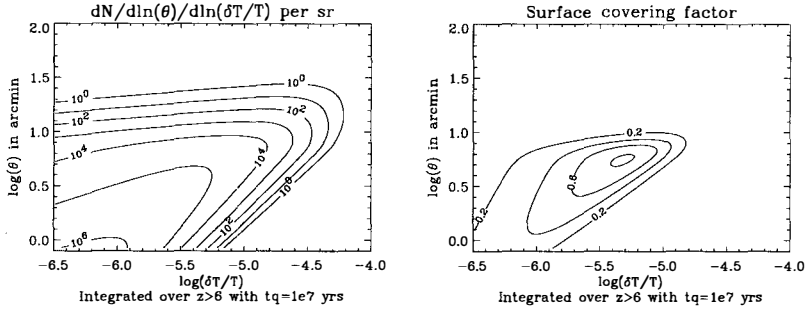

Figure 2: *Left: Number of ionized bubbles per unit solid angle, logarithmic interval of $|\delta_T|$ logarithmic interval of the angular radius θ plotted as a function of $log\delta_T$ and $log\theta$ integrated over $z > 6$ and computed for lifetime $t_q = 10^7$ yrs. Right: The surface covering factor as a function ($log\delta_T$) and $log\theta$ integrated over the redshifts ($z > 6$) for lifetime $t_q = 10^7$ yrs.*

quasars luminosity function is not well determined yet, in particular at high redshifts ($z > 3$), owing to the small number of observed sources. We use the luminosity function given by Boyle [3]. For $z > 3$, following [8] and [6] we introduce an exponential decay by a factor of 2 per unit redshift in the comoving number density.

The Gunn-Peterson test [5]for hydrogen shows that the universe is ionized at redshift smaller than 5. In order to evaluate the redshift z_{ion} of the reionization of the universe for hydrogen, we compute the porosity parameter P. The total reionization of the IGM occurs for P reaching 1 at $z_{ion} \approx 5.7$, which is compatible with the observed reionization of the universe.

Using expressions of the angular size, optical depth and temperature fluctuations of the ionized bubbles around quasars, we compute the number of bubbles at redshift z with angular size θ and temperature fluctuation δ_T in the universe, per unit of solid angle. See [1] for detailed computations. The results are plotted Fig. 2, left, integrated over the redshifts ($z > 6$) for $t_q = 10^7$ yrs.

We also compute the covering surface parameter which is the fraction of the sky covered by ionized bubbles inducing a distortion of amplitude δ_T and angular size θ at redshift z. The results plotted Fig. 2, right, are also integrated over z and given for $t_q = 10^7$ yrs.

7 Discussion and conclusions

We have discussed the effects of ionization of the IGM by early formed quasars on the cosmic microwave background as calculated in previous sections. We have shown the thermal SZ effect was negligible compared to the kinetic one. The amplitude of the largest temperature fluctuations induced by the latter mechanism are comparable to the the primordial fluctuations at scales comparable with the scales of the Doppler peaks ($10'$ to $1°$). These secondary fluctuations have no spectral signature to distinguish them from the primordial ones. Figure 1, left, shows that there are approximately 100 objects per unit solid angle with associated temperature fluctuations some 10^{-5} and angular radius 5 to 10 arcmin. The counts depend significantly on the quasar lifetime value, decreasing the lifetime t_q decreases the size of the bubbles and increases the number of bubbles. Figure 2, right, representing the surface covering factor, shows that the ionized bubbles around quasars are close to cover the whole sky although they do not fill the space until $z < z_{ion} = 5.7$.

We have simulated maps of these secondary anisotropies under simple geometrical assumptions (spherical bubbles), using the counts of ionized bubbles associated with quasars. The positions of the bubbles are random, this is a rather good assumption since the clustering of quasars is still uncertain. As could be expected, the distribution of the temperature fluctuations induced by quasars is far from

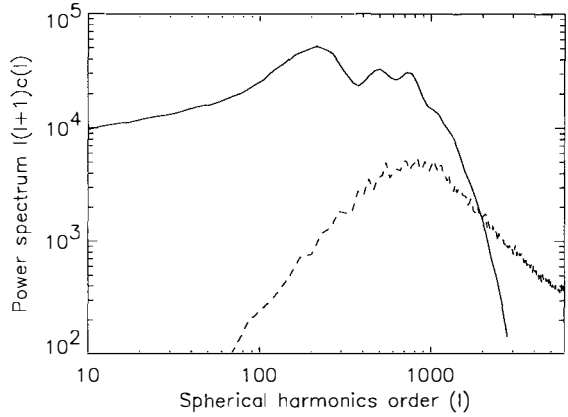

Figure 3: *Power spectra of the anisotropies in the spherical harmonics versus the multipoles. Solid curve for the primary CMB and ashed curve for the fluctuations induced by the bubbles for* $t_q = 10^7$ *yrs*

being gaussian. The presence of early ionizing sources induces additional non gaussian anisotropies. This is an important effect that might be taken into account if one wants to test the gaussiannity of the primordial anisotropies of the CMB.

Cosmological models show that there is an angular cut off in the spectrum of the primordial anisotropies. The bubbles contribution to the observed CMB could be important or may be dominant, in particular at scales where the primordial fluctuations are "washed out" because of the damping associated with the width of the the last scattering surface, as shown Fig. 3. Furthermore, Fig. 3 indicates that the secondary anisotropies due to ionized bubbles add a significant power ($\simeq$ 15%) at scales corresponding to the secondary Doppler peaks.

In the hypothesis of an ionization due to individual sources of radiation, the whole formalism we develop for early quasars [1] remains valid whatever the kind of sources, early galaxies, first generation of stars, ...

References

[1] Aghanim, N.,Désert, F.X., Puget, J.L., Gispert, R. 1995, *Astr. Astrophys.*, in press

[2] Bechtold, J. et al. 1987, *Astrophys. J.* **315**, 180

[3] Boyle, B. J 1991, in Texas/ESO-CERN Symposium on Relativistic Astrophysics, Cosmology and Fundamental Physics

[4] Faber, S. M., Courteau, S. J. A., Yahil, A. 1993, in Proc. 9^{th} *IAP Astrophysics Meeting, Cosmic Velocity Fields*, ed. M. Lachièze–Rey & F. R. Bouchet (Editions Frontières)

[5] Gunn, J. E., & Peterson, B. A. 1965, *Astrophys. J.* **142**, 1633

[6] Meiksin. A., & Madau. A. 1993, *Astrophys. J.* **412**, 34

[7] Sunyaev R. A., & Zeldovich, Ya. B. 1980, *M.N.R.A.S.* , **190**, 413

[8] Warren, S. J., Hewett, P. C., & Osmer, P. S. 1991, in *The Space Distribution of Quasars*, ed. D. Crampton (ASP Conf. Ser 21), 139

COBRAS/SAMBA AND MEASUREMENTS OF THE SUNYAEV-ZELDOVICH EFFECT

Martin G. Haehnelt[1]
[1] *Max-Planck-Institut für Astrophysik, Karl-Schwarzschild-Straße 1, 85740 Garching, Germany.*

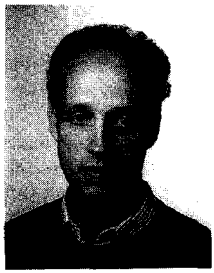

Abstract

The recently approved COBRAS/SAMBA cosmic microwave background (CMB) mission will also have a major impact on measurements of the Sunyaev-Zeldovich (SZ) effect. The frequency of three of the channels (150 GHz, 217 GHz, 353 GHz) are chosen to optimize measurements of the thermal and kinetic SZ effect mainly caused by hot gas in clusters of galaxies. Estimates of the number of detected clusters are somewhat uncertain due to incomplete knowledge of the gas mass function of clusters and the distribution of hot gas at large radii. Straightforward interpolation of X-ray observations of the 200 X-ray brightest clusters gives a firm lower limit of $\sim$ 3000 detected clusters of which roughly half should be resolved. If the gas distribution of clusters should turn out to be favourable and/or the cluster evolution with redshift is weak, this number could be higher by a factor of up to ten. Using an optimal filtering technique a measurement of the bulk peculiar velocity of a sample of about 200 of the resolved clusters will be possible with a 1σ error of $100 - 200\,\mathrm{km\,s^{-1}}$.

1 Sensitivity of COBRAS/SAMBA

For an unresolved cluster the "SZ-flux" due to Compton scattering by hot electrons can be written as

$$S_\nu = f_\nu \, g(h\nu/kT) \, Y, \tag{1}$$

where $g(h\nu/kT)$ describes the frequency dependence of the Compton distortion (Fig. 1), f_ν is a normalization constant and $Y = \int y \, \mathrm{d}\Omega$ is the Compton y parameter integrated over solid angle [1] [2] [3]. Y is proportional to the typical mass times the mass-weighted temperature within the radius where the density profile of the cluster becomes steeper than isothermal

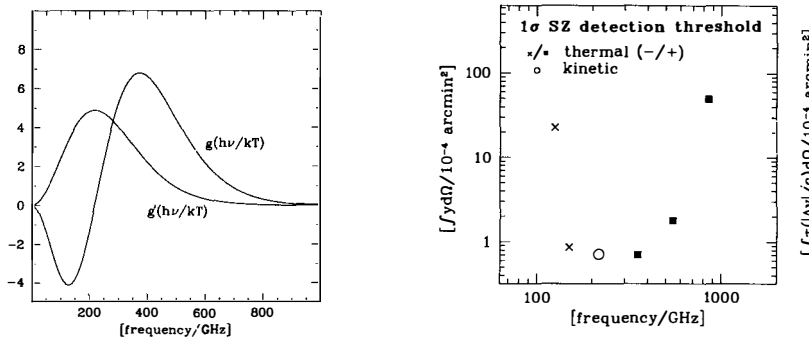

Figure 1: The left panel shows the frequency dependence of the thermal (g) and kinetic SZ (g') effect (equation 1 and 2). In the right panel the 1σ SZ detection threshold of the high frequency channels is shown in terms of the integrated Compton parameter $Y = \int y \mathrm{d}\Omega$.

(and/or the gas temperature starts to drop). The crosses and squares in Figure 1b show the 1σ SZ detection threshold of the high frequency channels in terms of Y . A typical value for the "SZ-channels" at 150 and 353 GHZ (maximum negative/positive SZ-flux) is 10^{-4}arcmin^2. This takes only detector noise into account and will be somewhat increased by residual noise from the foreground subtraction procedure. $3 - 10 \times 10^{-4}$arcmin^2 should be considered as a reasonable range for the expected detection threshold of an unresolved cluster (marked by the shaded region in Figure 2.)

2 SZ number counts of unresolved clusters

Straightforward interpolation of the properties of a flux-limited sample of the 200 X-ray brightest clusters by a factor 3-5 in flux gives a firm lower limit of $\sim$ 3000 detected clusters. More accurate estimates are difficult because the typical gas mass and mass-weighted temperature within the radius where the density profile of the cluster becomes steeper than isothermal (and/or the gas temperature starts to drop) are difficult to determine from X-ray observations which generally probe the gas and temperature distribution at considerably smaller radii. The typical Y-parameter of clusters of a given present-day number density is probably uncertain by a factor of two. The estimated number counts are also sensitive to

- the exact shape of the present-day mass function, especially the slope at large masses,
- the details of the assumed evolution of the cluster mass/temperature function,
- and the cosmological parameter.

Nevertheless, the Press-Schechter formalism can be used to evolve the observed present-day mass function of clusters backward in time to get a feeling for the influence of the uncertain

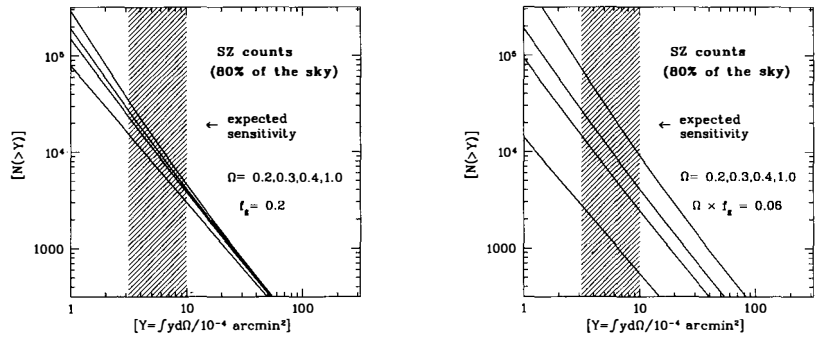

Figure 2: The expected number of detected clusters is plotted as function of the integrated Compton parameter $Y = \int y \, \mathrm{d}\Omega$ for different values of the total matter density Ω as indicated (Ω decreasing upwards). The present-day mass function of clusters was evolved backwards in time using the Press-Schechter formalism. An spectral index of $n = -1$ for the primordial density fluctuation spectrum on cluster scales is assumed. The expected sensitivity of COBRAS/SAMBA is indicated by the shaded area. The left panel is for fixed gas mass fraction $f_{\mathrm{g}} = 0.2$, while the right panel assumes compatibility with the nucleosynthesis constraint $\Omega \times f_{\mathrm{g}} = 0.06$.

parameter [4] [5]. Assuming the usual observationally normalized scaling of the cluster temperature $T \propto M^{2/3} \, (1 + z)$ we can work out the expected number counts $N(> Y)$. In Figure 2 these are shown for different values of Ω and different assumptions for the total fraction of hot gas. The left panel assumes a fixed gas mass fraction while the right panel assumes a gas mass fraction compatible with the nucleosynthesis constraint. The total number of clusters detected by COBRAS/SAMBA will depend strongly on the assumed sensitivity ($N \sim Y^{-3/2}$). The large difference between the two panels illustrates the uncertainties due to our insufficient knowledge of the total mass of hot gas in clusters.

3 Properties of the detected cluster sample

The properties of the detected cluster sample will also depend on the uncertainties mentioned above. If a detection threshold of 3×10^{-4}arcmin^2 and $\Omega = 1$ is assumed a sample of 10^4 clusters is expected. This is about a factor of two larger than the number of clusters in the extended Abell catalogue. As shown in Figure 3a the typical redshift would be $z = 0.1$, very similar to that in the Abell catalogue, while the typical mass would be somewhat smaller. Unfortunately, the sensitivity and spatial resolution of COBRAS/SAMBA will not be sufficient to make use of the fact that the "surface brightness" of the SZ effect is independent of redshift. Figure 3b shows that a flat redshift distribution would only be seen with considerably better sensitivity and in a low Ω universe. However, a high redshift tail might still be seen if Ω is low [6].

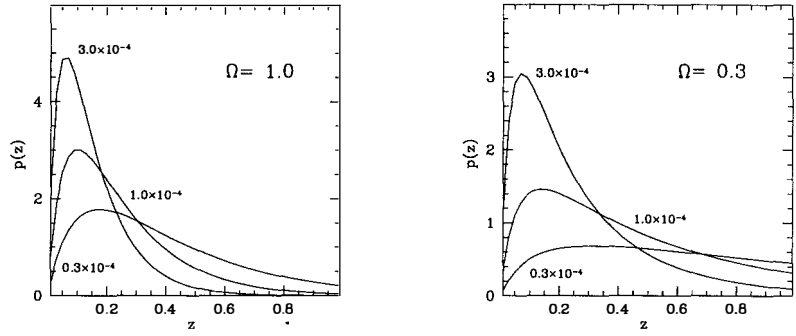

Figure 3: The left panel shows the expected redshift distribution for $\Omega = 1$ and for different sensitivity limits in terms of the integrated Compton parameter $Y = \int y \, d\Omega$ as indicated on the plot. The right panel is the same for $\Omega = 0.3$.

4 The kinetic SZ effect

For an unresolved cluster the kinetic "SZ-flux" due to peculiar motion of the hot gas in a cluster with respect to the CMB can be written as

$$S_\nu = f'_\nu \, g'(h\nu/kT) \int \tau |v_{\rm pec}/c| \, d\Omega, \tag{2}$$

where $g'(h\nu/kT)$ describes the frequency dependence of the kinetic distortion (Fig. 1a), f'_ν is a normalization constant, τ is the Thompson optical depth and $v_{\rm pec}$ is the peculiar velocity of the cluster. The frequency dependence is that of a temperature fluctuation in the CMB and for a typical cluster the change in brightness temperature at the cluster center is of order

$$\Delta T \sim 30 \left(\frac{n_e}{3 \times 10^{-3} \, {\rm cm}^{-3}} \right) \left(\frac{r_c}{0.4 \, {\rm Mpc}} \right) \left(\frac{v_{\rm pec}}{500 \, {\rm km \, s}^{-1}} \right) \mu{\rm K}, \tag{3}$$

where n_e is the electron density in the core, r_c is the core radius and we have scaled to the values of the Coma cluster (assuming a distance of 140 Mpc) [7] [2]. The open circle in Figure 1b shows the sensitivity of COBRAS/SAMBA for an unresolved cluster in terms of $\int \tau |v/c| \, d\Omega$.

5 Measuring bulk velocities of clusters

For the kinetic effect the expected noise level due to confusion with primary fluctuations is generally of order or larger than the expected signal. It is therefore essential to use the knowledge of the CMB "noise" properties and the gas distributions of the individual clusters (which can be obtained by the mission itself and from X-ray observations, respectively). This knowledge makes it possible to analyze the CMB maps of resolved clusters with a spatial filter optimized for individual clusters. An improvement in signal-to-noise by a factor of two is easily achievable, and even a factor of 10 is possible if the gas mass distribution is well known from a high-quality X-ray map [8]. The final signal-to-noise ratio depends crucially on the cosmological model and

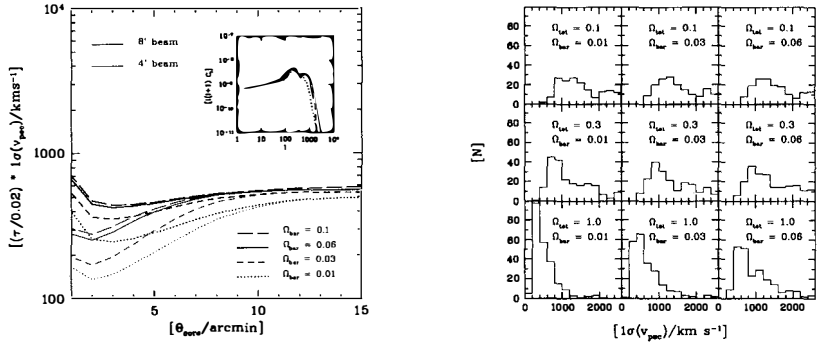

Figure 4: The left panel shows the 1σ error in the determination of the peculiar velocity as a function of the core radius of the cluster using an axisymmetric "optimal" filter function for a standard CDM scenario ($\Omega_{\rm tot} = 1$, $H_0 = 50\,{\rm km\,s^{-1}\,Mpc^{-1}}$) with varying baryonic fraction. The pixel noise is fixed and corresponds to $7\,\mu$K in the 4' (FWHM) beam. Thick curves are for a beam size of 8' and thin curves are for a beam size of 4'. The inset shows the angular power spectra of temperature fluctuations for the three cosmological models. The right panel shows the distribution of expected 1σ errors of peculiar velocity measurements for the XBACs cluster sample for different cosmological models. $\Omega_{\rm tot}$ and $\Omega_{\rm bar}$ vary as indicated in the plot. An axisymmetric optimal filter was applied using a β-model for the cluster gas distribution. The pixel noise is fixed and corresponds to $7\,\mu$K in the 4' beam.

the angular resolution of the instrument (Fig. 4a), and it is not currently clear whether a meaningful peculiar velocity measurement for individual clusters will be possible. Prime candidates are X-ray luminous clusters at intermediate redshift with core radii just below the Doppler peak scale. For a favourable but still rather standard cosmological scenario (standard CDM with low baryon fraction) and a good angular resolution (4' FWHM), the peculiar velocity of as many as 30 individual clusters might be determined accurately. Even if this is impractical, it should still be possible to determine the bulk motion of an ensemble of 200 X-ray luminous clusters at redshifts $\gtrsim 10000\,{\rm km\,s^{-1}}$ with an accuracy of order $100 - 200\,{\rm km\,s^{-1}}$ (Fig. 4b).

6 Concluding remarks

COBRAS/SAMBA will produce the first all-sky SZ maps. In these maps most known clusters of galaxies will be detected roughly half of which will be resolved. It will therefore be possible to study the gas distribution of a large sample of clusters out to the virial radius. Once the cosmological parameter are known with good precision (the primary aim of the COBRAS/SAMBA mission) problems like a possible clumping of the gas can be addressed. Relativistic corrections to equation (1) and (2) might also allow to achieve accurate measurements of the temperature of the cluster gas [3] [9]. Comparison of SZ and X-ray properties of clusters will significantly advance our understanding of cluster evolution. If the gas mass fraction in clusters is high and there is as little evolution in the cluster population as indicated by current X-ray observation the SZ effect might also be a suitable tool to detect clusters at high redshift in appreciable numbers. So far, not much is known about bulk velocities on scales larger than 5000 to $10000\,{\rm km\,s^{-1}}$.

The measurement of the bulk velocity of a volume-limited sample of 119 Abell clusters out to a distance of 15000 km s^{-1} gave a value considerably higher than expected in most cosmological scenarios [10]. The completely independent measurement by COBRAS/SAMBA on even larger scales should clarify this situation.

References

[1] Sunyaev R.A., Zeldovich Ya., 1970, Astroph. Sp. Sci., 7, 3

[2] Rephaeli Y., Lahav O.,1991, ApJ, 372,21

[3] Rephaeli Y., 1995, ARA&A, 33,541

[4] Bahcall N., Cen R. 1993, ApJ, 407, L49

[5] De Luca A., Désert F.X., Puget J.L., 1995, A&A, 300,335

[6] Barbosa D., Bartlett J.G., Blanchard A., Oukbir J., 1996, A&A, in press

[7] Sunyaev R.A., Zeldovich Ya.,1980, MNRAS, 190, 413

[8] Haehnelt M., Tegmark M., 1996, MNRAS, 279, 545

[9] Giard M., these proceedings

[10] Lauer T.R., Postman M., 1994, ApJ, 425, 418

Evolutionary Models of Galaxy Emission in the FIR/submm Range

Bruno Guiderdoni[1], Eric Hivon[2], François R. Bouchet[1], & Bruno Maffei[3]
[1] *Institut d'Astrophysique de Paris, CNRS, 98bis Boulevard Arago F-75014 Paris France*
[2] *Theoretical Astrophysics Center, Juliane Maries Vej 30, DK-2100 Copenhagen Denmark*
[3] *Queen Mary and Westfield College, Mile End Road, London E1 4NS UK*

Abstract

Most models of FIR/submm emission of galaxies are based on phenomenological extrapolations of the nearby IRAS luminosity function at 60 μm. They generally assume a single redshift of galaxy formation which acts as a cut-off in the extrapolation. Nevertheless, such an assumption is invalid in the paradigm of the hierarchical growth of structures which states that galaxy formation is a continuous process. In this framework, this paper proposes a new modelling of the evolution of the FIR and submm properties of galaxies which includes the following series of physical processes: growth of linear perturbations (gravitationally dominated by dark matter), non-dissipative collapse and virialization of haloes, shock-heating and subsequent cooling and dissipative collapse of baryonic gas, formation of a rotationally-supported disk-like core, star formation and stellar evolution, stellar feedback, stellar emission, absorption of star light by dust and re-emission in the FIR and submm. The model fairly reproduces the IRAS luminosity function and faint galaxy counts, and gives predictions of the deep counts and diffuse background of unresolved galaxies in the FIR and submm ranges, which are compared with the present upper limits and claimed detection. This first study should help to make specific predictions for the forthcoming satellites which will observe the submm sky with an unprecedented level of sensitivity and spatial resolution.

1 Introduction

After the great success of the COBE mission, new projects like the COBRAS/SAMBA satellite experiment aim at observing the anisotropies of the CMB on scales below the degree (see the presentation by Bouchet *et al.*, this Conference). On these scales, the separation of the various foregrounds and backgrounds which superimpose to the fluctuations of the CMB is more difficult than for the 7^o field of view of the COBE DMR experiment. In this perspective, the French RUMBA collaboration (standing for Research Upon Microwave Background Anisotropies) is developping simulations of the contributions of these various components to the fluctuations of the submm sky in order to study the

possible accuracy of their separation. The diffuse background of unresolved galaxies is one of these components. This background might have been observed for the first time as an isotropic component in FIRAS residuals (see Puget *et al.* 1996).

The numerous theoretical estimates of this diffuse background which are proposed in the literature are sensitive to the unknown evolution of galaxies at high redshift. This uncertainty has particularly strong consequences in the submm range, since there is a wavelength range, between $\sim$ 600 μm and $\sim$ 4 mm, where the distance effect is counterbalanced by the "negative k–correction" due to the huge rest–frame emission bump at $\sim$ 100 μm. In this range, the apparent flux of galaxies depends weakly on redshift. The modelling of the observer–frame submm fluxes, faint galaxy counts and diffuse background of unresolved galaxies is consequently very sensitive to the early stages of galaxy evolution. Moreover, this particular range brackets the maximum of emission of the CMB. Two classes of models have been proposed to predict the amplitude of the background, which could be called "backward evolution" and "forward evolution", following the good revue by Lonsdale (1996). Nevertheless, both classes of models assume that all galaxies form at the same redshift z_{for} and that there is no number evolution. As a matter of fact, the paradigm of the hierarchical growth of structures implies that there is no clear–cut redshift z_{for} since galaxy formation is a continuous process. Only Blain & Longair (1993) proposed a formalism to compute the redshift range of galaxy formation and consistently estimate the intensity of the submm background.

In order to implement a model of photometric and chemical evolution of galaxies into a more realistic scenario of dynamical formation, we have hereafter used ideas which have been elaborated by various authors during the last ten years (White & Rees 1978; Schaeffer & Silk 1985; Evrard 1989; Cole 1991; Blanchard *et al.* 1992; White & Frenk 1991; Lacey & Silk 1991; Lacey *et al.* 1993, Kauffmann *et al.* 1993, 1994; Cole *et al.* 1994; Heyl *et al.* 1995). The last seven papers of the previous list used various formalisms to compute the formation rate of dark matter haloes within the paradigm of the hierarchical growth of structures and implemented the astrophysics of galaxy formation and evolution in the haloes, with various levels of complexity. It turns out that, in spite of differences in the details of the models, these approaches share the same spirit and lead to conclusions in the UV, visible and (stellar) NIR which are remarkably similar. None of these models has been applied, up to now, to the prediction of the properties of galaxies in the FIR and submm ranges. This is the purpose of this paper. A preliminary version of these results is presented in Guiderdoni *et al.* (1996a). The results will be fully discussed in Guiderdoni *et al.* (1996b). A companion paper (Hivon *et al.* 1996) will show simulations of the anisotropies of the diffuse submm background due to galaxies and will study the possibility of their detection, especially with COBRAS/SAMBA. Forthcoming works will try to fix out some of the shortcomings detected in this preliminary study.

2 A Schematic View of Galaxy Formation

2.1 Physical Processes

We have to identify the main physical processes which connect the mass of the initial perturbation to the FIR and submm radiation emitted by the end–product galaxy. If we assume that the universe is dominated by non–baryonic dark matter, the formation and evolution of a galaxy in its dark matter halo can be briefly sketched as follows: the initial perturbation, which is gravitationally dominated by non–baryonic dark matter, grows and collapses. After the (non-dissipative) collapse, and subsequent violent relaxation, the halo virializes, through the formation of a mean potential well seen by all particles, which consequently share the same velocity distribution. The shock–heated baryonic component cools and collapses at the center of the potential well. Since the baryons initially share the small rotation velocity of the halo created by tidal interactions with other haloes, and because of angular momentum conservation, their collapse stops when they reach rotational equilibrium. Stars begin to form in this disk-like baryonic core and evolve through the main stages of stellar evolution. The luminosity and spectrum of the stellar population strongly change during this evolution. At the end

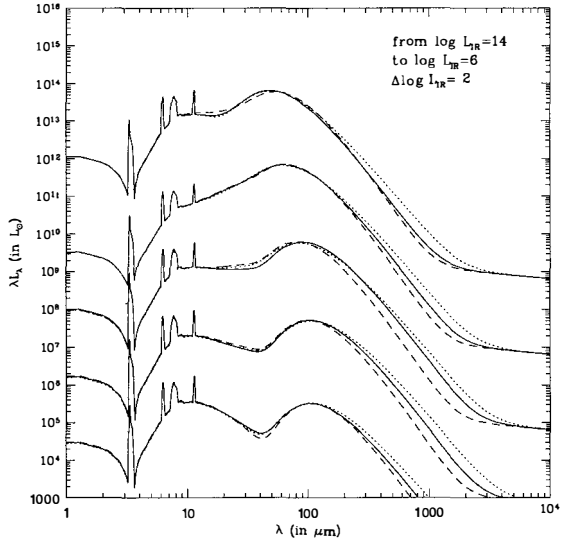

Figure 1: Models for emission spectra in the FIR and submm, for IR luminosities 10^6, 10^8, 10^{10}, 10^{12}, and $10^{14} L_{bol\odot}$. Emissivity index of big grains: $m = 2$ (dashes), $m = 1.5$ (solid lines), $m = 1$ (dots).

of their lifetime, stars explode and eject gas, heavy elements and energy into the interstellar medium. This energy feedback is likely to alter the star formation efficiency. Part of the UV and visible light is absorbed by dust and the energy is re–emitted in the FIR and submm ranges (hereafter L_{IR}). Finally, we have to conceive these evolutionary processes in the framework of the continuous, hierarchical growth of structures, in which small haloes merge to form bigger haloes. Moreover, galaxy merging in these merged haloes triggers bursts of star formation.

2.2 Haloes

We need simplifying assumptions to build semi–analytic models including these evolutionary processes. In particular, the initial, linear perturbation is assumed to be spherical and homogeneous. This is the so–called "top–hat" model, which has the friendly property of being entirely defined by two parameters, for instance the size R and the density contrast $(\delta\rho/\rho)_{z=0} \equiv \delta_0$ which are the linearly–extrapolated values at $z = 0$, or, equivalently, by its mass M and collapse redshift z_{coll}. If ρ_0 is the current mass density of the universe, we have $M = (4\pi/3)R^3\rho_0$. The extrapolated density contrast, and the ratio of the radius of maximal expansion r_m to the linearly–extrapolated size R, can be respectively computed as functions of the redshift of collapse z_{for}. After the collapse and violent relaxation, a mean potential well forms and the virialized halo results in a singular, isothermal sphere truncated at "virial radius" $r_V = r_m/2$. The properties of the virialized halo, such as its circular velocity V_c, its density profile $\rho(r)$ and its virial temperature T_V, are entirely computable as functions of M and z_{coll}.

We hereafter use the peaks formalism (Bardeen *et al.* 1986), as in Lacey & Silk (1991) and Lacey *et al.* (1993) to compute the formation rate and total number density of collapsed haloes. The method is fully discussed in Guiderdoni *et al.* (1996b). Our standard cosmological model is the CDM with $\Omega_0 = 1$, $h = 0.5$, $b = 1.5$ which stands below the COBE normalization, but gives a good fit on galaxy scales. We also take $\Omega_{bar} = 0.05$.

3 Galaxy Formation in Dark Matter Haloes

3.1 Cooling and dissipative collapse

The baryonic gas cools down in the potential well of the dark matter halo, by a process identical to cooling flows observed at the center of rich clusters. The cooling time at halo radius r is:

$$t_{cool}(r) = \frac{3}{2}\frac{n_{tot}(r)kT_V}{n_e^2(r)\Lambda(T_V)} = \frac{3\pi G\mu_e^2 m_p^2}{\Omega_{hot}}\frac{r^2}{\Lambda(T_V)} \quad (1)$$

with $\mu_e = 1.14$ for ionized primordial gas. The cooling curve $\Lambda(T)$ takes into account the various cooling processes. Hereafter, we do not take the Z dependence of $\Lambda(T)$ into account. Neglecting it leads to an *overestimate* of the cooling time, which is already very short. Ω_{hot} is the mass density in hot baryons in unit of the critical density. At the start of the cooling process, $\Omega_{hot} = \Omega_{bar}$. The equation $t_{cool}(r_{cool}) = t(z)$ defines a cooling radius r_{cool} as a function of redshift z. At this redshift, only gas inside r_{cool} (or r_V if $r_{cool} > r_V$) cools and is available for star formation. This cooling criterion introduces a high–mass cut-off in the mass distribution of cold baryonic cores.

When gas cools, the final radius of the gas in rotational equilibrium is related to the initial radius of the gas by conservation of angular momentum (Fall & Efstathiou 1980). Approximately, $r_D \sim \lambda \min(r_V, r_{cool})$, with the dimensionless spin parameter $\lambda \equiv J|E|^{1/2}G^{-1}M^{-5/2} \simeq 0.05 \pm 0.03$ (Barnes & Efstathiou 1987; Efstathiou *et al.* 1988; Zurek *et al.* 1988). Previous studies only used the mean value of λ in this formula. Hereafter, we introduce the λ distribution from Barnes & Efstathiou (1987) model C0–4 (their fig. 11). According to a fit based on fig. 3 of Fall & Efstathiou (1980), the exponential disk which forms from the dissipative collapse of the gas has a length scale $r_0 \simeq 1.26\lambda^{1.17}\min(r_V, r_{cool})$ and a radius including 50 % of the cold baryonic mass $r_{1/2}/r_0 = 1.68$. A dynamical time scale in the disk–like core is $t_{dyn} \equiv 2\pi r_{1/2}/V_c$. It is important to note that only disks can form in this formalism. The formation of elliptical galaxies (and of bulges of spiral galaxies) has to be explained by the merging of disks. Kauffmann *et al.* (1994) and Cole *et al.* (1994) showed that this merging process can easily explain the current fraction of gE among bright galaxies (about 10 %).

3.2 Star Formation

Then stars form according to a star formation rate history $SFR(t)$. Hereafter we consider two modes of star formation, which we called the *disk mode* and the *burst mode*.

Many phenomenological studies seem to show that, on galaxy scales, the disk mode SFR varies as a power law of the total gas content (the so–called Schmidt law), with index 1–2 (see e.g. Kennicutt 1989). Here we assume that the star formation time scale $t_\star$ is proportional to the dynamical time scale of the disk t_{dyn} and we introduce a first fudge factor f_1. With $t_\star \equiv f_1 t_{dyn}$, we take:

$$SFR(t) = \frac{M_{gas}(t)}{t_\star} \quad (2)$$

General arguments about star formation lead to $f_1 \sim 10^{-2}$. Guiderdoni *et al.* (1996b) show that it is possible to fit the observational distribution of $t_\star$ with a single value $f_1 = 0.01$. We keep a standard IMF with Salpeter index $x = 1.7$ for stars with masses $2 \leq m \leq 120 M_\odot$ (observational value from Scalo 1986), $x = 1.35$ between 1 and $2M_\odot$, and $x = 0.25$ for masses $0.1 \leq m \leq 1 M_\odot$. For this standard IMF, we assume that half of the mass involved in star formation goes into "dark objects" less massive that 0.1 $M_\odot$.

Alternatively, star formation could occur in the burst mode, which is defined by: 1) a rapid conversion of gas into stars; 2) an IMF favouring massive stars; 3) a strong extinction (see Sect. 4.2). As a typical case, we introduce a burst with a 2 Gyr duration. Anyhow, as long as the burst is short, the relevant quantity is the total mass involved in the burst, which is the product of its intensity by its duration. As a typical case for a "top–heavy" IMF, we hereafter take a Salpeter index $x = 1.1$ for stars with masses $2 \leq m \leq 120 M_\odot$. For this IMF, all mass goes into stars more massive than 2

no "dark objects". We also consider an "ultraluminous" burst, with only heavily–extincted massive stars radiating in the IR all the energy yielded by stellar nucleosynthesis (that is, $0.007xMc^2$). The luminosity of the burst is inversely proportional to its duration. For instance, if the burst is spread on 2 Gyr, its IR luminosity is 4 times that of the burst with the "top–heavy" IMF, that is: $L_{IR} = 52x\ L_{bol\odot}$ per solar mass of "cold baryons" initially available for star formation, versus 13 $L_{bol\odot}$. If the burst duration is as short as 0.1 Gyr, the IR luminosity can reach $L_{IR} = 10^3 x\ L_{bol\odot}$ per solar mass of "cold baryons"

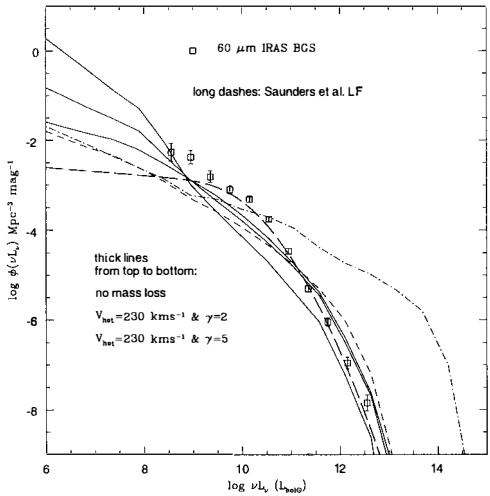

Figure 2: Upper panel: predicted 60 μm luminosity functions at $z = 0$ for the "standard" $\Omega_0 = 1$ CDM model (solid lines). Various mass loss parameters have been tested. Our standard model for mass loss is given by the intermediate curve. This will be called the "minimal" model. Dashes and dots: luminosity function with all star formation occurring according to the ultraluminous burst mode. Short dashes: luminosity function with a combination of disk mode and ultraluminous burst mode (see text for details). This will be called the "maximal" model. Squares: observational luminosity function for the IRAS Bright Galaxy Sample (Soifer & Neugebauer 1991). Thick long dashes: observational luminosity function from a compilation of various samples (Saunders *et al.* 1990).

3.3 Stellar feedback

The explosion of massive stars can expel gas from the galaxies and stop star formation, leading to a strong increase of the mass/luminosity ratios in small objects. Observationally, HI holes and X–ray superbubbles are good evidence that such galactic winds are present in galaxies. The stellar feedback is introduced in a similar way by most of the authors quoted in Sect. 1. By equating the gas binding energy to the thermal energy ejected by supernovae:

$$\frac{1}{2}M_{gas}(t)(\frac{V_{esc}}{V_c})^2V_c^2 = f_2\int_0^{tw}\tau_*(t')\eta_{SN}E_{SN}dt' \qquad (3)$$

where η_{SN} is the number of SNe per unit mass of stars, depending on the IMF. For our standard IMF, $\eta_{SN} = 4\ 10^{-3}\ M_\odot^{-1}$. The output mechanical energy of a SN is $E_{SN} \sim 10^{51}$ erg. The escape velocity at radius $r \leq r_V$ in a singular isothermal sphere truncated at radius r_V is $V_{esc}(r) = \sqrt{2}V_c(1-\ln(r/r_V))^{1/2}$.

The maximum of the λ distribution corresponds to $r_{1/2}/r_V \simeq 0.05$, leading to $V_{esc}/V_c \simeq 2.8$. Since much of this energy is subsequently radiated away, we insert a second fudge factor $0 \leq f_2 \leq 1$.

The mass fraction of stars forming before the triggering of the galactic wind at time t_W is $F_* = (1+\beta(V_c))^{-1}$ with $\beta(V_c) \equiv (V_{hot}/V_c)^\alpha$ with $\alpha = 2$ and $V_{hot} \equiv (V_c/V_{esc})(2\eta_{SN}E_{SN})^{1/2} f_2^{1/2} = 230 f_2^{1/2}$ km s^{-1} for the standard IMF. Because of the uncertainties, we do not consider the systematic changes of V_{hot}, the velocity below which more than half of the cold baryonic mass is returned to the hot phase, with the IMF. Hereafter, we take $\alpha = 2$ and $V_{hot} = 230$ km s^{-1} as a standard model. On the one hand, we can introduce higher values of V_{hot} which would correpond to shallower IMF's and/or larger values of E_{SN}. On the other hand, Cole *et al.* (1994) introduced a fit based on SPH simulations of galaxy formation in which most of the feedback effect is due to momentum exchange rather than to heating of the ISM. For a typical feedback parameter $f_V = 0.1$, the numerical simulations can be fitted with values $\alpha = 5$ and $V_{hot} = 130$ km s^{-1}.

4 Spectral Evolution

4.1 Stellar emission

A model of spectrophotometric evolution is used to compute the gas content, the UV to NIR spectra of the stellar population, and the mass–to–luminosity ratios in various photometric bands, at each age. The stars are placed on the Zero–Age Main Sequence of the HR diagram according to the Initial Mass Function. The models use compilations of stellar evolutionary tracks taking into account the various stages of stellar evolution in order to compute at each time step the distribution of the stellar populations in the HR diagram. This distribution is combined with a library of stellar spectra and gives the synthetic spectrum $F_{*\lambda}$. At the end of their life time, stars die and return a fraction of their mass to the ISM. The model which is used here is described in Guiderdoni & Rocca–Volmerange (1987, 1988), and Rocca–Volmerange & Guiderdoni (1988), with upgraded stellar tracks from Schaller *et al.* (1992).

4.2 Dust absorption

Part of the energy released by stars is absorbed by dust associated to the gaseous component and re–emitted in the IR and submm ranges. The estimate is this quantity is not an easy task since it depends on the chemical evolution of the dust, on the dust–to–gas ratio, and on the geometrical distribution of dust relatively to stars. As in Guiderdoni & Rocca–Volmerange (1987) and Franceschini *et al.* (1991, 1994), the optical thickness of the disk depends on the gas fraction $g(t)$ as:

$$\tau_\lambda(t) = 3.25(1-\omega_\lambda)^{1/2} (\frac{A_\lambda}{A_V})_{Z_\odot} (\frac{Z_g(t)}{Z_\odot})^s g(t) \qquad (4)$$

The extinction curve depends on the metallicity $Z_g(t)$ of the gas according to power–law interpolations based on the Solar Neighbourhood and the Magellanic Clouds, with $s = 1.35$ for $\lambda < 2000$ Å and $s = 1.6$ for $\lambda > 2000$ Å. The extinction curve for solar metallicity is taken from Mathis *et al.* (1983), and the albedo ω_λ from Draine & Lee (1984). The metallicity of the gas is estimated from the Instant Recycling Approximation $Z_g(t) = -y_Z \ln g(t)$ with a yield $y_Z = 1.23\ 10^{-2}$ for our standard IMF.

Finally, as in Guiderdoni & Rocca–Volmerange (1987) and Franceschini *et al.* (1991, 1994), we assume, as a simple geometric distribution, that the gas and the stars which contribute mainly to dust heating are distributed with equal height scales in the disks. The extinction correction (averaged over inclination angle i) is:

$$A_\lambda(t) = -2.5 \log < \frac{1-\exp(-\tau_\lambda(t)/\cos i)}{\tau_\lambda(t)/\cos i} >_i \qquad (5)$$

providing that the stars and gas have the same height scale. This "slab" geometry is intermediate between the "screen" geometry $\exp -\tau_\lambda / \cos i$ and the "sandwich" geometry (with zero scale height for dust) $(1 + \exp -\tau_\lambda / \cos i)/2$ which respectively lead to larger and smaller absorptions. Observational analyses seem to suggest that this "slab" geometry is the best guess to fit the data (see e.g. Franceschini & Andreani 1995).

For the burst model, we simply consider $A_B = 5$ mag of extinction on all stars. For the 2 Gyr burst, the IR emission drops soon after the end of the burst, when 2 $M_\odot$ stars finally die. The corresponding IR luminosity is $L_{IR} = 13\ L_\odot M_\odot^{-1}$. We also consider an "ultraluminous" starburst with only massive stars forming in a heavily-extincted environment.

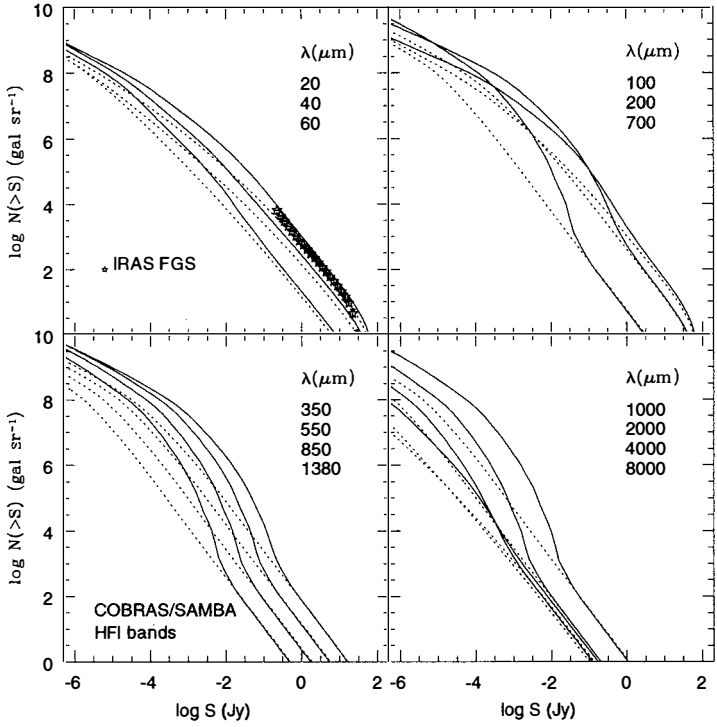

Figure 3: Predictions for faint galaxy counts at various wavelengths. Dots: "minimal" model (all disk mode). Solid lines: "maximal" model (combination of disk mode and ultraluminous burst mode). For increasing λ, the curves shift from bottom to top in the first panel, and from top to bottom in the other three panels. The counts at small λ show the typical bend due to the effect of curvature and positive "k-correction". The counts at submm λ show the bump due to the "negative k-correction" in the submm/mm range. Finally, the counts at large λ show a Euclidean behaviour. The IRAS Faint Galaxy Sample counts at 60 μm (Lonsdale *et al.* 1990) are given in the first panel. The left-hand lower panel show predictions for four bands of the COBRAS/SAMBA High-Frequency Instrument.

4.3 Dust Emission

The total star light in the UV and optical is absorbed by dust and re–emitted at longer wavelengths with a bolometric IR luminosity L_{IR}. The emission spectra of galaxies are computed as a sum of various components, according to the method developped by Maffei (1994). The guideline to compute the spectra are the observational correlations of the IRAS flux ratios 12μm/60μm, 25μm/60μm and 100μm/60μm with L_{IR} (Soifer & Neugebauer 1991). These correlations are extended at low L_{IR} from the samples of Smith *et al.* (1987) and especially Rice *et al.* (1988).

Several components are considered in the model spectra, as in Désert *et al.* (1990) and Maffei (1994): polycyclic aromatic hydrocarbons (PAH), very small grains (VSG), big grains (BG) and synchrotron radiation. The 60/100 colour gives the temperature T_{BG} of the BG, provided that an emissivity index m has been chosen. We hereafter take $m = 1$ (standard value), 1.5 and 2. Then the amount of BG, VSG and PAH are calculated iteratively from the 12/100, 25/100 and 60/100 ratios. The resulting spectra are computed from a few μm to several mm and evolve with L_{IR} such as more luminous galaxies emit preferentially at shorter wavelengths. By construction, these spectra fit the IRAS colour correlations. Fig. 1 shows examples of these model spectra for various L_{IR} and various emissivity indices for BG.

5 Predictions in the FIR and submm

5.1 The FIR Luminosity Function

Fig. 2 gives predictions for the $z = 0$ luminosity function at 60 μm compared with the observational determinations drawn from the IRAS Bright Galaxy Sample (Soifer & Neugebauer 1991) and from a compilation of various IRAS samples (Saunders *et al.* 1990). It is well known that this kind of semi–analytic models predicts too many low–luminosity galaxies in the optical bands at $z = 0$, with respect to the observational field luminosity functions (see the references quoted in Sect. 1). As a consequence, the optical luminosity functions are too steep and can be reconciled with the observations by invoking subtle selection effects based on surface brightness. The predicted steep luminosity functions are observed at $z > 0.3$ in the deep redshift surveys and can be responsible for the high number of faint blue objects seen in the ultradeep counts. The standard model also predicts too many low–luminosity galaxies in the IR, while the discrepancy is somewhat lower than in the blue. At $\nu_{60}L_{\nu_{60}} = 10^7 L_{bol\odot}$, the standard model with star formation occurring only in the disk mode (which we will call the "minimal" model) is a factor 30 over the data. The slope is $n(L_{IR})dL_{IR} \propto L_{IR}^{-1.8}dL_{IR}$ without mass loss, and decreases to -1.5 with the standard mass loss and to -1.3 with a stronger mass loss. On the other hand, the low Ω_0 cosmology (not plotted in fig. 2) also has less haloes and gives a better fit of the observations.

Finally, we introduce a model combining two modes of star formation: the disk mode as above and the burst mode. We take our so–called "ultraluminous" burst in which all the energy available from stellar nucleosynthesis is quickly radiated in the IR (massive stars in heavily–extincted environment). We assume that the mass fraction involved in the burst mode increases with the formation redshift as $f_b = 0.007(1 + z_{for})^{4.5}$, up to redshift $z_{for} \simeq 2$, above which all star formation occurs according to the ultraluminous burst mode. This power law comes from the increase of the galaxy pair rate observed by Zepf & Koo (1989). The remaining fraction $f_d = 1 - f_b$ is involved in the disk mode. We will call this model the "maximal" model.

Because of the sample–to–sample differences in the observational luminosity functions illustrated by the two published functions plotted in fig. 2 (the IRAS Bright Galaxy Sample and a compilation of various samples), both models seem to give similar fits to the data. They reproduce the high–luminosity cut–off, underestimate the number of galaxies at $\nu_{60}L_{\nu_{60}} = 10^{10}\ L_{bol\odot}$ by a factor ~ 3, and are within the observational sample–to–sample differences at $\nu_{60}L_{\nu_{60}} = 10^9\ L_{bol\bullet}$.

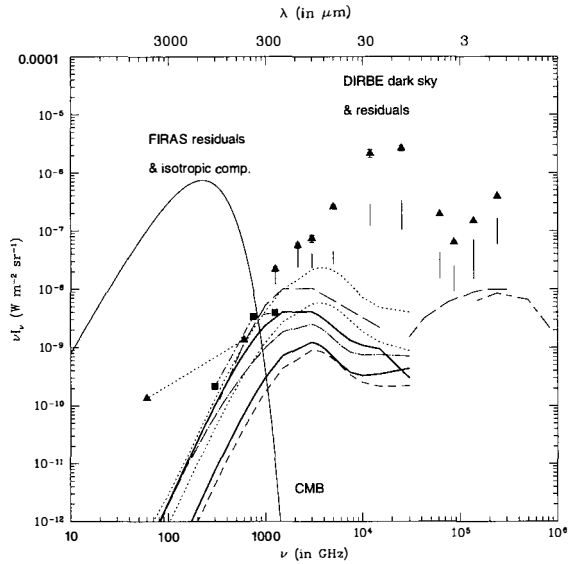

Figure 4: Predictions of the diffuse background of galaxies compared to the current upper limits for DIRBE and FIRAS, the CMB and other models. The DIRBE dark sky and residuals are from Hauser (1995) and the FIRAS residuals are from Mather *et al.* (1994). The squares are the isotropic component extracted by Puget *et al.* (1996) from the FIRAS data. The long dashes show a typical model by Franceschini *et al.* (1994), for strong evolution (his case c). The short and long dashes are predictions of the optical background from fits of the faint galaxy counts (Guiderdoni & Rocca–Volmerange 1990). The dashes and dots give predictions for no–evolution integrated up to redshifts $z_{for} = 8$. The two thick solid lines show the "minimal" and "maximal" models described in the text (respectively as the lower and upper curves), for the $\Omega_0 = 1$, $h = 0.5$, $b = 1.5$ standard CDM model. The dashes show the "minimal" model for $\Omega_0 = 0.2$. Finally, the two dotted lines respectively give the expected range for all–burst models with the top–heavy IMF and $A_B = 5$ mag of extinction (lower curve) and with "ultraluminous" bursts corresponding to quick IR emission of all the energy available from stellar nucleosynthesis (upper curve).

5.2 Faint Galaxy Counts

We hereafter explore the consequences of the two models proposed in the previous section. In the "minimal" model, all star formation occurs in a quiet mode, in disks. We hereafter assume that this "regular" behaviour is similar at high z. In the "maximal" model, the combination of the disk mode and the ultraluminous burst mode varies with redshift according to the observed z–dependence of the pair rate.

These models are used to generate evolving luminosity functions from $z = 0$ to $z = 8$, and predictions of faint galaxy counts at various wavelengths from 20 μm to 10 mm, which are shown in fig. 3. Clearly there are three regimes: at short wavelengths, the effect of curvature and the positive "k–correction" produce the bend of the faint counts; in the submm/mm range, the negative "k–correction" produces a bump in the faint counts, which reflects the passage of the 100 μm emission bump into the observing bands; finally, at larger wavelengths, the luminosity is so small that many galaxies at these flux levels are nearby, in the euclidean zone, with $N(> S) \propto S^{-3/2}$. The "maximal"

model has stronger evolution, and its bump regime is much larger than in the "minimal" model.

In the first panel, observational counts drawn from the IRAS Faint Galaxy Sample (Lonsdale *et al.* 1990) are superimposed. Both models fairly reproduce the faint counts of the IRAS FGS. The normalization can be improved by slight changes (a few hundredth dex) of the baryonic density Ω_{bar}, or of the baryonic mass–to–luminosity ratio, through the normalization of the "dark mass" in the IMF (see Sect. 3.2), with little relative influence on the luminosity function. We do not attempt to do this fine tuning. As a matter of fact, the models seem to bracket the data, since they respectivelty give slightly too shallow and too steep slopes. As shown by Bertin *et al.* (1996), the various data for the 60 μm faint counts below 0.1 Jy are discrepant by a factor of 0.25 dex, which turns out to be the difference between the "minimal" and "maximal" models. So we conclude that the IRAS data alone (the luminosity functions considered in Sect. 5.1 and the faint counts) are not sufficient to reject one of the models, or both of them.

At the typical sensitivity level of 0.1 Jy which will be reached for point sources by the COBRAS/SAMBA all–sky survey, and which is comparable to the 0.22 Jy level reached by the IRAS 60 μm Faint Source Catalogue, one expects 3 10^4 galaxies per steradian at 60 μm for the "maximal" model, and respectively 3 10^4, 10^3, 10^2 and 10 galaxies per steradian in the High–Frequency Instrument bands at 350, 550, and 850 and 1380 μm. At the better sensitivity level of 10 mJy, which can be reached by an ultra–deep survey with FIRST, the number of galaxies per steradian respectively reaches 3 10^6 and 10^5 at 350 and 550 μm. The predictions for the "minimal" model are much lower. So, while the IRAS data does not yield tight constraints on the evolution rate of galaxies, the COBRAS/SAMBA all–sky survey and the FIRST observatory will give a sufficiently large amount of information to constrain the various scenarios of evolution.

5.3 Diffuse Background

These faint counts can be summed up and yield predictions for the intensity of the diffuse background displayed in fig. 4, with other models and the current upper limits given by FIRAS and DIRBE. It turns out that, because of the non–conservation of the number density of galaxies with time (due to the continuous process of galaxy formation), the background is smaller than the predictions without number evolution, but with luminosity evolution, in which *all* galaxies already formed at $z_{for} = 4.5$ - 5 (Franceschini *et al.* 1991, 1994). The "minimal" model, in which all star formation occurs in disks, leads to background levels which are even *lower* than predictions without evolution, obtained by integrating the IRAS LF up to $z_{for} = 8$.

The isotropic component extracted by Puget *et al.* (1996) from a re–analysis of the FIRAS data is also plotted in fig. 4. If this component has an extragalactic origin, this is the first detection of the long–searched diffuse background of galaxies. The "minimal" model is unable to accomodate this component, because of the continuous process of galaxy formation in the CDM universe (without number density conservation) combined with the slow evolution of the disk mode of star formation. The "minimal" model in an $\Omega_0 = 0.2$ CDM universe does not lead to a better fit, in spite of its higher redshifts of galaxy formation (in agreement, for instance, with Heyl *et al.* (1995) in which the luminosity function in a low–Ω_0 universe is rather similar to the one in the $\Omega_0 = 1$ universe). There is simply not enough energy in the "minimal" model to reproduce the level of the isotropic component. Now, if we increase the luminosity of galaxies, for instance by reducing to zero the amount of dark mass in the IMF, by taking a shallower IMF or by increasing Ω_{bar}, the increasing luminosities of galaxies result in a background spectrum peaking at shorter wavelengths, according to the colour–luminosity correlations observed by IRAS and explicitly implemented in our spectra.

So, if we are to fit the isotropic background found by Puget *et al.* (1996), we must invoke a different type of evolution. In contrast with the "minimal" model, the "maximal" model, which gives a good fit of IRAS faint counts, also reproduces the level of the background. In this model, all star formation at $z_{for} > 2$ occurs in "ultraluminous" bursts which quickly radiate in the IR all the energy available from stellar nucleosynthesis. The mass fraction involved in bursts increases as $f_b = 0.007(1+z)^{4.5}$ for $z_{for} < 2$, and the fraction $f_d = 1 - f_b$ is involved in the quiet disk mode. The disk mode is dominant

at low z and small λ while the burst mode dominates at high z and large λ. The model correctly reproduces the level of the background, but it predicts that the light is to be found at wavelengths smaller than observed. This might be due to uncertainties in the spectral modelling of ultraluminous objects. Finally, two models in which all star formation occurs in bursts, with the top–heavy IMF and the "ultraluminous" burst, show the range of background which can be obtained. These "all burst models" violate the IRAS constraints.

6 Conclusions

In this paper, we attempt to test the IR predictions of a simple semi–analytic model of galaxy formation in the paradigm of the hierarchical growth of structures. Predictions of faint counts and diffuse background in the FIR/submm are finally given. We introduce two families of models corresponding to two modes of star formation. In the "disk mode", stars quietly form over a time scale 1 – 10 Gyr, in disks with moderate extinction, and the resulting IR luminosity per unit mass of "cold baryons" initially available for star formation amounts to 0.1 – 1 $L_{bol\odot}$. In the "burst mode", star formation occurs during a time interval as short as 0.1 – 1 Gyr, with an IMF favouring massive stars and strong extinction, and the resulting IR luminosity per unit mass of "cold baryons" reaches the range 100 – 1000 $L_{bol\odot}$. We design a "minimal" model in which all star formation occurs in disks, and a "maximal" model in which star formation progressively changes from the ultraluminous burst mode to the disk mode as time goes on. The redshift dependence of the change is given by observations of the galaxy pair rates.

As a matter of fact, no completely satisfactory solution has been found, if we are to accomodate simultaneously *all* the data (IRAS, FIRAS and DIRBE), under the assumption of continuous galaxy formation which is a consequence of hierarchical clustering. The "minimal" and "maximal" models seem to give fair fits of the IR luminosity function (based on nearby galaxies), within the differences between the published samples. Nevertheless, the computed slope is too steep. This feature is already found for the predicted luminosity functions in the optical bands. The models bracket the slope of the IRAS faint counts. Nevertheless, the uncertainties in the determination of the faint end of the luminosity function and in the level of the faint counts make the choice uneasy. The background predictions of the present paper stand significantly *below* the previous estimates, because of non–conservation of galaxy number density which is one of the main characteristics of models in the current paradigm of structure formation. As a result, the "minimal" model is unable to reproduce the isotropic component found by Puget *et al.* (1996), while the "maximal" model is designed to reproduce this background level without being rejected by the IRAS faint counts. If the isotropic component is actually extragalactic, this is evidence that the star formation mode strongly evolves with time.

In spite of its attempt to explicitly implement *all* the relevant physics of galaxy formation, the model has too many simplifying assumptions. Among the various improvements, we should try to explore, on the one hand, the modelling of cooling and feedback, and, on the other hand, the computation of the disk optical thickness. Non–standard dust at high z is another interesting possibility to be explored. The faint galaxy counts in the optical should be used as additional constraints in order to control the energy balance during all the galaxy evolution. The model of ultraluminous burst which is used here is very faint in the optical bands, since much of its energy is re–emitted in the IR. More refined solutions have to be found in order to reproduce the properties of high–redshift galaxies in the optical.

As it as already been noticed by previous studies, the forthcoming submm satellites such as COBRAS/SAMBA and FIRST will open a crucial new window on galaxy evolution. Many thousand galaxies will be potentially observable with these new instruments. The model gives predictions which can be used to prepare these observations. The separation of the sub–degree anisotropies due to the CMB and the various foregrounds/backgrounds, which would be observed by the second generation of submm satellites like the COBRAS/SAMBA project, can be prepared by an improved modelling

and realistic sky simulations (see Hivon *et al.* 1996). The information on the various backgrounds will help to optimize the design of the instrument, the choice of the observing channels and strategy, and the algorithm of component separation.

7 References

Andreani, P., & Franceschini, A. 1992. A&A, **260**, 89
Bardeen, J.M., Bond, J.R., Kaiser, N., & Szalay, A.S. 1986. Ap.J., **304**, 15
Barnes, J., & Efstathiou, G. 1987. ApJ, **319**, 575
Bertin, E., Dennefeld, M., & Moshir, M. 1996, *preprint*
Blain, A.W., & Longair, M.S. 1993, MNRAS, **264**, 509
Blanchard, A., Valls-Gabaud, D., & Mamon, G. 1992. A&A, **264**, 365
Cole, S. 1991. ApJ, **367**, 45
Cole, S., Aragón-Salamanca, A., Frenk, C.S., Navarro, J.F., & Zepf, S.E. 1994. MNRAS, **271**, 781
Désert, F.X., Boulanger, F., & Puget, J.L. 1990. AA, **237**, 215
Draine, B.T., & Lee, H.M. 1984. ApJ **285**, 89
Efstathiou, G., Frenk, C.S., White, S.D.M., & Davis, M. 1988. MNRAS, **235**, 715
Evrard, A.E. 1989. ApJ, **341**, 26
Fall, S.M., & Efstathiou, G. 1980. MNRAS, **193**, 189
Franceschini, A., Toffolatti, L., Mazzei, P., Danese, L., & De Zotti, G. 1991. ApJSS, **89**, 285
Franceschini, A., Mazzei, P., De Zotti, G., & Danese, L. 1994. ApJ, **427**, 140
Franceschini, A., & Andreani, P. 1995. ApJ, **440**, L5
Guiderdoni, B., & Rocca-Volmerange, B. 1987. A&A, **186**, 1
Guiderdoni, B., & Rocca-Volmerange, B. 1988. A&ASS, **74**, 185
Guiderdoni, B., & Rocca-Volmerange, B. 1990. A&A, **227**, 362
Guiderdoni, B., Hivon, E., Bouchet, F.R., Maffei, B., & Gispert, R. 1996a, in *Unveiling the Cosmic Infrared Background*, E. Dwek (ed), AIP Conference Proceedings 348
Guiderdoni, B., Hivon, E., Bouchet, F.R., & Maffei, B. 1996b, *submitted*
Hauser, M.G. 1995, in *Proceedings of the IAU Symp. n° 168, Examining the Big Bang and Diffuse Background Radiation*, The Hague, August 1994
Heyl, J.S., Cole, S., Frenk, C.S., & Navarro, J.F. 1995. MNRAS, **274**, 755
Hivon, E., Guiderdoni, B., & Bouchet, F. 1996, *in preparation*
Kauffmann, G.A.M., White, S.D.M., & Guiderdoni, B. 1993. MNRAS, **264**, 201
Kauffmann, G.A.M., Guiderdoni, B., & White, S.D.M. 1994. MNRAS, **267**, 981
Kennicutt, R.C. 1989. ApJ, **344**, 685
Lacey, C., & Silk, J. 1991. ApJ, **381**, 14
Lacey, C., Guiderdoni, B., Rocca-Volmerange, B., & Silk, J. 1993. ApJ, **402**, 15
Lonsdale, C.J., Hacking, P.B., Conrow, T.P., & Rowan-Robinson, M., 1990. ApJ, **358**, 60
Lonsdale, C.J. 1996. in *Unveiling the Cosmic Infrared Background*, E. Dwek (ed.), AIP Conference Proceedings 348
Maffei, B. 1994. PhD Dissertation, Université Paris VII
Mather, J.C., *et al.* 1994. ApJ, **420**, 439
Mathis, J.S., Mezger, P.G., & Panagia, N. 1983. A&A, **128**, 212
Puget, J.L., Abergel, A., Boulanger, F., Bernard, J.P., Burton, W.B., Désert, F.X., & Hartmann, D. 1996. *preprint*
Rice, W., Lonsdale, C.J., Soifer, B.T., Neugebauer, G., Kopan, E.L., Lloyd, L.A., de Jong, T., & Habing, H.J. 1988, ApJSS, **68**, 91
Rocca-Volmerange, B., & Guiderdoni, B. 1988. A&ASS, **75**, 93
Saunders, W., Rowan-Robinson, M., Lawrence, A., Efstathiou, G., Kaiser, N., Ellis, R.S., & Frenk, C.S. 1990. MNRAS, **242**, 318
Scalo, J.N. 1986. *Fundam. Cosmic Phys.*, **11**, 1
Schaeffer, R., & Silk, J. 1985. ApJ, **292**, 319
Schaller, G., Schaerer, D., Meynet, G., & Maeder, A. 1992. A&ASS, **96**, 269
Smith, B.J., Kleinmann, S.G., Huchra, J.P., & Low, F.J. 1987. ApJ, **318**, 161
Soifer, B.T., & Neugebauer, G. 1991. AJ, **101**, 354
White, S.D.M., & Rees, M.J. 1978. MNRAS, **183**, 341
White, S.D.M., & Frenk, C.S. 1991. ApJ, **379**, 52
Zurek, W.H., Quinn, P.J., & Salmon, J.K. 1988. ApJ, **330**, 519
Zepf, S.E., & Koo, D.C. 1989. ApJ, **337**, 34

CONTRIBUTION OF POINT SOURCES TO MICROWAVE BACKGROUND ANISOTROPIES

E. Hivon [1,2], B. Guiderdoni [2], F.R. Bouchet [2]
[1] *Theoretical Astrophysics Center, Juliane Maries Vej 30, DK-2100 Copenhagen Ø, Denmark.*
[2] *Institut d'Astrohysique de Paris, CNRS, 98 bis Bvd Arago, 75014 Paris, France*

Abstract

The high resolution and high sensitivity measurements of Cosmic Microwave Background Radiation (CMBR) anisotropies, scheduled in the next few years, should allow a high precision knowledge of the essential cosmological parameters. However, various foreground contributions, such as Galactic dust, free-free emission and other galaxies could impair the quality of these observations. In this paper we study microwave background anisotropies due to point sources and show that they could marginally hamper the observation of the primordial fluctuations at the smallest scales. At the same time, detection of these anisotropies by ISOPHOT seems possible.

1 Introduction

Triggered by the success of CMBR measurement by *COBE* mission, a host of new experiments, satellite-borne (COBRAS/SAMBA [1], MAP), air-borne (TOP-HAT, Maxima) as well as ground-based (CAT) have been scheduled for the next few years in the purpose of improving available data. They aim to measure CMBR anisotropies with high resolution (up to a few arcmin for the most ambitious experiments) and high sensitivity (up to $\Delta T/T = 10^{-6}$). Measurements of these anisotropies power spectrum would allow a high precision determination of the essential cosmological parameters like Ω_0, H_0, Ω_b, n ... (Jungman et al. 1996 [4]). However, various foreground contributions, such as Galactic dust, free-free emission and other galaxies could impair the quality of these measurements. In this paper we will consider the effect of remote galaxies on these measurements. In §2 we describe the model we used for galaxy formation and evolution. In §3 we study the origin and spectrum of these anisotropies associated with these remote galaxies. In §4 we discuss the effect of these anisotropies on CMBR experiments and their observability by ISO. A brief summary of our main conclusions is presented in §5.

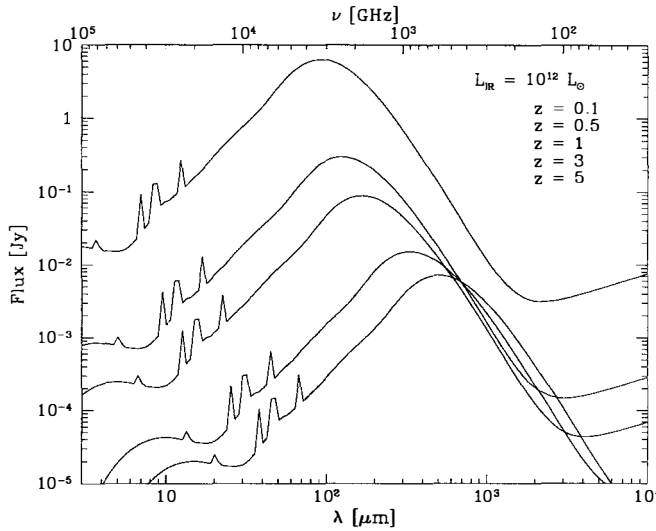

Figure 1: Spectrum of a $L_{\rm IR} = 10^{12} L_\odot$ galaxy observed at different redshifts z

2 Model

Our models are based on a Cold Dark Matter (CDM) cosmology with $H_0 = 50$ km/s/Mpc, $b = 1/\sigma_{8h^{-1}\rm Mpc} = 2.5$ and $\Omega = 1$. We used a Press-Schechter prescription for dark matter haloes formation and statistics. Radiative cooling allows baryonic gas collapse and star formation. Total emission is based on synthetic spectra assuming standard stellar evolution tracks. UV and visible light is absorbed by dust and reemitted in far-infrared and millimeter range. This re-emission is modeled as a sum of different components, according to the method developped by Maffei (1994 [5]). The respective emission of these components depends on the total infrared luminosity $L_{\rm IR}$ and is normalised thanks to IRAS observation. For more details see [2].

Puget et al. 1996 [6], from a reanalysis of the FIRAS data, extracted an isotropic component which could be parameterized as $\lambda B_\lambda \simeq 3.4 \times 10^{-9}\,(\lambda/400\,\mu\rm m)^{-3}$ W.m^{-2}.sr^{-1}, in the range 400-1000 μm. This measurement will be considered as an upper limit for contribution of primordial galaxies. We thus designed a maximal model, with a baryonic fraction $\Omega_b = 0.2$ and a strong star-burst which could fit these observations.[1] As a lower limit, we used a minimal model with $\Omega_b = 0.02$, in agreement with standard nucleosynthesis predictions, and weaker star-bursts.

These models have been used to create maps of the faint galaxy contribution to the CMBR anisotropies as COBRAS/SAMBA, or any other experiment, would observe them. For each redshift z, the number of galaxies located in the cone of observation is given by the model number density. Their position is picked at random or extracted from an external catalog, and their spectral luminosity is a Monte-Carlo simulation of the predicted luminosity function. We then compute the flux received from each of these galaxies on 500 × 500 pixels with an invidual size of 1.5 × 1.5 arcmin, for a set of frequencies lying between 15 and 15000 GHz. These maps can then be degraded, both in frequency and in spatial resolution, to meet an experiment specifications.

[1] Another strong star-burst model, not shown here, with $\Omega_b = 0.02$ also fit these observations.

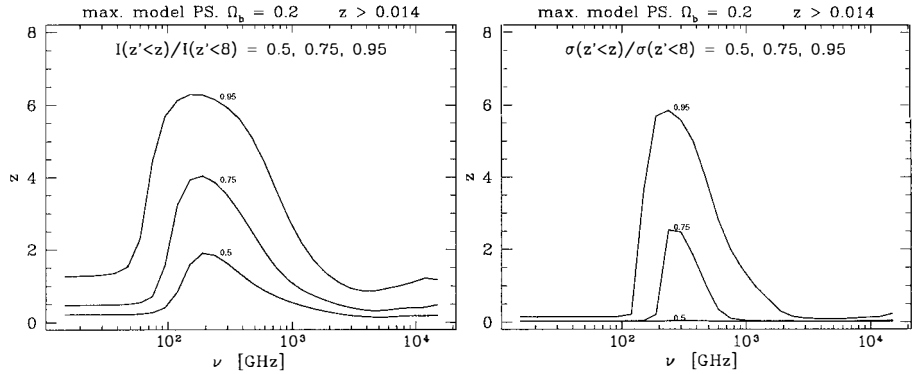

Figure 2: Redshift origin of 50, 75 and 95 % of the isotropic flux (left panel) and anisotropies on 1.5 arcmin pixels (right panel) after removal of galaxies with $0 < z < 0.014$ (see text) for our maximal model

3 Correlation of fluctuations at different frequencies

According to our models, the emission spectrum of a typical galaxy shows a strong bump at about 100 μm (in rest frame) because of dust emission. As shown on Fig. 1, in the range 70 – 500 GHz, the distance effect is couterbalanced by this negative k-correction, and the observed flux of a galaxy depends weakly on its redshift. We can then expect the contribution of high z galaxies to isotropic flux and fluctuations to be important in this frequency range.

In the case of our maximal model, figure 2 shows the frequency-dependent redshift up to which one has to integrate the contribution of point sources to, respectively, the isotropic flux and the anisotropies on a scale of 1.5 arcmin in order to get 50, 75 and 95 % of these quantities. In this model, galaxy emission started at $z = 8$. Sources with $0 < z < 0.014$ have been removed because most of them appear to cause fluctuations larger than 3 standard deviation of each map (and can thus can be singled out from the confusion noise due to crowding remote point sources) whereas their contribution to the total flux is negligible. The comparison of these two panels confirms that, at a given frequency, low-z sources (therefore rarer and brighter) contribute more to fluctuations than to isotropic flux. Nonetheless, as expected from Fig. 1, the contribution to isotropic flux of sources with $z \sim 3 - 4$ is important in the range $100 - 500$ GHz, and their contribution to anisotropies is non-negligible. On the other hand, outside this frequency range, only low redshift sources contribute to isotropic flux, whereas anisotropies are almost exclusively due to very close sources, $z \sim 0$. We verified that the same conclusions are valid for our minimal model.

Figure 3 shows the cross-correlation factor measured between the different bands

$$C_{\nu\nu'} = \frac{\langle i(x,\nu)\, i(x,\nu')\rangle_x}{\sqrt{\langle i(x,\nu)^2\rangle_x \langle i(x,\nu')^2\rangle_x}} \qquad (1)$$

where $i(x,\nu) = I(x,\nu) - \langle I(x,\nu)\rangle_x$, x identifies the pixel and $\langle \ldots \rangle_x$ is the average over all pixels. As expected the correlation is maximal along the first diagonal but also between the most distant frequencies (below 100 GHz and over 2000 GHz) to which contribute mainly the *same* low-z sources as seen in Fig. 2. The range 100–500 GHz, which brackets the maximum of emission of the CMBR, is thus poorly correlated with other frequencies. This fact could hamper the substraction process planed to clean up CMBR maps from point sources contribution, based on an extrapolation of spatial templates observed at other frequencies.

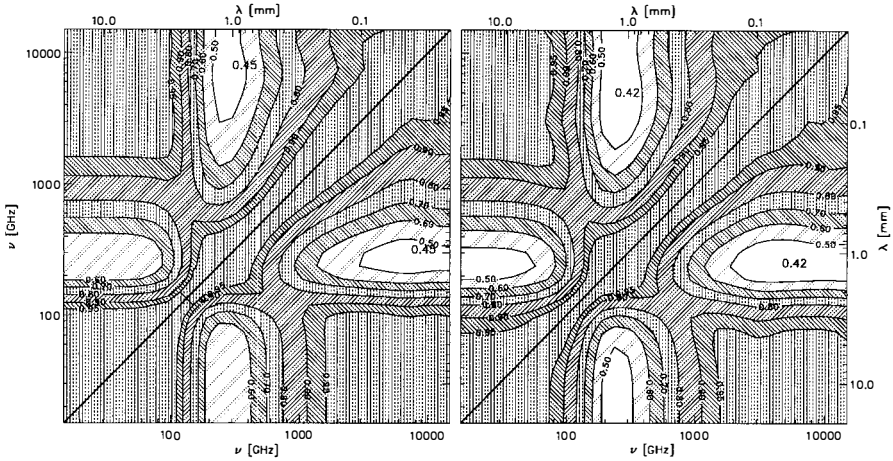

Figure 3: Cross correlation factor of fluctuations between different frequencies, in the case of our raw maximal model (left panel) and after removal of all pixel brighter than 3 standard deviation of maps containing point sources, CMBR fluctuations as expected in a standard CDM model, and dust at the median value observed over the whole sky (right panel). The different levels correspond to .5, .6, .7, .8, .9, .95

4 Observation

4.1 Angular-Frequency dependence of fluctuations

In the case of our maximal model, an analytical fit of the angular power spectrum of temperature fluctuations between 15 and 15000 GHz can be written as

$$\sqrt{\frac{\ell(\ell+1)C_\ell}{2\pi}} = 378\ 10^{-15}\ \ell\ \sinh\left(\frac{\nu}{0.113}\right)^2 \frac{1}{\nu^5}\left[\frac{1}{10}\,\nu^{1/4} + \frac{100\ \nu^4}{\sqrt{(1+(\nu/3)^8)(1+(\nu/2)^2)}}\right]\ \text{K}, \quad (2)$$

where ℓ is the multipole order and ν is the frequency in THz. For the minimal model, one simply has to divide the overall amplitude by a factor 16. The prediction of our maximal model for contribution of infrared galaxies is very close to what has been obtained with *purely luminosity evolution* models in parallel studies [7].

Figure 4 shows the power spectrum of point sources anisotropies at 125 GHz in our different models, as well as their angular-frequency dependence as compared to Galactic foregrounds (dust, free-free and synchrotron) in the frequency—multipole plan. The level of these foregrounds shown here correspond to the median value of fluctuations expected over the whole sky. One can see that at 125 GHz, where the sum of the various foregrounds is minimal, the point sources contribution in our maximal model exceeds 10% of the primordial CMBR (here for a standard *COBE* -normalised CDM) only for $\ell > 1000$. On the other hand, the observation of the frequency range 200-500 GHz, which is of particular interest to study high z formation and evolution of galaxies, requires high angular resolution as well as observation of regions of the sky with low Galactic foregrounds.

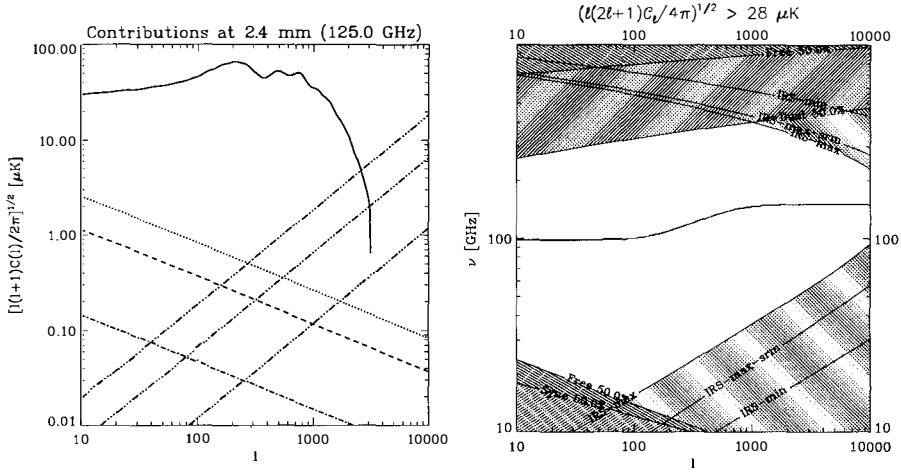

Figure 4: Angular dependence of different contributions. Left panel: power spectrum at 125 GHz of CMBR for a CDM model normalised to COBE observations (solid line), dust (dots), free-free (dashes), synchrotron (dot-dash) and our different models of point sources (dot-dot-dot-dash). Right panel: angular-frequency dependence of fluctuations due to point sources and Galactic foregrounds : dust, free-free and synchrotron. The shaded regions show where the power spectrum of each process is larger than the level of the *COBE* detection ($\ell(\ell+1)C_\ell/(2\pi))^{1/2} > 28\,\mu$K and the thick black line shows the location of the minimum contribution of the Galactic foregrounds and the maximal point source model. In both panels, galactic foregrounds are normalised to their median levels over the whole sky.

4.2 Observation of fluctuations by ISOPHOT

At the same time, we investigated the observation of these fluctuations in the range 50-200 μm with the photometer ISOPHOT (PHT-C) on board of ISO satellite. We studied the best strategy to observe these fluctuations. A fluctuation in a pixel is considered as being detected if its departure from the mean flux is larger (in absolute value) than the sum of instrumental noise and photon noise due to isotropic point sources background, by a ratio S/N. Figure 5 shows this number of detection as a function of the number of pixels observed and for different total times spent on observation, in the case of our maximal and minimal models at 1888 GHz (160 μm). In both cases, pixels with fluctuations larger than three standard deviations (less than 1% of the total number) are not considered. We can see that in the case of the maximal model, a significant number of detections, with a high signal to noise ratio, is easily feasible. In the minimal model, it would require a time of observation much longer but still within the ISOPHOT specifications. However, this study does not include fluctuations due to Galactic foreground which would make more difficult these detections [3].

5 Conclusion

Starting from a complete and consistent model for formation and evolution of galaxies, we studied their contribution to infrared and millimeter anisotropies. Because of the peculiar spectrum of galaxies in the infrared–millimeter range, anisotropies have different redshift origin,

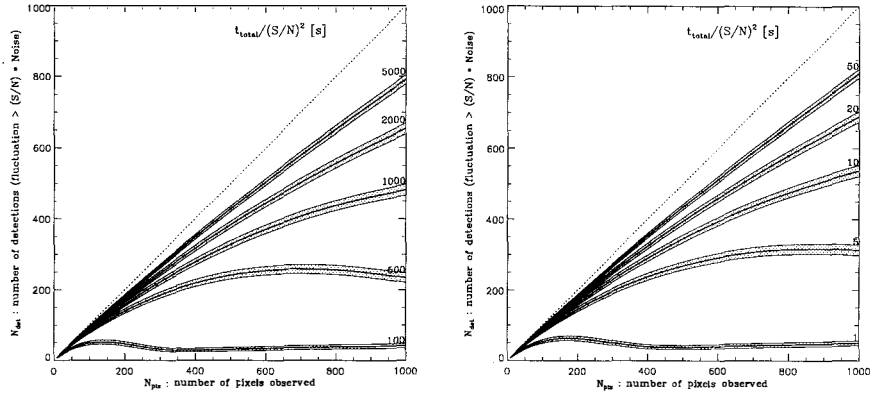

Figure 5: Number of fluctuations detected by ISOPHOT at 1888 GHz as a function of the number of pixels observed for different total time of observation $t_{\rm total}$ for our minimal (left panel) and maximal models (right panel). The thick line shows the number of detection most likely to occur and the shaded area shows ± 1 standard deviation of this number around its maximal probability. Each curve is labelled with $t_{\rm total}/(S/N)^2$ where S/N is the signal to noise ration used as a criterion for detection (see text).

depending on their frequency. In particular, anisotropies observed in the range 100-500 GHz, which brackets the maximum of emission of CMBR, and with the richest information on high-z formation and evolution of galaxies, are poorly correlated with those observed at different frequencies.

It seems that in the least foreground-contaminated frequency range, around 100 GHZ, point sources fluctuations would mainly hamper the observation of primordial CMBR anisotropies at the smallest angular scales. Observation of those fluctuations at higher frequency, which has great cosmological interest, should be possible at small scales in clear regions of the sky, or as soon as Galactic foreground can be efficiently removed. At the same time, we showed that, with ISOPHOT, anisotropies due to point sources can be singled out from the expected instrumental and photon noises in the range 1500-6000 GHz.

Exploration of parameter space (star burst, cosmology) and the effect of clustering of sources will be studied in forthcoming papers.

Acknowledgements. We are grateful to organizers for this interesting meeting and for providing financial support and to the Moriond's staff for his hospitality.

References

[1] Bouchet, F. R., these proceedings ; Tauber, J., these proceedings

[2] Guiderdoni, B., et al. these proceedings ; Guiderdoni, B., et al. in preparation.

[3] Hivon, E., et al. , 1996, in preparation

[4] Jungman, G., Kamionkowski, M., Kosowsky, A., Spergel, D. N, 1996, Phys. Rev. D, in press

[5] Maffei, B., 1994, PhD Dissertation, Université Paris VII

[6] Puget, J.-L., et al. , 1996, *Astr. Astrophys.* **308**, L5

[7] de Zotti, G., et al. , these proceedings.

FLUCTUATIONS DUE TO DISCRETE EXTRAGALACTIC SOURCES: PREDICTIONS FOR THE COBRAS/SAMBA MISSION

G. De Zotti[1], L. Toffolatti[1,2], F. Argüeso Gómez[3], A. Franceschini[4], P. Mazzei[1], L. Danese[5], C. Burigana[1]

[1] *Osservatorio Astronomico, Vicolo dell'Osservatorio 5, I-35122 Padova, Italy.*

[2] *Dep. de Física, Universidad de Oviedo, Av. Calvo Sotelo s/n, 33007 Oviedo, Spain.*

[3] *Dep. de Matematicas, Universidad de Oviedo, Av. Calvo Sotelo s/n, 33007 Oviedo, Spain.*

[4] *Dipartimento di Astronomia, Vicolo dell'Osservatorio 5, I-35122 Padova, Italy.*

[5] *SISSA, Via Beirut 2-4, I-34013 Trieste, Italy.*

Abstract

We discuss the properties of extragalactic sources in the COBRAS/SAMBA bands and present predictions for the expected counts and the contributions to fluctuations in each channel. It is shown that the central frequency bands are expected to be "clean", only a tiny fraction of high galactic latitude ($|b| > 20°$) pixels being contaminated by discrete extragalactic sources. The multifrequency observations anyway allow an efficient subtraction of contaminated pixels which may be identified by means of observations at neighbouring frequencies. Template spectra of sources of different classes will also be directly determined. Moreover, removal of contaminating signals is eased by the substantial difference between their power spectrum and that of primordial fluctuations.

On the other hand, the COBRAS/SAMBA mission will also provide the first all sky surveys of sources in a broad, essentially unexplored frequency region, which is unique for studying a wide variety of very interesting astrophysical phenomena.

1 Introduction

Accurate measurements of primordial small scale anisotropies of the microwave background are made a good deal easier by a lucky coincidence: the peak of the background intensity is roughly coincident with a minimum in the rest frame spectral energy distribution of our own galaxy as well as of most extragalactic sources.

In fact, both in the case of normal and of many active galaxies (as far as we can tell, based on the very limited information currently available), at wavelengths shorter than a few mm (in the rest frame), dust emission rapidly overwhelms the radio emission. Due to the very steep increase with frequency of the dust emission spectrum at mm and sub-mm wavelengths (spectral index $\alpha \simeq -3.5$, $F_\nu \propto \nu^{-\alpha}$), while the spectral index of the radio emission is $\alpha \simeq 0$ for compact "flat"-spectrum sources and $\alpha \simeq 0.7$–0.8 for steep-spectrum sources, the wavelength at which dust emission takes over does not change much between radio quiet and radio loud sources, in spite of the fact that the ratio of radio to far-IR emission for the former class is orders of magnitude lower than for the latter.

This means that the frequency range covered by COBRAS/SAMBA (from 30 GHz to 860 GHz, i.e., from 1 cm to 0.35 mm, with 9 channels) as the most favourable spectral region for primordial anisotropy studies is also of special interest for investigations of some astrophysical processes. Some examples follow.

At cm wavelengths star-forming galaxies have typical synchrotron spectra, with spectral index $\alpha \simeq 0.7$. At higher frequencies an increasing contribution of thermal emission is expected due to the HII regions associated to hot stars. Disentangling thermal and non-thermal radio emissions is important to understand the star formation rate, the SN rate, etc.

Compact radio sources are generally becoming optically thin, and their spectrum is correspondingly steepening, at wavelengths shorter than $\simeq 1$ cm, although some are observed to remain opaque up to mm wavelengths. Also, a high frequency cutoff must exhist, corresponding to a cutoff in the electron energy distribution caused either by the acceleration mechanism or by synchrotron or inverse Compton losses.

Sub-mm data are a very efficient indicator for the presence of interstellar material, the possible fuel for the central engine. In conjunction with data in other spectral bands, the COBRAS/SAMBA data will help to understand physical and evolutionary connections between nuclear activity and processes governing the abundance and the properties of the interstellar material, as well as to get insight into the relationships between different AGN classes. Tests for unified models can be performed by looking at the relative distributions of those isotropically emitted radiations (thermal emission by dust, low-frequency radio emission) which are least affected by obscuration versus possibly anisotropic components (e.g. radio core luminosities or nuclear optical-UV continua).

A survey for sub-mm dust emission from AGNs is also essential to understand the primary energy source of the huge far-IR emission from type 2 Seyferts and from some QSOs and radiogalaxies. A substantial emission from cold dust implies that the emitting region cannot be too small and strongly constrains the nuclear contribution to the energy budget.

A mm survey emphasizes "flat"-spectrum radiosources, such as blazars which should be easily recognizable directly from COBRAS/SAMBA measurements because of their smooth spectrum, free from any sub-mm excess.

In this paper we will discuss predictions for extragalactic sources in COBRAS/SAMBA channels, emphasizing uncertainties and areas in which more work is needed. The power spectrum of expected fluctuations due to such sources is estimated and the level at which measurements of primordial anisotropies may be affected is investigated.

2 Galaxies

Reliable estimates of the local luminosity functions in the frequency range of interest here are very difficult because of the very wide gap with the nearest frequencies where adequate surveys exist. Normal galaxies are anyway expected to contribute little to counts in the radio channels. Extrapolations of the 60 μm luminosity function face the problem that there is a considerable spread in the distribution of dust temperatures and there are not enough data to construct bivariate functions.

2.1 Evolution properties

In the sub-mm bands, the K-correction strongly amplifies evolutionary effects, so that indications of them might be present in COBRAS/SAMBA data.

Predictions can be only tentative at the present stage. At one extreme, there are models assuming that the comoving density of galaxies remained essentially constant after their formation, while they evolved in luminosity due to the ageing of stellar populations and the birth of new generations of stars (pure luminosity evolution). At the other extreme, it is proposed that big galaxies are formed by coalescence of large numbers of smaller objects (hierarchical clustering models). The observed properties of both disk and spheroidal galaxies imply that extensive merging cannot have occurred in the last several billion years (e.g. [2]). Furthermore, evolution depends on an impressive number of unknown or poorly known parameters: merging rate, star formation rate, initial mass function, galactic winds, infall, interactions, dust properties, ...

Strong evolution is expected in the far-IR/mm region particularly for early type galaxies since during their early phases they must have possessed a substantial metal enriched interstellar medium. This expectation is supported by evidences of large amounts of dust at high redshifts (cf. in particular the case of high-z radiogalaxies [14]) and by the intensity of the isotropic sub-mm component reported by [15] from an analysis of COBE/FIRAS data.

Observational constraints are extremely poor. The IRAS 60 μm counts span a limited range of flux and are rather uncertain at the faint end. The redshift survey by [1] of the deep IRAS field at the North Ecliptic Pole [9] has discovered a large supercluster at $z = 0.088$. On the other hand, [4] from a study of a set of deep IRAS fields covering a total area about three times larger than the NEP area, report counts higher by about a factor of 2 (note however that the adopted completeness limit is only 2.5 times the estimated rms confusion noise).

ISO surveys will, however, soon improve very much our understanding of far-IR evolution of galaxies.

2.2 Expected counts

Preliminary estimates (see Table 1) suggest that a significant number of star-forming (normal spiral and starburst) galaxies should be detected, over the high galactic latitude ($\mid b \mid > 20°$) portion ($\simeq 8$ sr) of the COBRAS/SAMBA survey in *all* channels except in the least sensitive one (125 GHz or 2.4 μm). The expected number of detectable galaxies at $\nu \leq 90$ GHz is very sensitive to the detailed shape of the spectrum. Different extrapolations of the data available at higher and lower frequencies yield estimates differing by factors of several; this uncertainty however has little effect on the total counts which are, by far, dominated by radiogalaxies.

Counts have been estimated following [5]. We have adopted the "opaque" models for the evolution of early-type galaxies; these models predict a far-IR/sub-mm extragalactic background in close agreement with the recent estimates by [15].

Table 1. Instrumental and confusion noise estimates for COBRAS/SAMBA and expected numbers of individually detectable sources at $|b| > 20°$.

$\nu_{\rm eff}$ (GHz)	$\lambda_{\rm eff}$ (mm)	beam (arcmin)	$\sigma_{\rm noise}$ (mJy)	$\sigma_{\rm conf}$ (mJy)	$\sigma^{(1)}_{\rm CMB}$ (mJy)	$S^{(2)}_{\rm lim}$ (mJy)	$N(>S_{\rm lim})_{\rm radio}$ (8 sr)	$N(>S_{\rm lim})_{\rm FIR}$ (8 sr)
31	10	30	38	35	60	320	1400	10
53	6	18	35	10	57	200	2000	16
90	3	12	76	4	90	400	800	7
125	2.4	10	300	10	81	1500	150	-
150	2	10	11	6	114	63	4600	130
217	1.4	7.5	11	5	66	60	3100	700
353	0.85	4.5	16	16	15	110	320	8000
545	0.55	4.5	19	40	3	220	160	30000
857	0.35	4.5	26	100	-	500	20	50000

(1) Flux density fluctuations of the cosmic microwave background corresponding to $\Delta T/T = 10^{-5}$

(2) Adopted detection limit for discrete sources, equal to $5 \times (\sigma^2_{\rm noise} + \sigma^2_{\rm conf} + \sigma^2_{\rm Galaxy})^{1/2}$. A rough estimate of anisotropies due to emission of the Galaxy at high latitudes, $\sigma_{\rm Galaxy}$ has been obtained following [20], exploiting the angular dependence determined by [7].

The number of galaxies that should be detected in the high frequency channels is large enough to allow statistical investigations of the properties of galaxies in this particularly interesting range and the definition of reliable luminosity functions.

3 Active galactic nuclei

3.1 Expected counts

Radio loud AGNs, including "flat"-spectrum radiogalaxies, quasars, BL-Lacs, mostly at substantial z, are expected to dominate the counts in the low frequency channels.

Estimates listed in Table 1 are based upon the models worked out by [6], encompassing both "flat-" and steep-spectrum radiosources. As for the former, which actually dominate, a spectral index $\alpha = 0$ has been adopted up to 100 GHz, with a break to $\alpha = 0.7$ at higher frequencies.

Once again, the extrapolations in frequency entail considerable uncertainties. On one side, there are indications of some steepening of the spectra of compact sources between $\simeq 20$ and $\simeq 100$ GHz, so that our assumptions may lead to an overestimate of the expected counts. On the other hand, the presence of excess mm emission over extrapolations from cm wavelengths has been established by [13] for a sample of nearby radio galaxies.

Observations of large mm fluxes attributed to dust emissions have been reported for several distant radio galaxies (see [14] and references therein). The inferred dust masses are 1–2 orders of magnitude higher than found for nearby radio galaxies [13].

Recently, [10] carried out sensitive 90 GHz observations of a sample selected at 5 GHz and observed at 8.4 GHz. They derived a distribution of spectral indices between 8.4 GHz and 90 GHz which allowed them to extrapolate to 90 GHz the 5 GHz source counts. They estimate that, over the entire sky, there are 178 sources with $S_{90\rm GHz} > 1$ Jy, almost a factor of 2 less than predicted by our model. As discussed by [10], their estimate is somewhat below the number of known sources with $S_{90\,\rm GHz} > 1$ Jy, so that it should be viewed as a lower limit.

The contributions of AGNs to the counts in the high frequency ($\geq$ 150 GHz) channels (where, however, star-forming galaxies should be the dominant population) are even more uncertain, since they depend on the evolution of both the non-thermal component and the dust emission, which in turn depend on several unknown or poorly known factors, such as the evolution of the nuclear energy source, the effect of possible circumnuclear starbursts, the abundance, properties and distribution of dust, and so on. The IRAS survey data do not help much, since the detection rate of quasars was extremely low.

It is then necessary to appeal to information available in other wavebands, where evolution of AGNs is best studied, i.e. the optical and X-ray bands. Rowan-Robinson and Pearson [17] adopted a luminosity evolution model fitting optical data, the local luminosity function data at 12μm of [18], and the average continuuum spectrum derived by [16] from a sample of bright, optically selected quasars.

Granato et al. [8] discussed several possibilities, considering evolution properties inferred from both optical and X-ray surveys. The spectral energy distributions were computed in the framework of unified AGN models, according to which nuclei are surrounded by dusty tori. Again the 12 μm local luminosity function of [18] was adopted.

Taking into account only the evolution of the non-thermal component, assumed to parallel that observed in X-rays, and adopting the spectral energy distributions used by [8] for type 1 and type 2 AGNs, we expect a detection rate of radio quiet AGNs increasing with increasing frequency: only a few of them are expected at 1.4 mm, but their number should increase up to a few hundreds at the highest frequencies.

Evidences of vast reservoirs of dust rich gas at high z is provided by mm/sub-mm detections of a number of mostly radio quiet QSOs ([11] and references therein).

Several high-z radio-loud QSOs were also detected ([12] and references therein), but the observed mm fluxes can generally be accounted for by synchrotron emission (but there are evidences of large dust emissions from several high-z radiogalaxies, see above).

To the extent that the mm/sub-mm emission of radio loud AGNs is dominated by synchrotron, we expect that their contribution to the counts in the high frequency COBRAS/SAMBA bands rapidly decreases with increasing frequency, depending also on the presence of a high-frequency cutoff.

4 Angular power spectra of fluctuations due to extragalactic point sources

Following Tegmark & Efstathiou [19] we have computed, and plotted in Fig. 1, the quantity $\delta T_\ell(\nu) = [\ell(2\ell+1)C_\ell(\nu)/4\pi]^{1/2}$ which is roughly the average r.m.s. temperature fluctuation in the multipole range $\ell_0 \leq \ell \leq \ell_1$ with $\ln(\ell_1/\ell_0) = 1$.

The plotted power spectra are the mean of 50 simulations of the all sky distribution of sources. Fluctuations are dominated by radio sources at the lowest frequencies (31, 53, and 90 GHz) and by the far-IR sources at the highest (350, 545 and 857 GHz); both classes of sources are important at the intermediate frequencies (125 – not plotted, 150, and 217 GHz).

It is assumed that sources brighter than 1 Jy are identified and removed from the maps (heavy solid line). The effect of a more efficient removal of the sources is illustrated by the heavy dot-dashed line (shown only for 31 and 90 GHz), corresponding to a source removal down to 100 mJy. Note that, as shown by Table 1, we do expect that it will be possible to directly detect, and subtract out, sources much fainter than 1 Jy, particularly at 150, 217, and 350 GHz.

As mentioned above, we have adopted the "opaque" models of [5] for the evolution of dust emission from early type galaxies. These imply very steep sub-mm counts when evolutionary

effects set in, and this happens at relatively bright fluxes. Correspondingly, predictions of these models at $\nu \geq 350\,\mathrm{GHz}$ are higher by about 20–70% (depending on frequency and angular scale) than those of the less extreme "moderate extinction" models (see [5]).

Altogether, it is likely that the confusion noise levels plotted in Fig. 1 are, if anything, somewhat overestimated at high frequencies.

Sources are assumed to have a Poisson distribution; as shown by [20], contributions due to clustering can safely be neglected except in the case of a very efficient subtraction of dicrete sources, down to very faint fluxes, which is not the case considered here.

Note that our results for a flux density cut of 100 mJy are substantially below those obtained by [19] adopting the same cut (dotted line in panels corresponding to 31, 90, and 217 GHz). This is due to their assumption of a spectral index $\alpha = 0$ for all sources selected at 1.5 GHz. This leads to a substantial overestimate of the expected counts at high frequencies, since most 1.5 GHz sources in the relevant flux density range are known to have a steep ($\alpha \simeq 0.7$) spectrum.

The long-dashed line shows the "unsmoothed" noise field (defined as in [19]) foreseen for the COBRAS/SAMBA detectors; the short-dashed line in the upper left corner of panels corresponding to 31, 53, and 90 GHz, shows, for comparison, that for COBE/DMR, calculated adopting the average pixel noise given by [3].

The roughly horizontal dot-dashed line shows the dependence on multipole of temperature fluctuations predicted by the standard CDM model (scale-invariant scalar fluctuations in a $\Omega = 1$ universe with $H_0 = 50\,\mathrm{km\,s^{-1}\,Mpc^{-1}}$, and baryon density $\Omega_b = 0.05$; cf. [19]).

5 Conclusions

Although the estimates of contributions of extragalactic sources are probably uncertain by a factor of two or three, particularly in the high frequency bands, it is clear from the conservative estimates plotted in Fig. 1 that at least the central bands allow a clean view of primordial anisotropies up to the maximum ℓ–values accessible to COBRAS/SAMBA. The availability of multifrequency data allows an efficient identification of pixels contaminated by discrete sources. Thanks to the large area surveyed, the number of clean pixels will be nevertheless very high (the total number of high galactic latitude – $|b| > 20^\circ$ – pixels ranges from $\simeq$ 830.000 at 90 GHz to $\simeq$ 2.100.000 at 217 GHz).

Table 1 also shows that many sources not directly detectable in the central frequency channels can be identified at higher or lower frequencies. The corresponding pixels can be simply removed, but a reliable subtraction of the contaminating flux may also be possible thanks to the fact that a significant number of sources of the various classes should be detectable in most or all frequency channels, allowing the definition of well defined template spectra.

On the other hand, COBRAS/SAMBA will bridge the gap between radio surveys, carried out at $\nu \leq 8.4\,\mathrm{GHz}$ ($\lambda \geq 3.6\,\mathrm{cm}$) and far-IR surveys (IRAS and ISO) at $\nu \geq 1500$–$3000\,\mathrm{GHz}$ ($\lambda \leq 100$–$200\,\mu\mathrm{m}$), providing the first exploration of the whole sky in a spectral region where many interesting astrophysical phenomena are most easily investigated. It will thus set the stage for the detailed studies to be carried out with FIRST. A pot-pourri of issues for which these data will be extremely relevant include: bremsstrahlung emission as a tracer of evolution of stellar populations; high-frequency behaviour of the spectra of compact radio sources and implications for their physical properties; definition of unbiased samples of blazars; cold dust in galaxies and hints on its evolution; physical and evolutionary connections between nuclear activity and processes governing the abundance and the properties of the interstellar material; the relationships between different AGN classes and tests for unified models; energy source(s) of the huge far-IR emission from type 2 Seyferts and from some QSOs and radiogalaxies.

Acknowledgements. Work supported in part by ASI and CNR.

References

[1] Ashby M.L.N., Hacking P.B., Houck J.R., Soifer B.T., Weisstein E.W., 1996, *Astrophys. J.* **456**, 428

[2] Babul A., Ferguson H.C., 1996, *Astrophys. J.* **458**, 100

[3] Bennett C.L., et al., 1994, *Astrophys. J.* **436**, 423

[4] Gregorich D.T., Neugebauer G., Soifer B.T., Gunn J.E., Herter T.L., 1995, *Astron. J.* **110**, 259

[5] Franceschini A., Mazzei P., De Zotti G., Danese L., 1994, *Astrophys. J.* **427**, 140

[6] Franceschini A., Toffolatti L., Danese L., De Zotti G., 1989, *Astrophys. J.* **344**, 35

[7] Gautier T.N., Boulanger F., Perault M., Puget J.-L., 1992, *Astron. J.* **103**, 1313

[8] Granato G.L., Franceschini A., Danese L., 1996, in *Unveiling the Cosmic Infrared Background, AIP Conf. Proc. 348, p. 226, ed. E. Dwek, AIP Press*

[9] Hacking P., Houck J.R., 1987, *Astrophys. J. Suppl. Ser.* **63**, 311

[10] Holdaway M.A., Owen F.N., Rupen M.P., 1994, NRAO report, unpublished

[11] Ivison R.J., 1995, *MNRAS* **275**, L33

[12] Klein U., Vigotti M., Gregorini L., Reuter H.-P., Mack K.-H., Fanti R., 1996, *Astr. Astrophys.*, in press

[13] Knapp G.R., Patten B.M., 1991, *Astron. J.* **101**, 1609

[14] Mazzei P., De Zotti G., 1996, *MNRAS* **279**, 535

[15] Puget J.-L., Abergel A., Bernard J.-P., Boulanger F., Burton W.B., Désert F.-X., Hartmann D., 1996 *Astr. Astrophys.* **308**, L5

[16] Rowan-Robinson M., 1995, *MNRAS* **272**, 737

[17] Rowan-Robinson M., Pearson C., 1996, in *Unveiling the Cosmic Infrared Background, AIP Conf. Proc. 348, p. 192, ed. E. Dwek, AIP Press*

[18] Rush B., Malkan M., Spinoglio L., 1993, *Astrophys. J. Suppl. Ser.* **89**, 1

[19] Tegmark M., Efstathiou G., 1996, *MNRAS*, submitted

[20] Toffolatti L., et al., 1995, *Astrophys. Lett. Comm.* **32**, 125

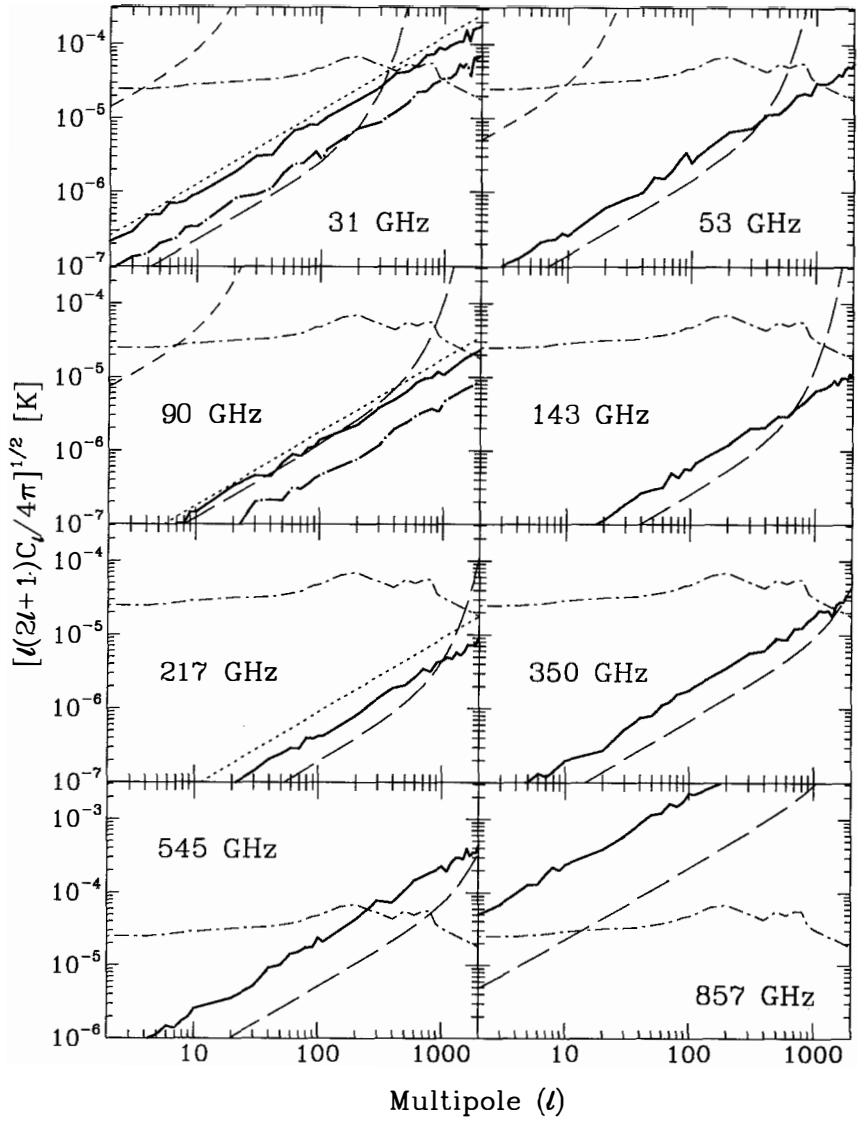

Figure 1. – Angular power spectrum of fluctuations due to discrete sources (see text).

HIGH-LATITUDE GALACTIC EMISSION IN THE COBE-DMR 4-YEAR SKY MAPS

Al Kogut
Hughes STX
Code 685
NASA Goddard Space Flight Center
Greenbelt, MD 20771 USA

We search for faint Galactic emission at high latitudes by cross-correlating the *COBE* DMR 4-year sky maps with spatial templates dominated by Galactic emission. We detect a statistically significant cross-correlation with the DIRBE far-infrared maps whose frequency dependence indicates a superposition of dust and free-free emission. The dust emission corresponds to antenna temperature fluctuations $\Delta T_{\rm dust} = 2.7 \pm 1.3$ μK at 53 GHz and may be used to place limits on enhanced emissivity at long wavelengths, $\beta_{\rm dust} > 1.1$ at 95% confidence. The free-free emission is spatially correlated with the dust on angular scales larger than the DMR beam, with *rms* fluctuations $\Delta T_{\rm ff} = 7.1 \pm 1.7$ μK at 53 GHz. We detect no significant correlation with either the 408 MHz synchrotron survey or a synchrotron model with spatially varying spectral index and place upper limits on the spectral index of emission traced by either map.

1 Introduction

Diffuse microwave emission at high Galactic latitudes is dominated by the cosmic microwave background and optically thin emission from Galactic synchrotron, dust, and free-free emission. These components may be distinguished by their different spatial morphology and frequency dependence. A number of authors have attempted to separate Galactic and cosmic emission on angular scales above a few degrees[1-7]. Unfortunately, there is currently no emission component for which both the spatial distribution and frequency dependence are well determined. Synchrotron radiation dominates radio-frequency surveys, but the spectral index $\beta_{\rm synch}$ steepens with frequency and has poorly-determined spatial variation[4,8]. Dust emission dominates far-infrared surveys, but its spectral behavior at longer wavelengths depends on the shape, composition, and size distribution of the dust grains, which are poorly known[9]. Free-free emission from electron-ion interactions has well-determined spectral behavior but lacks an obvious template map: free-free emission never dominates the high-latitude radio sky, while other tracers of the warm ionized interstellar medium (WIM) such as Hα emission, pulsar dispersion measure, or NII emission are either incomplete, undersampled, or noise-dominated[4,10,11]. At least one component of the WIM is spatially correlated with the far-infrared dust distribution on large angular scales; however, the fraction of the total WIM contained in the correlated component has substantial uncertainties[7,12]

The ratio of cosmic to Galactic emission depends on the angular scale and observing frequency. CMB anisotropies have antenna temperature[1]

$$\Delta T_A \;=\; \frac{x^2 e^x}{(e^x-1)^2}\,\Delta T$$

where $x = h\nu/kT$ and T is thermodynamic temperature. The angular power spectrum of CMB anisotropy is well described[13] by a power-law spectrum $P_{\rm CMB} \propto \frac{1}{\ell(\ell+1)}$ while Galactic emission follows a steeper law[12,14] $P_{\rm Gal} \propto \ell^{-3}$ where $\ell \propto \theta^{-1}$ is the spherical harmonic multipole order. Galactic emission reaches a minimum near 60 GHz. In this paper I present models of Galactic emission based on Galaxy-dominated sky surveys and the 4-year *COBE* DMR microwave maps.

2 Techniques

A number of authors have addressed the problem of identifying and modelling foreground emission in multi-frequency sky surveys[3,7,15,16]. There are (at least) three techniques that can be used. The simplest is a pixel-by-pixel least-squares fit to components whose spectra are fixed *a priori*. For example, the set of antenna temperatures $T_A(\nu)$ measured in several frequency bands in the same spatial pixel could be fitted to a CMB anisotropy plus a set of Galactic components (dust, free-free, and synchrotron). The Galactic spectral indices can then be varied and the process repeated until a global "best" solution (defined by some goodness-of-fit criterion such as χ^2) is achieved. This method is simple and fast, but suffers confusion and signal-to-noise considerations. The different frequency spectra do not form an orthogonal basis; the resulting covariance between the fitted components typically amplifies the instrument noise

[1] Antenna temperature T_A is defined in terms of the power received per unit bandwidth, $P = kT_A\Delta\nu$ where k is Boltzmann's constant. It is related to the intensity I_ν by $I_\nu = 2kT_A\frac{\nu^2}{c^2}$.

Table 1: DMR-Galactic Template Cross-Correlation Coefficients

DMR Frequency	Galactic Template		
(GHz)	408 MHz[a]	Cosmic-Ray[b]	DIRBE 140 μm[c]
31.5	1.17 ± 1.13	1.88 ± 1.24	6.37 ± 1.52
53	0.69 ± 0.77	0.88 ± 0.81	2.69 ± 1.06
90	-0.14 ± 0.74	0.43 ± 2.55	2.79 ± 1.01

[a] α has units μK K^{-1} since the template map has units K.
[b] α is dimensionless since the template map has units μK.
[c] α has units μK (MJy/sr)$^{-1}$ since the template map has units MJy sr^{-1}.

by a factor of 3 to 10 in the fitted parameters. Uncertainty in the Galactic spectral indices adds further systematic uncertainty to the derived maps.

A second method uses a spatial "template" map to trace one or more components of Galactic emission. We assume that a microwave sky map $\Delta T^{\rm obs}$ consists of emission traced by a template map $\Delta X^{\rm Gal}$ plus instrument noise,

$$\Delta T^{\rm obs} = \alpha \Delta X^{\rm Gal} + n$$

and derive the coupling coefficient α from a global least-squares fit to all map pixels. This has the advantage of using information from all pixels simultaneously, allowing detection of faint diffuse emission. The frequency dependence need not be specified *a priori*, but can be inferred from the coefficient α.

Least-squares templates perform well when instrument noise is the dominant contaminant. If other emission sources are present, chance alignment between bright features in the template map and these other emission sources can result in systematic shifts in the coefficient α. This is of particular concern to CMB maps at millimeter wavelengths, where cosmic anisotropy is brighter than the high-latitude Galactic emission. We may account for these additional sources by extending the least-squares method to include a statistical description of these sources. For specificity, we will work with the high-latitude portion of the DMR 4-year maps, defined as the region $|b| > 20°$ with custom cutouts at Orion and Ophiuchus[17]. We assume that the DMR maps are a superposition of CMB emission, Galactic emission, and noise,

$$\Delta T^{\rm DMR} = \Delta T^{CMB} + \alpha \Delta X^{\rm Gal} + n,$$

where $\Delta T^{\rm DMR}$ is the antenna temperature in a DMR map, $\Delta X^{\rm Gal}$ is the intensity of the Galactic template map (not necessarily in temperature units), and n is the instrument noise, related to the number of observations N in each pixel by $n = \frac{\sigma_0}{\sqrt{N}}$. The coefficient α converts the units of the Galactic map to antenna temperature at the DMR frequency.

We estimate the correlation coefficient α by minimizing

$$\chi^2 = \sum_{a,b} (T - \alpha X)_a \, (\mathbf{M}^{-1})_{ab} \, (T - \alpha X)_b, \qquad (1)$$

where T is a vector consisting of the DMR temperatures in each high-latitude pixel[9], X is a similar vector for the Galactic template map, and $\mathbf{M}$ is the covariance matrix between the

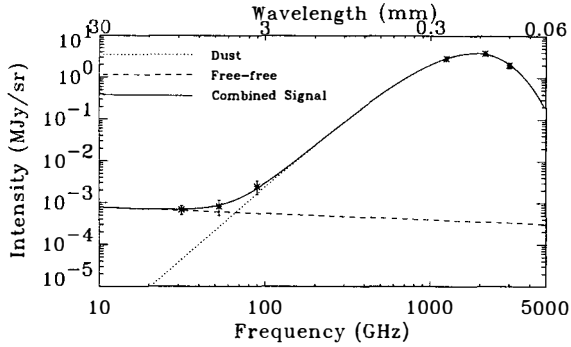

Figure 1: Spectrum of correlated intensity fluctuations in the DMR and DIRBE data at $|b|>20°$. Far-infrared points represent the standard deviation of the DIRBE maps after subtracting a fitted monopole and dipole, and include calibration uncertainties. Long-wavelength points are the values inferred from the cross-correlation of the DMR and DIRBE maps. The fitted free-free emission and single-component dust model are also shown.

elements of T. For a power-law spectrum of CMB anisotropy, the covariance matrix (including instrument noise) becomes

$$M_{ab} = \langle T_a T_b \rangle = \frac{1}{4\pi} \sum_\ell (2\ell+1) W_\ell^2 C_\ell P_\ell(\hat{n_a} \cdot \hat{n_b}) + \frac{\sigma_0^2}{N_a} \delta_{ab} \tag{2}$$

where W_ℓ^2 is the experimental window function that includes the effects of beam smoothing and finite pixel size, C_ℓ is the power spectrum, $P_l(\hat{n_a} \cdot \hat{n_b})$ is the Legendre polynomial of order ℓ, $\hat{n_a}$ is the unit vector towards the center of pixel a, and N_a is the number of observations for pixel a. We assume a scale-invariant power spectrum[18],

$$C_\ell = C_\ell(Q_{rms-PS}, n) \equiv (4\pi/5) Q_{rms-PS}^2 \frac{\Gamma(\ell + (n-1)/2)\Gamma((9-n)/2)}{\Gamma(\ell + (5-n)/2)\Gamma((3+n)/2)} \tag{3}$$

with amplitude $Q_{rms-PS} = 18\ \mu$K and index $n = 1$[13]. In the limit that only instrument noise is considered ($Q_{rms-PS} = 0$), the covariance matrix $\mathbf{M}$ is diagonal and Eq. 1 reduces to a noise-weighted least-squares estimate of α.

3 Galactic Microwave Emission

We cross-correlate the DMR maps with three Galactic templates: the synchrotron-dominated 408 MHz survey[19] a "cosmic-ray" synchrotron model[4] with spatially varying, frequency-dependent spectral index $\beta_{\rm synch}$, and the dust-dominated DIRBE 140 μm survey, from which a model of zodiacal dust emission has been removed. All templates are convolved with the DMR

[2]For computational reasons, the direct pixel basis uses maps degraded one step in pixel resolution, leaving 954 high-latitude pixels, each of diameter 5°.2.

beam prior to analysis. Table 1 shows the fitted correlation coefficients between the 4-year DMR maps and the Galactic templates, derived using Eq. 1 in a maximum-likelihood analysis with the "brute-force" pixel basis. We evaluate the three DMR frequencies simultaneously, $T = [T_{31}, T_{53}, T_{90}]$, and account for possible cross-talk between the synchrotron and far-IR templates by fitting both templates simultaneously, $X = [X^{\rm synch}, X^{\rm DIRBE}]$. The uncertainties in Table 1 include the errors from instrument noise, chance alignments between the CMB and Galactic features, and cross-talk between the two Galactic templates.

We find no statistically significant correlation between the DMR sky maps and either the 408 MHz survey or the cosmic-ray synchrotron model. Both synchrotron templates have deficiencies and it is possible that neither template accurately reflects the distribution of synchrotron emission at millimeter wavelengths, regardless of overall normalization. The large-scale structure in the 408 MHz survey at $|b| > 20°$ is dominated by the North Polar Spur (Loop I), but this region has steeper spectral index and becomes increasingly less important at higher frequencies[20]. The cosmic-ray model accounts for both the spatial variation in $\beta_{\rm synch}$ and the steepening of the spectrum at higher frequencies, but the spatial structure of this model at the DMR frequencies is dominated by regions of flattened index at the southern declination limits of the 1420 MHz survey[21] used to generate this model. The DMR maps show no evidence for such bright regions, suggestive instead of sidelobe pickup at the southern declination limits of the 1420 MHz survey. Table 2 shows the *rms* fluctuations in antenna temperature corresponding to the fitted coefficients. We adopt an upper limit $\Delta T_{\rm synch} < 11$ μK (95% confidence) at 31.5 GHz for emission traced by either synchrotron template. This limit corresponds to synchrotron spectral index $\beta_{\rm synch} < -3.0$ between 408 MHz and 31.5 GHz.

Tables 1 and 2 show a statistically significant correlation between the DMR maps and the DIRBE 140 μm map; we obtain nearly identical results using the DIRBE maps at 100 or 240 μm. Note that the Galactic emission has nearly equal amplitude in the DMR 53 and 90 GHz channels but rises sharply at 31.5 GHz (Table 2). Figure 1 shows the intensity of the correlated emission fluctuations in the high-latitude portion of the DMR and DIRBE maps. The frequency dependence of the correlated signal is well described by a superposition of dust and free-free emission. We fit the *rms* DMR and DIRBE signals to emission models of the form

$$I_\nu = \tau(\frac{\nu}{\nu_0})^\beta B_\nu(T) \; + A_{\rm ff}(\frac{\nu}{\nu_0})^{-0.15}, \qquad (4)$$

i.e., a model with free-free emission plus a single dust population with enhanced submillimeter emissivity. The best fit occurs for dust temperature $T = 20.0^{+2.5}_{-4.0}$ K and emissivity $\beta = 1.5^{+1.1}_{-0.3}$, with opacity $\tau = (1.2^{+0.7}_{-0.4}) \times 10^{-5}$ (68% confidence). We may use these data to limit enhanced dust emissivity at long wavelengths: $\beta_{\rm dust} > 1.1$ at 95% confidence. Figure 2 shows the spectra of high-latitude Galactic emission derived from the DMR maps and Galactic templates. The fitted amplitudes correspond to $\Delta T_{\rm dust} = 2.7 \pm 1.3$ μK and $\Delta T_{\rm ff} = 7.1 \pm 1.7$ μK for the *rms* fluctuations in dust and free-free antenna temperature at 53 GHz. The anisotropy in Galactic emission reaches a minimum between 50 and 90 GHz.

The correlation technique is insensitive to emission whose spatial distribution is uncorrelated with the Galactic template maps. We estimate the amplitude of the total free-free emission (including any uncorrelated component) by analyzing a linear combination of the DMR maps designed to be sensitive to free-free emission (spectral index -2.15 in units of

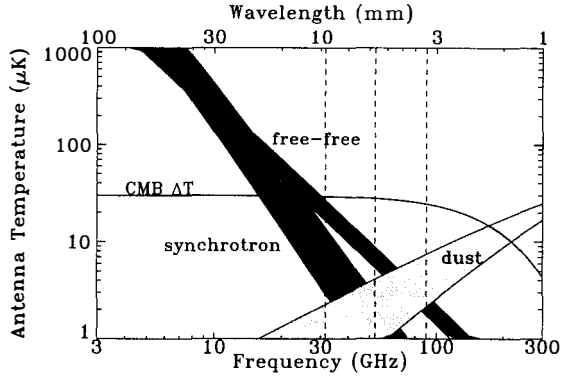

Figure 2: Frequency spectra of *rms* fluctuations in high-latitude Galactic emission. Free-free emission dominates synchrotron emission at frequencies above 20 GHz. Dashed lines indicate DMR observing frequencies.

antenna temperature), cancel emission with a CMB spectrum, and minimize instrument noise:

$$T_{\rm ff} = 0.37 \times \frac{1}{2}(T'_{31\rm A} \pm T'_{31\rm B}) + 0.02 \times \frac{1}{2}(T'_{53\rm A} \pm T'_{53\rm B}) - 0.47 \times \frac{1}{2}(T'_{90\rm A} \pm T'_{90\rm B}), \qquad (5)$$

where T' is the antenna temperature in each DMR channel after subtracting synchrotron and dust emission using the cosmic-ray and DIRBE models, respectively. We smooth the maps with a 7° FWHM Gaussian to further reduce the effects of noise, remove a fitted monopole and dipole, and compare the variance of the (A+B)/2 sum map to the (A-B)/2 difference map. The result is an estimate for the fluctuations in free-free antenna temperature at 53 GHz from all sources, $\Delta T_{\rm ff} = 5.2 \pm 4.2$ μK. This value compares well with the correlated component at the same effective smoothing, $\Delta T_{\rm ff} = 6.8 \pm 2.6$ μK. We further test for free-free emission uncorrelated with the far-IR dust by removing the correlated free-free component from each DMR channel prior to forming the free-free linear combination (Eq. 5). A power spectrum analysis of this uncorrelated free-free map shows no statistically significant signal at any $\ell < 30$. The correlated component must form at least 1/3 of the total free-free emission (95% confidence) and may form the bulk of this emission.

The observed correlation between the free-free and dust components on large angular scales implies that the far-IR dust distribution may be used (within certain limits) as a template for the free-free emission from the diffuse warm (electron temperature $T_e \sim 10^4$ K) ionized interstellar medium. We may fit the correlation coefficients from Table 1 to dust and free-free frequency dependences to derive the microwave free-free scaling of the DIRBE 140 μm maps:

$$\Delta T_{\rm ff} = \alpha_{\rm ff} X^{\rm DIRBE} [\frac{\nu}{53\ {\rm GHz}}]^{-2.15}$$

in units μK antenna temperature, where $\alpha_{\rm ff} = 2.07 \pm 0.20$ μK MJy^{-1} sr.

The *rms* fluctuations in free-free emission traced by the DIRBE maps on 7° angular scales are small, $\Delta T_{\rm ff} = 7.1 \pm 1.7$ μK at 53 GHz. Assuming that free-free emission remains

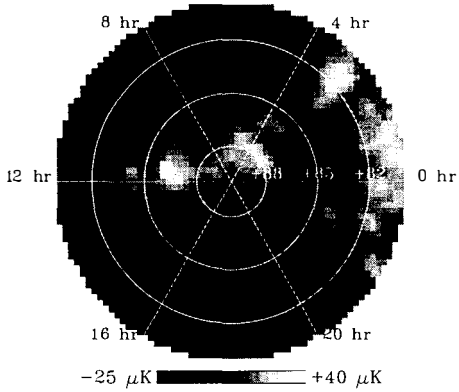

Figure 3: Fluctuations in the DIRBE 100 μm dust emission over the north celestial polar cap, scaled to free-free antenna temperature at 40 GHz assuming the same correlation observed by DMR at 7° resolution.

correlated with the dust at smaller angular scales, we may scale the DIRBE power spectrum to estimate the free-free contribution at angular scales of interest to the next generation of CMB anisotropy experiments. The far-IR dust emission traced by the DIRBE and IRAS maps has a steeply-falling power spectrum[12,14], $P_{\rm dust} \propto \ell^{-3}$. A full-sky map at 53 GHz with angular resolution 0.°5 would observe *rms* free-free emission of 6.1 ± 2.0 μK averaged over the high-latitude sky. Surveys restricted to smaller regions exclude power from Fourier modes with wavelength larger than the survey size. A $10° \times 10°$ survey (corresponding to modes $\ell > 18$) with angular resolution 0.°5 would measure *rms* free-free emission of 1.5 ± 0.5 μK, where the quoted errors reflect only the uncertainty in the free-free normalization and do not include the variation from patch to patch on the sky. Emission at this level is well below the expected magnitude of CMB anisotropy, although individual patches may show free-free emission significantly larger than the high-latitude average. If the correlation persists unchanged to smaller angular scales, free-free emission should not be a serious contaminant to CMB anisotropy measurements at 0.°5 angular scales.

The assumption above that the dust/free-free correlation persists to smaller angular

Table 2: RMS Galactic Signal in DMR Sky Maps (μK)[a]

DMR Frequency		Galactic Template	
(GHz)	408 MHz	Cosmic-Ray	DIRBE 140 μm
31.5	5.7 ± 5.5	8.4 ± 5.5	22.7 ± 5.4
53	3.4 ± 3.7	3.9 ± 3.6	9.6 ± 3.8
90	-0.7 ± 3.6	1.9 ± 3.5	10.0 ± 3.6

[a] Units are antenna temperature. The quadrupole has not been subtracted. Results are quoted for $|b| > 20°$ with custom cutouts at Orion and Ophiuchus.

scales is testable. Many experimental groups have detected CMB anisotropy on angular scales below 1°, and could cross-correlate the detected anisotropy in each frequency channel with the IRAS or DIRBE far-IR dust templates (Eq. 1) to search for emission with the characteristic free-free spectrum. Figure 3 shows the pattern of intensity variations in the DIRBE 100 μm map over the north celestial polar region observed by the Saskatoon and MSAM experiments[22,23]. The pattern has been normalized to free-free antenna temperature at 40 GHz, assuming that the correlation observed over the full sky at 7° resolution persists to 0.°5 resolution over the polar cap. The *rms* fluctuations over the region $\delta > 82°$ correspond to $\Delta T_{\rm ff} = 11 \pm 3$ μK at 40 GHz. Beam chopping will remove the large-scale gradients and reduce the free-free contribution to small-scale CMB experiments, but a detectable signal may remain at the few μK level.

References

1) Fixsen, D.J., Cheng, E.S., & Wilkinson, D.T. 1983, PRL, 50, 620
2) Lubin, P., Villela, T., Epstein, G., & Smoot, G. 1985, ApJ, 298, L1
3) Wright, E.L., et al. 1991, ApJ, 381, 200
4) Bennett, C.L., et al. 1992, ApJ, 396, L7
5) Bensadoun, M., Bersanelli, M., De Amici, G., Kogut, A., Levin, S.M., Limon, M., Smoot, G.F., & Witebsky, C. 1993, ApJ, 409, 1
6) Gutiérrez de la Cruz, C.M., Davies, R.D., Rebolo, R., Watson, R.A., Hancock, S., & Lasenby, A.N. 1995, ApJ, 442, 10
7) Kogut, A., Banday, A.J., Bennett, C.L., Górski, K.M., Smoot, G.F., & Wright, E.L./ 1996, ApJ, 464, L5
8) Banday, A. & Wolfendale, A.W. 1991, MNRAS, 248, 705
9) Désert, F.-X., Boulanger, F., & Puget, J.-L. 1990, A&A, 327, 215
10) Reynolds, R.J. 1992, ApJ, 392, L35
11) Bennett, C.L., et al. 1994, ApJ, 434, 587
12) Kogut, A., Banday, A.J., Bennett, C.L., Górski, K.M., Hinshaw, G., & Reach, W.T. 1996a, ApJ, 460, 1
13) Górski K.M., Banday, A.J., Bennett, C.L., Hinshaw, G., Kogut, A., Smoot, G.F., & Wright, E.L., 1996, ApJ, 464, L11
14) Gautier, T.N., Boulanger, F., Pérault, M., & Puget, J.L. 1992, AJ, 103, 1313
15) Fixsen, D.J, Cheng, E.S., Gales, J.M., Mather, J.C., Shafer, R.A., & Wright, E.L. 1996, ApJ, submitted
16) Brandt, W.N., Lawrence, C.R., Readhead, A.C.S, Pakianathan, J.N., and Fiola, T.M., 1994, ApJ, 424, 1
17) Bennett, C.L., et al. 1996, ApJ, 464, L1
18) Bond, J.R., and Efstathiou, G., 1987, MNRAS, 226, 655
19) Haslam, C.G.T., Salter, C.J., Stoffel, H., and Wilson, W.E., 1982, A&A Suppl., 47, 1
20) Lawson, K.D., Mayer, C.J., Osborne, J.L, & Parkinson, M.L. 1987, MNRAS, 225, 307
21) Reich, P., & Reich, W. 1988, A&AS, 74, 7
22) Netterfield, C.B., Devlin, M.J., Jarosik, N., Page, L., & Wollack, E.J. 1996, ApJ, submitted
23) Cheng, E.S., et al. 1996, ApJ, 456, L71

RADIO FREQUENCY FOREGROUND EMISSION AND THE SEPARATION OF MICROWAVE ANISOTROPIES FROM FOREGROUND CONTAMINATION

A.N. Lasenby
MRAO, Cavendish Laboratory
Cambridge, U.K.

Abstract

The effects on CMB measurements of foreground contamination due to synchrotron radiation, free-free emission and discrete sources are considered. Estimates of the level and power spectrum of the Galactic fluctuations are made using low frequency maps and recent Tenerife data. New methods for achieving a frequency-based separation of Galactic and CMB components are discussed, and a positive/negative maximum entropy algorithm shown to be particularly powerful in this respect.

1 Introduction

A common feature of all current and future CMB experiments is that contamination of the CMB signal by foreground components must be dealt with. The most important contaminants over the frequency range of interest for the CMB are the effects of discrete radio and sub-mm sources, and the effects of our own Galaxy. Discrete sources can in principle be discriminated against on the basis of their quite different angular size compared to the CMB fluctuations of interest. For Galactic effects however, no such assumption can be made, and we must discriminate between them and CMB purely on the grounds of their differing behaviour with frequency.

In this context it is very important to have as good an estimate as we can of the likely level of Galactic anisotropies, and to be armed with good algorithms for separating out their effects. This is an area which will see great development over the next few years as we prepare for the

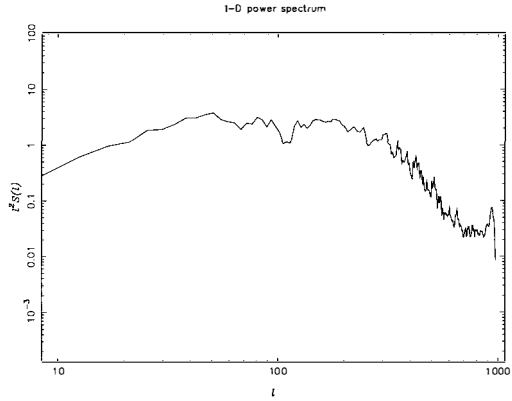

Figure 1: 1-d power 408 MHz spectrum for Tenerife patch

next generation of experiments, but as a preliminary effort in this direction we consider here, in schematic form, some recent estimates of Galactic variation gathered using current CMB experiments and low frequency maps. Data on a new type of discrete source whose spectrum can mimic a thermal source is also discussed. In the main part of the contribution, methods of performing the Galactic frequency separation are briefly reviewed, and the good performance for this purpose of a maximum entropy algorithm allowing both positive and negative fluctuations is highlighted.

2 Power spectrum and level of Galactic fluctuations

It is difficult to use the low frequency 408 MHz [6] and 1420 MHz [11] maps to extrapolate Galactic variations to CMB observing frequencies. The problems include difficulties with base-levels, scanning effects and of course with only two frequencies available only one spectral index can be estimated, whereas in principle the maps are mixtures of synchrotron and free-free emission, which have different spectral indices. As further problems, the synchrotron spectral index probably varies with frequency (on physical grounds it is expected to steepen with increasing frequency), and the maps are of a limited resolution (0.85° and 0.6° at 408 and 1420 MHz respectively) which makes it difficult to assess effects on scales below where the first Doppler peak is expected to lie for CMB fluctuations in an inflationary picture.

However, one thing we *can* use the low frequency maps for is to estimate the spatial power spectrum of high-latitude Galactic variations, at least on angular scales above the point where scanning effects and/or the limited resolution become significant. Figs. 1 and 2 (prepared by M.P. Hobson) show the 1-dimensional spatial power spectra at 408 and 1420 MHz for a patch of sky which has been extensively sampled by the 'Tenerife' experiments. The section used is 165° to 225° in Right Ascension and 35° to 45° in Declination. A Hanning window has been applied and an overall mean subtracted. The spectrum is given in terms of spherical multipole l and multiplied by l^2, so that it can be directly compared to the usual plots of CMB power — in particular, a scale invariant spectrum would have zero slope on this plot. It has recently been suggested, on a number of grounds, that the Galactic power spectrum behaves as l^{-3} as one approaches smaller angular scales [12]. The observational basis of this for dust emission seems

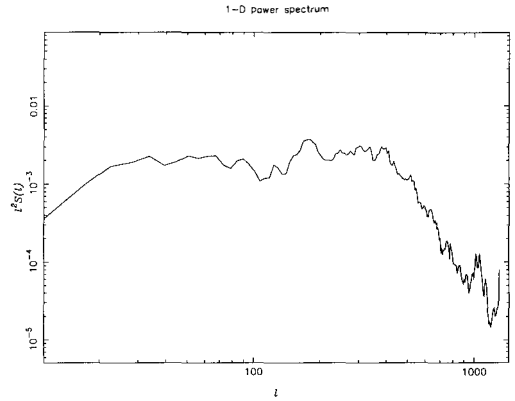

Figure 2: 1-d power 1420 MHz spectrum for Tenerife patch

well established, but the plots presented here favour a slightly less steep index for synchrotron emission (assuming this is the dominant component at 408 and 1420 MHz). In fact, the fall off at higher l away from an l^{-2} scale-invariant behaviour, begins in both plots at an angular scale which corresponds to the effects one would expect given the limited resolution of the maps. In any case, these results make it clear that the Galactic foreground problem will not get any *worse* compared to the CMB levels as one goes to higher resolutions, and this is encouraging for future experiments.

2.1 Estimating the fluctuation level

The Tenerife experiments constitute a suite of three instruments, operating at 10, 15 and 33 GHz, on angular scales of $\sim 5°$, and are therefore potentially well-suited to providing an estimate of the Galactic component on these scales. They were designed and built at Jodrell Bank [3, 4] and are operated by the IAC in-situ on Tenerife island. In fact, the level of anisotropy seen does not change very much in passing from 15 to 33 GHz [5] and this makes it difficult to assess the Galactic contribution, the implication being that the majority of the signal detected is CMB. However, we can set upper limits on the Galactic contribution as follows. Using the COBE DMR 2 year data and an assumed scale invariant CMB spectrum, we can predict a level of 31 μK that should be the *rms* observed in the Tenerife scans (at all frequencies since the beam geometry is the same at each frequency). We can then estimate other contributions to the signal (in particular the point source contribution) and then subtract in quadrature from the *observed rms* in order to obtain a residual, which can be interpreted as an estimate of the Galactic contribution. This process is shown in Table 1, with the result and 68% error bounds given in the row labelled 'residual'. In the next two rows, the predicted Galactic contribution is shown assuming first a spectral index ($T \propto \nu^{-\beta}$) of $\beta = 2.75$ in going from 1420 MHz to the Tenerife frequencies and secondly using the 408 and 1420 MHz maps themselves to provide the spectral index to use in the extrapolation. In the final row, the β necessary to get the residuals found starting from 1420 MHz is shown, and indicates a considerable steepening over the canonical 2.75 value. The area of sky included in generating these figures is the same as used for the power spectral plots shown above.

The fact that the residuals do not change too much between 10 and 15 GHz suggests that

Component	10GHz signal μK	15GHz signal μK
Point sources	12.8	6.5
Signal	39^{+16}_{-14}	37^{+11}_{-8}
CMB pred. ($n = 1$)	31	31
Residual	24^{+22}_{-24}	20^{+16}_{-20}
1420 MHz $\beta = 2.75$	89	33
408/1420 MHz	185	76
β from 1420 MHz	3.4	3.0

Table 1: Breakdown of different contributions to the measured anisotropy in the Tenerife experiments at 10 and 15 GHz.

they do not represent a true Galactic level. (For example, even wholly free-free would reduce by a factor ~ 2.3 in passing from 10 to 15 GHz.) However, we could takes these numbers as 'worst case' levels. Thus, if we assume a free-free spectrum and take the numbers at 15 GHz, we can now predict the levels that will be seen in the COBRAS/SAMBA lower channels on the $\sim 5°$ scale.

$$\begin{array}{ccccc} \nu(\mathrm{GHz}) & 31.5 & 53 & 90 \\ \Delta T_{\mathrm{Gal}}(\mu\mathrm{K}) & < 4^{+4}_{-4} & < 1.4^{+1.1}_{-1.4} & < 0.46^{+0.37}_{-0.46} \end{array}$$

We can compare these levels with the ($|b| > 20°$) all-sky free-free levels suggested by Kogut's analysis (this volume) of the COBE DMR – DIRBE 140 μm cross-correlation:

$$\begin{array}{ccccc} \nu(\mathrm{GHz}) & 31.5 & 53 & 90 \\ \Delta T_{\mathrm{ff}}(\mu\mathrm{K}) & 21 \pm 5 & 7 \pm 2 & 2.3 \pm 0.5 \end{array}$$

This suggests that the Tenerife region (approx 600 square degrees) is ~ 5 times better than average over the $|b| > 20°$ sky. The availability of such large patches with relatively low Galactic levels is encouraging for future ground-based and balloon experiments, especially when coupled with the conclusion that things get no worse as one moves down in angular scale from the Tenerife/COBE scales.

3 Discrete sources

As mentioned above, discrete radio and sub-mm sources can be discriminated from CMB fluctuations via their quite different angular scale. This requires having higher resolution available than the resolution at which the CMB information is desired of course. As an example of how trying to eliminate radio sources using spectral information alone could go wrong, we show in Fig. 3 the spectrum of the source RXJ1459.9+3337 over the radio sub-mm region. (This figure and associated information were kindly provided by Alistair Edge.) The data are from multi-frequency VLA observations taken in April 1996 and JCMT photometry in May 1996. RXJ1459.9+333 is a quasar that was discovered first in X-rays, and only later measured as a radio source. The spectrum 'turns over' at a point somewhere between 20 and 40GHz, and on the rising side has a slope of ~ 1.8, virtually indistinguishable from the CMB over this range.

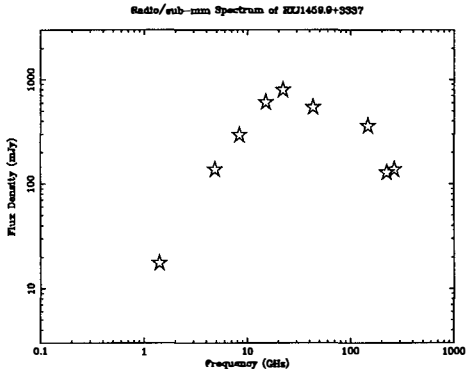

Figure 3: The radio/sub-mm spectrum for the X-ray selected quasar RXJ1459.9+3337. (Figure courtesy of A. Edge)

Since the source was selected at X-ray, rather than on the basis of its radio properties, we do not how how rare such sources are — it would not have turned up in previous radio surveys. Some indication of the frequency of occurrence of such sources may come from another such source, slightly weaker, which was found serendipitously in a search of $\sim$ 0.5 square degrees in a ROSAT cluster field using the Ryle Telescope at 15GHz. One such source in each $\sim$ 0.5 square degrees area would not pose a formidable threat to CMB astronomy, but shows that we do have to be on our guard for the unexpected.

4 Algorithms for frequency separation

Methods for separating foreground contamination from the CMB include pixel by pixel separation using least squares [2], marginalization [7, 10], Wiener filtering [1, 12] and maximum entropy methods (MEM) [8, 9]. Here we wish to consider particularly the use of 2-channel (positive/negative) maximum entropy, which can simultaneously achieve both deconvolution and frequency separation.

The classical MEM approach to combining observations, and removing the effects of a switched beam etc., uses an assumption of positivity (e.g. White and Bunn [13]). The CMB sky, however, apart from an unobservable monopole, has zero mean and is expected to fluctuate equally between positive and negative. White and Bunn try to repair this by adding a positive constant to the data, but the need to include a default measure as well results in less space in which to reconstruct negative as opposed to positive features, and a consequent bias in the results. This may be verified by numerical simulations. Instead 2- channel MEM may be used, in which positive and negative channels are reconstructed simultaneously. This has been shown to work well in deconvolution of switched beam data [8] and avoids the problem with bias. Recently, Maisinger *et al.* [9] have applied this technique to foreground/CMB separation using multifrequency data in the context of simulated interferometer observations, and the results below are taken from that paper. This method can be contrasted with that of Wiener filtering. The latter provides the optimal linear method in the case that the power spectrum of the separate components is known. MEM is a non-linear method, which does not rely on any

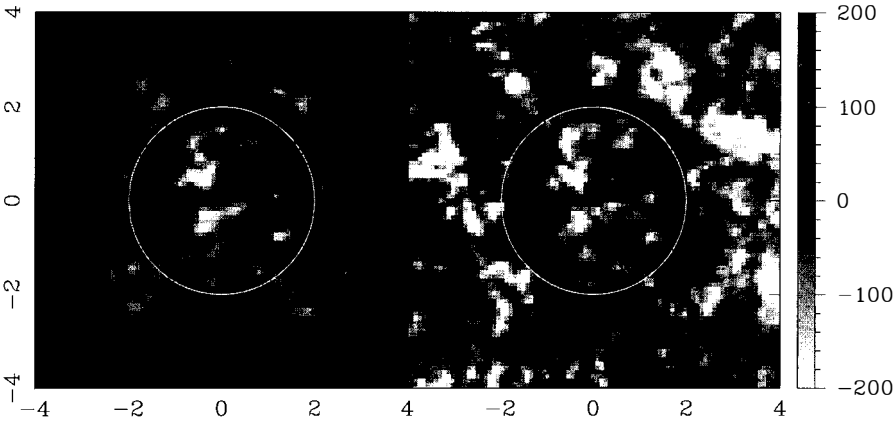

Figure 4: The MEM reconstruction of the CMBR component at 30 GHz in a $8° \times 8°$-field compared to the true underlying CMBR map used in the simulation. The grey-scales denote temperature fluctuations in μK. Neither of the maps is convolved with a synthesised beam, and the image is kept on the reconstruction grid. The circles indicate the FWHM of the primary telescope beam.

assumption about the power spectra, but just that the skies it reconstructs have the smallest information content consistent with the actual data.

The examples given in the following figures concentrate on the case of the VSA (see Jones, this volume). Two channels of data are used, at 28 and 38 GHz, each with bandwidth 2 GHz, with observations made for 30× 12 hours at each frequency. Fig. 4 shows the true (CDM) sky used in the simulation on the right, and its MEM reconstruction on the left. An important point which must be made is that the reconstruction can only be made within the sky area sampled by the telescope, and this is controlled by the circular primary beam. This is why the reconstruction fades to zero (the default) near the edges. In Fig. 5 the power spectrum recovered from the reconstructed map is shown together with the real power spectrum and errors estimated by Monte Carlo simulations. The real power spectrum of course deviates from the underlying ensemble CMB power spectrum since only the realization corresponding to the single sky patch used is available. Figs. 6 and 7 show the same but for an implementation of the Wiener filtering approach to this problem. Note in each case (MEM and Wiener), the true Galactic frequency spectral index used in the simulations ($\beta = 2.7$) is assumed known by the algorithm. However, it is not too difficult to relax this assumption, for example by including *two* channels for frequency reconstruction, each with a different assumed spectral index, and letting the algorithms decide how much weight to give each channel.

Overall it can be seen that this application of MEM is very successful, clearly outperforming the Wiener method in this case. We are investigating its use for frequency based foreground/CMB separation in a variety of other contexts also.

Acknowledgements. I am grateful to all the members of the CAT and Tenerife teams at Jodrell Bank and Cambridge for help with the preparation of material, particularly Mike Hobson, Stephen Hancock, Mike Jones, Klaus Maisinger, Carlos Gutiérrez and Aled Jones.

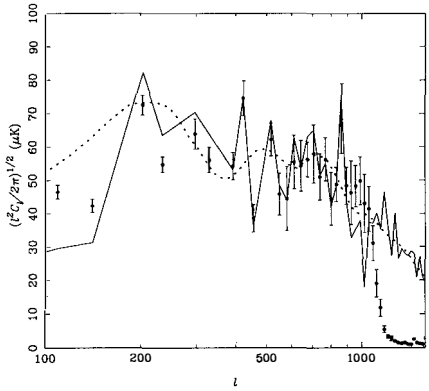

Figure 5: Comparison of power spectra of original (solid line) and reconstructed (points) CMBR maps. The error-bars indicate the 68-percent confidence limits as derived from 100 Monte-Carlo simulations with different noise realisations. Also plotted is the ensemble average CDM power spectrum (dotted line) from which the input map was generated.

References

[1] F.R. Bouchet, R. Gispert and J.L. Puget, 1995, in E. Dwek, ed., Proceedings of the COBE workshop *"Unveiling the Cosmic Infrared Background"*, Baltimore, Maryland, USA

[2] W.N. Brandt, C.R. Lawrence, A.C.S. Readhead, J.N. Pakianathan and T.M. Fiola, 1994, *Ap J.*, 424, 1

[3] R.D. Davies, R.A. Watson, E.J. Daintree, J. Hopkins, A.N. Lasenby, J. Sanchez-Almeida, J.E. Beckman, and R. Rebolo, 1992, *Mon. Not. R. astr. Soc.*, 258, 605

[4] R.D. Davies, C.M. Gutiérrez, J. Hopkins, S. Melhuish, R.A. Watson, R. Hoyland, R. Rebolo, A.N. Lasenby, and S. Hancock, 1996, *Mon.Not.R.astr.Soc*, 278, 883

[5] S. Hancock, R.D. Davies, A.N. Lasenby, C.M. Gutiérrez, R.A. Watson, R. Rebolo, and J.E. Beckman, 1994, *Nature*, 367, 333

[6] C.G.T. Haslam, C.J. Salter, H. Stoffel, and W.E. Wilson., 1982, *Astr. Astrophys. Suppl.*, 47, 1

[7] M.P. Hobson, A.N. Lasenby and M. Jones, 1995, *Mon. Not. R. astr. Soc.*, 275, 863

[8] A.W.Jones, S. Hancock, A.N. Lasenby, R.D. Davies, C.M. Gutiérrez, G. Rocha, R.A. Watson and R. Rebolo, 1996, *Mon. Not. R. astr. Soc.*, submitted

[9] K. Maisinger, M.P. Hobson and A.N. Lasenby, 1996, *Mon. Not. R. astr. Soc.*, submitted

[10] P.F. Scott *et al.*, 1996, *Ap J.*, 461, L1

[11] P. Reich and W. Reich, 1988, *Astr. Astrophys. Suppl.*, 74, 7

[12] M. Tegmark and G. Efstathiou, 1996, *Mon. Not. R. astr. Soc.*, in press

[13] M. White and E. Bunn, 1995, *Ap J.*, 443, L53

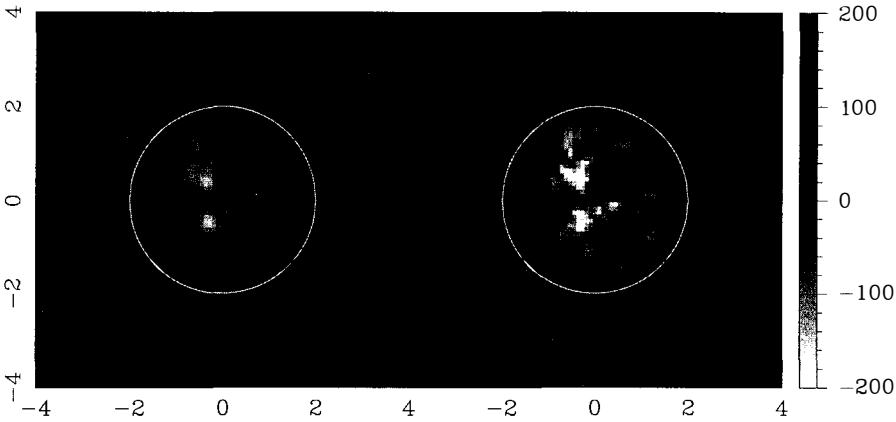

Figure 6: The Wiener filter reconstruction of the CMBR component at 30 GHz in a $8° \times 8°$-field compared to the true underlying CMBR map used in the simulation, multiplied by the primary beam. In contrast to Fig. 4, no deconvolution has been attempted in this case. The circles indicate the FWHM of the primary telescope beam.

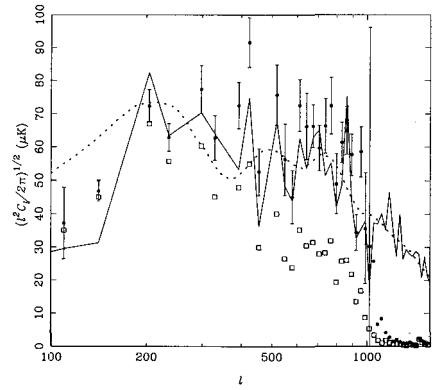

Figure 7: Comparison of power spectra of original (solid line) and reconstructed CMBR maps as obtained from linear filtering methods. Power spectra for both Wiener filtering (squares) and the rescaling method (dots) are plotted. Also plotted is the ensemble average CDM power spectrum (dotted line) from which the input map was generated.

PART V

DESIGN & DATA ANALYSIS ISSUES

THE OBSERVABILITY OF SECONDARY DOPPLER PEAKS

Michael P. Hobson
Mullard Radio Astronomy Observatory, Cambridge, UK.

Abstract

By proposing a statistic for the detection of secondary (Doppler) peaks in the CMBR power spectrum, the significance level at which such peaks may be detected are computed for a large range of model CMBR experiments. In particular, we investigate experimental design features required to distinguish between competing cosmological theories, such as cosmic strings and inflation, by establishing whether or not secondary peaks are present in the CMBR power spectrum.

1 Introduction

Experimental measurement of the Doppler peaks' positions and heights would fix at least some combinations of cosmological parameters (e.g. H_0, Ω_0 etc.) which are left free in inflationary models [1]. Furthermore, as shown by [2, 3], the *absence* of secondary Doppler peaks is a robust prediction for cosmic strings, although this may or may not be the case for textures [4, 5]. Therefore it appears that even determining whether or not there are secondary Doppler peaks offers an important alternative motivation for measuring the CMBR power spectrum.

We address this issue by proposing a statistic for detecting secondary oscillations, and studying how it performs for various models, using different experimental strategies. The results are encoded in a detection function Σ which indicates to within how many sigmas we can claim a detection of secondary oscillations, given a particular model and experiment.

We apply the statistic to both the standard CDM scenario and an open CDM model which is tuned to confuse inflation and cosmic strings in all but the existence or otherwise of secondary oscillations. For a wide range of experiments we allow the beam size, sky coverage, and detector noise to vary, and use this framework to compute the detection function for secondary peaks.

2 Power spectrum estimation from real observations

There are several factors affecting how well one can measure the CMBR power spectrum from real observations, which we now discuss.

(i) Distortion of the underlying spectrum due to the finite size of the observed field. For (square) fields of size $L \geq 4$ degrees (suitably windowed with a cosine bell or Hann window) this is not a severe problem for detecting secondary peak structure.

(ii) Cosmic/sample variance, which places constraints on the minimum sky-coverage necessary to achieve a given accuracy. Roughly speaking, if f_s is the fraction of sky observed, then $\sigma^2(C_\ell)/C_\ell^2 \approx 1/(\ell f_s)$.

(iii) Instrumental noise, which we shall assume is uncorrelated for simplicity, and characterised by $\sigma_{\rm pix}$, the rms pixel noise, and $\Omega_{\rm pix}$, the area of a pixel. If we consider the most general case where only a fraction f_s of the sky is mapped, then for a detector of fixed sensitivity, and for a fixed total observing time, then by varying $\Omega_{\rm pix}$ and f_s the quantity $w^{-1} = \sigma_{\rm pix}^2 \Omega_{\rm pix}(4\pi/f_s)$, remains constant, and is therefore an important qualifier for noise on maps obtained using different scanning strategies.

(iv) Diffuse foreground emission, which can severely hamper the measurement of CMBR anisotropies. A discussion of these foreground components, and the regions of frequency/multipole space in which each dominates, is given by [6]. The main components of this foreground are Galactic dust, synchrotron and free-free emission. Algorithms for separating these components from the CMBR signal are discussed by [6] and [7]. Typically the errors associated with the separation process are of a similar magnitude to the average errors on an individual frequency channel due to instrumental noise alone, but details depend on the separation algorithm used.

(v) Point sources, which cannot be removed from spectral information alone. This requires the identification of the sources by higher-resolution observations at a frequency close to that of the CMBR observations, with sufficient flux sensitivity to indentify all point sources down to some flux limit roughly equal to the instrumental noise of the CMBR observations. We note here that although it is generally believed that point source contamination becomes less important as the observing frequency increases above about 100 GHz, there is no direct evidence for this. Moreover, even the population of radio point sources at frequencies above about 10 GHz is rather uncertain, and it may be inadvisable to rely on low frequency surveys such as the 1.5 GHz VLA FIRST survey [8] to subtract point sources from CMBR maps made at much higher frequencies.

3 Observing Doppler peaks in standard CDM

The idea is to apply to a particular model a statistic sensitive only to the existence or absence of secondary oscillations in the power spectrum. In this section we consider the power spectrum predicted by the standard inflation/CDM scenario with $\Omega_0 = 1$, $h_0 = 0.5$ and $\Omega_b = 0.05$ (which we shall call sCDM).

To this end we first compute the average broad band power C_i in each of several equally spaced-bins, denoted by horizontal bars in Fig. 1. We then infer the convexity $\mathcal{C}_i$ of the spectrum at each bin position (apart from the first and last bins) from $\mathcal{C}_i = (C_{i-1} + C_{i+1})/2 - C_i$. These convexities are all negative if there are no secondary peaks, but alternate in sign for sCDM. If the overall error in $\mathcal{C}_i$ is $\sigma^2(\mathcal{C}_i)$ then one can define an oscillation detection function as

$$\Sigma_i = \frac{|\langle \mathcal{C}_i \rangle|}{\sigma(\mathcal{C}_i)}, \tag{1}$$

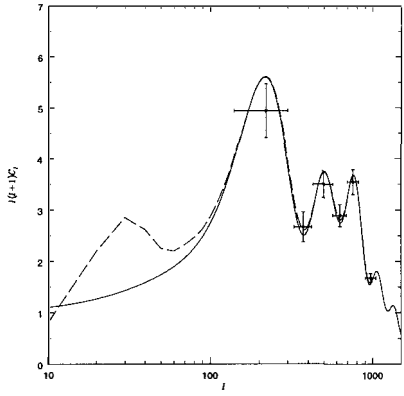

Figure 1: The ensemble average power spectrum predicted by sCDM (solid line), and the ensemble average power spectrum for a square observing field of size 10 degrees after windowing with a cosine bell (dashed line). The points indicate the corresponding power spectrum estimates for a particular realisation in each of the bins indicated by the horizontal error bars. The vertical error bars indicate the theoretical cosmic/sample variance in the absence of noise.

for $i = 2$ and $i = 4$, which tells us to within how many sigmas we can claim a detection of secondary peaks. The method for computing the estimates C_i of the power spectrum in each bin, and their associated standard errors, taking into account limited sky-coverage and instrumental noise, are discussed in detail in [9] and [10].

From Fig. 1 we see that the first dip in the sCDM power spectrum is more easily detected than than the second one, a situation only exacerbated by finite resolution and the presence of instrumental noise. Therefore we shall confine ourselves to considering the detection function Σ_2, which from now on we refer to simply as Σ.

The detection function $\Sigma = \Sigma(L, \theta_b, w^{-1})$, where L is the linear size of the observed (square) field [the all-sky limit can be recovered by setting $L^2 = 4\pi$ sr $\approx$ (202 deg)^2], θ_b is FWHM of the observing beam, and w^{-1} is the noise level discussed above. This function is plotted in Fig. 2 for the low noise case $w^{-1} = (25\mu\text{K})^2(\text{deg})^2$ and the high-noise case $w^{-1} = (60\mu\text{K})^2(\text{deg})^2$.

For any beamsize there is a maximum sky coverage beyond which the detection is not improved. If anything the level of the detection decreases, but typically not by much. The ideal scanning strategy is then defined by a line $L_i(\theta_b)$ which intersects the contours of Σ at the lowest L-value at which a plateau has been achieved in the detection function. The significance of the detection obtained for an ideally scanned experiment depends on the beam size. For example, in the low-noise case, if $\theta_b = 0.6°$, the ideal coverage is a patch of $L_i(0.6°) = 5$ degrees, which results in a 3-sigma detection. If $\theta_b = 0.5°$, on the other hand, an 8-sigma detection can be obtained with $L_i = 35$ degrees. The detection provided by an optimally scanned experiment increases at first very quickly as the beam is reduced below $\theta_b = 0.6°$ (from 3-sigma at $\theta = 0.6°$ to 33-sigma at $\theta_b = 0.2°$). By reducing θ_b from 0.2° to zero, however, the detection is only increased by 2-sigma (from 33 to 35). For this level of noise the maximal detection is 35 sigma and is achieved with $\theta_b < 3'$ and all-sky coverage. For low noise levels all-sky coverage is never harmful, but it is the beamsize that determines how good a detection can be achieved, and how much sky coverage is actually required for an optimum level of detection.

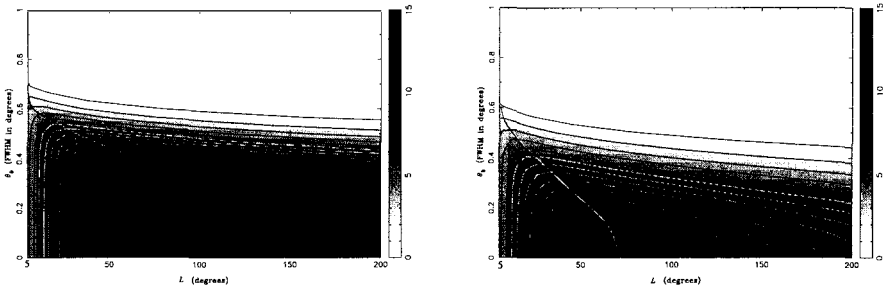

Figure 2: (Left) Low noise $w^{-1} = (25\mu K)^2(\mathrm{deg})^2$ contours of the Σ function. Sky coverage L varies between 5 degrees and all sky ($L = 202$ degrees), and the beamsize FWHM between 0 and 1 degrees. (Right) High noise $w^{-1} = (60\mu K)^2(\mathrm{deg})^2$ contours of the Σ function.

For noise levels of the order $w^{-1} = (25\mu K)^2(\mathrm{deg})^2$ the overall picture is always as in Fig. 2. In particular, there is always a top contour indicating the maximal detection allowed by the given noise level. The maximum Σ is always achieved with infinite resolution, but one falls short of this maximum by only a couple of sigmas if $\theta_b \approx 0.1°$. If the noise is much smaller than this, however, the summit of Σ is beyond $L = 202°$. For $w^{-1} = (15\mu K)^2(\mathrm{deg})^2$, for instance, all-sky coverage becomes ideal for any $\theta_b < 0.3°$.

If, on the other hand, the noise is much larger than $w^{-1} = (25\mu K)^2(\mathrm{deg})^2$ then the Σ contours are qualitatively different, as shown in Fig. 2 for $w^{-1} = (60\mu K)^2(\mathrm{deg})^2$. The beamsize is now a crucial factor. A beamsize of $\theta_b = 0.5°$ would provide a 3-sigma detection (with $L_i = 10°$), but reducing the beamsize to about $\theta_b = 0.4°$ improves the detection to 6-sigma (with $L_i = 20°$). It is also clear from the figure that, for high noise levels, forcing all-sky coverage dramatically decreases the detection.

4 Open CDM models and cosmic strings

We may repeat the above analysis for different cosmological models. We therefore consider the case of maximal confusion between inflation/CDM and cosmic string scenarios by comparing a cosmic strings model with a CDM model for which the main peak in the power spectrum has the same position and shape (but the latter exhibits secondary peaks). For definiteness we have chosen a CDM theory with a flat primordial spectrum, $\Omega_0 = 0.3$, $h_0 = 0.6$, and $\Omega_b h_0^2 = 0.02$. We shall call this theory stCDM, the CDM competitor of cosmic strings. As before we simply study the first dip detection function of stCDM, and then take this detection function as a cosmic string rejection function.

In Fig. 3 we show the angular power spectrum of stCDM (solid line) and a possible power spectrum for cosmic strings (dotted line). We then simply repeat the same exercise as in the previous section to obtain the detection function of the first dip of stCDM. The results are shown in Fig. 4 for the same noise levels as before.

Overall we see that in signal dominated regions the detection is much better for stCDM than for sCDM. This is because features at higher ℓ have a smaller cosmic/sample variance (which is proportional to $1/\ell$). It can be checked that the cosmic/sample variance limit, obtained with a single-dish experiment with no noise, is now $\Sigma \approx 197L^2/(4\pi)$ (as opposed to $\Sigma \approx 77L^2/(4\pi)$ for sCDM). Even in the presence of noise, wherever the signal dominates, the detection is better

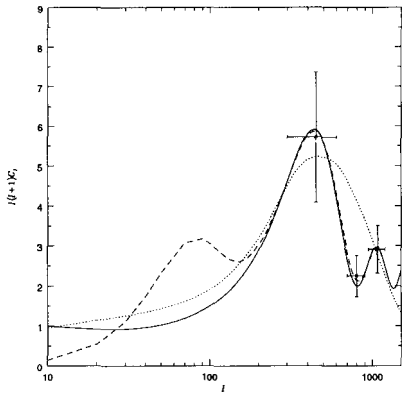

Figure 3: The angular power spectrum of stCDM (solid line) and one possible cosmic string scenario (dotted line). The dashed line is the ensemble average stCDM power spectrum as sampled by an experiment with a field size $L = 2$. The points indicate the average power in each bin for stCDM. The horizontal errorbars denote the width of the bins, and the vertical errorbars show the sample variance of the power estimates for such an experiment assuming no instrumental noise.

for stCDM. However, in noise-dominated regions the behaviour of the detection function for stCDM and CDM is very different.

The signal-dominated region is greatly reduced in stCDM. Much smaller beamsizes θ_b are now required for any meaningful detection. As shown in Fig. 4, one would now need $\theta_b < 0.3°$ and $\theta_b < 0.25°$, for noises $w^{-1} = (25\mu K)^2(\mathrm{deg})^2$ and $w^{-1} = (60\mu K)^2(\mathrm{deg})^2$ respectively, in order to obtain a reasonable detection. Again one can plot an ideal scanning line in the beam/coverage sections defined by a fixed noise w^{-1}. The ideal sky coverage is much smaller for stCDM than for sCDM. In general the contours of Σ for stCDM compared to sCDM are squashed to lower θ_b, lower L, and achieve higher significance levels, with steeper slopes. Following an ideal scanning line for any fixed w^{-1} one reaches a maximal detection allowed by the given level of noise, which is always better for stCDM than for sCDM. This maximal detection is normally obtained with a small sky coverage, and infinite resolution. Nevertheless, one falls short of this maximum by only a few sigma if the resolution is about $\theta_b = 0.05° - 0.1°$. From Fig. 4, for $w^{-1} = (25\mu K)^2(\mathrm{deg})^2$, one may now obtain a maximal 43-sigma detection for an ideal scanning area of $L = 65$ degrees. If $\theta_b = 0.1°$ a 36-sigma detection is still obtained. We also see that a beamsize of $\theta_b < 0.25°$ is required to obtain a 3-sigma detection (with $L = 4$ degrees), and a 10-sigma detection can be achieved only with $\theta_b \approx 0.15°$ (and $L_i = 18$ degrees). All-sky coverage for an experiment targeting stCDM is generally inadvisable, and it would only be optimal for the extremely low level of noise $w^{-1} < (11\mu K)^2(\mathrm{deg})^2$.

5 Conclusions

The results obtained here are useful for future CMBR projects in two different ways. Firstly they allow the choice of an ideal scanning strategy (choice of resolution and sky coverage) for

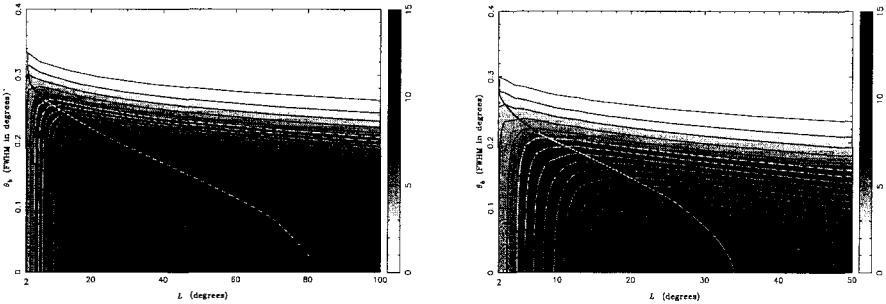

Figure 4: (Left) Low noise $w^{-1} = (25\mu K)^2(\mathrm{deg})^2$ contours of the detection function Σ for stCDM. (Right) High noise $w^{-1} = (60\mu K)^2(\mathrm{deg})^2$ contours of the detection function.

detecting secondary Doppler peaks, given observational constraints such as the instrumental noise level and the total observing time. Secondly, one may compute the expected value of the detection, assuming ideal scanning, as a function of these parameters. This provides lower bounds on experimental conditions for a meaningful detection as well as an estimate of how fast detections will improve thereafter.

These results also indicate that in order to study Doppler peak features for sCDM, depending on the noise levels, a large sky coverage might be desirable, even for a resolution of about $\theta_b = 0.4° - 0.5°$. If, however, one is instead to test the high-l opposition between low Ω CDM and cosmic strings, then a rather higher resolution is required. Furthermore, in this context, all-sky scanning is not only unnecessary, but in fact undesirable.

Acknowledgements. Thanks to Joao Magueijo for many useful discussions.

References

[1] Jungman G., Kamionkowski M., Kosowsky A., Spergel D., 1996, Phys. Rev. Lett., submitted.

[2] Albrecht A., Coulson D., Ferreira P., Magueijo J., 1996, Phys.Rev.Lett., 76, 1413

[3] Magueijo J., Albrecht A., Coulson D., Ferreira P., 1996, Phys.Rev.Lett., in press

[4] Crittenden R., Turok N., 1995, Phys. Rev. Lett., 75, 2642

[5] Durrer R., Gangui A., Sakellariadou M., 1996, Phys. Rev. Lett., 76, 579

[6] Tegmark M., Efstathiou G., 1996, *MNRAS*, in press

[7] Maisinger K., Hobson M. P., Lasenby A., 1996, *MNRAS*, submitted

[8] Becker R. H., White R. L., Helfand D. J., 1995, *Astrophys. J.* **450**, 559

[9] Hobson M. P., Mageuijo J.,1996, *MNRAS*, submitted

[10] Magueijo J., Hobson M. P., 1996, Phys.Rev.Lett., submitted

ASSESSING OBSERVING STRATEGIES

L. Knox
Canadian Institute for Theoretical Astrophysics, Toronto, Canada.

Abstract

Given an instrument and a strategy for measuring the cosmic microwave background anisotropy, one should be able to calculate the expected uncertainties on the angular power spectrum, or on the parameters of a model spectrum. Here I present a semi-analytic method for doing so that is applicable to both differential and map-making observations. As an example, I examine the case of a balloon-borne bolometric instrument to be flown this spring (MSAM2) and find that a smoothly scanning secondary is better than a chopping one.

1 Method

The task at hand is to estimate, for a given instrument and observing strategy, the uncertainties to expect on the parameters, a_p, of some model angular power spectrum, C_l. The problem is simplified by transforming the data so that both the signal and noise covariance matrices are diagonal. The desired transformation is the Karhunen-Loeve [9] transformation independendently discovered and brought to cmb phenomenology by Bond [2] who calls it the signal-to-noise eigenmode transformation (S/N transformation). Bond [1] and White and Bunn [15] use it in their analyses of the COBE DMR maps. Vogeley and Szalay have shown how it is useful for analysis of galaxy redshift surveys [14].

The transformation is a non-unitary mapping of the data in the pixel basis, D_i, into the "signal-to-noise eigenmode" basis, D'_i:

$$D'_i = R_{ij}((C^N)^{-1/2})_{jk} D_k \tag{1}$$

where S_i and N_i are the signal and noise components of the data, $C^N_{ij} \equiv \langle N_i N_j \rangle$, R is the rotation matrix that diagonalizes $M \equiv (C^N)^{-1/2} C^S (C^N)^{-1/2}$ and $C^S_{ij} \equiv \langle S_i S_j \rangle$. It is straightforward to show that

$$\langle D'_i D'_j \rangle = (\lambda_i + 1)\delta_{ij} \tag{2}$$

where λ_i are the eigenvalues of the S/N matrix, M. Thus we have the desired transformation, since the signal and noise covariance matrices are diagonal in the new basis.

We can now think of the experiments as measuring the λ_i which are a function of the power-spectrum and therefore of the parameters, a_p. We can build a quadratic estimator for λ_i from D'_i by squaring it and subtracting unity:

$$\lambda_i^{\rm est} = D_i'^2 - 1 \tag{3}$$

This estimator has variance $2(\lambda_i + 1)^2$ since D'_i is a Gaussian random variable with variance $\lambda_i + 1$.

From here it is straightforward to calculate uncertainties on the parameters. First calculate the curvature matrix α:

$$\alpha_{pp'} = \sum_i \frac{1}{\sigma^2(\lambda_i)} \frac{\partial \lambda_i}{\partial a_p} \frac{\partial \lambda_i}{\partial a_{p'}}. \tag{4}$$

where $\sigma^2(\lambda_i) = 2(\lambda_i + 1)^2$. Then invert to get the desired result, the parameter covariance matrix [12, 8, 13]:

$$C^P_{pp'} = \left(\alpha^{-1}\right)_{pp'}. \tag{5}$$

Equation 5 is strictly true only if our estimates of a_p are Gaussian random variables. This will be approximately true as long as the data constrain the parameter well.

The covariance matrix is simply given by the inverse of the curvature matrix for the case when we have no prior information on the parameters. At the other extreme, if the parameters other than a_p are perfectly known then $\sigma^2(a_p) = 1/\alpha_{pp}$. The intermediate case is easily treated if the prior information is expressed as a covariance matrix $C_{\rm prior}$. Then

$$\sigma^2(a_p) = \left(\left(\alpha + C^{-1}_{\rm prior}\right)^{-1}\right)_{pp}. \tag{6}$$

To summarize, the procedure is straightforward. First choose a parametrized theory and calculate the signal and noise covariance matrices. This step requires a specific choice of theory parameters. Calculate the rotation matrix, R and the eigenvalue spectrum and its derivatives. Cacluate the curvature matrix, add any prior information and invert to get the estimated parameter covariance matrix.

The method is, in principle, analytic but I refer to it as semi-analytic since the necessary high-dimensional linear algebra requires numerical computation. By far, the most time-consuming of the above calculations is that of the eigenmode window function. However, this step is unnecessary for calculation of a specific parameter covariance matrix. The second most time-consuming step is the calculation of the signal covariance matrix, C^S. This calculation will have to be done eventually in order to analyze the data and hence it is worth while figuring out how to do it efficiently.

Before moving on to an application I make the connection with a well-known, less general, method for estimating parameter uncertainties. For a map with uniform full-sky coverage and Gaussian angular resolution, σ_b, the eigenmodes are the spherical harmonics with eigenvalues equal to $wC_l e^{-l^2\sigma_b^2}$ where w is the weight per solid angle. There are $2l+1$ modes for each l and thus $\sigma^2(\lambda_i) = 2(\lambda_i + 1)^2$ leads to the formula (derived by other means in [10]):

$$\sigma^2(C_l) = \frac{2}{2l+1}\left(C_l + w^{-1}e^{l^2\sigma_b^2}\right)^2. \quad (7)$$

Jungman et al. [8] used this formula and the analogs of Eq. 4 and 5 to calculate standard errors for an eleven parameter adiabatic gravitational instability model.

2 Application to MSAM2

In this section I apply the above formalism to the particular case of the second Medium Scale Anisotropy Measurement instrument (MSAM2). The MSAM instruments are balloon-borne off-axis Cassegraine telescopes with bolometric radiometers. The MSAM1 instrument is described in [5]. Detections have been reported from two of the flights [3] with the second flight confirming the results of the first [7]. The MSAM2 instrument uses the same gondola as MSAM1 but has a different radiometer and secondary mirror.

The largest component of atmospheric contamination dependends only on elevation and is slowly varying in time. Thus a standard technique to reduce atmospheric contamination is to rapidly sample a stretch of sky at constant elevation by motion of a secondary mirror from $-\theta_c$ to θ_c. Only linear combinations of the data that have no sensitivity to a spatially homogeneous signal are kept for further processing. In some cases those combinations sensitive to a gradient are discarded as well. Each linear combination corresponds to a "synthesized antenna pattern". The MSAM1 secondary motion was a three point chop. From the time stream, two antenna patterns were synthesized.

The MSAM2 secondary motion will be a triangle wave pattern of period T. Here we model the time stream of data as follows:

$$d(t) = A_0(\theta_i)/2 + \sum_{\mu=1}^{8} D_\mu^c(\theta_i)cos(2\pi\mu\frac{t}{T}) + \sum_{\nu=1}^{8} D_\nu^s(\theta_i)sin(2\pi\nu\frac{t}{T}). \quad (8)$$

where θ_i is a slowly changing function of time and refers to the point on the sky observed when the chopper is in its central position.

We cut the Fourier decomposition off at $\nu = \mu = 8$ because the peak-to-peak chop amplitude is 8 beam full-widths; higher frequency modes would have very little signal. Since the secondary motion is symmetric about $t = T/2$, the asymmetric Fourier modes will contribute zero signal. Thus the odd ν components are ignored.

If we assume that the noise in the time stream $d(t)$ is white, then the noise in each of the above modes will be independent; the noise covariance matrix C^N will be diagonal. A better model would also have terms that vary in time but not in space, as is the case for instrumental and atmospheric drifts. Having to fit for the coefficients of these terms would induce correlations in the noise covariance matrix C^N. Given a model of the drifts, it is straightforward to calculate C^N [6]. Here we ignore the effects of drifts and take the matrix to be diagonal. From a model of the bolometer and the foregrounds [4] (a one component dust model) we expect the sensitivity to CMB to be NET $\simeq 266\ \mu K\sqrt{\text{sec}}$.

Although the noise matrix is diagonal, the signal matrix is not. The off-diagonal correlations exist for three conceptually distinct reasons. First, the Fourier decomposition in Eq. 8 is for functions of period T but because of the triangle wave motion of the secondary, the same stretch of sky is scanned twice in that one period. The $D_\mu^c(\theta_i)$ and $D_\mu^s(\theta_i)$ are the cosine and sine coefficients of the sky sampled from $\theta_i - \theta_c$ to $\theta_i + \theta_c$, with fundamental frequency half what it would be for a Fourier decomposition. Second, the decompositions are not all done with the same origin. Thus, even if the fundamental mode had the right frequency, the modes

with $\theta_i \neq \theta_j$ are not orthogonal. Third, since the sky is not "white" like the noise (there are intrinsic correlations) the different modes are correlated – even when $|\theta_i - \theta_j| >> 2\theta_c$.

For a specific application, we examine the motion of the secondary. Is it better to move it in a step motion between two or three spots, or to smoothly scan it back and forth? Here I have addressed that question by computing the S/N eigenvalue spectra, shown in Figure 1, for a three-point chop and a triangle wave.

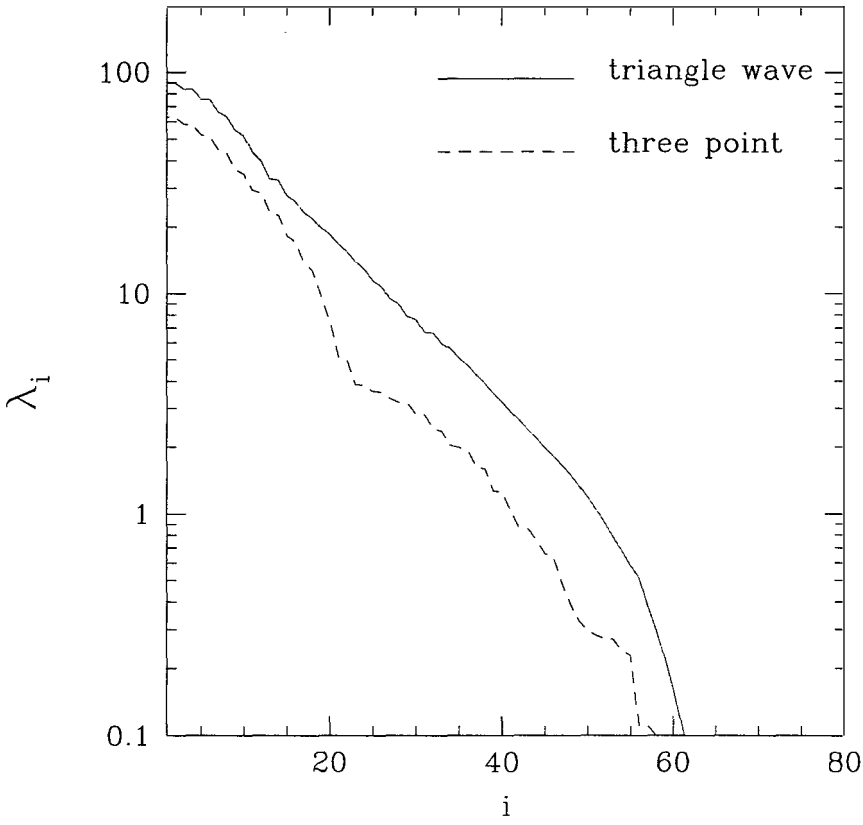

Figure 1: The S/N eigenvalue spectrum for a three-position secondary and for a smoothly scanning secondary.

The two curves shown in Fig. 1 are all S/N spectra for observing strategies that are the same in all respects except for the motion of their secondaries. They all point at a declination of $\delta = 78$ degrees on the transit meridian and the secondary moves back and forth $\pm 80'$ at constant declination for five hours. The beam is taken to be a Gaussian with $\sigma_b = 20'/(\sqrt{8ln2})$. The sky is observed in this manner for five hours. The rotation of the sky leads to coverage of a

strip 15.6 degrees long. For a theory I took a flat spectrum with:

$$\delta T_l^2 \equiv \frac{l(l+1)C_l}{2\pi} = (50\ \mu K)^2. \tag{9}$$

The dashed curve is for the secondary that executes a three-point chop. The single difference and double difference signals are analyzed. The solid curve is for the triangle wave motion. In this case the signals from the 12 different synthesized antenna patterns were analyzed. One can see that the chopping secondary is inferior to the smoothly scanning ones since its eigenvalue spectrum is lower for every mode.

As a rough guide to the power-spectrum sensitivity of the experiment, we can simply count the number of modes with $\lambda_i > 1$. This is because modes with $\lambda_i >> 1$ all have the same fractional error ($\sqrt{2}$) while those with $\lambda_i << 1$ have very large uncertainties. For a more precise comparison we can perform the sum

$$\sigma^2(A) = \left(\sum_i \frac{\lambda_i^2}{2(\lambda_i+1)^2}\right)^{-1} \tag{10}$$

where A is the amplitude of the spectrum whose shape has been assumed.

It is easy to see how sensitivity to the amplitude of the spectrum will change with varying sky coverage. Increasing the sky coverage by a factor of n will increase the number of modes by a factor of n. If the observing time remains fixed, then the noise in each pixel will increase, reducing each eigenvalue by a factor of n. From Fig. 1, we see that it would be highly beneficial to greatly increase the sky coverage.

Further applications of this method, as well as an appendix detailing the calculation of C^S and C^N, can be found in [11].

3 Acknowledgments

For useful discussions I would like to thank Andrew Jaffe and my collaborators on MSAM2, especially Grant Wilson whose questions stimulated this work.

References

[1] J.R. Bond, Phys. Rev. Lett. **74** 4369 (1995).

[2] J.R. Bond, *Cosmic Structure Formation and the Background Radiation*, in "Proc. IUCAA Dedication Ceremonies," Pune, India, Dec. 1992, ed. T. Padmanabhan, Wiley (1994).

[3] E. S. Cheng, *et al.*, Ap. J. **422**, L37 (1994); E. S. Cheng, *et al.*, Ap. J. **456**, L71 (1996).

[4] S. Dodelson, astro-ph/9512021.

[5] D. J. Fixsen *et al.*, Ap. J. (1996), astro-ph/9512006.

[6] M. Gladders, L. Knox and M. Kowitt, work in progress.

[7] C. A. Inman, *et al.*, submitted to Ap. J., astro-ph/9603017.

[8] G. Jungman, M. Kamionkowski, A. Kosowsky and D.N. Spergel, *Phys. Rev. Lett.* **76**, 1007 (1996); Jungman et al., astro-ph/9512139.

[9] Karhunen, K. 1947, *Uber lineare Methoden in der Wahrschleinlichkeitsrechnung*, Helsinki: Kirjapaino oy. sana

[10] L. Knox, *Phys. Rev. D* **52**, 4307 (1995).

[11] L. Knox, astro-ph/9606066.

[12] W.H. Press, B. Flannery, S.A. Teukolsky and W.T. Vetterling, "Numerical Recipes in Fortran", 2nd ed.

[13] M. Tegmark, astro-ph/9511148, to appear in Proc. Enrico Fermi, Course CXXXII, Varenna, 1995.

[14] M.S. Vogeley and A.S. Szalay, Ap. J., in press (1996).

[15] M. White and E. Bunn, astro-ph 9503054.

AN IMPROVED METHOD FOR PIXELIZING CMB SKY MAPS

Max Tegmark[1,2]
[1]*Max-Planck-Institut für Physik, Föhringer Ring 6,D-80805 München.*
[2]*Max-Planck-Inst. für Astrophysik, Karl-Schwarzschild-Str. 1, D-85740 Garching.*
Email: max@mppmu.mpg.de

Abstract

For power spectrum estimation
it's important that the pixelization
of a CMB sky map be
smooth and regular to high degree.
With this criterion in mind
the "COBE sky cube" was defined.
This paper has as central theme
to further improve on this elegant scheme
which uses a cube as projective base
- here an icosahedron is used in it's place.
Although the sky cube is excellent,
a further reduction of 20 percent
of the number of pixels can be obtained
while the filling factor is maintained,
and without any degradation
of accuracy for integration.
The pixels are rounder in this scheme where
they are hexagonal rather than square,
and the faces are small in this implementation
which simplifies area-equalization.
The reason distortion is lessened is that
the faces are smaller and therefore more flat.
To use the method, you can get
a FORTRAN code from the Internet.

1 Introduction

In astronomy and cosmology, this is the age of map-making. Recent ground-based and satellite-borne experiments have produced all-sky maps at a wide range of wavelengths, spanning from radio frequencies to the infra-red, ultraviolet and x-ray bands. Although the brightness distributions being measured are always continuous functions of position, the maps are in practice compiled and distributed with values only at some finite number of points, or *pixels*. As discussed below, a good choice of pixelization scheme can often substantially simplify the subsequent analysis of the data, and for this reason, considerable amounts of work have been spent on developing good schemes for pixelizing the celestial sphere. Arguably the best and most

elaborate method to date is the so-called *COBE sky cube* scheme [1, 4], which has been successfully employed for the DMR, DIRBE and FIRAS maps of the COBE satellite. This method has a number of desirable properties, and it is rather obvious that it is quite a good one that cannot be radically improved upon. However, the next generation of cosmic microwave background (CMB) maps from instruments such as the MAP and COBRAS/SAMBA satellites will be subjected to very extensive and time-consuming processing in order to obtain measurements of cosmological parameters. In view of this, it is timely to search for still better pixelization schemes, since even quite modest improvements can translate into substantial numerical gains.

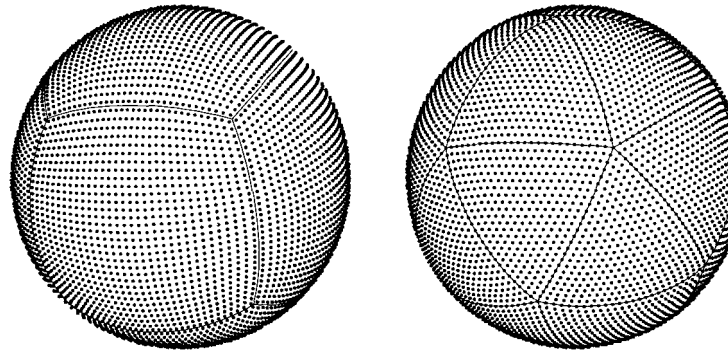

Figure 1. The cube-based (left) and icosahedron-based (right) pixelization schemes.

The purpose of this paper is to present such an improved method for pixelizing the sphere, akin to the sky cube method but replacing the cube by an icosahedron.

1.1 What is a "good" pixelization?

What do we mean by a pixelization scheme being good? Specifically, if we are to place N points (pixel centers) on the sphere, where is the best place to put them? We will use the following two criteria:

1. The distance to the nearest pixel should be minimized.
2. To a good approximation, we should be able to approximate integrals by sums.

Defining d as the maximum distance that a point on the sphere can be from the pixel closest to it, criterion 1 says to minimize d. Criterion 2 states that the integral of a function over the sphere should be well approximated by $(4\pi/N)$ times the sum of the function values at the pixel locations. This is important for applications such as CMB maps, where one wants to expand the brightness distribution in some set of functions, *e.g.*, spherical harmonics. Intuitively, we expect that both of these goals can be attained if the pixel distribution is in some sense as regular as possible. So if $N = 6$, for instance, one might opt for the 6 corners of a regular octahedron. Unfortunately, there is only a finite number of platonic solids (SO(3) has only a finite number of discrete subgroups), so there is in general no obvious "most regular pixelization scheme.

1.2 The icosahedron advantage

The COBE sky cube pixelization scheme is illustrated in Figure 1 (left), and consists of the following steps:

1. The sphere is inscribed in a cube, whose faces are pixelized with a regular square grid.
2. The points are mapped radially onto the sphere.
3. The points are shifted around slightly, to give all pixels approximately equal area.

A pixel (the area which is closer to a given point than to all other points) is thus approximately square, with a side of length $\sim \sqrt{4\pi/N}$. The points furthest from the pixels lie at the corners of these squares, so

$$d_{cube} \approx \sqrt{2\pi/N}. \tag{1}$$

It is well-known that the filling factor is better for a triangular grid as illustrated in Figure 2. Here a pixel is hexagonal, and one readily computes that

$$d_{icosa} \approx \sqrt{8\pi/3\sqrt{3}N}, \tag{2}$$

a value which is about 12% smaller than that for the square grid case. To take advantage of this, one could thus replace the sky cube by a Platonic solid with triangular faces, *i.e.*, by the tetrahedron, the octahedron or the icosahedron.

The above-mentioned area-equalization is carried out for the sake of our second criterion, loosely speaking so that the equal weights that the pixels get when summed over correspond to equal weights $d\Omega$ in an integral (we return to this issue in the discussion section). Since the pixels originally where on a rectangular grid on the cube faces (on the tangent plane of the sphere), the amount of "stretching" required increases toward the edges of the faces. Both this and the radial projection makes the pixels slightly deformed, so that the further out on a face one goes, the more the corresponding pixels on the sphere depart from a regular grid. Because of this, it is clearly desirable to use *as small faces as possible*, so that the corresponding regions of the sphere are as flat as possible. The Platonic solid with the smallest faces is the one with the largest number of faces: the icosahedron, whose faces are 20 triangles (see Figure 1). Not only does it have the advantage of having more than three times as many faces as the cube, which one would expect to help with criterion 2, but since the faces are triangles rather than squares, it is better according to criterion 1 as well.

2 Method

The icosahedron pixelization scheme is illustrated in Figure 1 (bottom), and is akin in spirit to the COBE sky cube method:

1. The sphere is inscribed in an icosahedron, whose faces are pixelized with a regular triangular grid.
2. The points are mapped radially onto the sphere.
3. The points are shifted around slightly, to give all pixels approximately equal area.

A FORTRAN package implementing this is available at
http://www.mpa-garching.mpg.de/~max/icosahedron.html (faster from Europe)
and from **http://www.sns.ias.edu/~max/icosahedron.html** (faster from the US). The user interface is identical to that for the COBE sky cube package: for any specified resolution, one subroutine converts a pixel number to a unit vector, and a second subroutine converts a unit vector to a pixel number, the number of the pixel closest to that vector. Below we merely summarize the geometrical issues that specify the method.

2.1 Part I: mapping to and from the icosahedron

The 3D aspects of the problem are computationally trivial, since any of the 20 icosahedron faces can be rotated to lie in the $z = 1$ plane by multiplication by an appropriate rotation matrix, and all these rotation matrices can be precomputed once and for all. The mapping between the $z = 1$ tangent plane and the surface of the unit sphere preserves the direction of a vector and simply changes its length appropriately, either to be unity (on the sphere) or to have $z = 1$. It is easy to see that straight lines on the tangent plane correspond to great circles on the sphere. Thus each icosahedron face gets mapped onto a region on the sphere bounded by three great circles.

2.2 Part II: the area equalization

The area equalization step is illustrated in Figure 2. After mapping part of the sphere onto a triangle in the tangent plane as above, we want to map this triangle onto itself ("shift the pixels around") in such a way that the combined mapping becomes an equal-area mapping, *i.e.*, gets a constant Jacobian. The Jacobian of the mapping from the sphere to the plane is

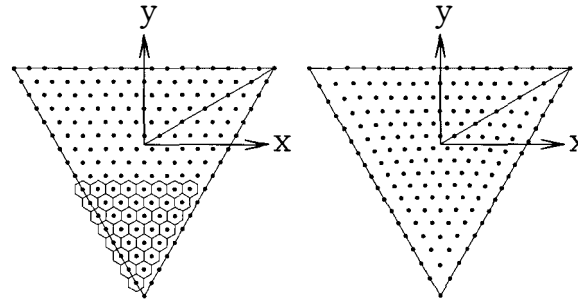

Figure 2.
A regular triangular grid (left) is adjusted (right) to give all pixels the same area. As illustrated, the pixels have a hexagonal shape. A triangular icosahedron face can be symmetrically decomposed into six identical right triangles (one is shaded), and the area equalization mapping is seen to respect this symmetry.

$$|\partial(x,y)/\partial\Omega| = (1 + x^2 + y^2)^{3/2}, \tag{3}$$

so we want to find find a second mapping $(x, y) \mapsto (x', y')$ whose Jacobian is proportional to the inverse of this. In other words, we wish to find two functions (x', y') that map the boundary of the triangle onto itself and satisfy the nonlinear partial differential equation

$$\det \begin{pmatrix} \partial x'/\partial x & \partial x'/\partial y \\ \partial y'/\partial x & \partial y'/\partial y \end{pmatrix} = \eta^2 (1 + x^2 + y^2)^{-3/2} \tag{4}$$

for some proportionality constant η. Since the icosahedron has 20 faces, the area of the triangular region on the sphere is clearly $4\pi/20$. The sides of the equilateral triangle in the tangent plane have length $a = \left[9 \tan^2\left(\frac{\pi}{5}\right) - 3\right]^{1/2} \approx 1.323$, so its area is $a^2\sqrt{3}/4$. Taking the ratio of these two areas fixes the above proportionality constant to be

$$\eta = \left[\frac{15\sqrt{3}}{4\pi}\left(3\tan^2\frac{\pi}{5} - 1\right)\right]^{1/2} \approx 1.098. \tag{5}$$

The partial differential equation equation (4) is under-determined and admits infinitely many solutions, which allows us to impose additional simplifying requirements. As illustrated in Figure 2, the triangle can be decomposed into six right triangles of identical shape that can all

be mapped into the one in the upper right corner (shaded) by a combination of 120° rotations and reflections. We require our solution to respect this symmetry, so we merely need to find a solution to equation (4) in the shaded triangle that maps its boundary onto itself. We use the additional freedom to require that horizontal lines in this region get mapped onto horizontal lines. This is enough to determine the solution uniquely, and we find that

$$\begin{cases} y' &= \eta\sqrt{\frac{2}{\sqrt{3}}\tan^{-1}\left[\sqrt{3}\frac{\sqrt{1+4y^2}-1}{\sqrt{1+4y^2}+3}\right]}, \\ x' &= \left(\frac{\eta x y'}{y}\right)\sqrt{\frac{1+4y^2}{1+x^2+y^2}}, \end{cases} \tag{6}$$

which can be verified by direct substitution. These equations are readily inverted, giving

$$\begin{cases} y &= \frac{1}{2}\sqrt{3\left[\frac{1+\sqrt{3}\tan(\sqrt{3}y'^2/2\eta^2)}{\sqrt{3}-\tan(\sqrt{3}y'^2/2\eta^2)}\right]^2-1}, \\ x &= x'y\sqrt{\frac{1+y^2}{y'^2(1+4y^2)-x'^2y^2}}. \end{cases} \tag{7}$$

This area-equalizing mapping is illustrated in Figure 2, where the regular triangular grid of points (left) has been adjusted (right) to give equal-area pixels when projected onto the sphere. The pixels in Figure 1 have also been equal-area adjusted — otherwise a slight excess would be visible near the corners of the triangles.

3 Discussion

As far as practical issues goes, our icosahedron method is essentially equivalent to the COBE sky cube method: the pair of subroutines that convert between unit vectors and pixel numbers are for all practical purposes instantaneous. How does its geometric performance compare with that of the COBE sky cube method according to the two criteria described in the introduction? As discussed above, the fact that the pixels are hexagons rather than squares gives a 12% improvement with regard to criterion 1. We will now examine criterion 2 in more detail.

The study of how to best approximate integrals over various manifolds with sums has a long tradition in the mathematics literature. The sphere case is notoriously difficult since it permits no completely regular point distributions for $N > 20$ — see *e.g.* [2, 3, 5, 6] for theoretical work on this so-called cubature problem. We can clearly write our approximation of the integral $I \equiv \int f d\Omega$ as $\int w f d\Omega$ for some *weight function* $w(\hat{\mathbf{r}}) = \sum_{i=1}^{N} w_i \delta(\hat{\mathbf{r}}, \hat{\mathbf{r}}_i)$. If we expand the integrand f in spherical harmonics, we see that the integral I is proportional to the monopole. Defining the *window function* W_ℓ as

$$W_\ell \equiv \frac{1}{4\pi}\sum_{m=-\ell}^{\ell}\left|\int Y^*_{\ell m}(\hat{\mathbf{r}})w(\hat{\mathbf{r}})d\Omega\right|^2 = \frac{1}{4\pi}\sum_{m=-\ell}^{\ell}\left|\sum_{i=1}^{N} w_i Y^*_{\ell m}(\hat{\mathbf{r}}_i)\right|^2, \tag{8}$$

where the $Y_{\ell m}$ denote spherical harmonics, we thus see that an integration scheme is exact if $W_\ell = \delta_{0\ell}$. Such window function are plotted in Figure 3 for the COBE sky cube method and the icosahedron method using a comparable number of points, both with all weights $w_i = 4\pi/N$. Apart from the monopole (which gives the integral), both window functions are seen to vanish for all polynomials of degree $\ell \ll 100$, which means that these integration methods are essentially exact in Gauss' sense to that order. Comparing the two methods, the icosahedron scheme is seen to remain accurate out to approximately 10% greater ℓ-values, so in this sense, the method is about 10% better. This gain factor was found be remain around 10% over the range of N-values likely to be of astrophysical interest.

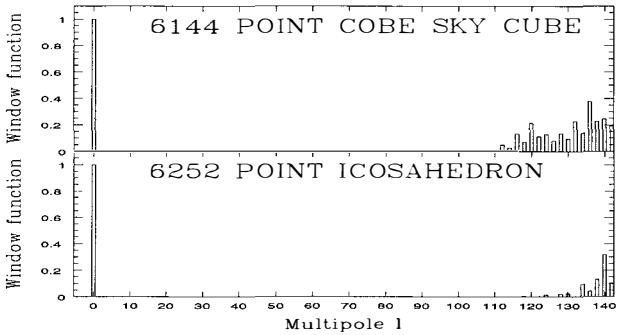

Figure 3.
Window function comparison. The histograms show the errors obtained when approximating integrals by sums, multipole by multipole. The icosahedron method generally remains accurate down to about 10% smaller scales than a COBE sky cube with a similar number of pixels, which means that it can produce comparable results using about 20% fewer pixels.

How close to perfect is the icosahedron method? Although no strictly optimal method has been found for general N (which is one of the main foci of the mathematics literature, together with proofs of various bounds on how well one can do), an approximate answer to the question follows from simple constraint-counting. There are ℓ^2 spherical harmonics of degree less than ℓ, whereas w is specified by $3N$ free parameters (N weights w_i and N unit vectors $\hat{\mathbf{r}}_i$), so one might hope to obtain a perfect window function up to $\ell \approx \sqrt{3N}$, *i.e.*, to make the integration exact for polynomials of degree up to $\sqrt{3N}$. For the examples in Figure 3, we have $\sqrt{3N} \approx 136$ and 137, respectively, *i.e.*, values quite close to where the icosahedron window function becomes substantial.

Given the great efforts that will be spent on collecting and analyzing future CMB data sets, there should be no reason to use anything but the best scheme when pixelizing them. We have found that the icosahedron method improves upon the COBE sky cube method with about 10% when it comes to both filling factor and integration accuracy. A 12% better window function allows 25% fewer pixels, which corresponds to halving the CPU time for data-analysis steps such as ordo N^3 matrix inversions. Since this improvement is computationally speaking free, it is hoped that the icosahedron method will be useful for future mapping experiments.

Acknowledgements. The author wishes to thank James Binney, Angélica de Oliveira-Costa, Krystof Górski, Vikram Seth, Harold Shapiro and Ned Wright for useful comments, and Schwabinger Krankenhaus for hospitality during the visit where this work was carried out. This work was partially supported by European Union contract CHRX-CT93-0120 and Deutsche Forschungsgemeinschaft grant SFB-375.

References

[1] Chan, F.K. & O'Neill, E.M. 1976, *Feasibility study of a quadrilateralized spherical cube Earth data base*, Computer Sciences Corp. EPRF Technical Report

[2] Konjaev, S. I. 1979, *Mat. Zametki*, **25**, 629

[3] Mysovskikh, I. P. 1976, in *Quantitative Approximation*, eds. R. A. Devore & K. Scherer (New York: Academic Press)

[4] O'Neill, E.M. & Laubscher, R.E. 1976, *Extended studies of a quadrilateralized spherical cube Earth data base*, Computer Sciences Corp. EPRF Technical Report

[5] Sobolev, S. L. 1974, *Introduction to the theory of cubature formulae* (Moscow: NAUKA)

[6] Stroud, A. H. 1971, *Approximate Calculation of Multiple Integrals* (Englewood Cliffs: Prentice-Hall)

COMPARING PERFORMANCES OF CMB EXPERIMENTS

François R. Bouchet[1], Richard Gispert[2], François Boulanger[2], Jean-Loup Puget[2]
[1] *Institut d'Astrophysique de Paris, CNRS, Paris,France.*
[2] *Institut d'Astrophysique Spatiale, CNRS-Université Paris-Sud, Orsay, France.*

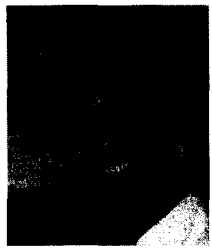

Abstract

This paper first summarizes the present knowledge on the spectral and spatial distributions of Galactic foregrounds: dust, free-free and synchrotron emission. We also discuss the emission from infrared galaxies and radio sources. This information comes in support of a modelization of the microwave sky including all relevant components. We then introduce an indicator, based on the Wiener filtering method, of the effective resolution of an experiment once the effect of foregrounds is taken into account. We finally use both our sky model and the indicator to assess the ability of different experiments to separate the true Cosmic Microwave Background (CMB) anisotropies from the foregrounds.

1 Introduction

A comparison of the relative performances of CMB experiments implies a detailed discussion of the foregrounds, Galactic and extragalactic. To avoid repetitions and make the discussion easier to follow we have combined in this paper the oral contributions of Bouchet, Puget and Boulanger. Undoubtly new aspects of the foreground emission will be discovered in future CMB experiments but we feel that the present observations and understanding of foregrounds is already sufficient to build a model of the microwave sky realistic enough to test the ability of planned experiments to disentangle foregrounds from true CMB anisotropies.

Section 2 discusses the foregrounds. Research on foregrounds has thrived on the analysis of the Infrared Astronomy Satellite (*IRAS*) and the Cosmic Background Explorer (*COBE*) all-sky surveys as well as on ground based observations in the millimeter and centimeter range. The Galactic emission are associated with dust, free-free emission from ionized gas and synchrotron

emission from relativistic electrons. We here summarize the present knowledge on the spectral and spatial distributions of these three emission components. The extragalactic foregrounds are due to infrared galaxies and radio–sources. Also, the Sunyaev-Zeldovich effect on clusters of galaxies induces anisotropies of the CMB which need to be separated from the primordial ones.

In the section 3, the present understanding on foregrounds is used to build a model of the microwave sky. This model is then used to discuss the relative importance of the different components as a function of frequency, angular scale and region of sky. Section 4 present a component separation method based on Wiener filtering. This method is used on the model of section 3 to estimate the quality of the component separation for various experiments as well as for different choices and hypotheses relevant for these experiments.

2 Galactic Foregrounds

Many detailed studies have been devoted to effects that may blur the primordial signature of the CMB anisotropies. Gravitational lensing by mass concentrations along the light ray paths may for instance alter the detailed map patterns and add a stochastic component. Or photons passing through a fast evolving potential well might be redshifted (Rees-Sciama effect). Secondary fluctuations might be generated during a reionization phase of the Universe. For all this processes, the answer is that their impact should be negligible at scales corresponding to $\ell \simeq 1/\theta \lesssim 1000$. On the other hand, the dust, free-free, and synchrotron emission of our own galaxy, those of radio-sources and infrared galaxies, and the Sunyaev-Zeldovich effect of clusters of galaxies all contribute detectable microwave anisotropies, at least at some frequencies and angular scales of interest. Here we review the current state of knowledge of these sources, with the perspective of creating a realistic model of the microwave sky.

2.1 Dust emission

The spectrum of the dust emission at millimeter and sub-millimeter wavelengths has been measured by the Far–Infrared Absolute Spectrophotometer (*FIRAS*) aboard *COBE* with a 7 degree beam. In addition, several balloon experiments have detected the dust emission at high galactic latitude in a few photometric bands with angular resolution between 30 arcminutes and 1 degree (see for example Fischer et al. (1995) and De Bernardis, Masi, & Vittorio (1992) for recent results). The spectrum of the Galaxy as a whole (Wright et al., 1991) and more specifically that measured in the Galactic plane (Reach et al., 1995) cannot be fitted with a single dust temperature and emissivity law. These authors have proposed a two temperatures fit including a very cold component with $T \sim 7\,K$. The interpretation of this result for the Galactic plane is not straightforward because dust along the line of sight is expected to spread over a rather wide range of temperatures just from the fact that the stellar radiation field varies widely from massive star forming regions to shielded regions in opaque molecular clouds. By providing maps of the sub-mm dust emission with an angular resolution comparable to that of *IRAS*, the *COBRAS/SAMBA*experiment will probably make it possible to separate the contributions from cold and warm regions but this is not directly the topic of this paper and in the following we focus on the emission at high Galactic latitude.

2.1.1 Emission at High Galactic Latitude: At high Galactic latitudes, Reach et al. (1995) also argued for the presence of a very cold dust component with an optical depth much larger than that of the warm component. This study however was based on the analysis

of total power spectra which could include a non–Galactic emission component. Later, two independent studies based on spatial correlations have not confirmed this result (Boulanger et al., 1996; Dwek et al., 1996). The first of this study derived the dust emission spectrum from the spatial correlation between the *FIRAS* maps and the 21cm line emission from H I. The second one used the spatial correlation of the *FIRAS* data with the 100μm all-sky map from the Diffuse Infrared Background Experiment (*DIRBE*).

For their analysis, Boulanger et al. used the fraction of the sky, north of $-30°$ declination, for which the H I emission is weaker than 250 K.Km/s (36% of the sky). The declination limit was set by the H I survey made with the Dwingeloo telescope (Burton & Hartmann, 1994). For an optically thin emission this threshold corresponds to $N(HI) = 5 \times 10^{20}\,H\,cm^{-2}$. Above this threshold the correlation between dust emission and H I emission shows an increased slope and scatter. This is probably related to the contribution of dust associated with molecular hydrogen since the column density threshold coïncides with that inferred from UV absorption data for the presence of H_2 along the line of sight (Savage et al., 1977). The far–IR sub-mm spectrum derived by Boulanger et al. is well fitted by one single dust component with $T = 17.5\,K$ and $\tau/N_H = 1.0 \times 10^{-25}(\lambda/250\mu m)^{-2}\,cm^2$. The residuals to this one temperature fit allow to put an upper limit on the sub-mm emission from a very cold component almost one order magnitude lower than the value claimed by Reach et al. (1995). Assuming a temperature of 7 K for this purported component we can set an upper limit on the optical depth ratio $\tau(7K)/\tau(17.5K) \sim 1$.

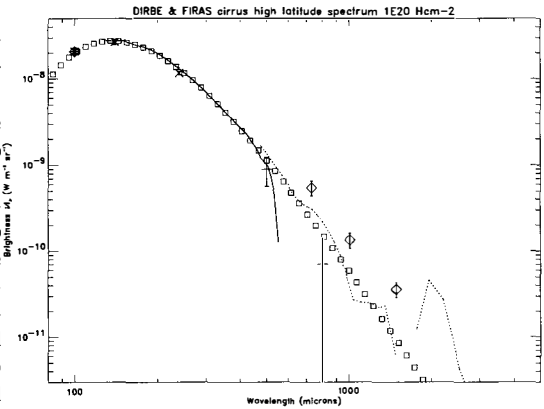

Figure 1: Far–IR and sub–mm spectrum of dust at high Galactic latitude. The solid and dotted lines represent the *FIRAS* data (from Boulanger et al. (1996)), the boxes the 17.5K fit. The points with error bars correspond to the cirrus spectrum deduced from the balloon experiments of Fischer et al. (1995) (diamonds) and De Bernardis, Masi, & Vittorio (1992) (crosses).

Dwek et al. have derived the emission spectrum for dust at Galactic latitudes larger than 40° and compared this spectrum with a dust model not including any cold component. The residuals of this comparison shows a small excess which could correspond to emission from a very cold component at a level just below the upper limit set by the Boulanger et al. analysis. Both studies thus raise the question of the nature of the very cold component measured by Reach et al.. Puget et al. (1996) have shown that the sub-mm excess is isotropic over the sky. To be Galactic it would have to originate in a halo large enough ($> 50\,kpc$) not to contradict the lack of Galactic latitude and longitude dependence. Since such halos are not observed in external galaxies, Puget et al. conclude that the excess is the extragalactic background from galaxies unless it is an instrumental component.

The spectrum presented by Puget et al. (1996) for the residuals of the *FIRAS*- H I correlation in the regions of lowest H I column densities contains a fraction of the emission in the far–IR from dust emission associated with the diffuse ionized gas seen at high latitude. This statement may not yet be quantified since it is still unclear how much dust emission comes from this gas

component and also what fraction of it is left after subtraction of the dust emission correlated with H I gas (Boulanger et al., 1996). Assuming that the dust in H II gas has an emission spectrum similar to that of the dust correlated with H I emission, Puget et al. show that the contribution from ionized gas can account for only a minor fraction of the residual spectrum at $\lambda > 400\,\mu$m. This is due to the fact that the residual spectrum has a marked sub-mm excess with respect to the dust emission spectrum. The presence of a non-Galactic emission component is thus firmly established at long wavelengths.

2.1.2 Cold component: There is now converging evidence that the dust emission spectrum from *high* latitude regions with low H I column densities can be well approximated with a single dust temperature and ν^2 emissivity with no evidence for a very cold dust component. In this section we show that the emission spectrum from higher column density lines of sight with molecular clouds comprise an emission component with a colder temperature than that measured at high latitude.

Lagache et al. (1996) have combined *DIRBE*and *FIRAS* data to study the emission spectrum from nearby molecular clouds not heated by luminous stars (e.g. the Taurus molecular complex). Analysis of *IRAS* images of these clouds show that there is a dust component seen at 100μm and not at 60μm. This cold *IRAS* component is well correlated with dense molecular gas as traced by ^{13}CO emission (Laureijs, Clark, & Prusti, 1991; Abergel et al., 1994). The change of the 60μm/100μm color between the dense and more diffuse gas shows a sudden jump between two distinct values. It is understood as a change in the abundance of very small grains emitting at temperatures higher than the equilibrium temperature of large dust grains. Lagache et al. (1996) have studied the cold *IRAS* component with the *DIRBE*100, 140 and 240μm all-sky maps with a 40' resolution. The dust temperature obtained for this component is found to be around 14K. For the understanding of the evolution of dust properties within the interstellar medium this is an interesting result since it shows that the change in abundance of very small grains is correlated with a change in the temperature of large grains. We believe that the difference in temperature cannot be accounted for by the attenuation of the radiation field but that it reflects a change in the emissivity of large grains.

Lagache et al. have extended their analysis to sub-mm wavelengths with the *FIRAS* data. This is particularly difficult because dense clouds are highly diluted in the 7° beam of *FIRAS*. This analysis shows that *FIRAS* spectra for pixels including cold *IRAS* emission are not well fitted by a combination of two dust components (the H I like with T $\sim$ 17.5 K and the one associated with the cold *IRAS* component with T $\sim$ 14 K) with an emissivity index of 2. When averaged together these spectra show an excess which could be accounted for by an even colder dust component. But it could as well be that the emissivity law for the cold *IRAS* component is flatter than ν^2. There is thus some evidence that the dust in molecular clouds differs from that in the more diffuse gas components. With respect to future space mission, we cannot estimate with the present data the fraction of the sky which will include detectable emission from dense gas with cold dust.

There are a few measurements done with balloon borne experiments which have detected the dust emission from clouds with a significant visible opacity ($A_v \sim 1$ mag, $N_H \sim 2 \times 10^{21}$ cm^{-2}) outside of the Galactic plane. These observations were made in a few photometric bands with an angular resolution between 30 arc-minutes and 1 degree. Fischer et al. (1995) combined their data with *IRAS* data at 100 μm and found they get a best fit with a modified Planck function with $T = 24$ K and $\alpha = 1.4$. This could be mistakenly taken for evidence of cold dust in thin cirrus clouds. Firstly, one must note that Fischer et al. (1995) correct the *IRAS* 100 μm by a factor 0.7 given in the *COBE* Explanatory Supplement (NASA, 1995). This photometric correction factor is only relevant for very large scale emission. For point sources,

the photometry of *IRAS* and *COBE* are in good agreement. Thus the correction factor to be applied for structures smaller than one degree is between 0.7 and 1, and likely to be closer to 1. Various galactic dust emission spectra are plotted in Figure 1. They are all normalized to 100 μm. The data from De Bernardis, Masi, & Vittorio (1992) are also shown. It is clear in that comparison that the emission of cirrus clouds with typical optical depth around unity has a spectrum very similar to the one found by Boulanger et al. (1996) for dust correlated with H I emission.

Concerning the scale dependence of the amplitude of the fluctuations, we verified that the power spectrum of the DIRBE fluctuations is decreasing approximately like the 3^{rd} power of the spatial frequency, ℓ, in agreement with the determination of Gautier et al. (1992) who used instead the $100\mu m$ IRAS data down to a resolution of 4 arc minutes.

2.2 Free-free emission

Observations of H_α emission at high Galactic latitude and dispersion measurements in the direction of pulsars indicate that low density ionized gas (the Warm Ionized Medium, WIM) accounts for about 25% of the gas in the Solar Neighborhood (Reynolds, 1989). The column density from the mid-plane is estimated to be in the range 0.8 to 1.4×10^{20} cm^{-2}. Until recently, little was known about the spatial distribution of this gas but numerous H_α observing programs are currently in progress. An important project is the northern sky survey started by Reynolds (WHAM Survey). This survey will consist of H_α spectra obtained with a Fabry-Perot through a 1° aperture. The spectra will cover a radial velocity interval of 200 Km/s centered near the LSR with a spectral resolution of 12 Km/s and a sensitivity of 1 cm^{-6} pc (5σ). Several other groups are conducting H_α observations with wide field camera (10°) equipped with a CCD and a filter. These surveys with an angular resolution of a few arc minutes should be quite complementary to the WHAM data. From these H_α observations one can directly estimate the free-free emission from the WIM.

Kogut et al. (1996) have found a correlation at high latitudes between the *DMR*emission after subtraction of the CMB dipole and quadrupole and the *DIRBE*240μm map. The observed change of slope of the correlation coefficients at 90 GHz is just what is expected from the contribution of the free-free emission as predicted by Bennett et al. (1994). The spectrum of the free-free emission may be described by $I_\nu \propto \nu^{-0.16}$ (the index is the best fit value of Kogut et al.).

The correlation observed on large angular scales between the free-free and dust emission is statistical in nature and one should not interpret it as a one to one correlation between the two emission. In particular the result of Kogut et al. (1995) does not allow to use the higher angular resolution *DIRBE*maps to assess potential contamination of CMB maps by free-free emission. The power spectrum measured for the spatial distribution of dust emission cannot either be extrapolated to the free-free emission. This is well illustrated by a comparison between H_α and H I emission done over one region by Reynolds et al. (1995) which shows a significant but not complete correlation between the two gas components. We stress also that the WIM is distributed over a scale height of 1.5 Kpc much larger than that of the neutral gas (Reynolds, 1989). Half of the WIM is at a z distance from the mid-plane larger than 1 Kpc while this fraction is less than 15% for the H I gas (Lockman, Hobbs, & Shull, 1986). The power spectrum in the limited H_α maps available is compatible with an l^{-3} spectrum but does not constrain it strongly.

2.3 Synchrotron emission

Away from the Galactic plane region, synchrotron emission is the dominant signal at frequencies below ~5 GHz, and it has become standard practice to use the low frequency surveys of Haslam et al. (1982) at 408 MHz and Reich & Reich (1988) at 1420 MHz to estimate by extrapolation the level of synchrotron emission at the higher CMB frequencies. This technique is complicated by a number of factors. The synchrotron spectral index varies spatially due to the varying magnetic field strength in the Galaxy (Lawson et al., 1987). It also steepens with frequency due to the increasing energy losses of the electrons. Although the former can be accounted for by deducing a spatially variable index from a comparison of the temperature at each point in the two low frequency surveys, there is no satisfactory information on the steepening of the spectrum at higher frequencies. As detailed by Davies, Watson, & Gutierrez (1996), techniques that involve using the 408 and 1420 MHz maps are subject to many uncertainties, including errors in the zero levels of the surveys, scanning errors in the maps, residual point sources and the basic difficulty of requiring a very large spectral extrapolation (over a decade in frequency) to characterize useful CMB observing frequencies. Moreover, the spatial information is limited by the finite resolution of the surveys: 0.85° FHMW in the case of the 408 MHz map and 0.6° FWHM in the case of the 1420 MHz one.

Additional information is available from existing CMB observing programs in the frequency range 5–15 GHz on $\sim 7°$ and $\sim 1°$ angular scales. Using data at frequencies higher than 408 or 1420 MHz improves the spectral leverage. For instance, the Jodrell Bank 5 GHz interferometer has been used to make a high sensitivity survey of the northern sky in the declination range $35° - 45°$ on a scale of $\sim 2°$. A full analysis of the data has been undertaken by Jones (1996), and we consider here the results for the quietest region of the sky as identified from the 1420 MHz map and from the Green Bank discrete source catalogue (Condon, Broderick, & Seielstad, 1989). A comparison of the (Jodrell Bank) observed *rms* signal levels and those at 1420 MHz yields a best fit spectral index between 1.4 and 5 GHz: over the 800 square degrees of sky included in the analysis, the best fit spectral index is $\alpha = -0.9 \pm 0.3$.

In the frequency range 10–33 GHz the best information comes from the Tenerife CMB project (Hancock et al., 1994; Davies et al., 1996), which has observed a large fraction of the northern sky with high sensitivity. At 10.4 GHz and 14.9 GHz the window from RA $161° - 230°$, dec $35.0° - 45.0°$ is fully covered, whilst at the higher 33 GHz frequency only data at declination $+40°$ have been analyzed. At these frequencies this sky area is free from significant discrete source contribution. The most accurate figures are obtained from the signal levels derived from a joint likelihood analysis of all of the sky area, which implies a residual *rms* signal of 24μK at 10 GHz and 20μK at 15 GHz. The confidence bounds on these figures have yet to be calculated, but assuming that these best fit values are correct, one can derive spectral indices of $\alpha = -1.4$ between 1.4 and 10.4 GHz and $\alpha = -1.0$ between 1.4 and 14.9 GHz. These values, which apply on scales of order 5°, are in agreement with those obtained from the 5 GHz observations on $\sim 2°$ scales.

Finally, the lack of detectable cross-correlation between the Haslam data and the *DMR*data leads Kogut et al. (1995) to impose an upper limit of $\alpha = -0.9$ for any extrapolation of the Haslam data in the millimeter wavelength range at scales larger than $\sim 7°$. In view of the other constraints at higher frequencies, it seems reasonable to assume that this spectral behavior also holds at smaller scales.

The spatial power spectrum of the synchrotron emission is not well known and despite the problems associated with the 408 and 1420 MHz maps it is best estimated from these. We have computed the power spectrum of the 1420 MHz map for the sky region discussed above. The results show that at $\ell \gtrsim 100$ the power spectrum falls off as ℓ^{-3} (i.e. with the same behavior

as the dust and free–free emission).

2.4 A pessimistic galactic model

The galactic emission is strongly concentrated toward the galactic plane. But what is the geography of the galactic fluctuations? Do we expect large connected patches with low levels of fluctuations? What is the amplitude of fluctuations typical of the best half of the sky?

To answer these questions, we created a galactic model valid at scale $\gtrsim 1°$ from spectral extrapolations of spatial templates taken from existing observations. The 408 MHz full-sky map of Haslam is our template for the *synchrotron* emission, extrapolated to other frequencies with a spectral index of $\alpha = -0.9$. We use the *DIRBE*240 μm map as a template for the H I-correlated dust and the free-free emission.

Comparisons with other tracers of the free-free emission show that the H I correlated free-free emission accounts for most (at least 50%), and maybe all, of that component. We conservatively assume that there may be a second, uncorrelated, component accounting for 5% of the total dust and 50% of the free-free emission. There is of course no known template for such a component, but we assume that it should have the same "texture" than the correlated component: we simulate it by using again the *DIRBE*240 μm map, but North/South inverted (in galactic coordinates). While arbitrary, this choice preserves the expected latitude dependence of the emission, and the expected angular scale dependence of the fluctuations. The dust spectral behavior is modeled as a single temperature component with $T_d = 18$K and ν^2 emissivity. We assume that the free-free emission will behave according to $I_\nu \propto \nu^{-0.16}$, and normalize it to give a total *rms* fluctuation level of 6.2 μK at 53 GHz. The spectral model we use for the three galactic component is summarized in figure 2. Since the weakest emissions in *DIRBE*are at the 1 MJy/sr (and at the 10K level for Haslam), we immediately see that the corresponding fluctuations should be at the level of a few μK around 100 GHz.

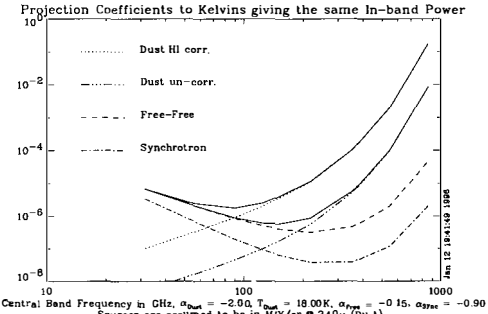

Figure 2: Conversion coefficients from template units to Kelvin. The two solid lines convert MJy/sr at 240μm (*DIRBE*and *DIRBE*North/south inverted, for our model of dust and free-emission, see text) while the dot-dashes convert Kelvin at 408 GHz (Haslam et al., 1982), for the synchrotron emission.

Using this model, we can now create full sky maps of the total galactic emission converted to an equivalent thermodynamical temperature at any chosen frequency. Note that at this resolution, extragalactic point sources and the SZ effect should contribute negligible signal. In order to obtain *local* estimates of the level of fluctuations, we have computed their *rms* amplitude (σ_T), over square patches of 3 degrees on each side (i.e. containing about 11 beams of 1 degree FWHM). Thus, this estimator only retains perturbations at angular scales roughly between 1 and 3 degrees, equivalent to restricting the contribution to the variance to a range of angular modes, with ℓ between $\sim$ 20 and 60. Figure 3 shows an example of such a map at $\lambda = 2.4$ mm (125 GHz). The two darkest shades of grey ($\sigma_T \gtrsim 10$ μK) delimit the area

where galactic fluctuations would be comparable to those of a *COBE*-normalized CDM model[1]; they only represent 20% of the total sky area at this scale. This map provides direct graphical evidence that a large fraction of the sky is quite "clean" around the degree scale (Bouchet, Gispert, & Puget, 1995b,a).

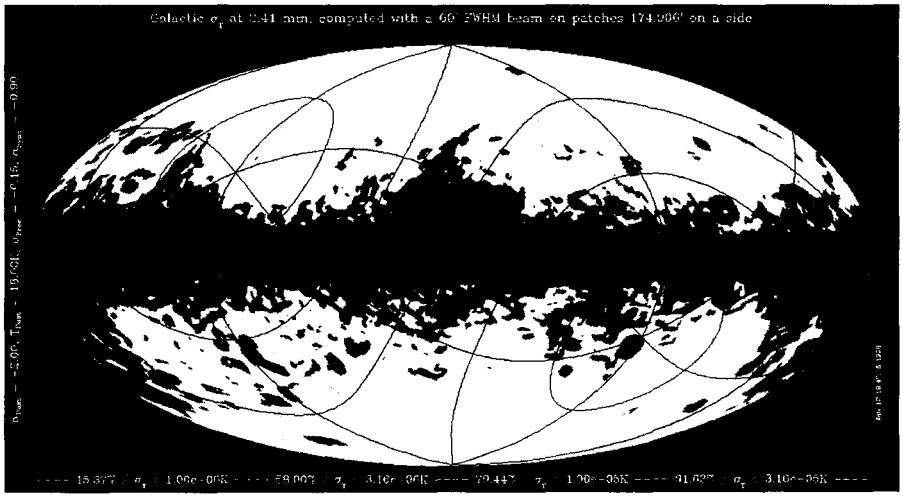

Figure 3: Map of the temperature fluctuations due to the galactic foregrounds at $\lambda = 2.4$ mm. The fluctuation levels, denoted by 5 shades of grey, are obtained by computing the local variance over square patches with 3 degrees on a side (see text). From the lightest (small σ_T) to the darkest regions close to the galactic plane, the levels correspond to $\sigma_T < 1.0, 3.16, 10.0, 31.1\mu$K, and $\sigma_T > 31.1\mu$K. CMB fluctuations (in a standard CDM model) would correspond to $\sigma_T \gtrsim 10\ \mu$K, i.e. span the 2 darkest shades of grey.

Analyzing figure 3 more quantitatively, figure 4.a shows the fraction of the sky for which the *rms* fluctuations of each of the foregrounds and of their total contribution are less than a given value at $\lambda = 2.4$ mm. These curves are steep for low fluctuation levels; the best half of the sky (median value) is only a factor of ~ 4 noisier than the best regions, but a factor ~ 10 below the CDM level. The high level "plateaus" correspond to low galactic latitude regions. Indeed the maps tell us that that the "clean" sky essentially corresponds to the areas at high galactic latitudes, excepting only a few hot spots like the Magellanic clouds. Figure 4.b, which plots the median fluctuation values as a function of frequency, shows a clear minimum around 100 GHz (as could be expected from figure 2), at a level lower than 10 % of the expected level of the CMB anisotropies. Thus measurements restricted to that frequency would already be sufficient to achieve better than 10% accuracy around the degree scale (provided a few high latitude "hot or cold spots" are flagged out with higher and lower frequency channels).

As was shown above, the angular power spectra $C(l)$ of the galactic components all decrease strongly with ℓ, approximately as $C(\ell) \propto \ell^{-3}$. Smaller angular scales thus bring increasingly small contributions per logarithmic interval of ℓ to the variance, $\ell(\ell+1)C(\ell)$: the galactic sky get smoother on smaller angular scales. We set the normalization constants of the spectra to

[1]The parameters of this model are $\Omega_b = 0.05$ for the baryonic abundance, $\Omega_c = 0.95$ for that of CDM, $\Lambda = 0$, $H_0 = 50$ Km/s/Mpc, no reionization, and only scalar modes

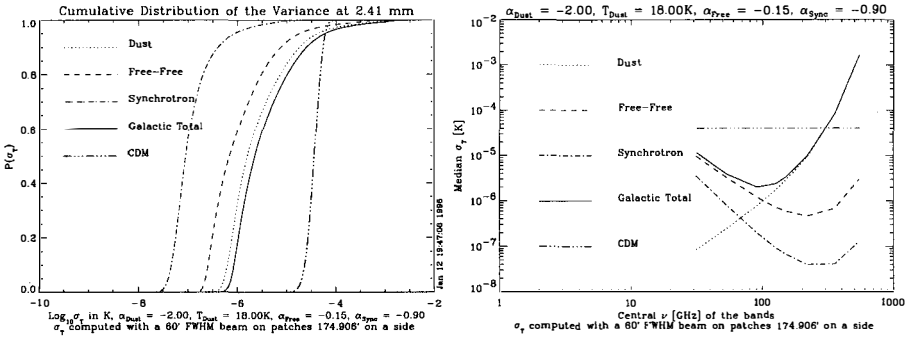

Figure 4: a) Cumulative distribution functions of the galactic foreground fluctuations at $\lambda =$ 2.4 mm (125 GHz) in 3 degree patches for a 1 degree FWHM Gaussian beam. It gives directly the the fraction of the sky in which the rm fluctuation level is lower than a certain value. The CDM curves gives for comparison the expected range of fluctuations for a *COBE* normalized CDM model. b) Median fluctuation values (i.e. corresponding to 50% of the sky) for the galactic components around the degree scale as a function of frequency. The galactic fluctuations have a clear minimum around 100 GHz.

obtain a level of fluctuations representative of the best half of the sky, i.e. the local fluctuations in regions of interest for CMB measurements would actually be even lower. In practice, this was achieved by generating an artificial maps with $C(\ell) = \ell^{-3}$. We then measured its σ_T using our previous procedure of measuring the variance in 3 degree patches after convolving with a one degree beam. This gives the required normalization factor of the power spectra by comparisons with the median values plotted in fig.4.b. We find that

$$\ell\, C_\ell^{1/2} = c\, \ell^{-1/2}\ \mu\mathrm{K}, \tag{1}$$

with $c_{sync} = 2.1$, $c_{free} = 13.7$, and $c_{dust} = 13.5$ at 100 GHz. In addition, one has $c_{HI-U} = 8.5$ and $c_{HI-C} = 20.6$ for the Dust+Free-free components, uncorrelated and correlated (respectively) with H I.

Of course, by their very construction, these normalizations are only appropriate for intermediate and small scales, about $\ell \gtrsim 10$. The corresponding fluctuation levels at 3.3 mm and 1.4 mm are shown in figure 6.

2.5 Radio-sources and infrared galaxies

In order to estimate the contribution of radio-sources and infrared galaxies to the anisotropies of the microwave sky, we have created a simple physical model using ideas developed previously for modeling optical emissions. In short, we start from a matter power spectrum (here a standard, *COBE*-normalized CDM), and estimate the number of dark matter halos at any redshift using the Press-Schechter approach. Standard cooling rates are used to estimate the amount of baryonic material that forms stars. The stellar energy release is obtained from a library of stellar evolutionary tracks and the part reradiated in the microwave range is estimated with a simple geometrical model. This results in an infrared luminosity function at all redshifts; for more details, see Guiderdoni et al. (1996) in this volume. Monte-Carlo realizations of these infrared galaxies, together with an assignment of synthetic spectra to a given infrared

luminosity, allow creating maps at any frequency of this contribution of faint galaxies to the CMB anisotropies; for more details, see Hivon, Guiderdoni, & Bouchet (1996) in this volume.

Once sources creating more than 3-σ fluctuations are removed, one can fit the frequency-dependent power spectrum of the maps of the unresolved background by

$$\ell C_\ell^{1/2} = \frac{2.07}{\nu^5} \sinh^2\left(\frac{\nu}{113.6}\right) \left[\nu + \frac{10^{-15}\,\nu^8}{[1+(\nu/2500)^8]\,[1+(\nu/1500)^2]}\right]^{1/2} \mathrm{K}, \qquad (2)$$

where ν is the frequency in GHz (and $\ell C_\ell^{1/2}$ is in Kelvin). This corresponds to the "maximal" model (and it gives $\ell C_\ell^{1/2} = 2.2 \times 10^{-3}\ \ell\ \mu$K at 100 GHz).

The corresponding fluctuation levels at 90 and 217 GHz are compared in figure 6 and they are quite low (at least at $\ell \lesssim 1000$) as compared to the expected fluctuations from the CMB or from the galaxy.

2.6 Clusters of galaxies

The mass function of clusters of galaxies at low redshift can be inferred from X-ray and optical surveys (Bahcall & Cen, 1993) and models based on the Press-Schechter formalism have been used to predict the evolution of their mass function (Bartlett & Silk, 1994). On the basis of such models a minimum contribution of the Sunyaev-Zeldovich effect to the fluctuations of the CMB on 10 arcminute scale, including the kinematic effect due to peculiar velocities can be estimated and is shown in figure 5 (De Luca, Désert, & Puget, 1995). It shows that measurements of the CMB fluctuations at a sensitivity of $\delta T/T \simeq 2.\,10^{-6}$ require the removal of the S-Z component (Colafrancesco et al., 1994). Fortunately, the Sunyaev-Zeldovich effect has a well-defined spectral signature (ignoring the relativistic correction for high temperature clusters) which makes it relatively easy to identify, if the experiment covers the range 500 μm to 2 mm with high sensitivity and good angular resolution (better than 10 arcminute).

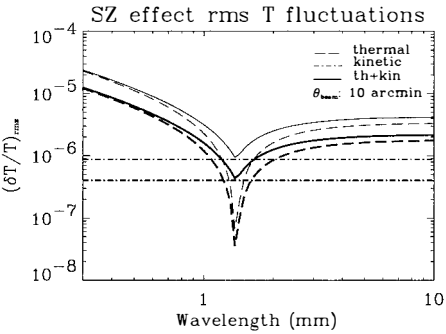

Figure 5: An estimate (see text) of the *rms* contribution as a function of wavelength of the Sunyaev-Zeldovich effects of a cluster background at the 10' scale. The bold set of lines corresponds to the contribution of all sources weaker than 100 mJy for the thermal part and 30 mJy for the kinetic part. The light set of lines corresponds to the contributions of sources weaker than 1 Jy.

Actual realizations of patches of the sky were generated by using the same Press-Schechter approach. This procedure yields the number density of clusters per unit of redshifts, solid angles and flux density interval. Thus one can simply lay down in each redshift slice the appropriate number of clusters. The gas profiles in the clusters were simply modeled by a β-model. To generate temperature maps, the radial peculiar velocities v_r of each cluster were drawn randomly from an assumed initial Gaussian velocity distribution with a standard deviation at z =0 of σ_0 = 400 Km/s. A $\Delta T/T$ profile was then computed for each of the resolved clusters. The resulting maps (Aghanim et al., 1996) were found to agree reasonably well with those generated using more sophisticated algorithms (such as the "peak-patch" method, Myers & Bond (1993)).

3 Comparing contributions to the microwave sky

3.1 Angular Scale Dependence of the Fluctuations

Figure 6 compares the power spectrum at 3.3 mm and 1.4 mm of the expected primary anisotropies (in a standard CDM model) with the power contributed by the galactic emission (eq. [1]), and the unresolved background of radio and infrared sources (eq. [2]). It is interesting to see that even at 90 GHz, the dust contribution might be stronger than the one coming from the synchrotron emission. Since point processes have flat ("white noise") spectra, their logarithmic contribution to the variance, $\ell(\ell+1)C(\ell) \propto \ell^2$, increases and becomes dominant at very small scales. These levels must now be compared with those from the noise of the detector of an experiment, in order to evaluate what is measurable in practice.

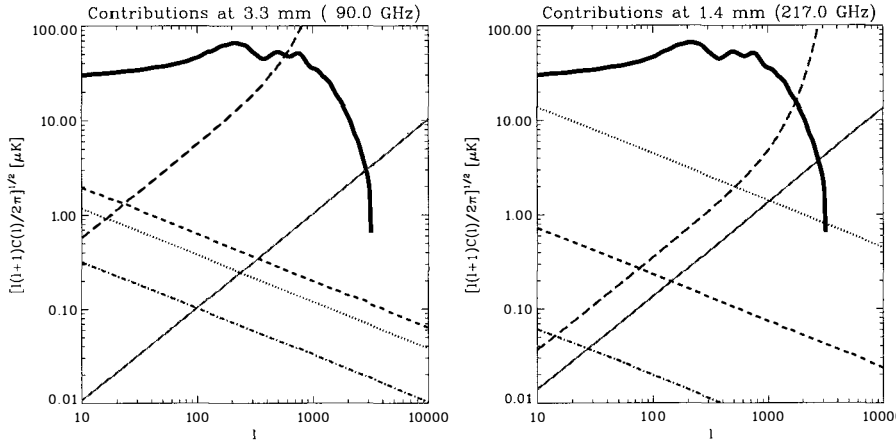

Figure 6: Contributions to the fluctuations of the various components, as a function of angular scale. The thick solid line corresponds to a *COBE*-normalized CDM model. The dots, dashes and dot-dashes refer respectively to the dust, free-free and synchrotron emissions of the galaxy. The triple dots-dashes displays the contributions from unresolved infrared sources. Long dashes show "on-sky" noise level (see text).

The detector noise is added to the total signal *after* the sky fluctuations have been convolved by the beam pattern. Its level depends on the observing strategy, e.g. the total integration time per sky pixel. When the time-ordered data is converted into a map, the pixel noise will depend on the size of the map pixels, which must in practice be at least a factor of 2.4 smaller than the beam FWHM to preserve all the angular information available. We assume at this stage that the detector noise can be modeled as isotropic white noise[2].

In order to directly compare the astrophysical fluctuations with those coming from the detectors, it is convenient to derive a fictitious noise field "on the sky" which, once convolved with the beam pattern and pixelized, will be equivalent to the real one (Knox, 1995). Modeling

[2]This assumption leaves aside the effect of low frequency $1/f$ noise which, if uncorrected, would translates into "stripping" of the maps. Here we assume that redundancy in the sky coverage will allow the removal of this component.

the angular response of channel i, $w_i(\theta)$, as a gaussian of FWHM θ_i, the sky or "unsmoothed" noise spectrum is then

$$C_i(\ell) = c^2_{noise} \exp\left(-\frac{(\ell+\frac{1}{2})^2}{2(\ell_i+\frac{1}{2})^2}\right) \simeq c^2_{noise} \exp(-\frac{\ell^2\theta_i^2}{2\sqrt{2\ln 2}}),\ \text{with}\ (\ell_i+\frac{1}{2})^{-1} = 2\sin\left(\frac{\theta_i}{2\sqrt{8\ln 2}}\right)$$

and $c^2_{noise} = \sigma_i^2\Omega_i = \sigma_i^2 \times 2\pi[1-\cos(\theta_i/2)]$, if σ_i stands for the $1\text{–}\sigma$ $\Delta T/T$ sensitivity per field of view. As an example, the long dashes in figure 6 correspond to detector noise at the level of 35.5 μK per FWHM of 17.4′ for the 90 GHz plot and at the level of 5.5 μK per FWHM of 7.1′ at 217 GHz (both being representative of what HEMTs and bolometers might respectively achieve at these frequencies in a space mission with a 1.5 m mirror and respectively 36/12.5 seconds of integration per FWHM, see table 1 below).

3.2 Angular-Frequency Dependence of the Fluctuations

An extensive series of angular power spectra at many frequencies (such as those in figure 6), or of amplitudes of fluctuations as a function of frequency for a series of angular scales (such as figure 4), provides a detailed picture of the behavior of the various components. Still, it proves convenient to consider the fluctuation amplitudes as simultaneous functions of frequency and angular scale to build a more synthetic view of the fluctuations "landscape".

Figure 7 shows the contours in the $\nu - \ell$ plane where the fluctuations, as estimated from $\ell(\ell+1)C(\ell)/2\pi$, reach the large scale *COBE* level ($\ell(\ell+1)C(\ell)/2\pi = (30\mu\text{K})^2$). These contours map the three dimensional topography of the fluctuations of individual components in the $\nu - \ell$ plane. Tickmarks show the "downhill" directions. The synchrotron component (when expressed in equivalent temperature fluctuations) defines a valley which opens towards large ℓ, since $\ell^2 C(\ell)$ decreases with ℓ as $1/\ell$. The free-free component defines a shallower and gentler valley (see also fig.4.b), while the dust emission creates a high frequency cliff. The large ℓ end of the valley is barred by the point sources "dam".

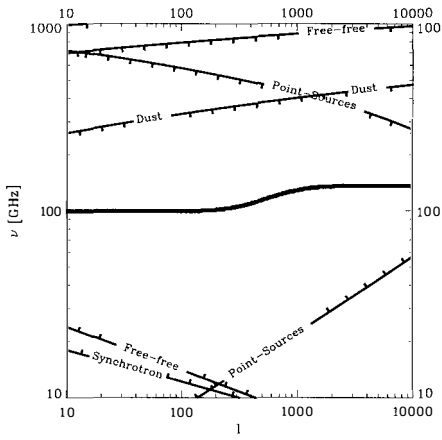

Figure 7: Contour levels of the different components in the angular scale–frequency plane. The levels indicate when the power spectra of the various components reach $\sim (30\mu\text{K})^2$ - the level of the *COBE* detection; tickmarks show the downhill direction. Thus the central area is the region where a CMB signal at COBE level will dominate over all other components. The central line materializes the locus of weakest overall contamination by foregrounds.

The heavy black line shows the path followed by a stream lying at the bottom of the valley, i.e. it traces the lowest level of total fluctuations . Its location confirms that $\nu \simeq 100$ GHz is the best frequency for low-ℓ measurements. At $\ell \gtrsim 200$, the optimal frequency moves to higher values and is determined by the minimum of the fluctuations from unresolved sources; its exact value ($\simeq 150 - 200$ GHz) depends on the uncertain modeling of the point sources background and to which level can point sources may be resolved at different frequencies.

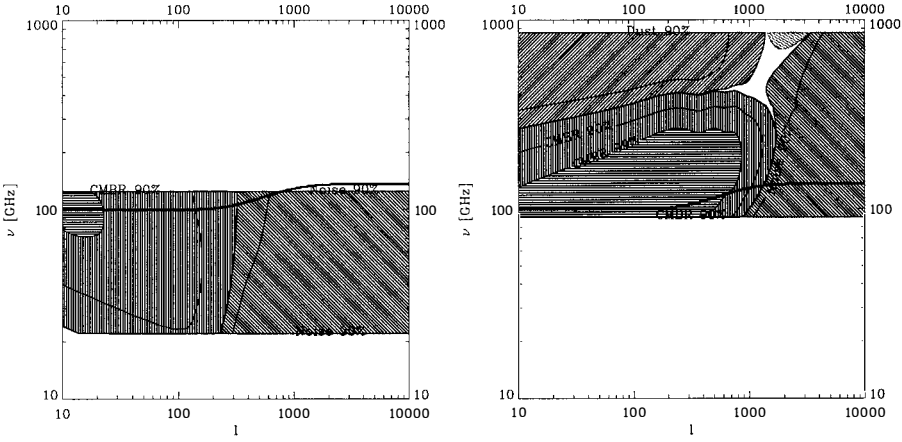

Figure 8: Each hatched areas delimits the regions where a given component accounts for 50% of the total contribution to the variance, including detector noise chosen to be representative of what HEMTs (on the left) and bolometers (on the right) can achieve. Each panel has been restricted to the frequency range that each technology can cover. Inner contours show when a component accounts for 90% of the signal, and the central contour (horizontal hatches) delimits the region where the CMB anisotropies should contribute 99% of the signal.

In order to identify the dominant processes, Figure 8 shows the regions where the contribution from a given process $\ell C_p(\ell)$ accounts for half of the total including the noise, $\ell \sum_p C_p(\ell)$ (i.e. of the contribution per logarithmic interval centered around that scale ℓ to the variance of the measurement at frequency ν). The inner contours show when that process accounts for 90% of the total (and 99% for the CMB). This figure thus shows the areas in the ν-ℓ plane where a given component will be sampled directly by the measurements. Two cases were considered. On the left (case I) the noise level and the frequency. range have been chosen to be representative of what passively cooled HEMTs can achieve with a 1.5 m mirror in a year spent observing all the sky while on the right (case II) the case of bolometers is presented. Each technology allows a cover a decade on either side of 100 GHz. The noise levels plotted were computed using a

CASE I: Passively cooled HEMTS						
ν	22.0	30.0	40.0	60.0	90.0	125.0
FWHM	54.0	39.5	31.8	23.4	17.4	12.0
1-σ $\frac{\Delta T}{T}$	9.5	12.0	10.0	13.0	13.0	45.
$c_{noise}T$	20.7	18.9	12.8	12.3	9.11	21.8

CASE II: Bolometers at 0.1 K						
ν	90.0	143.0	217.0.	353.0	545.0	857.0
FWHM	17.5	10.3	7.1	4.4	4.4	4.4
1-σ $\frac{\Delta T}{T}$	2.0	1.2	2.0	12.1	76.6	4166.
$c_{noise}T$	1.41	0.50	0.57	2.14	13.6	739

Table 1: Summary of the two cases considered. Frequencies are in GHz, FWHM are in arc minute, sensitivities are in 10^{-6} units, and $c_{noise}T$ is in μK.deg (instead of K.steradian$^{1/2}$). They should be representative of what can be achieved in satellite missions using each technology and mapping the full sky in a year.

spline interpolation between the columns of the summary table 1.

In the latter case, reaching 10% accuracy on the CMB anisotropies over all modes between a few and a thousand in the cleanest 50% of the sky should be easily accessible. A 1% accuracy can only be obtained though in a much smaller angular range, if no foreground subtraction is performed. We now turn to that issue.

4 Separation of components

4.1 Linear Inversion

As was shown earlier, it is possible to reach 10% accuracy (in $\Delta C(\ell)/C(\ell)$) on the CMB anisotropies by simply using a low and high frequency channels to monitor regions with high foregrounds, and then using the central, least polluted, channel (~ 100 GHz) to measure directly the CMB fluctuations. However, with a larger number of spectral channels, more information is available that can be used to achieve higher accuracy. We start by describing the simplest, linear, approach to this "inversion problem".

We make the hypothesis that the flux $f(\mathbf{r}, \nu)$ measured in the direction $\mathbf{r}$ and at a frequency ν is a superposition of n_p processes (physical components) whose contributions can be factorized[3] as a spatial template $x_p(\mathbf{r})$ at a reference frequency (e.g. at 100 GHz), times a spectral coefficient $s_p(\nu)$

$$f(\mathbf{r}, \nu) = \sum_{p=1}^{n_p} s_p(\nu) x_p(\mathbf{r}). \tag{3}$$

Note that this assumption does not restrict the analysis to components with a spatially constant spectral behavior. Indeed, these variations are expected to be small, and can thus be linearized too[4].

If there are n_ν channels, each transmitting a frequency $\nu\prime$ according to $t_\nu(\nu\prime)$, the observation in each direction can be arranged as an n_ν component vector $y(\mathbf{r})$ given by

$$y(\mathbf{r}) = Px(\mathbf{r}) + B(\mathbf{r}), \tag{4}$$

where x is an n_p elements vector, B is a vector whose n_ν elements are the noise contributions in each channel, and the $n_\nu \times n_p$ design matrix P describes the "projection" of each component p on each channel ν:

$$P_{\nu p} = \int_0^\infty t_\nu(\nu\prime) s_p(\nu\prime) d\nu\prime. \tag{5}$$

If all the observations are at the same angular resolution, equation (4) applies also to spatially smoothed (beam-convolved) quantities.

On the other hand, since maximum resolution is to be retained, each channel might be at or near the diffraction limit, and it becomes more convenient to work in Fourier space (or with spherical harmonics for larger maps) where convolutions reduce to products. Then

$$y(\ell) = A(\ell)x(\ell) + B(\ell), \tag{6}$$

[3]This is unlikely to be realistic for the unresolved contribution from galaxies, since at different frequencies different redshift ranges dominate, and thus different sources. We defer a discussion of the contribution of point sources to §4.3.2.

[4]For instance, in the case of a varying spectral index whose contribution can be modeled as $\nu^{\alpha(\mathbf{r})} x_p(\mathbf{r})$, we would decompose it as $\nu^{\overline{\alpha}}[1 + (\alpha(\mathbf{r}) - \overline{\alpha}) \ln \nu] x_p(\mathbf{r})$. We would thus have two spatial templates to recover, $x_p(\mathbf{r})$ and $(\alpha(\mathbf{r}) - \overline{\alpha}) x_p(\mathbf{r})$ with different spectral behaviors, $\propto \nu^{\overline{\alpha}}$ and $\propto \nu^{\overline{\alpha}} \ln \nu$ respectively. But given the low expected level of the high latitude synchrotron emission, this is unlikely to be necessary.

with $A_{\nu p}(\ell) = P_{\nu p}\, w_\nu(\ell)$, if w_ν is the angular response of channel number ν (and the dependence on ℓ recalls that we consider transformed quantities). Every "pixel" in Fourier space (i.e. every mode) is then independent and it is natural to define a figure of merit

$$\chi^2(\ell) = |y - Ax|^2 \tag{7}$$

for each mode ℓ. The matrix inversion algorithm by singular value decomposition is precisely designed to solve the problem of finding the vector x that minimizes this figure of merit.

4.2 Improving the Separation

The inversion scheme described above is really only a first guess which can be considerably refined. One can for instance apply "Wiener" filtering techniques (Tegmark & Efstathiou, 1996; Bouchet, Gispert, & Puget, 1995b). Any *linear* recovery procedure may be written as an $n_p \times n_\nu$ matrix W which applied to the $y(\ell)$ vector yields an estimate $\widehat{x}(\ell)$ of the $x(\ell)$ vector, i.e.

$$\widehat{x}(\ell) = W(\ell) y(\ell) \tag{8}$$

The simple inversion of § 4.1 was designed to best reproduce the observed data set by minimizing the residuals between the observations and the model (eq. [7]). Another possibility is to require a *statistically minimal* error in the recovery, when the method is applied to an ensemble of data sets with identical statistical properties. One then obtains the "Wiener" matrix W, by demanding that the difference between the initial and recovered *processes* be of minimal variance

$$\varepsilon_p^2(\ell) \equiv < |Wy - x|_p^2 > = < |W(Ax + B) - x|_p^2 > . \tag{9}$$

In practice, we require that the derivatives of

$$\varepsilon_p^2(\ell) = (W_{p\nu} A_{\nu p\prime} - \delta_{pp\prime})(W_{p\nu\prime} A_{\nu\prime p\prime\prime} - \delta_{pp\prime\prime}) < x_{p\prime} x_{p\prime\prime} > + W_{p\nu} W_{p\nu\prime} < B_\nu B_{\nu\prime} > \tag{10}$$

versus all $W_{p\nu}$ be zero for each ℓ (repeating indices implying summation), which yields

$$W_{p\nu}\,(A_{\nu p\prime} < x_{p\prime} x_{p\prime\prime} > A_{\nu\prime p\prime\prime} + < B_\nu B_{\nu\prime} >) = A_{\nu\prime p\prime} < x_{p\prime} x_p > . \tag{11}$$

If we further assume that the decomposition in the model (6) is on a basis of uncorrelated spatial templates[5], i.e. $< x_p x_{p\prime} > = \delta_{pp\prime} C_p(\ell)$, and that the noise is not correlated between channels, i.e. $< B_\nu B_{\nu\prime} > = \delta_{\nu\nu\prime} C_{\nu\prime}$ the expression above simplifies to

$$W_{p\nu}(A_{\nu p\prime} A_{\nu\prime p\prime} C_{p\prime} + \delta_{\nu\nu\prime} C_{\nu\prime}) = \delta_{pp\prime} A_{\nu\prime p\prime} C_{p\prime}. \tag{12}$$

Since $A_{\nu p}\sqrt{C_p}$ indicates the typical amplitude of the signal in the channel ν which is due to the process p (which we shall denote below as $\mathcal{S}_{\nu p}$), we see that the Wiener matrix simply weights the n_ν observations to obtain a process p according to a generalization of signal/(signals + noise). One can thus think of Wiener filtering as a "polishing" stage of a first inversion as in § 4.1 yielding an estimate of the power spectra needed to have optimal weights. Note though that the "typical amplitude" of a signal $\mathcal{S}_{\nu p}(\ell)$ might be a rather poor indicator for a non-Gaussian process like the Sunyaev-Zeldovich effect from clusters. This needs be checked by direct simulations of the observations and of their inversion, and is presented in a separate paper by Gispert & Bouchet (1996), in this volume.

[5]In our case, it means that our templates are the HI correlated emmission and the uncorrelated one, not that of the dust and free-free emission. If one wants to keep decomposing on simpler spectral components, e.g. dust and free-free, one would then have to keep the cross-correlation terms.

Note that we never had to assume the statistical independence of different modes of a process in deriving this optimal recovery of the Fourier modes. On the other hand, if we required that $< |\widehat{x}_p(\mathbf{r}) - x_p(\mathbf{r})|^2 >$ be minimal for a convolution kernel W (such that $\widehat{x}(\mathbf{r}) = W \star y(\mathbf{r})$), we would have to further assume $< x_p(\ell) x_p(\ell') >= \delta(\ell - \ell') C_p(\ell)$. In other words, the best linear recovery of Fourier modes is also the best linear recovery of pixel values when the modes are statistically independent.

4.3 Quality of the component separation

It is illuminating to compute the matrix $\mathcal{Q}_{pp\prime} =< \widehat{x}_p \widehat{x}_{p\prime} > / \sqrt{< x_p^2 >< x_{p\prime}^2 >}$ which should be equal to the identity matrix $\delta_{pp\prime}$ if we were able to recover perfectly the initial processes. One has

$$\mathcal{Q}_{pp\prime} =< W_{p\nu} y_\nu W_{p\prime\nu\prime} y_{\nu\prime} > / [C_p C_{p\prime}]^{1/2} = W_{p\nu} A_{\nu p\prime} [C_{p\prime}/C_p]^{1/2}, \tag{13}$$

where we have used the definition equation (12) of the W matrix to write the last equality. By using the matrix of typical amplitudes $\mathcal{S}_{\nu p}$, this equation may be written in matrix form

$$\mathcal{Q} = \mathcal{S}^T [\mathcal{S}\mathcal{S}^T + N]^{-1} \mathcal{S}, \tag{14}$$

which clearly shows that $\mathcal{Q}$ is the identity matrix in the absence of noise.

In the following we focus on the trace elements of $\mathcal{Q}$, $Q_p = W_{p\nu} A_{\nu p}$, with $< \widehat{x}_p(\ell) >= Q_p(\ell) < x_p(\ell) >$, so that a value of Q_p nearly equal to unity indicates that enough information has been collected by the experiment on the process p at scale ℓ for the initial and recovered process to have nearly identical power spectra values. Contrariwise, if Q_p is close to zero, the information collected is not sufficient, and the Wiener filter sets this mode of that process to nearly zero. In other words, $Q_p(l)$ may be used as a "quality factor" which evaluates the ability of a given experiment to recover process p at scale ℓ.

This indicator generalizes the real space "Foreground Degradation Factor" introduced by Dodelson & Stebbins (1994). It may be viewed as an extension of the usual window functions used to describe an experimental setup. Indeed, let us imagine a noiseless experiment mapping directly the CMB anisotropies with a beam profile $w(\theta)$. Then the power spectrum of the map will be the real power spectrum times the square of the spherical harmonic transform of the beam, $< \widehat{x}_p(\ell) >= w(\ell)^2 < x_p(\ell) >$. The spherical transform of $Q_p^{1/2}(\ell)$ is thus the beam profile of a thought experiment directly measuring CMB anisotropies. The shape of $Q_p(\ell)$ thus gives us a direct insight on the real angular resolution of an experiment when foregrounds are taken into account.

In addition, one often considers (e.g. for theoretical studies of the accuracy of parameter estimation from power spectra) a somewhat less idealized experiment which still maps directly the CMB, with a beam profile $w(\theta)$, but including also detector noise, characterized by its power spectrum C_N. Then we know (Knox, 1995) that the errors on the power spectrum in the Gaussian case are given by

$$\Delta C_{CMB}(\ell) = \sqrt{\frac{2}{2\ell+1}} \left(C_{CMB}(\ell) + C_N(\ell)\, w(\ell)^{-2} \right). \tag{15}$$

Since this experiment would have $w^2 C_{CMB}/(w^2 C_{CMB} + C_N) = Q$, we find that $1/Q_{CMB} - 1$ gives us the effective noise power spectrum "on the sky" and thus

$$\frac{\Delta C_{CMB}}{C_{CMB}} = \sqrt{\frac{2}{2\ell+1}}\, \frac{1}{Q_{CMB}}. \tag{16}$$

Determining the quality factor thus allows estimating directly the final errors on the power spectrum determination from a foreground model and the summary table of performance of an experiment.

4.3.1 Comparing technologies: Figure 9 shows the quality factor that obtain for 2 different experiments, representative of what can be achieved with HEMTs and with cryogenically cooled bolometers (cases I & II above, summarized in table 1), when the contribution from unresolved sources is ignored.

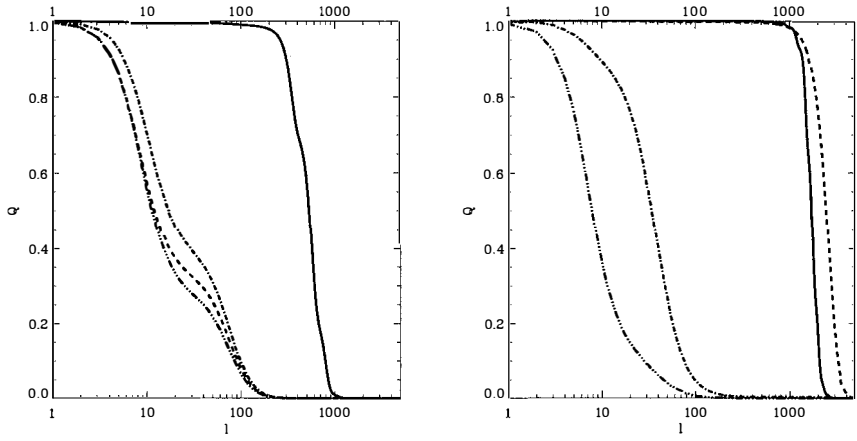

Figure 9: Quality factors (or square of the ℓ-space effective windows) for a typical HEMT experiment (case I, left) and for a typical bolometer experiment (case II, right). The dashes, dot-dashes, triple dots-dashes refer respectively to the H I correlated & uncorrelated component, and to the synchrotron with levels typical of the best half of the sky. The effect of point sources is ignored. The solid line corresponds to the CMB (CDM).

In order to allow quick quantitative comparison between different cases, it is convenient to note the numerical values of the angular scale ℓ when the quality of the recovery (the effective beam) drops below a given threshold, for instance 0.25, the half maximum value[6] of $Q^{1/2}$. One can also view this scale as that for which the relative error on the power spectrum [eq. (16)] is 4 times greater than it's minimal value due to cosmic variance (i.e. $(\ell + 1/2)^{-1/2}$).

Table 2 compares these scales for the cases I and II when the CMB spectrum $\ell(\ell+1)C(\ell)/2\pi$ is taken to be a constant equal to $30^2(\mu\mathrm{K})^2$ at all scales , or twice that value, or in a *COBE* normalized CDM case as in figure 9. It shows that indeed Q_p does not depend too much on the underlying spectrum for the CMB. Furthermore, when we assumed that the spatially uncorrelated components are those with a dust and a free-free spectrum, we found instead (for the CDM case) that $\ell_{CMB} = 645/1862$, $\ell_{Dust} = 17/2818$, $\ell_{Free} = 102/77$, $\ell_{Sync} = 24/12$ where the 2 numbers correspond to case I and II, as in the table. While the recovery of the galactic components is not surprisingly rather different, that of the CMB remains remarkably stable.

[6] Alternatively one may define an equivalent width for the effective beams $Q_p^{1/2}$, equal to $\int Q_p^{1/2}(\ell)\, d\ell$, which is thus the width in ℓ of a top-hat filter having the same transmission. We found that this leads to fairly similar numerical values.

assumed CMB	ℓ_{CMB}	ℓ_{HI-C}	ℓ_{HI-U}	ℓ_{Sync}
$30^2(\mu K)^2$	531/2493	51/2968	62/52	40/13
$60^2(\mu K)^2$	611/2714	51/2968	62/52	40/13
CDM	628/1886	51/2856	62/52	40/13

Table 2: Angular scale ℓ when the quality of the recovery drops below 0.25. The two numbers separated by a slash correspond respectively to case I (left) and II (right).

4.3.2 Effect of a Background of Unresolved Sources: We now address the degrading effect of unresolved sources. Since the fluctuations at different frequencies might not be well correlated, we have performed the calculation under the two extreme assumptions that these fluctuations might be either totally correlated between different frequencies, or totally uncorrelated. In the first case, this amounts to add one more physical process which one tries to recover, while in the second case, this background is treated as noise and added to the detectors fluctuations. In addition, since the prediction of the unresolved component from sources is rather uncertain at this time, we have also computed these two extreme cases when the level of this sources background has been increased by a factor of 5.

Assumed sources	ℓ_{CMB}	ℓ_{HI-C}	ℓ_{HI-U}	ℓ_{Sync}
None	628/1886	51/2856	62/52	40/13
Correlated	628/1885	51/2031	61/52	39/13
Uncorrelated	628/1873	51/2310	61/50	39/9
Correlated $\times$ 5	628/1885	43/742	52/52	34/13
Uncorrelated $\times$ 5	628/1804	45/997	45/43	33/4

Table 3: Angular scale ℓ when the quality of the recovery drops below 0.25. The two numbers separated by a slash correspond respectively to case I (left) and II (right). The CMB was taken to be a *COBE*-normalized CDM. The first line is when sources are ignored altogether, while the 2 next other lines should bracket what to expect realistically. The final two lines correspond to a background of sources 5 times stronger.

As can be seen from table 3, the CMB recovery remains essentially unaffected by the assumptions made concerning the sources, and the range in ℓ available for CMB measurements is about 3 times better in case II than in case I. For the H I–correlated component, the range available is substantially narrowed in case II, although it still remains nearly 40 times larger than in case I. Both cases probe equally well the H I–uncorrelated emission, while the range for the synchrotron emission is about three times larger in case I than in case II.

4.3.3 Effect of the noise level: As a final example of use of the quality factor, we vary the assumed performance level of the detectors of cases I and II, to see the impact of e.g. the time spent on each pixel, or the detectors' operating temperature, etc...

As can be seen from table 4, HEMTs would improve their CMB ℓ coverage by ~ 30 % (45%) if they could be operated in such a way as to improve by a factor of two (four) the nominal noise level. Contrariwise, bolometers could tolerate a substantial degradation of their noise level ands still allow mapping all the most interesting scales for the primary anisotropies (with a 12% degradation in ℓ coverage for an increase by a factor of 2 of the noise).

Noise level	ℓ_{CMB}	ℓ_{HI-C}	ℓ_{HI-U}	ℓ_{Sync}
$1/4\ \sigma$	910/2280	109/2728	130/112	83/12
$1/2\ \sigma$	815/2073	77/2546	92/77	59/11
Nominal σ	628/1873	51/2310	61/50	39/9
2σ	525/1667	33/2010	40/32	25/7
4σ	333/1441	21/1466	25/21	16/5

Table 4: Angular scale ℓ when the quality of the recovery drops below 0.25. The CMB was taken to be a *COBE*-normalized CDM, and the unresolved source background was treated as noise. The two numbers separated by a slash correspond respectively to case I (left) and II (right) for global variations (i.e. by the same factor in each band)of the detector noise level.

5 Discussion

We have developed a simple measure of the effective resolution of an experiment in the presence of foregrounds by computing a quality factor assuming a model of foregrounds based on current knowledge. It arises naturally when using multi-frequency multi-resolution observations and power spectrum estimates to build optimal spatial templates of the underlying physical processes, as defined by their spectral behaviour.

If one were interested not in the best maps in the previous χ^2 sense, but rather in power spectrum estimation, we saw that the minimization performed leads to maps whose power spectrum is biased compared to the real one in a way which Q_p precisely quantifies. It follows that an unbiased estimate $\widehat{C}_p$ of the power spectrum is $\widehat{C}_p =< \widehat{x}^2 > /Q_p$.

Of course, if instead of $W_{p\nu}$ we were to use $W_{p\nu}/Q_p^{1/2}$ to construct maps, there power spectra would yield the same unbiased estimators of the underlying power spectra (i.e. $< \widehat{x}^2 >=< x^2 >$), but these maps would be more noisy and contain spurious features. Indeed one finds in that case

$$\varepsilon\prime_p^2(\ell) =< \widehat{x}_p^2 > -2 < \widehat{x}_p x_p > + < x_p^2 >= 2(1 - Q_p^{1/2}) < x^2 > \tag{17}$$

which is always greater than the minimum value $\varepsilon_p^2(\ell) = (1 - Q_p) < x^2 >$ obtained by straight Wiener filtering. On the other hand, the reconstructed maps would be less sensitive to the assumed behavior of the different components. Indeed, suppose we reconstruct the process r and replace the assumed power spectra $C_r(\ell)$ by $C'_r(\ell) = \alpha(\ell)C_r(\ell)$. Then $W_{r\nu}(\ell)$ becomes $W'_{r\nu}(\ell) = \beta(\ell)W_{r\nu}(\ell)$ and $Q_r(\ell)$ becomes $Q'_r(\ell) = \beta(\ell)Q_r(\ell)$, so that the weights $W_{p\nu}/Q_p^{1/2}$ now only scale as $\beta^{1/2}(\ell)$. On the other hand, β is already quite a weak function of α when Q is sizable, at least for our model of the microwave sky (see table 2 above).

In addition, if one were to use the matrix $W_{p\nu}/Q_p$ to do a component separation which is independent of the assumed power spectrum of the recovered process, one would then have

$$< \widehat{x}_p^2 >=< x_p^2 > + O_p =< x_p^2 > /Q_p, \tag{18}$$

where O_p stands for the contributions of the other processes and of detector noise. In that case an unbiased estimate of the power spectrum would be $< \widehat{x}_p^2 > - O_p$, but the corresponding maps would be even noisier since then $\varepsilon\prime\prime_p^2(\ell) =< x_p^2 > (1/Q_p - 1) \geq \varepsilon\prime \geq \varepsilon$ (the equality holding when $Q_p = 1$).

The previous developments focused on the recovery of Fourier modes and their inherent errors for variants of Wiener filtering. To estimate the induced errors on the derived power spectra would entail computing $< |\widehat{C}(\ell) - C(\ell)|^2 >$ which involves the poorly known fourth order correlations $< x_p x_q x_{p\prime} x_{q\prime} >$ of the processes. In case of experiments with sufficiently

good signal-to-noise ratio for yielding reasonable first estimates of these fourth order quantities (and not only of the C_p's), one would then derive new weights, optimal for power spectrum estimation by linear combinations, by requiring instead that $< |\tilde{C}(\ell) - C(\ell)|^2 >$ be minimal.

In conclusion, the quality factor introduced in this paper allows a quick appraisal of the *effective* resolution (or noise level, using L. Knox formalism) of an experiment once foregrounds are taken into account. It is flexible enough to allow checking easily the effect of changing the sky model, or the instrumental configurations.

Acknowledgements. We are grateful to S. Hancock for useful informations on experimental constraints on some galactic foregrounds, as well as D. Bond and the french RUMBA group for stimulating discussions.

References

Abergel, A., Boulanger, F., Mizuno, A., & Fukui, Y. 1994, Astrophys. J. Lett., 423, L59–L62

Aghanim, N., De Luca, A., Bouchet, F. R., Gispert, R., & Puget , J.-L. 1996, Astr. Astrophys., submitted

Bahcall, N. A., & Cen, R. 1993, Astrophys. J. Lett., 407, L49–L52

Bartlett, J. G., & Silk, J. 1994, Astrophys. J., 423, 12–18

Bennett, C. L., Kogut, A., Hinshaw, G., Banday, A. J., Wright, E. L., Gorski, K. M., Wilkinson, D. T., Weiss, R., Smoot, G. F., Meyer, S. S., Mather, J. C., Lubin, P., Loewenstein, K., Lineweaver, C., Keegstra, P., Kaita, E., Jackson, P. D., & Cheng, E. S. 1994, Astrophys. J., 436, 423–442

Bouchet, F. R., Gispert, R., & Puget, J.-L. 1995a. The COBRAS/SAMBA CMB project. In Clustering in the Universe; Proceedings of the 30^{th} Moriond meeting, Les Arcs, France, astro-ph9507032, S. Maurogordato, C. Balkowski, C. Tao, and J. Trân Thanh Vân, editors, Editions Frontières, pages 537–544

Bouchet, F. R., Gispert, R., & Puget, J.-L. 1995b. The mm/sub-mm Foregrounds and Future CMB Space Missions. In Unveiling the Cosmic Infrared Background; AIP Conference Proceedings 348, Baltimore, Maryland, USA, E. Dwek, editor, pages 255–268

Boulanger, F., Abergel, A., Bernard, J. P., Burton, W. B., Desert, F. X., Hartmann, D., Lagache, G., & Puget, J. L. 1996, Astr. Astrophys., 312, 256–262

Burton, W. B., & Hartmann, D. 1994, Astrophys.and Space Sc., 217, 189–193

Colafrancesco, S., Mazzotta, P., Rephaeli, Y., & Vittorio, N. 1994, Astrophys. J., 433, 454–463

Condon, J. J., Broderick, J. J., & Seielstad, G. A. 1989, Astron. J., 97, 1064–1073

Davies, R. D., Watson, R. A., & Gutierrez, C. M. 1996, MNRAS, 278, 925–939

Davies, R. D., Gutierrez, C. M., Hopkins, J., Melhuish, S. J., Watson, R. A., Hoyland, R. J., Rebolo, R., Lasenby, A. N., & Hancock, S. 1996, MNRAS, 278, 883–896

De Bernardis, P., Masi, S., & Vittorio, N. 1992. CMB and galactic maps in the millimetric region. In The infrared and submillimetre sky after COBE; Proceedings of the NATO Advanced Study Institute, Les Houches, France, Mar. 20-30, 1991, pages 315–330

De Luca, A., Désert, F. X., & Puget, J. L. 1995, Astr. Astrophys., 300, 335

Dodelson, S., & Stebbins, A. 1994, Astrophys. J., 433, 440–453

Dwek, E., Arendt, R. C., Fixsen, D. J., Sodroski, T. J., Odegard, N., Weiland, J. L., Reach, W. T., Hauser, M. G., Kelsall, T., Moseley, S. H., Silverberg, R. F., Shafer, R. A., Ballester, J., Bazell, D., & Isaacman, R. 1996, Astrophys. J., in press

Fischer, M. L., Clapp, A., Devlin, M., Gundersen, J. O., Lange, A. E., Lubin, P. M., Meinhold, P. R., Richards, P. L., & Smoot, G. F. 1995, Astrophys. J., 444, 226–230

Gautier, T. N., I., Boulanger, F., Perault, M., & Puget, J. L. 1992, Astron. J., 103, 1313–1324

Gispert, R., & Bouchet, F. R. 1996. Simulation of CMB Experiments. In these proceedings

Guiderdoni, B., Hivon, E., Bouchet, F. R., & Maffei, B. 1996. Evolutionary Models of Galaxy Emission in the FIR/Submm Range. In these proceedings

Hancock, S., Davies, R. D., Lasenby, A. N., Gutierrez, C. M., Watson, R. A., Rebolo, R., & Beckman, J. E. 1994, Nature, 367, 333

Haslam, C. G. T., Stoffel, H., Salter, C. J., & Wilson, W. E. 1982, Astronomy and Astrophysics Supplement Series, 47, 1

Hivon, E., Guiderdoni, B., & Bouchet , F. R. 1996. Contribution of point sources to microwave background anistropies. In these proceedings

Jones, A. W. e. a. 1996, in preparation

Knox, L. 1995, Phys Rev D, 52, 4307–4318

Kogut, A., Banday, A. J., Gorski, K. M., Hinshaw, G., Bennett, C. L., & Reach, W. T. 1995, BAAS, 187, 2002

Kogut, A., Banday, A. J., Bennett, C. L., Gorski, K. M., Hinshaw, G., Smoot, G. F., & Wright, E. I. 1996, Astrophys. J. Lett., 464, L5

Lagache, G., Abergel, A., Bernard, J.-P., Boulanger, F., Désert, F.-X., Puget, J.-L., & Reach, W. T. 1996, Astr. Astrophys., in press

Laureijs, R. J., Clark, F. O., & Prusti, T. 1991, Astrophys. J., 372, 185–193

Lawson, K. D., Mayer, C. J., Osborne, J. L., & Parkinson, M. L. 1987, MNRAS, 225, 307–327

Lockman, F. J., Hobbs, L. M., & Shull, J. M. 1986, Astrophys. J., 301, 380–394

Myers, S. T., & Bond, J. R. 1993, BAAS, 182, 7707

NASA 1995, COBE Explanatory Supplement, Version 2.0, http://www.gsfc.nasa.gov/astro/cobe/dirbe_ exsup.html

Puget, J. L., Abergel, A., Bernard, J. P., Boulanger, F., Burton, W. B., Desert, F. X., & Hartmann, D. 1996, Astr. Astrophys., 308, L5

Reach, W. T., Dwek, E., Fixsen, D. J., Hewagama, T., Mather, J. C., Shafer, R. A., Banday, A. J., Bennett, C. L., Cheng, E. S., Eplee, R. E., J., Leisawitz, D., Lubin, P. M., Read, S. M., Rosen, L. P., Shuman, F. G. D., Smoot, G. F., Sodroski, T. J., & Wright, E. L. 1995, Astrophys. J., 451, 188

Reich, P., & Reich, W. 1988, Astronomy and Astrophysics Supplement Series, 74, 7–20

Reynolds, R. J. 1989, Astrophys. J. Lett., 339, L29–L32

Reynolds, R. J., Tufte, S. L., Kung, D. T., McCullough, P. R., & Heiles, C. 1995, Astrophys. J., 448, 715

Savage, B. D., Drake, J. F., Budich, W., & Bohlin, R. C. 1977, Astrophys. J., 216, 291–307

Tegmark, M., & Efstathiou, G. 1996, MNRAS, 281, 1297

Wright, E. L., Mather, J. C., Bennett, C. L., Cheng, E. S., Shafer, R. A., Fixsen, D. J., Eplee, R. E., J., Isaacman, R. B., Read, S. M., Boggess, N. W., Gulkis, S., Hauser, M. G., Janssen, M., Kelsall, T., Lubin, P. M., Meyer, S. S., Moseley, S. H., J., Murdock, T. L., Silverberg, R. F., Smoot, G. F., Weiss, R., & Wilkinson, D. T. 1991, Astrophys. J., 381, 200–209

SIMULATIONS OF CMB EXPERIMENTS

Richard Gispert[1] and François R. Bouchet[2]
[1]*Institut d'Astrophysique Spatiale, CNRS-Université Paris-Sud, Orsay, France.*
[2] *Institut d'Astrophysique de Paris, CNRS, Paris, France.*

Abstract

In this paper, we present the current state of detailed simulations performed during the phase A study of the satellite project COBRAS/SAMBA, which since the meeting has been selected by ESA to become the next medium size mission of the agency. We start by describing how we simulated the microwave sky and the observational process. Then we perform on these fake but fairly realistic observations a separation into physical components using the Wiener filtering method described in Bouchet, Gispert, & Puget (1996), this volume. This yields estimates of the precision on the products (maps of CMB anisotropy, of the galactic emissions, of the Sunyaev-Zeldovich effect of clusters) that may be achieved with such data. It promises a revolution at the beginning of the next century.

Future satellite experiments offer the promise of mapping the microwave sky with unprecedented sensitivity and angular resolution. Many studies have shown (see e.g. Efstathiou (1996)) that some effects of cosmological parameters on the Cosmic Microwave Background (CMB) anisotropies are degenerate. This degeneracy may be lifted though once a highly accurate determination of the power spectrum of the CMB becomes available till $\ell \gtrsim 1000$, corresponding to angular scales of about 10 arc minute. The COBRAS/SAMBA satellite project precisely aims to reach that goal with an accuracy close to 1 %. Reaching that ambitious requirement depends of course on our ability to separate the multi-frequency, multi-resolution observations into separate contributions from different physical components.

Bouchet, Gispert, & Puget (1996) in this volume (hereafter BGBP) presented an analytical estimation of the achievable quality of the separation by using a model of the microwave sky and a method based on the concept of Wiener filtering. This method of separation yields the best linear estimates of the spatial templates of the underlying physical processes since it minimizes the variance of the residuals between the input and recovered templates, i.e. the power spectrum of the difference map. While quite useful, this tells us little on the quality of

the overall distributions and phases (the maps) in presence of non-gaussian processes like the galactic emissions or the Sunyaev-Zeldovich effect of clusters (oversighting the fact that the CMB anisotropies themselves might be non-gaussian in case topological defects exists). This and other issues (like the impact of errors on the assumed spectral behavior of the physical components) is best addressed by direct numerical simulations of patches of the sky as observed by *COBRAS/SAMBA* (see also Bouchet, Gispert, & Puget (1995a,b); Bouchet & Gispert (1996)).

We shall include the three galactic components, the primary fluctuations, and the Sunyaev-Zeldovich effect from clusters. The only astrophysical source of fluctuations missing from the simulation are those arising from the background of unresolved sources, which are at very faint levels where the CMB contribution is strongest (but they should be included later to test in particular the removal of resolved sources). We do however include galaxy clusters, to allow an assessment of how well faint extended clusters can be recovered through their Sunyaev-Zeldovich effect.

1 Simulations of the microwave sky and of its observations

We have chosen to construct 12.5×12.5 degree fields with 1.5'×1.5' pixels, and have created spatial templates for all the components. For the primary $\Delta T/T$ fluctuations, the realizations generated correspond to a COBE-normalized CDM model. Realizations of the thermal and kinetic effects of clusters (stored respectively as maps of the y parameter and of $\Delta T/T$) were generated using the Press-Schechter formalism, as described in BGBP. To simulate galactic emissions, we have also used the spectral model presented by BGBP. The spatial templates need be different though since here we want angular resolutions much better than the degree.

There is no template available for the synchrotron emission, even over relatively small areas of the high latitude sky. We instead use patches of the 408 MHz radio map of Haslam et al. (1982) with its 0.85° resolution and add to them small scale structures with a $C(l) \propto l^{-3}$ power spectrum [1], thereby extrapolating to small scales the observed behavior of the spatial spectrum. For the dustand free-free emissions, the DIRBE data lacks the proper resolution (42'), but we can use instead 100μ IRAS maps as spatial templates. The IRAS sky was divided into 300 maps , which were then sorted according to their *rms* level, so that we could check for systematic effects depending on the foreground level on the CMB recovery. When we pick a map as a template for the HI correlated component (see BGBP), we used a contiguous map for the uncorrelated component.

COBRAS/SAMBA Main Characteristics									
Frequency	31.5	53	90	125	143	217	353	545	857
Bandwidth	0.15	0.15	0.15	0.15	0.37	0.37	0.37	0.37	0.37
Resolution	30	18	12	12	10.3	7.1	4.4	4.4	4.4
Sensitivity	9.9	9.6	18.3	45.1	1.2	2.0	12.1	76.6	4166

Table 1: Proposed payload characteristics. Central band frequencies ν are in GHz, bandwidth are in $\frac{\Delta\nu}{\nu}$, angular resolutions (FWHM) in arc minute, and sensitivities $\frac{\Delta T}{T}$ per FWHM, at $1\sigma, 10^{-6}$ units (for 12 months of mission).

[1] To do so, the map is Fourier transformed (which is equivalent to a spherical harmonics decomposition if the size of the map is much smaller than a radian) and its spectrum till the cutoff is computed. New harmonics are then generated at larger l, and globally normalized so that their spectrum smoothly extends the measured one. The results are then transformed back in real space.

The measurement process by the *COBRAS/SAMBA* instruments was simulated in the following way. We have assumed unit transmission across each spectral channel (with $\Delta\nu/\nu = 0.15$ for the LFI and $\Delta\nu/\nu = 0.37$ for the HFI, see Table 1), and integrated across each waveband the different spectral components. The angular response of each channel was assumed to be Gaussian (of the corresponding FWHM width, see Table 1), and the sky maps were convolved with these beams. Finally, we have added isotropic noise maps, assuming a spatial sampling at 1/2.4 of the beam FWHM. That is we assumed that a prior de-stripping procedure had been efficient enough for the residuals to be negligible.

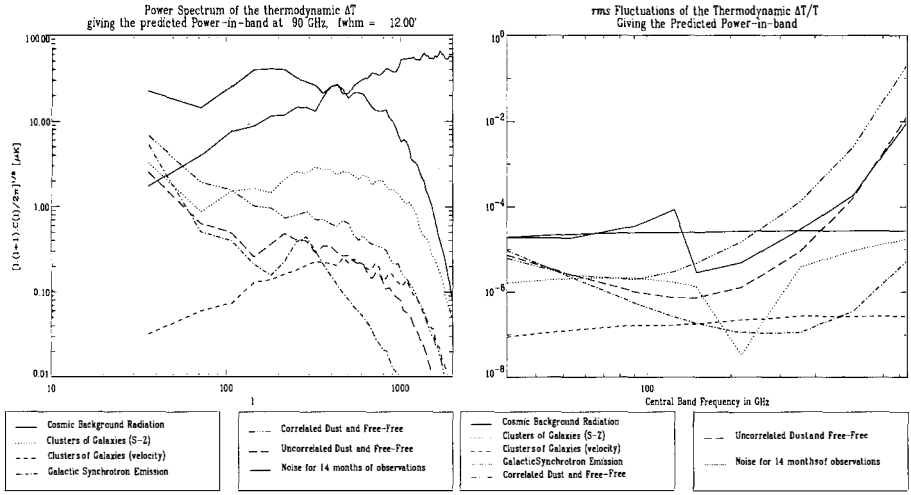

Figure 1: Characteristics of the "observed" maps of the color plate III: a) power spectra at 90 GHz; b) *rms* contribution of the various components as compared to the nominal noise level of *COBRAS/SAMBA* .

The color plate III shows an example of (simulated) "observed" maps in a region with nearly median foregrounds. This can be seen on figure 1.a which shows the power spectra of the various templates included. Their amplitude is similar to those of figure 2 of BGBP at low ℓ, the high-ℓ difference comes from the fact that the the spectra in the color plate III correspond to the signal detected (i.e. after beam convolution) while those of BGBP are "on the sky". The corresponding *rms* contributions in $\delta T/T$ units of the various components (at the proper resolution for the frequency) are shown in figure 1.b.

Having created simulated observations, we now turn to the problem of separating the "observed" data into component maps.

2 Separation of the components

We the apply the Wiener filtering method, as described in BGBP, assuming perfect knowledge of the spectral behavior and the power spectra of the components (from a prior analysis, e.g. a simple linear inversion). All the processes are adequately recovered, even in this region with foregrounds fluctuations amplitudes exceeding the expected one in (the best) half of the sky. The color plate IV show a comparison between the input templates of the simulated maps of the

color plate III, and those recovered after Wiener analysis for the CMB and Sunyaev-Zeldovich effect.In order to show maps with enough strong sources for the Sunyaev-Zeldovich effect on clusters, the input simulation of this process have been multiplied by a factor XXX. In that sense, this map (and the corresponding restored map) is not representative of a 12.5×12.5 degree field on the sky but shows what can be achieved for brightest clusters with a Wiener method.

2.1 Accuracy of the Recovery of the CMB Anisotropies

We computed the mean relative error $\Delta C(\ell)/C(\ell)$ and found an overall value of 1.8% in the range $30 < \ell < 1000$. This was done assuming negligible error in the assumed spectral behaviors of the foregrounds. In addition, we checked that this good figures would not be jeopardized by different input assumptions. Table 2 shows that this is indeed the case. In the worst case, when we made a 10% positive error on the dust emissivity index, the error did not even reach 2.2 %, up by less than 0.4% from the best case. Such a large error on the dust emissivity is quite unlikely though, given the high frequency information which will be available by combining together IRAS and COBRAS/SAMBA data. In addition, relatively large errors on the synchrotron and free-free spectral index have very low impact on the final CMB accuracy.

α_{Sync}	α_{Free}	α_{Dust}	$\Delta C(\ell)/C(\ell)$
0.9	0.15	2.0	1.80 %
0.7	0.15	2.0	1.90 %
1.1	0.15	2.0	1.80 %
0.9	0.10	2.0	1.80 %
0.9	0.20	2.0	1.82 %
0.9	0.15	1.8	1.81 %
0.9	0.15	2.2	2.14 %

Table 2: The last column of this table indicates the mean relative error on the recovered CMB spectra in the range $30 < \ell < 1000$ for different assumed spectral behaviors of the foregrounds. These numbers correspond to analyses of of the simulated observations of the color plate III, i.e. for strong foregrounds. The value α_{Dust} of the third column corresponds to the dust emissivity index. The first line recalls the result obtained without spectral errors, while the other lines demonstrate that the CMB recovery is not very sensitive to reasonable spectral errors.

Because the simulated maps are very small in spatial extent compared to the area to be observed by *COBRAS/SAMBA* , we have analyzed the variation in accuracy as a function of sky coverage. We have done this numerically by generating many realizations (maps) of patches of the sky, and by comparing the input CMB maps to the extracted ones. Figure 2.a compares the average input CMB spectrum over 128 maps with the average recovered spectrum, and displays the corresponding error $[\Delta C(l)/C(l)]^{1/2}$ (on a different scale, at left). This error is the overall "inversion noise" which depends in a complicated fashion on a combination of the detector's noises and of the beam width at all frequencies (the obtained $C(\ell)$ are "on the sky"), as well as the varying amplitudes of the foregrounds with scale and location (see below). In any case, if we assume that this noise spectrum remains flat toward low ℓ, by summing over ℓ from $\ell = 1$ $\ell \sim 1100$ this inversion noise, we find an *rms* $\Delta T/T \sim 1.6\ 10^{-6}$ on a scale $\theta \sim 10'$.

The maps used to obtain figure 2 are the first 128 maps in our series ordered by increasing variance of the *IRAS* maps in that area, *i.e.*the first one is the cleanest region of our simulated

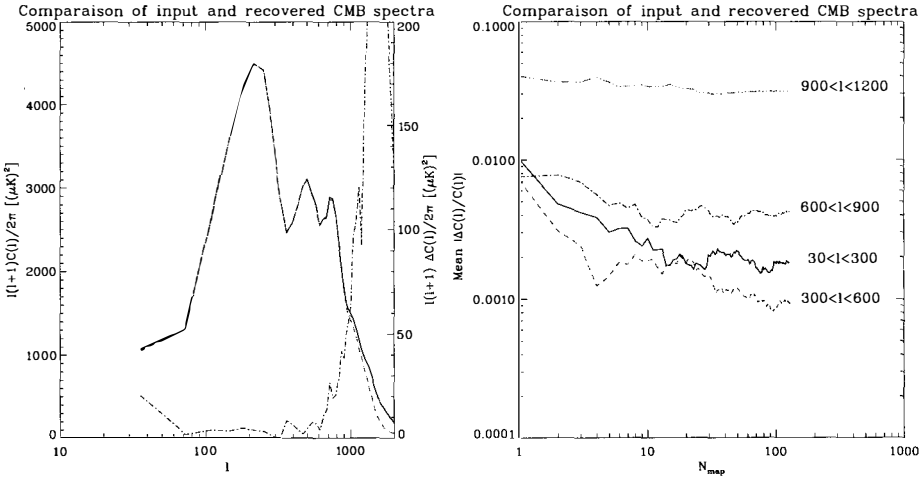

Figure 2: Errors in the recovery of the mean CMB spectrum (an average over 128 maps). a) The input (solid) and recovered (dashes) average CMB spectrum (scale on the left), and the error $[\ell(\ell+1)\Delta C(\ell)/2\pi]^{1/2}$ (scale on the right). The accuracy is $\lesssim 2\mu$K up to $l \sim$ 700b) The mean relative error on the power spectrum recovery, binned within ranges of ℓ, when an increasing number of maps (N_{map}) is taken into account.

sky, and the last one has about a median level. We found that the error on the $C(l)$ of each individual map is nearly constant, i.e. it does not depend strongly on the level of the foregrounds. Figure 2.b shows how the mean error $\Delta C(l)/C(l)$ within different l ranges *decreases* as the average is taken over an increasing number of maps. Note that the combined area of these 128 maps amounts to only $\sim$ 20% of the sky. Thus analyzing the best half of the sky should lead to even more accurate determination of the high ℓ part of the CMB power spectrum.

The analysis outlined above (e.g. Figure 2) demonstrates that it will be possible for *COBRAS/SAMBA* to achieve accuracies on the $C(\ell)$ better than 1 % for $\ell \lesssim$ 1000 in the recovery of the spectrum of CMB anisotropies.

In addition, we have run the Kolmogorov–Smirnoff to check to what extent the input and output *distributions* are compatible with each other. This test involves the overall shape of the distribution of the differences per pixel and not only their variance, but also their skewness, kurtosis, etc.... We have applied this test to 64 pairs of input and recovered distribution and found on average a probability greater than 0.99 that the two distributions are identical (with a pair to pair dispersion smaller than 0.02. In other words, measurements of how non-gaussian the CMB distribution is will be faithful to the underlying physics.

2.2 Sunyaev-Zeldovich Effect of Clusters:

As mentioned previously, because the SZ effect from clusters has a non-gaussian distribution, measuring the accuracy of the recovery in terms of power spectrum is not adequate. For this reason, we present below a separate analysis (Aghanim et al., 1996).

Starting from one recovered map of y (e.g. color plate IV), we have searched for local maxima. For each peak found, we have built a radial y profile, assuming circular symmetry,

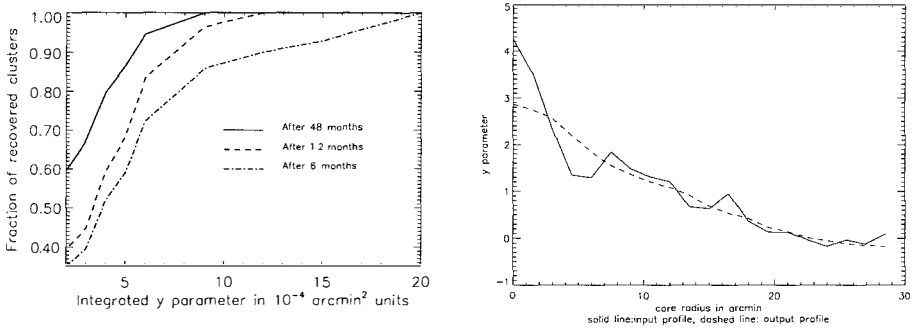

Figure 3: Recovery of the Sunyaev-Zeldovich effect of clusters. a) Fraction of clusters recovered from a typical simulated map (solid line) for three sensitivity levels as a function of the integrated Y parameter. The nominal mission of the *COBRAS/SAMBA* allows for 14 months of observations (left) b) Initial (solid) and recovered (dashes) profiles for a weak cluster with $Y \simeq 2.7\,10^{-4}$ (right).

and computed the integrated Y parameter, $Y = \int y \mathrm{d}\Omega$ (Y is proportional to the typical mass times the mass-weighted temperature within an outer radius where the density profile of the cluster becomes steeper than isothermal and/or the gas temperature starts to drop). Figure 3.a shows the fraction of clusters found in the recovered map as a function of Y. Fig. 3.b for a cluster with $Y \simeq 3\,10^{-4}$ exemplifies the type of accuracy to be expected close to the detection limit. Approximately 70% of the clusters with Y $> 5 \times 10^{-4}$ arcmin^2 are recovered after one year of observations, or 40% if the threshold is set at a very low Y$\sim 2 \times 10^{-4}$ arcmin^2. These percentages increase rather steeply as the noise level is decreased. However, the sensitivity for the nominal duration of the *COBRAS/SAMBA* mission is such that it will be possible to use the observed cluster density variation with limiting flux as a sensitive cosmological test.

3 Conclusion

While this study should and will be refined in many ways, it exemplifies the type of accuracy we may anticipate when bolometer detectors will be flown aboard a satellite.

Acknowledgements. We are grateful to Jean-Loup Puget and the french RUMBA group for their substantial work in the frame of the simulations and for stimulating discussions.

References

Aghanim, N., De Luca, A., Bouchet, F. R., Gispert, R., & Puget , J.-L. 1996, Astr. Astrophys., submitted

Bouchet, F. R., & Gispert, R. 1996, in preparation

Bouchet, F. R., Gispert, R., & Puget, J.-L. 1995a. The COBRAS/SAMBA CMB project. In Clustering in the Universe; Proceedings of the 30^{th} Moriond meeting, Les Arcs, France, astro-ph9507032, S. Maurogordato, C. Balkowski, C. Tao, and J. Trân Thanh Vân, editors, Editions Frontières, pages 537–544

Bouchet, F. R., Gispert, R., & Puget, J.-L. 1995b. The mm/sub-mm Foregrounds and Future CMB Space Missions. In Unveiling the Cosmic Infrared Background; AIP Conference Proceedings 348, Baltimore, Maryland, USA, E. Dwek, editor, pages 255–268

Bouchet, F. R., Gispert, R. Boulanger, F., & Puget, J.-L. 1996. Comparing performances of CMB Experiments. In these proceedings

Efstathiou, G. 1996. ??? In these proceedings

Haslam, C. G. T., Stoffel, H., Salter, C. J., & Wilson, W. E. 1982, Astronomy and Astrophysics Supplement Series, 47, 1

DETERMINATION OF THE OPTIMAL SET OF FREQUENCY BANDS FOR THE COBRAS/SAMBA CMBR SATELLITE MISSION

M.J.D. Linden-Vørnle[1] and H.U. Nørgaard-Nielsen[2]
[1]*Niels Bohr Institute for Astronomy, Physics and Geophysics, Astronomical Observatory, Copenhagen, Denmark*
[2]*Danish Space Research Institute, Copenhagen, Denmark*

Abstract

The COBRAS/SAMBA satellite is the most likely candidate to become the next medium sized mission in ESAs Horizon 2000 programme. It is intended to observe anisotropies in the cosmic microwave background radiation (CMBR) with a sensitivity and angular resolution which is far better than previous CMBR-experiments like the COBE satellite mission.

In order to assess COBRAS/SAMBAs ability to retrieve the temperature fluctuations in the presence of disturbing foreground sources and noise, we have performed model calculations based on a single-pixel approach and a non-linear least squares spectral fitting technique.

We find that even worst-case foreground scenarios do not prohibit a measurement accuracy for $\frac{\Delta T}{T}$ in the order of 10^{-6}.

These model calculations have been applied to different mission configurations in order to determine the optimal combination of frequency bands for the mission. We find that only a large frequency coverage allows a clean separation of CMBR anisotropies and foreground signals.

1 Introduction

As it can be clearly seen in Fig. 1, the signals from various disturbing foreground sources have intensities comparable to that of $\frac{\Delta T}{T} = 10^{-6}$ fluctuations in the CMBR. For any experiment aiming at the detection of such extremely weak temperature fluctuations in the CMBR it is thus imperative to document the ability to overcome the disturbing effect of these foregrounds. The choise of optimal frequency bands enters this discussion as a crucial parameter.

In this work this ability is tested for the CMBR mission COBRAS/SAMBA (see Bersanelli et al. 1996) which is most likely to become ESAs next medium sized satellite mission. We discuss the ability to overcome the difficulties induced by foregrounds for the COBRAS/SAMBA baseline as well as for alternate configurations in order to assess the question of the optimum set of frequency bands.

2 Model calculations

The general outline for the model calculations in this study is inspired by the work of Brandt et al. (1994). The concept is to simulate differential observations of the CMBR with disturbing foreground sources on a single pixel basis, to add realistic instrument noise and then try to recover the original model parameters by using a non-linear least squares spectral fitting technique.

By doing so one should be able to address the interesting issue of how well COBRAS/SAMBA and other mission concepts will be able to extract the anisotropies in the CMBR in the presence of hampering foregrounds.

A number of simplifying assumptions are made both with respect to the instrument, the simulated observations and in the actual fitting process. These assumptions, the models and the fitting are described below.

2.1 The instrument

- Frequency bands are assumed to have a zero bandwidth.
- Noise (sensitivity) assumes a 2 year mission, an angular resolution of 30 arcmin for all bands and only gaussian noise. The noise values for the different frequency bands are adapted from Bersanelli et al. (1996).
- Modelling is done on a single pixel basis only regarding one single measurement in one resolution element (pixel) of the size 30×30 arcmin^2.

The fact that the modelling is done on a single pixel basis implies, that any spatial correlation in the CMBR and in the foregrounds is ignored making the modelling a conservative estimate.

2.2 The simulated observations

The following disturbing foregrounds are included in the simulated observations: Synchrotron radiation, free-free emission and Galactic dust emission.

Both the synchrotron radiation and the free-free emission are modelled as perfect power-laws, whereas the dust is modelled in two different ways: As a perfect power-law and as the sum of the thermal emission from two dust components with different temperatures following

the analysis of Wright et al. (1991) and Reach et al. (1995). The total model used to produce the simulated observations is given by:

$$\begin{aligned}\Delta I_{\nu,model} &= \Delta I_{CMBR} + \Delta I_{Synchrotron} + \Delta I_{Free-free} \\ &\quad + \Delta I_{Dust} + \Delta I_{Noise} \end{aligned} \tag{1}$$

where

$$\begin{aligned}\Delta I_{CMBR} &= B_\nu(T) - B_\nu(\overline{T}) \\ \Delta I_{Synchrotron} &= I_{sync}(\tfrac{\nu}{\nu_0})^{\alpha_{sync}} - \overline{I_{sync}}(\tfrac{\nu}{\nu_0})^{\overline{\alpha_{sync}}} \\ \Delta I_{Free-free} &= I_{free}(\tfrac{\nu}{\nu_0})^{\alpha_{free}} - \overline{I_{free}}(\tfrac{\nu}{\nu_0})^{\overline{\alpha_{free}}} \\ \Delta I_{Dust} &= I_{dust}(\tfrac{\nu}{\nu_0})^{\alpha_{dust}} - \overline{I_{dust}}(\tfrac{\nu}{\nu_0})^{\overline{\alpha_{dust}}} \\ \Delta I_{Noise} &= G \times I_{Noise}.\end{aligned}$$

Here $T = \overline{T} + \Delta T$, where $\overline{T} = 2.726$ K and ΔT is allowed to vary within ± 100 μK. I_{Noise} is the 1σ sensitivity in intensity and G is a gaussian random variable yielding random values with $\langle G \rangle = 0.0$ and $1\sigma = 1.0$.

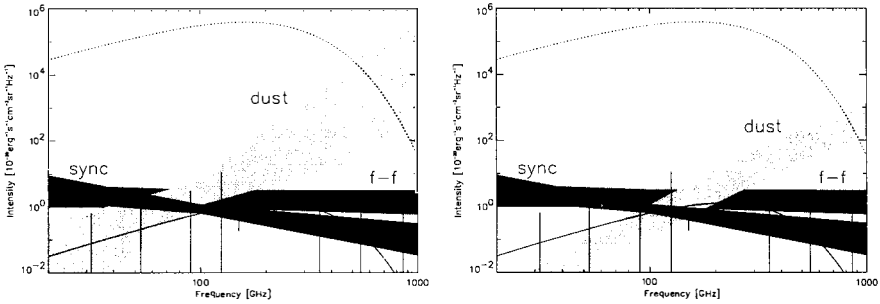

Figure 1: The range of foregrounds given the parameter ranges covered by the model calculations. To the left the parameters for the simulations with the perfect power-law dust model and to the right ranges for the two-temperature dust simulations. The dashed line is the 2.726 K black-body, the solid line corresponds to a $\frac{\Delta T}{T}$ of 10^{-6}, the darkest grayshaded region is the synchrotron radiation (marked 'sync'), the intermediate grayshaded region is the free-free emission (marked 'f-f') and finally the lightest grayshaded region is the dust component (marked 'dust'). The solid vertical lines illustrate the instrumental noise levels.

The parameters and parameter ranges for the foregrounds are given below with $\nu_0 = 100$ GHz and all intensities in units of 10^{-20} erg s^{-1} cm^{-2} Hz^{-1} sr^{-1}.

$\overline{\alpha_{sync}}$	=	-0.93	$\overline{\alpha_{free}}$	=	-0.12	$\overline{\alpha_{dust}}$	=	3.43
$\overline{I_{sync}}$	=	0.89	$\overline{I_{free}}$	=	2.11	$\overline{I_{dust}}$	=	3.72
α_{sync}	=	$\overline{\alpha_{sync}} \pm 0.35$	α_{free}	=	$\overline{\alpha_{free}} \pm 0.10$	α_{dust}	=	$\overline{\alpha_{dust}} \pm 1.60$
I_{sync}	=	$\overline{I_{sync}} \pm 0.27$	I_{free}	=	$\overline{I_{free}} \pm 1.16$	I_{dust}	=	$\overline{I_{dust}} \pm 2.60$

When the two-temperature dust model is used, ΔI_{Dust} is given by:

$$\begin{aligned}\Delta I_{Dust} &= \left(\frac{\nu}{\nu_0}\right)^2 \times \tau[B_\nu(18.0\text{K}) + 7B_\nu(4.0\text{K})] \\ &\quad - \left(\frac{\nu}{\nu_0}\right)^2 \times \overline{\tau}[B_\nu(18.0\text{K}) + 7B_\nu(4.0\text{K})]\end{aligned}$$

In this model the parameter and range is given with $\nu_0 = 900$ GHz by:

$$\begin{array}{|rcl|}\hline \overline{\tau} & = & 0.3 \\ \tau & = & \overline{\tau}^{+0.7}_{-0.2} \\ \hline\end{array}$$

The allowed ranges of foregrounds are sketched in Fig. 1. The ranges of model parameters, originally adapted from Bennett et al. (1992), yield contributions corresponding to situations which can be encountered in most of the sky. The exact fractions are: 99.6% of the sky for the synchrotron radiation, 86% for the free-free emission and 100% for the power-law dust. These estimates are based on extrapolation of the model-parameters to all-sky maps and comparision with Hα data for the free-free emission. The two-temperature dust parameters cover 100% of the areas at high Galactic latitudes where very cold dust is located according to Reach et al. (1995).

For each model a set of parameters (ΔT, I_{sync}, α_{sync}, I_{free}, α_{free} and either I_{dust} and α_{dust} or τ depending on the dust model) is chosen randomly staying within the limits listed above and sketched in Fig. 1. Using expression (1) the observed differential intensity, $\Delta I_{\nu,model}$, is then calculated for each frequency band.

2.3 The parameter recovery process

The recovery of the model parameters is performed by fitting a function similar to expression (1)[1] to the simulated observations. The fitting is performed using the program ADAPTION (Brosa 1994) for non-linear least squares fitting. An important assumption is made by choosing to fit the combined synchrotron radiation and free-free emission using a single power-law. The dust component is fitted with a power-law in the case where it is modelled as such and similar with a two-temperature component in case of this model. For the two-temperature dust model the coldest fitting temperature is chosen 1 K too high compared to the simulated data in order to simulate limited knowledge of this disturbing foreground.

In order to get a statistical sample 100 different models are calculated and the differences between the input parameters (ΔT, ($I_{sync} + I_{free}$), $\frac{(\alpha_{sync}+\alpha_{free})}{2}$, I_{dust} and α_{dust} or τ) and the fitted parameters (ΔT_{fit}, $I_{s/f,fit}$, $\alpha_{s/f,fit}$ and $I_{dust,fit}$ and $\alpha_{dust,fit}$ or τ_{fit}) are registered (e.g. $\Delta T - \Delta T_{fit}$). For these differences means and standard deviations are calculated.

3 Results

Below the results of calculations are given for the standard COBRAS/SAMBA baseline and for a revised COBRAS/SAMBA concept only including frequency bands 31.5, 53, 150, 217, 545 and 857 GHz. Further modelling and a more detailed discussion of other configurations is given in Linden-Vørnle & Nørgaard-Nielsen (1996). Here only the resulting means and standard deviations for $\Delta T - \Delta T_{fit}$ are given in units of μK.

COBRAS/SAMBA Baseline:		
Dust model:	$\langle \Delta T - \Delta T_{fit} \rangle$	$\sigma_{\Delta T - \Delta T_{fit}}$
Perfect power-law	0.06	0.65
Two-temperature dust	0.51	1.08
COBRAS/SAMBA Revised:		
Dust model:	$\langle \Delta T - \Delta T_{fit} \rangle$	$\sigma_{\Delta T - \Delta T_{fit}}$
Perfect power-law	−0.03	0.82
Two-temperature dust	−0.24	1.13

[1]Omitting the noise term (ΔI_{Noise}).

4 Discussion

At a first glance it is clear, that the COBRAS/SAMBA baseline concept will actually be able to extract CMBR anisotropies in the presence of disturbing foreground sources with an accuracy and a sky coverage[2], which will allow the detection of very small temperature fluctuations in the CMBR. It can be seen, that the recovery of the anisotropies in the presence of the two-temperature dust does not cause any severe problems, except for a small systematic error seen in $\langle \Delta T - \Delta T_{fit} \rangle$. This error is most likely due to the fact, that the temperature of the coldest dust component in the fitting function is chosen 1 K higher than the corresponding temperature in the simulated observations.

Including IR/FIR point sources and the Sunyaev-Zel'dovich effect in the calculations might turn things to the worse for the high frequency part of the experiment, and strengthen the need for lower frequency bands in order to achieve a satisfactory anisotropy extraction. This is however an important point for further investigation. Furthermore the low frequency bands are indispensable when attempting to constrain the synchrotron radiation and especially the free-free emission by making the first all-sky maps of these Galactic emission components at these frequencies, at a high level of sensitivity and with fairly high angular resolution. The production of such maps will undoubtively have considerable impact on the actual data processing of COBRAS/SAMBA observations, not to mention the astrophysical information about our Galaxy, which is embedded in such maps.

The revised COBRAS/SAMBA configuration, which is largely the same concept as the baseline but with three bands omitted, perfoms almost as well as the COBRAS/SAMBA baseline. This is most likely due to the fact that the two most sensitive bands placed at the peak of the CMBR are also included in this configuration. The larger gaps between the frequency bands could however prove to be problematic for obtaining an accurate description of the known foreground sources and to insure that no unknown source of confusion lurks at the frequencies not yet gauged with high sensitivity and resolution.

The noteworthy fact established in this work is, that a range of foreground parameters which covers most possible values does not prevent the extraction of CMBR anisotropies with an accuracy of about 1 μK. It can be very useful to search for patches with the lowest possible foreground contamination, but it is not imperative for the success of a CMBR anisotropy experiment like COBRAS/SAMBA, at least not on angular scales of about $30'$. From the above considerations it furthermore seems clear, that a broad continous frequency coverage will allow a better extraction of the CMBR anisotropies with the intended accuracy. The COBRAS/SAMBA baseline seems to very qualified for this task.

Tegmark & Efstathiou (1995) describe a different approach towards the removal of foreground effects from multi-frequency CMBR sky maps. They use an optimal Wiener filtering method to recover CMBR anisotropies in the presence of disturbing foregrounds. This method exploits the fact, that the foregrounds have both spectral behaviours and angular power spectra, which differ substantially from that of the CMBR.

They find, that a pixel-by-pixel subtraction by the COBRAS/SAMBA concept yields an accuracy in the extraction of anisotropies of a few μK at a resolution of $30'$ in good agreement with the results achieved in this study, whereas their optimal filtering technique yields results, which are about 100 times better.

This very persuasive scheme has however a major weakness, by being very dependent on the knowledge of the foregrounds, since the highly non-linear spectral behaviour of the foregrounds is treated as a linear problem. If the frequency dependencies of the foregrounds were perfectly

[2]The assesment of the sky coverage is based on the choise of foreground parameters (see 2.2).

known and independent of the position in the sky, this optimal Wiener filtering method could recover the CMBR anisotropy power spectrum out to multipoles of at least $\ell \sim 1000$ with an accuracy of about one tenth of a percent (Tegmark & Efstathiou 1995).

Since most of the foreground parameters are rather uncertain and since they are definitely not independent of the position in the sky, the above stated accuracy is not directly achievable. In the reduction and analysis of data obtained with a mission like COBRAS/SAMBA, the very detailed all-sky maps also depicting the foregrounds could be utilized by first making a single-pixel spectral analysis as demonstrated above and then use these results in an optimal Wiener filtering technique to improve the accuracy in the determination of the CMBR anisotropies, thus combining the strength of both methods.

5 Conclusions

1. Even in a worst-case foreground scenario the COBRAS/SAMBA baseline is able to achieve an accuracy in the measurement of CMBR fluctuations in the order of $\frac{\Delta T}{T} \sim 10^{-6}$. The dynamic range is wide meaning that even severe limitations in our knowledge of the foreground parameters will not prevent the above stated accuracy.

2. Increased knowledge of the foregrounds and exploitation of the spatial correlations in the foregrounds will provide even better results than those stated above. Using the results from spectral fitting as shown here could be used as input for the optimal Wiener filtering technique outlined by Tegmark & Efstathiou (1995) to yield truly stunning results.

3. With respect to the choise of frequency bands for the COBRAS/SAMBA mission the above considerations indicate that the present baseline seems to be optimal regarding both instrumental limitations, scientific objectives, which are not just cosmological but also include desires to map the sky and especially the Galaxy at hitherto unobserved frequencies and finally the need of 'spectral redundancy' both in case of unexpected phenomena turning up and in case of failure of one or more detectors.

References

Bennett C.L., et al., 1992, ApJ 396, L7
Bersanelli M., et al., 1996, COBRAS/SAMBA. Report on the Phase A Study, ESA
Brandt W.N., et al., 1994, ApJ 424, 1
Brosa U., 1994, ADAPTION Program Manual
Linden-Vørnle M.J.D., Nørgaard-Nielsen H.U., 1996, under preparation
Reach W.T., et al., 1995, ApJ 451, 188
Tegmark M., Efstathiou G., 1995, submitted to MNRAS, preprint astro-ph/9507009
Wright E.L., et al., 1991, ApJ 381, 200

FOREGROUNDS REMOVAL IN PRACTICE: A TEST WITH ARGO DATA

S. Masi[1], E. Aquilini[3], A. Boscaleri[2], P. de Bernardis[1], M. De Petris[1], M. Gervasi[1] L. Martinis[3], F. Scaramuzzi[3]
[1] *Dipartimento di Fisica, Universita' La Sapienza, Roma, Italy*
[2] *IROE-CNR, Firenze, Italy*
[3] *ENEA, Frascati, Italy*

Abstract

The problem of foregrounds removal is of outmost importance for the planned satellite mappers of the CMB. Several groups have developed sophisticated simulations in order to investigate the problem. Here we take a different approach and we use real data from a multiband experiment. We analyze the data of the ARGO experiment in a sky region moderately contaminated by foreground dust emission. We show that taking advantage of the multiband nature of the ARGO experiment it is possible to separate efficiently CMB anisotropy data from cirrus dust emission data.

1 The ARGO experiment

The experiment, a balloon telescope measuring CMB anisotropies with an angular resolution of 53 arcmin FWHM in four spectral bands (2.0, 1.2, 0.8 and 0.5 mm center wavelengths) has been described in [2]. The CMB anisotropy detection in the Hercules region has been described in [3] and [4]. Thermal emission from cirrus dust has been ubiquitously detected, at different levels, in several observed regions [5]. Here we focus on the Aries-Taurus region, where dust emission is evident in the high frequency channel and well correlated to the IRAS-ISSA maps. In this region we have a set of 147 independent data, sparsely sampling a sky region about 45 deg wide in R.A. and 15 deg wide in declination. Two well known sources (IC348 and M45) have been scanned in the sidelobes of the telescope, producing distinctive signals in the higher frequency channels. Since other cirrus signatures are evident in the high frequency channel, we guess that some dust contamination must be present even in the lowest frequency channel

(the 2 mm one). The guess is confirmed by a simple correlation test: the cross correlation coefficient between the 0.5 and the 2 mm channels is $R_{0.5mm,2mm} = 0.5416$ (147 data) and $R_{0.5mm,2mm} = 0.3394$ (142 data, known sources removed). A scatter plot of the two channels is shown in fig.1a (full data set) and fig.1b (known sources removed). The probability to get larger correlation values from random data sets of the same size is $\sim 8 \times 10^{-13}$ and $\sim 2 \times 10^{-5}$ respectively. We conclude that some dust contamination has to be present in the bulk of the 2 mm data. We try to clean the data using a best fit method similar to [1]. This is described in detail in [6].

2 The method

We analyze the data in the framework of a simple model in which the sky signal $S_{i,j}$ (j is the index of the band, i is the index of the observed direction) is the sum of interstellar dust emission (single temperature, optical depth Δn_i) and CMB anisotropies (ΔT_i). We perform the linear best fit

$$S_{i,j} = C_j \Delta n_i + D_j \Delta T_i$$

for the 147 observed directions. In this way for each direction we get the dust and CMB data Δn_i and ΔT_i. We have two additional parameters: the temperature of the dust and the spectral index of dust emissivity. These are found by global minimization of the χ^2. The minimum $\chi^2(\alpha, T_d)$ is 302 with 294 DOF, and is found for $\alpha_0 = 1.55$ and $T_{d0} = 19.5K$. The values of the two parameters are strongly correlated, and equally good fits can be found for $18K < T_d < 22K$ with $1.4 < \alpha < 1.6$. None of the results in the following is significantly changed either if we use different best fit couples T_d, α in place of T_{d0}, α_0, or if we include an additional free-free contribution as large as 30% of the dust contribution at 2 mm. Once α_0 and T_{d0} have been selected, we estimate the dust column density fluctuation Δn_i (dust channel in the following) and the CMB temperature fluctuation ΔT_i (CMB channel in the following). To check if these new channels (dust and CMB) are still correlated we compute the correlation coefficient: we find $R_{dust,CMB} = -0.0489$ (147 data) and $R_{dust,CMB} = -0.0384$ (142 data): the new channels are not significantly correlated. On the other hand most of the fluctuations visible in the orignal 2.0 mm channel are maintained in the CMB channel, strongly suggesting a cosmological origin, while the dust channel resembles a lot of the 0.5 mm channel. In fact, we have $R_{CMB,2.0mm} = 0.8827$, and $R_{dust,0.5mm} = 0.9997$ (142 data).

3 CMB anisotropy

The fluctuations in the CMB channel data are not much larger than the error bars. A statistical analysis is needed to understand if the data contain significant sky signal contributions in addition to detector noise fluctuations. To get a meaningful value for $\Delta T/T$ we must take into account the effects of sine-wave sky chop and beamsize. The result of our sine wave modulation plus square demodulation is that the observed rms ΔT_{sky} is roughly three times lower than the rms observed by a single beam experiment with the same beamsize.

The rms sky temperature fluctuation we measure in the CMB channel can be transated in a band-power estimate of the power spectrum C_ℓ of CMB anisotropies by means of the window function w_ℓ of the ARGO experiment. We define the measured mean square temperature fluctuation as $\Delta T^2_{sky} = \sum_\ell C_\ell w_\ell$. We get $\langle C_{\ell=109} \rangle = (20 \pm 9)\mu K^2$ (the quoted 95% confidence interval includes the 10% calibration error). This has to be compared to $C_{109} = (13 \pm 6)\mu K^2$ for

Fig.1 : Correlation between the original 0.5 and 2 mm channels

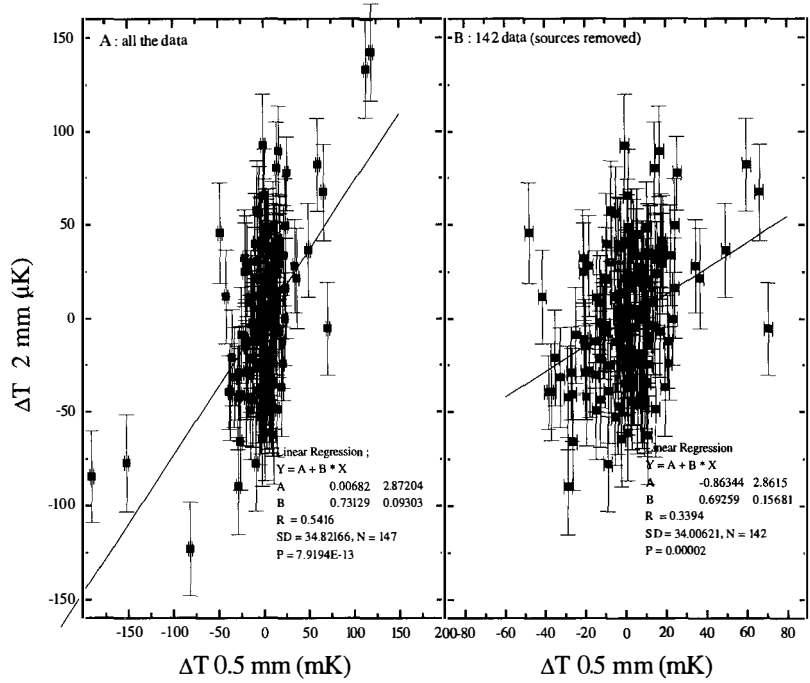

Fig.2 : Likelihood analysis before and after removing the foreground

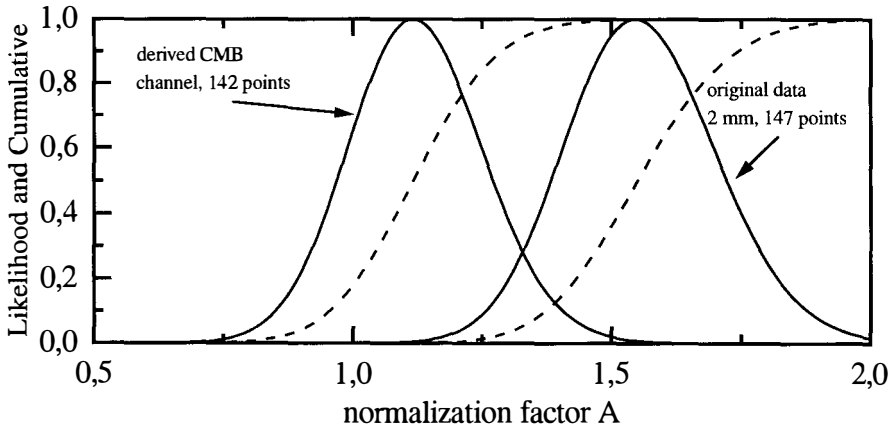

a standard, n=1, $\Omega_b = 0.05$ spectrum of anisotropies normalized to the rms anisotropy detected by COBE-DMR (95% confidence interval).

A detailed analysis, simultaneously taking into account beamsize, modulation, detector noise and sky scan strategy, can be done using a maximum likelihood approach as in [3], [4]. We renormalize the CMB anisotropy power spectrum ($n = 1$, $\Omega_b = 0.05$, no reionization, $h = 0.5$) by a factor A^2, and we search for the maximum likelihood changing A ($A = 1$ if the ARGO data were perfectly consistent with COBE-DMR and with the standard model). The likelihood profiles for the original 2 mm data and for the derived CMB channel are compared in fig.2. The effect of dust removal is evident. We derive 95% confidence limits for the parameter A by means of integration under the Likelihood profile. From the data of the 2 mm channel we get a 95% confidence interval $A = (1.5 \pm 0.3)$, while for the CMB channel we get $A = (1.1 \pm 0.3)$ (again the error bars include the 10% calibration error of these ARGO measurements). We conclude that the ARGO data presented here are in good agreement with the power spectrum of CMB anisotropy fluctuations, with n=1 and normalized to the COBE-DMR detection (29 μK rms with a 10^o FWHM beam).

4 Conclusions

Multiband measurements of faint sky brightness gradients at mm wavelengths are quite effective in distinguishing and separating different components of diffuse emission. In our case we were able to derive a "dust" channel and a "CMB" channel from four original channels centered at 2.0, 1.2, 0.8 and 0.5 mm. This separation procedure allows us to conclude that the 2.0 mm channel is really dominated by CMB anisotropy. The procedure affects significantly the CMB anisotropy estimates, which are decreased by $\sim 30\%$. Future bolometric experiments will be more sensitive than ARGO (few μK per pixel is the forecast sensitivity for experiments like COBRAS/SAMBA, MAP, BOOMERANG etc.) and will operate in darker Galactic regions. So the problem of foreground removal will be faced at a level comparable to the case we have studied here. We think that the above described data and procedures represent a useful working bench for planning deeper searches for CMB anisotropy at mm wavelengths.

References

[1] Cheng E.S., et al. 1994, *Ap.J.* 422 L37

[2] de Bernardis P., et al. 1993, *Astron. Astrophys.* 271 683

[3] de Bernardis P., et al. 1994, *Ap.J.L.* 422 L33

[4] de Bernardis P., et al. 1994, *Ap.J.L.* 433 L1

[5] Masi S., et al. 1995, *Ap.J.* 452 253

[6] Masi S., et al. 1996, *Ap.J.* 463 L47

ANNEX

RESUMES EN FRANÇAIS DES CONTRIBUTIONS

PARTIE I. – LA SCENE DE L'ACTION

L'héritage de COBE

GEORGE F. SMOOT

Les informations fournies par COBE (Cosmic Background Explorer), premier satellite de la NASA dédié à la cosmologie, constituent une étape marquante pour l'étude de l'univers primordial. La plupart de ses résultats proviennent des observations du fond diffus cosmologique (CMB). Le CMB est un pilier du modèle du Big Bang, et contient des informations sur les perturbations primordiales et la géométrie de l'Univers, ainsi que sur les paramètres cosmologiques critiques comme Ω_0, Ω_B, Ω_Λ, et H_0. L'héritage de COBE porte sur la mesure précise du spectre du CMB, la découverte, et la première cartographie, du spectre de puissance des anisotropies du CMB. Il permet ainsi de tester nos théories cosmologiques, et de comprendre plus précisément l'Univers primordial.

L'agenda du théoricien dans les recherches sur le CMB

J. RICHARD BOND

Nous décrivons le terrain couvert par les théoriciens dans cet âge d'or du CMB. Nous sondons la physique de l'univers primordial à la recherche du générateur des fluctuations. Nous explorons les vertus de l'inflation et des défauts. Nous transportons les champs, la matière et le rayonnement dans le régime linéaire (anisotropies primaires) et dans le régime non-linéaire (anisotropies secondaires). Nous validons nos codes linéaires pour fournir des prédictions précises aux expérimentateurs afin qu'ils puissent les démolir. Nous nous battons aux frontières du calcul pour que nos simulations non-linéaires passent du stade simplement illustratif à un stade complètement prédictif. Nous sommes maintenant des phénoménologistes, qui optimisons des techniques statistiques sur les données des expériences actuelles et à venir, pour en extraire des vérités et leurs barres d'erreurs. Nous commençons à nettoyer les émissions d'avant-plan. Nous rejoignons les équipes expérimentales sur le CMB. Nous cherchons à rendre cohérentes les observations du CMB avec celles des structures à grande échelle et des galaxies, ainsi qu'avec d'autres observations cosmologiques. Les courageux utilisent toutes les données sur le sujet. Les autres sélectionnent avec attention les données pour en réduire le nombre. Nous ne sommes jamais "biaisés". Nous déclarons nos théories laides, malades, mortes. Parfois nous les soignons ou les ressuscitons, mais nous les rendons rarement plus belles. Notre but est de comprendre comment toutes les structures cosmiques que nous voyons se sont créées, de quoi l'univers est fait, et d'utiliser cette compréhension pour découvrir les lois de la physique à très haute énergie. Les théoriciens sont humbles, sans *hubris*.

INTRODUCTION À L'ÉTAT ACTUEL DES TECHNOLOGIE DE DÉTECTION

Récepteurs millimétriques à transistor à effet de champ hétérostructure à ultra–bas bruit

MARIAN W. POSPIESZALSKI

Les récents développements en technologie des récepteurs à transistors à effet de champ hétérostructure à ultra-bas bruit pour des fréquences jusqu'à la bande W sont discutés, en particulier:
- les propriétés du bruit et du signal des transistors à effet de champ hétérostructure (HFET), également connus comme transistors à haute mobilité électronique (HEMT) à des températures cryogéniques,
- des exemples de réalisations d'amplificateurs HFET à large bande, bas bruit, refroidis à des températures cryogéniques, et de récepteurs dans la gamme 20 - 100 GHz, et
- une comparaison des récepteurs HFET avec des récepteurs à mélangeur SIS et à amplificateurs HFET IF.

Bolomètres: les détecteurs ultimes pour les mesures du CMB ?

JEAN-MICHEL LAMARRE

Le bruit d'un bolomètre optimisé dépend essentiellement de sa température, de la constante de temps requise, et de la puissance incidente. Il peut être rendu inférieur au bruit de photons du ciel dans la gamme millimétrique, pourvu que: (1) la réponse fréquencielle du bolomètre requise par la stratégie d'observation n'excède pas quelques dizaines de Hertz; (2) la température du bolomètre soit suffisamment basse, à savoir 0.3 K ou même 0.1 K; (3) la bande passante du rayonnement observé soit large, afin de maximiser le flux détecté. Ainsi, la meilleure technologie des bolomètres disponible permet d'effectuer de la photométrie limitée par le bruit de photons du fond micro-ondes cosmologique. Ces conditions sont présentes dans les projets actuels basés sur la détection bolométrique pour la mesure des anisotropies du CMB, et en particulier pour COBRAS/SAMBA. La qualification spatiale pour les systèmes cryogéniques nécessaires a été démontrée pour des températures de 0.3 K, et est en préparation pour 0.1 K. Pour ce type de photométrie à bande large, les bolomètres sont les meilleurs types de détecteurs dans la gamme 200 μm - 5 mm.

PROJETS SPATIAUX

FIRE: Far InfraRed Explorer

ANDREW E. LANGE

La carte définitive du fond micro-ondes cosmologique (CMB) sera réalisée par une expérience en orbite, au point L_2 du système Terre-Soleil, où les effets systématiques sont minimisés. Le concept de FIRE, mission de la classe Midex, est d'obtenir, à partir de L_2, des images du CMB sur tout le ciel, avec une résolution de 8' et une sensibilité de 20 mK par pixel. FIRE a accès à ces hautes performances en utilisant un système avancé de détecteurs bolométriques. Nous décrivons le concept de la mission FIRE, en insistant sur la technologie des détecteurs développée spécifiquement pour cette mission. Beaucoup d'aspects du système de détection développé pour FIRE ont été adoptés par l'instrument à haute fréquence (HFI) de COBRAS / SAMBA.

SAMBA: SAtellite for Measurements of Background Anisotropies, satellite de mesure des anisotropies du fond cosmologique

YVAN BLANC

SAMBA est une proposition de petite mission, dont le but est de cartographier les fluctuations du CMB à des résolutions angulaires allant de 20 minutes d'arc à quelques degrés, avec une sensibilité et une résolution angulaire meilleures que celles de COBE d'un ordre de grandeur. L'objet de cet article n'est pas de décrire les buts scientifiques de SAMBA, ni le détail des détecteurs, mais de décrire brièvement quelques aspects particuliers de la mission SAMBA et de ses développements techniques.

COBRAS/SAMBA: une mission définitive pour les anisotropies du fond micro–ondes.

JAN A. TAUBER

L'objectif principal de la mission COBRAS/SAMBA est d'obtenir des images des anisotropies du fond micro-ondes cosmologique (CMB), avec une sensibilité $\Delta T/T \sim 2 \times 10^{-6} (T \sim 2.726K)$ et une résolution angulaire de 10 minutes d'arc. Pour atteindre ce but, COBRAS / SAMBA observera le ciel entier à neuf fréquences entre 30 et 900 GHz, avec une résolution angulaire entre 30 et 4.5 minutes d'arc. L'information spectrale sera utilisée pour soustraire du signal observé l'émission de notre Galaxie et d'autres sources ponctuelles, et déterminer ainsi l'information primordiale. Les cartes des fluctuations du CMB seront utilisées pour tester les modèles de l'univers primordial, mesurer les paramètres cosmologiques fondamentaux avec une précision de l'ordre de 1 %, et contraindre les modèles de matière sombre. De surcroît, la détection de l'effet Sunyaev-Zeldovich dans des milliers d'amas de galaxies riches permettra l'étude de leurs caractéristiques et de leur évolution. Finalement, les catalogues de sources extragalactiques et les cartes de notre Galaxie permettront une grande diversité d'études astrophysiques.

PARTIE II.– STATUT OBSERVATIONNEL DES ANISOTROPIES DU CMB & IMPLICATIONS

RÉSULTATS RÉCENTS DE L'ANALYSE DES DONNÉES COBE

Le dipôle CMB: la mesure la plus récente, et un peu d'histoire

CHARLES H. LINEWEAVER

La plus grande anisotropie du fond micro-ondes cosmologique (CMB) est le dipôle à $\sim 3mK$, supposé être la conséquence de notre mouvement par rapport au CMB. Durant les dix dernières années, la précision de nos connaissances de ce dipôle a augmenté d'un facteur dix. Nous discutons les mesures de ce dipôle les plus récentes, obtenues avec 4 ans d'observations de DMR (voir Lineweaver et al. 1996). Le meilleur ajustement du dipôle est $3.358 \pm 0.001 \pm 0.023 mK$ dans la direction $(l, b) = (264°.31 \pm 0°.04 \pm 0°.16, +48°.05 \pm 0°.02 \pm 0°.09)$, où les premières incertitudes sont statistiques, et les secondes incluent l'étalonnage et les incertitudes systématiques. La vitesse du Groupe Local qui en est inférée est $v_{LG} = 627 \pm 22$ km/s dans la direction $l = 276° \pm 3°, b = 30° \pm 2°$. Nous comparons ce résultat le plus récent à une compilation de plus de trente ans d'observations du dipôle.

Contraindre la topologie avec le CMB

ANGELICA DE OLIVIERA-COSTA, GEORGE F. SMOOT & ALEXEI A. STAROBINSKY

Nous présentons une nouvelle méthode d'analyse des données pour étudier les "petits univers" rectangulaires T^3, avec une ou deux de ses dimensions significativement plus petites que l'horizon actuel (qui se rapporte aux modèles T^1- et T^2- respectivement). Nous trouvons que les données de 4 ans COBE–DMR donnent une limite inférieure sur la taille de la plus petite cellule pour les modèles T^1- et T^2- à $3000h^{-1}$ Mpc, à 95% de confiance, pour un spectre de puissance invariant d'échelle ($n = 1$).

Normalisation de modèles cosmologiques avec les données de 4 ans COBE-DMR

RADEK STOMPOR

Je résume les résultats d'ajustement précis du vaste ensemble de modèles cosmologiques, aux données de 4 ans de COBE-DMR. Les normalisations obtenues, exprimées en termes de Q_{rms-PS} sont données par des formules d'ajustement approchées (précises jusqu'à 3%), mais utiles.

Analyse spatiale et fréquencielle des données de COBE et spectre des anisotropies du CMB

D.P. Skulachev, A.A. Brukhanov, I.A. Strukov, T.V. Konkia

Nous discutons le problème de l'estimation du spectre des anisotropies du CMB quand la procédure de soustraction de la contribution de la Galaxie a été appliquée. Nous proposons une méthode en deux étapes, le filtrage spatial et fréquenciel, qui conserve l'orthogonalité des harmoniques sphériques. Cette méthode est utilisée pour analyser les 4 ans de données de COBE. Après l'analyse des cartes de différences contenant seulement du bruit, les multipôles l= 13, 14, 23 et 25 ont été exclus des données considérées, parce que leur puissance de bruit dans les cartes de différences étaient statistiquement anormales. Nous montrons que cette procédure n'introduit pas d'erreur systématique significative dans le modèle employé de spectre de bruit. Après que les multipôles anormaux en termes de bruit ont été supprimés, l'analyse a donné l'indice de la loi de puissance pour le spectre de puissance des anisotropies du CMB : $n = 1.87 \pm 0.25$, et une moyenne quadrupolaire de $Q_{rms-PS} = 13.79 \pm 3.0$ à 53 GHz, ainsi que $n = 1.51 \pm 0.24$ et une moyenne quadrupolaire de $Q_{rms-PS} = 15.58 \pm 2.9$ à 90 GHz.

Les expériences actuelles et leur suite planifiée

Mesures précises du spectre de puissance du CMB

P. M. Lubin

Durant les 5 à 10 prochaines années, il sera possible d'effectuer des cartes de précision du CMB à partir d'expériences tant sub-orbitales qu'orbitales. En théorie, les cartes couvrant une portion significative du ciel, à haute sensibilité et à petit lobe ($\ll$ taille de l'horizon au découplage), permettront l'extraction des paramètres cosmologiques fondamentaux. Ces mesures précises du spectre de puissance du CMB promettent de révolutionner notre compréhension de l'univers primordial.

"Expérience froide" au RATAN–600, et anisotropie du CMB

Y. Parijiski, A. Chepurnov, N. Bursov

Nous présentons un résumé et les projets de l'"expérience froide" au RATAN-600, que nous avons commencée il y a plus de 15 ans. On peut trouver tous les détails dans Parijiski et Korolkov (1986), avec les premiers résultats des estimations des anisotropies du CMB, après la réduction des données de 1980-1981.

Observations millimétriques des anisotropies du CMB à Tenerife

R. Rebolo et coll.

Nous présentons les résultats d'une expérience de mesure des anisotropies du CMB, effectuées au sol à l'observatoire du Teide (Tenerife). L'instrument est un système de bolomètres à quatre voies (3.1, 2.1, 1.3 et 1.1 mm) couplé à un télescope composé d'un miroir primaire parabolique de *chopping* hors axe, et d'un secondaire hyperbolique hors axe. La configuration résultante est sensible à des structures angulaires d'environ 1°-2°. Nous utilisons les canaux des deux plus hautes fréquences pour visualiser l'émission atmosphérique, et corriger ainsi les deux plus basses fréquences. Nous avons prouvé qu'une simple méthode d'échelle était très efficace en réduisant de manière significative la contribution atmosphérique dans chaque balayage individuel. Nos balayages finaux à 3.1 et 2.1 mm à $\delta = +40°$ obtenus par l'addition des différentes nuits indépendantes, atteignent des sensibilités d'environ $40\mu K$ par lobe. L'analyse statistique montre la présence de signaux communs. L'analyse de ces deux canaux par maximum de vraisemblance, en utilisant des fonctions d'autocorrélation gaussiennes, donne une détection des fluctuations avec une amplitude intrinsèque $C_0^{1/2} = 76^{+23}_{-21}\mu K$ à $\theta_c = 1.3°$. Nous considérons que ces fluctuations sont dominées par le signal CMB. Elles ne peuvent être expliquées en termes de contamination par le fond galactique ou de bruit résiduel atmosphérique.

Observations de structures du CMB avec les expériences de Tenerife

C. M. Gutiérrez

Les expériences à Tenerife sur le CMB cartographient une région de 5000 deg^2 sur le ciel. Plusieurs radiomètres à *beam-switching* à des fréquences de 10, 15 et 33 GHz ont fonctionné à l'Observatoire du Teide (Tenerife) pendant plus de dix ans. Nous présentons le statut observationnel actuel de ces expériences, avec une attention particulière pour les données à $\delta = +35°$. Dans cette bande, les données à 15 GHz ont un rapport signal sur bruit ~ 2, et mettent clairement en évidence la présence de structures individuelles à haute latitude galactique. En supposant un spectre Harrison-Zel'dovich pour les fluctuations primordiales, une analyse de ces données à 15 GHz par maximum de vraisemblance montre la présence d'un signal avec une amplitude $Q_{RMS-PS} = 20^{+8}_{-6}\mu K$, en accord avec nos précédents résultats à $\delta = +40°$, et avec les résultats de COBE DMR. Nous concluons des résultats à 10 GHz que la possible contamination galactique diffuse est $\leq 25\%$ du signal détecté. Une comparaison préliminaire de nos résultats avec les prédictions de COBE DMR pour les expériences de Tenerife indique clairement la présence de structures individuelles communes. L'invariance en amplitude sur une gamme de fréquence aussi étendue (10 – 90 GHz) indique fortement une origine cosmologique intrinsèque de ces structures.

Résultats récents de mesures d'anisotropie à moyenne échelle / Programme TOPHAT

Robert F. Silverberg

Nous décrivons un programme ballon de mesures complémentaires pour l'étude de l'anisotropie du CMB et des avants-plans astrophysiques, à des échelles angulaires de $\sim 0.°5$. La première série de mesures, à des fréquences comprises entre 5 et 22 cm^{-1} avec le Medium Scale Anisotropy

Measurement (MSAM1) a été achevée en 1995. Nous effectuons ici une comparaison entre les résultats récents provenant de vols pour lesquels nous avons des mesures répétées. Dans la seconde phase du programme, nous observerons à des fréquences plus basses (2 à 5 cm^{-1}) en utilisant un radiomètre multicanal et un lobe plus petit (∼20'). La troisième phase du programme utilisera une expérience légère, TopHat, montée au sommet d'un ballon pour permettre d'obtenir une grande sensibilité et de diminuer les erreurs systématiques. Cette expérience aura l'avantage d'utiliser les possibilités d'un vol ballon de longue durée, désormais ouvertes en Antarctique.

Les expériences MAX et MAXIMA

S. Hanany, et les collaborations MAX et MAXIMA

Nous résumons les performances de l'expérience MAX, pendant ses 5 ans d'opération, et nous présentons une compilation des résultats à ce jour. Nous décrivons MAXIMA, une expérience ballon employant une mosaïque de détecteurs dans le plan focal, ce qui permettra d'effectuer des mesures sensibles du spectre de puissance entre $l \sim 60$ et $l \sim 650$.

Projets de mesures futures des anisotropies du CMB avec la mosaïque MAXIMA

A. Lee et coll.

BOOMERanG: observations en ballon du rayonnement millimétrique extragalactique et géophysique

P. de Bernardis et coll.

L'expérience BOOMERanG (balloon observations of millimetric extragalactic radiations and geophysics) est un projet international de mesure des anisotropies du fond micro-onde cosmologique (CMB) à des résolutions angulaires de 12 à 20 minutes d'arc, avec une sensibilité, une couverture spatiale et spectrale sans précédents. Le télescope sera lancé en Antarctique par le NASA-NSBF avec un ballon stratosphérique à longue durée de vol (7-14 jours), et est actuellement programmé pour un vol de test en 1996, et pour un vol en Antarctique en 1997. L'expérience est conçue pour mesurer le spectre de puissance des anisotropies du CMB jusqu'à $l \sim 700$ et pour produire une image du ciel CMB avec une grande sensibilité et une bonne résolution angulaire. Il sera un précurseur important des missions spatiales à venir, en produisant des données cosmologiques cruciales, et en testant de nouvelles technologies essentielles pour concevoir un satellite effectuant la cartographie du CMB.

Résultats de CAT, et perspectives pour le VSA

Michael E. Jones

Nous avons produit une image du ciel micro-ondes avec une résolution de 30' dans un champ de 2° en utilisant le CAT (Cosmic Anisotropy Telescope). L'analyse des données prises à trois fréquences proches de 15 GHz indique que l'essentiel du signal est dû au CMB, avec une puissance équivalente en bande large $\Delta T/T = 1.9^{+0.5}_{-0.5} \times 10^{-5}$ à des échelles angulaires correspondant aux multipôles $l = 320 - 500$, et $\Delta T/T = 1.8^{+0.7}_{-0.5} \times 10^{-5}$ à $l = 500 - 680$. Nous construisons actuellement un instrument plus perfectionné, le VSA (Very Small Array), qui couvrira les échelles $l = 130 - 1800$ avec une sensibilité par élément de résolution de $\Delta T/T \sim 10^{-6}$.

Résultats du premier vol de BAM

G. S. Tucker, H. P. Gush, M. Halpern, W. Towlson

Un nouvel instrument, BAM (Balloon-borne Anisotropy Measurement), concu pour mesurer les anisotropies du fond micro-ondes cosmologique (CMB) à des échelles angulaires moyennes, a volé pour la première fois en juillet 1995. BAM est unique en ce sens qu'il utilise un spectromètre cryogénique différentiel à transformée de Fourier, couplé à un télescope léger "hors axe". Le grand succès du premier vol de BAM démontre le potentiel de l'instrument pour obtenir des données de grande qualité sur les anisotropies du CMB.

Imagerie et calibration des anisotropies du CMB en dessous de 130 GHz

M. Bersanelli et coll.

Nous soulignons les principales caractéristiques de l'instrument basse fréquence (LFI) de COBRAS/ SAMBA, qui est destiné à effectuer des images des anisotropies du CMB dans la gamme 30 - 130 GHz. L'instrument est composé d'un réseau de cornets striés couplés avec des récepteurs HEMT bas-bruit refroidis passivement, employant une technologie de circuits intégrés micro-onde. Nous décrivons le concept de ces récepteurs et présentons des simulations de l'étalonnage de l'instrument en vol utilisant le signal dipolaire du CMB.

Combinaison des résultats des expériences actuelles pour contraindre les théories

Une première détermination de la position du pic "Doppler"

Stephen Hancock et Graca Rocha

Les théories cosmologiques sur l'origine et l'évolution des structures dans l'univers prédisent à un haut degré la forme du spectre de puissance angulaire des fluctuations du CMB. Nous présentons de nouveaux résultats à partir d'une étude complète des observations du CMB, qui donnent les premières mesures du spectre de puissance jusqu'à des échelles angulaires de $\sim$ 10 minutes d'arc. Pour les grandes échelles, l'analyse des données de COBE et de Tenerife par maximum de vraisemblance fixe la normalisation du spectre de puissance à $Q_{rms-ps} = 21.0 \pm 1.6\mu K$ pour un spectre des fluctuations initial invariant d'échelle. La combinaison des données est compatible avec cette hypothèse, en placant la limite à $n = 1.3 \pm 0.3$ sur la pente du spectre. A des échelles intermédiaires, nous trouvons une évidence claire d'un pic "Doppler" dans le spectre de puissance, localisé autant en échelle angulaire qu'en amplitude. Cette première estimation de la position angulaire du pic sert à donner une nouvelle limite directe à la courbure de l'univers, correspondant à une densité de $\Omega = 0.7^{+1.0}_{-0.4}$. Les modèles d'univers peu dense et ouvert ne sont pas compatibles avec cette limite, à moins qu'il y ait une contribution significative de la constante cosmologique.

Implications théoriques des expériences sur l'anisotropie du CMB

Graca Rocha

Nous considérons les résultats observationnels de plusieurs expériences comme COBE, SP, Saskatoon, PYTHON, ARGO, MAX, MSAM, Tenerife et CAT, et effectuons la comparaison avec les prédictions de plusieurs modèles. Des conclusions sont données sur la viabilité des modèles actuels de formation des structures.

Estimation des paramètres cosmologiques en combinant les expériences CMB sub–degré avec COBE

J.R. Bond et A.H. Jaffe

Nous décrivons une méthode bayesienne des valeurs propres du signal sur bruit pour l'estimation de paramètres cosmologiques, nous montrons comment elle peut être utilisée pour compresser, de manière optimale, les données des anisotropies du CMB à des tailles gérables, et nous l'appliquons aux données DMR sur 4 ans, Pôle Sud et Saskatchewan, de manière individuelle et combinée. Une méthode simple de probabilités *a priori* est utilisée pour inclure les observations des structures à grande échelle. Nous donnons des estimations du paramètre du Hubble, de la densité d'énergie du vide, de la fraction de baryons, et de la distorsion du spectre primordial, à partir de la combinaison des données.

Le CMB et les structures à grande échelle

Joseph Silk

Je discute de la reconstruction du spectre de puissance des fluctuations de matière, sous-jacentes aux fluctuations de température du CMB. Il existe une concordance remarquable, à un petit facteur près, entre la puissance observée sur des échelles comobiles s'étendant entre des dizaines et des milliers de Mpc, et le modèle canonique inflationnaire de "cold dark matter" (matière sombre froide), bien qu'une comparaison détaillée avec la structure à grande échelle requiert une révision sérieuse du modèle le plus simple.

Contraintes sur la réionisation à l'aide des fluctuations du CMB

Paolo de Bernardis et coll.

PARTIE III.– THEORIE DU CMB & IMPACT DES FUTURES EXPERIENCES

THÉORIE DES ANISOTROPIES PRIMAIRES

Connaissons–nous la géométrie de l'univers ?

MARC KAMIONKOWSKI ET NICOLAOS TOUMBAS

Il est assez remarquable que, soixante-dix ans après la découverte de l'expansion de l'univers par Hubble, nous ne sachions toujours pas dans laquelle des trois géométries de Friedmann-Robertson-Walker nous vivons. La majeure partie de la littérature s'est concentrée sur les modèles plats ou ouverts. Ici, nous construisons un modèle viable de l'univers qui a une géométrie fermée, même si la densité de matière non-relativiste est sous-critique. De plus, dans ce modèle, le fond cosmologique pourrait provenir d'une région causalement connectée à l'antipode de l'univers fermé. Ce modèle illustre le fait que la géométrie de l'univers n'est pas contrainte par les données actuelles. Nous discutons des observations qui pourraient déterminer, dans un proche avenir, la géométrie de l'univers de façon certaine.

Anisotropies du fond micro–ondes sans inflation

R. TRIAY

Des spéculations sur le problème de la platitude, et le problème de l'horizon, montrent que les modèles cosmologiques fermés avec une constante cosmologique non nulle, sont des solutions possibles, et ne requièrent pas le scénario de l'inflation. Nous considérons les conséquences sur l'interprétation des anisotropies du fond micro-ondes.

Calculs numériques des anisotropies du CMB

NAOSHI SUGIYAMA

Les nouvelles générations de satellites vont bientôt donner des données de très grande qualité sur les anisotropies du CMB. Il sera possible de déterminer les paramètres cosmologiques, i.e. le paramètre de densité Ω_0, la constante de Hubble H_0, la densité baryonique Ω_B etc., et de comparer ces données avec les prédictions théoriques. Dans cette perspective, nous avons besoin de spectres de puissance très précis obtenus à partir de calculs théoriques. Nous discutons ici de la précision des calculs numériques d'évolution des fluctuations de température, et contrôlons la validité des hypothèses habituelles dans ces calculs numériques.

Une méthode rapide pour calculer les spectres du CMB

U. Seljak et M. Zaldarriaga

Nous avons développé une nouvelle méthode rapide et précise pour calculer les anisotropies linéaires du CMB. La méthode est basée sur l'intégration des sources dans le cône de lumière passé du photon. Le $l^{ème}$ moment multipolaire du spectre du CMB C_l est écrit comme une intégrale temporelle sur le produit de la fonction de Bessel sphérique d'ordre l et d'un terme de source exprimé comme les perturbations des photons, des baryons et de la métrique. Dans cette formulation, les moments du multipôle dépendent seulement d'un petit nombre de variables, qui peuvent évoluer dans le temps sans faire croître la fonction de distribution des photons dans un grande hiérarchie. De plus, le terme source est une fonction lentement variable de la longueur d'onde, et a besoin d'être évalué seulement en un petit nombre de points, tandis que les fonctions de Bessel sphériques, qui oscillent rapidement, ne dépendent pas du modèle. Cette nouvelle approche conduit à une réduction de temps de CPU d'environ deux ordres de grandeur, comparée aux méthodes standards, tout en gardant une précision supérieure à 1% dans le spectre du CMB. La méthode pourrait être spécialement utile pour la détermination précise des paramètres cosmologiques à partir de mesures du CMB, ce qui va devenir possible avec la nouvelle génération de satellites.

Simulations précises du ciel micro–ondes aux petites échelles angulaires

D. Sáez et J. V. Arnau

Nous décrivons des simulations précises du ciel micro-ondes. Nous utilisons le scénario minimal "cold dark matter" (matière sombre froide) pour la formation des structures, et considérons des échelles angulaires plus petites que celles des simulations précédentes. Les spectres obtenus à partir des cartes simulées sont comparés avec les spectres théoriques, de manière appropriée. Des couvertures de ciel et des niveaux de bruit blanc variés sont étudiés. Nous présentons des commentaires préliminaires à propos de l'intérêt de couvertures modérées du ciel micro-ondes (~ 1600 deg^2).

La formation des structures dans les cosmologies inflationnaires

Andrew R. Liddle

Nous présentons brièvement la modélisation des structures à grande échelle, en supposant que les perturbations initiales sont dues à l'inflation. Nous résumons les implications de l'inflation pour les grandes structures; dans le paradigme de la "descente douce" (*slow roll*) appliqué très largement, l'inflation ajoute exactement deux paramètres supplémentaires aux scenarii normaux, que l'on peut identifier avec la pente du spectre initial des perturbations et l'amplitude des ondes gravitationnelles. Nous effectuons quelques commentaires sur la normalisation de COBE. Nous décrivons brièvement une analyse qui utilise à la fois les données du fond diffus cosmologique et celles des grandes structures, pour contraindre les paramètres cosmologiques, et nous considérons le cas des modèles de la matière sombre froide avec une constante cosmologique, comme illustration spécifique.

Univers ouverts à partir de bulles: introduction et mise à jour

J. D. Cohn

Cet article est une introduction aux modèles d'univers ouverts, provenant de bulles, et inclut un résumé des résultats récents sur le spectre de puissance.

Anisotropies dues aux défauts

Cohérence et oscillations Sakharov dans le ciel micro–ondes

A. Albrecht

Je discute de l'origine des "oscillations Sakharov" (ou "pics Doppler secondaires") dans le spectre de puissance angulaire standard du CMB, calculées pour des modèles d'inflation. Je montre que ces oscillations apparaissent parce que les perturbations provenant de l'inflation ont des propriétés qui les rendent "passives". Toutes les perturbations passives connaissent une période de *squeezing* linéaire résultant d'un fort degré de cohérence de phase (classique) des ondes de pression du fluide photons-baryons. Cette cohérence de phase est, par la suite, reproduite dans des structures oscillatoires dans le spectre de puissance angulaire des anisotropies de température observées actuellement. Les perturbations provenant de défauts cosmiques sont des "perturbations actives" qui ont des propriétés très différentes. Les perturbations actives sont hautement non-linéaires, et le degré de cohérence de phase dans un modèle donné traduit la concurrence d'effets complémentaires. Une grande classe de modèles actifs ont des spectres de puissance angulaire *non*–oscillants, et seulement une classe très exotique de modèles a le même degré de cohérence que celui trouvé dans les modèles passifs. Je discute du caractère significatif de la recherche de telles oscillations (qui transcende la vérification de n'importe quel modèle) et jette un regard critique sur l'état de la question de la cohérence dans la littérature.

Anisotropies micro–ondes en provenance de sources aléatoires

Pedro G. Ferreira

Je traite des derniers développements dans la théorie des perturbations du CMB. Je décris des manières de modéliser des alternatives aux théories gaussiennes canoniques à l'intérieur du cadre de travail standard de la théorie des perturbations cosmologiques. Je commente l'utilisation de ces techniques pour lever les incertitudes dans les théories de formation des structures avec défauts topologiques.

Les pics Doppler à partir d'un défaut générique

João Magueijo

Nous examinons lesquelles des caractéristiques des pics Doppler exotiques trouvés pour les textures et les cordes cosmiques, sont des nouveautés génériques propres aux défauts. Nous trouvons que la signature "hors phase" des textures est un accident. Les défauts génériques, quand ils génèrent une structure de pic secondaire similaire à l'inflation, créent un décalage additif. Il n'est pas nécessaire que ce décalage soit "hors phase". Nous montrons également quels facteurs sont responsables de l'absence d'oscillations secondaires trouvée pour les cordes cosmiques. Nous considérons enfin, dans cette analyse générale, les conditions dans lesquelles les défauts topologiques et l'inflation peuvent être confondus, et la seule chance qu'ils le soient est l'inflation avec $\Omega = 1$ et un défaut avec une longueur de cohérence de la taille de l'horizon. Tous les autres modèles d'inflation et de défaut diffèrent toujours distinctement.

Cordes cosmiques et cohérence

M. Hindmarsh, M. Sakellariadou, G. Vincent

Les cordes cosmiques fournissent un paradigme pour la formation des structures radicalement différent de celui de l'inflation, qui prédomine. Elle créent quelques complications techniques supplémentaires: par exemple, le calcul du spectre de puissance des perturbations de la matière et du rayonnement nécessite la connaissance de l'histoire et de l'évolution des défauts sous la forme de fonctions de corrélation à deux temps. Nous décrivons quelques simulations numériques de réseaux de cordes, dans le but de mesurer les corrélations à deux temps pendant leur évolution.

Anisotropies à grande échelle dans le rayonnement du corps noir cosmologique engendrées par des textures globales

Ruth Durrer

Je présente une méthode pour calculer les anisotropies à grande échelle angulaire dans le CMB, en utilisant des perturbations locales et invariantes de jauge. Cette méthode est appliquée au modèle de formation de structures avec des textures globales. On trouve un spectre de fluctuations Harrison–Zel'dovich dans ce scénario comme dans les modèles avec inflation. Je compare ces résultats avec les travaux précédents et je trouve une différence substantielle dans les conditions initiales pour le modèle CDM. Cette différence représente une vraie différence dans les modèles physiques qui sont discutés.

Fluctuations non–gaussiennes à partir de textures

Alejandro Gangui

L'un des outils les plus puissants pour sonder l'existence de défauts cosmologiques dans l'univers primordial, est le fond de rayonnement micro-ondes. Il est bien connu que les calculs avec sources causales sont plus compliqués que leurs contreparties adiabatiques basées sur l'inflation, ce qui a, en partie, ralenti le développement de prédictions fines et détaillées. Bien que leur pouvoir soit nécessairement limité, les modèles analytiques peuvent nous dire les principales caractéristiques du CMB dues aux défauts et indiquer de nouvelles pistes d'analyse. Nous appliquons un modèle analytique pour les textures afin d'étudier les motifs non–gaussiens du CMB, puis de comparer nos prédictions avec la campagne observationnelle de quatre années du satellite COBE.

Pics Doppler: un test pour les défauts topologiques

MAIRI SAKELLARIADOU

Les anisotropies du CMB peuvent nous donner le critère nécessaire pour discriminer entre les deux classes de modèles qui sont proposées pour expliquer l'origine des fluctuations primordiales nécessaires à la formation des grandes structures. Nous étudions la position et l'amplitude du premier pic Doppler dans le spectre de puissance angulaire du CMB, dans un modèle où les perturbations sont générées par des défauts topologiques globaux et de la matière cachée non-relativiste. Nous avons trouvé que les signatures sont différentes du cas où les perturbations sont produites par l'amplification de fluctuations quantiques pendant une période d'inflation.

IMPACT SCIENTIFIQUE DES FUTURES EXPÉRIENCES

Conséquences des mesures de l'anisotropie du CMB pour la cosmologie inflationnaire

GEORGE EFSTATHIOU

La cosmologie inflationnaire peut expliquer beaucoup des caractéristiques essentielles de notre univers, comme l'homogénéité et l'isotropie observées à grande échelle. Cependant, il n'existe actuellement pas de consensus sur la réalité de l'inflation, ni sur ses mécanismes détaillés. Dans cet article, je passe en revue les perspectives pour contraindre les modèles d'inflation à partir des observations des anisotropies du CMB. Les observations du CMB avec une résolution angulaire meilleure que 30' sont essentielles si les paramètres des modèles inflationnaires doivent être séparés des petites variations dues aux autres paramètres cosmologiques. Heureusement, de telles observations sont programmées avec la prochaine génération de satellites dédiés à l'étude du CMB – MAP et COBRAS/SAMBA. Ces satellites permettront la mesure simultanée des paramètres spectraux qui pourront tester les modèles inflationnaires et des paramètres cosmologiques fondamentaux comme la constante de Hubble et la densité baryonique, à des précisions bien au–delà de celles accessibles par des techniques astronomiques conventionnelles. En conséquence, les observations du CMB promettent de révolutionner la cosmologie de la prochaine décennie.

Anisotropies micro–ondes provenant de défauts cosmiques

NEIL TUROK

Une carte à haute résolution du ciel micro-ondes constitue une opportunité unique pour chercher des défauts topologiques macroscopiques prévus par beaucoup de théories de physique des hautes énergies. Cette présentation résume les raisons théoriques pour lesquelles il faut sérieusement prendre en compte l'existence de tels défauts cosmiques, à la fois d'un point de vue de physique fondamentale, et parce qu'ils nous donnent des théories de formation des structures qui sont des alternatives viables aux perturbations quantiques inflationnaires. Je décris également le travail récent sur les signatures des défauts dans le ciel micro-ondes, à savoir le décalage des pics Doppler vers des échelles angulaires plus petites, le problème de l'atténuation de ces pics par décohérence de la source, et le motif de *hot spots* caractéristiques produit par les théories de monopôles et de textures à des échelles inférieures au degré.

Mesurer la courbure de l'univers

Wayne Hu et Martin White

Nous discutons comment la courbure de l'univers peut être mesurée de manière robuste, en employant seulement les caractéristiques les plus manifestes du spectre des anisotropies du CMB. Bien que la position du premier pic ne soit pas robuste, les incertitudes dans le modèle de formation des structures peuvent être éliminées en utilisant l'espacement des pics acoustiques et la localisation de la queue d'amortissement. Cette combinaison permet d'obtenir des tests importants de cohérence, qui peuvent être utilisés pour faire la différence avec des modèles vraiment exotiques.

Tester l'inflation avec les anisotropies à petite échelle du CMB

Martin White et Wayne Hu

Nous discutons de la capacité du profil harmonique des pics dans le spectre de puissance angulaire du CMB pour tester l'inflation. En étudiant les caractéristiques robustes de modèles alternatifs, qui doivent tous être isocourbures par nature, nous caractérisons les signatures propres à l'inflation. L'inflation pourrait donc être validée par la prochaine génération d'expériences.

Sonder la géométrie de l'univers avec les pics de température du CMB

J. L. Sanz et coll.

Nous discutons de quelques discriminateurs pour les modèles de matière sombre froide ("cold dark matter"), basés sur les propriétés statistiques du CMB: nombre de pics, distribution de la courbure gaussienne et de l'excentricité au-delà d'un certain seuil. Pour les anisotropies de température représentées par un champ aléatoire gaussien à 2D, toutes ces quantités peuvent être exprimées comme fonctions de deux paramètes spectraux. Nous considérons des résolutions angulaire de 7.5′ à 30′, correspondant aux valeurs les plus sensibles de l'expérience COBRAS/SAMBA. Nous trouvons que le nombre de pics, et la distribution de la courbure gaussienne sont des discriminateurs valides de la géométrie de l'univers, alors que la distribution de l'excentricité y est insensible.

L'influence des mesures de l'anisotropie et de la polarisation sur la physique des particules

M. V. Sazhin, V. V. Shulga

Dans cet article, nous discutons la contribution des perturbations scalaires et des ondes gravitationnelles aux anisotropies. La séparation de ces deux contributions est un objectif important des futures mesures. Un des moyens possibles pour séparer ces deux contributions est de mesurer la polarisation. Nous discutons l'influence des mesures de l'anisotropie et de la polarisation sur la physique des particules, ainsi que la limite supérieure dans la "descente douce" (*slow roll*) du potentiel de l'inflation.

PARTIE IV.– THEORIE ET OBSERVATIONS DES EMISSIONS D'AVANT–PLAN

Anisotropies secondaires moléculaires

ROBERTO MAOLI

Nous décrivons une nouvelle sorte d'anisotropies secondaires : les raies primordiales qui peuvent être produites par une diffusion élastique résonnante des photons du CMB par un milieu moléculaire à grand redshift. La molécule LiH est la meilleure candidate pour une interaction efficace. Nous calculons les principales caractéristiques du signal émis par un nuage primordial pendant ses différentes phases d'évolution. Les anisotropies secondaires moléculaires sont probablement les seules distorsions du CMB associées à des perturbations dans leur phase d'évolution linéaire, et les plus importantes sont émises par l'effondrement des nuages primordiaux, avant que le milieu cosmologique ne soit réionisé, et que l'effet Sunyaev-Zel'dovich ne devienne prédominant.

Comparaison des données de COBE–DMR et du relevé complet du ciel par ROSAT

RÜDIGER KNEISSL

Les comparaisons statistiques des cartes micro-ondes dans la gamme du GHz, et des cartes X vers 1 keV constituent un sondage intéressant pour contraindre différents phénomènes astrophysiques. Des corrélations possibles à des échelles angulaires diverses, et avec des dépendances en fréquence (énergie) différentes, bien qu'elles ne soient pas attendues avec les sensibilités des expériences actuelles, devraient en principe être dues à l'émission/absorption galactiques, à l'effet Sunyaev-Zel'dovich, à l'effet intégré Sachs-Wolfe dans les modèles cosmologiques avec une constante cosmologique ou à faible densité, ou à des sources radio lumineuses en X, comme les AGNs émettant en radio. Je décris le travail de corrélation croisée entre les données de COBE–DMR et celles du relevé du ciel complet de ROSAT, dans une région choisie du ciel. Cette portion du ciel ($+40° < b$, $70° < l < 250°$) est actuellement la meilleure qui soit disponible pour sonder le fond extragalactique X autour de 1 keV. Nous n'avons pas trouvé de corrélation significative sur des échelles astrophysiques pertinentes, mais il sera possible de placer des contraintes à partir de ces limites.

Diffusions Compton

(Effet Sunyaev–Zel'dovich dans les amas)

L'effet Sunyaev–Zel'dovich à 1 et 2 mm en direction des amas ROSAT

P. Andreani et coll.

Une campagne d'observations a été dédiée à la recherche de l'effet Sunyaev-Zel'dovich (S-Z) en direction des amas X ROSAT dans le domaine spectral millimétrique. Un photomètre à deux canaux (1.2 et 2 mm) a été installé au foyer du SEST, le télescope submillimétrique suédois de 15 mètres de l'ESO au Chili, en septembre 94 et 95, et les observations de S1077, A2744, S295 et RXJ0658-5557 ont été menées. Nous avons effectué des détections à 1 mm vers A2744, et dans les deux canaux vers RXJ0658-5557. Pour la première fois, il existe une évidence pour l'accroissement S-Z, et nous avons détecté sur la même source celui–ci et le décrément. Nous discutons des effets astrophysiques et systématiques qui peuvent être à l'origine de ces signaux.

Observations de l'effet Sunyaev–Zel'dovich avec le télescope Ryle

Richard Saunders

Le télescope Ryle a été utilisé pour obtenir des images à 15 GHz des décréments Sunyaev-Zel'dovich en direction d'une douzaine d'amas choisis pour leur forte luminosité en rayons X. Jusqu'à présent, les données en rayons X ont permis l'estimation de H_0 en direction de deux d'entre eux, donnant, dans les deux cas, des valeurs "basses" qui sont auto-cohérentes, bien qu'il soit essentiel d'en obtenir beaucoup autres pour diminuer les effets de projection des amas. Nous avons également découvert un décrément S-Z en direction de la paire de quasars PC1643+4631 A&B (séparation 198") située à $z = 3.8$. De nombreuses observations supplémentaires en X, optique, et infrarouge, montrent que l'amas responsable doit être situé à $z = 1$, ou bien être anormalement peu lumineux, et qu'un effet de lentille gravitationnelle très marqué est certainement en jeu.

L'effet de la température des électrons sur la pente du spectre S–Z

M. Giard et E. Pointecouteau

L'effet des électrons moyennement relativistes, $\frac{v}{c} > 0.1$, n'est pas correctement pris en compte dans les expressions usuelles de la distorsion spectrale S-Z du CMB à travers un gaz chaud à $T_e > 5$ keV. Nous montrons comment obtenir des spectres exacts, en utilisant une intégration Monte-Carlo des diffusions Compton inverses. L'utilisation du spectre exact est nécessaire pour déterminer correctement le paramètre Compton et la vitesse particulière des amas de galaxies à partir de données millimétriques. Les calculs exacts montrent un excès submillimétrique, qui croît avec la température électronique. Cet excès peut être utilisé pour déterminer la température des électrons à partir de futures mesures sensibles dans le millimétrique et le submillimétrique, indépendamment de toute mesure X.

L'effet Sunyaev–Zel'dovich et la valeur de Ω_0

Domingos Barbosa et coll.

Nous étudions comment l'effet Sunyaev-Zel'dovich (S-Z) des amas de galaxies peut contraindre Ω_0. En utilisant des modèles auto-cohérents d'amas X dans le contexte des modèles de formation hiérarchique des structures, nous montrons que le paramètre Compton y moyen, ainsi que le nombre d'amas observés via l'effet S-Z, dépendent fortement de Ω_0. Ces quantités sont plus grandes dans les modèles cosmologiques ouverts, à cause d'une formation de structures qui commence plus tôt. Nous comparons spécifiquement deux modèles capables de reproduire l'abondance d'amas X observés aujourd'hui, l'un avec $\Omega_0 = 0.2$, et l'autre avec $\Omega_0 = 1$. Pour $\Omega_0 = 0.2$, $< y >$ dépasse la limite mesurée par FIRAS de 1.5×10^{-5}. La distribution en redshift des sources S-Z est aussi très différente entre les deux modèles cosmologiques analysés. Ces résultats montrent donc qu'une amélioration de nos connaissances sur la distorsion spectrale du CMB et la réalisation de relevés en millimétrique sur une grande surface du ciel pour observer des sources S-Z, devraient produire des contraintes intéressantes sur Ω_0 et sur l'évolution de la fraction baryonique des structures virialisées.

Evolution des amas de galaxies

S. Collafrancesco, N. Vittorio, et P. Mazzotta

Dans cet article nous discutons les prédictions théoriques de l'abondance locale des amas de galaxies, et leur évolution. Nous discutons également des contraintes apportées par deux bases de données différentes: la fonction de luminosité X (XRLF) et la fonction de température (TF).

Comptonisation intra–amas du CMB dans les cosmologies CDM

N. Vittorio et coll.

Nous présentons les calculs du paramètre de Comptonisation moyenné sur le ciel, décrivant la diffusion du CMB par le gaz chaud dans les amas de galaxies, pour un choix de cosmologies CDM (matière sombre froide) plates et ouvertes. Les modèles sont globalement normalisés pour coller aux données X, et la gaz intra–amas est supposé avoir évolué d'une manière compatible avec les observations actuelles. Nous discutons également des fluctuations rms de température induites par une population d'amas en évolution. Enfin, nous prédisons le nombre d'amas pour lesquels un flux net (par rapport au CMB) supérieur à une certaine valeur limite peut être détecté. De tels comptages sont prédits spécifiquement pour la mission COBRAS/SAMBA.

Fluctuations de température et réionisation inhomogène

N. Aghanim, J.L. Puget, et R. Gispert

Nous étudions la photoionisation du milieu intergalactique par des quasars à grands décalages spectraux. Les premiers quasars produisent autour d'eux des bulles ionisées. Nous évaluons les effets Sunyaev-Zel'dovich thermique et cinématique associés à ces bulles. Le premier effet est négligeable, mais le second produit des anisotropies secondaires à petites et moyennes échelles avec des amplitudes $\delta_T \simeq 10^{-6}$ à $\delta_T \simeq 10^{-4}$; de plus, cet effet introduit un caractère non-gaussien dans la statistique des fluctuations de températures primordiales.

COBRAS/SAMBA et les mesures de l'effet Sunyaev–Zel'dovich

MARTIN G. HAEHNELT

La mission COBRAS/SAMBA, récemment approuvée, aura un impact majeur sur les mesures de l'effet Sunyaev-Zel'dovich (S-Z). Les fréquences de trois des canaux (150 GHz, 217 GHz, 353 GHz) sont choisies pour optimiser les mesures de l'effet S-Z thermique et cinétique, causé principalement par le gaz chaud dans les amas de galaxies. Les estimations du nombre d'amas détectés sont quelquefois incertaines, à cause de la connaissance incomplète de la fonction de masse du gaz des amas, et de la distribution du gaz chaud à grand rayon. Une interpolation directe des observations X des 200 amas les plus brillants donne une limite inférieure ferme de $\sim$ 3000 amas détectés, dont environ la moitié devraient être résolus. Si la distribution du gaz des amas s'avérait favorable, et/ou l'évolution de l'amas avec le redshift était faible, ce nombre pourrait être plus grand, d'un facteur allant jusqu'à dix. En utilisant une technique optimale de filtrage, une mesure de la vitesse particulière d'ensemble, pour un échantillon d'environ 200 amas résolus, sera possible avec une erreur à 1σ de $100 - 200$ km s^{-1}.

FLUCTUATIONS DUES AUX SOURCES, RÉSOLUES OU NON

Modèles d'évolution de l'émission des galaxies dans la gamme IR lointain – submillimétrique

BRUNO GUIDERDONI ET COLL.

La plupart des modèles d'émission des galaxies en IR lointain et en submillimétrique sont basés sur des extrapolations phénoménologiques des fonctions de luminosité des galaxies IRAS proches à 60 μm. Ils supposent généralement un seul redshift pour la formation des galaxies qui agit comme une coupure dans l'extrapolation. Néanmoins, de telles hypothèses ne sont pas valides dans le paradigme de la croissance hiérarchique des structures, qui stipule que la formation des galaxies est un processus continu. Dans ce cadre, cet article propose une nouvelle modélisation de l'évolution des propriétés des galaxies dans l'IR lointain et dans le submillimétrique, qui inclut les processus physiques suivants: croissance des perturbations linéaires (dominées gravitationnellement par la matière sombre), effondrement non–dissipatif, et virialisation des halos, chauffage par ondes de choc, refroidissement consécutif et effondrement dissipatif du gaz baryonique, formation d'un disque supporté par la rotation, formation d'étoiles et évolution stellaire, rétroaction stellaire sur le MIS, émission stellaire, absorption de la lumière des étoiles par la poussière et réémission en IR lointain et en submillimétrique. Le modèle reproduit assez bien la fonction de luminosité IRAS et les comptages de galaxies lointaines, et donne des prédictions pour le comptage des galaxies faibles et le fond diffus de galaxies non-résolues dans l'IR lointain et le submillimétrique, qui sont comparées avec les limites supérieures actuelles. Cette première étude devrait conduire à des prédictions spécifiques pour les satellites à venir, qui observeront le ciel en submillimétrique avec une sensibilité et une résolution spatiale sans précédents.

Contribution des sources ponctuelles au fond micro–ondes cosmologique

E. Hivon, B. Guiderdoni, F. R. Bouchet

La grande résolution et la grande sensibilité des mesures des anisotropies du CMB, prévues pour les prochaines années, devraient permettre la connaissance des paramètres cosmologiques essentiels, avec une grande précision. Cependant, des contributions d'avant–plan variées, comme la poussière galactique, l'émission free-free et les autres galaxies, peuvent altérer la qualité de ces observations. Dans cet article, nous étudions les anisotropies du CMB dues aux sources ponctuelles, et nous montrons qu'elles peuvent gêner maginalement l'observation des fluctuations primordiales aux plus petites échelles. En revanche, la détection de ces anisotropies par ISOPHOT semble possible.

Fluctuations dues à des sources extragalactiques discrètes: prédictions pour la mission COBRAS/SAMBA

G. De Zotti et coll.

Nous discutons des propriétés des sources extragalactiques dans les bandes de COBRAS / SAMBA, et présentons des prédictions pour les comptages attendus et les contributions des fluctuations dans chaque canal. Nous montrons que les bandes de fréquence centrales seront "propres" : seule une petite fraction des pixels à haute latitude galactique ($> 20°$) sera contaminée par des sources extragalactiques ponctuelles. Les observations multifréquences permettent de toute façon une soustraction efficace des pixels contaminés, qui peuvent être identifiés au moyen d'observations à des fréquences voisines. Les spectres étalons de différentes classes de sources seront également directement déterminés. De plus, l'élimination des signaux contaminants est facilitée par la substantielle différence entre leur spectre de puissance et celui des fluctuations primordiales. D'autre part, la mission COBRAS/SAMBA fournira le premier survey sur l'ensemble du ciel, dans un vaste domaine de fréquences largement inexploré, qui sera unique pour étudier une grande variété de phénomènes astrophysiques très intéressants.

Emissions Galactiques : Poussières, Synchrotron, Bremsstrahlung

Emission galactique à haute latitude dans les cartes du ciel de 4 ans de COBE–DMR

Al Kogut

Nous cherchons l'émission galactique faible à haute latitude par corrélation croisée entre les cartes du ciel COBE–DMR après 4 ans d'intégration, et des étalons spatiaux dominés par l'émission galactique. Nous détectons une corrélation croisée statistiquement significative avec les cartes en IR lointain de DIRBE, dont la dépendance en fréquence indique une superposition d'émissions des poussières et du free-free. L'émission des poussières correspond à une fluctuation de température d'antenne de $\Delta T_{dust} = 2.7 \pm 1.3 \mu K$ à 53 GHz, et peut être utilisée pour placer des limites sur l'émissivité plus élevée à grande longueur d'onde, $\beta_{dust} > 1.1$ à 95% de confiance. Le rayonnement free-free est corrélé spatialement avec la poussière, sur des échelles angulaires plus grandes que le lobe de DMR, avec des fluctuations rms de $\Delta T_{ff} = 7.1 \pm 1.7 \mu K$ à 53 GHz. Nous ne détectons pas de corrélation significative avec le relevé synchrotron à 408 MHz, ni avec un modèle synchrotron ayant un indice spectral variant spatialement, et nous plaçons des limites supérieures sur l'indice spectral de l'émission tracée par chacune des cartes.

Emission d'avant–plan en radio, et séparation des anisotropies micro–ondes et de la contamination d'avant–plan

A. N. Lasenby

Nous considérons les effets de la contamination d'avant–plan due au rayonnement synchrotron, à l'émission free-free et aux sources discrètes, sur les mesures du CMB. Nous effectuons des estimations du niveau des fluctuations galactiques et de leur spectre de puissance, en utilisant les cartes à basse fréquence et des données récentes de Tenerife. Nous discutons de nouvelles méthodes pour effectuer une séparation de la composante galactique et du CMB basée sur la fréquence, et nous montrons qu'un algorithme positif / négatif par maximum d'entropie est particulièrement puissant pour remplir cet objectif.

PARTIE V. – STRATEGIES ET ANALYSE DES DONNEES

Optimisation des concepts expérimentaux

L'observabilité des pics Doppler secondaires

Michael P. Hobson

En proposant une statistique pour la détection des pics secondaires Doppler dans le spectre de puissance du CMB, nous calculons, pour une large gamme de modèles d'expériences sur le CMB, le niveau de signification auquel de tels pics peuvent être détectés. En particulier, nous examinons les caractéristiques requises des projets expérimentaux pour faire la distinction entre des théories cosmologiques rivales, comme les cordes cosmiques et l'inflation, en établissant si les pics secondaires sont présents ou non dans le spectre de puissance du CMB.

Evaluation des stratégies d'observation

L. Knox

Etant donnés un instrument et une stratégie pour mesurer les anisotropies du fond cosmologique, il serait possible de calculer les incertitudes prévues sur le spectre de puissance angulaire, ou sur les paramètres d'un spectre théorique. Je présente ici une méthode semi-analytique pour le faire, qui est applicable à la fois aux observations différentielles et à la cartographie. Comme exemple, j'examine le cas d'un instrument bolométrique porté par un ballon dont le lancement est prévu pour ce printemps (MSAMS2). Je mets en évidence l'avantage d'un secondaire à balayage continu par rapport à un secondaire à balayage par saccade.

Une méthode améliorée pour pixéliser les cartes du CMB

Max Tegmark

Pour estimer le spectre de puissance, il est important que la pixélisation de la carte du ciel CMB soit lisse et régulière à un haut degré. Le "cube de ciel COBE" a été défini dans cette idée. Cet article a pour objectif de perfectionner encore ce schéma élégant, qui utilise un cube comme base de projection : nous utilisons ici un icosaèdre. Bien que le cube soit excellent, nous pouvons obtenir une réduction supplémentaire de 20% du nombre de pixels, tout en maintenant le facteur de remplissage, et sans dégradation de la précision d'intégration. Les pixels sont plus ronds dans ce schéma, puisqu'ils sont hexagonaux plutôt que carrés, et les petites faces dans cette méthode simplifient l'égalisation de la surface. La diminution de la distorsion vient des faces plus petites, et donc plus plates. Pour utiliser cette méthode, on peut charger le code FORTRAN par Internet.

Séparation des fluctuations primaires et secondaires

Comparaison des performances des expériences de mesure du CMB

François R. Bouchet et coll.

Cette article résume les connaissances actuelles sur le comportement spectral et la distribution spatiale des émissions galactiques d'avant-plan: poussière, rayonnement de freinage, et synchrotron. Nous discutons aussi l'émission des galaxies infra-rouge et des radio-sources. Nous nous appuyons sur ces données pour modéliser le ciel micro-onde en incluant toutes les composantes nécessaires. Nous introduisons ensuite un indicateur, inspiré du filtrage de Wiener, qui estime la résolution effective d'une expérience quand l'effet des émissions d'avant-plan est inclus. Nous utilisons enfin notre modèle du ciel et cet indicateur pour déterminer l'aptitude de différentes expériences à séparer les véritables anisotropies du rayonnement cosmique de fond de celles issues des émissions d'avant-plan.

Simulations d'expériences de mesure du CMB

Richard Gispert et François R. Bouchet

Nous présentons dans cette article l'état actuel de développement de simulations détaillées effectuées au cours de l'étude de phase A du projet de satellite COBRAS/SAMBA. Depuis la tenue du congrès, ce projet a été sélectionné par l'ESA comme future mission de taille moyenne de l'Agence. Nous commençons par décrire comment nous avons simulé le ciel micro-onde et le processus d'observation. Nous effectuons ensuite sur ces observations fausses (mais relativement réalistes) une séparation en composantes utilisant le filtrage de Wiener décrit par Bouchet et coll. dans ce même ouvrage, ce qui donne une estimation de la précision atteignable avec de telles données. Elle fait anticiper une révolution au début du siècle prochain.

Détermination de l'ensemble optimum des bandes de fréquence pour la mission satellite COBRAS/SAMBA

M.J.D. Linden-Vornle et H.U. Norgaad-Nielsen

Le satellite COBRAS/SAMBA est le mieux placé pour devenir la prochaine mission de taille moyenne dans le programme Horizon 2000 de l'ESA. Il a été conçu pour observer les anisotropies du fond cosmologique micro-ondes (CMB) avec une sensibilité et une résolution angulaire bien meilleures que les expériences CMB effectuées jusqu'à présent.

Afin d'évaluer la capacité de COBRAS/SAMBA pour récupérer les fluctuations de température en présence de sources perturbantes d'avant–plan et de bruit, nous avons mis au point des calculs de modélisation basés sur une approche "pixel unique" et une technique non–linéaire d'ajustement spectral des moindres carrés. Nous trouvons que les pires scenarii d'avant–plan n'empêchent pas une précision de mesure pour $\Delta T/T$ de l'ordre de 10^{-6}. Ces calculs de modélisation ont été appliqués à différentes configurations de mission afin de déterminer la combinaison optimale de bandes de fréquence pour la mission. Nous trouvons que seule une large couverture en fréquence permet une séparation propre des anisotropies du CMB et des signaux d'avant–plan.

Enlèvement des émissions d'avant–plan en pratique : un test avec les données ARGO

S. Masi et coll.

MICROWAVE BACKGROUND ANISOTROPIES
Participants electronic addresses

Aghanim	Nabila	aghanim@iaslab.ias.fr	Inst. d'Astrophysique Spatiale	France
Albrecht	Andreas	a.albrecht@ic.ac.uk	Imperial College	U.K
Andreani	Paola	andreani@pdmida.pd.astro.it	Universita' di Padova	Italy
Aussel	Hervé	aussel@ariane.saclay.cea.fr	CE - Saclay	France
Banday	Tony	banday@mpa-garching.mpg.de	M.P.I für Astrophysik	Germany
Barbosa	Domingos	barbosa@wirtz.u-strasbg.fr	Obs. Astron. de Strasbourg	France
Bartlett	James G.	bartlett@wirtz.u-strasbg.fr	Obs. Astron. de Strasbourg	France
Bernardeau	Francis	fbernard@amoco.saclay.cea.fr	CE - Saclay	France
Bersanelli	Marco	marco@ifctr.mi.cnr.it	Istituto di Fisica Cosmica	Italy
Bignami	Giovanni F.	gfb@ifctr.mi.cnr.it	Istituto di Fisica Cosmica	Italy
Blanc	Yvan	blanc@tortue.cst.cnes.fr	C.N.E.S.	France
Bond	Dick	bond@cita.utoronto.ca	C.I.T.A	Canada
Bouchet	François R.	bouchet@iap.fr	Inst. d'Astrophysique de Paris	France
Boulanger	François	boulanger@ias.fr	Inst.d'Astrophysique Spatiale	France
Bruni	Marco	bruni@tsmix3.sissa.it	I.C.T.P.	Italy
Cohn	Joanne	jdc@asterix.lbl.gov	Lawrence Berkeley Nat. Lab.	U.S.A
Colafrancesco	Sergio	cola@axtov1.roma2.infn.it	Oss. Astronomico di Roma	Italy
de Bernardis	Paolo	debernardis@roma1.infn.it	Univ. Roma I "La Sapienza"	Italy
de Oliveira-Costa	Angelica	angelica@mpa-garching.mpg.de	M.P.I für Astrophysik	Germany
de Zotti	Gianfranco	dezotti@pdmida.pd.astro.it	Osservatorio Astronomico	Italy
Degrange	Bernard	degrange@frcpn11.in2p3.fr	Ecole Polytechnique&IN2P3	France
Delabrouille	Jacques	jacques@ias.fr	Inst.d'Astrophysique Spatiale	France
Dodelson	Scott	dodelson@hermes.fnal.gov	Fermilab Astrophysics Center	U.S.A
Durrer	Ruth	durrer@karystos.unige.ch	Université de Genève	Switzerland
Efstathiou	George	g.efstathiou@physics.oxford.ac.uk	University of Oxford	U.K
Fernenia	Bruno	bfernenia@ll.iac.es	Instituto de Astrofisica de	Spain
Ferreira	Pedro	pgf@physics.berkeley.edu	University of California	U.S.A
Fontaine	Gérard		IN2P3	France
Gaertner	Siegfried	gaertner@cesr.cnes.fr	C.E.S.R	France
Gangui	Alejandro	gangui@gandalf.sissa.it	Observatoire de Meudon	France
Giard	Martin	giard@cesr.cnes.fr	C.N.R.S	France
Giraud-Heraud	Yannick	giraud-heraud@cdf.in2p3.fr	Collège de France	France
Gispert	Richard	gispert@ias.fr	Inst.d'Astrophysique Spatiale	France
Gorski	Krzysztof	gorski@stars.gsfc.nasa.gov	N.A.S.A	U.S.A
Guiderdoni	Bruno	guider@iap.fr	Inst. d'Astrophysique de Paris	France
Gutierrez	Carlos M.	cgc@iac.es	Inst.Astrofisica de Canarias	Spain
Haehnelt	Martin G.	haehnelt@mpa-garching.mpg.de	M.P.I für Astrophysik	Germany
Hanany	Shaul	hanany@physics.berkeley.edu	Center for Particle	U.S.A
Hancock	Stephen	stephen@mrao.cam.ac.uk	M.R.A.O	U.K
Hindmarsh	Mark	m.b.hindmarsh@sussex.ac.uk	University of Sussex	U.K
Hivon	Eric	hivon@tac.dk	Theoretical Astrophysics	Denmark
Hobson	Michael Paul	mph@mrao.cam.ac.uk	M.R.A.O	U.K
Hu	Wayne	whu@sns.ias.edu	Inst. for Advanced Study	U.S.A
Jaffe	Andrew	jaffe@cita.utoronto.ca	C.I.T.A	Canada
Janssen	Michael A.	michael.a.janssen@jpl.nasa.gov	Jet Propulsion Laboratory	U.S.A
Jewell	Jeff	jewell@oddjob.uchicago.edu	University of Chicago	U.S.A

Jones	Michael	mike@mrao.cam.ac.uk	M.R.A.O	U.K
Jones	Aled Wynne	awj10@mrao.cam.ac.uk	M.R.A.O	U.K
Juszkiewicz	Roman	roman@camk.edu.pl	Copernicus Astronomical	Poland
Kamionkowski	Marc	kamion@phys.columbia.edu	Columbia University	U.S.A
Kneissl	Rüdiger	ruk@mpa-garching.mpg.de	M.P.I für Astrophysik	Germany
Knox	Lloyd	knox@cita.utoronto.ca	C.I.T.A	Canada
Kogut	Alan	kogut@stars.gsfc.nasa.gov	Godard Space Flight Center	U.S.A
Lamarre	Jean-Michel	lamarre@ias.fr	Inst.d'Astrophysique Spatiale	France
Lange	Andrew	ael@astro.caltech.edu	CALTECH	U.S.A
Lasenby	Anthony	anthony@mrao.cam.ac.uk	M.R.A.O	U.K
Lee	Adrian	atl@physics.berkeley.edu	Center for Particle	U.S.A
Liddle	Andrew	A.Liddle@sussex.ac.uk	University of Sussex	U.K
Linden-Voemle	Michael J.D.	mykal@dsri.dk	Danish Space Research	Denmark
Lineweaver	Charles	charley@cdsxb6.u-strasbg.fr	Obs. Astron. de Strasbourg	France
Lubin	Philip	lubin@cfi.ucsb.edu	University of California	U.S.A
Lucchin	Francesco	lucchin@astrpd.pd.astro.it	Universita' di Padova	Italy
Lukash	Vladimir	lukash@dpc.asc.rssi.ru	Astro Space Center	Russia
Magueijo	Joao	jcr@amtp.cam.ac.uk	University of Cambridge	U.K
Maino	Davide	maino@ifctr.mi.cnr.it	I.F.C.T.R	Italy
Mandolesi	Reno	reno@botes1.tesre.bo.cnr.it	Istituto TESRE	Italy
Maoli	Roberto	maoli@mesioa.obspm.fr	Observatoire de Paris	France
Martinez-Gonzalez	Enrique	martinez@astax1.unican.es	Facultad de Ciencias	Spain
Mauron	Nicolas	mauron@merlin.graal.univ-montp2.fr	CNRS - CC 072	France
Meyer	Stephan	meyer@oddjob.uchicago.edu	University of Chicago	U.S.A
Pace	Oscar	opace@estec.esa.nl	European Space Agency	The Netherlands
Parijskij	Yuri N.	par@sao.stavropol.su	Obs. Russian Academy of	Russia
Perdereau	Olivier	perderea@frcpn11.in2p3.fr	Lab. de l'Accélérateur Linéaire	France
Pierpaoli	Elena	pierpa@neumann.sissa.it	SISSA	Italy
Piran	Tsvi	tsvi@shemesh.fiz.huji.ac.il	Hebrew University	Israel
Pointecouteau	Etienne		C.E.S.R	France
Polarski	David	polarski@balzac.univ-tours.fr	Univ. Tours Fac. Sciences	France
Pompilio	Maria-Paola	pompilio@roma1.infn.it	Univ. di Roma I "La	Italy
Pospieszalski	Marian W	mpospies@nrao.edu	N.R.A.O	U.S.A
Puget	Jean-Loup	puget@ias.fr	Inst.d'Astrophysique Spatiale	France
Punch	Michael	punch@polhp1.in2p3.fr	Ecole Polytechnique	France
Rebolo	Rafael	rrl@ll.iac.es	Inst.Astrofisica de Canarias	Spain
Richards	Paul	richards@physics.berkeley.edu	University of California	U.S.A
Rocha	Graca	graca@mrao.cam.ac.uk	M.R.A.O	U.K
Saez	Diego	diego.saez@uv.es	Universidad de Valencia	Spain
Sakellariadou	Mairi	mairi@karystos.unige.ch	Université de Genève	Switzerland
Sanz	Jose Luis	sanzjl@besaya.unican.es	Inst. de Fisica de Canterbria	Spain
Saunders	Richard	rdes@mrao.cam.ac.uk	M.R.A.O	U.K
Sazhin	Mikhail	sazhin@sai.msu.su	Sternberg Astronomical	Russia
Seljak	Uros	useljak@cfa.harvard.edu	Harvard-Smithsonian CfA	U.S.A
Silk	Joe	silk@pac2.berkeley.edu	University of California	U.S.A
Silverberg	Robert	silverberg@stars.gsfc.nasa.gov	Godard Space Flight Center	U.S.A

XVIth Moriond Astrophysics meeting 16-23 mars 1996
MICROWAVE BACKGROUND ANISOTROPIES
Participants electronic addresses

Skulachev	Dmitri P.	dskulach@vmcom.lz.space.ru	Russian Academy of Sciences	Russia
Smoot	George	smoot@cosmos.lbl.gov	University of California	U.S.A
Souradeep Tarun	Ghosh	tarun@cita.utoronto.ca	C.I.T.A	Canada
Starobinsky	Alexei A.	alstar@landau.ac.ru	Russian Academy of Sciences	Russia
Stompor	Radek	r.stompor1@physics.oxford.ac.uk	University of Oxford	U.K
Strukov	Igor A.	istrukov@esoc1.iki.rssi.ru	Russian Academy of Sciences	Russia
Sugiyama	Naoshi	sugiyama@utaphp1.phys.s.u-tokyo.ac.jp	University of Tokyo	Japan
Tauber	Jan	jtauber@astro.estec.esa.nl	European Space Agency	The Netherlands
Taylor	Brian G.	btaylor@astro.estec.esa.nl	Space Science Dept. ESA	The Netherlands
Tegmark	Max	max@mppmu.mpg.de	M.P.I für Astrophysik	Germany
Triay	Roland	triay@cpt.univ-mrs.fr	C.N.R.S	France
Tucker	Gregory S.	gst@physics.ubc.ca	Univ. of British Columbia	Canada
Turok	Neil	neil@puhep1.princeton.edu	D.A.M.T.L	U.K
Vittorio	Nicola	vittorio@roma2.infn.it	Universita' di Roma "Tor	Italy
Volonte	Sergio		E.S.A	France
Vozzi	Beatrice	vozzi@roma1.infn.it	Univ. di Roma I "La	Italy
White	Simon D.M.	swhite@mpa-garching.mpg.de	MPI für Astrophysik	Germany
White	Martin	white@oddjob.uchicago.edu	Enrico Fermi Institute	U.S.A

XVIth Moriond Astrophysics meeting 16-23 mars 1996
MICROWAVE BACKGROUND ANISOTROPIES

Dr. Nabila Aghanim
Inst. d'Astrophysique Spatiale
Université Paris-Sud Bâtiment 121
F - 91405 Orsay
France

Dr. Francis Bernardeau
CE - Saclay
Service de Physique Théorique
F - 91191 Gif-sur-Yvette Cedex
France

Dr. Andreas Albrecht
Imperial College
The Blackett Lab. Prince Consort Rd
SW7 2BZ London
U.K

Dr. Marco Bersanelli
Istituto di Fisica Cosmica
C.N.R via Bassini 15
I - 20133 Milano
Italy

Dr. Paola Andreani
Universita' di Padova
Dipartimento di Astronomia Vic. dell'Osservatorio 5
I - 35122 Padova
Italy

Dr. Giovanni F. Bignami
Istituto di Fisica Cosmica
C.N.R via Bassini 15
I - 20133 Milano
Italy

Dr. Hervé Aussel
CE - Saclay
Service d'Astrophysique L'Orme des Merisiers
F - 91191 Gif-sur-Yvette Cedex
France

Dr. Yvan Blanc
C.N.E.S.
CNES/ED/TU/BPI 2003 18, avenue Edouard Belin
F - 31055 Toulouse Cedex
France

Dr. Tony Banday
M.P.I für Astrophysik
Karl-Schwarzschild-Strasse 1
D - 85740 Garching
Germany

Dr. Dick Bond
C.I.T.A
University of Toronto 60, Saint George Street
ON M5S 1A1 Toronto
Canada

Dr. Domingos Barbosa
Obs. Astron. de Strasbourg
Université Louis Pasteur 11, rue de l'Université
F - 67000 Strasbourg
France

Dr. François R. Bouchet
Inst. d'Astrophysique de Paris
C.N.R.S 98bis, boulevard Arago
F - 75014 Paris
France

Dr. James G. Bartlett
Obs. Astron. de Strasbourg
Université Louis Pasteur 11, rue de l'Université
F - 67000 Strasbourg
France

Dr. François Boulanger
Inst.d'Astrophysique Spatiale
Université Paris-Sud
F - 91405 Orsay Cedex
France

Dr. Marco Bruni
I.C.T.P.
Strada Costiera 11
I - 34014 Trieste
Italy

Dr. Jacques Delabrouille
Inst.d'Astrophysique Spatiale
Université Paris-Sud Bâtiment 121
F - 91405 Orsay Cedex
France

Dr. Joanne Cohn
Lawrence Berkeley Nat. Lab.
MS 50A - 3115
CA 94720 Berkeley
U.S.A

Dr. Scott Dodelson
Fermilab Astrophysics Center
N.A.S.A MS 209 P.O. Box 500
IL 60510 Batavia
U.S.A

Dr. Sergio Colafrancesco
Oss. Astronomico di Roma
Via dell'Osservatorio, 2
I - 00040 Monteporzio
Italy

Dr. Ruth Durrer
Université de Genève
Département de Physique Théorique 24, quai Ernest-Ansermet
CH-1211 Genève
Switzerland

Dr. Paolo de Bernardis
Univ. Roma I "La Sapienza"
Dipartimento di Fisica P. le Aldo Moro 2
I - 00185 Roma
Italy

Dr. George Efstathiou
University of Oxford
Nuclear & Astrophysics Laboratory Keble Road
OX1 3RH Oxford
U.K

Dr. Angelica de Oliveira-Costa
M.P.I für Astrophysik
Karl-Schwarzchild Strasse 1
D - 85740 Garching
Germany

Dr. Bruno Femenia
Instituto de Astrofisica de Canarias
c/ via lactea s/n
E - 38200 La Laguna
Spain

Dr. Gianfranco de Zotti
Osservatorio Astronomico
Vicolo dell' Osservatorio 5
I - 35122 Padova
Italy

Dr. Pedro Ferreira
University of California
CfA Astrophysics 301 LeConte Hall
CA 94720 - 7304 Berkeley
U.S.A

Dr. Bernard Degrange
Ecole Polytechnique&IN2P3
L.P.N.H.E
F - 91128 Palaiseau Cedex
France

Dr. Gérard Fontaine
IN2P3
3, rue Michel Ange
F - 75781 Paris Cedex 16
France

Dr. Siegfried Gaertner
C.E.S.R
9, avenue du Colonel Roche
F - 31029 Toulouse Cedex
France

Dr. Alejandro Gangui
Observatoire de Meudon
D.A.R.C 7, place Janssen
F - 92195 Meudon Cedex
France

Dr. Martin Giard
C.N.R.S
C.E.S.R B.P 4346
F - 31029 Toulouse
France

Dr. Yannick Giraud-Heraud
Collège de France
Lab. de Physique Corpusculaire 11, place Marcelin Berthelot
F- 75231 Paris Cedex
France

Dr. Richard Gispert
Inst.d'Astrophysique Spatiale
Université Paris-Sud Bâtiment 121
F - 91405 Orsay Cedex
France

Dr. Krzysztof Gorski
N.A.S.A
Hughes STX NASA/GSFC Code 685
MD 20771 Greenbelt
U.S.A

Dr. Bruno Guiderdoni
Inst. d'Astrophysique de Paris
C.N.R.S 98bis, boulevard Arago
F-75014 Paris
France

Dr. Carlos M. Gutierrez
Inst.Astrofisica de Canarias
c/ Via Lactea s/n
E - 38200 La Laguna
Spain

Dr. Martin G. Haehnelt
M.P.I für Astrophysik
Karl-Schwarzchild Strasse 1
D - 85740 Garching
Germany

Dr. Shaul Hanany
Center for Particle Astrophysics
UC Berkeley 301 LeConte Hall
CA 94720 Berkeley
U.S.A

Dr. Stephen Hancock
M.R.A.O
Cavendish Laboratory Madingley Road
CB3 0HE Cambridge
U.K

Dr. Mark Hindmarsh
University of Sussex
Dept. of Physics&Astronomy
BN1 9QH Brighton
U.K

Dr. Eric Hivon
Theoretical Astrophysics Center
Juliane Maries Vej 30
D K - 2100 Copenhagen
Denmark

Dr. Michael Paul Hobson
M.R.A.O
Madingley Road
CB3 0HE Cambridge
U.K

Dr. Wayne Hu
Inst. for Advanced Study
School of Natural Sciences
NJ 08540 Princeton
U.S.A

Dr. Andrew Jaffe
C.I.T.A
60, Saint George Street
ON M5S 1A1 Toronto
Canada

Dr. Michael A. Janssen
Jet Propulsion Laboratory
4800 Oak Grove Dr
CA 91109 Pasadena
U.S.A

Dr. Jeff Jewell
University of Chicago
Dept. of Astronomy&Astrophysics 5640 South Ellis Avenue
IL - 60637 Chicago
U.S.A

Dr. Michael Jones
M.R.A.O
Cavendish Laboratory Madingley Road
CB3 0HE Cambridge
U.K

Dr. Aled Wynne Jones
M.R.A.O
Cavendish Laboratory Madingley Road
CB3 0HE Cambridge
U.K

Dr. Roman Juszkiewicz
Copernicus Astronomical Center
Bartycka 18
PL - 00716 Warsaw
Poland

Dr. Marc Kamionkowski
Columbia University
Department of Physics 538 West 120th Street
NY 10027 New York
U.S.A

Dr. Rüdiger Kneissl
M.P.I für Astrophysik
Postfach 1523
D - 85740 Garching
Germany

Dr. Lloyd Knox
C.I.T.A
McLennan Labs 60, Saint George Street
ON M5S 1A7 Toronto
Canada

Dr. Alan Kogut
Godard Space Flight Center
Lab. for Astronomy &Solar Physics Hughes STX
MD 20771 Greenbelt
U.S.A

Dr. Jean-Michel Lamarre
Inst.d'Astrophysique Spatiale
Université Paris-Sud Bâtiment 121
F - 91405 Orsay Cedex
France

Dr. Andrew Lange
CALTECH
59 - 33
CA 91125 Pasadena
U.S.A

Dr. Anthony Lasenby
M.R.A.O
Cavendish Laboratory Madingley Road
CB3 0HE Cambridge
U.K

Dr. Adrian Lee
Center for Particle Astrophysics
University of California 301 LeConte Hall
CA 94720 Berkeley
U.S.A

Dr. Andrew Liddle
University of Sussex
Astronomy Centre
BN1 9QH Brighton
U.K

Dr. Michael J.D. Linden-Voernle
Danish Space Research Institute
Gl. Lundtoftevej 7
DK-2800 Lyngby
Denmark

Dr. Charles Lineweaver
Obs. Astron. de Strasbourg
11, rue de l'Université
F - 67000 Strasbourg
France

Dr. Philip Lubin
University of California
Physics Department
CA - 93106 Santa Barbara
U.S.A

Dr. Francesco Lucchin
Universita' di Padova
Dipartimento di Astronomia Vic. dell' Osservatorio 5
I - 35100 Padova
Italy

Dr. Vladimir Lukash
Astro Space Center
Lebedev Physical Institute Profsoyuznaya 84/32
117810 Moscow
Russia

Dr. Joao Magueijo
University of Cambridge
DAMTP & MRAO Silver Street
CB3 9WE Cambridge
U.K

Dr. Davide Maino
I.F.C.T.R
C.N.R Via E.Bassini 15
I - 20133 Milano
Italy

Dr. Reno Mandolesi
Istituto TESRE
C.N.R via Gobetti 101
I - 40129 Bologna
Italy

Dr. Roberto Maoli
Observatoire de Paris
DEMIRM 61, avenue de l'Observatoire
F - 75014 Paris
France

Dr. Enrique Martinez-Gonzalez
Facultad de Ciencias
Instituto de Fisica de Cantabria Avda. Los Castros s/n
E - 39005 Santander
Spain

Dr. Nicolas Mauron
CNRS - CC 072
Université de Montpellier II Place Eugène Bataillon
F - 34095 Montpellier Cedex 5
France

Dr. Stephan Meyer
University of Chicago
Enrico Fermi Institute
IL 60637 Chicago
U.S.A

Dr. Oscar Pace
European Space Agency
ESA/ESTEC-PF Keplerlann 1
NL - 2200 Noordwijk
The Netherlands

Dr. Yuri N. Parijskij
Obs. Russian Academy of Science
Nignij Arkhyz Special Astrophysical
Karachay-Cherkessia
357147 Karachay-Cherkessia
Russia

Dr. Olivier Perdereau
Lab. de l'Accélérateur Linéaire
Université de Paris - Sud Bâtiment 200
F - 91405 Orsay Cedex
France

Dr. Elena Pierpaoli
SISSA
SISSA-ISAS via Beirut 2-4
I-34013 Trieste
Italy

Dr. Tsvi Piran
Hebrew University
Racah Instute of Physics
IL - 91904 Jerusalem
Israel

Dr. Etienne Pointecouteau
C.E.S.R
9, avenue du Colonel Roche
F - 31029 Toulouse Cedex
France

Dr. David Polarski
Univ. Tours Fac. Sciences
Lab. Modèles Phys. Mathématique Parc de Grandmont
F - 37200 Tours
France

Dr. Maria-Paola Pompilio
Univ. di Roma I "La Sapienza"
Dipartimento di Fisica P. le Aldo Moro 2
I - 00185 Roma
Italy

Dr. Marian W Pospieszalski
N.R.A.O
Central Development Laboratory 2015 Ivy Road
VA 22901 Charlottesville
U.S.A

Dr. Jean-Loup Puget
Inst.d'Astrophysique Spatiale
Université Paris - Sud Bâtiment 121
F - 91405 Orsay
France

Dr. Michael Punch
Ecole Polytechnique
L.P.N.H.E
F - 91128 Palaiseau Cedex
France

Dr. Rafael Rebolo
Inst.Astrofisica de Canarias
c/ Via Lactea s/n
E - 38200 La Laguna
Spain

Dr. Paul Richards
University of California
Department of Physics
CA - 94720 Berkeley
U.S.A

Dr. Graca Rocha
M.R.A.O
Cavendish Laboratory Madingley Road
CB3 0HE Cambridge
U.K

Dr. Diego Saez
Universidad de Valencia
Dept. de Astronomia y Astrofisica C/ Dr. Moliner 50
E - 46100 Burjassot
Spain

Dr. Robert Silverberg
Godard Space Flight Center
Code 685
MD 20771 Greenbelt
U.S.A

Dr. Mairi Sakellariadou
Université de Genève
Département de Physique Théorique 24, quai
Ernest-Ansermet
CH-1211 Genève 4
Switzerland

Dr. Dmitri P. Skulachev
Russian Academy of Sciences
Space Research Institute Profsojuznaja 84/32
117810 Moscow
Russia

Dr. Jose Luis Sanz
Inst. de Fisica de Canterbria
Facultad de Ciencias Av. de los Castros sn
E - 39005 Santander
Spain

Dr. George Smoot
University of California
LBNL & Physics Department
CA 94720 Berkeley
U.S.A

Dr. Richard Saunders
M.R.A.O
Cavendish Laboratory Madingley Road
CB3 0HE Cambridge
U.K

Dr. Ghosh Souradeep Tarun
C.I.T.A
University of Toronto McLennan Labs 60, Saint
George Street
ON M5S 1A7 Toronto
Canada

Dr. Mikhail Sazhin
Sternberg Astronomical Institute
Universitetsky pr. 13
119899 Moscow
Russia

Dr. Alexei A. Starobinsky
Russian Academy of Sciences
Landau Institute for Theoretical Physics Kosygina 2
V - 334 Moscow
Russia

Dr. Uros Seljak
Harvard-Smithsonian CfA
60 Garden Street MS51
MA 02138 Cambridge
U.S.A

Dr. Radek Stompor
University of Oxford
Nuclear & Astrophysics Laboratory Keble Road
OX1 3RH Oxford
U.K

Dr. Joe Silk
University of California
Dept. of Astronomy
CA 94720 Berkeley
U.S.A

Dr. Igor A. Strukov
Russian Academy of Sciences
Space Research Institute ul. Profsoyuznaya 84/32
117810 Moscow
Russia

Dr. Naoshi Sugiyama
University of Tokyo
Department of Physics 7-3-1 Hongo,Bunkyo-ku
113 Tokyo
Japan

Dr. Jan Tauber
European Space Agency
Astrophysics Division Postbus 299
NL-2201AZ Noordwijk
The Netherlands

Dr. Brian G. Taylor
Space Science Dept. ESA
Astrophysics Division ESTEC
NL-2201AZ Noordwijk
The Netherlands

Dr. Max Tegmark
M.P.I für Astrophysik
Karl-Schwarzchild Strasse1
D - 85740 Garching
Germany

Dr. Roland Triay
C.N.R.S
Centre de Physique Théorique Case 907 - Luminy
F - 13288 Marseille Cedex 9
France

Dr. Gregory S. Tucker
Univ. of British Columbia
Physics Department 6224 Agricultural Road
BC Vancouver
Canada

Dr. Neil Turok
D.A.M.T.L
Silver Street
CB3 9WE Cambridge
U.K

Dr. Nicola Vittorio
Universita' di Roma "Tor Vergata"
Dipartimento di Fisica Via della Ricerca Scientifica, 1
I - 00133 Roma
Italy

Dr. Sergio Volonte
E.S.A
8-10, rue Mario-Nikis
F - 75738 Paris Cedex 15
France

Dr. Beatrice Vozzi
Univ. di Roma I "La Sapienza"
Dipartimento di Fisica P. le Aldo Moro 2
I - 00185 Roma
Italy

Dr. Simon D.M. White
MPI für Astrophysik
Karl-Schwarzschild-Str. 1 P.O.Box 1523
D - 85740 Garching
Germany

Dr. Martin White
Enrico Fermi Institute
5640 S. Ellis Avenue
IL 60637 Chicago
U.S.A